

ENGINEERING CHARACTERIZATION OF TIRE DERIVED AGGREGATE FOR
GEOTECHNICAL APPLICATIONS

by

Mauricio Miguel Garcia-Theran

A dissertation submitted to the faculty of
The University of North Carolina at Charlotte
in partial fulfillment of the requirements
for the degree of Doctor of Philosophy in
Infrastructure and Environmental Systems

Charlotte

2015

Approved by:

Dr. Miguel A. Pando

Dr. Tara Cavalline

Dr. Vincent Ogunro

Dr. Brett Tempest

Dr. Sheng-Guo Wang

©2015
Mauricio Miguel Garcia-Theran
ALL RIGHTS RESERVED

ABSTRACT

MAURICIO MIGUEL GARCIA-THERAN. Engineering characterization of tire derived aggregate for geotechnical applications. (Under the direction of Dr. MIGUEL A. PANDO)

According to the Rubber Manufacture Association about 230.7 million scrap tires are generated in the United States every year. Reduction of scrap tire disposal, through recycling and reutilization, has become an important environmental priority. In this regard, several reutilization options of scrap tires have been implemented within the field of civil engineering. This dissertation examines one of these reutilization alternatives involving shredded scrap tires that are processed to produce a granular material often referred to as tire derived aggregates (TDA). The specific civil engineering application that this research investigates is the use of TDA as a potential sustainable backfill for retaining walls. The backfill of retaining walls induces lateral pressures which are a key input in the design process. For conventional mineral soils these lateral pressures are computed using classical theories of lateral earth pressures. The applicability of these theories to TDA materials, which have deformable particles, needs to be confirmed due to the very limited experimental data available on TDA generated lateral pressures. The work plan involved centrifuge laboratory experiments, geotechnical laboratory testing, and finite element analyses designed to help fill this important knowledge gap.

Results from the Centrifuge laboratory experimental program revealed that the at-rest lateral pressures generated by TDA and TDA/sand mixtures (50/50 by volume) were found to be approximately 80% and 35% lower than those induced by a conventional Nevada sand backfill, respectively. This large reduction in lateral pressures by TDA and TDA/sand mixtures has the potential to translate into important cost savings

associated to reduced material amounts of a likely smaller cantilever wall associated to the lower TDA backfill load demand. The centrifuge tests confirmed that classical earth pressure theories for at-rest (Jaky 1944) and active conditions (Rankine theory) considerably overpredict the measured lateral pressures generated by TDA and TDA/sand mixtures.

The geotechnical laboratory experiments indicate that TDA backfills exhibit a high degree of compressibility which may be an important design consideration for retaining walls where surcharge loading acts on the backfill. The triaxial compression tests on TDA indicated that this material is contractive and did not exhibit a marked peak deviatoric stress. Additionally friction angle values are highly dependent on the axial strain level used. Friction angle values varying from 8 to 21 degrees were found for axial strains between 5% and 27%, respectively. For design purposes it is recommended that the TDA shear strength be based on a limiting axial strain value associated to allowable deformations or service limit states. The granulated rubber TDA tested showed a significant apparent cohesion attributed to particles deforming and pressing against each other to develop some interlocking. A 50/50 by volume TDA/sand mixture was found to have improved mechanical properties, shear strength, and a drastically reduced compressibility compared to the 100% TDA.

The finite element analyses (FEA), carried out using three different constitutive models, suggest that FEA is reasonably good approach for predicting geotechnical behavior of TDA materials within certain limitations.

ACKNOWLEDGMENTS

I am especially grateful to my advisor and mentor, Dr. Miguel Pando for his guidance and encouragement during this long journey of graduate studies. His advice and trust in me played an important role in my professional and academic growth not only at the University of North Carolina-Charlotte but also at University of Puerto Rico-Mayaguez, our former institution. I would like to thank my committee members: Dr. Tara Cavalline, Dr. Vincent Ogunro, Dr. Brett Tempest, and Dr. Sheng-Guo Wang for their time and contribution to this work.

Special thanks to Dr. Youngjin Park for offering his advice and expertise with the triaxial testing system when I needed it. I would also like to thank Dr. Tarek Abdoun, Dr. Inthuorn Sasanakul, and the now Drs. Anthony Tessari and Hesham El-Ganainy for their guidance and training during the centrifuge testing at Rensselaer Polytechnic Institute. Interacting with undergrad students was an important component and enriching experience during my Ph.D. studies. Therefore, I would like to thank the faculty members who allowed me to serve as their teaching assistants for several semesters: Dr. Rajaram Janardhanam, Dr. Vincent Ogunro, Dr. Kimberly Warren, and Dr. David Young.

I acknowledge the financial support from the Infrastructure and Environmental Systems program; and the Civil and Environmental Engineering department in forms of teaching assistantships. The tuition awards offered by UNCC graduate school every year through the Graduate Assistant Support Plan (GASP) was also an important support to fund my studies. Thanks to all my family and friends in Colombia and in the United States for their support and understanding during this process.

TABLE OF CONTENTS

LIST OF TABLES	ix
LIST OF FIGURES	xi
LIST OF SYMBOLS AND ABBREVIATIONS	xxv
CHAPTER 1. INTRODUCTION	1
1.1 Introduction	1
1.2 Motivation	3
1.3 Objectives	6
1.4 Organization	7
CHAPTER 2. BACKGROUND AND LITERATURE REVIEW	8
2.1 Introduction	8
2.2 Tire Derived Aggregates (TDA)	8
2.3 Common Civil Engineering Applications of TDA	9
2.4 Engineering Properties of TDA	16
2.4.1 Shear Strength Parameters of TDA	16
2.4.2 Triaxial Compression Stress-Strain Behavior	22
2.4.3 Shear Strength and Stress-Strain Behavior of TDA/Soil Mixtures	24
2.4.4 Short Term 1-D Compressibility of TDA Materials	26
2.4.5 Long Term 1-D Compression Characteristics of TDA Materials	30
2.4.6 Lateral Pressures Generated on Retaining with TDA Backfill Materials	32
2.4.7 Permeability and Leaching Characteristics	40
2.4.8 Spontaneous Combustion or Self Heating	41
2.5 Analytical Studies of TDA Fill Materials	46

	vi
2.6 Literature Review Summary	51
CHAPTER 3. INVESTIGATION OF TDA LATERAL PRESSURES ON RETAINING STRUCTURES BY MEANS OF CENTRIFUGE TESTING	52
3.1 Introduction	52
3.2 Concepts of Centrifuge Modeling	53
3.3 Materials Tested and Methodology	57
3.3.1 Description of the Centrifuge Experimental Program	60
3.3.2 Model Preparation and Instrumentation	62
3.4 Centrifuge Test Results for At-rest Condition	68
3.4.1 Comparison Between TDA and Nevada Sand Lateral Pressure Results	71
3.4.2 Effect of Time in TDA At-rest Lateral Pressures	75
3.4.3 Discussion of at-rest Lateral Pressures for 50/50 (by volume) TDA/sand Mixture	77
3.4.4 Comparison of At-rest Lateral Pressure Results with Classical Earth Pressure Theory	81
3.5 Summary of Lateral Pressure Measurements From Retaining Wall Centrifuge Tests	83
3.5.1 Comparison of Cantilever Retaining Wall Centrifuge Test Results with Rankine Theory	91
3.5.2 Analysis of the Retaining Wall Movement Mechanisms From Centrifuge Test Model	94
CHAPTER 4. TRIAXIAL COMPRESSION STRESS-STRAIN BEHAVIOR OF TDA AND TDA/SAND MIXTURES	103
4.1 Introduction	103
4.2 General Description of the Triaxial Compression Test and Methodology	103
4.2.1 Triaxial Tests Set-up and Sample Preparation Procedure	106

	vii
4.3 Stress-Strain Behavior of TDA Materials From CD Triaxial Tests	113
4.3.1 Shear Strength Parameters for TDA Materials Under Drained Conditions	119
4.3.2 Effect of Particle Size in TDA Stress-Strain Characteristics	125
4.4 Triaxial Compression for TDA/sand Mixtures	134
4.5 Stress-Strain Behavior of TDA Material Under CU Triaxial Compression	145
4.6 Effect of Strain Rate in TDA Stress-Strain Behavior	152
CHAPTER 5. SIMPLE SHEAR BEHAVIOR OF TDA AND TDA/SAND MIXTURES	164
5.1 Introduction	164
5.2 Simple Shear Test Set-up and Methodology	165
5.3 1-D Compression and Creep Results	169
5.4 TDA Simple Shear Stress-Strain Characteristics	181
5.4.1 TDA Particle Size and Shearing Strain Rate Effects on Simple Shear Behavior	187
5.4.2 Estimation of the Friction Angle from the Simple Shear Test Results	192
5.4.3 Comparison Simple Shear vs Triaxial Friction Angles	195
CHAPTER 6. FINITE ELEMENT MODELLING OF TDA TRIAXIAL COMPRESSION STRESS-STRAIN BEHAVIOR	197
6.1 Introduction	197
6.2 Hyperelastic Constitutive Models	197
6.2.1 Selection of a Suitable Strain Energy Density Function for TDA Modeling	201
6.2.2 TDA Triaxial Simulations Using the Hyperelastic Yeoh Model	203
6.3 Soil Hardening Constitutive Model	209
6.3.1 FE Predictions of TDA, TDA-Mixtures and Nevada Sand CD Triaxial Tests Using the SH Model	213

	viii
6.4 Porous Elasticity Constitutive Model	218
6.4.1 Porous Elasticity Model for the Consolidation Phase of CD Triaxial Tests	219
6.4.2 Predicted CD Triaxial Compression Behavior Using Porous Elasticity Model	225
6.4.3 Summary of Porous Elasticity Model Predictions	230
CHAPTER 7. SUMMARY, CONCLUSIONS AND RECOMMENDATIONS FOR FUTURE WORK	231
7.1 Summary	231
7.2 Conclusions	233
7.2.1 Centrifuge Tests Under At-rest Condition	233
7.2.2 Centrifuge Tests Under Active Conditions Using a Model Cantilever Wall	234
7.2.3 Triaxial Compression Tests	235
7.2.4 Simple Shear Tests	238
7.2.5 Finite Element Predictions of CD Triaxial Compression Tests Using Three Different Constitutive Models	239
7.3 Recommendations for Future Work	240
REFERENCES	242
APPENDIX A: INDEX PROPERTIES	250
APPENDIX B: ADDITIONAL INFORMATION ON CENTRIFUGE MODELS	257
APPENDIX C: ADDITIONAL INFORMATION ON TRIAXIAL AND SIMPLE SHEAR TESTS	280

LIST OF TABLES

TABLE 2.1: TDA classification according to ASTM D6270 (ASTM 2012)	9
TABLE 2.2: TDA Civil Engineering Applications (RMA 2013)	11
TABLE 2.3: Summary of key shear strength studies on TDA materials	18
TABLE 2.4: Coefficients of permeability for TDA materials	40
TABLE 2.5: Parameters used for the finite element analyses of the retaining wall (Lee et al. 1999)	46
TABLE 3.1: Centrifuge tests program	53
TABLE 3.2: Centrifuge scaling relations (Whitman and Arulanandan 1985)	56
TABLE 3.3: Summary of index properties of centrifuge test materials	59
TABLE 3.4: Comparison of experimental coefficients of lateral earth pressures (K_o) and Jaky equation	82
TABLE 3.5: Lateral force in retaining structure using centrifuge results and Jaky equation	83
TABLE 3.6: Comparison of experimental coefficients of lateral earth pressures (K) and Rankine theory	92
TABLE 4.1: Test matrix of triaxial testing program for TDA, Nevada sand, and TDA/sand mixtures	105
TABLE 4.2: TDA shear strength parameters (CD triaxial tests)	119
TABLE 4.3: TDA $D_{50}=2.60\text{mm}$ shear strength parameters (CD triaxial tests)	131
TABLE 4.4: Shear strength parameters for TDA/sand mixture (30/70 by weight or 50/50 by volume)	137
TABLE 4.5: Shear strength parameters for TDA/sand mixture (10/90 by weight or 20/80 by volume)	137
TABLE 4.6: Effective TDA shear strength parameters (CU triaxial tests)	150
TABLE 4.7: Effective TDA shear strength parameters based on CU triaxial tests	161
TABLE 5.1: Test matrix for simple shear test program	167
TABLE 5.2: Summary of simple shear strength and G_{50} modulus	186

TABLE 6.1: Summary of parameters determined for Hyperelastic Yeoh model	209
TABLE 6.2: Summary of parameters required for soil hardening model	210
TABLE 6.3: Summary of parameters used for soil hardening model predictions	215
TABLE 6.4: Summary of parameters used for soil porous elasticity model predictions	228
TABLE A.1: Sieve analysis for Nevada sand ($D_{50}=0.15$ mm) ASTM D 422	250
TABLE A.2: Sieve analysis for TDA ($D_{50}=1.2$ mm) ASTM D 422	250
TABLE A.3: Sieve analysis for TDA ($D_{50}=2.6$ mm) ASTM D422	251
TABLE A.4: Specific gravity results for materials tested (ASTM D854)	252
TABLE A.5: Minimum and maximum density tests (ASTM D 4253)	254
TABLE B.1: At-rest lateral pressures at 40 g for backfills tested	266
TABLE B.2: TDA lateral pressure at different times for 40g-level	267
TABLE B.3: Earth pressure lateral pressure retaining wall models at 5 g	275
TABLE B.4: Earth pressure lateral pressure retaining wall models at 15 g	276
TABLE B.5: Earth pressure lateral pressure retaining wall models at 25 g	277
TABLE B.6: Earth pressure lateral pressure retaining wall models at 35 g	278
TABLE B.7: Earth pressure lateral pressure retaining wall models at 50 g	279
TABLE C.1: Triaxial tests initial conditions	284
TABLE C.2: Shear strength parameters determination at 5% axial strain	290
TABLE C.3: Shear strength parameters determination at 10% axial strain	290
TABLE C.4: Shear strength parameters determination for TDA at peak	291

LIST OF FIGURES

FIGURE 1.1: US Scrap tire disposition as percent of total tons generated annually (RMA 2013)	2
FIGURE 1.2: Schematic of 1-D compression of a mineral soil	3
FIGURE 1.3: At-rest earth pressure distribution against a smooth, rigid retaining wall	5
FIGURE 2.1: Equipment commonly used to produce TDA	9
FIGURE 2.2: Embankment construction in US 101 using TDA (Baker et al. 2003)	12
FIGURE 2.3: Subgrade frost insulation applications (EPA 2015)	12
FIGURE 2.4: Retaining walls applications using TDA for scale models and bridge abutments (Humphrey 2008; Tweedie et al. 1998)	13
FIGURE 2.5: Landfill gas collection trenches applications (Patenaude and Wright 2014)	13
FIGURE 2.6: Reconstruction of a embankment failure using TDA (Mills 2008)	15
FIGURE 2.7: Shear stress vs. horizontal displacement for sand, and TDA materials under direct shear condition (Edinclair et al. 2004)	20
FIGURE 2.8: Mohr-Coulomb failure envelope for different TDA sizes (Moo-Young et al. 2003)	20
FIGURE 2.9: Graphical comparison of the shear strength parameters from previous studies	21
FIGURE 2.10: Stress-strain behavior of TDA and Monterey sand from triaxial tests (Zornberg et al. 2004)	23
FIGURE 2.11: Variation of shear stress with normal stress on samples with 4 x 8 cm shred tires (Ghazavi et al. 2005)	25
FIGURE 2.12: Variation of initial friction angle versus shred aspect ratio (Ghazavi et al. 2005)	25
FIGURE 2.13: Friction angles for different TDA-Sand mixtures (Youwai et al. 2003)	26
FIGURE 2.14: Volume changes in TDA (tire chips) under saturated, drained isotropic compression (Wartman et al. 2007)	29
FIGURE 2.15: Vertical strain vs normal stress for TDA specimens (Wartman et al. 2007)	29

	xii
FIGURE 2.16: 1-D compression test results for TDA specimens (Celis and Pando 2008)	30
FIGURE 2.17: Time dependent volumetric strains vs time for Tire chip-sand mixtures at $\sigma_v = 80$ kPa (Wartman et al. 2007)	31
FIGURE 2.18: Time dependent volumetric strains vs time for different TDA contents (Celis and Pando 2008)	31
FIGURE 2.19: Comparison of horizontal stress distributions for three TDA backfill materials under active conditions (Tweedie et al. 1998b).	33
FIGURE 2.20: Comparison of horizontal stress distributions using TDA backfill materials for at-rest conditions (Tweedie et al. 1998a).	33
FIGURE 2.21: Results of TDA Lateral pressures study using retaining wall prototype (Garcia-Theran et al. 2014)	35
FIGURE 2.22: Merrymeeting bridge north abutment as built (Helstrom et al. 2010)	36
FIGURE 2.23: Limestone Run bridge abutment as built (Helstrom et al. 2010)	37
FIGURE 2.24: Measured horizontal pressure versus calculated vertical stress in TDA layers for at-rest conditions (Helstrom et al. 2010)	38
FIGURE 2.25: Measured horizontal pressure versus calculated vertical stress in TDA layers for active conditions (Helstrom et al. 2010)	39
FIGURE 2.26: Spontaneous combustion in SR 100, Ilwaco, Washington (Baker et al. 2003)	42
FIGURE 2.27: Variation of temperature inside an embankment with TDA (Yoon et al. 2006)	44
FIGURE 2.28: TGA derivate weight curves (Moo-Young, 2003)	45
FIGURE 2.29: Variation of earth pressure with depth from Lee et al. (1999)	47
FIGURE 2.30: Comparison between drained triaxial compression tests and numerical simulation (Youwai et al. 2004)	49
FIGURE 2.31: Comparison of global response for experimental and numerical 1-D loading tests (Valdes et al. et al. 2008)	50
FIGURE 3.1: Scaling of physical models (Madabhushi 2004)	55
FIGURE 3.2: Photos of test materials used in centrifuge testing	58

FIGURE 3.3: Grain size distribution for Nevada Sand and Granulated Rubber TDA material	59
FIGURE 3.4: Schematic of centrifuge box set up for model 1 and 2	60
FIGURE 3.5: Schematic of centrifuge box set up for model 3 and 4 (dimensions in cm)	61
FIGURE 3.6: 150 g-ton geotechnical centrifuge @ RPI	62
FIGURE 3.7: Sensors used during centrifuge tests	63
FIGURE 3.8: Preparation and placement of the tactile pressure sensors	64
FIGURE 3.9: Construction of centrifuge models in the lab	65
FIGURE 3.10: At rest lateral pressure test (Model 1)	66
FIGURE 3.11: Retaining wall centrifuge tests (Model 4)	66
FIGURE 3.12: Retaining wall geometry for centrifuge model 3 and 4	68
FIGURE 3.13: At-rest lateral pressures for Nevada sand backfill	70
FIGURE 3.14: At-rest lateral pressures for TDA/sand mixture backfill	70
FIGURE 3.15: TDA and Nevada sand lateral pressures for at-rest condition from 40 g centrifuge tests	72
FIGURE 3.16: Comparison of at-rest TDA lateral pressures from Helstrom et al. (2010), Tweedie et al. (1998a) and centrifuge test results	74
FIGURE 3.17: Comparison of at-rest TDA lateral pressures from Tweedie et al. (1998b) and centrifuge test results	75
FIGURE 3.18: Time variation of at-Rest lateral pressures of the 100% TDA backfill	76
FIGURE 3.19: Effect of time in at-rest lateral pressure for TDA and Nevada sand at 40g	77
FIGURE 3.20: At-rest lateral pressures from centrifuge tests of TDA/sand mixture (50/50 ratio by volume)	78
FIGURE 3.21: Photo showing rich sand zones in the TDA/sand mixture backfill after testing	79
FIGURE 3.22: Illustration of retained spherical particle b in the pore space between 3 spheres a (Adapted from Taylor 1948)	80

FIGURE 3.23: Centrifuge tests results for the three backfills tested at 40 g	81
FIGURE 3.24: Lateral pressure vs depth at different g-levels retaining wall model with Nevada sand backfill	84
FIGURE 3.25: Lateral pressure vs depth at different g-levels for retaining wall model with 50/50 TDA/sand backfill	85
FIGURE 3.26: Comparison of lateral pressures from retaining wall centrifuge test at 25 g	85
FIGURE 3.27: Comparison of lateral pressures from retaining wall centrifuge test at 35 g	86
FIGURE 3.28: Comparison of lateral pressures from retaining wall centrifuge test at 50 g	86
FIGURE 3.29: Retaining wall displacement variation along the depth at different g-levels for Nevada sand backfill	88
FIGURE 3.30: Retaining wall displacement variation along the depth at different g-levels for TDA/sand backfill	89
FIGURE 3.31: Lateral pressure distribution using a curve fitting for Nevada sand backfill	89
FIGURE 3.32: Comparison between retaining wall movement at the top of the wall for Nevada sand and TDA/sand mixture backfills	90
FIGURE 3.33: Retaining wall lateral displacements variation with depth for TDA/sand mixture at different g-levels (prototype dimensions)	90
FIGURE 3.34: Variation of lateral pressure coefficient versus normalized displacement	92
FIGURE 3.35: Lateral displacements from Nevada sand retaining wall centrifuge test	95
FIGURE 3.36: Representation of retaining wall model using beam theory	96
FIGURE 3.37: Rotation + Translation retaining wall movement at 15 g	97
FIGURE 3.38: Rotation + Translation retaining wall movement at 25 g	98
FIGURE 3.39: Rotation + Translation retaining wall movement at 35 g	98
FIGURE 3.40: Rotation + Translation retaining wall movement at 50 g	99

	xv
FIGURE 3.41: Variation of translation in retaining wall with g-level (prototype dimensions)	99
FIGURE 3.42: Variation of translation in retaining wall with wall height (prototype dimensions)	100
FIGURE 3.43: Translation of the retaining wall due to sliding vs total deflections (prototype dimensions)	100
FIGURE 3.44: Variation of earth pressure coefficient with depth (prototype dimensions)	101
FIGURE 3.45: Variation of the factor of safety with height of the wall	102
FIGURE 4.1: TDA with different particle size tested in the triaxial experimental program	106
FIGURE 4.2: Geocomp triaxial system	107
FIGURE 4.3: Mold set up used for specimen preparation	108
FIGURE 4.4: TDA triaxial tests and failure after shearing	110
FIGURE 4.5: Nevada sand triaxial tests and failure after shearing	110
FIGURE 4.6: TDA/sand mixture triaxial test and failure after shearing	111
FIGURE 4.7: CD Triaxial compression tests results for TDA material ($D_{50}=1.20\text{mm}$)	114
FIGURE 4.8: CD drained triaxial compression tests for dense Nevada sand ($D_{50}=0.15\text{mm}$)	115
FIGURE 4.9: Comparison between TDA material and Nevada sand for CD triaxial test at 55.16 kPa confining pressure	118
FIGURE 4.10: Stress paths for TDA material during CD triaxial tests at 25% axial strain	120
FIGURE 4.11: Stress paths for Nevada sand material during CD triaxial tests at peak	120
FIGURE 4.12: Shear strength parameters determination for TDA at 5% axial strain	121
FIGURE 4.13: Shear strength parameters determination for TDA at 15% axial strain	121
FIGURE 4.14: Shear strength parameters determination for TDA at 20% axial strain	122

FIGURE 4.15: Comparison between TDA and Nevada sand friction angles for different strain levels	123
FIGURE 4.16: Blocks of TDA after applying an isotropic confining pressure	125
FIGURE 4.17: Consolidated drained triaxial tests results for TDA material ($D_{50}=2.60\text{mm}$)	126
FIGURE 4.18: Consolidated drained triaxial tests results for TDA materials at 13.79 kPa	127
FIGURE 4.19: Consolidated drained triaxial tests results for TDA materials at 27.58 kPa	128
FIGURE 4.20: Consolidated drained triaxial tests results for TDA materials at 55.16 kPa	128
FIGURE 4.21: Consolidated drained triaxial tests results for TDA materials at 82.74 kPa	129
FIGURE 4.22: Secant modulus (E_{50}) for both TDA particle size	129
FIGURE 4.23: Shear strength parameters determination for TDA ($D_{50}=2.60\text{mm}$) at 15 % axial strain	130
FIGURE 4.24: Stress path for TDA ($D_{50}=2.60\text{mm}$) at peak axial strain	131
FIGURE 4.25: Comparison between TDA $D_{50}=1.20\text{ mm}$ and $D_{50}=2.60\text{mm}$ friction angles for different strain levels	132
FIGURE 4.26: Consolidated drained triaxial tests results for TDA/sand mixture (30/70 by weight)	135
FIGURE 4.27: Consolidated drained triaxial tests results for TDA/sand mixture (10/90 by weight)	136
FIGURE 4.28: Shear strength parameters determination for TDA/sand mixture (30/70 by weight or 50/50 by volume) at peak strain ($\approx 10\%$)	138
FIGURE 4.29: shear strength parameters determination for TDA/sand mixture (10/90 by weight or 20/80 by volume) at peak strain ($\approx 5\%$)	138
FIGURE 4.30: Stress-strain curves for all aggregates tested at $\sigma'_3 = 27.58\text{ kPa}$	140
FIGURE 4.31: Stress-strain curves for all aggregates tested at $\sigma'_3 = 82.74\text{ kPa}$	140
FIGURE 4.32: Variation of the secant modulus with the confining pressure	141
FIGURE 4.33: Variation of the secant modulus with TDA content	141

FIGURE 4.34: Variation of the friction angle with TDA content	143
FIGURE 4.35: Consolidated undrained triaxial tests results for TDA material	147
FIGURE 4.36: Effective shear Strength Parameters determination for TDA at peak from CU triaxial tests	149
FIGURE 4.37: Comparison between effective and total stress paths for TDA CU tests	149
FIGURE 4.38: Comparison between effective and total stress paths for TDA CU tests	151
FIGURE 4.39: Shear strength parameters using peak deviatoric stress and principal stress ratio criteria	151
FIGURE 4.40: CU triaxial compression tests for TDA strain rate = 2.0%/min	153
FIGURE 4.41: Comparison for consolidated undrained test at two different strain rates and 82.74 kPa confining pressure	154
FIGURE 4.42: Comparison for consolidated undrained test at two different strain rates and 55.16 kPa confining pressure	155
FIGURE 4.43: Effect of strain rate in the stress path for CU triaxial tests	156
FIGURE 4.44: Consolidated drained triaxial tests results for TDA strain rate = 2.0%/min	157
FIGURE 4.45: Comparison for consolidated drained test at two different strain rates and 82.74 kPa confining pressure	157
FIGURE 4.46: Secant modulus for consolidated undrained triaxial test	159
FIGURE 4.47: Secant modulus for consolidated drained triaxial test	159
FIGURE 4.48: Comparison between CD and CU triaxial test at 0.2%/axial strain at 27.58 kpa confining pressure	160
FIGURE 4.49: Comparison between CD and CU triaxial test at 0.2%/axial strain at 55.16 kPa confining pressure	160
FIGURE 4.50: Secant modulus for both drained conditions at 2.0%/min	162
FIGURE 4.51: Secant modulus for both drained conditions at 0.2%/min	163
FIGURE 5.1: Advanced simple shear machine used in this research	165
FIGURE 5.2: Simple shear sample membrane and stack of rings	167

FIGURE 5.3: Simple shear sample preparation	168
FIGURE 5.4: Simple shear sample installation in main machine	168
FIGURE 5.5: Simple shear specimen during shearing phase	168
FIGURE 5.6: 1-D vertical strain versus time for dense fine TDA	170
FIGURE 5.7: Comparison of strains from 1-D compression at 40 kPa normal stress	172
FIGURE 5.8: Comparison of strains from 1-D compression at 120 kPa normal stress	172
FIGURE 5.9: TDA vertical deformation for all materials at the end of the normal stress application	173
FIGURE 5.10: Analysis of deformations after vertical stress (20 kPa) is fully applied	174
FIGURE 5.11: Analysis of deformations after vertical stress (80 kPa) is fully applied	175
FIGURE 5.12: Creep compression index at different vertical stresses	177
FIGURE 5.13: Comparison of 1-D compression for two TDA sizes at 40 kPa normal stress	179
FIGURE 5.14: Comparison of 1-D compression for two TDA sizes at 120 kPa normal stress	179
FIGURE 5.15: TDA vertical deformation for both TDA at the end of the normal stress application	180
FIGURE 5.16: Creep vertical deformations for both TDA particle size	180
FIGURE 5.17: Simple shear stress-strain curves for fine TDA	181
FIGURE 5.18: Simple shear stress-strain curves for Nevada sand	182
FIGURE 5.19: Simple shear stress-strain curves for TDA/sand mixture	182
FIGURE 5.20: Stress-strain curves for TDA for the different specimens at 20 kPa	183
FIGURE 5.21: Stress-strain curves for TDA for the different specimens at 40 kPa	183
FIGURE 5.22: Stress-strain curves for the different specimens at 120 kPa	184
FIGURE 5.23: Determination of secant shear modulus for all specimens	185

FIGURE 5.24: Variation of secant shear modulus with the vertical stress	186
FIGURE 5.25: Stress-strain curves for coarser TDA ($D_{50} = 2.60$ mm) under simple shear	187
FIGURE 5.26: Stress-strain curves for different TDA particle size at $\sigma'_v = 20$ kPa	188
FIGURE 5.27: Stress-strain curves for different TDA particle size at $\sigma'_v = 80$ kPa	188
FIGURE 5.28: Secant shear modulus (G_{50}) for both TDA particle sizes	189
FIGURE 5.29: Simple shear stress-strain curves for fine TDA at $\dot{\gamma} = 2.0\%/min$	190
FIGURE 5.30: Simple shear stress-strain curves at different strain rates at $\sigma'_v = 120$ kPa	190
FIGURE 5.31: Simple shear stress-strain curves at different strain rates at $\sigma'_v = 40$ kPa	191
FIGURE 5.32: TDA secant shear modulus (G_{50}) at different strain rate	192
FIGURE 5.33: Stress state approach to estimate friction angles from simple shear test	193
FIGURE 5.34: Estimation of friction angles from simple shear tests results	195
FIGURE 5.35: Comparison between simple shear and triaxial friction angle results	196
FIGURE 6.1: Stress-strain relationship as a function of energy function in hyperelastic material and elastic material (Jakel 2010)	198
FIGURE 6.2: Axisymmetric representation of triaxial tests (Surarak et al. 2012)	204
FIGURE 6.3: Screenshot from ABAQUS specifying displacement boundary condition BC-3 and confining pressure applied	205
FIGURE 6.4: Screenshot of ABAQUS showing boundary conditions and applied confining pressure	206
FIGURE 6.5: Screenshot of ABAQUS showing stresses for consolidation and shear phase	206
FIGURE 6.6: Screenshot of ABAQUS showing axial strains during initial stage, consolidation and shear phase	207
FIGURE 6.7: Comparison between FEM simulation and experimental results	208
FIGURE 6.8: Hyperbolic stress-strain relation for soil-hardening model (PLAXIS 2014)	211

	xx
FIGURE 6.9: Triaxial axisymmetric model implemented in PLAXIS	214
FIGURE 6.10: Soil hardening model results for Nevada Sand	215
FIGURE 6.11: Soil hardening model results for TDA-Sand mixture (20/80 by volume)	216
FIGURE 6.12: Soil hardening model results for TDA-Sand mixture (50/50 by volume)	216
FIGURE 6.13: Soil hardening model results for TDA	217
FIGURE 6.14: Volumetric change prediction during shearing for TDA	217
FIGURE 6.15: Porous elastic volumetric behavior (adapted from Abaqus 2011)	219
FIGURE 6.16: Analytical solution of k parameter obtained from the porous elasticity model	223
FIGURE 6.17: Analytical solution of p_{tel} parameter from the porous elasticity model	223
FIGURE 6.18: Predicted volumetric strains at the end of consolidation using Porous Elasticity Model	224
FIGURE 6.19: Drucker-Prager yield criteria for porous elasticity (ABAQUS 2011)	226
FIGURE 6.20: Porous elasticity model results for 100% fine TDA	228
FIGURE 6.21: Porous elasticity model results for Nevada Sand	229
FIGURE 6.22: Porous elasticity model results for TDA-Sand mixture (50/50 by volume)	229
FIGURE 6.23: Deviatoric peak stress estimation for different TDA contents	230
FIGURE A.1: Sieve analysis curves for TDA materials tested	251
FIGURE A.2: Sieve analysis for TDA material	252
FIGURE A.3: Specific gravity test for TDA and Nevada sand	253
FIGURE A.4: Minimum and maximum density test	253
FIGURE A.5: Optical microscope x 25 Fine TDA	255
FIGURE A.6: Optical microscope x 25 Nevada sand	255
FIGURE A.7: Optical microscope x 100 Nevada sand	256

	xxi
FIGURE A.8: Coarse TDA material tested in this research	256
FIGURE B.1: Aluminium retaining wall used in centrifuge tests	257
FIGURE B.2: Detail of aluminium retaining wall placement and sensor attachment to the wall for models 3 and 4	257
FIGURE B.3: Detail of laser sensors in front of the retaining wall face for model 4 in the centrifuge room	258
FIGURE B.4: Retaining wall model using Nevada sand	258
FIGURE B.5: Model 2 set up in the centrifuge room	259
FIGURE B.6: Model 4 in centrifuge room to start spinning	259
FIGURE B.7: Laser displacement sensor operation mechanism (www. sensorland.com)	260
FIGURE B.8: Laser displacement sensor components (Ubilla 2007)	261
FIGURE B.9: Tactile sensor calibration equipment (Ha 2007)	263
FIGURE B.10: Tactile sensor calibration equipment	264
FIGURE B.11: Tactile pressure sensor print screen from I-Scan software	265
FIGURE B.12: Increase in lateral pressure with time for TDA backfill	268
FIGURE B.13: Retaining wall centrifuge tests results at 5 g	268
FIGURE B.14: Retaining wall centrifuge tests results at 15 g	269
FIGURE B.15: Retaining wall displacements measurements for middle laser sensor	269
FIGURE B.16: Retaining wall displacements measurements for lower laser sensor	270
FIGURE B.17: Retaining wall displacements measurements for TDA/sand backfill mixture	270
FIGURE B.18: Pressure distribution with depth using a second degree polynomial regression for Nevada sand backfill at 25 g (retaining wall)	271
FIGURE B.19: Pressure distribution with depth using a second degree polynomial regression for Nevada sand backfill at 50 g (retaining wall)	271
FIGURE B.20: Rotation + Translation retaining wall movement at 10 g	272
FIGURE B.21: Rotation + Translation retaining wall movement at 20 g	272

	xxii
FIGURE B.22: Rotation + Translation retaining wall movement at 30 g	273
FIGURE B.23: Rotation + Translation retaining wall movement at 40 g	273
FIGURE B.24: Variation of the earth pressure coefficient K with depth for Nevada sand backfill in retaining wall model at 5 g	274
FIGURE B.25: Variation of the earth pressure coefficient K with depth for TDA/sand backfill in retaining wall model	274
FIGURE C.1: Filling of triaxial cell in the lab and pre-saturation process	280
FIGURE C.2: CD Triaxial test from beginning of shearing phase to the end	281
FIGURE C.3: TDA sample after shearing (right : sample inside chamber, left: sample outside chamber)	282
FIGURE C.4: Triaxial sample preparation mold and sample after mold removal	282
FIGURE C.5: 3/7 ratio TDA/sand mixture preparation and shearing failure	283
FIGURE C.6: 1/9 ratio TDA/sand mixture preparation and shearing failure	283
FIGURE C.7: Variation of density with confining pressure during consolidation phase	285
FIGURE C.8: Variation of volume during consolidation phase for both TDA materials tested in this research	285
FIGURE C.9: Variation of volume during consolidation phase for all different aggregates	286
FIGURE C.10: Comparison between TDA material and Nevada sand for CD triaxial test at 13.79 kPa confining pressure	287
FIGURE C.11: Comparison between TDA material and Nevada sand for CD triaxial test at 27.58 kPa confining pressure	288
FIGURE C.12: Comparison between TDA material and Nevada sand for CD triaxial test at 82.74 kPa confining pressure	289
FIGURE C.13: Shear strength parameters determination for TDA at 10% axial strain (CD triaxial test)	291
FIGURE C.14: Shear strength parameters determination for TDA ($D_{50}=2.60\text{mm}$) at peak for CD triaxial test .	292
FIGURE C.15: Shear strength parameters determination for TDA ($D_{50}=2.60\text{mm}$) at 5 % axial strain (CD triaxial test)	292

FIGURE C.16: Shear strength parameters determination for TDA ($D_{50}=2.60\text{mm}$) at 10 % axial strain (CD triaxial test)	293
FIGURE C.17: Shear strength parameters determination for TDA ($D_{50}=2.60\text{mm}$) at 20 % axial strain (CD triaxial test)	293
FIGURE C.18: Shear strength parameters determination for TDA/sand mixture (30:70 by weight) at 5% axial strain	294
FIGURE C.19: Stress-strain curves for all aggregates tested at $\sigma'_3 = 55.16 \text{ kPa}$	294
FIGURE C.20: Effective shear strength parameters determination for TDA at 5% axial strain (CU triaxial test)	295
FIGURE C.21: Effective shear strength parameters determination for TDA at 10% axial strain (CU triaxial test)	295
FIGURE C.22: Effective shear strength parameters determination for TDA at 15% axial strain (CU triaxial test)	296
FIGURE C.23: Comparison for consolidated undrained test at two different strain rates at 13.79 kPa confining pressure	297
FIGURE C.24: shear strength parameters for CU-Triaxial test at 2.0%/min strain rate	298
FIGURE C.25: Comparison for consolidated drained test at two different strain rates at 27.58 kPa confining pressure	298
FIGURE C.26: Comparison for consolidated drained test at two different strain rates and 55.16 kPa confining pressure	299
FIGURE C.27: Shear strength parameters determination for CD-Triaxial test at 2.0%/min strain rate	299
FIGURE C.28: Comparison between CD and CU triaxial tests at 0.2%/min strain rate (13.79 kPa confining pressure)	300
FIGURE C.29: Comparison between CD and CU triaxial tests at 0.2%/min strain rate (82.74 kPa confining pressure)	300
FIGURE C.30: Nevada sand deformation at different normal stresses during consolidation	301
FIGURE C.31: TDA ($D_{50} = 2.60 \text{ mm}$) deformation at different normal stresses during consolidation	301
FIGURE C.32: TDA/sand mixture (50/50 by volume) deformation at different normal stresses during consolidation	302

FIGURE C.33: Deformation of the different types of materials during consolidation at 20 kPa	302
FIGURE C.34: Deformation of the different types of materials during consolidation at 80 kPa	303
FIGURE C.35: Secondary deformation for the different types of materials during consolidation at 120 kPa	304
FIGURE C.36: Comparison of deformation during consolidation for both TDA particle size at 20 kPa	305
FIGURE C.37: Comparison of deformation during consolidation for both TDA particle size at 80 kPa	305
FIGURE C.38: Secondary deformation for both TDA particle size at 80 kPa	306
FIGURE C.39: Effect of TDA particle size in stress-strain behavior during simple shear at 40 kPa	307
FIGURE C.40: Effect of TDA particle size in stress-strain behavior during simple shear at 120 kPa	307
FIGURE C.41: Effect of strain-rate in TDA stress-strain behavior during simple shear at 20 kPa	308
FIGURE C.42: Effect of strain-rate in TDA stress-strain behavior during simple shear at 80 kPa	308

LIST OF SYMBOLS AND ABBREVIATIONS

A_c	Specimen corrected area
A_0	Specimen initial area
B	Cauchy-Green deformation tensor
c'	Cohesion
C_α	Compression Index
C_c	Coefficient of curvature
C_u	Coefficient of uniformity
$^{\circ}\text{C}$	Temperature in Celsius
CD	Consolidated drained triaxial test
CU	Consolidated undrained triaxial test
Δ/h	Normalized lateral displacement
Δ_u	Excess pore pressure
D_{10}	Grain diameter corresponding to 10% of the material being smaller
D_{30}	Grain diameter corresponding to 30% of the material being smaller
D_{50}	Grain diameter corresponding to 50% of the material being smaller
D_{60}	Grain diameter corresponding to 60% of the material being smaller
D_r	Relative density
ε	Axial Strain
ε_{vol}	Volumetric strain
e	Void ratio
E	Modulus of elasticity
E_{50}	Secant modulus of elasticity at 50% deviatoric stress

E_{50}^{ref}	Reference stiffness modulus from triaxial test
ϕ'	Effective friction angle
FEM	Finite element model
f_r	Fraction of rubber
f_t	Threshold rubber content
γ	unit weight
γ_{min}	Minimum unit weight
γ_{max}	Maximum unit weight
g	Gravity acceleration
G	Shear modulus
G_s	Specific gravity
H	Wall height
H_0	Initial Height
I	Stress invariants
I_a	Moment of inertia aluminum beam
J	Jacobian
J^{el}	Elastic volume change for porous elasticity model
K_a	Active lateral earth pressure coefficient
K_0	At-rest lateral earth pressure coefficient
K_p	Passive lateral earth pressure coefficient
λ	Stretch ratio
L	Length of aluminum beam
m	Power modulus evolution depending on confining pressures

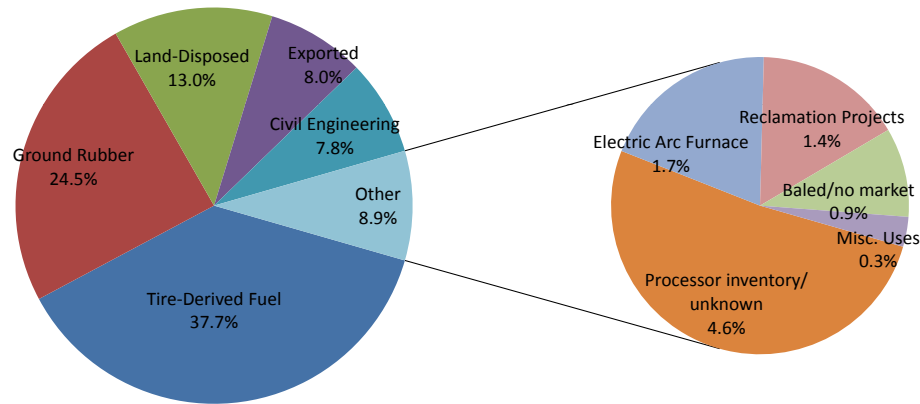
n	Scaling factor for centrifuge tests
p'	Mean effective principal stress
P_a	Active lateral pressure
p^{ref}	Reference confining pressure
q	Deviator stress
R_f	failure ratio
(σ'_1 / σ'_3)	Principal stress ratio
σ'_h	Horizontal stress
σ'_{peak}	Failure deviatoric stress
σ'_v	Normal Stress
S	Stress change in hyperelastic model
τ	Shear stress
t	Time
TDA	Tire derived aggregate
ν	Poisson's ratio
W	Strain energy density
w_o	Linear load at the bottom of the stem wall
x	Location along the wall where deflection is being calculated

CHAPTER 1. INTRODUCTION

1.1 Introduction

This research was undertaken to investigate the mechanical behavior and shear strength characteristics of recycled tire particle granular media and to evaluate the performance of such aggregates as backfill for retaining structures. The base granular material with deformable particles used in this dissertation is finely shredded scrap tires which as per ASTM D6270 (ASTM 2012) is referred to as tire-derived aggregate or TDA.

In addition to the information gaps that have motivated this research, the environmental concern in terms of waste management has also promoted research towards finding sustainable solution and uses of disposal materials rather than continuing to fill up landfills. According to the Rubber Manufacturer Association (RMA 2013) as of 2011 the net scrap tires generated in the United States was 230.7 million, and 13% of this amount (30 million) were disposed of or stockpiled in landfills. Civil engineering applications only account for only 7.8% percent of the market as shown in Figure 1.1.



* Numbers may not add due to rounding.

Figure 1.1: US Scrap tire disposition as percent of total tons generated annually (adapted from RMA 2013)

Civil engineering projects traditionally use mineral soil as construction material for embankments or for retaining wall backfills. For mineral soil the basic assumption of non-deformable or rigid particles is the cornerstone of granular material mechanics. In recent years, the use of recycled materials as an environmentally friendly granular material alternative has been reported in the literature. Examples of these recycled materials include shredded scrap tires, cullet glass, roofing shingles, blast furnace slag, steel slag, coal bottom ash/boiler slag, reclaimed asphalt and concrete pavement, and flue gas desulfurization scrubber. Some of these materials are composed of deformable particles. The underlying premise assumed when these materials are used in functional projects and demonstrations have been that classical soil mechanics theories and methodologies apply to these recycled granular materials. However, this premise of soil mechanics theory having universal applicability to deformable recycled materials has not been evaluated.

This dissertation investigates whether classical lateral earth pressure theories apply to granular media with deformable particles. Specifically the experimental program used TDA material. A study of the stress-strain characteristics of TDA is also part of this research.

1.2 Motivation

Classical soil mechanics has been developed under the basic assumption that soil particles are rigid (Lambe and Whitman 1969). For example as shown in Figure 1.2, deformation of a soil under 1-D compression is primarily due to particle rearrangement, which results in a decrease in void ratio. Using tire derived aggregates in the same manner as soils would result in a granular particulate media with deformable particles, which may not be subject to traditional soil mechanics principles. The change in sample height (ΔH) is directly related to particle rearrangement which results in the soil sample going from an initial void ratio e_1 to a denser void ratio e_2 .

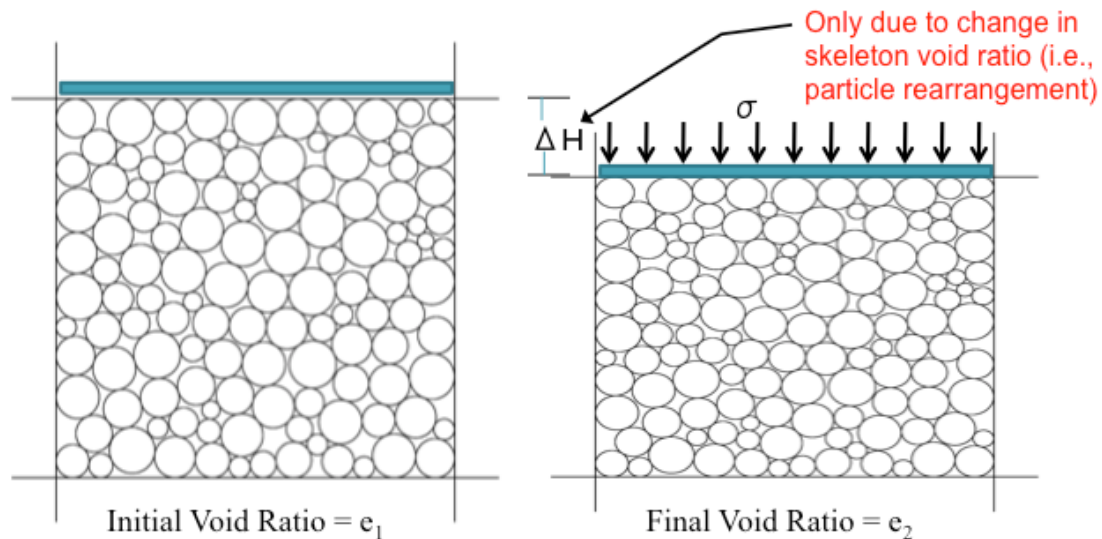


Figure 1.2: Schematic of 1-D compression of a mineral soil

The above discussion did not include any sample height drop due to particle deformability. The deformable nature of the particles of recycled granular material may be an important factor that can affect the validity and applicability of classical soil mechanics theories and methodologies. For instance, deformations and associated strains of recycled granular materials will likely lead to a cause and effect quite different from the norm where (i) a change in void ratio of the skeleton of the granular medium (classical soil mechanics); will cause (ii) deformation of the particles themselves (the effect). Deformation is not a normal reaction to a change in void ratio. A thorough understanding of the deformation and stress-strain mechanics of recycled granular materials with deformable particles is necessary in order to safely and adequately design and implement civil engineering projects involving these new types of materials.

Although several authors have reported engineering properties of tire-derived materials in terms of shear strength, short and long term compressibility, drainage and permeability, and lateral pressure, there is still an information gap which asks whether conventional earth pressure theories used for conventional soils are applicable to these kinds of materials and will they allow us to predict lateral pressure magnitude. This gap exists in the current state of knowledge due to the lack of experimental data obtained from field and scaled earth-retaining structures using TDA and TDA/soil mixtures as backfills.

Conventional retaining structures are commonly designed in the geotechnical field following conventional earth pressure theories and concepts (at-rest, active, and passive condition). However, these theories were developed for conventional mineral soils in which particles are rigid.

For mineral soils composed of rigid particles, the lateral pressure against a retaining structure is directly proportional to the backfill unit weight as shown in Figure 1.3. Another factor involved in conventional lateral earth pressure theories is the earth pressure coefficient (K_o). The applicability of conventional lateral earth pressures theories and the distribution shown in Figure 1.3 for retaining walls with backfills consisting of deformable particles has to be confirmed. To date only limited data has been published in this regard.

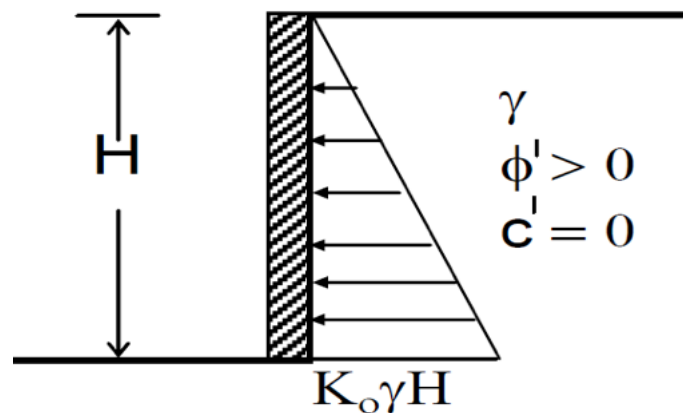


Figure 1.3: At-rest earth pressure distribution against a smooth, rigid retaining wall

The proposed dissertation research plan will assess whether conventional lateral earth pressure theories produce acceptable estimates of the lateral pressure for backfill composed of deformable particles such as tire-derived aggregates. If confirmed, the expected reduction in lateral pressure would translate into economic and environmental benefits. In terms of stress-strain behavior and shear strength characteristics, most studies have focused on the use of large shredded tire particles; however, for this research, it was decided to focus on studying the mechanical behavior of small TDA particles. The

selection of shear strength parameters when using TDA materials has been also questioned due to the high level of compressibility expected.

1.3 Objectives

This research has two main objectives. First, to develop a better understanding of TDA stress-strain behavior and shear strength characteristics for geotechnical engineering applications. Second to study the generation of lateral pressures induced by TDA on retaining structures applications.

Specific objectives associated with the above main objectives are as follows:

1. Carry out geotechnical centrifuge tests to assess lateral pressures development (magnitude and distribution with depth) for TDA, TDA/soil mixture and conventional soil backfills.
2. Carry out a detailed experimental program based on triaxial tests to evaluate the stress-strain behavior and shear strength characteristics of TDA, TDA/soil mixture and how the behavior compares to conventional sand material.
3. Evaluate the stress-strain behavior of TDA under drained and undrained conditions as well as the effect of particle size and strain rate effect on the resulting behavior.
4. Carry out an experimental program based on simple shear techniques to evaluate the stress-strain behavior of TDA, TDA/soil mixture and how the behavior compares to conventional sand material.
5. Carry out an analytical study based on different constitutive models to investigate their suitability in predicting the mechanical behavior of TDA.

1.4 Organization

This dissertation is organized into seven chapters. The methodology followed in each phase is described at the beginning of each chapter rather than creating a separate methodology chapter. Chapters are organized as follows:

Chapter Two presents important definitions and background regarding TDA materials as well as civil engineering applications. A literature review describing previous studies regarding mechanical properties and lateral earth pressures is also included. Chapter Three presents and discusses retaining structures' lateral pressure results obtained from the centrifuge-testing program. Chapter Four presents the stress-strain behavior and shear strength characteristics obtained from a series of consolidated drained and undrained triaxial shear tests. Chapter Five presents experimental results obtained from a series of simple shear tests as well a discussion of how the results compare to those in the triaxial testing program discussed in chapter four. Chapter Six presents the triaxial testing simulations carried out using three different constitutive models. Finally, Chapter Seven discusses the principal conclusions and findings obtained in this research. Recommendations for future studies are also indicated. Appendix A includes index properties of the materials tested while Appendices B and C includes information not included in the corresponding chapters.

CHAPTER 2. BACKGROUND AND LITERATURE REVIEW

2.1 Introduction

This chapter presents a brief section with relevant background in terms of definitions and Civil Engineering applications for tire derived aggregate (TDA) materials. Additionally this chapter includes a comprehensive literature review. The literature review summarizes previous studies on mechanical properties of TDA (alone and mixed with sand), lateral pressures of TDA, and other general characteristics of TDA topics aligned to the scope of this study such as: permeability and leachate properties, spontaneous combustion, and analytical studies.

2.2 Tire Derived Aggregates (TDA)

The general term tire derived aggregate (TDA) refers to pieces of chopped or shredded scrap tires. These pieces of scrap tires can range in size depending on the procedure used to shred or chop the tires. In general TDA material sizes range from 0.5 to 305 mm as summarized in Table 2.1. This size classification of TDA materials is based on ASTM Standard D6270 (ASTM 2012) which also provides general guidance when considering TDA materials for civil engineering applications. Figure 2.1 presents photos of some of the shredding equipment commonly used to produce TDA materials. The larger TDA sizes typically involve use of only a primary shredder. Smaller TDA sizes often require use of additional stages of shredding (e.g., secondary shredders) and for very small TDA sizes the production also includes the removal of metal filaments.

Table 2.1: TDA classification according to ASTM D6270 (ASTM 2012)

TDA Type	Particle Size Description
Scrap Tire	A tire which can no longer be used for its original purpose due to wear or damage
Tire Shreds	Pieces of scrap tires that are generally between 50 mm and 305 mm in size
Tire Chips	Generally between 12 mm and 50 mm in size and have most of the wire removed
Granulated Rubber	Particles sizes ranges from 0.425 mm (40 mesh) to 12 mm
Ground Rubber	Particle sizes ranges from 0.425 mm (40 mesh) to 2 mm
Powder Rubber	Particle sizes bellow 0.425 mm (40 mesh)



Figure 2.1: Equipment commonly used to produce TDA

2.3 Common Civil Engineering Applications of TDA

In recent years TDA materials have been actively used in Civil Engineering applications such as a light weight material for road fills, backfills of retaining walls, rubber asphalt pavements, sound barrier walls, and others (Humphrey 2004). Some of the most common Civil Engineering applications where TDA has been reported are listed in Table 2.2. Use of TDA materials has an obvious environmental benefit as it involves the

recycling or reusing of scrap tires that otherwise often end up in landfills. TDA also have the engineering benefit that they are light weight as compared to conventional geomaterials. TDA materials have been reported as having compacted unit weights about one third the unit weight of conventional mineral soils (Humphrey 1999; Humphrey 2004; RMA 2006). The lower unit weight of TDA materials compared to regular mineral soils translate into economical benefits. For example, lower cost in retaining walls since the lighter TDA backfill would require a smaller wall cross section, smaller foundation, and less reinforcing steel (Cecich et al. 1996; Garcia-Theran et al. 2014). TDA technical design benefits are also present particularly associated to projects where light weight materials are needed when dealing with poor compressible foundation soil conditions.

One of the Civil Engineering applications listed in Table 2.2 is the use of TDA materials in the construction of highway embankments. This application is attractive because TDA is a lightweight fill ideal for highways with soft subgrades and because the TDA can act as a thermal insulation to limit frost penetration beneath roads applications. Additionally, it has been reported as a potential backfill for retaining structures, as well as an excellent drainage material due to TDA high permeability characteristics even if they are compressed under the weight of overlying fill (Humphrey 1999; Humphrey and Blumenthal 2011; Humphrey et al. 1998; Reddy and Marella 2001). Figures 2.2 through 2.5 show some of the most important TDA Civil Engineering applications.

Table 2.2: TDA Civil Engineering Applications (adapted from RMA 2013)

Application	Comments
Subgrade fill and highway embankments	The principal engineering that TDA brings to these projects is lighter weight (one-third to one-half of conventional backfill). TDA allows construction of embankments on weak, compressible foundation soils.
Landfill construction and operation	Drainage layer in cap closures, as permeable backfill in gas venting systems, as a material for daily cover, permeable aggregate for leachate collection systems, and in operational layers.
Cap closures	Final cover system for landfills.
Gas Venting Systems	A 3 to 4 inch maximum size is used as the bedding material for gas extraction pipes. This reduces shifting or damage to the gas venting pipes.
Leachate collection systems	TDA replaces the upper foot of the two to three feet of sand that is required in a leachate collection system in landfills.
Septic system drain fields	TDA has a greater void space percentage compared to stone which allows TDA to hold more water than stone.
Backfill for walls and bridge abutments	The weight of TDA produces lower horizontal pressure on the wall, allowing for construction of walls with less with less reinforcing steel. TDA is free draining and provides good thermal insulation; eliminating problems with water and frost build up behind the walls.
Subgrade freeze insulation for roads	The insulation that is provided by a TDA layer keeps the subgrade soils from freezing throughout the winter.
Vibration dampening layers	Attenuation of ground born vibrations



Figure 2.2: Embankment construction in US 101 using TDA (Baker et al. 2003)



Figure 2.3: Subgrade frost insulation applications (EPA 2015)



Figure 2.4: Retaining walls applications using TDA for scale models and bridge abutments (Humphrey 2008; Tweedie et al. 1998)



Figure 2.5: Landfill gas collection trenches applications (Patenaude and Wright 2014)

TDA has not only been implemented in new infrastructure projects but also as a lightweight material to remediate existing geotechnical structures. For example, an embankment failure occurred during the construction of a highway in Stephen, New Brunswick in Canada was remediated using recycled tire shreds. Figure 2.6 (a) shows the

embankment failure which was found to be caused to a combination of a low strength foundation soil and the rate and intensity of embankment loading (Mills 2008).

Therefore, it was necessary to find a light material that would reduce the load over the foundation soil. TDA alternative was viable since the recycling facility was near the site, which reduced transportation costs. The subgrade of the embankment was prepared followed by the placement of a woven geotextiles and placement and compaction of TDA in lifts as shown Figure 2.6 (b).

Despite some of the potential benefits, the use of TDA in Civil Engineering applications has been a slow process. This may be due to the perceived potential environmental concerns such as leachability and combustion characteristics, as well as compressibility effects that have been under debate in the past. At least 15 states have incorporated the material for embankments and backfills: California, Colorado, Indiana, Maine, Minnesota, New Jersey, North Carolina, Oregon, Pennsylvania, South Carolina, Vermont, Virginia, Washington, Wisconsin, and Wyoming (DOT 2012). Other states such as Alabama, Florida and Georgia allow tire shreds to be used in construction of drain fields for septic systems (EPA 2015). Lack of acceptance in some states can be due to institutional obstacles or policy preferences. Institutional obstacles are generally permitting conditions that make the use of TDA very difficult. For example, a regulatory agency might require development of its own testing protocol for applications that have been used elsewhere; which adds costs to the price of TDA and delays the approval process (RMA 2006).



a) Embankment failure remediated using TDA



b) Placement of TDA in the construction site

Figure 2.6: Reconstruction of a embankment failure using TDA (Mills 2008)

2.4 Engineering Properties of TDA

The use of TDA in Civil Engineering applications requires knowledge of engineering properties. For example, mechanical properties such as elastic stiffness, strength, and creep are needed in order to assess structural performance and safety. Environmental properties such as permeability and spontaneous combustion are needed to evaluate leachability, durability as well as potential environmental hazards. The following subsections provide a literature review for each of these key properties with emphasis on those related to the focus of this research (retaining wall backfills and stress-strain characteristics).

2.4.1 Shear Strength Parameters of TDA

Shear strength characteristics of TDA materials have been studied by several researchers (Ahmed 1993; Benda 1995; Cecich et al. 1996; Celis and Pando 2008; Edinclair et al. 2004; Lee et al. 1999; Masad et al. 1996; Moo-Young et al. 2003; Soganci 2014; Wartman et al. 2007; Wu et al. 1997; Xiao et al. 2014; Yang et al. 2002; Zornberg et al. 2004). Most of these studies report shear strength in terms of a drained or effective friction angle based on a linear Mohr-Coulomb shear strength envelope. The general observation made by these studies is that shear strength parameters of TDA materials exhibit a lower friction angle as compared to typical soils under similar conditions. In practice the TDA friction angle can be commonly taken to be about 25° (Strenk et al. 2007), which is lower comparing to values higher than 30° for most soils used in conventional fills. Table 2.3 presents a summary of the shear strength parameters characteristics of relevant previous studies. This table indicates the TDA size considered in each study. It is noted that most studies have included TDA with larger particles sizes

(> 4.75 mm) which corresponds to TDA materials classified as tire chips or tire shreds as per Table 2.1.

The shear strength parameters summarized in Table 2.3 show a wide range of variation. The effective friction angle (ϕ') varies from 6 to 54 degrees while the effective cohesion intercept (c') ranges from 0 to 82 kPa. There are several possible factors and reasons for this large variability including: (i) size, shape and type of TDA; (ii) type of shear strength laboratory tests; (iii) range of stress level used in testing program; (iv) failure criterion used; (v) rate of loading; etc. As discussed in the following subsections the stress-strain behavior of TDA materials usually does not exhibit a sharp or well-defined peak and for instances where a peak is observed, they usually occur at much larger levels of axial strain (triaxial tests) or shear box displacements (direct shear tests). Therefore, many references in Table 2.3 report shear strength parameters for a limiting axial strain level ($\epsilon_a \text{ max}$) or limiting shear box displacement. For engineering design purposes using shear strength parameters based on a limiting axial strain or displacement is considered more appropriate in order to ensure Φ' and c' values correspond to anticipated field deformations and displacements which must be within service limit states.

Table 2.3: Summary of key shear strength studies on TDA materials

Reference	Maximum Size (mm)	Ranges of stresses (kPa) ⁽¹⁾	Cohesion (kPa) (c')	Effective Friction Angle (ϕ')	Failure Criteria ⁽²⁾	Type of Test
Ahmed (1993)	13	36-199	22.7	11.2	10	Triaxial
			35.8	20.5	20	Triaxial
Benda (1995)	9.5	35-55	0	20.6	10	Triaxial
			0	32.1	20	
Cecich et al. (1996)	12.5	3.5-27.6	7.0	27	15	Direct shear
Masad et al. (1996)	4.75	150-350	70	6	10	Triaxial
			82	15	20	
Wu et al. (1997)	38	34.5-55	0	57	At peak	Triaxial
	19		0	54		
	9.5		0	47		
Lee et al. (1999)	30	28-193	7.6	21	At peak	Triaxial
Yang et al. (2002)	10	20-60	21.6	11	10	Triaxial
			18.8	37.7	20	
		20.7-82.7	0	32	10	Direct shear
Moo-Young et al. (2003)	50	4.0- 17.0	0.39	15	At peak	Direct Shear
	50-100	7.0-37.0	0.37	32		
	100-200	10.0-20.0	0.37	27		
	200-300	10.0-20.0	0.35	29		
Edinlier et al. (2004)	40	20-80	0	22	15	Direct shear
Zornberg et al. (2004)	25.4	48.3-207	0	26.5	15	Triaxial
			22.8	21.4		
Celis et al. (2008)	4.75	13.7-68.9	0	19	At peak	Triaxial
Soganci (2014)	3.0	100-400	3.5	24.3	At peak	Direct shear
Xiao et al. (2014)	100	24-144	14.3	36.1	At peak	Direct shear

Notes: (1) Range of stresses for triaxial testing refers to effective confining stress and for direct shear normal stress.

(2) Failure criteria for direct shear tests were defined as a horizontal deformation percentage of the sample diameter. For triaxials tests, failure criteria corresponds the axial strain percentage.

Edinclier et al. (2004) studied the shear strength characteristics of tire waste materials using large scale direct shear tests. The TDA tested in this study had sizes ranging from between 1 and 4 mm and lengths ranging from 2 to 40 mm. Figure 2.7 shows the shear stress versus horizontal displacement curves obtained for selected normal stress levels. The effective friction angle at peak shear displacement angle of the tire derived materials was found to be 22° compared to 33° in sand (Edinclier et al. 2004). Other authors have studied the influence of TDA particle size in the shear strength parameters. For example, Moo-Young et al. (2003) reported angles of friction between 15° and 29° for TDA materials sizes ranging from 50 mm to 300 mm as shown in Figure 2.8. The authors indicated that in general, as the particle size increases, the shear strength of TDA increases as well (Moo-Young et al. 2003). However, as shown in Figure 2.8 particle sizes ranging from 50 to 100 mm exhibited the higher shear strength parameters which may be the result of other factors such as effect of steel belts and wires which creates interlocking forces during shearing and increased dry density (Moo-Young et al. 2003).

Despite the several studies on shear strength characteristics of TDA materials, there are still some concerns in regards to the appropriateness of using a linear shear strength failure envelope (Yang et al. 2002). Shear strength parameters of TDA materials might be highly dependent on the level of confining stresses and the level of axial strain. Hence recommend selecting the shear strength parameters of the TDA material based on the actual range of confining pressures and deformation levels expected in a particular project should be clarified. Graphical comparison of the shear strength parameters listed

in Table 2.3 is presented in Figures 2.9a and 2.9b for the tire chips TDA and granular rubber TDA, respectively.

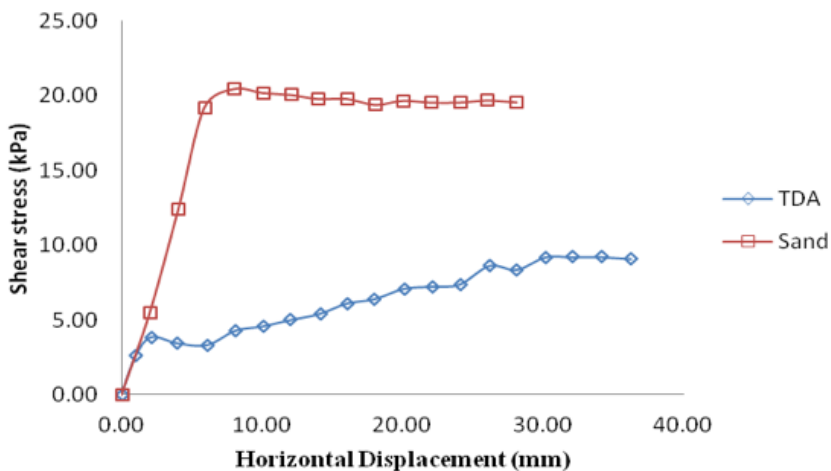


Figure 2.7: Shear stress vs. horizontal displacement for sand, and TDA materials under direct shear condition at vertical stress of 20 kPa (Edinclair et al. 2004)

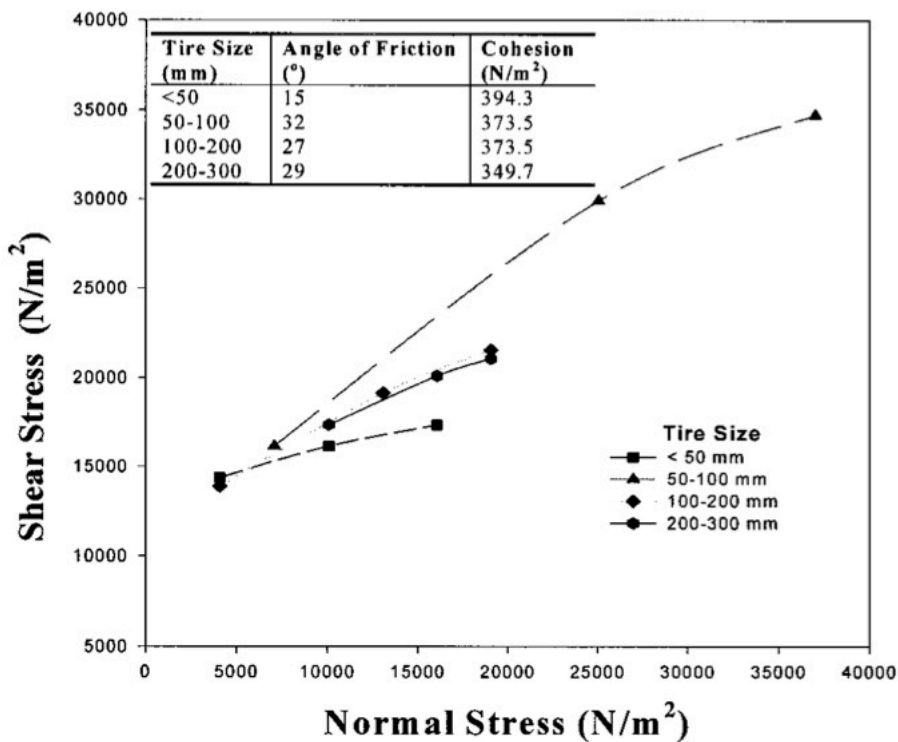
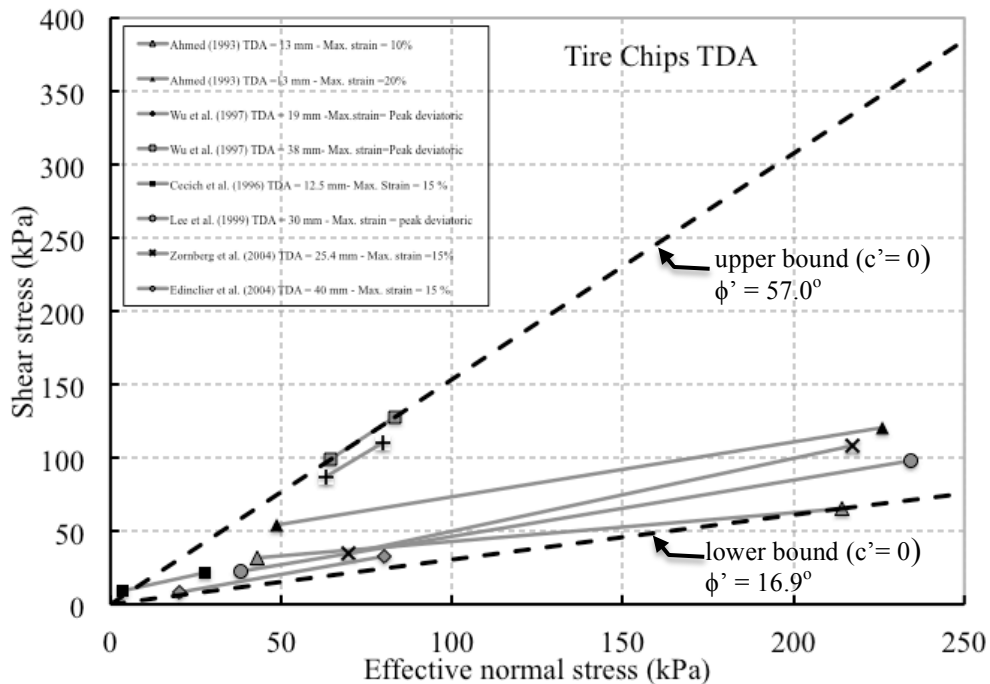
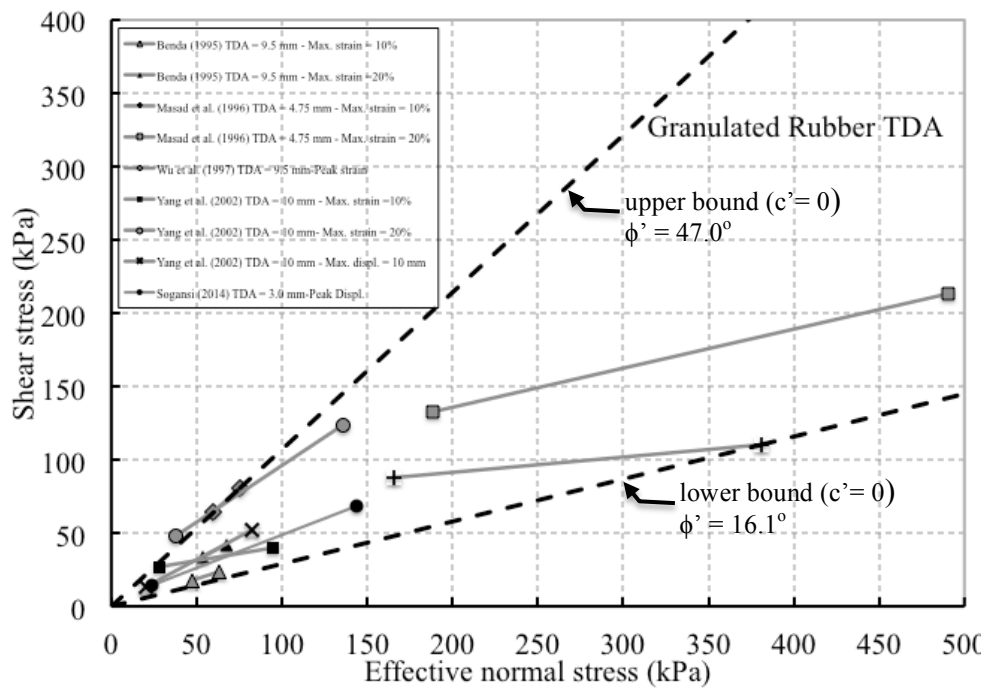


Figure 2.8: Mohr-Coulomb failure envelope for different TDA sizes (adapted from Moo-Young et al. 2003)



a) Tire chips TDA



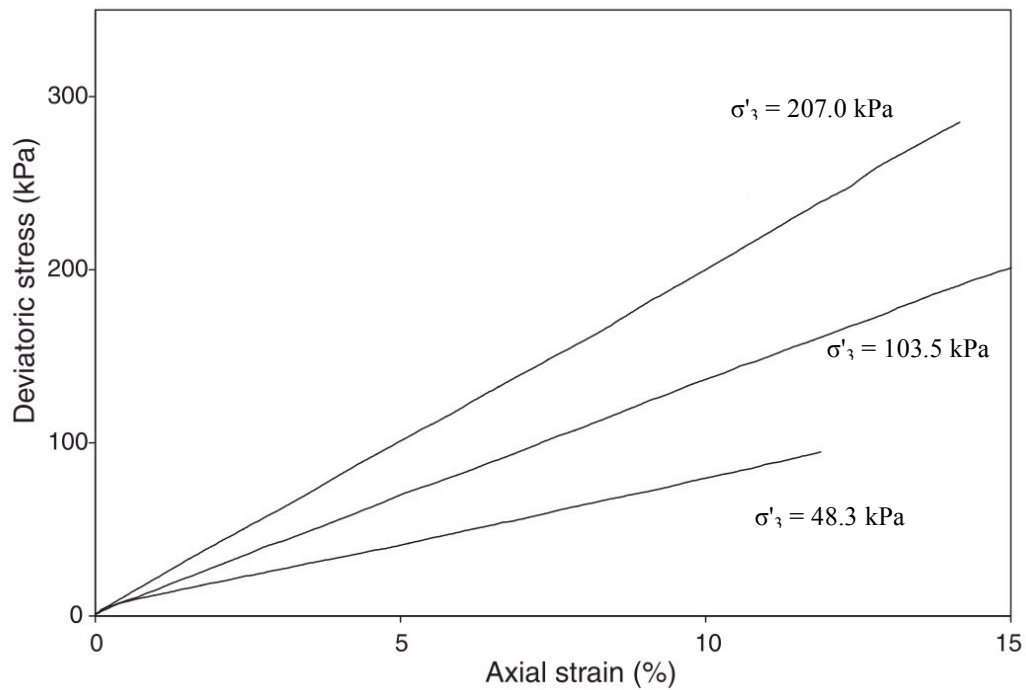
b) Granulated rubber TDA

Figure 2.9: Graphical comparison of the shear strength parameters from previous studies

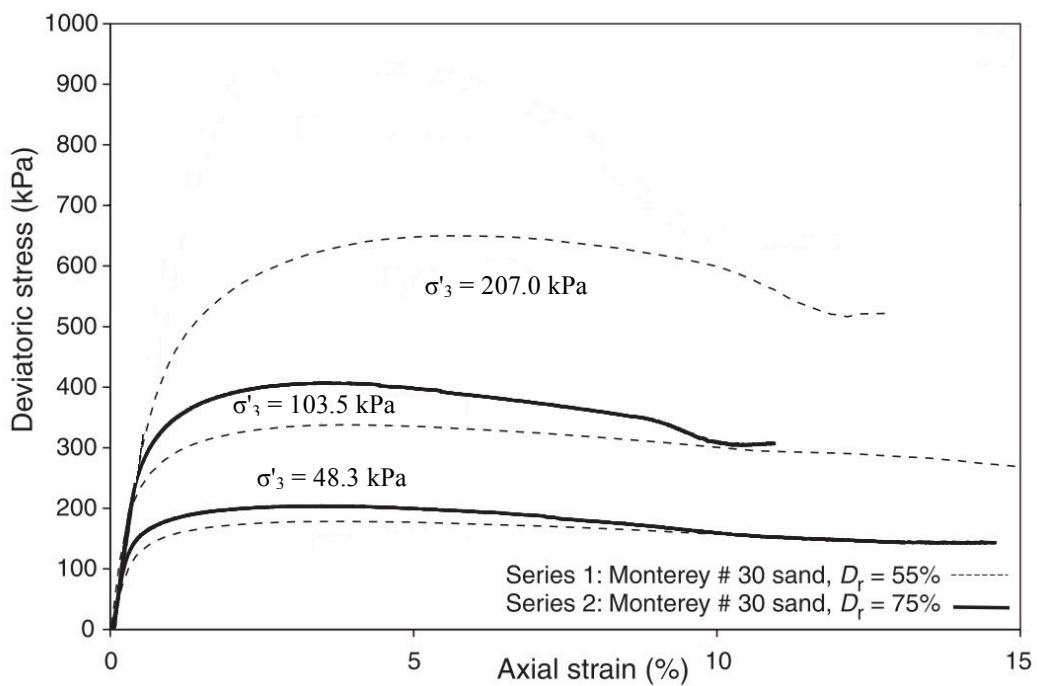
2.4.2 Triaxial Compression Stress-Strain Behavior

Several authors have reported triaxial compression stress-strain behavior of TDA materials (most listed in Table 2.3). For example, Zornberg et al. (2004) reported a series of consolidated drained triaxial tests on tire chips TDA (25.4 mm) with effective confining pressures of 48.3, 103.5 and 207 kPa. The deviatoric stress-strain relationship obtained for the tire chips are presented in Figure 2.9 (a). The stress-strain behavior observed was approximately linear up to axial strain levels of up to 15%. This same study carried out similar triaxial compression tests on sands. Stress-strain curves obtained on Monterey # 30 sand are shown in Figure 2.9 (b). This figure shows a much stiffer response for sands tested under similar relative densities and levels of isotropic effective confinement. Additionally, it can be seen that tests on Monterey # 30 sands reached a peak or a plateau at axial strain levels below 10%. This is an important difference compared to the tire chips TDA results where a softer and linear response without a peak was observed at axial strain levels of about 15%. However, other authors (Wu et al. 1997) have reported clear peak deviatoric stress at about 15% axial deformation for tire chips.

Yang et al. (2002) studied the stress strain behavior of tire chips with a 10 mm maximum size by means of triaxial compression test. The deformation behavior was characterized by high compressibility and low Young modulus. The authors reported that the stress-strain curves are nearly linear up to strain levels of about 15% which is consistent with the findings observed by Zornberg et al (2004). However, beyond the 15% axial deformation threshold, chips TDA started exhibiting strain softening with a clearly defined maximum deviatoric stress at about 25% axial strain (Yang et al. 2002).



a) Stress-strain behavior of TDA



b) Stress-strain behavior Monterey sand

Figure 2.10: Stress-strain behavior of TDA and Monterey sand from triaxial tests (Zornberg et al. 2004)

2.4.3 Shear Strength and Stress-Strain Behavior of TDA/Soil Mixtures

Mechanical behavior of TDA-Soil mixtures have been studied taking into consideration variables such as different mixing proportions and effect of TDA sizes. For example, the influence of different tire shreds contents by volume and aspect ratio (ratio between the length of tire shred and its width) has been studied by Ghazavi et al. (2005) and Zornberg et al. (2004). The principal findings in these studies indicate that at a given normal stress applied on specimens, the shear resistance of the shred-sand mixtures tends to be greater than that of the sand alone at the same sand matrix unit weight, and the shear resistance of the mixtures increases with increasing tire shred content (Ghazavi and Sakhi 2005) as shown in Figure 2.11. Increments in shear strength parameters using tire shreds/sand mixtures has also been reported by other authors (Foose et al. 1996; Zornberg et al. 2004) who have reported higher friction angles in TDA-Sand mixtures depending on the mixing proportions as aspect ratios. As can be observed in Figure 2.12, the addition of tire shreds to sand can increase the initial friction of the sand significantly. It is also noted from Figure 2.12, the aspect ratio has also a significant influence in the initial friction angle of the mixtures. It can be seen that for a given shred width, there is solely an optimized length giving the greatest friction angle regardless of the shred content (Ghazavi et at. 2005).

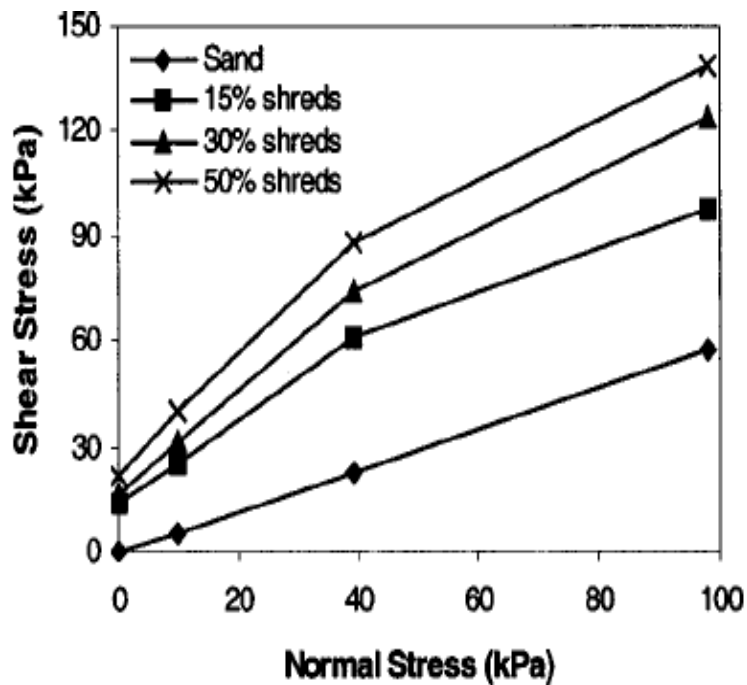


Figure 2.11: Variation of shear stress with normal stress on samples with 4 x 8 cm shred tires (adapted from Ghazavi et al. 2005)

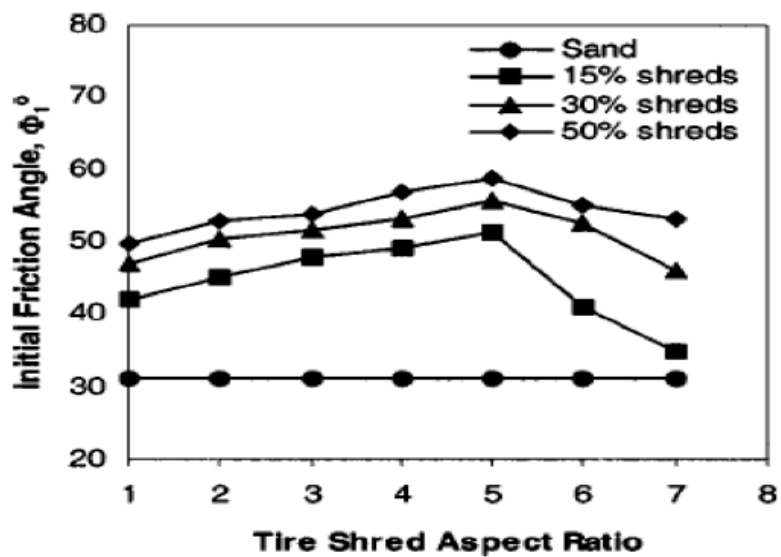


Figure 2.12: Variation of initial friction angle versus shred aspect ratio (adapted from Ghazavi et al. 2005)

Other authors (Celis and Pando 2008; Youwai and Bergado 2003) have reported improvements in the shear strength parameters of TDA/sand mixtures when compared to TDA specimens alone, but not necessarily higher than the parameters found for Sand alone as the previous studies indicated as shown in Figure 2.13. Therefore, key factors that can influence TDA strength such as tires sizes, aspect ratios, mixing proportions and densities can lead to different results among researchers.

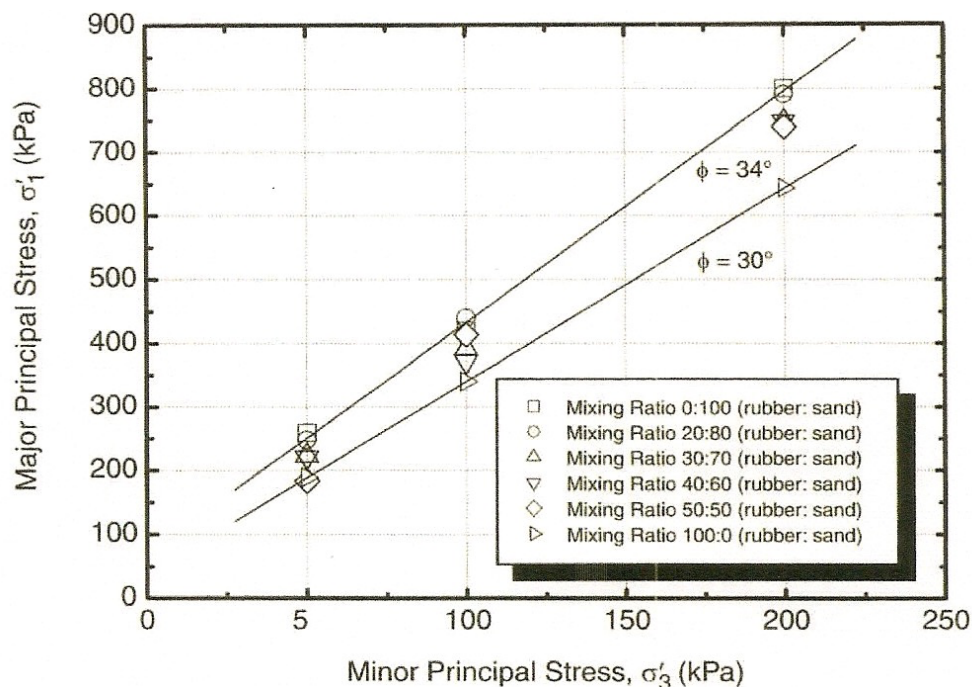


Figure 2.13: Friction angles for different TDA-Sand mixtures (adapted from Youwai et al. 2003)

2.4.4 Short Term 1-D Compressibility of TDA Materials

Short term 1-D compressibility of TDA and TDA/sand mixtures has also been studied extensively primarily from field test studies of embankment fills (Bosscher et al. 1997; Dickson et al. 2001; Hoppe and G. 2004; Tandon et al. 2007; Yoon et al. 2006;

Zornberg et al. 2004) and has also been studied in the laboratory (Celis and Pando 2008; Drescher et al. 1999; Tatlisoz et al. 1997; Wartman et al. 2007).

These studies show that TDA materials exhibit a high degree of compressibility upon initial loading, especially at low stress levels (below 100 kPa). This is an important difference with conventional soil backfills where the soil particles are practically non-deformable and the deformation is associated to rearrangement of the soil particles which results in a reduction in the pore volume of the soil skeleton. In the TDA material, deformation is believed to be related to reduction of pore volume (similar to conventional soils) as well as to the deformation of the particles themselves (Youwai and Bergado 2003). The immediate compressibility of TDA/sand mixtures has been found to be inversely proportional to the sand content (Tatlisoz et al. 1997). In order to minimize the short term compressibility these authors recommend having sand contents of at least 30%.

Wartman et al. (2007) carried out an experimental program to study the mechanisms of immediate and time-dependent 1D compression of TDA materials. Most one-dimensional compression experiments were performed under stresses of 200 kPa. Experiments were performed under both one-dimensional confined compression and isotropic compression. Volume changes were normalized by the initial global volume of the specimen to express the results in terms of the volumetric strain.

Figure 2.14 shows the changes in water volume within the specimen, which is also expressed as volumetric strain. Because the specimens were fully saturated, water expelled from the specimen during compression is directly attributable to pore volume reduction. Differences between the specimen and pore volume strains which solely result

from the reduction of pore space. Figure 2.14 shows that the modulus (slope of stress-strain curve) decreases with increasing applied stress, whereas the unload curve indicates that a significant fraction of the immediate compression is recoverable. At applied stresses up to approximately 120 kPa the volume of water expelled from the specimen is nearly identical to the specimen volume change, implying that at these stress levels immediate compression is entirely a result of pore volume reduction. At larger stresses the differences between the specimen and pore volume response implies that the tire particles are compressing; however, volume change in the specimen is still largely dominated by reduction of pore volume. Therefore, it appears that particle compression does not contribute to immediate deformation of TDA at low to intermediate stresses (up to 120 kPa). Figure 2.14 shows that even under high stresses, the contribution of particle compression to immediate deformations can be negligible for practical purposes (Wartman et al. 2007).

The 1-D compression behavior of the same tire chip TDA ($D_{\max} = 30$ mm) was also investigated in this study. The variation of volumetric strain during 1-D compression is shown in Figure 2.15. This figure shows the TDA reached a volumetric strain of 27% at a vertical stress level of 200 kPa. It is observed that for large TDA contents, the first increments of stresses result in significant compression after which the specimens become less compressible as strain accumulates and the material strain hardens. In contrast this same TDA under isotropic compression experienced a volumetric strain of 23% at a stress level of 200 kPa. Wartman et al. (2007) compared the 1-D compression behavior of their test TDA with mixtures with sand. The TDA contents by volume considered were 0%, 50%, 65%, 85% and 100%. The 1D compression results for TDA-Sand mixtures are also shown in Figure 2.15. Celis and Pando (2008) also investigated the short term 1-D compression behavior of crumb rubber TDA material with a D_{\max}

=4.75 mm. This study investigated mixtures by volume with a uniform quartzitic sand with $D_{50} = 3.0$ mm.

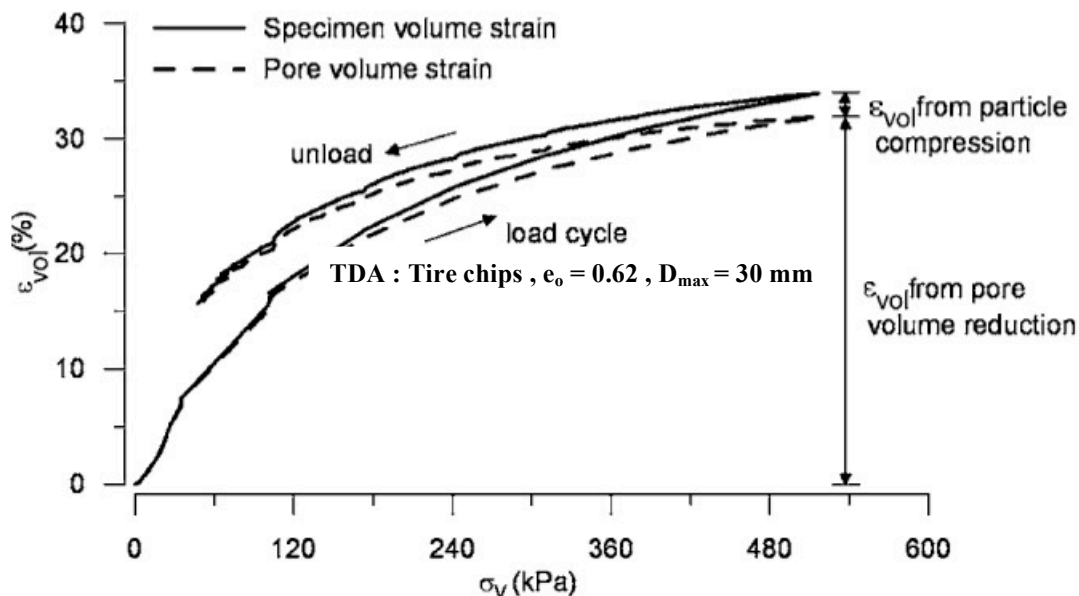


Figure 2.14: Volume changes in TDA (tire chips) under saturated, drained isotropic compression (adapted from Wartman et al. 2007)

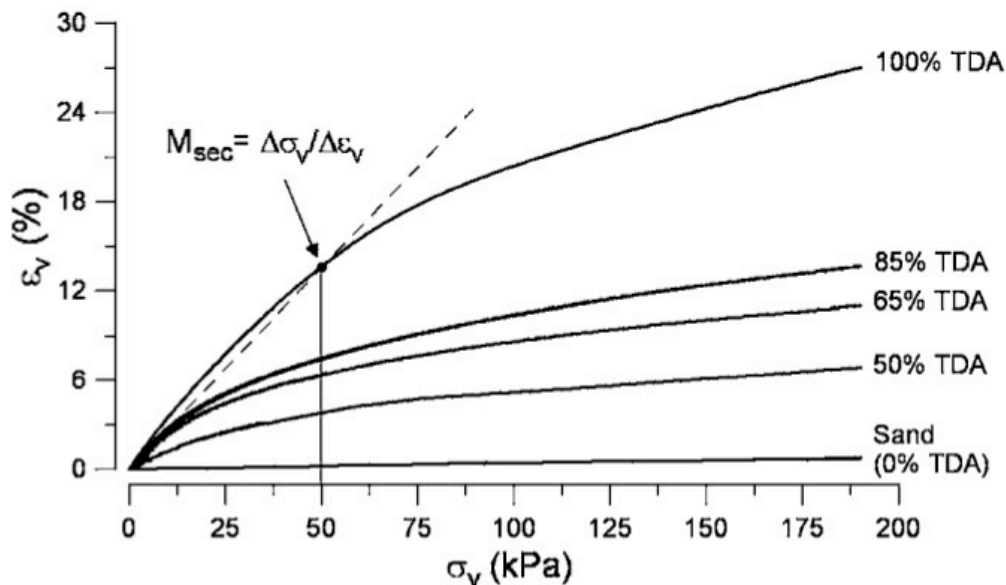


Figure 2.15: Vertical strain vs normal stress for TDA specimens (Wartman et al. 2007)

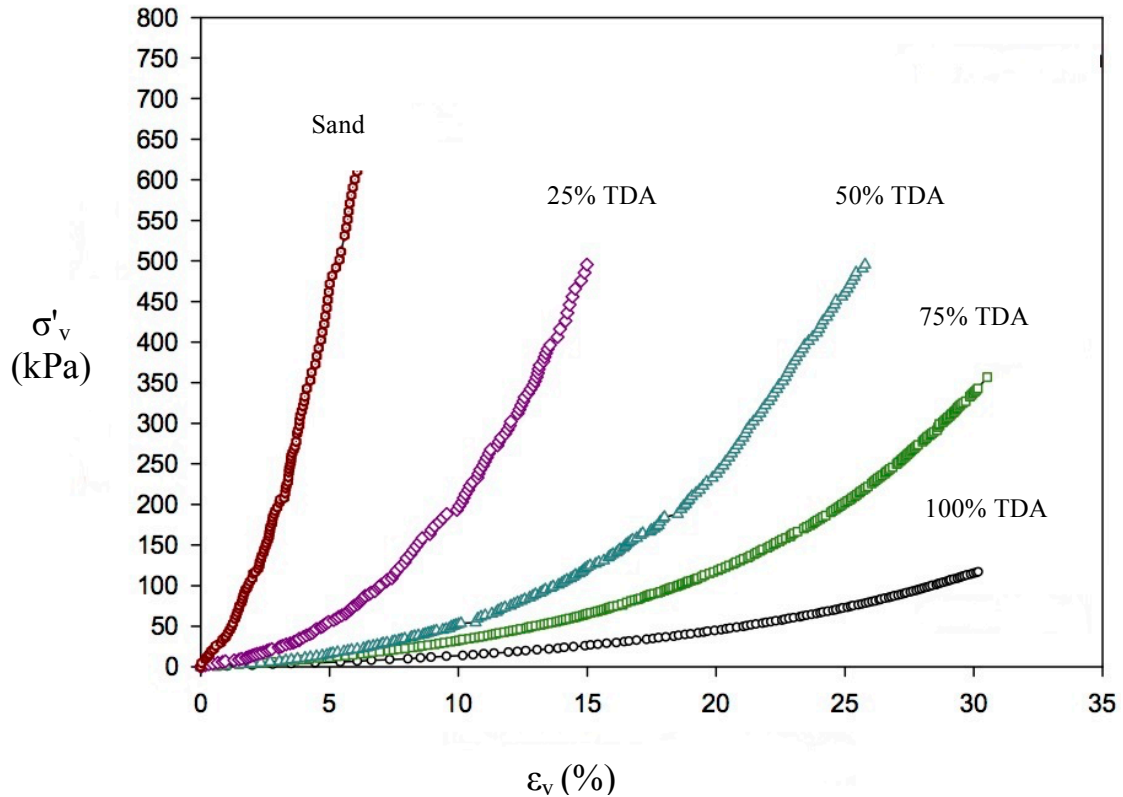


Figure 2.16: 1-D compression test results for TDA specimens (Celis and Pando 2008)

2.4.5 Long Term 1-D Compression Characteristics of TDA Materials

Regarding long term compression of TDA materials and TDA /sand mixtures, laboratory tests have been carried out by Tatlisoz et al. (1997), (Humphrey et al. 1993), Wartman et al. (2007), and Celis (2008), among others. These laboratory studies all showed that TDA materials exhibit high long term compressibility and creep. For example, Wartman (2007) investigated the long terms compressibility behavior of TDA on specimens subjected to 35, 80 and 192 kPa under laterally restrained conditions using the same odometer apparatus as in the short term 1-D compression tests described in 2.44. Figure 2.17 show tire chips materials tested under a vertical stress of 80 kPa.

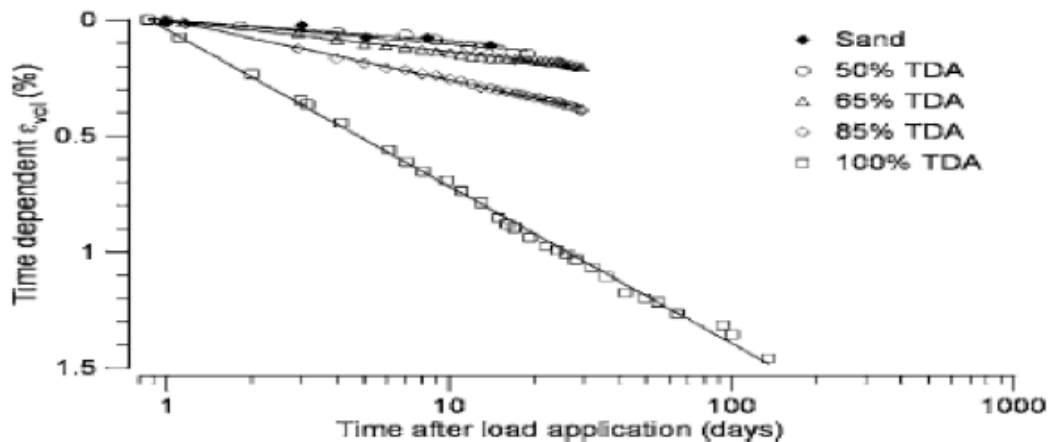


Figure 2.17: Time dependent volumetric strains vs time for Tire chip-sand mixtures at $\sigma_v = 80$ kPa (Wartman et al. 2007)

Celis and Pando (2008) carried out creep odometer tests on crumb rubber TDA ($D_{max} = 4.75$ mm) for applied periods of time between 38 and 71 days. Constant vertical stress levels of 25, 50, 100 and 200 kPa. Figure 2.18 shows the time dependent volumetric strains for this study at a constant vertical stress of 50 kPa.

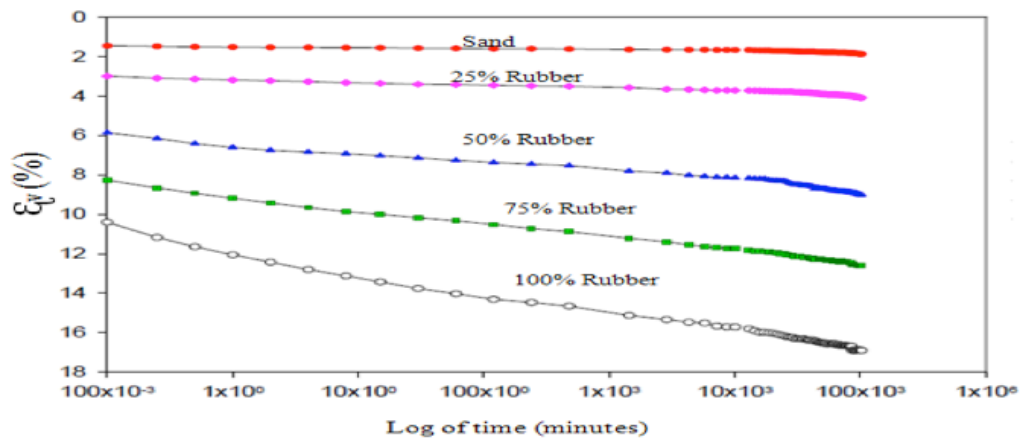


Figure 2.18: Time dependent volumetric strains vs time for different TDA contents (adapted from Celis 2008)

From Figures 2.17 and 2.18, the long term-compressibility of TDA materials seems to be an important design consideration for samples with TDA contents (by volume) greater than 50%.

2.4.6 Lateral Pressures Generated on Retaining with TDA Backfill Materials

An important aspect for using TDA materials as a retaining wall backfill is the study of the lateral pressures generated by these materials. Tweedie et al. (1988a and 1998b) carried out large scale laboratory experiments using a 4.88m-high instrumented retaining wall. Tests were carried out using three TDA materials ranging in sizes from 38 to 76 mm and under at-rest and active conditions. Figures 2.19 and 2.20 shows the results for active and at-rest conditions respectively.

For this study the authors assumed the lateral induced pressure varied linearly with depth, as typically for conventional backfills. Tweedie et al. (1998b) reported levels of lateral pressures, under active conditions (lateral wall movement of 0.01 H), about 35% lower than those expected for a conventional soil backfill (Figure 2.19). All pressure distributions in this figure correspond to a 35.9 kPa surcharge.

The pressure cells installed in the inside face of the instrumented wall showed that lateral pressures increased if the wall movement was stopped. This was attributed to creep of the TDA backfill. For the three TDA materials tested, and for the particular wall dimensions and test setup, the authors found that active conditions were achieved when an outward rotation of the top of the wall reached about 2.2 degrees (equivalent translation of about 0.04H). The observed failure plane was between 61 and 70 degrees with respect to the horizontal. The authors estimated an equivalent active lateral earth pressure coefficient of 0.25 (Tweedie et al. 1998).

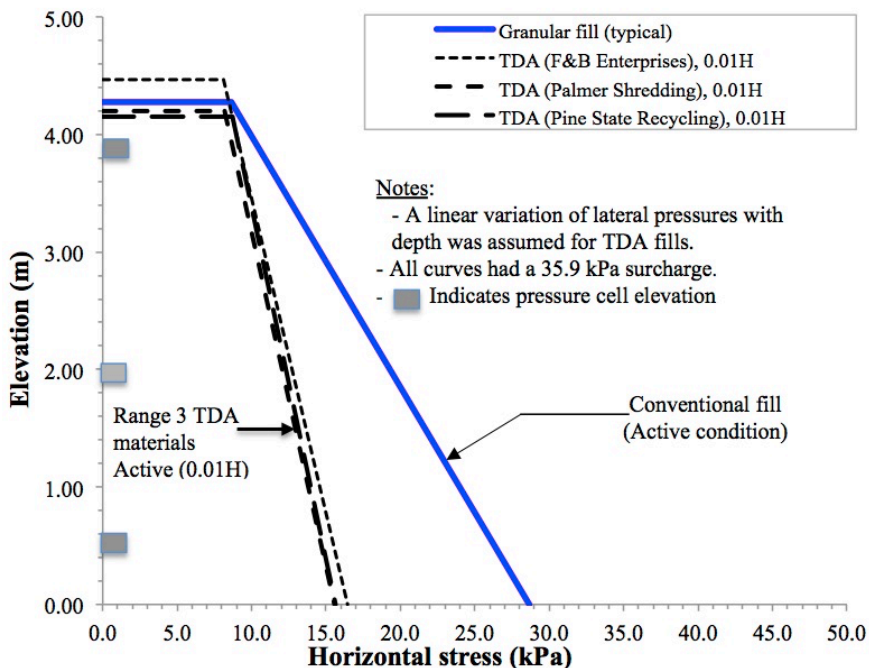


Figure 2.19: Comparison of horizontal stress distributions for three TDA backfill materials under active conditions (adapted from Tweedie et al. 1998b).

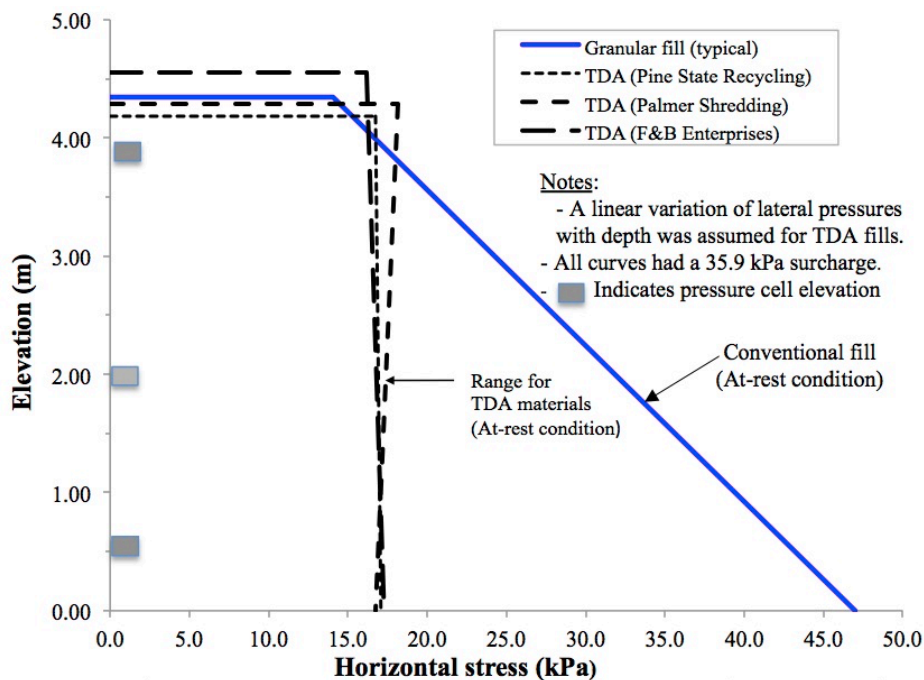


Figure 2.20: Comparison of horizontal stress distributions using TDA backfill materials for at-rest conditions (adapted from Tweedie et al. 1998a).

Tweedie et al. (1998a) report the experimental results for the same instrumented wall and TDA materials but under at-rest conditions. Figure 2.20 shows the deduced lateral earth pressure distributions for the three TDA materials tested under at-rest conditions (again the authors assumed a linear distribution). From the results shown in Figure 2.21, the authors concluded that for their test configuration and TDA materials used, the at-rest horizontal stresses were about 45% lower than the values expected for a conventional granular backfill (Tweedie et al. 1998). The results shown in Figure 2.20 also show an almost constant variation of the at-rest lateral pressures with depth for the TDA backfills. This constant variation is related to the compaction and surcharge load.

To further investigate this area, an exploratory experimental study was carried out at the University of Puerto Rico at Mayaguez using crumb rubber TDA ($D_{50} = 2.5$ mm) and a small plexiglass prototype retaining wall device specially designed and built for the project. Results of this study have been summarized by Celis and Pando (2008), and Garcia-Theran et al. (2014). Acknowledging the presence of scale and side friction effects in the small retaining wall prototype, the authors carried out a series of lateral pressure measurements to further explore the lateral pressure characteristics of TDA backfill materials and TDA-Sand mixtures.

Comparison of prototype wall measurements for rubber crumb TDA backfill and conventional sand with similar relative density are shown in Figures 2.21a and 2.21b for the active and passive conditions, respectively. The results of this exploratory study show similar results as found by Tweedie et al. (1998a and b). For example for the active conditions, shown in Figure 2.21a, we can see that the experiment with the crumb rubber TDA resulted in the lowest equivalent earth pressure coefficient, K_a , of about 0.23

compared to $K_a = 0.32$ for the silica sand backfill (Tweedie et al. 1998b estimated $K_a = 0.25$ from their experiments). The sand and crumb rubber mixture (at 50% by volume) yielded an passive earth pressure coefficient K_p of 5.5 at an inward relative wall displacement of 0.16, however the lateral pressures developed for intermediate wall displacements were slightly smaller than those measured in for the sand case. A big difference was observed for the case of a backfill made of crumb rubber only under passive conditions.

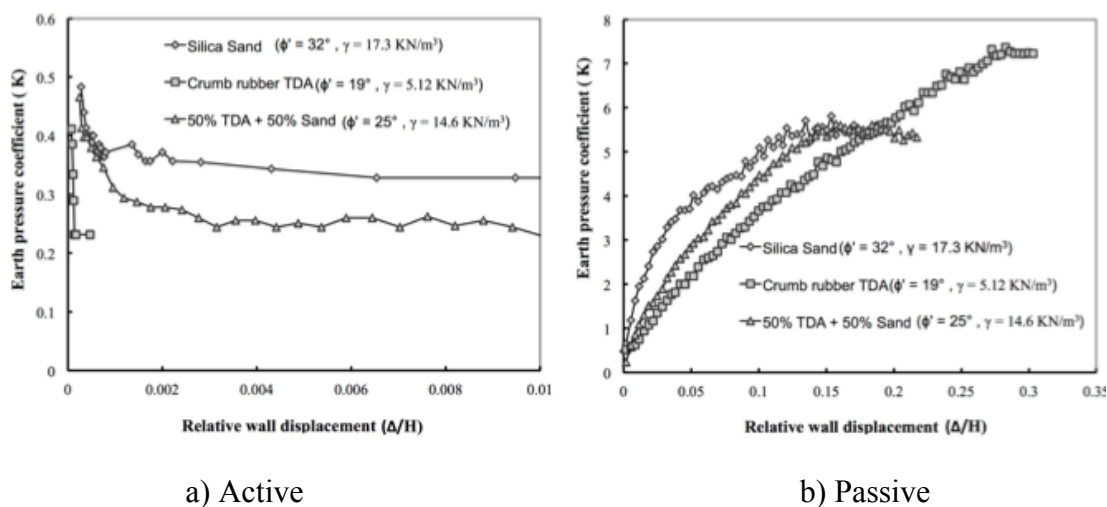


Figure 2.21: Results of TDA lateral Pressures study using retaining wall prototype (Garcia-Theran et al. 2014)

Successful use of TDA backfill in constructed highway projects have been reported by Helstrom et al. (2010) in bridge abutments in Maine (Merrymeeting bridge) and Pennsylvania (Limestone Run bridge) as shown in Figure 2.22 and 2.23, respectively. TDA material was placed in layers overlaid by soil. At the Merrymeeting bridge, the TDA was chosen as a light weight fill solution in Merrymeeting bridge considering that the north abutment was underlain by weak compressible clay; and prior to construction the existing slope had a calculated factor of safety of 1.1 (close to failure). Cell pressures

were installed to measure the horizontal pressures exerted by TDA, and based on the massive nature of the abutments and the fact they were supported on pile foundations, horizontal deflections were expected to be less than 1% of the abutment height and at-rest conditions were generally anticipated (Helstrom et al. 2010).

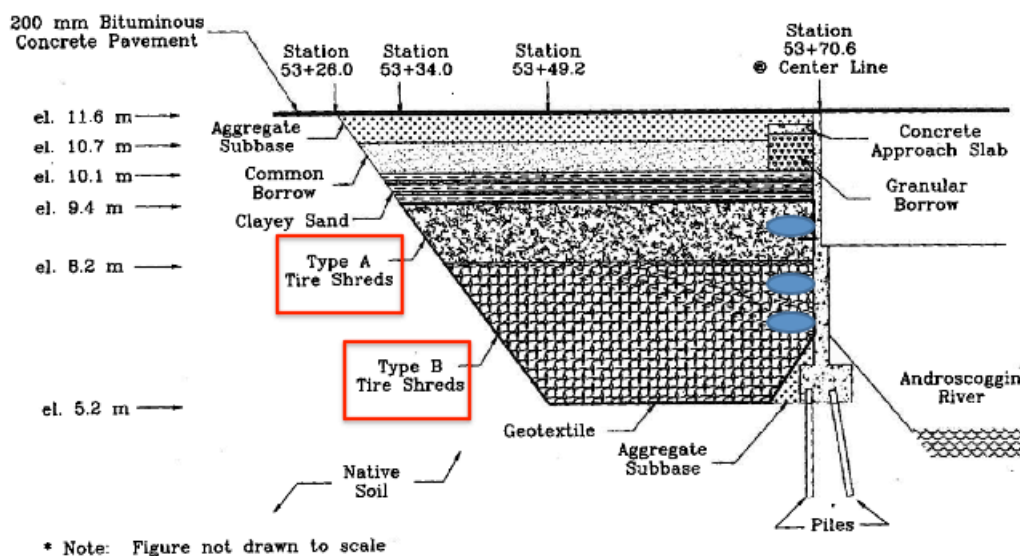


Figure 2.22: Merrymeeting bridge north abutment as built (Adapted from Helstrom et al. 2010)

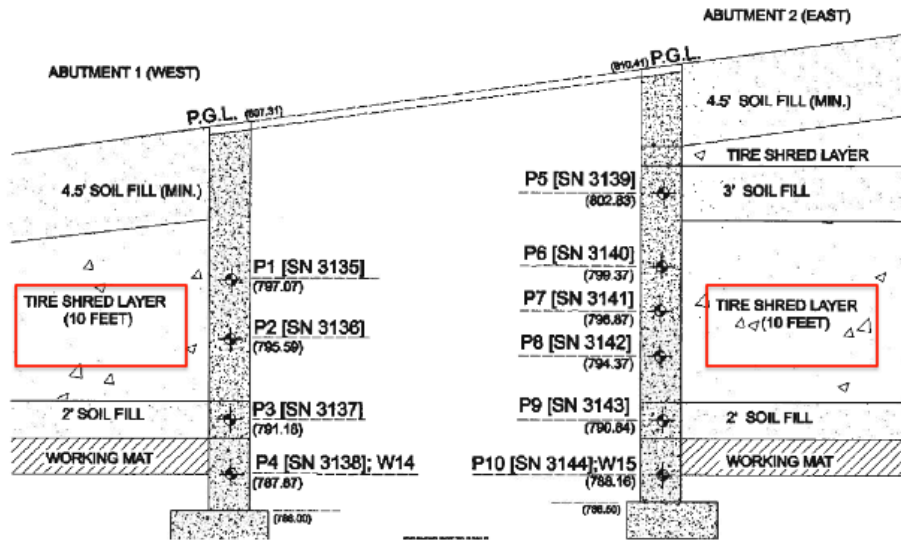


Figure 2.23: Limestone Run bridge abutment as built (Adapted from Helstrom et al. 2010)

Helstrom et al. (2010) compared lateral pressure measurements with the results reported by Tweedie et al. (1998). Figures 2.24 and 2.25 show the measured horizontal stress from the sensors installed in TDA layers for at-rest and active condition, respectively. Acknowledging the fact that there is considerable scatter among the data points, the authors considered the results are reasonable well when using an earth lateral pressure coefficient $\left(k = \frac{\sigma'_h}{\sigma'_v}\right)$ equal to 0.3. This approximate value was deemed reasonable for both cases of at-rest and active lateral pressure conditions.

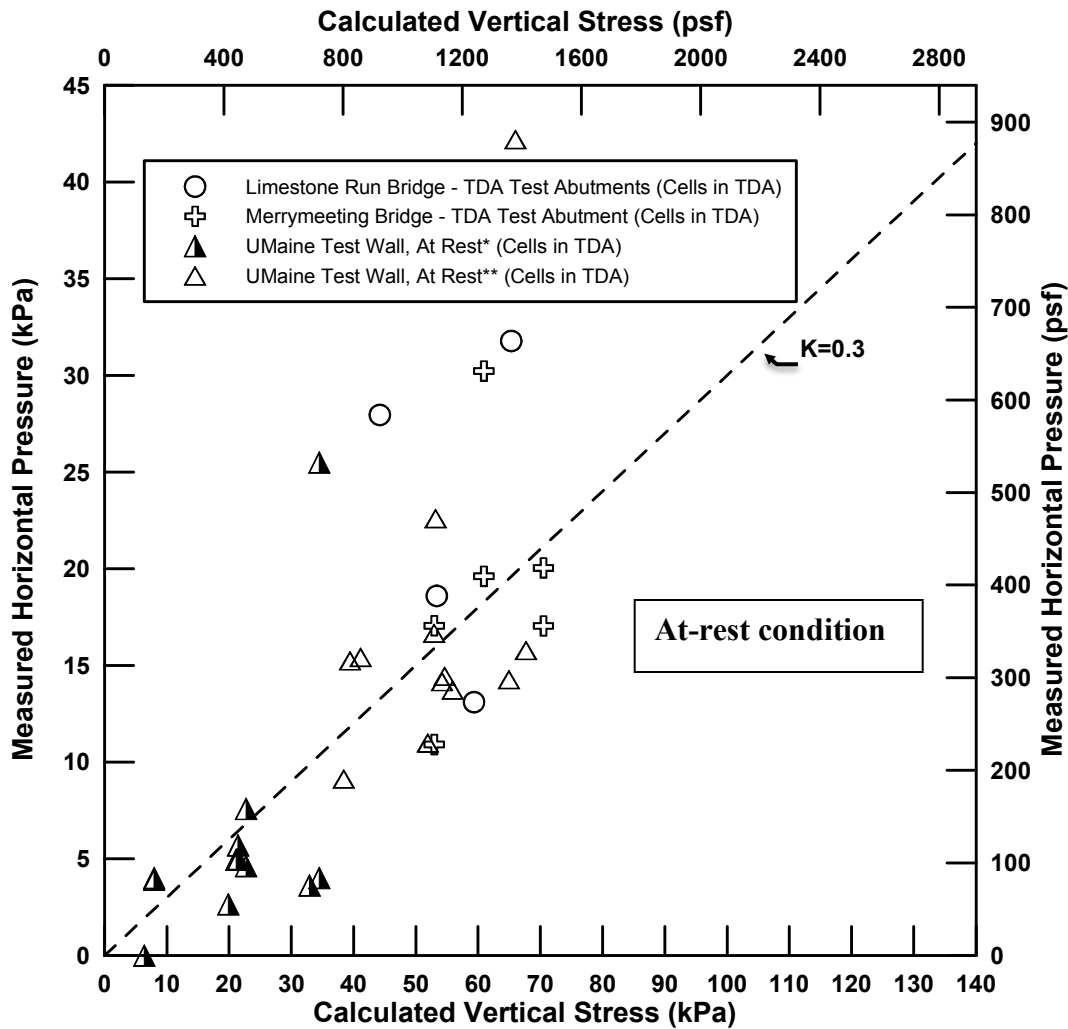


Figure 2.24: Measured horizontal pressure versus calculated vertical stress in TDA layers for at-rest conditions (adapted from Helstrom et al. 2010)

2.4.7 Permeability and Leaching Characteristics

Permeability and leaching characteristics are not within the scope of this research. However are important for actual retaining wall design since backfills usually require good drainage conditions and must not pose environmental risks related to their leaching characteristics. Several authors (Cecich et al. 1996; Collins 1997; Reddy and Marella 2001) have reported measured permeability values of TDA materials and it has been found that these materials exhibit high hydraulic conductivity which make them a promising selecting choice for drainage applications. Reported values range from 0.0005 to 59.3 cm/s and it has included studies using TDA and TDA/sand mixtures. The wide range in permeability is attributed to the variability in sizes availability and normal stress. Table 2.4 shows hydraulic conductivity values reported in the literature.

Table 2.4: Coefficients of permeability for TDA materials

Reference	% TDA by weight	TDA Size (mm)	Unit weight (kN/m ³)	Coefficient of permeability (cm/s)
Cecich et al. (1996)	100	10	5.6 to 6.1	0.033 to 0.034
Masad et al. (1996)	100	4.57	6.19	0.0005
Collins (1997)	100	30	5.35	0.00685 at 30 kPa 0.00584 at 160 kPa
	53	30	10.82	0.00548 at 20 kPa 0.0044 at 160 kPa
Reddy and Marella (2001)	100	2 to 381	2.45 to 8.5	0.01 to 59.3

Leaching studies has been carried out motivated by the environmental hazards the TDA leachate could potentially produce in the groundwater quality. Most of the TDA related research indicates that water permeating through this material will not be adversely contaminated (Aydilek et al. 2006; Humphrey and Katz 2001; Humphrey and

Swett 2006; Liu et al. 1998). For example, Humphrey and Swett (2006) carried out a comprehensive literature review of US EPA related to water quality and environmental toxicology effects of TDAs. This literature review found that previous studies on TDAs have consistently reported limited effects on drinking water quality and fresh water aquatic toxicity for a wide range of applications including lightweight backfill for walls. This study indicated that TDAs are unlikely to increase the concentration of substances with primary drinking water standards above those naturally occurring in the groundwater. However, Humphrey and Swett (2006) indicate that it is likely that TDA will increase the concentration of iron and manganese, but the data indicates that these elements have limited ability to migrate away from the TDA installation. Another concern is that in severe conditions, leaching of metals can occur due to exposure of the metal reinforcements present in the tire shreds (O'Shaughnessy and Garga 2000). Under such conditions, zinc is often used as an indicator that leaching has occurred (Collins et al. 1995; Vashisth et al. 1998).

2.4.8 Spontaneous Combustion or Self Heating

Humphrey (1996) reported internal combustion at three TDA embankment fill projects located in Ilwaco, WA, Garfield County, WA (Figure 2.26); and Glenwood Canyon, CO. All three projects presented serious self-heating reactions within 6 months of construction completion (Humphrey 1996). Unfortunately these cases of self-burning of tire shred embankments has significantly impacted their widespread use. The use of tire shreds in civil engineering applications was reduced from 15 million to 5 million tires after the reports of tire burning at the two projects in the state of Washington

(Nightingale and Green 1997). The authors indicated that the negative publicity from these events adversely affected 5 years of positive experience.



Figure 2.26: Spontaneous combustion in SR 100, Ilwaco, Washington (Baker et al. 2003)

One of the key factors favoring spontaneous combustion, identified by Humphrey (1996) and Nightingale and Green (1997), is the use of very thick layer of shredded tires. Based on these forensic investigations, the presence of pyrolytic reactions; thermochemical decomposition of a material at elevated temperatures, were identified as leading to burning of TDAs, but the exact cause of reaction is debatable. Nightingale and Green (1997) suggested that one or a combination of the following conditions could trigger the pyrolytic reaction:

- 1) Exothermic steel oxidation of the beads and steel belts,
- 2) Microbial decomposition of the tire materials, and
- 3) Chemical oxidation of the fine tire particles.

Humphrey (2004) reported that the occurrence of spontaneous combustions of these three case histories was caused by oxidation of exposed steel belts and freshly cut rubber pieces. Humphrey (2004) proposes to minimize the use of small TDA sizes (recommend using sizes larger than 1.5 inches), avoid or limit the presence of steel belts, and limiting the thickness of TDA layers to 3 m (10 ft), as well restricting the access of water and air to the TDA layers. The author indicates that oxidation of 3.4% of the steel fragments present in the TDA can raise the temperature by about 10° C. The oxidation of the rubber of the TDA can also raise the temperature of the fill. Humphrey (2004) indicates the existence of a hypothesis where the rubber polymer chains are severed during the cutting process and that freshly cut rubber surfaces must oxidize to return to chemical equilibrium. This factor needs to be further investigated but would indicate that smaller TDA sizes would be more prone to combustion given the larger proportion of cut surfaces compared to larger TDA materials.

Some authors (Tandon et al. 2007; Yoon et al. 2006) have monitored the variation of temperature in the field especially in embankment applications. For example, in a study carried out by Yoon, et al. (2006), the temperature variation inside a embankment, constructed using 50/50 mixture by volume of tire shreds and sand, was monitored at the center for one year. Figure 2.27 shows the temperature variations observed in this study. Only in the four months around winter time, higher temperatures inside than outside the embankment (outside air temperature) were observed. The higher embankment temperature was due to the insulation effect of the fill material. However, the difference between the temperature inside the embankment and the outside temperature was small. The highest temperature observed within the embankment during the monitoring period

was 20 C. This clearly shows that there is no evidence of exothermic reactions. This data confirms the idea that if tire shreds are combined with soil, internal exothermic reactions do not seem to be a concern. Similar results were reported by Tendon et al. (2007).

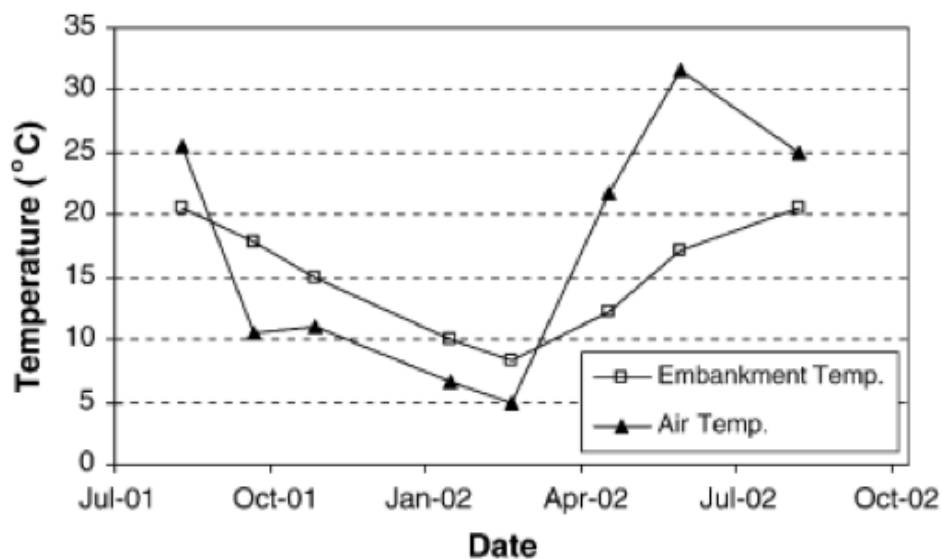


Figure 2.27: Variation of temperature inside an embankment with TDA (Yoon et al. 2006)

Although, no combustion concern was observed in Yoon et al. (2006), the authors indicate that in order to evaluate exothermic reactions that can cause heating within embankments for a broader set of conditions; more laboratory tests should be conducted since the results might vary according to the site temperature and construction techniques.

Moo-Young et al. (2003), have studied the thermal stability of tired shreds in laboratory studies using thermal gravimetric analyses (TGA) experiments. TGA experiments involve a thermal analysis technique used to measure changes in the weight of a sample as a function of temperature and/or time. TGA is commonly used to determine degradation temperatures, residual solvent levels, absorbed moisture content,

and the amount of inorganic noncombustible filler in material compositions (Moo-Young et al. 2003). Figure 2.28 shows the TGA derivate weight curves for TDA sample, tire sample + fiber, and tire sample + fiber + steel wire. According to Moo-Young (2003), it seems that the sample with fibers lost more weight, suggesting that some components of the rubber evaporate first, but the majority of components is more stable. The fibers in the rubber matrix have good stability up to 311°C, but then a sudden decomposition begins which involves large parts of fiber. In the analysis of the sample with steel wire, the steel has a large contribution to the total sample weight. This explains the greater stability of the tires with steel in comparison to tires with fiber.

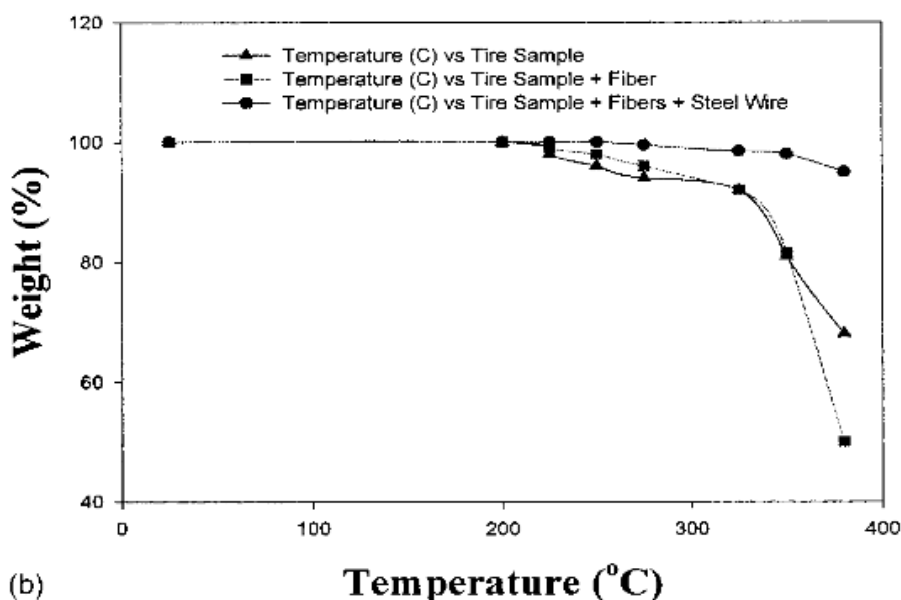


Figure 2.28: TGA derivate weight curves (adapted from Moo-Young 2003)

2.5 Analytical Studies of TDA Fill Materials

Lee et al. (1999) carried out finite element analyses of a retaining wall model using tire-sheds TDA as backfill material. For the analyses these authors used the FE commercial software ABAQUS. TDA was modeled using the Duncan and Chang (1970) hyperbolic constitutive model commonly used for conventional soils. The authors used the TDA hyperbolic model parameters obtained by Gharegrat (1993) for the retaining wall model in order to represent better the behavior of the material used in the scale model used experimentally by Tweedie et al. (1998). Although, rubber-sand backfills were not used in the finite element analyses, the authors determined rubber-sand mixture hyperbolic model parameters based on consolidated drained triaxial test data (Lee et al. 1999). The parameters used for the retaining wall model and those obtained for rubber-sand mixture (40% TDA by weight) are summarized in Table 2.5

Table 2.5: Parameters used for the finite element analyses of the retaining wall (adapted from Lee et al. 1999)

Parameter	Meaning	Tire shreds TDA	TDA/sand mixture
$\gamma(\text{kn/m}^3)$	Unit weight	6.3	12.5
K	Modulus number (loading)	33.5	83.7
n	Modulus exponent	1.10	0.47
c (kPa)	Cohesion intercept	7.6	17.5
$\Phi(^{\circ})$	Friction angle	21	42
R_f	Failure ratio	0.61	0.70
K_b	Bulk modulus number	24.8	120.0
m	Bulk modulus exponent	1.09	0.33

The model was a 2D plane strain thus both backfill and wall were modeled using 2-D eight-noded finite elements with four integration points inside the element.

Figure 2.29 shows the computed earth pressures variation as a function of depth. For comparison, this figure also shows the experimental data published by Tweedie et al. (1998a). The predicted values of horizontal pressure found by Lee et al. (1999) overestimated the measured values on average by 20 and 30%. This difference was attributed by the authors due to the fact that the hyperbolic model is not ideal for modeling materials undergoing large deformations such as in these experiments since it was developed based on conventional soil materials. Furthermore, authors noted that the hyperbolic model was not able to reproduce the strong interlocking observed in the tire shred TDA (Lee et al. 1999).

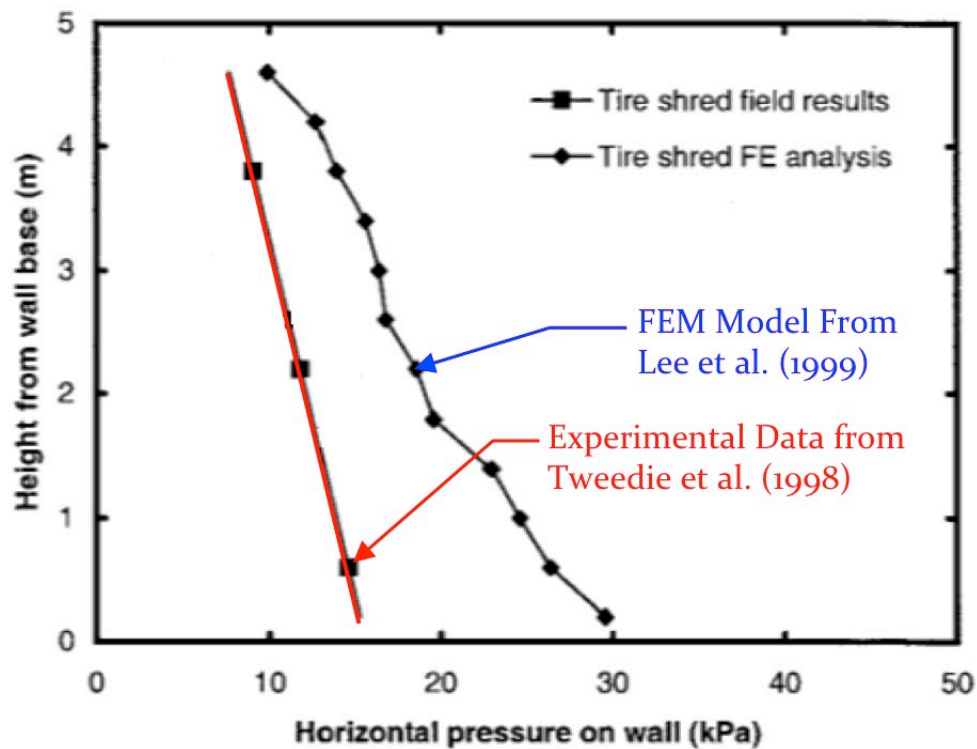
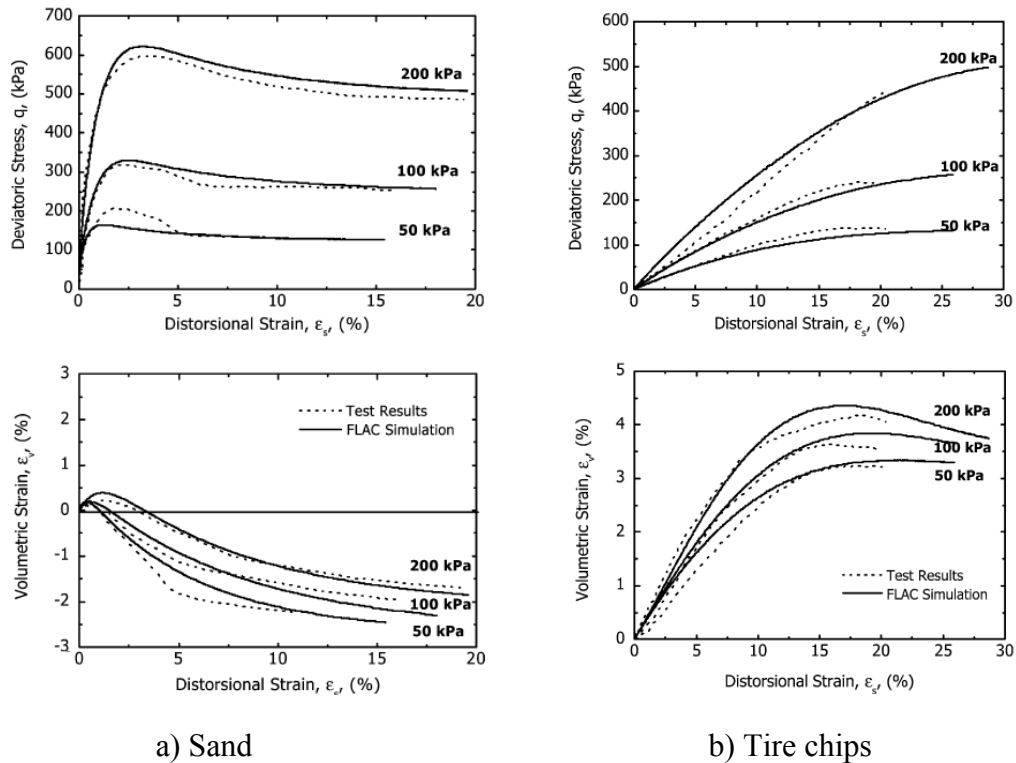


Figure 2.29: Variation of earth pressure with depth from Lee et al. (1999)

Youwai et al. (2004) performed numerical analyses of drained triaxial compression tests on samples of rubber tire chips. The numerical analyses were implemented using the commercial software FLAC (ITASCA 2015). FLAC is a software based on using finite difference analyses, which is capable of performing large strain nonlinear analyses using a number of built-in constitutive models. For rubber tire chip mixed with sand, the state-dependent constitutive model developed by Li and Dafalias (2000) was implemented in order to calibrate their models (Li and Dafalias 2000).

The simulations were done using the unit cell. The unit cell was set to be an axisymmetric stress condition. Boundary conditions were set to fix displacement in vertical direction at the top and the bottom of the unit cell to simulate an equal strain loading condition (Yowwai and Bergado 2004). In the right side of the cell, constant pressure was applied to simulate the confining pressure in the triaxial test. Comparisons between the simulations and the triaxial test results of sands, and rubber tire chips are illustrated in Figure 2.30. The results showed that the model captures the overall strength and deformation characteristics of the mixed materials. However, at low confining pressures, simulations underestimated peak strength (Yowwai and Bergado 2004).



a) Sand
b) Tire chips
Figure 2.30: Comparison between drained triaxial compression tests and numerical simulation (adapted from Youwai et al. 2004)

Valdes et al. (2008) carried out numerical analyses of 1-D compression experiments of TDA materials using discrete element methods (DEM). The DEM model method represents the material as an assemblage of independent particles interacting with one another. DEM numerical simulations for rubber and sand-rubber mixtures were performed by Valdes et al. (2008). The emphasis of this study was placed on studying the load-deformation behavior and selecting appropriate parameters for the discrete element modeling of sand-rubber with relevance to the use of compressible particulate systems for filtration control. Experimental tests were conducted under 1-D compression tests and the results were used to calibrate the discrete element model. In this study, the authors defined the parameter F_R as the volume fraction of rubber particles with respect to the volume of solids in the mixture (e.g., a specimen with $F_R = 1$ is composed of

rubber particles only). Specimens were loaded in 1-D compression (sample mold diameter equal to 50.8 mm, height equal to 20 mm) using a standard loading frame. The discrete element simulations were performed using the commercially available DEM program PFC-2D for F_R values of 1 and 0.6. An approximation of the Hertz-Mindlin contact model was used in the simulations with a strain-dependent shear modulus and a stress-dependent contact friction values obtained from the literature. The experimental and numerical simulations results are presented in Figure 2.31. According to the authors the macroscale agreement between the experimental and numerical results is reasonable given the drawback of 2-D simulations. The $F_R = 1$ simulation captures the nonlinear stress-strain relationship including the peak very well. Significant residual strains post-unloading are observed due to the interlocking effects and side friction promoted by the rigid boundary conditions (Valdez and Evans 2008).

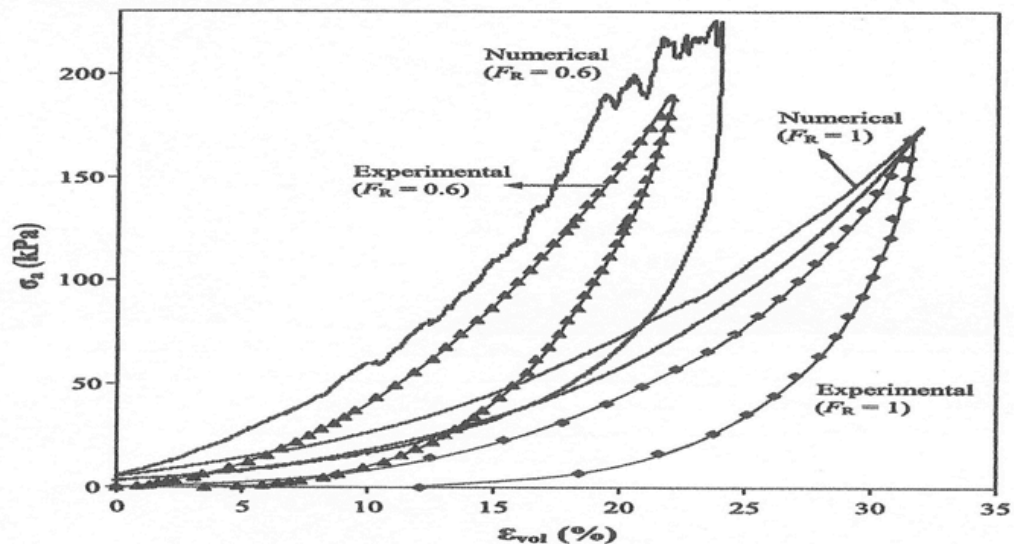


Figure 2.31: Comparison of global response for experimental and numerical 1-D loading tests (adapted from Valdes et al. et al. 2008)

2.6 Literature Review Summary

A literature review covering topics relevant to this research and others of environmental concern was carried out in order to identify gaps and topics where there are previous studies but more experimental and analytical results are needed. Few studies have been carried out regarding the generation and magnitude of TDA lateral pressures on retaining structures. The data available to the best knowledge of this author corresponds to important studies using scale models and field built retaining structures using large tire shreds as backfills. However, experimental lateral pressures data is scarce and more data is needed to clarify issues such as if conventional earth pressure theories applies to TDA materials. Additionally, lateral pressures using TDA/Soil mixtures backfills seems not to be available in the literature. Scale models and field data are either expensive or rarely available. Therefore, the use of other most cost effective scale models is needed to provide more TDA lateral pressures data.

In terms of engineering properties and deformation characteristics, stress-strain behavior and shear strength characteristics of TDA materials have been broadly studied for TDA sizes above 4.75 mm. Few studies have focused on the use of TDA granulated rubber with sizes smaller than 4.75 mm. Additionally, the majority of the studies have focused on TDA behavior under drained conditions. This research examines the behavior of TDA for both drained and undrained conditions to evaluate pore pressure generation in TDA. Most testing techniques have focused on Triaxial and direct shear. This research includes triaxial testing but also simple shear techniques to study the shear strength characteristics of TDA.

CHAPTER 3. INVESTIGATION OF TDA LATERAL PRESSURES ON RETAINING STRUCTURES BY MEANS OF CENTRIFUGE TESTING

3.1 Introduction

This chapter presents and discusses results of the centrifuge geotechnical experimental program carried out as part of this research. The chapter starts with a brief overview of basic centrifuge modeling concepts for the reader who is not familiar with this technique. Then, a description of the materials tested and the methodology followed to build the models is provided. The chapter also includes the experimental results obtained from the four series of centrifuge tests as follows: i) at-rest condition test for TDA granulated rubber and Nevada sand; ii) at-rest condition for TDA/sand mixture tests acknowledging the limitations and challenges faced during the mixture process; and iii) lateral pressures on two cantilever retaining wall centrifuge tests using Nevada sand alone and a TDA/sand mixture as backfills. Table 3.1 summarizes the tests carried out during this research and their purpose. The chapter ends with a discussion of the movement mechanism observed in the retaining structure during the spinning process.

Table 3.1: Centrifuge tests program

Model	Test Condition	Backfill material	Purpose/Comments
1	At rest Condition. Rigid box was divided into two parts which allowed to test two different backfills at the same time (See Fig. 3.4)	100% sand and Sand/TDA mixture (50/50 by volume)	Examine lateral pressure distribution and magnitude at rest condition.
2		Sand/Crumb rubber mixture (50/50 by volume) and 100% TDA	Same purpose as Model 1. Sand/Crumb rubber mixture (50/50) was repeated to check results. Effect of time in TDA
3	Retaining wall (See Fig. 3.5)	100% Sand	Assess magnitudes and distribution of lateral pressure along inner face of retaining wall. Wall movement was monitored during the tests.
4		Sand/TDA (50/50 by volume)	Same purpose as Model 3

3.2 Concepts of Centrifuge Modeling

Geotechnical centrifuge modeling is a powerful technique for testing soil and soil-structure interaction under static or dynamic loading conditions. It was first proposed by Edouard Phillips (1869), and the first mentioned of applied centrifuge modeling in the literature appears to be that of Philip Bucky (1931), working at the University of Columbia in New York (Craig 2002). It is based on the principal of testing a small model under a higher gravitational field (N_g) that results from the centrifugal accelerations when the model is spun at a high rpm. A number of geotechnical research centers in different countries around the world have acquired the capability of geotechnical centrifuge modeling, as it offers the ability to create fairly realistic full-scale stress states

with uniform and measurable soil properties. Centrifuge modeling is considered a cost-effective method for modeling and predicting the properties and behavior of soil deposits (Urbilla 2007).

The attractiveness of centrifuge model is related to being able to capture behavior that is sensitive to stress levels. Small-scale models at 1g would not capture field stress levels for many problems. If small-scale models at 1g are tested, the corresponding stresses and strains will be quite small and therefore incorrect stiffness of the soil might be invoked (Madabhushi 2004). For example, a concrete dam 40 m high can generate a vertical stress of approximately 960 kPa, while a 1/40th scale model of this dam (1m high) in laboratory will generate a vertical stress of only 24 kPa. Clearly, the soil beneath the model dam will respond with much higher stiffness under this low vertical stress compared to the soil below the real dam, which is under much higher stress. Based on this situation, it is important in geotechnical research that prototype stresses and strains are correctly generated in small-scale models in order to get the right stiffness and engineering properties of soils; this can be achieved by centrifuge modeling (Madabhushi 2004).

The main principle in centrifuge modeling is that a 1/N model subject to a gravitational acceleration of Ng will be subjected at comparable points in the soil mass to the same stresses as the prototype. Under such increased gravitational field of Ng , N is the scaling factor and g is the acceleration of gravity (Urbilla 2007). For example, consider a rectangular block of dimensions $L \times B \times H$ that has a mass M standing on a soil bed as shown in Figure 3.1.

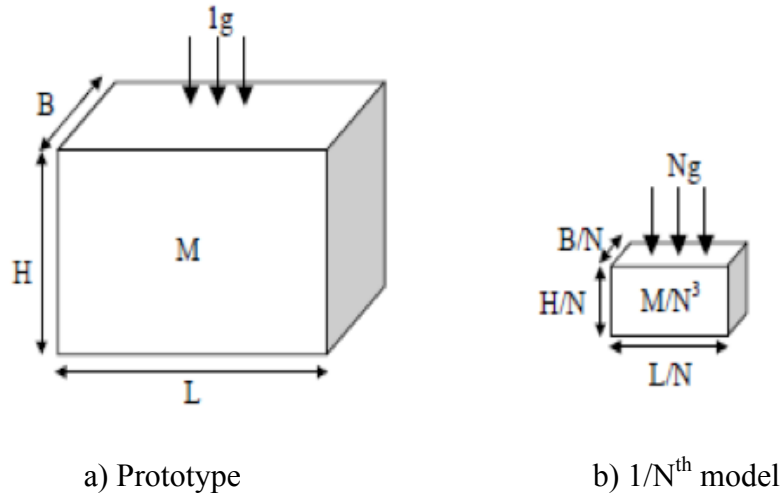


Figure 3.1: Scaling of physical models (Madabhushi 2004)

The vertical stress and strain on the soil imposed by this block would be:

$$\sigma_v = \frac{M \times 1g}{L \times B} \quad (3.1)$$

$$\varepsilon_l = \frac{\Delta H}{H} \quad (3.2)$$

Now, consider a 1/Nth scale model of the rectangular block as seen in Figure 3.1b. Each of the dimensions of the block is scaled down by a factor N. Then, the mass of the scaled model would be $\frac{M}{N^3}$. This scaled model is subjected to a gravity field Ng that has been also increased by a factor N compared to the normal earth's gravity field g. The vertical stress in the scaled model now would be:

$$\sigma_v = \frac{\frac{M}{N^3} \times Ng}{\frac{L}{N} \times \frac{B}{N}} = \frac{M \times g}{L \times B} \quad (3.3)$$

It can be seen from equation 3.3 that the vertical stress imposed in the scaled model is the same as that in equation 3.1 (full-sized prototype model). Similarly, the strains in the scaled model can be obtained as:

$$\varepsilon_l = \frac{\frac{\Delta H}{N}}{\frac{H}{N}} = \frac{\Delta H}{H} \quad (3.4)$$

In general, the main principle in centrifuge modeling is that a 1/N model subject to a gravitational acceleration of N x g will be subjected at comparable points in the soil mass to the same stresses as the prototype, where N is the scaling factor and g is the acceleration of gravity. Arulandan et al. (1988) have found that using the same soil type i.e. granular or cohesive, in the prototype and the model will preserve the stress-strain relation at equivalent points in model and prototype. A complete set of scaling relationships governing various geotechnical problems can be developed by dimensional analysis or through a thorough analysis of the physics of the problem. A list of common centrifuge scaling relations is given in Table 3.2 (Whitman and Arulanandan 1985).

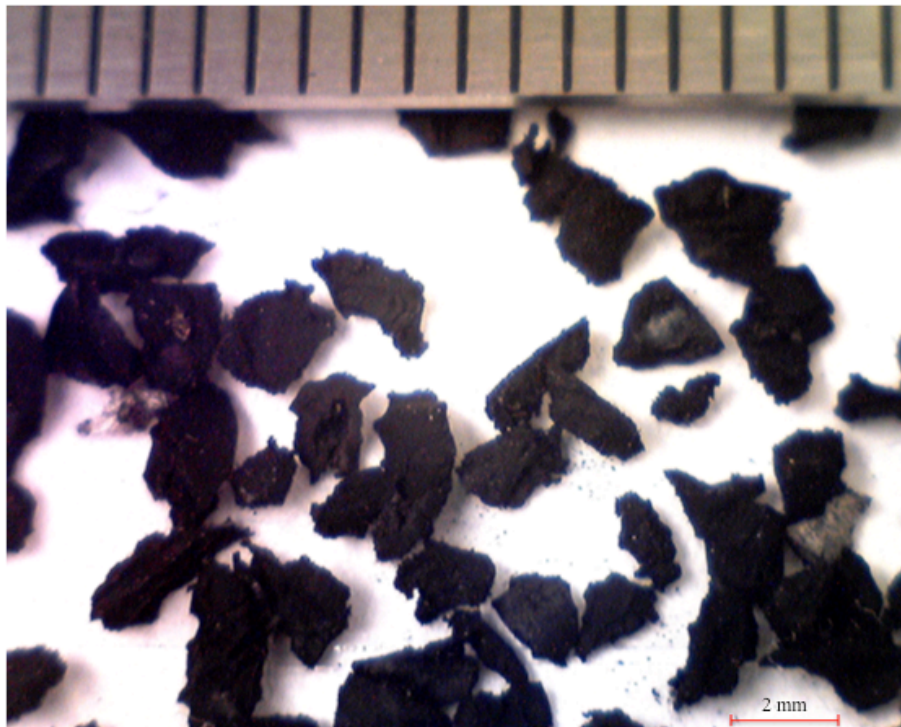
Table 3.2: Centrifuge scaling relations (Whitman and Arulanandan 1985)

Quantity	Prototype Scale	Centrifuge Model (N*g)
Length	1	1/N
Area	1	1/N ²
Volume	1	1/N ³
Acceleration	1	N
Dynamic Frequency	1	N
Force	1	1/N ²
Stress	1	1
Strain	1	1
Dynamic Time	1	1/N
Time (Consolidation)	1	1/N ²
Displacement	1	1/N
Energy	1	1/N ³

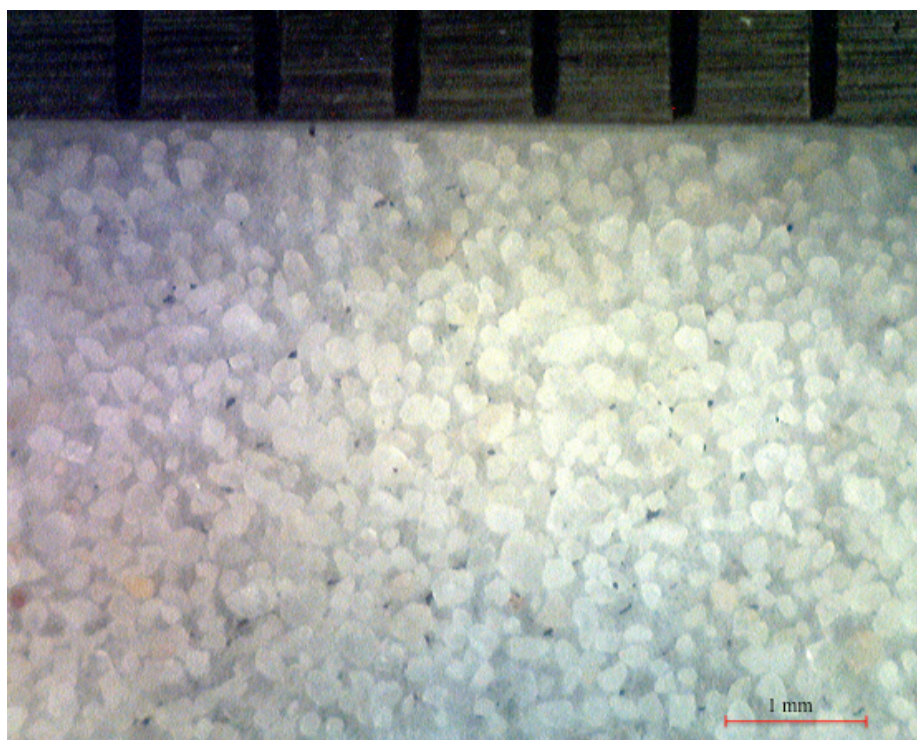
Particles sizes are not conventionally scaled in centrifuge tests as indicated in Table 3.2 which is considered one of the main limitations of the test. Grain size particles are not scaled because this would lead to the use of geomaterials that are totally different in their classification and mineralogy as required in the prototype. An appropriate representation of the stress-strain behavior of the material would not be feasible. For example, if a prototype model requires a fine sand with average size particles of 0.4 mm. These particles would have to be represented by fine clayey silts with a particle size of 0.004 mm at 100g (Madabhushi 2015). It is well known that the behavior of clay and sands differ significantly. Therefore, it would be considered erroneous to use clay in centrifuge models to represent sand in the prototype (Madabhushi 2015). For this research, in order to minimize scale effect the finest TDA available was used. Nevada sand is typically used for centrifuge testing due to its fine grain size.

3.3 Materials Tested and Methodology

Two materials were selected for the centrifuge experimental program. A granulated rubber TDA and a fine grained uniform Nevada sand. Photos of both tests materials are presented in Figure 3.2. The TDA material was classified as granulated rubber as per ASTM D6270 with a mean particle size of $D_{50} = 1.20$ mm. The gradation curves for both test materials are shown in Figure 3.3. The test sand used was Nevada sand which is a uniform, sub-rounded fine sand commonly used in centrifuge studies. Table 3.3 summarizes the index properties of the materials. Additional information regarding index properties and microscopic images of both materials can be found in Appendix A.



a) Granulated TDA



b) Nevada Sand

Figure 3.2: Photos of test materials used in centrifuge testing

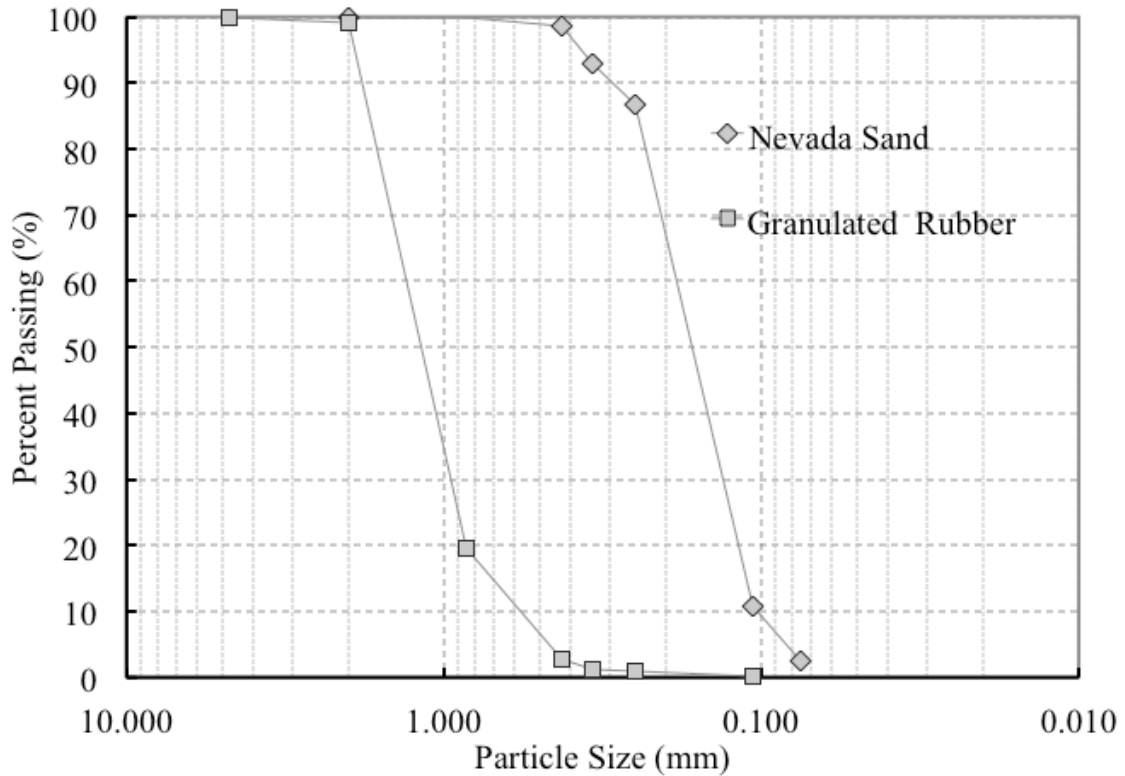


Figure 3.3: Grain size distribution for Nevada Sand and Granulated Rubber TDA material

Table 3.3: Summary of index properties of centrifuge test materials

Parameter	Nevada Sand	Granulated Rubber TDA	Standard
D_{50} (mm) ⁽¹⁾	0.15	1.20	ASTM D 422
D_{10} (mm) ⁽²⁾	0.105	0.70	
D_{30} (mm) ⁽³⁾	0.12	0.95	
D_{60} (mm) ⁽⁴⁾	0.18	1.4	
C_u ⁽⁵⁾	1.7	2.0	
C_c ⁽⁶⁾	0.8	0.90	ASTM D 854
G_s ⁽⁷⁾	2.67	1.15	
γ_{min} ⁽⁸⁾	13.92	4.75	
γ_{max} ⁽⁸⁾	17.04	5.80	ASTM D 4253

Notes : (1) D_{50} : Grain diameter corresponding to 50% of the material being smaller by weight

(2) D_{10} : Grain diameter corresponding to 10% of the material being smaller by weight

(3) D_{30} : Grain diameter corresponding to 30% of the material being smaller by weight

(4) D_{60} : Grain diameter corresponding to 60% of the material being smaller by weight

(5) C_u : Coefficient of uniformity

(6) C_c : Coefficient of curvature

(7) G_s : Specific Gravity

(8) γ_{min} : Minimum unit weight, γ_{max} : Maximum unit weight

3.3.1 Description of the Centrifuge Experimental Program

The primary purpose of the centrifuge experimental program was to generate high quality data on the lateral pressures generated by TDA and Sand/TDA mixture-based retaining wall fill materials. A total of four centrifuge models were performed for this research. The four models were previously listed and described in Table 3.1. Figures 3.4 and 3.5 show the layout of the different centrifuge models. Models 1 and 2 aimed to provide valuable experimental lateral pressures generated by TDA and TDA-Sand mixtures for at-rest conditions. Models 3 and 4 were performed in order to observe the tendencies and magnitudes of lateral pressures on a retaining wall under active conditions.

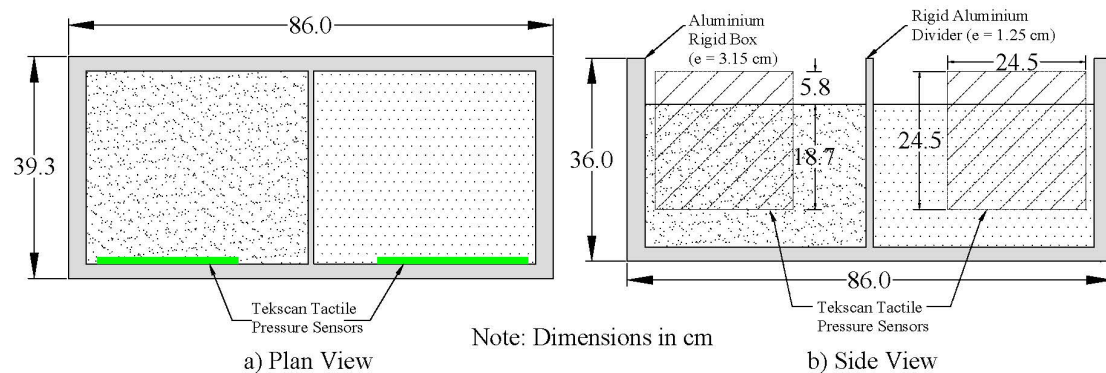


Figure 3.4: Schematic of centrifuge box set up for model 1 and 2

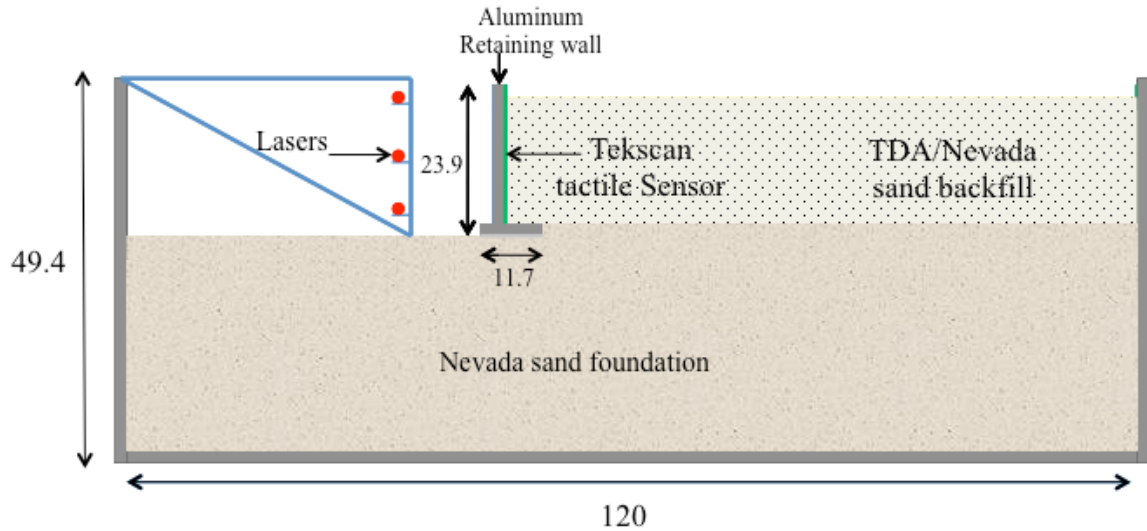


Figure 3.5: Schematic of centrifuge box set up for model 3 and 4 (dimensions in cm)

All centrifuge tests were performed at the 150 g-ton geotechnical centrifuge NEES facility at Rensselaer Polytechnic Institute (RPI). This 150g-ton geotechnical centrifuge has a radius of 2.7 m and can rotate at a maximum speed of 265 rpm which allows subjecting centrifuge models to gravitational fields to up to 150 g. A photo of the centrifuge used is shown in Figure 3.6. This research facility not only offers services to RPI graduate students and faculty but also visiting students and researchers from other states and around the world. Besides the centrifuge room, the facility includes two model preparation rooms, state-of-the art control and teleconference room with plasma screens to monitor models while spinning, and a geotechnical laboratory. More information can be found at www.nees.rpi.edu.

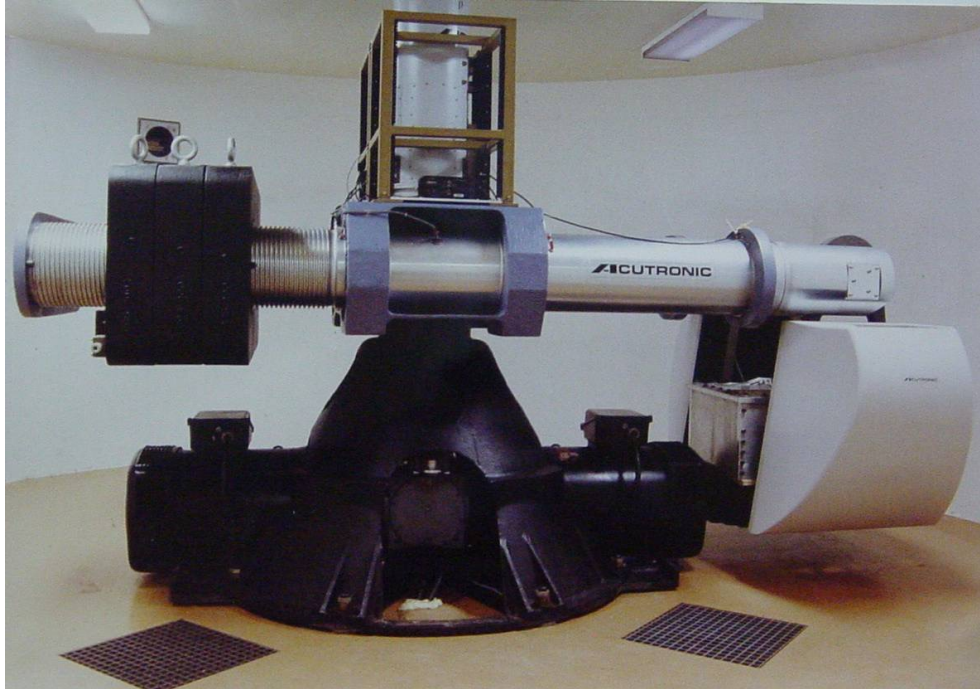


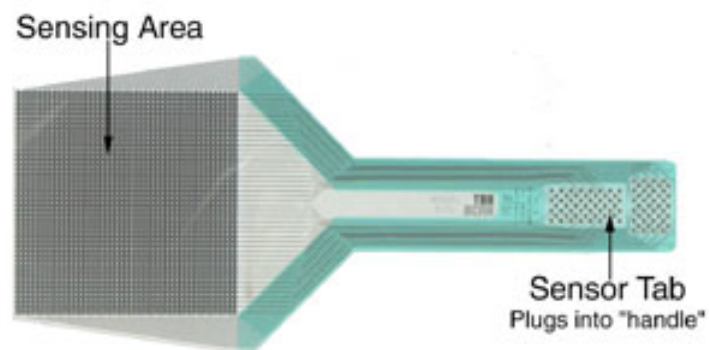
Figure 3.6: 150 g-ton geotechnical centrifuge @ RPI

3.3.2 Model Preparation and Instrumentation

All tests were tested in a dry state which precluded consideration of pore water pressures. The main instrumentation used to measure the generated lateral pressures was a Tekscan force and pressure tactile measurement system. The Tekscan system; fabricated by Tekscan, Inc., is shown in Figure 3.7(a). This sensing film allowed measuring the pressure distribution between the inner face of the retaining wall and the backfill. All pressure data can be obtained using I-Scan software, which can record and saves static pressure data directly to the PC. Every Tekscan Industrial system, including *I-Scan*, uses a specially designed sensor interface electronic called a "handle." The handle connects to the sensor, gathers the data from the sensor, and then processes and sends this data to the computer. The handle connects to the PC via a USB cable. The usefulness and accuracy of the tactile pressure sensors used have been discussed by Palmer et al. (2009).

In this study the authors report errors in the Teskan measured pressures of less than 5% (Palmer et al. 2009).

Displacements in Models 3 and 4 were measured using Keyence laser displacement sensors as shown in Figure 3.7(b). The displacement range of these laser displacement sensors is 100 mm +/- 40 mm. Each sensor consists of a sensor head and an associated controller. The sensor head consists of an infrared semiconductor laser, an in-range stability indicator, and a heavy-duty sensor cable that connects to the controller. Details regarding the different sensor specifications and calibrations can be found in Appendix B.



a) Tekscan tactile sensor pressure to measure lateral pressures



b) Keyence laser displacement sensors

Figure 3.7: Sensors used during centrifuge tests

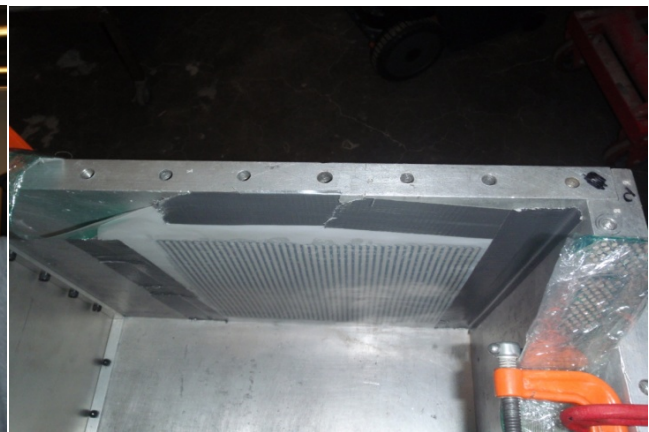
The Tekscan tactile sensor preparation consisted in attaching one Teflon sheet at each side of the sensor in order to avoid or minimize shear effects (Figures 3.8(a) and (b)). Teflon sheets were attached to the sensor using vacuum grease. The laminated tactile sensor was attached directly to the inside face of the wall using duct tape along its perimeter as shown in Figure 3.8 (c).



a) Vacuum grease application



b) Teflon sheets attached



c) Sensor attached to the model container

Figure 3.8: Preparation and placement of the tactile pressure sensors

The weight of each lift or layer of sand, TDA, or TDA/sand mixture was monitored carefully. The test materials were placed in layers of 25 mm (1 inch) thickness. The pluviation process was carried out using a funnel to place the materials backfill. The TDA/sand mixture proportion was 50/50 by volume approximately, which corresponds to 300 grams of granulated rubber TDA per 700 grams of Nevada sand. Segregation tendencies due to the difference in size particle were observed while mixing both materials. TDA/sand mixture for at-rest condition test was repeated in Model 2 in order to confirm results due to the mixing challenges. A photo showing the material placement of a centrifuge model is shown in Figure 3.9. Figures 3.10 and 3.11 show Model 1 (at-rest) and Model 4 (retaining wall) respectively.



Figure 3.9: Construction of centrifuge models in the lab

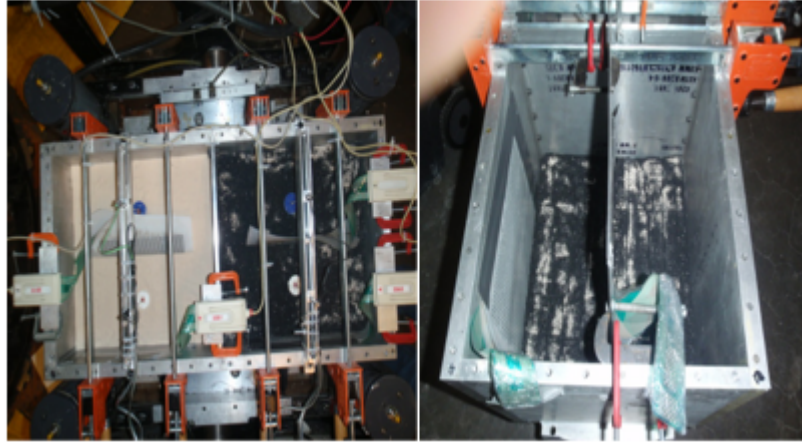


Figure 3.10: At rest lateral pressure test (Model 1)

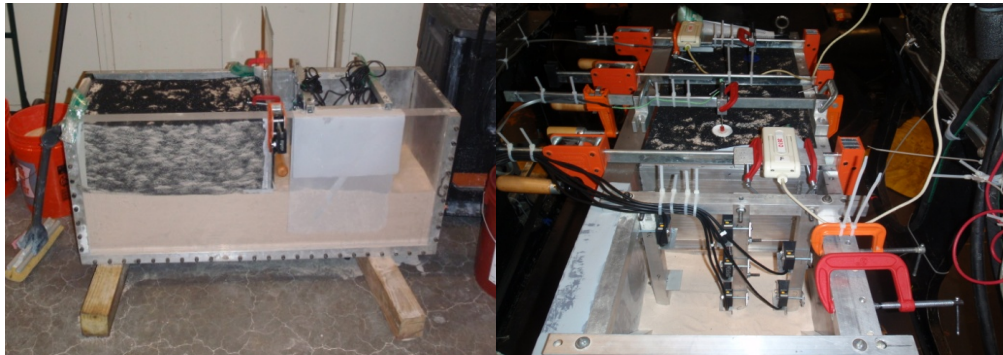


Figure 3.11: Retaining wall centrifuge tests (Model 4)

As can be seen in Figures 3.10 and 3.11, large confining clamps were used to help prevent lateral deformation of the full width of the box as the g level was increasing. For Model 1 (at rest condition) the g level was increased up to 50 g at a velocity of 2.0 g/min, with hold periods of about 20 minutes at 20, 30, 40 and 50 g. The selection of this rate was based following conventional protocol for this type of centrifuge test as suggested by RPI staff and faculty. Model 2 was similar to model 1, except that one of the partitions was filled with just TDA and the other half was used to repeat the sand/TDA mixture proportion used in model 1 (at-rest of a 50/50 mixture). Model 2 was spun up to 40 g

without making holding periods at lower g levels, and at the target g level the centrifuge was left spinning at a constant g level for up to 2 hours. This final holding period was carried out to investigate possible time effects of the induced lateral pressures.

The centrifuge models carried out to investigate lateral pressures on a cantilever retaining wall were Models 3 and 4. The main objective was to study tendencies in earth pressure generations against the retaining structure using sand/TDA backfills at different g-levels. For these centrifuge tests a rigid box with a plexiglass side was used to allow viewing the model while it is in flight spinning was used for these tests (Figure 3.11). A series of laser sensors located at 100% (top of the wall), 52.9%, and 10.4% the height of the wall were installed at a distance of 10 cm from the wall face to monitor the wall movement. Figure 3.12 shows the geometry of the aluminum retaining wall and the location of the laser sensors and Tekscan tactile sensor. Models 3 and 4 were spun up to 50 g at a rate of 2.0 g/min with 15 minutes holding periods at 25, 35 and 50 g. An aluminum plate was clamped at the face of the wall to avoid movement while building the model.

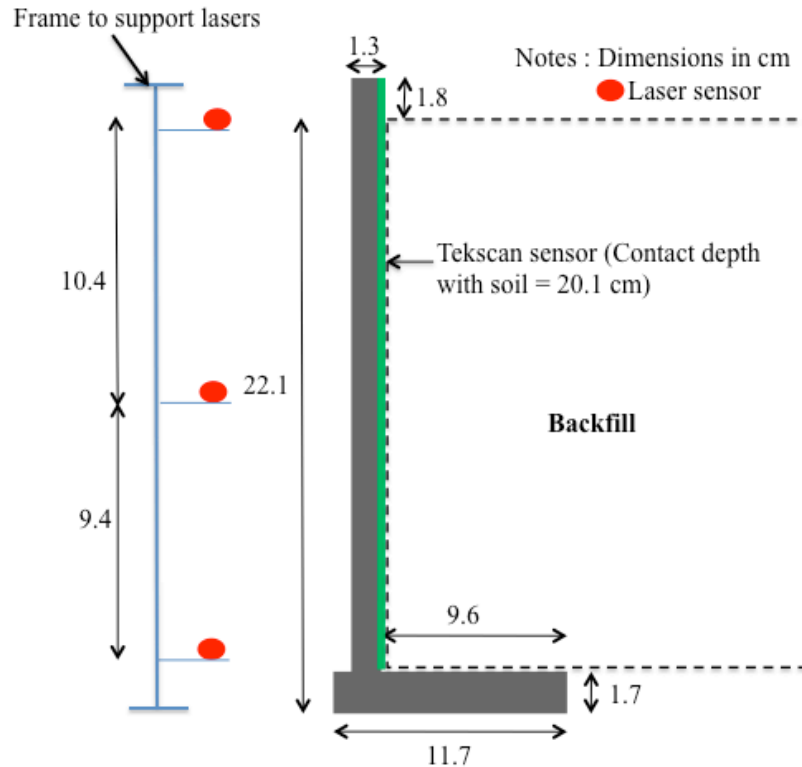


Figure 3.12: Retaining wall geometry for centrifuge model 3 and 4

Additional details and information regarding the construction and instrumentation of the different centrifuge models is provided in Appendix B.

3.4 Centrifuge Test Results for At-rest Condition

Lateral pressures measurements using the tactile pressure sensors for the at-rest conditions at different g-levels using Nevada sand and TDA/sand mixture as backfill are shown in Figures 3.13 and 3.14, respectively. These figures present results in terms of a normalized depth considering that as the g-level increases the corresponding prototype backfill depth increases proportionally with g-level. Lateral pressures increases proportionally with g-level as seen in Figures 3.13 and 3.14. However, the variation of lateral pressure with depth differs significantly for both types of backfills. For the Nevada sand results, shown in Figure 3.13 a linear variation of lateral pressures with depth seems

a reasonable approximation ($R^2 = 0.978$). However, the lateral pressures measured with the Tekscan tactile system show a slight change of slope at a normalized depth of about 0.5. A possible explanation for this decrease of slope in the lower half may be due to small deformations of the aluminum box that are not experienced in the upper portion due to the clamps.

A power or polynomial variation with depth seems to capture the lateral pressures shown in Figure 3.14 for 50/50 TDA/sand backfill. Results for the TDA/sand mixtures show considerable scatter or variation with depth. This scatter is believed to be associated with the particle segregation observed when mixing these models. For model 1 Nevada sand and TDA were mixed together at the specified proportions (300:700). However, segregation tendency was observed during preparation and after the test was completed possibly due to the evident particle size difference. A small proportion (75:175) in mixing the materials was used in model 2 to evaluate the effect of the mixing procedure in the results and with the objective to improve or minimize the segregation effects. However, the segregation problem was recurrent during and after test 2 was completed as well. Segregation tendencies in the TDA/sand mixture models will be further discussed in this chapter.

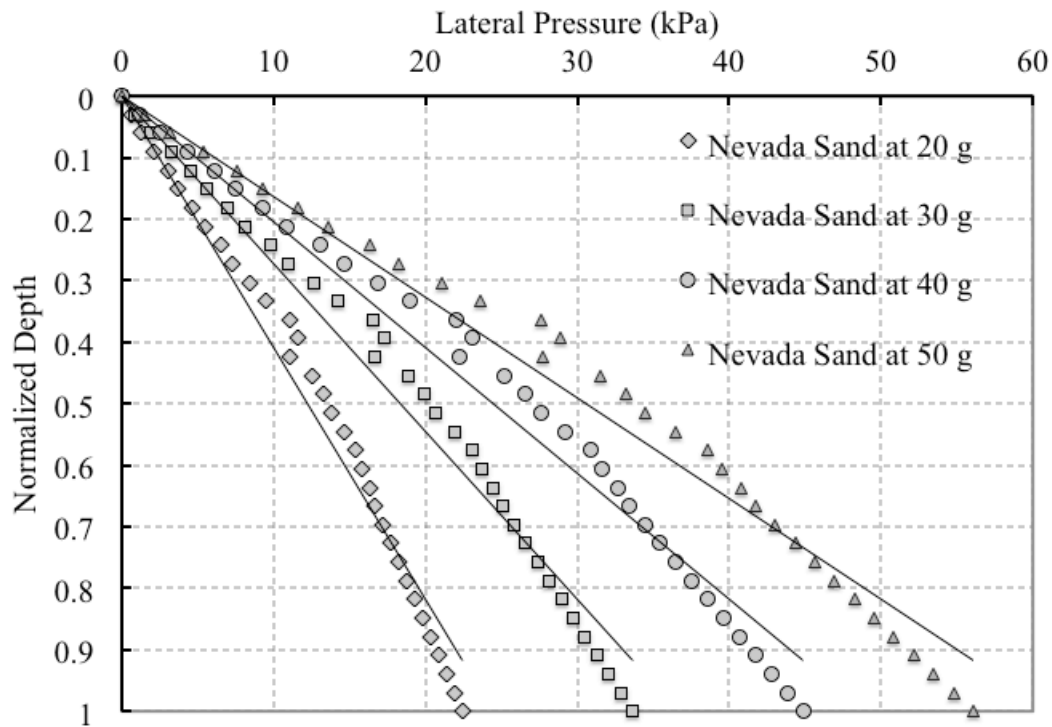


Figure 3.13: At-rest lateral pressures for Nevada sand backfill

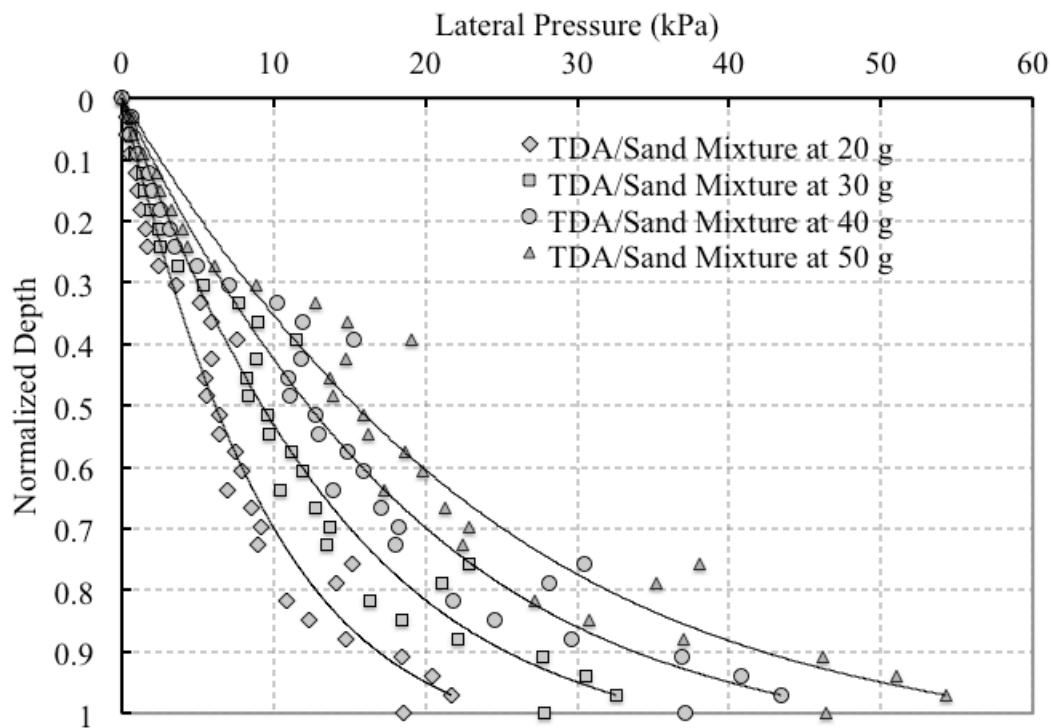


Figure 3.14: At-rest lateral pressures for TDA/sand mixture backfill

3.4.1 Comparison Between TDA and Nevada Sand Lateral Pressure Results

Lateral pressure measurements for the TDA alone at an at-rest condition for TDA alone was only tested at 40 g. A comparison of the lateral pressure versus prototype measured depth for TDA and Nevada sand are shown in Figure 3.15. The final depth reported corresponds to the embedded length of the tactile sensors which was 18.7 cm in the model. This embedded sensor length at 40 g corresponds to a prototype depth of about 7.5 m. The at-rest lateral pressures measurements presented in this figure show a reasonably linear variation of lateral pressures with depth for both test materials. The lines shown in this figure correspond to linear regressions (equation and R^2 coefficient displayed in the figure). Based on the slope of the linear regressions shown in Figure 3.15, the at-rest coefficients of lateral pressure (K_o) were estimated to be 0.401 and 0.235 for the Nevada sand and the 100% TDA backfills, respectively.

The values of K_o are based on the following equations:

$$K_o = \frac{\sigma'_h}{\sigma'_v} \quad (3.5)$$

Where σ'_h is the lateral pressure (measured) at a depth z and σ'_v is the vertical effective stress at the same depth Z . The vertical effective stress for the different centrifuge backfills (dry) were computed using:

$$\sigma'_v = \gamma_{FILL} \times Z \quad (3.6)$$

Where γ_{FILL} is the total unit weight of the backfill and Z is the depth where σ'_v is being evaluated.

For model 1 the average total unit weight of the Nevada sand was 16.29 kN/m³. For the 100% TDA backfill, used in Model 2, the average total unit weight was 5.49

16.29 kN/m³. Using these unit weights, the slopes in Figure 3.15, and equations 3.5 and 3.6, yielded the K_0 coefficients of 0.401 and 0.235 for the Nevada sand and TDA backfills, respectively.

The at-rest lateral pressure measured in the TDA crumb rubber was found to be about 19.74% of the values recorded for the Nevada sand which corresponds to a reduction in at-rest lateral pressures of about 80%. When used the TDA backfill. This significant reduction in lateral pressures is in part due to the lower unit weight of the TDA compared to the value of The Nevada sand. As mentioned before the average unit weight of the TDA is about 66% lower than the average unit weight of the Nevada sand backfill. However, this difference in unit weight does not fully explain the measured reduction of 80%.

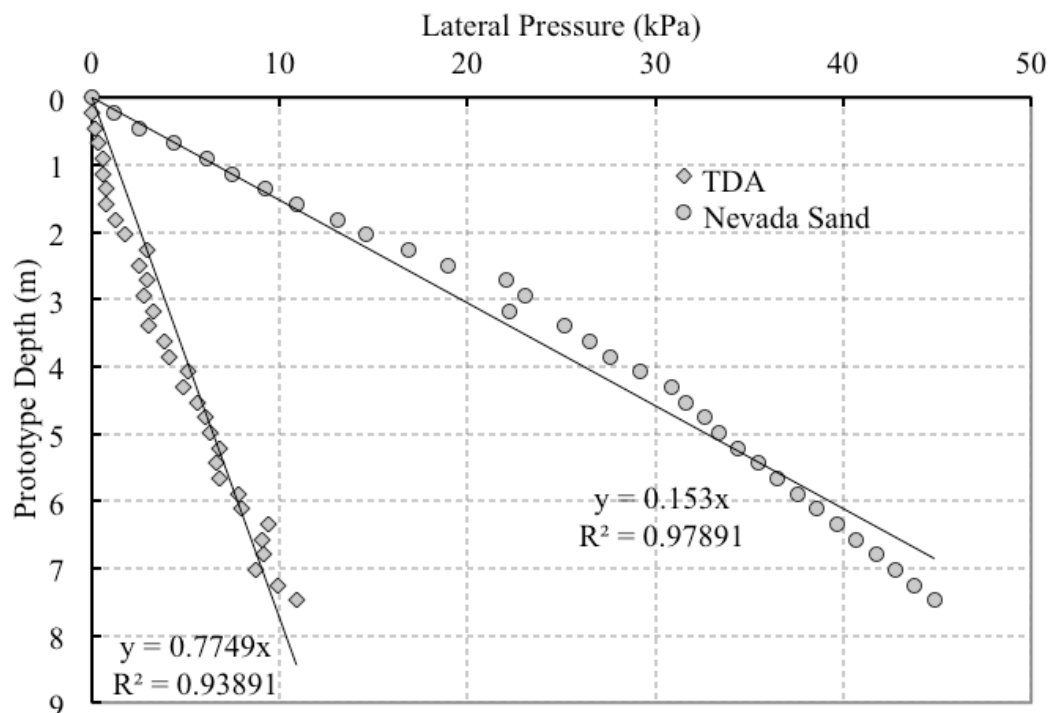


Figure 3.15: TDA and Nevada sand lateral pressures for at-rest condition from 40 g centrifuge tests

As described in Chapter 2, other authors have reported lateral pressures measurements and the earth pressure coefficient (K) values for TDA backfills. Specifically Helstrom et al. (2010) reported values from bridge abutment projects and Tweedie et al. (1998) from large scale retaining wall tests. Helstrom et al. (2010) reported data from pressure cell measurements. These authors also acknowledged that the measurements showed considerable scatter. As mentioned in Chapter 2, Helstrom et al. (2010) indicated that an average at-rest lateral pressure coefficient (K_o) of 0.3 was a reasonable first approximation as shown in Figure 3.16. The scatter in the data may be to the fact that all these projects are not completely comparable among them. Although, measurements have been taken in the TDA layers, Limestone Run and Merrymeeting bridge projects contained layers of TDA materials overlaid by soil with unit weights considerably higher than the TDA layers which increased the measured vertical stress and the compaction process involved may have produced an interlocking effect among the tire shreds which could have produced higher lateral residual stresses in the TDA layers.

Figure 3.16 also shows the results from Tweedie et al. (1998a) and the results from the centrifuge tests carried out for this dissertation. It is observed that the measurements obtained in this research are reasonably comparable with Tweedie et al. (1998a) for the no-surcharge case retaining wall which is consistent with the test conditions of this research. The dashed line corresponding to an at-rest coefficient $K_o = 0.235$ based on this research, is also shown in Figure 3.16 which seems to be in good agreement with other measurements as well while Figure 3.17 shows the comparison between the at-rest tests from Tweedie et al. (1998a) and the centrifuge test results obtained this research. The results compare reasonable well but the slight scatter could be

related to differences in TDA particle sizes, field densities, and particle characteristics used in these studies used among the studies. Tweedie et.al (1998a) used large tire shreds while this research used granulated rubber TDA.

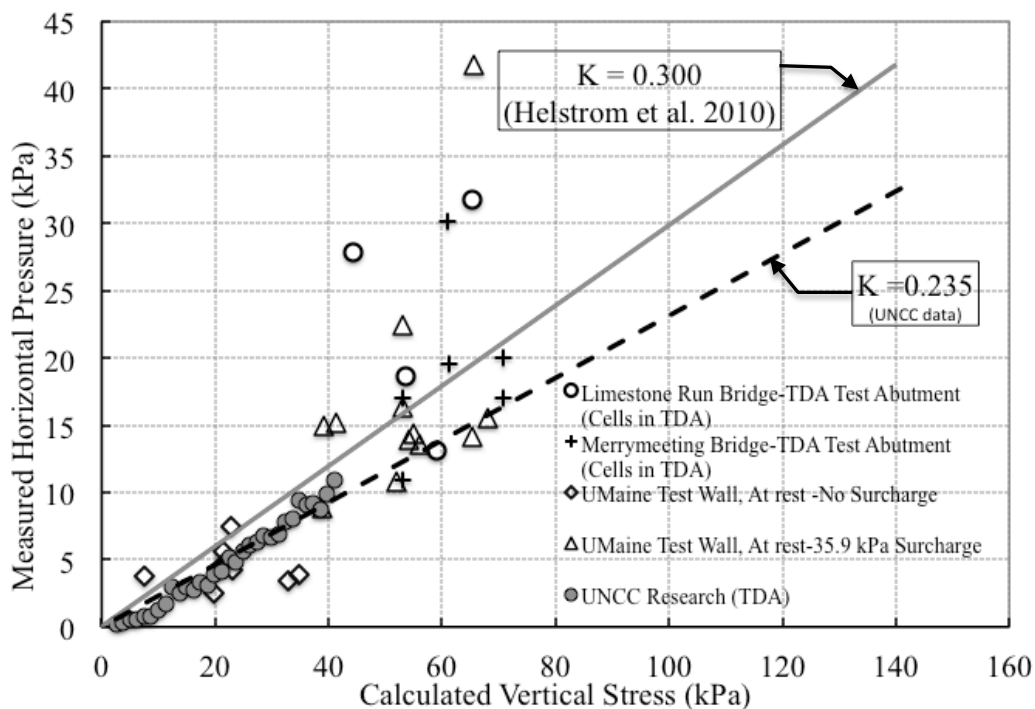


Figure 3.16: Comparison of at-rest TDA lateral pressures from Helstrom et al. (2010), Tweedie et al. (1998a) and centrifuge test results

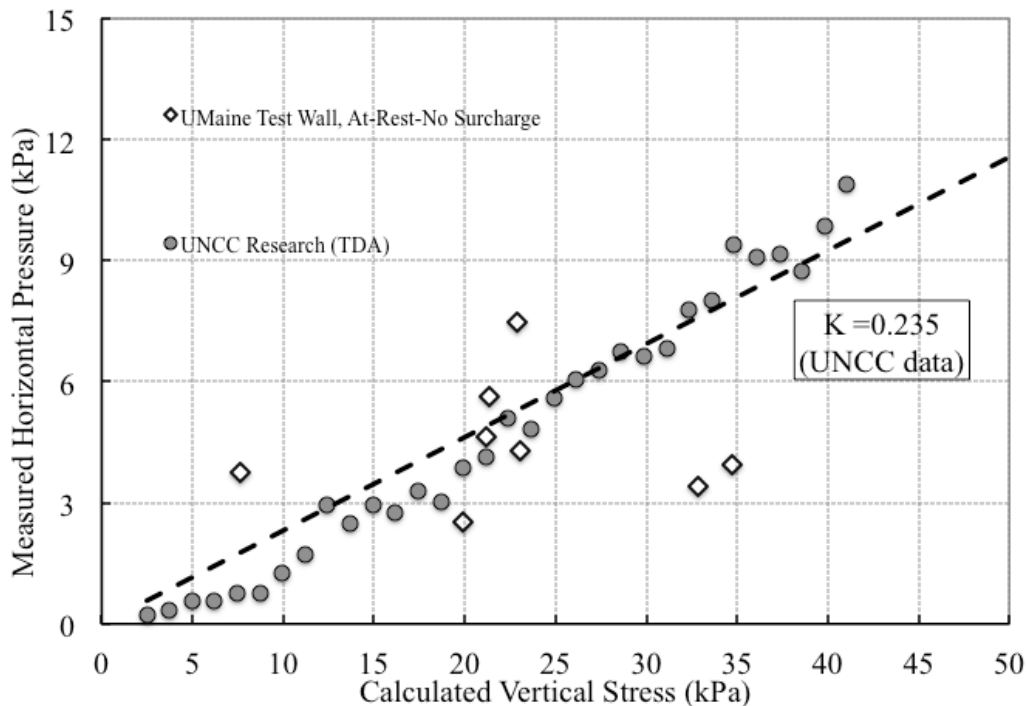


Figure 3.17: Comparison of at-rest TDA lateral pressures from Tweedie et al. (1998b) and centrifuge test results

3.4.2 Effect of Time in TDA At-rest Lateral Pressures

Centrifuge Model 2 allowed assessment of the variation of the at-rest lateral pressures induced by the granulated TDA over time. Results of at-rest lateral pressures measured for different times are shown in Figure 3.18 for Model 2 at 40g. The maximum duration of the lateral pressure time dependency was 120 minutes. The results, although limited in duration, are useful to show some increase of lateral pressures with time for the 100% TDA backfill. This variation was more noticeable below the scaled prototype depth of 3 meters, and the rate of increase seems to diminish after 20 minutes.

An eight percent increase of at-rest lateral pressure was measured during the first 20 minutes of sustained 40g level. The increase in lateral pressures during the first 20 minutes may be due to the compressibility of the TDA particles, but more experimental

data is required to confirm this hypothesis. Model 1 also included a test section to evaluate at-rest lateral pressures of Nevada sand. The variation of lateral pressures for both the TDA and Nevada sand are shown in Figure 3.19. As shown in this figure the Nevada sand showed little to no variation of lateral pressures with time.

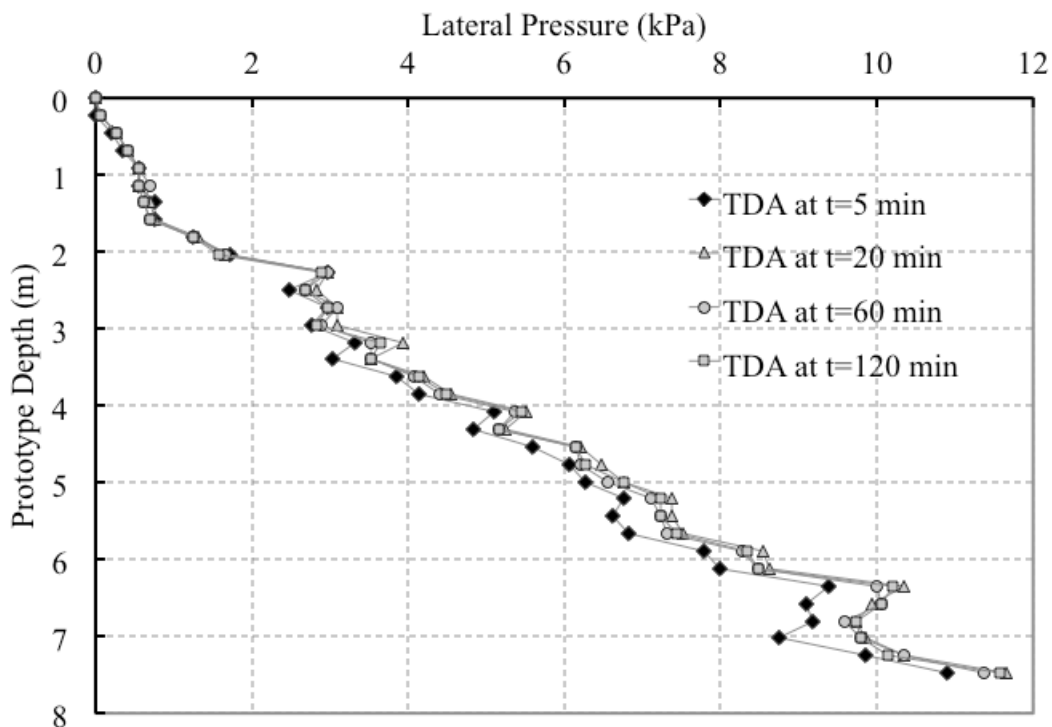


Figure 3.18: Time variation of at-Rest lateral pressures of the 100% TDA backfill

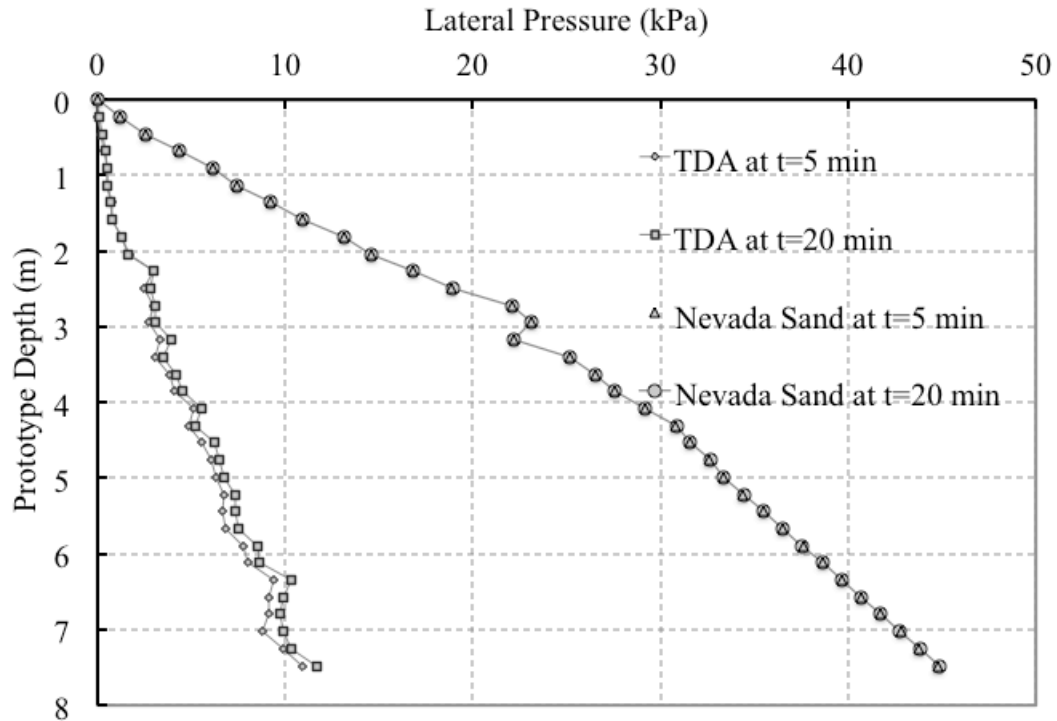


Figure 3.19: Effect of time in at-rest lateral pressure for TDA and Nevada sand at 40g

3.4.3 Discussion of at-rest Lateral Pressures for 50/50 (by volume) TDA/sand Mixture

Testing of the TDA/sand mixtures was more challenging due to the difference in particle sizes between both materials which created the potential for segregation problems during model preparation as well as during the spinning of the models during the centrifuge tests. The TDA/sand mixture backfill was tested twice during Model 1 and Model 2 of the centrifuge test plan. Figure 3.20 shows the results at 40 g (obtained from both centrifuge models). As mentioned in section 3.4, the at-rest lateral pressures for the 50/50 (by volume) mixture of TDA/sand was not linear with depth and it was well represented by a third degree polynomial curve fit. The large increase of lateral pressures near the bottom (prototype depths of 6 m and lower) could have been caused by the high concentration of sand particles at the bottom of the aluminum tank. This is feasible given

the smaller D_{50} size of the Nevada sand ($D_{50} = 0.15$ mm) compared to the TDA ($D_{50} = 1.20$ mm).

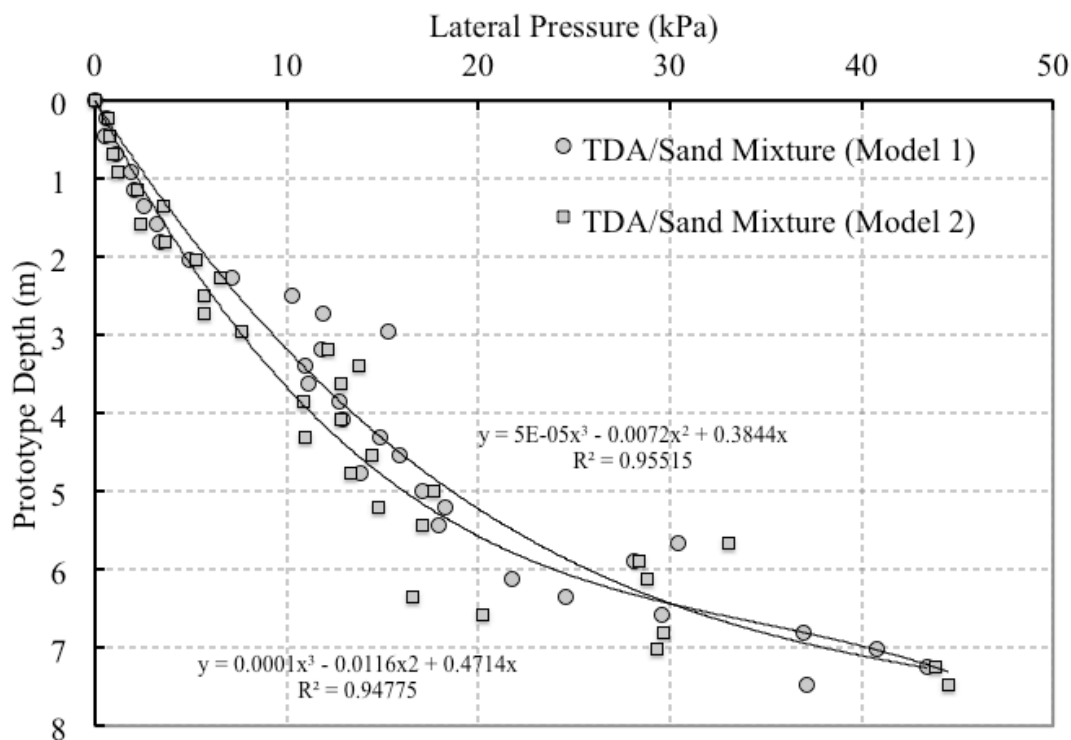


Figure 3.20: At-rest lateral pressures from centrifuge tests of TDA/sand mixture (50/50 ratio by volume)

Although the segregation problem observed in the laboratory while preparing the model and after finishing spinning is not easy to quantify. Visual examination of the model was accessed after the tests were completed trying to keep intact the integrity of the backfill as close as possible. From Figure 3.21, it can be observed a high concentration of TDA particles at the top of the backfill, and it could be implied that Nevada sand particles that were originally in those areas mixed with the TDA could have started segregated and moved towards the bottom of the backfill.

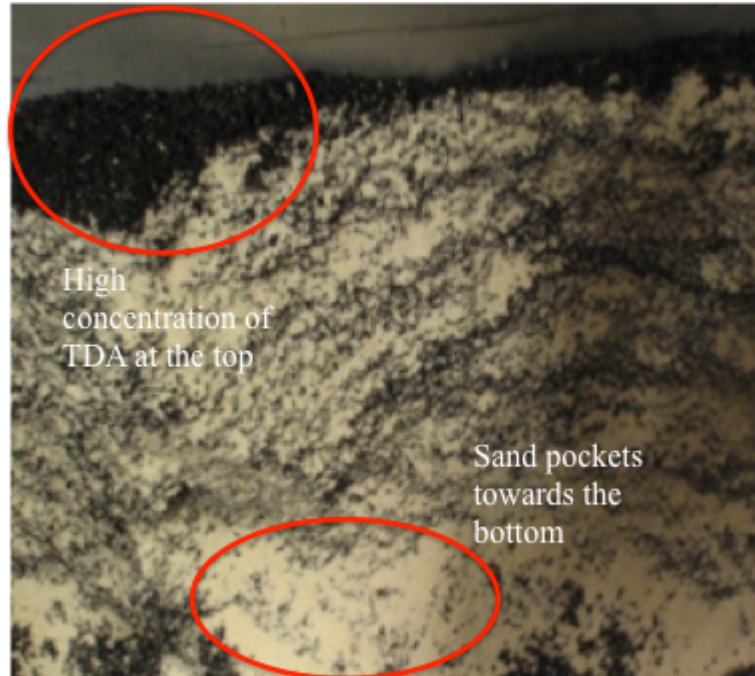


Figure 3.21: Photo showing rich sand zones in the TDA/sand mixture backfill after testing

Additionally, Taylor (1948) proposed a relationship that could be useful to check the feasibility of segregation for spherical particles of two sizes as shown in Figure 3.22. In this figure, the small particle b would be retained by three particles a (with higher particle size D_{50}). Particle b would not segregate if the following condition is satisfied (Taylor 1948):

$$D_{50_b} \geq (D_{50_a})/6.5 \quad (3.7)$$

Where:

D_{50_b} = mean particle size of finer soil

D_{50_a} = mean particle size of the coarser soil

Therefore for the variables involved for this research equation 3.7 becomes:

$$D_{50_Nevada\ sand} \geq (D_{50_TDA})/6.5 \quad (3.8)$$

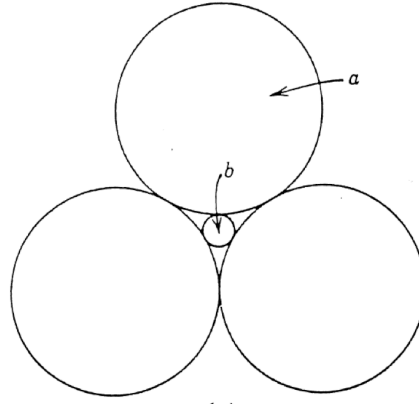


Figure 3.22: Illustration of retained spherical particle b in the pore space between 3 spheres a (Adapted from Taylor 1948)

From the sieve analysis performed on both test materials used in the centrifuge tests carried out for this research (shown in Figure 3.2), it was found that $D_{50_TDA} = 1.20$ mm, and $D_{50_Nevada\ sand} = 0.15$ mm; therefore, the ratio $D_{50_TDA}/6.50 = 0.18$. Therefore, the relationship proposed by Taylor (1948) relationship is not satisfied which would suggest the Nevada sand particles would not be easily retained by the TDA particles thus segregation would be feasible when these two materials are mixed.

Despite the challenges faced when mixing both materials, the data shows that the use of TDA/sand mixture will lead to a substantial decrease in lateral pressure when compared to conventional soil backfills for at-rest conditions as shown in Figure 3.23. An approximate reduction of 30 percent in lateral pressure using TDA/sand mixture (50/50 by volume) was found when compared to the Nevada sand backfill. This decrease in lateral pressures is expected to bring economic benefits in structures that are usually designed under at-rest conditions (e.g, basement retaining walls, bridge abutments) since

the amount of concrete and reinforcement steel bars to be required in such structures could be potentially reduced under a lower loading demand from the retained backfill.

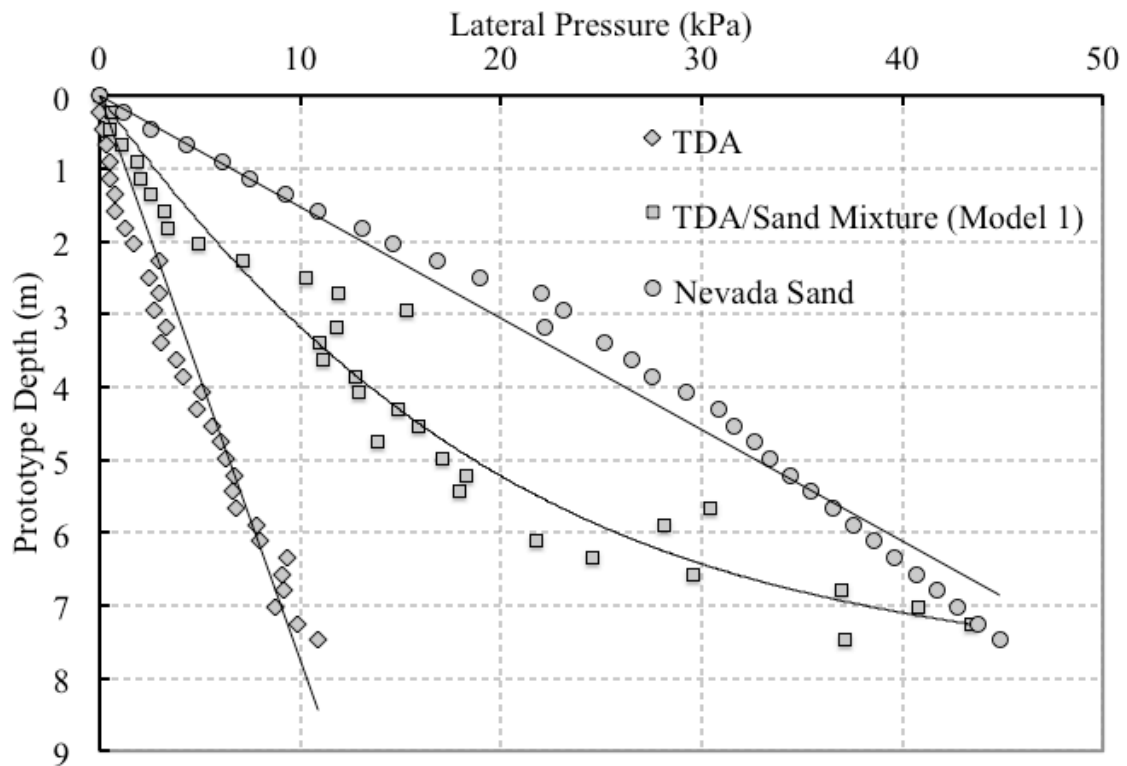


Figure 3.23: Centrifuge tests results for the three backfills tested at 40 g

3.4.4 Comparison of At-rest Lateral Pressure Results with Classical Earth Pressure Theory

Jaky (1944) proposed the following equation which is widely used by geotechnical engineers to calculate the at-rest earth pressure coefficient (K_o)

$$K_o = 1 - \sin(\phi') \quad (3.9)$$

Where ϕ' is the effective soil friction angle.

In order to calculate the theoretical earth pressure coefficient using the above equation, a series of dry triaxial tests were carried out on samples of the two test

materials prepared at the same density in the centrifuge test. As discussed in chapter 2, the effective friction angle of TDA materials is highly dependent on the axial strain level used to define failure criterion. A detailed discussion of the shear strength parameters of the TDA material will be presented in Chapter 3. Table 3.4 shows the earth pressure coefficients obtained from the centrifuge test compared to the values obtained using the Jaky's equation.

Table 3.4: Comparison of experimental coefficients of lateral earth pressures (K_o) and Jaky equation

Property	Backfill Material		
	TDA	TDA/sand Mixture	Nevada Sand
Unit Weight (kN/m^3)	5.49	12.18	16.29
Friction Angle ϕ' (deg)	11.2-24.6 ⁽¹⁾⁽²⁾	27.4-32.7 ⁽¹⁾⁽³⁾	35.5 ⁽¹⁾⁽⁴⁾
K_o from $1 - \sin \phi'$ (Jaky, 1944)	0.806-0.584	0.534-0.460	0.419
K_o from Centrifuge Test Measurements	0.235 ⁽⁵⁾	0.378 ⁽⁵⁾	0.401 ⁽⁵⁾
Ratio K_o measured versus K_o Jaky	29.2%-40.2%	70.8%-82.2%	95.7%

Notes : (1) Friction angles were determined from dry triaxial tests at the same densities

(2) Range of friction angle for TDA between 5 and 25% axial strain

(3) Range of friction angle for TDA/sand mixture between 5 % and peak ($\approx 10\%$)

(4) Determine at peak strain ($\approx 2\%$)

(5) All earth pressure coefficients were calculated assuming lineal regression slopes

The results presented in Table 3.4 indicate that Jaky's equation overestimates considerably the at-rest earth pressure coefficient for the TDA and the 50/50 TDA/sand mixture backfills. Experimental earth pressure coefficients are between 29% and 40% lower than those obtained using Jaky (1944) equation which would result in an overprediction of the lateral forces when designing earth retaining structures for at-rest conditions. In order to quantify the level of overprediction that would occur in

conventional geotechnical design, the acting lateral force (P_a) as a function of the unit weight (γ) and the height of the wall (H) can be calculated as follows:

$$P_a = \frac{1}{2} K_o \gamma H^2 \quad (3.10)$$

Table 3.5 shows the calculated lateral forces, using equation 3.10, for all three backfills. The results indicate that lateral pressures would be overpredicted between 3.4 to 2.5, and 1.4 to 1.2 times compared to the experimental data for the TDA and TDA/sand backfill, respectively when Jaky (1944) equation is used. The ranges reported in Table 3.5 correspond to the angle selected which as mentioned before is highly dependent for the level of limit axial strain used to define ϕ' . In contrast, lateral pressures using Jaky's equation for Nevada sand are about 1.05 times higher than the lateral pressure measured in the centrifuge test. The high level of overprediction may result in extremely conservative designs specially when the TDA backfill is used alone.

Table 3.5: Lateral force in retaining structure using centrifuge results and Jaky equation

TDA			TDA/sand Mixture			Nevada Sand	
Pa from Centrifuge Results K=0.235	Pa from Jaky K=0.806	Pa from Jaky K=0.584	Pa from Centrifuge Results K=0.378	Pa from Jaky K=0.534	Pa from Jaky K=0.460	Pa from Centrifuge Results K=0.401	Pa from Jaky K=0.419
36.10	123.79	89.69	128.80	181.95	156.74	182.74	190.95

Notes : (1) p_a in kN-m

3.5 Summary of Lateral Pressure Measurements From Retaining Wall Centrifuge Tests

Variation of lateral pressures with depth for the cantilever wall centrifuge tests using Nevada sand (Model 3) and TDA/sand mixture (Model 4) are shown in Figures 3.24 and 3.25, respectively. Results shown are for 25, 35, and 50 g which correspond to the three g-levels where the centrifuge machine was kept at a constant g-level for a

certain period of time to allow reading of the lateral pressures. It is observed in all figures that the lateral pressures increase proportionally with the g-level which is similar to the at-rest test results. For the Nevada sand lateral pressure readings approximate reasonably well with a linear variation with depth. Figure 3.24 results show a marked increase of the lateral pressures in the lower 10% of the wall. The lateral pressures recorded for the 50/50 TDA/sand backfill are bilinear with a marked slope increase in the lower half of the wall. Figures 3.26 through 3.28 compare the lateral pressures measured at prototype dimensions for both backfills. An approximate reduction of 35 percent in lateral pressure is obtained when TDA/sand mixture (50/50 by volume) is used. Lateral pressures at lower g levels were necessary for further analysis in this chapter and they were measured instantaneously as the spinning process was progressing. Information at lower g-levels can be found in Appendix B.

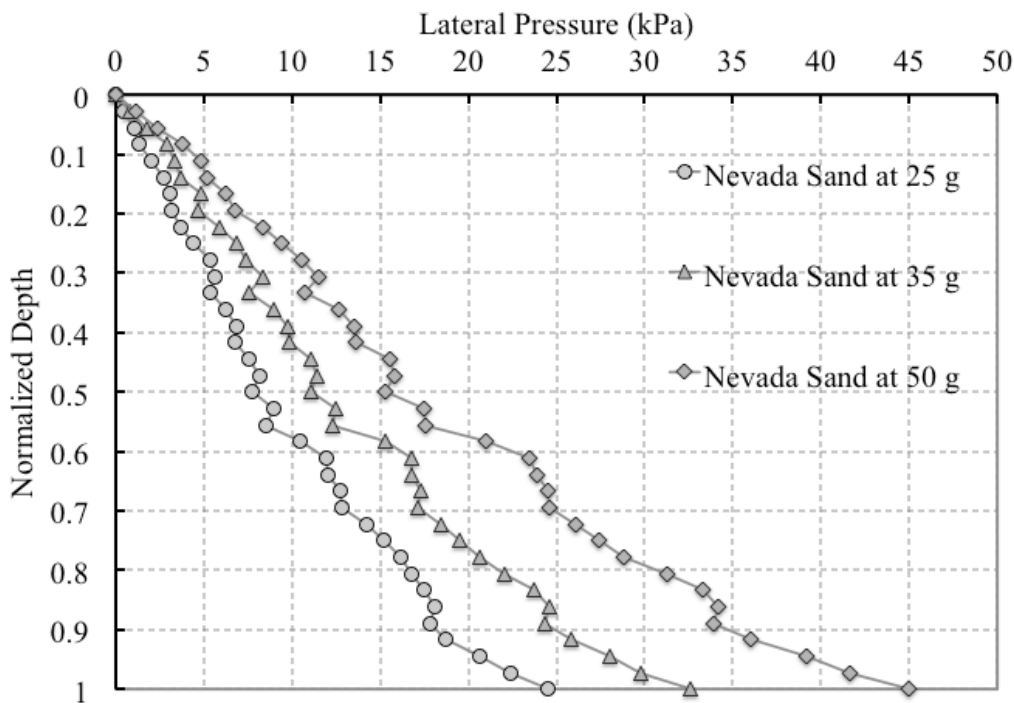


Figure 3.24: Lateral pressure vs depth at different g-levels retaining wall model with Nevada sand backfill

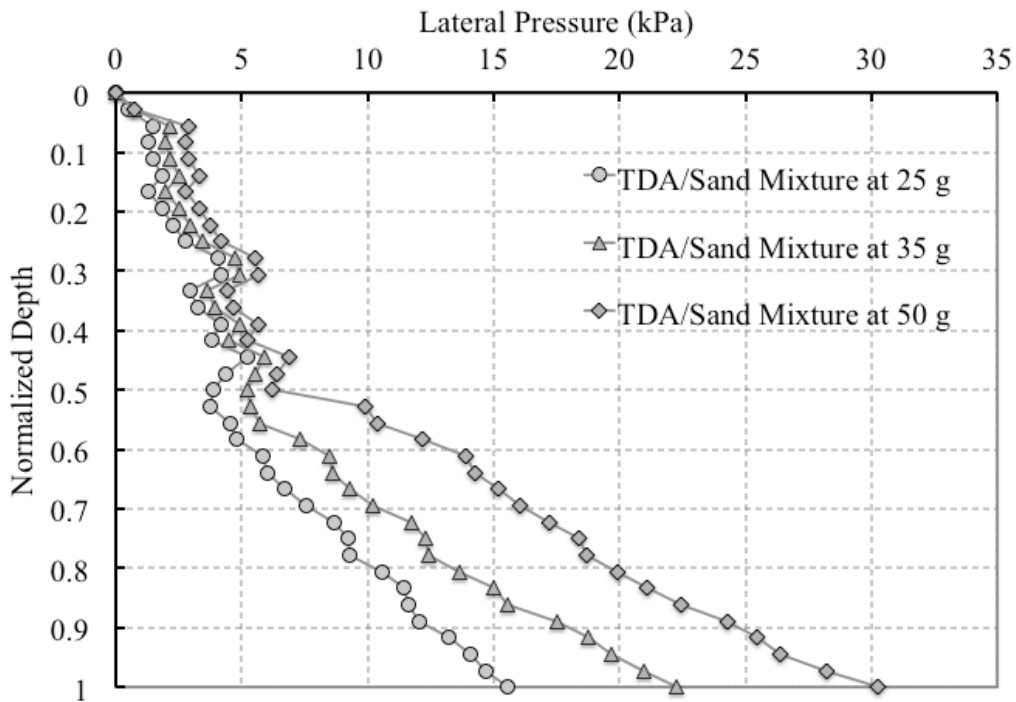


Figure 3.25: Lateral pressure vs depth at different g-levels for retaining wall model with 50/50 TDA/sand backfill

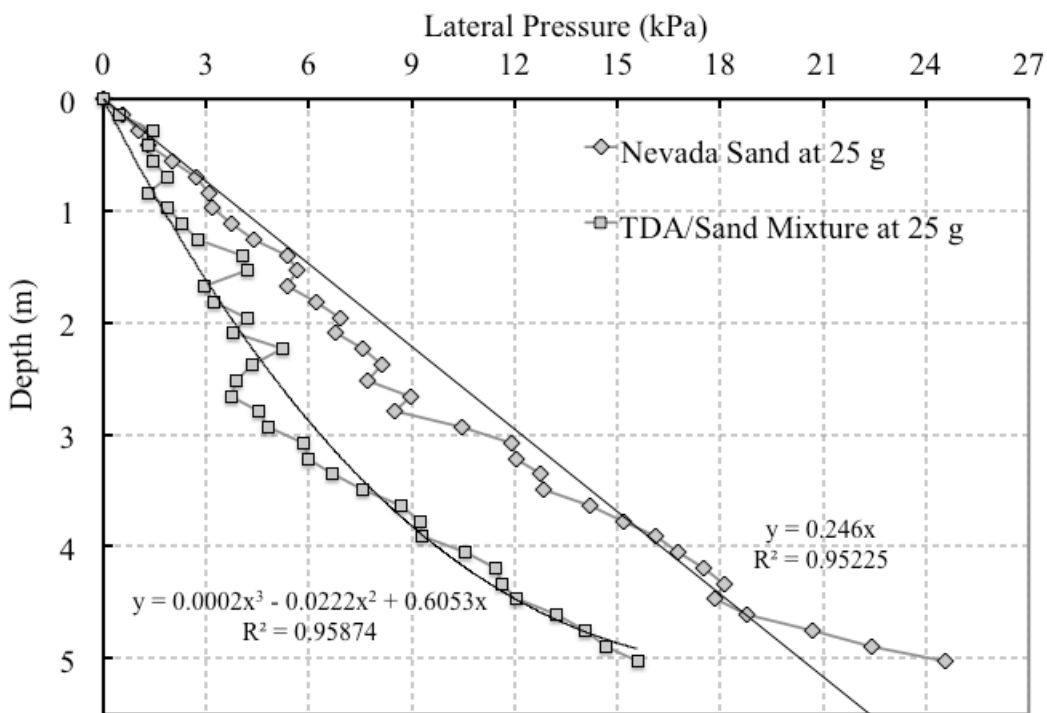


Figure 3.26: Comparison of lateral pressures from retaining wall centrifuge test at 25 g

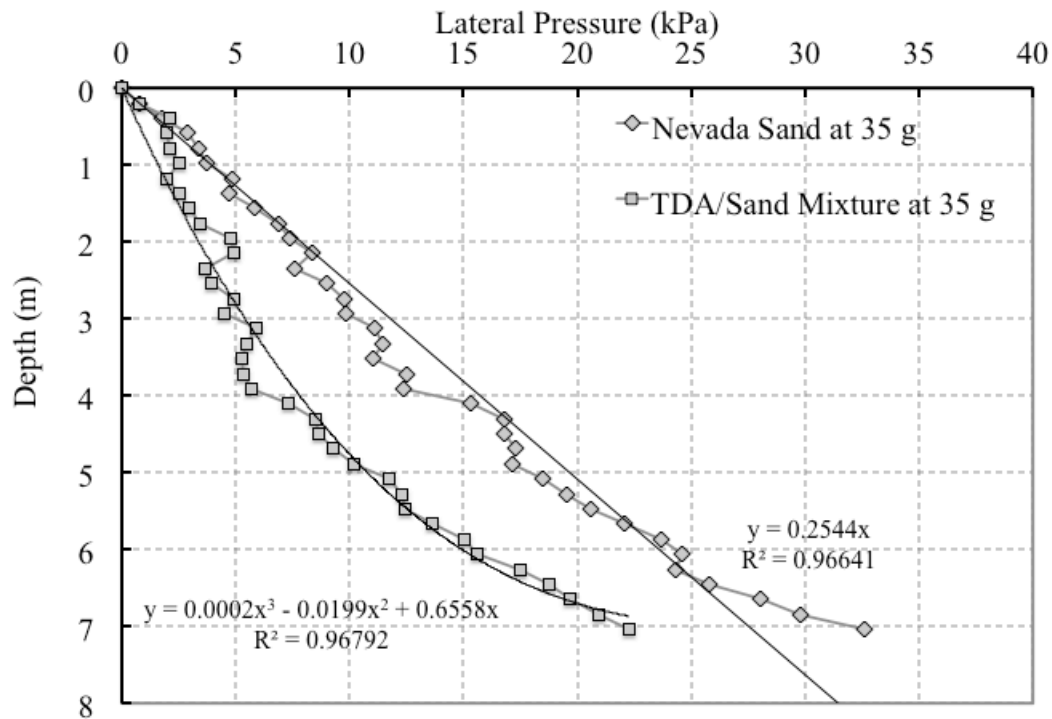


Figure 3.27: Comparison of lateral pressures from retaining wall centrifuge test at 35 g

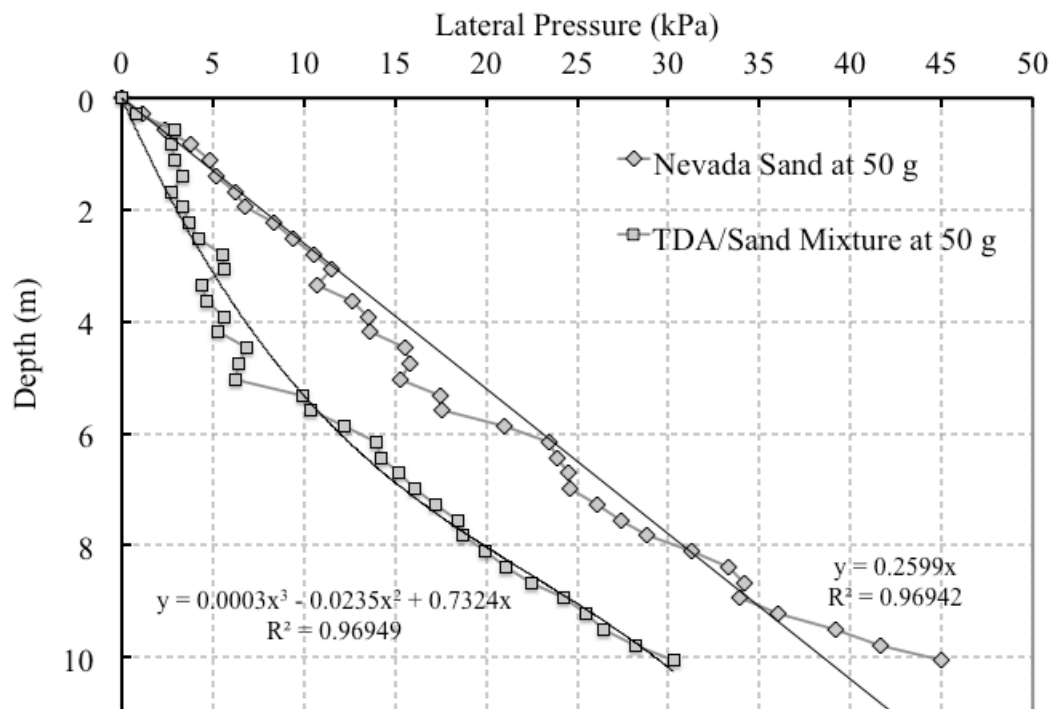


Figure 3.28: Comparison of lateral pressures from retaining wall centrifuge test at 50 g

Higher lateral pressures at the bottom of the wall (lower 10%) for the Nevada sand backfill may be the result of the lower movement levels along the depth of the wall. Displacements at the top the wall are considerable higher than those observed at the middle and near the bottom of the retaining structure for both backfills as shown in Figures 3.29 and 3.30. Higher amounts of displacements would produce a substantial decrease in lateral pressure at the top of the wall when compared to those at the bottom of the wall where the amount of movement is less.

Higher pressures at the bottom of retaining wall rotating at the base have also been reported in the literature by other researchers (Fang and Ishibashi 1986; Harrop-Williams 1989). These authors agreed that although conventional geotechnical engineering practice and theory assumes that earth pressure distribution on retaining wall is triangular, experimental data shows that a triangular distribution is almost never the case; and pressure distributions are better represented in the form of a curve (Harrop-Williams 1989). The previous statement can be compared with the data obtained in this research. Although R^2 values obtained in Figures 3.26 through 3.28 are reasonable when using a linear regression ($R^2 > 0.95$), a fitting curve of second-degree considerable improves the R^2 as shown in Figure 3.31 for 35 g. The same observation was found at 25 and 50 g which are presented in Appendix B.

Lateral displacements of the wall are shown in Figures 3.29 and 3.30 for the Nevada sand and 50/50 TDA/sand mixture backfill, respectively. These figures show not only that the displacements at the top of the wall are the highest but also indicate that the deflected shape of the retaining structure is a result of combining two movements of the

wall. Namely rotation of wall about the base and the translation mode or sliding along the base.

Figure 3.32 shows the laser sensor readings at the top of the wall for both backfill at model dimensions (i.e, not scaled). A comparison of the middle and lower laser sensor can be found in Appendix B. The amount of lateral displacement that the Nevada sand retaining wall exhibited at the end of the test was 1.55 times higher compared to the TDA/sand mixture wall. The same conclusion was achieved from Figure 3.33 where the lateral movement was expressed as a function of retaining wall height (prototype dimensions). Higher amounts of lateral displacements should be expected in the Nevada sand backfill since earth lateral pressures are higher compared to the TDA/sand mixture backfill.

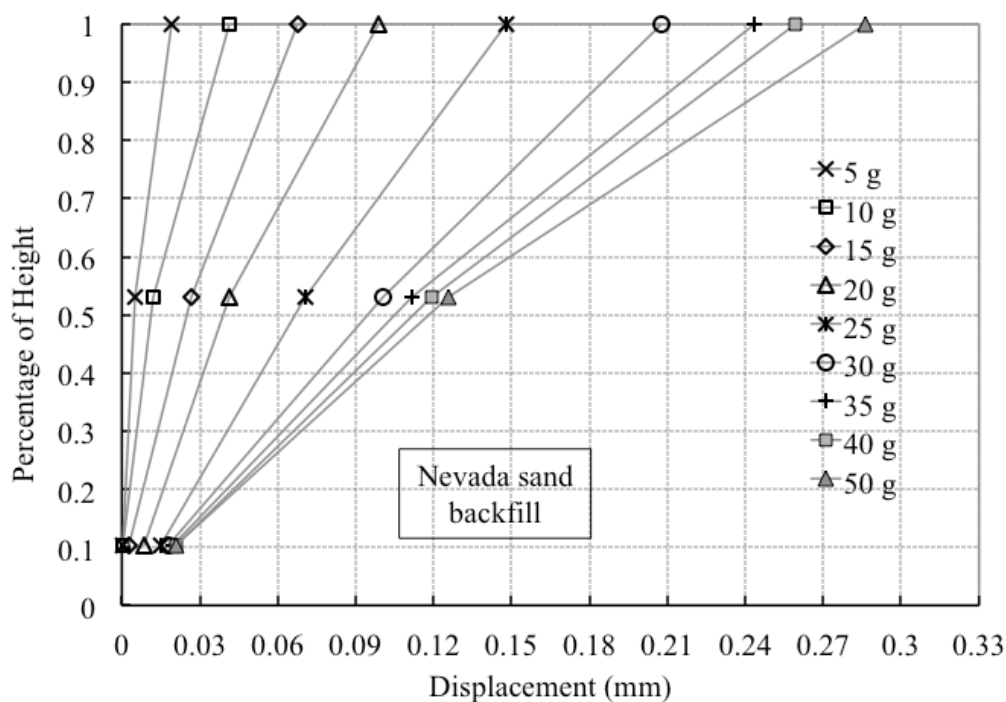


Figure 3.29: Retaining wall displacement variation along the depth at different g-levels for Nevada sand backfill

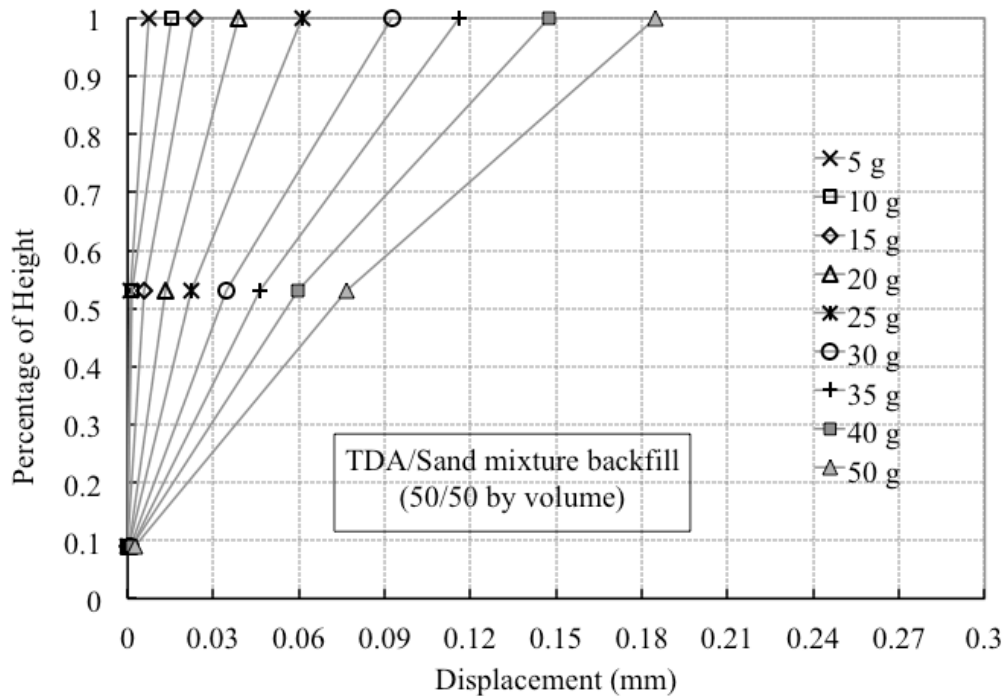


Figure 3.30: Retaining wall displacement variation along the depth at different g-levels for TDA/sand backfill

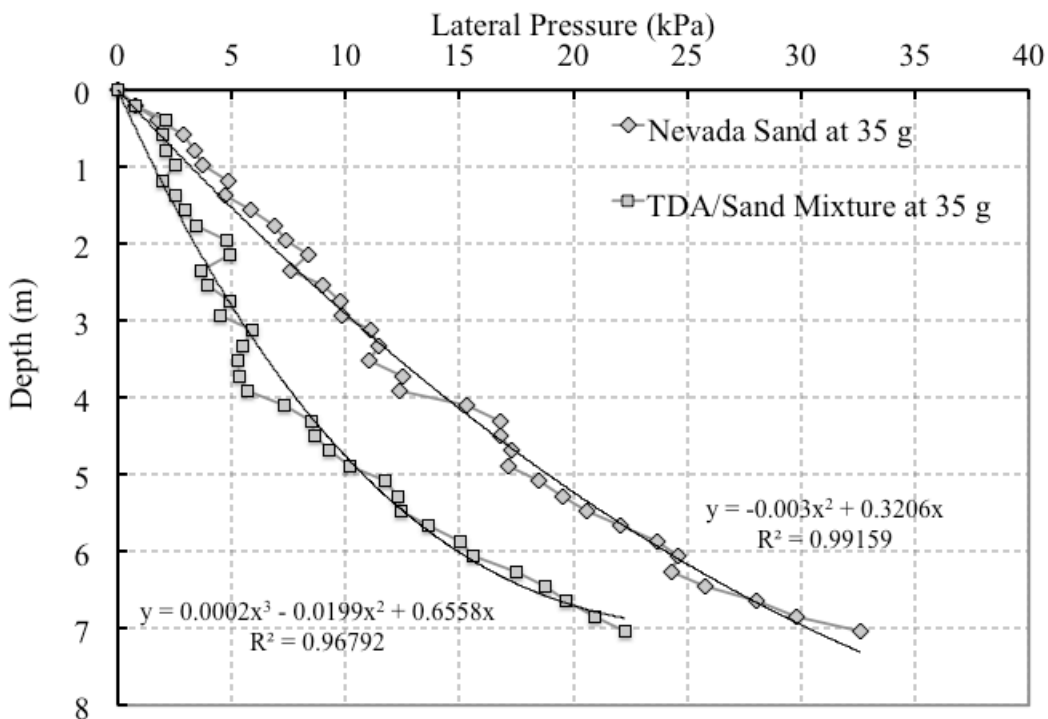


Figure 3.31: Lateral pressure distribution using a curve fitting for Nevada sand backfill

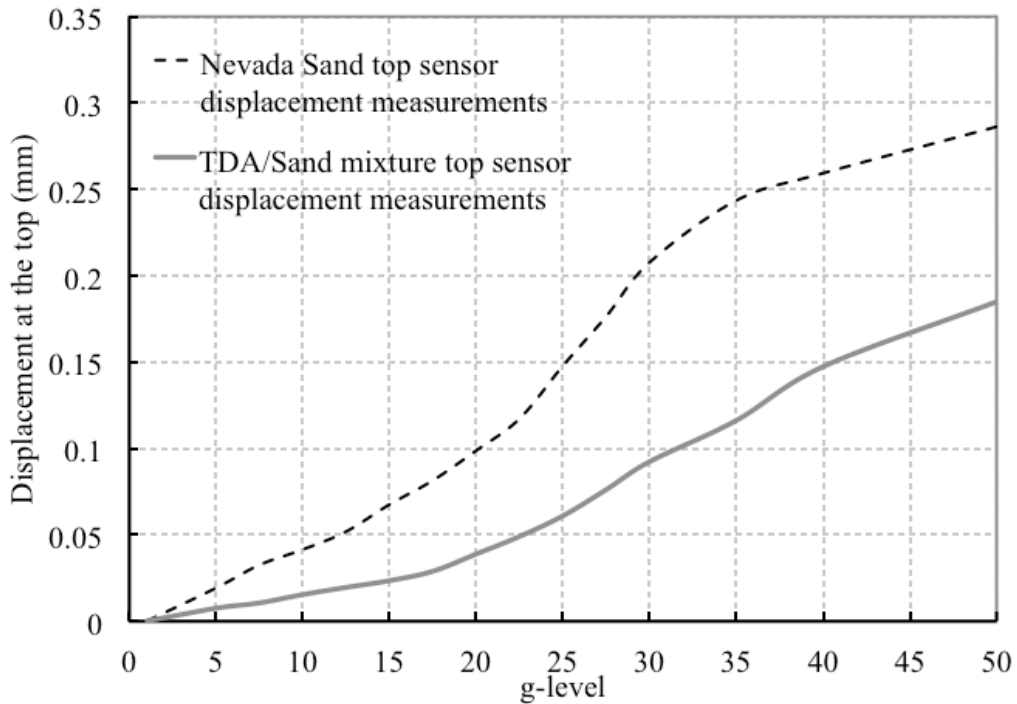


Figure 3.32: Comparison between retaining wall movement at the top of the wall for Nevada sand and TDA/sand mixture backfills (Model dimensions)

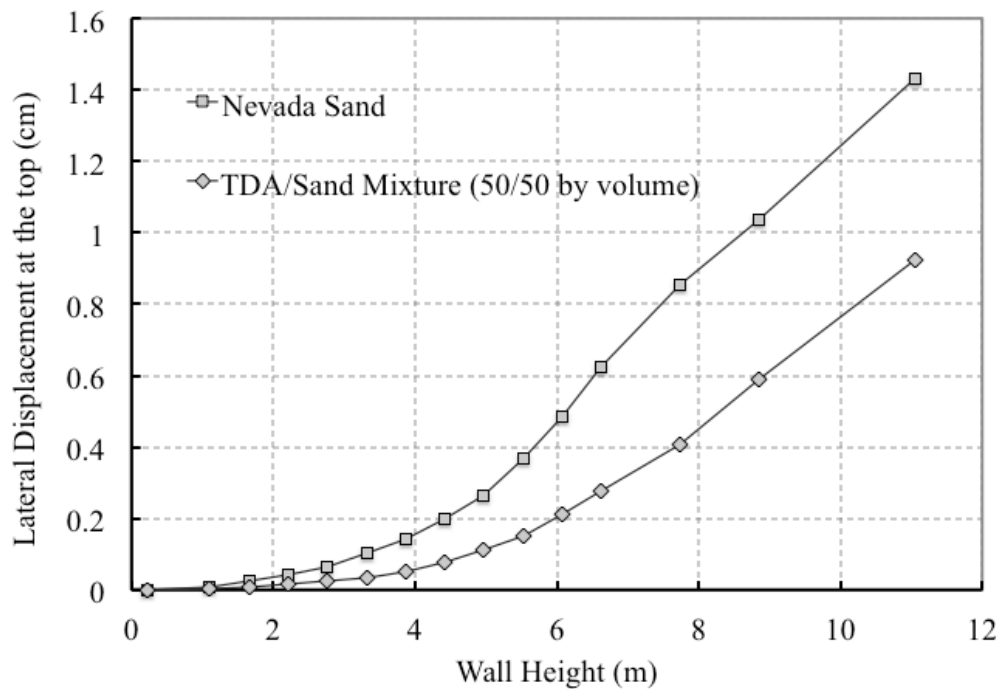


Figure 3.33: Retaining wall lateral displacements variation with depth for TDA/sand mixture at different g-levels (prototype dimensions)

3.5.1 Comparison of Cantilever Retaining Wall Centrifuge Test Results with Rankine Theory

The amount of lateral displacements measured using the laser sensors were used to calculate the ratio displacement/height of the wall (Δ/h) to compare the results with the widely used Rankine theory where the earth pressure coefficient for active state can be calculated as follows:

$$K_a = \frac{1 - \sin \phi'}{1 + \sin \phi'} \quad (3.11)$$

Lateral displacements to calculate the ratio Δ/h were taken as the maximum displacement at the top of the wall which is consistent with the same type of analysis carried out by other authors for rotating walls (Mei et al. 2009; Sherif et al. 1984). Figure 3.34 shows the variation of the earth pressure coefficient with Δ/h . It is observed that although the experimental result for the active coefficient of earth pressure (K_a) for the Nevada sand is lower than the one obtained using Rankine theory, it is still within an acceptable range of prediction between experimental data and theory; and typical friction angles for Nevada sand. Active earth pressure coefficient for the Nevada sand backfill using Rankine theory was found to be 12 percent higher than the experimental value. However, the level of over prediction for TDA/sand mixture backfill may not be within acceptable ranges even for the value calculated using the friction angle at failure. Figure 3.34 shows that the theoretical active earth pressure coefficient for the TDA/sand mixture can be between 45% and 80% higher than the experimental value for the friction angle at failure and at 5% axial strain deformation respectively. Table 3.6 shows a summary of the results and the percentage of the experimental values when compared to Rankine theory.

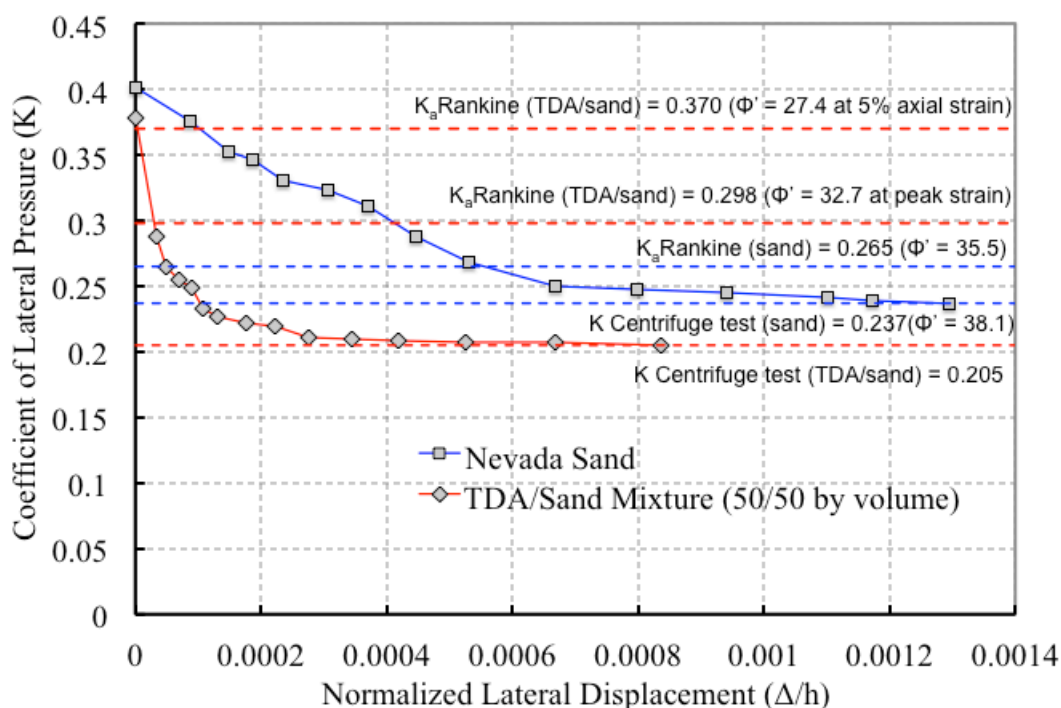


Figure 3.34: Variation of lateral pressure coefficient versus normalized displacement

Table 3.6: Comparison of experimental coefficients of lateral earth pressures (K) and Rankine theory

Property	Backfill Material	
	TDA/sand Mixture	Nevada Sand
Unit Weight (kN/m^3)	12.18	16.29
Friction Angle ϕ' (deg)	27.4-32.7 ⁽¹⁾⁽²⁾	35.5 ⁽¹⁾⁽³⁾
K_a from Rankine Theory	0.370-0.298	0.265
K_a from Centrifuge Test Measurements	0.205 ⁽⁴⁾	0.237 ⁽⁴⁾
Ratio K measured versus K_a Rankine	55.4%-68.8%	89.4%

Notes : (1) Friction angles were determined from dry triaxial tests at the same densities
 (2) Range of friction angle for TDA/sand mixture between 5% and peak ($\approx 10\%$)
 (3) Determined at peak strain ($\approx 2\%$)
 (4) All earth pressure coefficients were calculated assuming lineal regression slopes

Discrepancies between experimental and theory results may be the result of experimental errors during the test. For example, although tactile sensors are a versatile way to measure lateral pressure since it allows to obtain several data points along the depth of the wall, the accuracy the sensors have been discussed in the literature by (Palmer et al. 2009) where the authors report errors in the measured pressures were less than 5% which may be a low error but it may be result in lower lateral pressures. The amount of movement during spinning was not self-controlled like in most of the experimental and analytical studies where similar analyses for the relation between K and Δ/h have been carried out (Celis and Pando 2008; Clough and Duncan 1971; Fang and Ishibashi 1986; Mei et al. 2009). For the TDA/sand backfills in addition to possible unavoidable experimental errors, the high discrepancy may be the result of the assumptions Rankine theory was based on. One of the main assumptions for Rankine theory is that the soil is cohesionless which is indicated in equation 3.11, where the only shear strength parameter involved in the calculation of the earth pressure coefficient is the soil friction angle (ϕ'). For TDA and TDA/sand mixture backfills this assumption may not be totally valid since as it will be discussed in Chapter 4, TDA and TDA/sand mixtures may exhibit cohesion. Other authors have reported cohesion values for TDA materials as it was described in Chapter 2 as well. However, the objective of this research was to evaluate the distribution with depth and magnitude of earth lateral pressures using TDA materials and verifies the validity of commonly used earth pressure theory.

From Figure 3.34, it also observed that the amount of movement required to achieve apparent active condition for Nevada sand is for a ratio of Δ/h equal to 0.0013 which is within the acceptable ranges reported by other authors for granular materials and

rotating walls around the base (Mei et al. 2009). However, the amount of movements obtained in this study should be considered carefully when compared to other studies, since as it will be explained in the following sub-section, it was found that the movement mechanism presented in the wall was a combination of both rotation and translation models while previous studies have been able to control displacements in their models. Other factors influencing the amount of movements in the centrifuge tests were the manipulation of the model in the centrifuge room prior to testing that could have caused additional small movements and velocity at which the centrifuge machine was rotating. However, since conditions were kept constant for both tests, it is observed that the amount of movement required to achieve apparent active condition for the TDA/sand mixture backfill is less than the amount required for the Nevada sand backfill. Active condition was achieved at an approximate ratio of Δ/h equal to 0.0008 which corresponds to a 38% reduction in the amount of movement required to achieve active conditions as compared to the Nevada sand backfill. Reduction in the amount of movement for TDA/sand mixtures has also been reported by Celis and Pando (2008).

3.5.2 Analysis of the Retaining Wall Movement Mechanisms From Centrifuge Test Model

Based on the initial geometry of the aluminum retaining wall (Figure 3.12) used in the centrifuge tests, it was suspected that the wall would experience mainly rotation mode movement. However, it was not possible to control a desired amount of movement during the test while spinning making necessary to interpret the overall movement behavior from the laser sensors data located along the depth of the wall from the beginning to the end of the test as shown in Figure 3.35. It has to be noted that a passive force was not acting the model since a certain depth of soil covering the toe of the wall

was not provide during the model construction process. Therefore, the wall was theoretically free to translate as well.

It is observed that the lower displacement sensor located close to the base of the wall as explained in Section 3.4 and shown in Figure 3.12 recorded an abrupt change in lateral displacement at approximate 15 g level. It seems that the middle and top sensors presented a change in slope from this point as well. The abrupt change experienced in the lower sensor could give an indication that the retaining wall might have started sliding from this point, and that a combination of rotation and translation could have been the governing movement mode from this point.

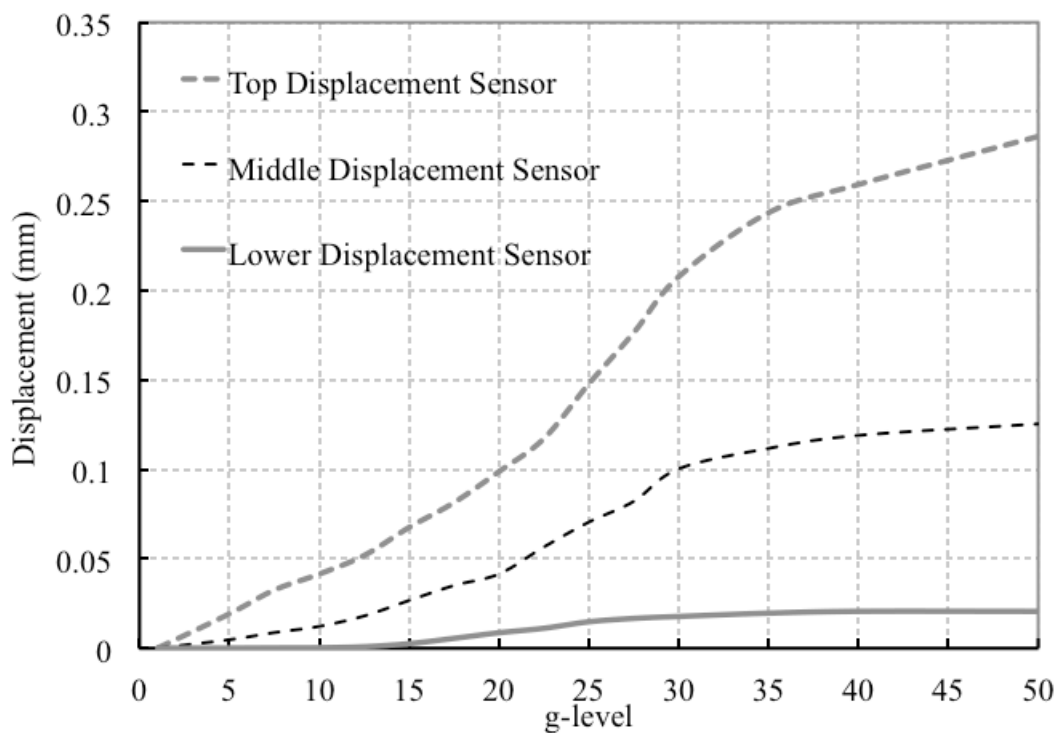


Figure 3.35: Lateral displacements from Nevada sand retaining wall centrifuge test

Acknowledging the unavoidable experimental sources of error such as slight movements of the cantilever wall during model construction, handling, and installation;

velocity and vibrations during spinning could have affected in a minor manner the exact displacements of the wall. The combined translation-rotation movement mechanism could be explained by means of the classical theory of beams where the deflection curve of a cantilever beam (which can represent the retaining wall) can be calculated as:

$$v = -\frac{w_0 x^2}{120 LEI} (10L^3 - 10L^2x + 5Lx^2 - x^3) \quad (3.12)$$

Where w_0 is the linear load at the bottom of the stem that was obtained from the tekscan pressure sensor, x is the location along the length where the deflection is being calculated, E is the aluminium modulus of elasticity, I is the moment of inertia; and L is the length of the beam as shown in Figure 3.36. The deflected shape using beam theory was calculated for different g-levels and compared with the displacements obtained using the three laser sensors readings. Corresponding data and derivation of the procedure followed for the rotation-translation mode of movement is shown in Appendix B.

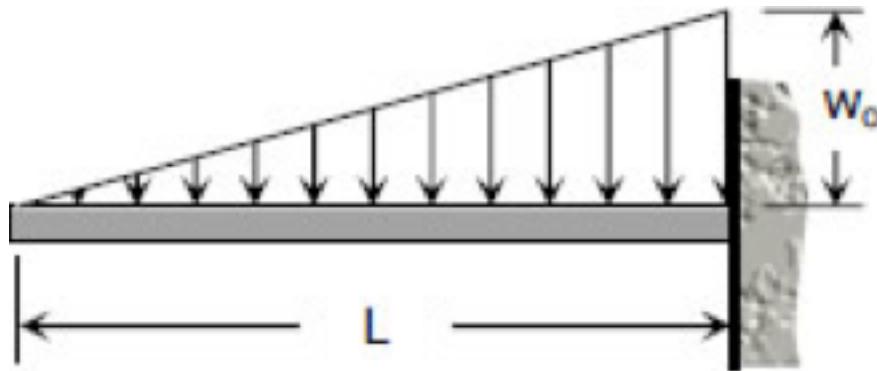


Figure 3.36 Representation of retaining wall model using beam theory

Figures 3.37 through 3.40 show the calculated deflected shape of the wall obtained beam theory and the loads per unit length obtained from the Tekscan sensor (black line) at different g-levels. Laser sensor readings are found to be shifted a certain

amount toward the left with respect to the theoretical deflected shape. This shift is related to a translation of the wall Δ_T that produces an additional rotation in the wall as well.

Translation and rotation were estimated by displacing an additional deflected shape parallel to the initial curve without translation (gray curve) calculated using beam theory. Additional g-level curves and corresponding data can be found in Appendix B.

Figures 3.41 and 3.42 shows the estimated translation of the wall due to sliding at the base with g-level and the height of the wall respectively. The final translation at end of the test was 0.77 mm, and when the results are compared with the total lateral deflections as shown in Figure 3.43, it is observed that translation movements are much lower than the total deflections (14.3 mm at the end of the test). Therefore, the overall movement of the wall was predominantly rotation mode, but the resulting total deflections were highly impacted by sliding in the base of the wall.

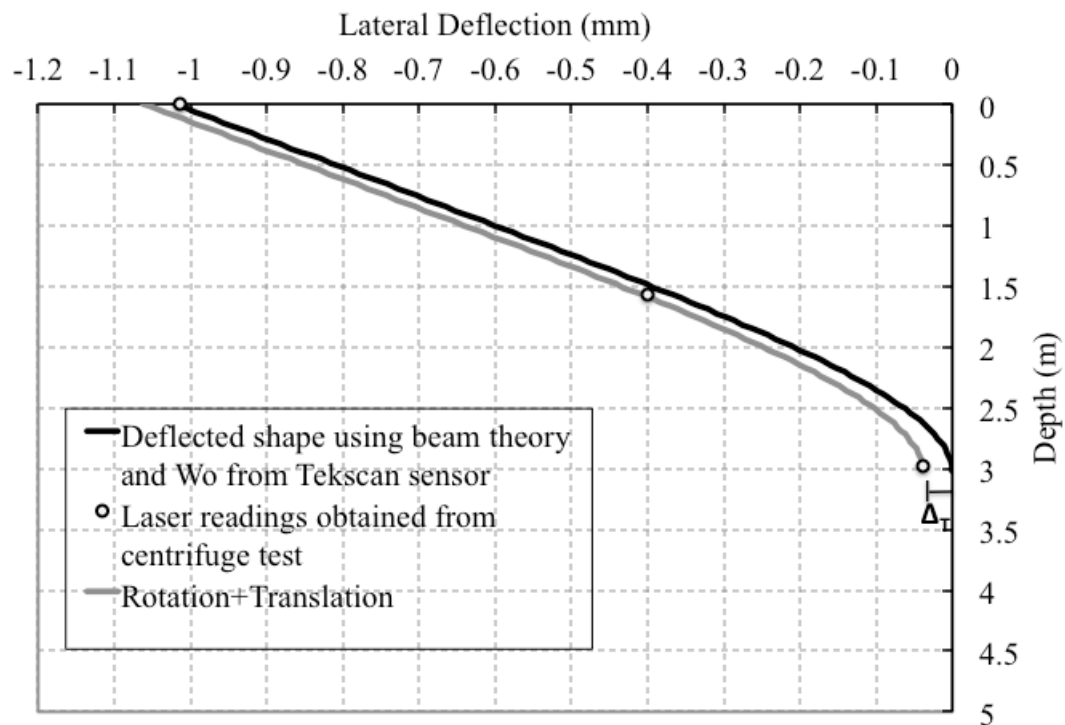


Figure 3.37: Rotation + Translation retaining wall movement at 15 g

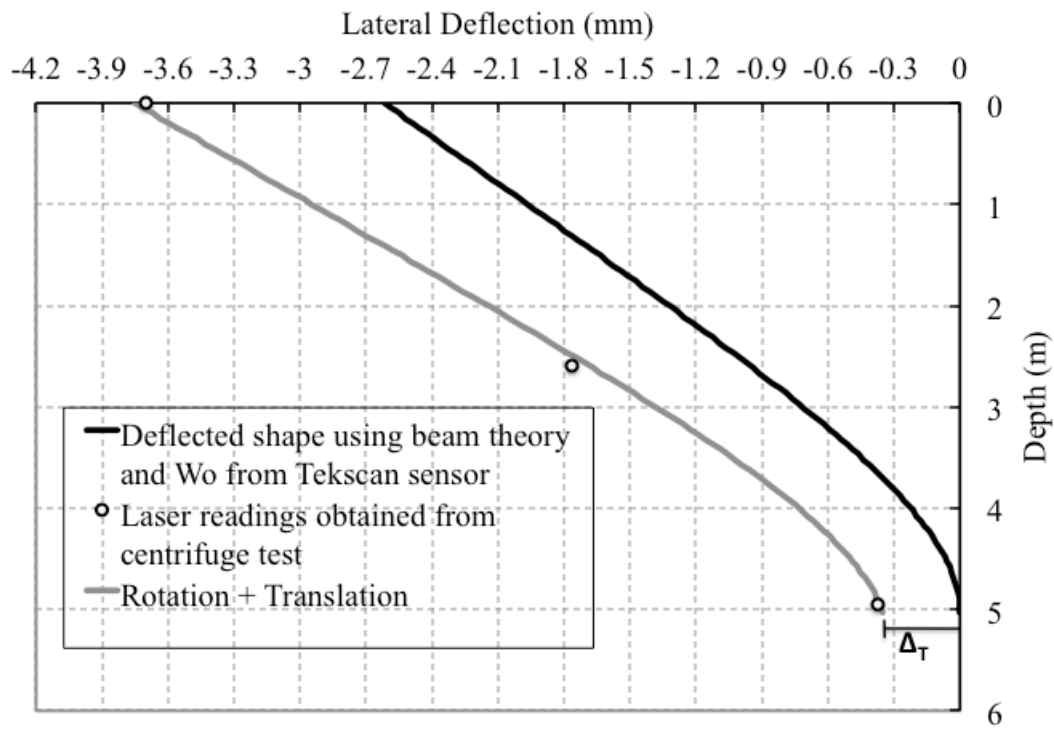


Figure 3.38: Rotation + Translation retaining wall movement at 25 g

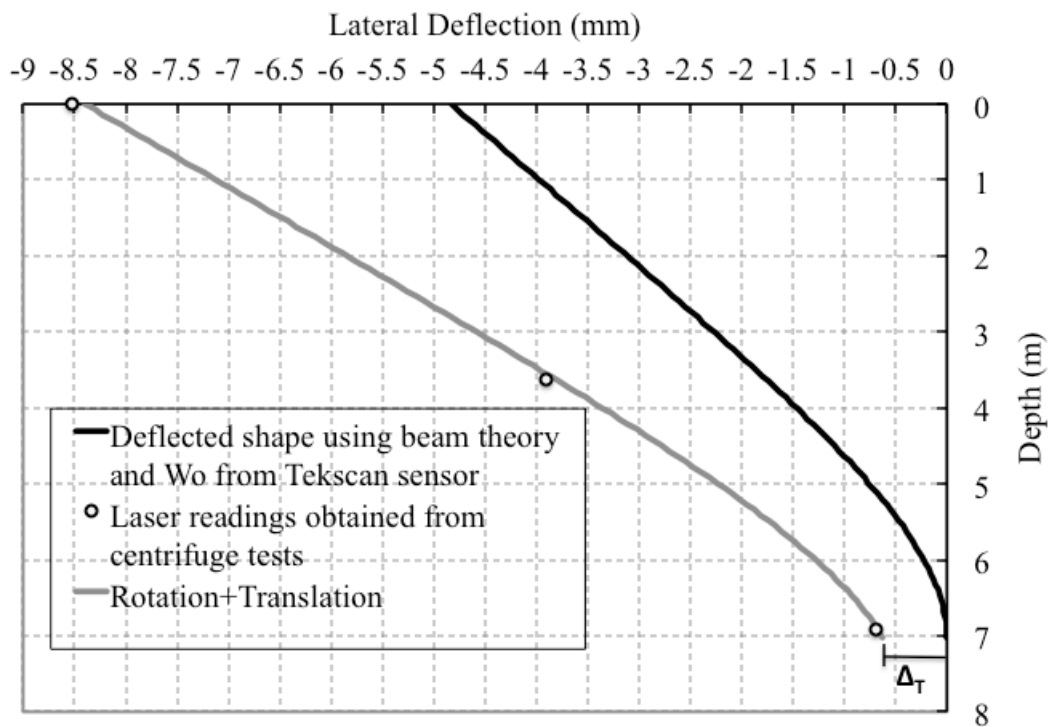


Figure 3.39: Rotation + Translation retaining wall movement at 35 g

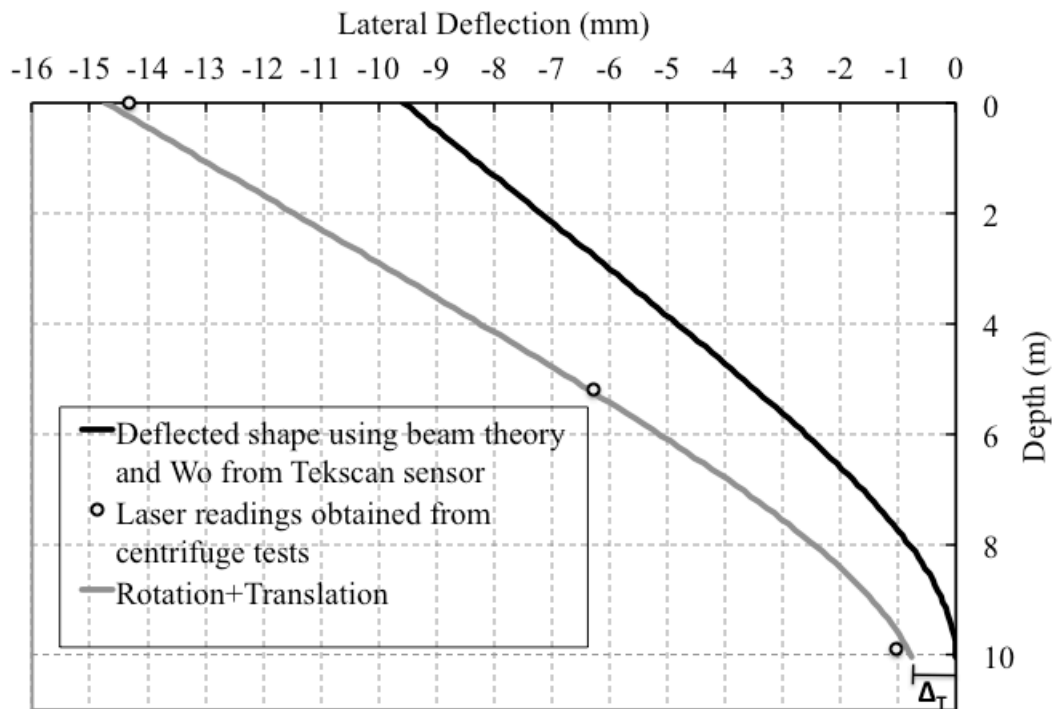


Figure 3.40: Rotation + Translation retaining wall movement at 50 g

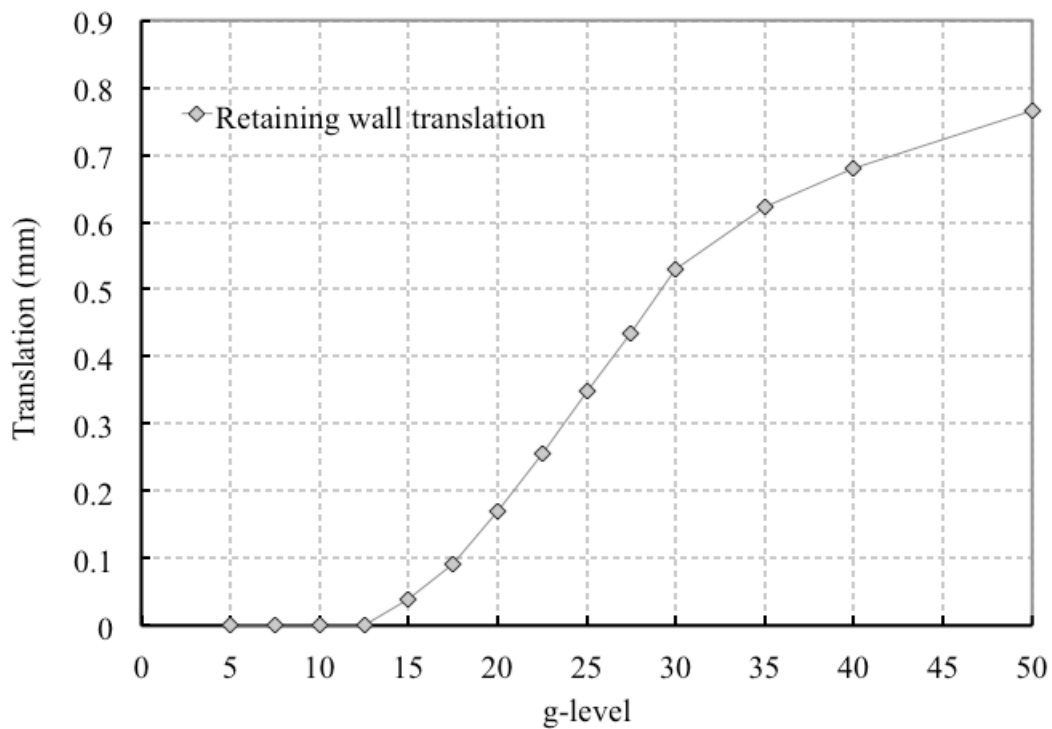


Figure 3.41: Variation of translation in retaining wall with g-level (prototype dimensions)

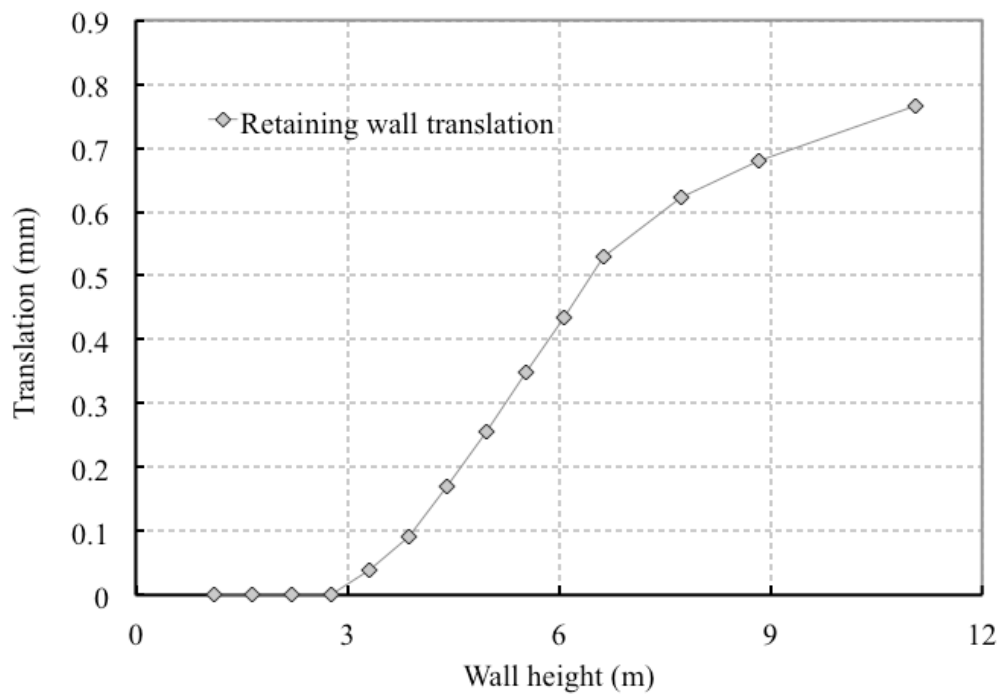


Figure 3.42: Variation of translation in retaining wall with wall height (prototype dimensions)

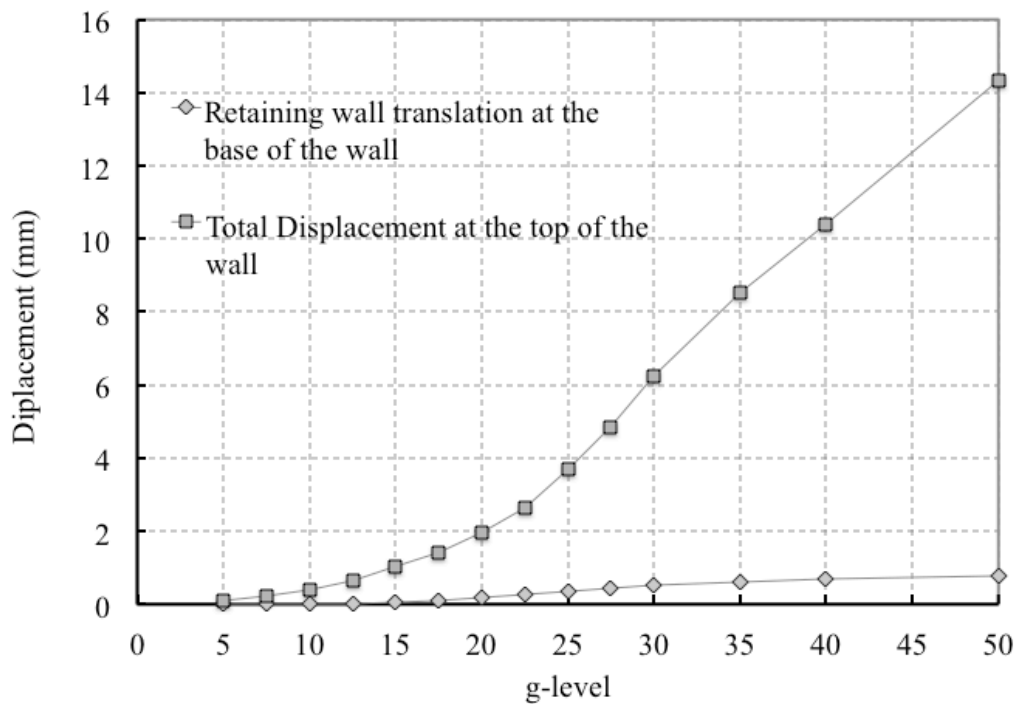


Figure 3.43: Translation of the retaining wall due to sliding vs total deflections (prototype dimensions)

Sliding at the base of the wall may have been provoked due to the fact that lateral earth pressures tends to be higher towards the bottom of the retaining wall as it was previously discussed. Figure 3.44 shows the variation of the earth pressure coefficient (K) with depth, and it is observed that not only K values at the bottom are higher than the overall value for the entire wall obtained from a linear regression but also in general K values are considerable higher bellow 3.5 meters below the retaining wall (prototype dimension) when compared to the values obtained above this depth. These high concentrations of stresses at the bottom of the stem could have caused sliding at the base.

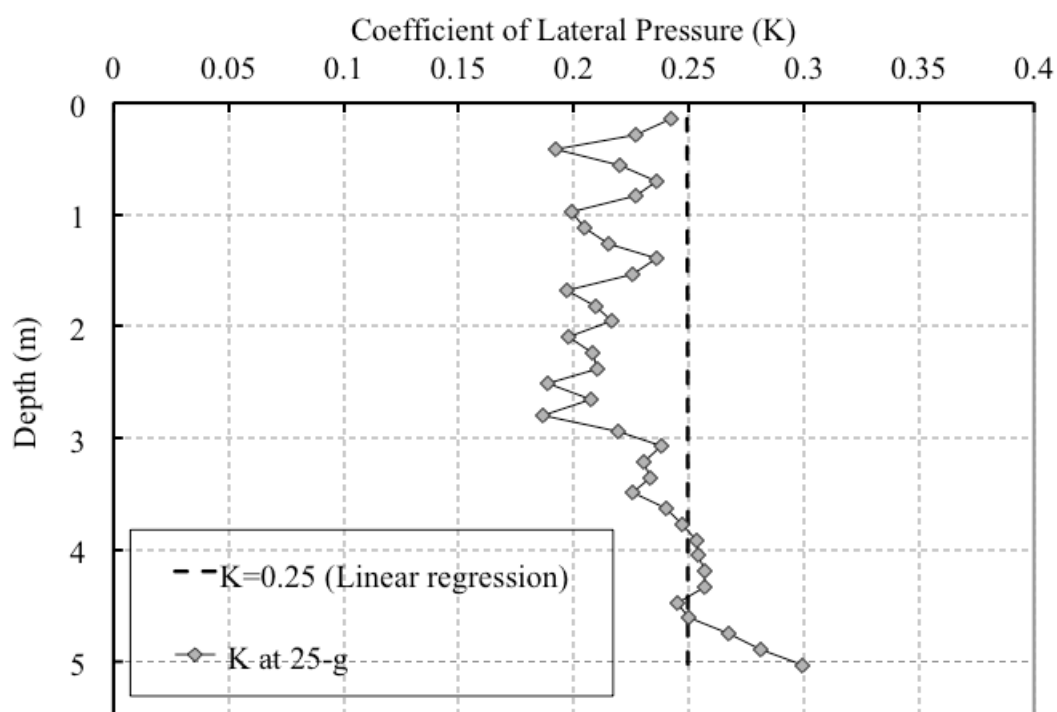


Figure 3.44: Variation of earth pressure coefficient with depth (prototype dimensions)

Factor of safety analysis against sliding and overturning were carried out for different wall heights as shown in Figure 3.45. Factor of safety tends to increase because as the g-level increases, resisting forces in the retaining wall are also scaled in the same proportion. The driving force acting on the retaining wall was also increasing as the g-level went up. However, the acting force was not being scaled at the same proportion because it depends on the amount of movement which is reflected in the reduction of the earth pressure coefficient (K) values.

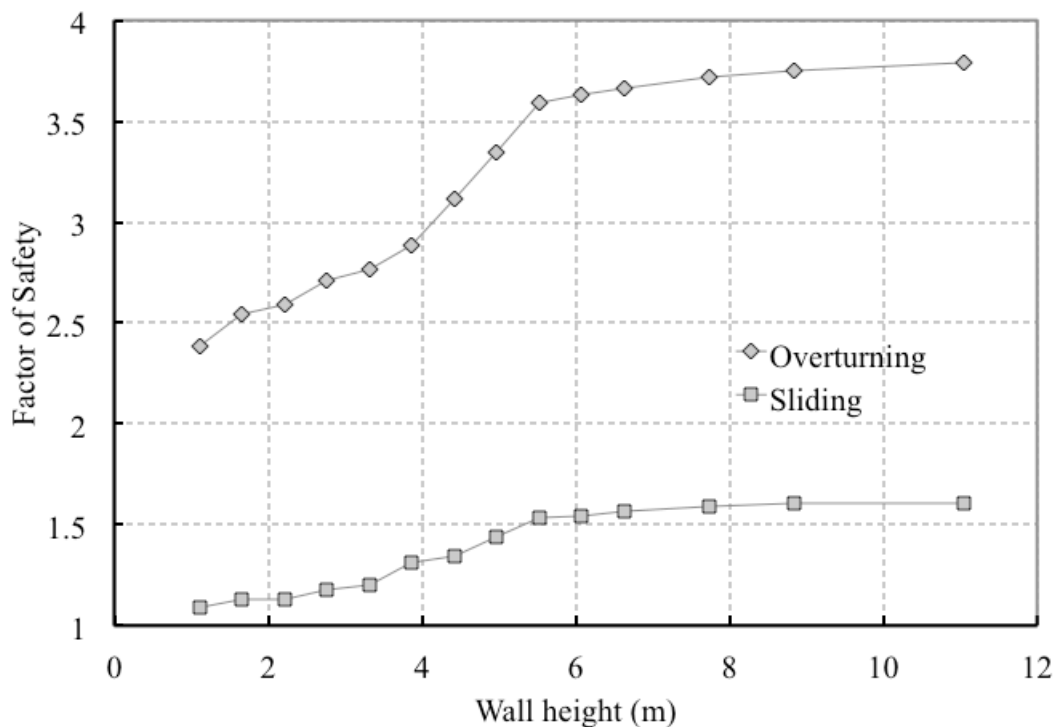


Figure 3.45 Variation of the factor of safety with height of the wall

CHAPTER 4. TRIAXIAL COMPRESSION STRESS-STRAIN BEHAVIOR OF TDA AND TDA/SAND MIXTURES

4.1 Introduction

This chapter describes the experimental methodology and the results obtained from a series of triaxial compression tests carried out on TDA, TDA/sand mixtures, and Nevada sand. The chapter is divided into 3 main sections. First, a description of the procedures used for isotropic consolidated drained (CD) and isotropic consolidated undrained (CU) triaxial compression tests performed and equipment used is presented. Next, the triaxial stress-strain behavior and shear strength parameters of TDA materials using both triaxial techniques are presented. Finally, the chapter presents the analysis and discussion of other variables included in the experimental program such as the use of TDA/sand mixture, strain-rate, and particle size effect in the mechanical response and shear strength characteristics of TDA materials.

4.2 General Description of the Triaxial Compression Test and Methodology

As part of this research, a series of isotropic consolidated drained triaxial compression tests (CD) were carried out on Nevada sand, TDA granulated rubber materials, and mixtures of TDA/sand material. The purpose was to evaluate the triaxial compression stress-strain behavior and shear strength parameters of the different test materials as a function of axial strain levels. Additionally, a series of isotropic consolidated undrained triaxial compression tests (CU) were performed but only on the TDA materials. The purpose of the CU triaxials was to examine the mechanical behavior

of TDA material under undrained condition as well as to investigate the pore pressure generation characteristics. All triaxial tests were performed using 4 different levels of effective confining pressures (2,4,8 and 12 psi) and two different strain rates (0.20%/min and 2.0%/min). All specimens were prepared to an initial relative density of 90%. Generally, the diameter and height of the specimens were approximately 71 mm and 152 mm, respectively. However, detailed data regarding initial dimensions and densities of all test specimens can be found in Appendix C. Table 4.1 shows the test matrix summarizing the triaxial experimental program.

Most triaxial tests involved the same granulated rubber TDA material ($D_{50} = 1.20\text{mm}$) used in the centrifuge tests presented in Chapter 3. However, tests TR-9 through TR-12 were carried out using a rubber granulated TDA material ($D_{50} = 2.60\text{mm}$) with the objective to study the influence of particle size in the stress-strain behavior. Figure 4.1 shows a photo of both TDA test materials. Additional microscope pictures and sieve analysis of the materials can be found in Appendix C.

Table 4.1: Test matrix of triaxial testing program for TDA, Nevada sand, and TDA/sand mixtures

Test number	Test type	Material	Confining pressure (kPa)	Strain rate (%/min)
TR-1	Consolidated Drained (CD)	TDA (D ₅₀ =1.20mm)	13.79 (2 psi)	0.20
TR-2			27.58 (4 psi)	
TR-3			55.16 (8 psi)	
TR-4			82.74 (12 psi)	
TR-5	Consolidated Drained (CD)	Nevada-Sand (D ₅₀ =0.15mm)	13.79 (2 psi)	0.20
TR-6			27.58 (4 psi)	
TR-7			55.16 (8 psi)	
TR-8			82.74 (12 psi)	
TR-9	Consolidated Drained (CD)	TDA (D ₅₀ =2.60mm)	13.79 (2 psi)	0.20
TR-10			27.58 (4 psi)	
TR-11			55.16 (8 psi)	
TR-12			82.74 (12 psi)	
TR-13	Consolidated Drained (CD)	TDA (D ₅₀ =1.20mm)	13.79 (2 psi)	2.0
TR-14			27.58 (4 psi)	
TR-15			55.16 (8 psi)	
TR-16			82.74 (12 psi)	
TR-17	Consolidated Undrained (CU)	TDA (D ₅₀ =1.20mm)	13.79 (2 psi)	0.20
TR-18			27.58 (4 psi)	
TR-19			55.16 (8 psi)	
TR-20			82.74 (12 psi)	
TR-21	Consolidated Undrained (CU)	TDA (D ₅₀ =1.20mm)	13.79 (2 psi)	2.0
TR-22			27.58 (4 psi)	
TR-23			55.16 (8 psi)	
TR-24			82.74 (12 psi)	
TR-25	Consolidated Drained (CD)	TDA/sand Mixture (3/7 by weight) (50/50 by volume)	13.79 (2 psi)	0.20
TR-26			27.58 (4 psi)	
TR-27			55.16 (8 psi)	
TR-28			82.74 (12 psi)	
TR-29	Consolidated Drained (CD)	TDA/sand Mixture (1/9 by weight) (20/80 by volume)	13.79 (2 psi)	0.20
TR-30			27.58 (4 psi)	
TR-31			55.16 (8 psi)	
TR-32			82.74 (12 psi)	

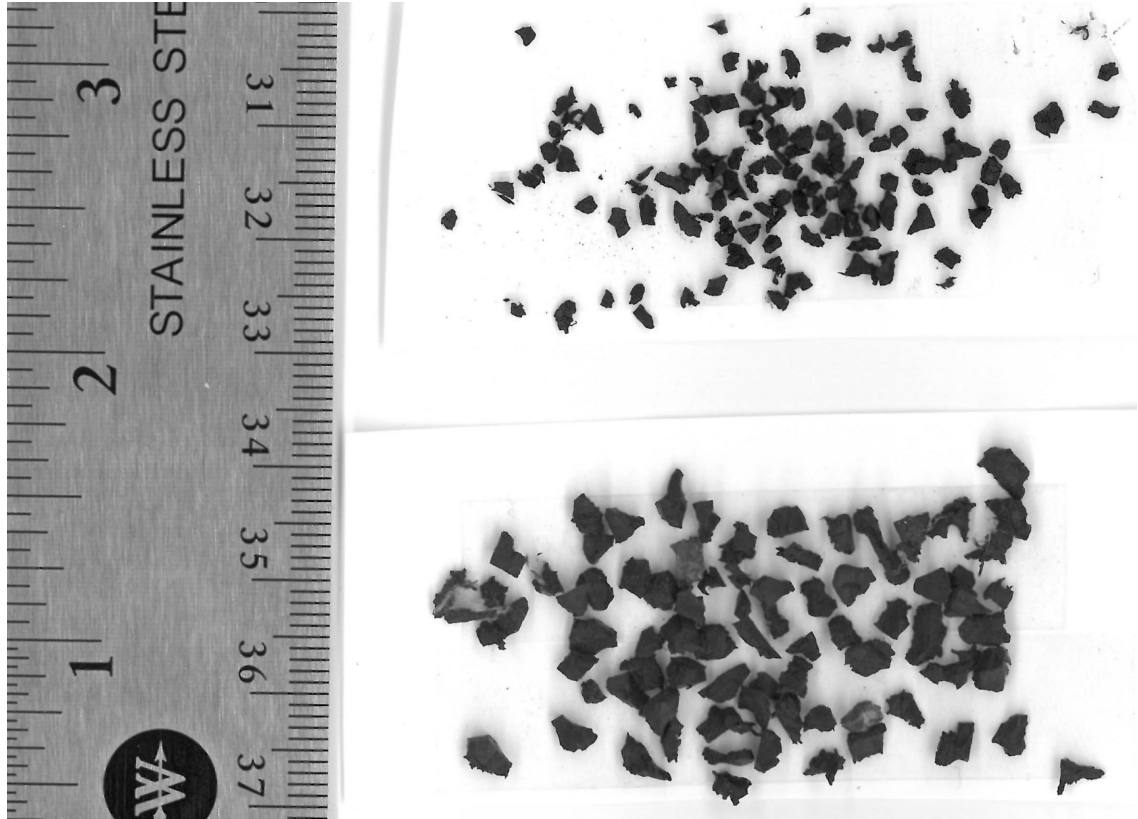


Figure 4.1: TDA with different particle size tested in the triaxial experimental program

4.2.1 Triaxial Tests Set-up and Sample Preparation Procedure

Triaxial tests were performed using the automatic LoadTrac II/FlowTrac II triaxial system manufactured by Geocomp Corp. as shown in Figure 4.2. This testing system consists of three main components: a load frame (LoadTrac-II) which applies the vertical deviatoric load to the specimen, and two volume-pressure controllers (FlowTrac-II) which measure and control the cell and sample pressures and track changes in volume. More details of this machine can be found in Geocomp Corp (2011).



Figure 4.2: Geocomp triaxial system

Sample preparation consisted of positioning a latex membrane within a forming split mold using a vacuum, which held the membrane open to approximately 71 mm diameter as shown in Figure 4.3. The latex membrane had an average wall thickness of 0.25 mm. The membrane was securely attached to the top and bottom of the mold with aid of O-rings. All specimens were prepared by pouring consecutive layers (1 inch thickness) of the materials into the latex membrane and tamping each layer before the next one is placed. Each layer was compacted with a tamping rod keeping track of the mass and height required to achieve the desired target initial relative density.



Figure 4.3: Mold set up used for specimen preparation

After the removal of the split mold, at least three diameter and height measurements were taken to determine the specimen dimensions and initial sample density. Then, the triaxial cell was carefully assembled, and filled with water. A pre-saturation process was also performed in order to shorten the amount of time required for saturation during the tests. Figures showing the procedure used for the triaxial cell filling and for sample pre-saturation can be found in Appendix C.

Once the triaxial cell was completely filled, it was carefully transported to the triaxial frame for testing. All tests consisted primarily of three phases: saturation, consolidation and shearing. Saturation was achieved through a back pressure saturation to the specimens. The automatic system applied successive increments of cell and sample pressure until a B pore pressure parameter value of at least 0.97 was obtained. After saturation, consolidation phase consisted in applying an isotropic confining pressure.

Four different levels of effective, isotropic confining pressures were selected for this research, namely 2,4,8 and 12 psi (13.79,27.58, 55.16 and 82.74 kPa) for each set of tests listed in Table 4.1. The system applied and maintained the target confining pressure until reaching 100% of primary consolidation in the sample. Finally, either drained or undrained shearing (see Table 4.1) was applied. All triaxial compression tests were strain-controlled tests performed at rates of 0.20% or 2.0% axial strain per minute.

Figures 4.4 through 4.6 shows photos of representative samples before and after shearing for the initial set up of the triaxial tests and failure shapes after shearing for TDA, Nevada sand, and TDA/sand mixture (50/50 by volume), respectively. For TDA samples, a failure plane was not typically observed as shown in Figure 4.4. The failure mode was sample bulging which was in line with the observed high level of axial deformation and compressibility of the TDA aggregate. The Nevada sand and TDA/sand mixture presented a failure mode with a well-defined failure plane as shown in Figure 4.5 and 4.6, respectively. More details about triaxial tests can be found in Appendix C.

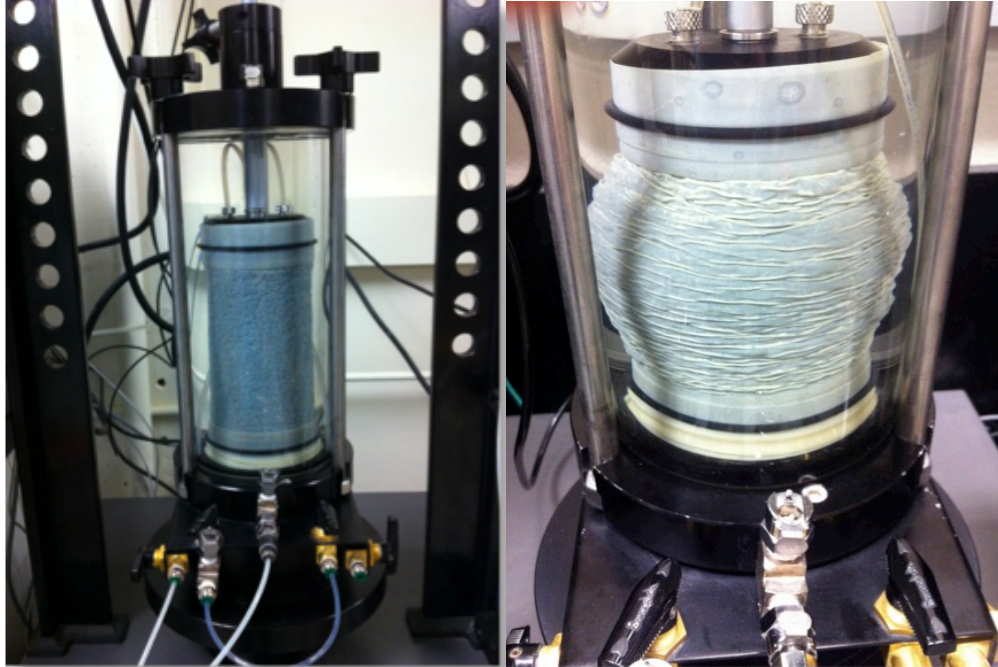


Figure 4.4: TDA triaxial tests and failure after shearing

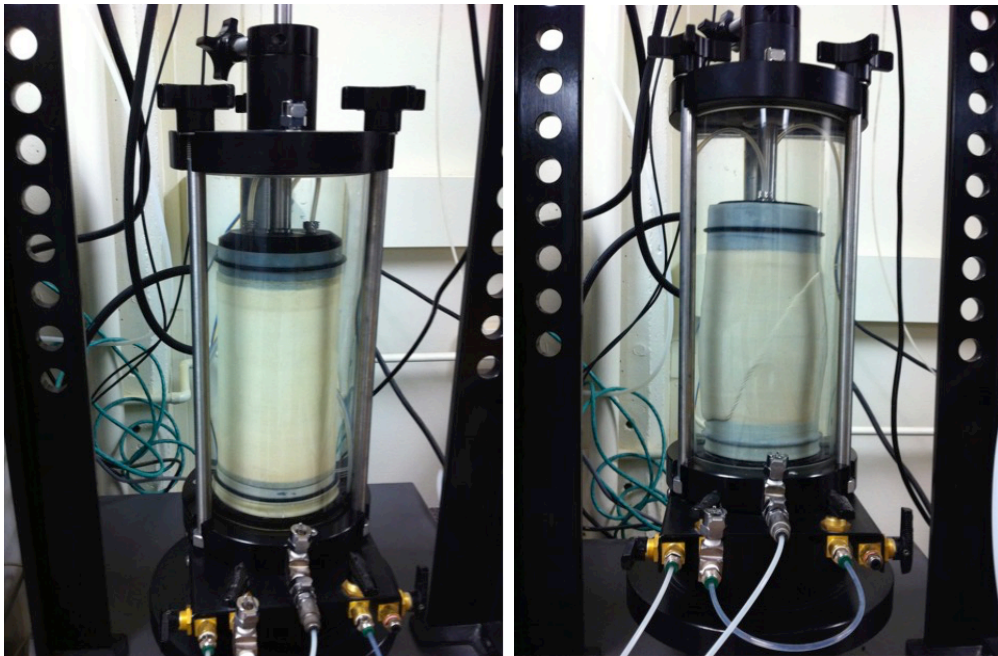


Figure 4.5: Nevada sand triaxial tests and failure after shearing

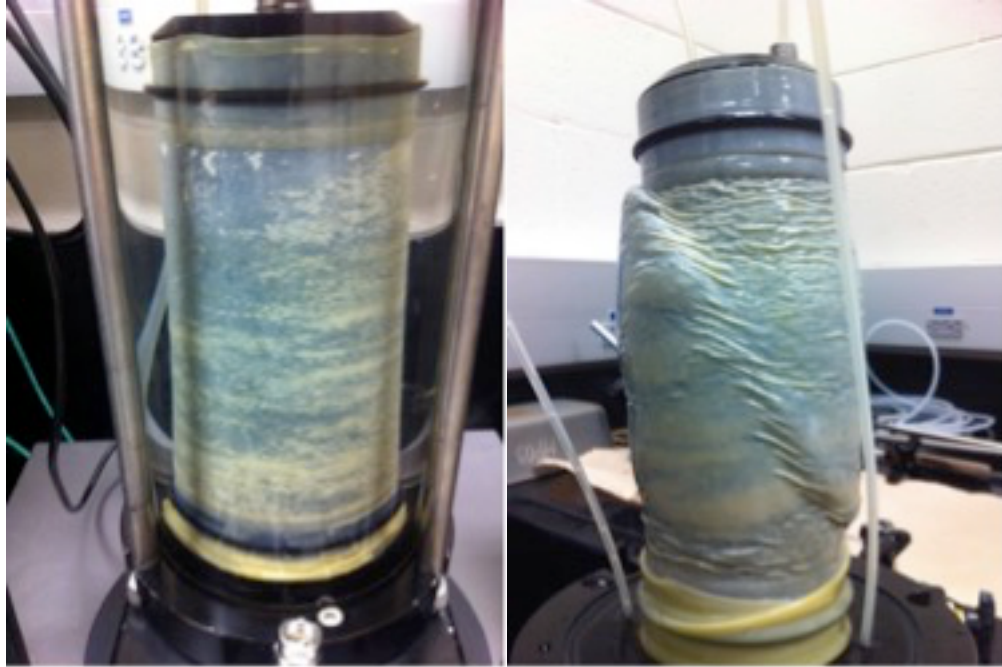


Figure 4.6: TDA/sand mixture triaxial test and failure after shearing

Before presenting test results, it is important to discuss the cross-section area correction used given the large vertical and radial deformations observed in most samples during shearing. These deformations play an important role when correcting the cross-sectional area needed to calculate stresses. Radial deformations are an important factor to consider in the TDA specimens since All TDA triaxial samples deformed in a parabolic fashion as shown in Figure 4.4. Therefore, the following parabolic area correction was used:

$$\text{Specimen Area} = A = A_0 \frac{1 - \varepsilon_{vol}}{1 - 1.5\varepsilon_v} \quad (4.1)$$

Where A_0 is the initial cross sectional area of the specimen; ε_{vol} is the volumetric strain; and ε_v is the axial strain. Axial strains, volumetric strains, and deviatoric stresses needed for further analysis were computed using a detailed spreadsheet prepared for this

research. For example, the change in height that the specimen experienced during saturation, and consolidation required to calculate the axial strain during shearing was computed by taking the LVDT displacement sensor measurements from the beginning of the test to the end of each phase. This procedure allowed determining accurately the initial height of the sample at the beginning of the shearing phase. Changes in height during shearing were calculated from the raw LVDT displacement data as well in order to calculate corresponding axial strains. Changes in volume were obtained by taking the cell and sample motors steps raw data, which were converted, into cell and sample volume changes using the cell and sample cell multiplier. This value is equal to 5.363×10^4 cc/step (Geocomp-Corp. 2011). Therefore, the change in volume in each step could be calculated according to Geocomp-Corp as:

$$\Delta \text{Micro steps} \times 5.363 \times 10^{-4} \frac{\text{cc}}{\text{step}} = \Delta \text{Volume change in cc} \quad (4.2)$$

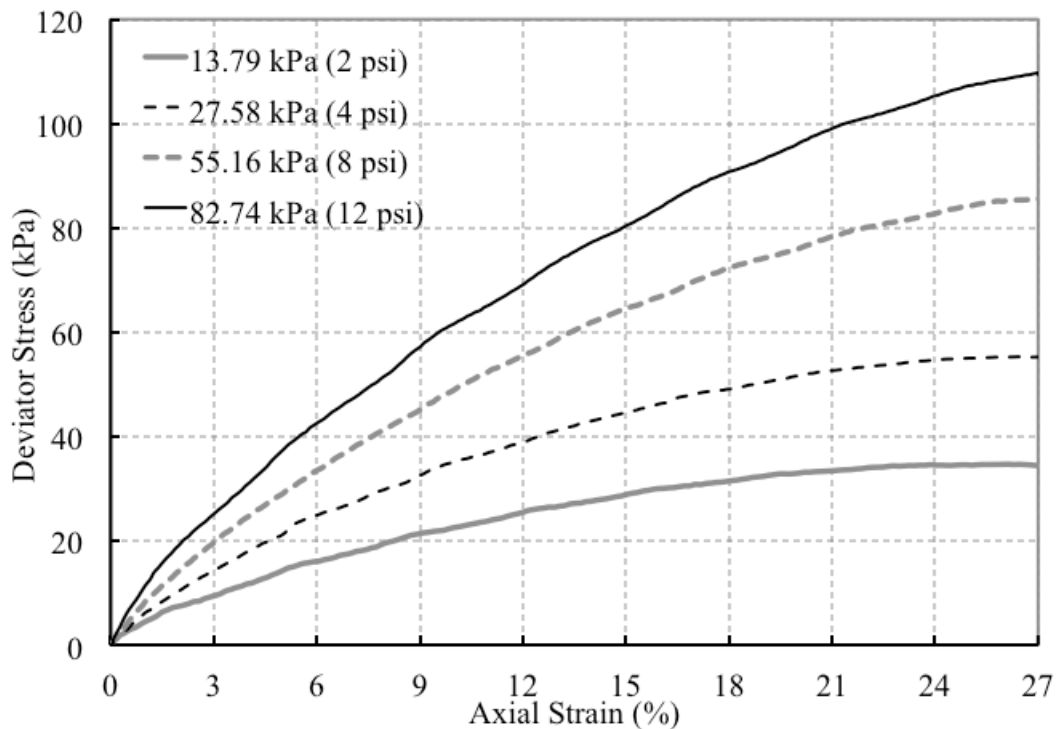
where cc = cm³.

The previous expression allowed calculating the volume change in the specimen at the end of consolidation in order to determine its volume before shearing. Volumetric strains during shearing were also calculated using Equation 4.2. Volume changes during all shearing steps and the initial volume during that phase.

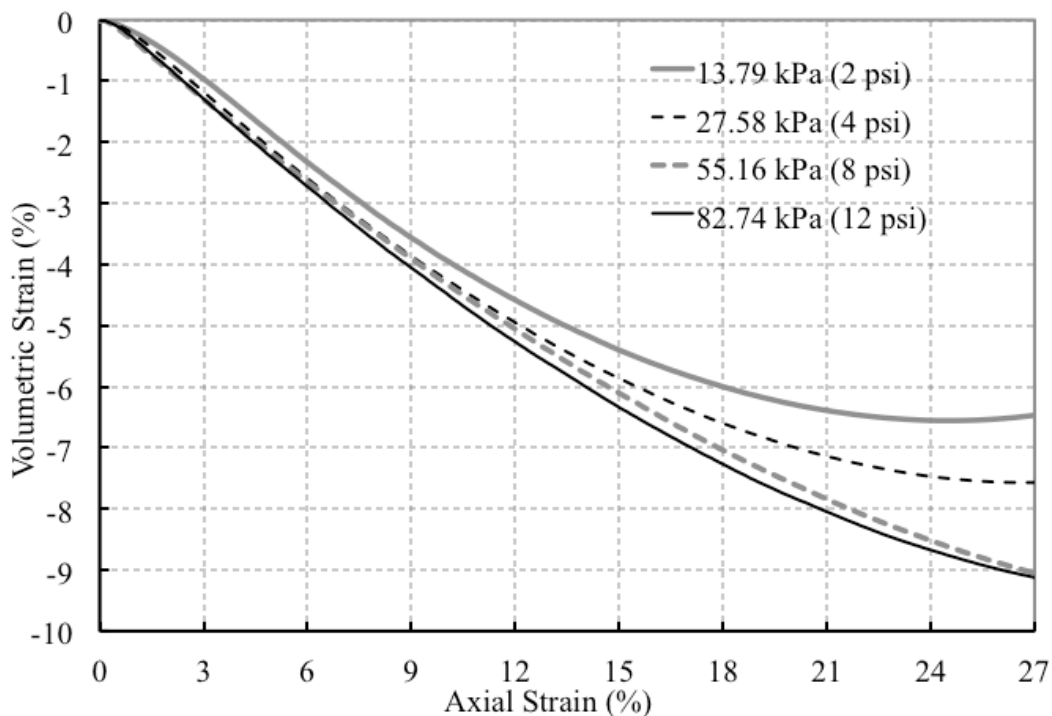
4.3 Stress-Strain Behavior of TDA Materials From CD Triaxial Tests

CD triaxial compression tests for the TDA granulated rubber material were carried out for the four levels of effective confining pressures mentioned earlier. Samples were prepared in a very dense state ($\sim 90\%$ relative density). Figure 4.7 shows the deviator stress versus axial strain, and the volumetric change versus axial strain during the shear phase for all four different confining pressures. Figure 4.8 shows the corresponding results obtained for the Nevada sand specimens. As expected, no build-up in excess pore pressure was observed during the tests at the strain-rate of $0.2\%/min$. Therefore, fully drained conditions were achieved which was expected specially given the high permeability characteristics broadly reported in the literature.

As shown in Figure 4.7, the drained stress-strain behavior observed in the TDA materials ($D_{50} = 1.2 \text{ mm}$) showed a gradual monotonic increase of the deviatoric stress even to very high axial strain levels of 27% . Furthermore, the volumetric-strain behavior was contractive and approximately linear to an axial strain of about 10% . The levels of axial strains reached for TDA material is not commonly exhibited by conventional soil materials. This is illustrated in Figure 4.8 where the results for the Nevada sand are reported. Therefore, failure can be defined recommendations by ASTM D4767 (ASTM 2011) which suggests using a limiting axial strain of 15% . It is observed that for TDA materials there is a not well-defined peak for all four tests. However, for purposes of this dissertation an analysis of the variation of the shear strength parameters as a function of different limiting axial strain levels was undertaken which included axial strain levels of up to 27% .

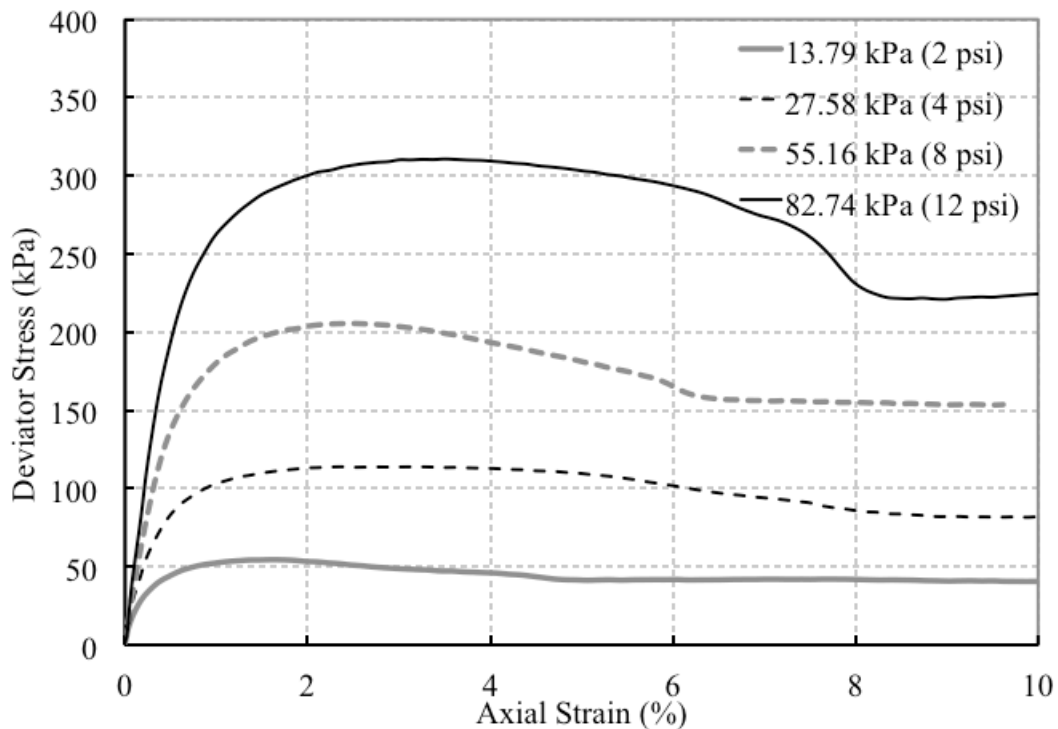


a) Deviator stress vs axial strain

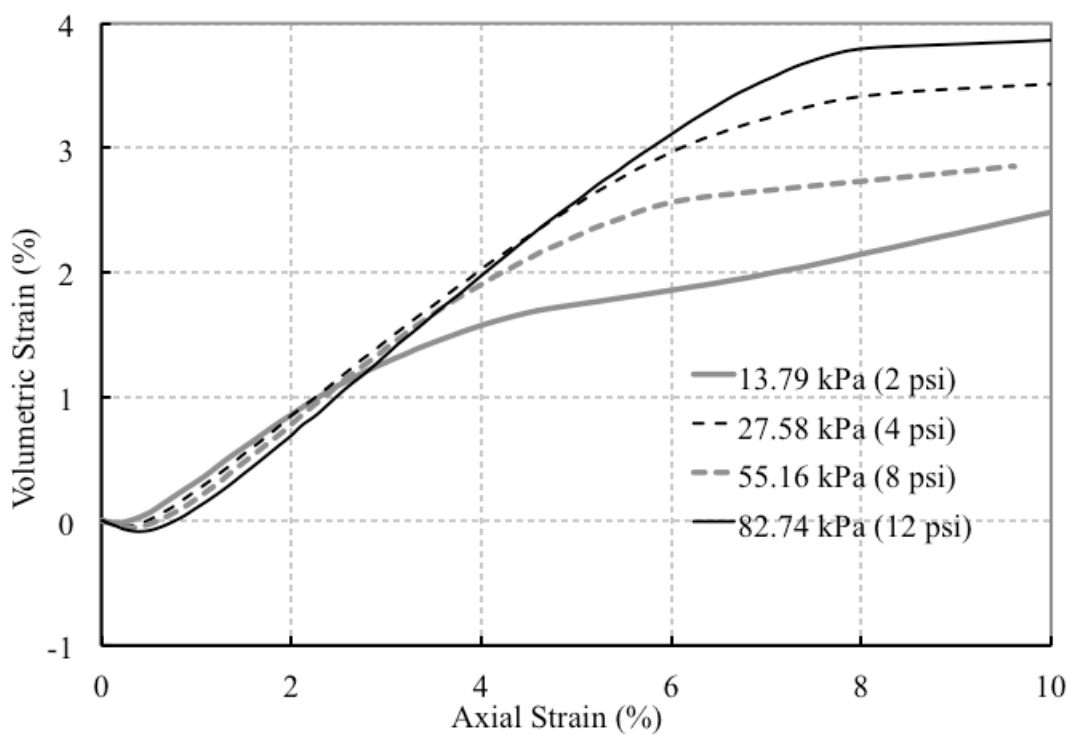


b) Volumetric strain versus axial strain

Figure 4.7: CD Triaxial compression tests results for TDA material ($D_{50}=1.20\text{mm}$)



a) Deviator stress versus axial strain



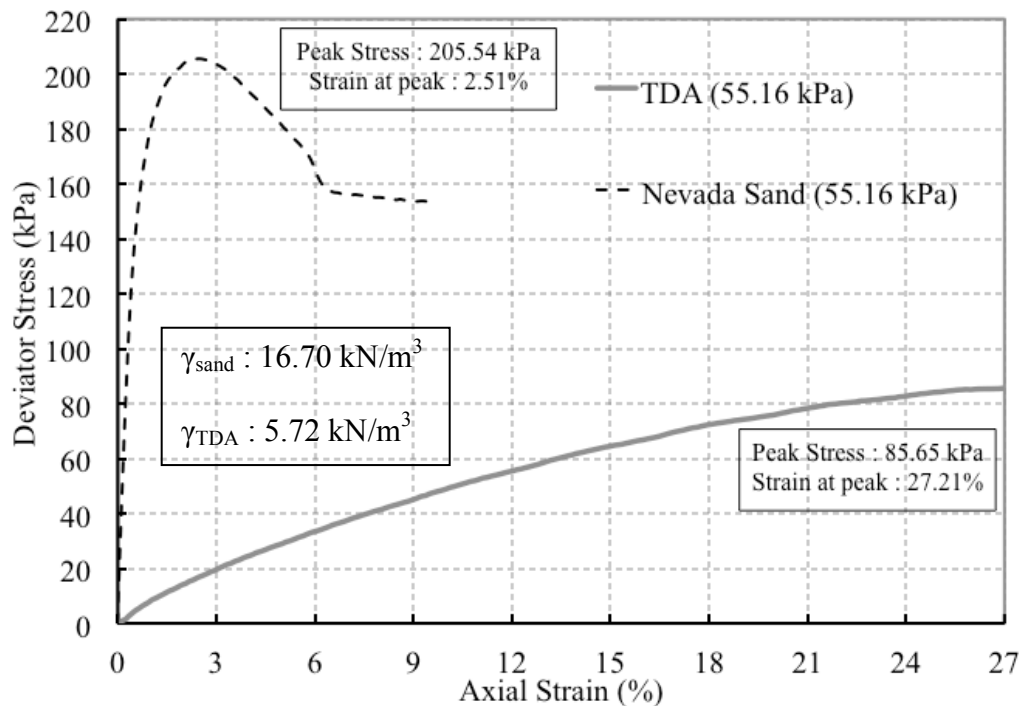
b) Volumetric strain versus axial strain

Figure 4.8: CD drained triaxial compression tests for dense Nevada sand ($D_{50} = 0.15\text{mm}$)

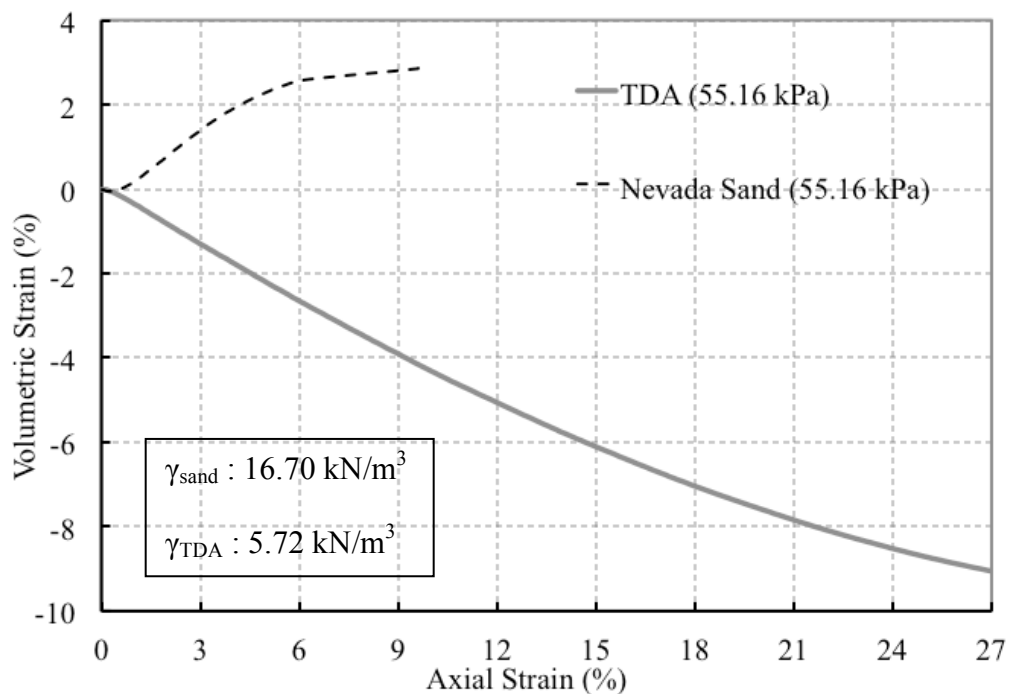
The results for the two materials are very different despite being tested at the same initial very dense state, and similar effective stress levels. The Nevada sand results are similar to those widely reported in the literature for granular mineral backfills. At the initial stage of shearing, all specimens exhibited a short contraction, which is related to initial particle rearrangement and reorientation followed by dilation as the shearing continued as shown in Figure 4.8 (b). A clear peak deviatoric stress was observed in all tests and occurred at axial strain levels of approximately 2%. In contrast TDA samples, experienced a peak deviatoric even at axial strain levels beyond 20% axial strain at dense state. Additionally, Nevada sand specimens exhibit strain-softening characteristics after reaching the peak deviatoric stress. Conversely TDA specimens did not exhibit strain-softening behavior. However, TDA specimens seem to start approaching a shearing state of constant volumetric change at around 25% axial deformation strain. This may imply that TDA might be close to achieving a steady state of deformation (constant volume) condition at these very large levels of axial strain.

Figure 4.9 shows a comparison of the stress-strain behavior of both materials for a confining stress level of 55 kPa. The same tendency was observed for the other three confining pressures as shown in Appendix C. it is observed that Nevada sand samples are quite stiffer compared to TDA samples. Secant Young's modulus for the different test materials will be discussed later in this chapter. The loss in volume during consolidation phase was dramatically higher in all TDA samples when compared to Nevada sand. This loss of volume was highly dependent on the confining pressure applied for the TDA samples whereas in the Nevada sand specimens, the small loss in volume had relative similar values for all four levels of confining pressures. This is an important difference

between both materials, TDA are too sensitive to the level of confining pressure applied due to its intrinsic deformable characteristics of the skeleton and particles. In fact, it has been reported that compacting energy has only a small effect on the resulting density of TDA (ASTM 2012) which is consistent with the narrow range between maximum and minimum relative densities reported in Appendix A. TDA specimens when compacted during the preparation process would tend to rebound but not when subject to the different confining pressures which is maintained constant and not removed during the consolidation pressure. Under these conditions, TDA specimens cannot rebound, and thus their loss of volume will be higher as the confining stress level increases. This is due to its high deformability which is not the case for the Nevada sand specimens, specially prepared at a dense state where there are not as many voids in the sample and because the sand particles are rigid. The high deformable characteristic of TDA samples make triaxial testing challenging since these techniques are mainly designed to test rigid granular materials. However, other authors have reported TDA mechanical properties using triaxial tests as well; and it is important to use conventional geomaterials characterization techniques in TDA in order to properly compare both behaviors. Appendix C presents additional information regarding density variation with confining pressure and volume loss during consolidation for the reader.



a) Deviator stress versus axial strain



b) Volumetric strain versus axial strain

Figure 4.9: Comparison between TDA material and Nevada sand for CD triaxial test at 55.16 kPa confining pressure

4.3.1 Shear Strength Parameters for TDA Materials Under Drained Conditions

Shear strength parameters (ϕ' and c') were determined for the TDA material using the data obtained from the consolidated drained tests. Figures 4.10 show the stress paths for TDA up to 25% axial strain. For the Nevada sand samples stress paths are shown in Figure 4.11 until peak deviatoric stress is achieved. It is noted that for the TDA, the failure envelope seems to be better represented passing through a y-intercept that would correspond to cohesion intercept in the material. For more clarity, Figures 4.12 through 4.14 show the stress paths, the linear regressions for the failure envelope considering both: a line passing through the origin ($c'=0$), and a best fit line passing allowing a y-intercept ($c' \neq 0$). The mobilized shear strength parameters different strain levels are shown for $c' \neq 0$ while Table 4.2 shows the data for both different regressions. Data for the rest of different axial strains considered in the analysis is presented in Appendix C. It was found that the TDA shear strength parameters drastically change as the axial strain level increases for the TDA.

Table 4.2: TDA shear strength parameters (CD triaxial tests)

Axial Strain (%)	Failure Envelope with y-axis intercept			Failure Envelope Through origin ($c' = 0$)	
	ϕ' (°)	c' (kPa)	R^2	ϕ' (°)	R^2
5	8.00	4.75	0.991	11.69	0.725
10	12.47	6.97	0.989	17.32	0.810
15	15.58	8.23	0.991	20.89	0.858
20	18.13	8.61	0.994	23.33	0.900
25	20.08	8.18	0.995	24.83	0.933
27	20.52	7.94	0.996	25.11	0.941

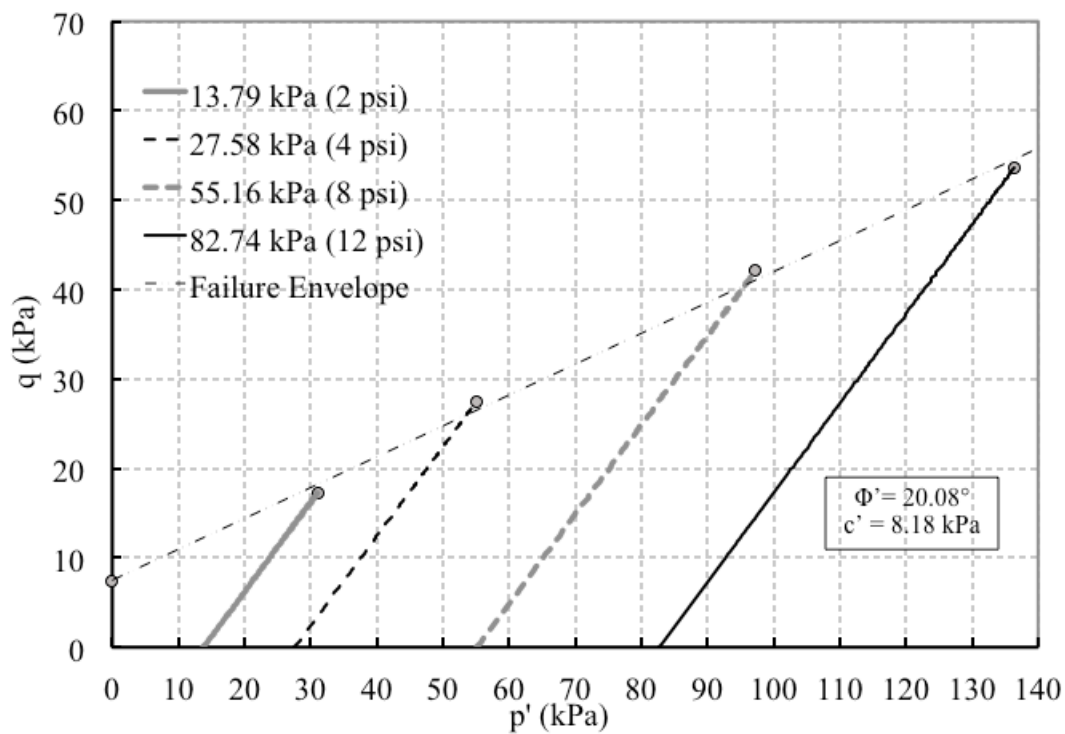


Figure 4.10: Stress paths for TDA material during CD triaxial tests at 25% axial strain

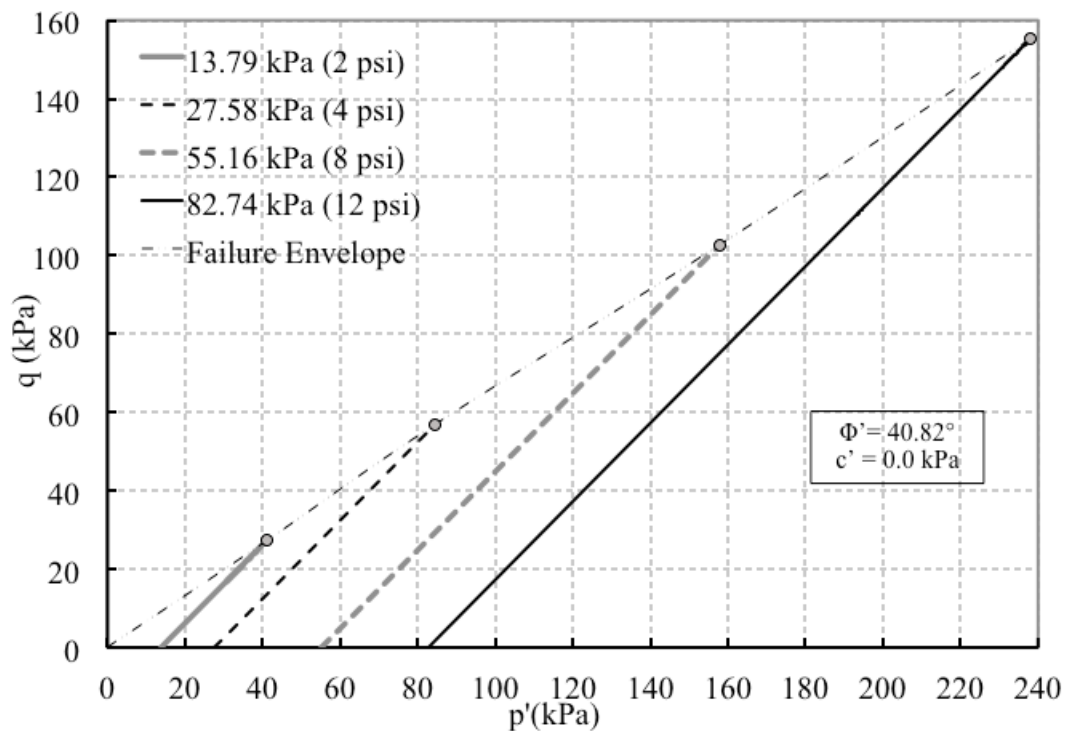


Figure 4.11: Stress paths for Nevada sand material during CD triaxial tests at peak

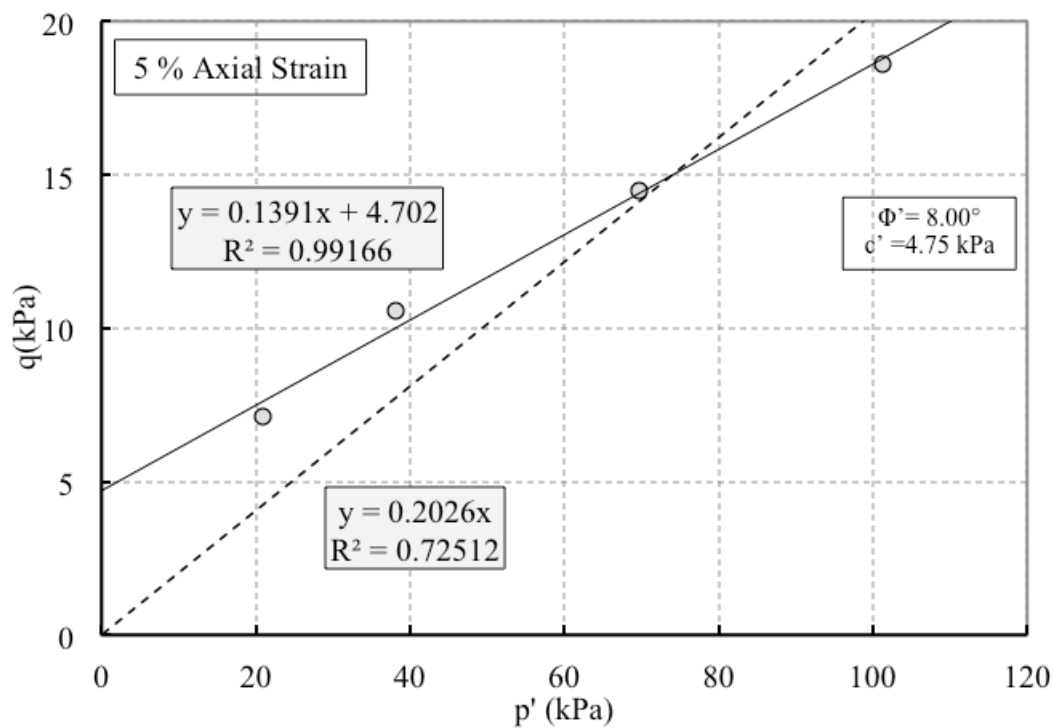


Figure 4.12: Shear strength parameters determination for TDA at 5% axial strain

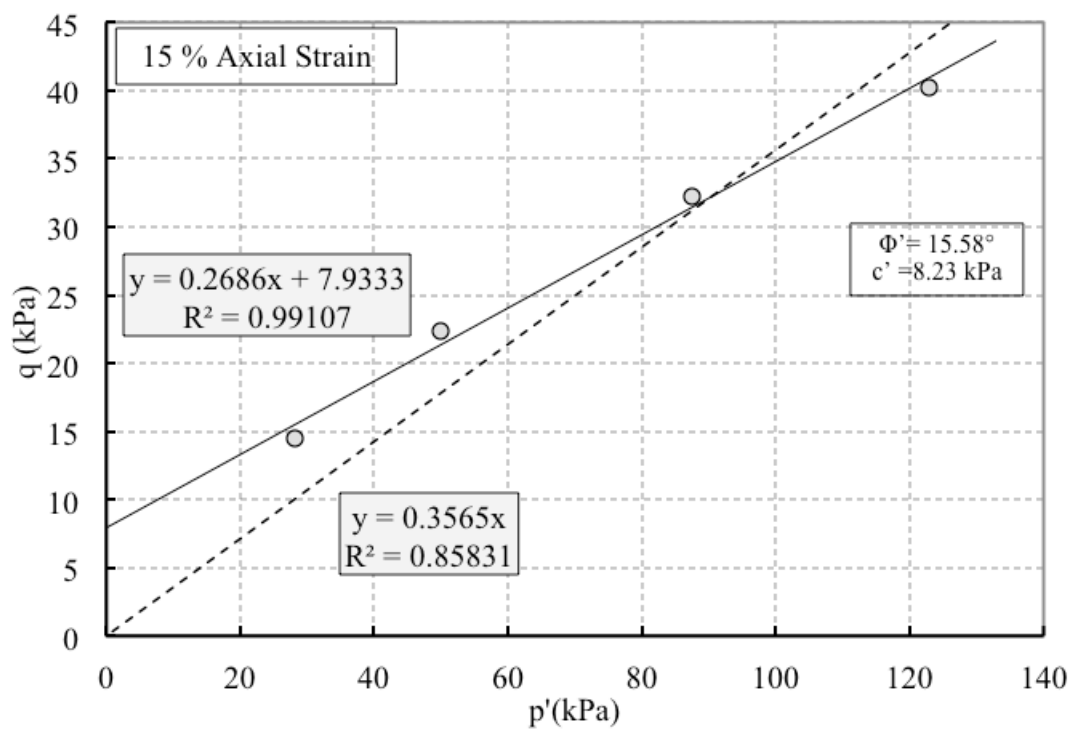


Figure 4.13: Shear strength parameters determination for TDA at 15% axial strain

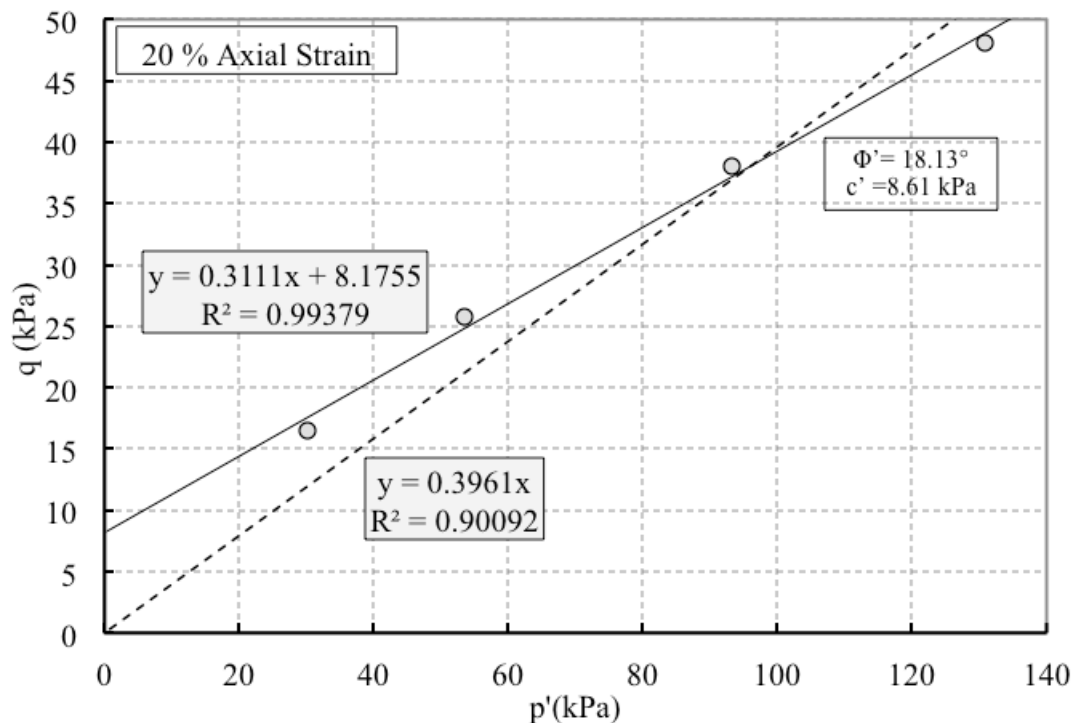


Figure 4.14: Shear strength parameters determination for TDA at 20% axial strain

Despite the fact that conventional granular soils exhibits low degree of deformation to reach a peak failure, the same analysis was performed for the Nevada sand at very low axial strain levels. It is common practice to report the frictional angle at peak for sands; however as seen in Figure 4.15 frictional angles in Nevada sand changes between 33.41 to 39.78 degrees for axial strains ranges between 0.5 and 1.5% reaching a frictional angle at failure equal to 40.82 degrees as it was shown in Figure 4.11. Although, mechanical properties of Nevada sand may vary with each batch delivered; similar friction angles for drained conditions at a dense state have been reported in the literature by other authors (Arulmoli et al. 1992; Kutter and Chen 1997). The increase in frictional angle may be due to particle rearrangement and reorientation during shearing.

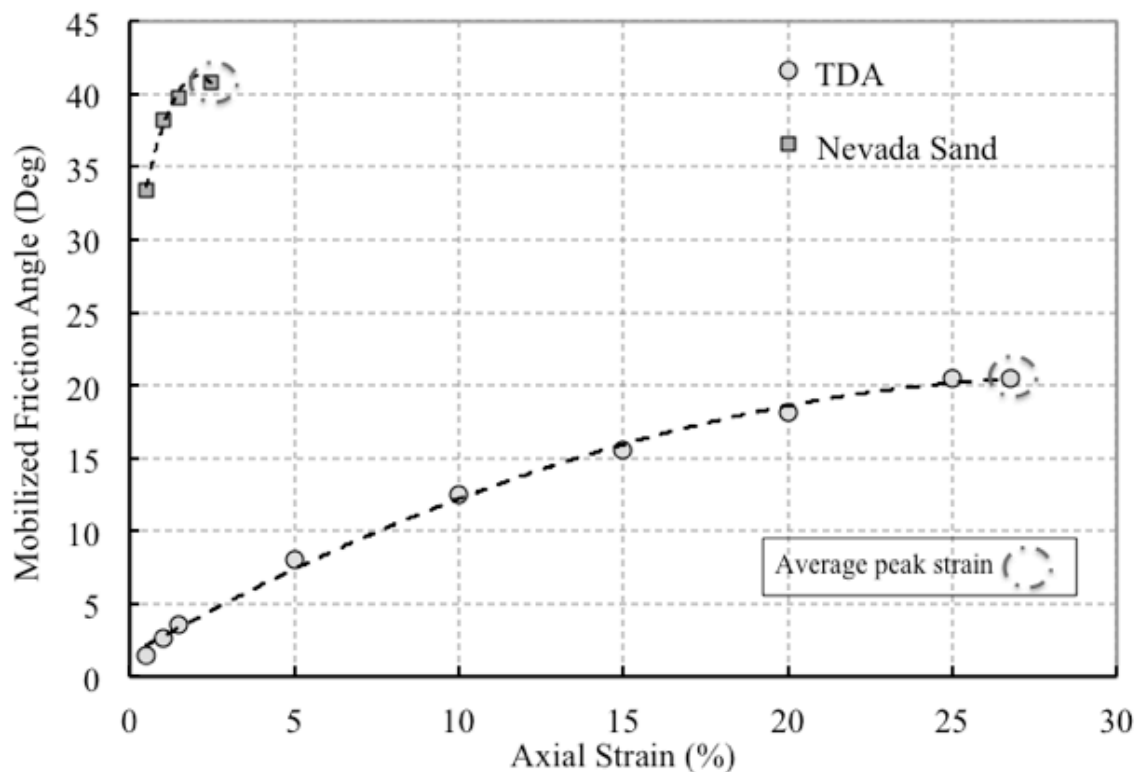


Figure 4.15: Comparison between TDA and Nevada sand friction angles for different strain levels

The selection of shear strength parameters for TDA materials as shown in Table 4.2 and Figure 4.15 is not as straightforward as for conventional granular soils. Such high levels of axial deformations most likely would not be permissible for most civil engineering applications. Frictional angles can vary between 8.0 to 20.5 degrees for axial deformations ranges between 5 and 27%. The increase in frictional angle with the axial strain levels for TDA materials might be less influenced by particle rearrangement as in the case of the Nevada Sand. The main driving factor for the increase in friction angle in TDA may be the deformability of the particles. As the axial strain level increases the contact area between particles increases as well while shearing.

The increase in contact area between particles is not a mechanism present in the Nevada sand triaxial test results because its particles are considered rigid or practically non-deformable. The apparent cohesion observed in the TDA shear strength best fit envelopes may be the results as well of the increasing contact area and the ability of TDA particles to interlock as they press each other. Several authors have reported cohesion values for larger TDA sizes as previously mentioned in the literature review chapter. A separate test using both TDA sizes ($D_{50} = 1.20$ mm and 2.60 mm) in this research where an isotropic confining pressure was applied and let constant for a period of time (no shearing) produced blocks of TDA, which aggregate particles remained quite stuck and undisturbed when the membrane was removed as shown in Figure 4.16. Wide variability in friction angles, cohesion intercepts has been reported in the literature for TDA (see Section 2.4). Although most of the studies have focused on large tire shreds TDA, the values obtained for granulated rubber in this research seems to be within acceptable ranges of published data (see Table 2.3). Discrepancy between studies is also due to the fact that most of the studies tended to report shear strength parameters at a specific axial strain while it has been shown in this research that TDA shear strength parameters are highly dependent on the level of strain attained, and a single friction angle or cohesion parameters could not be specified considering that a peak failure does not occur at low axial strain levels.

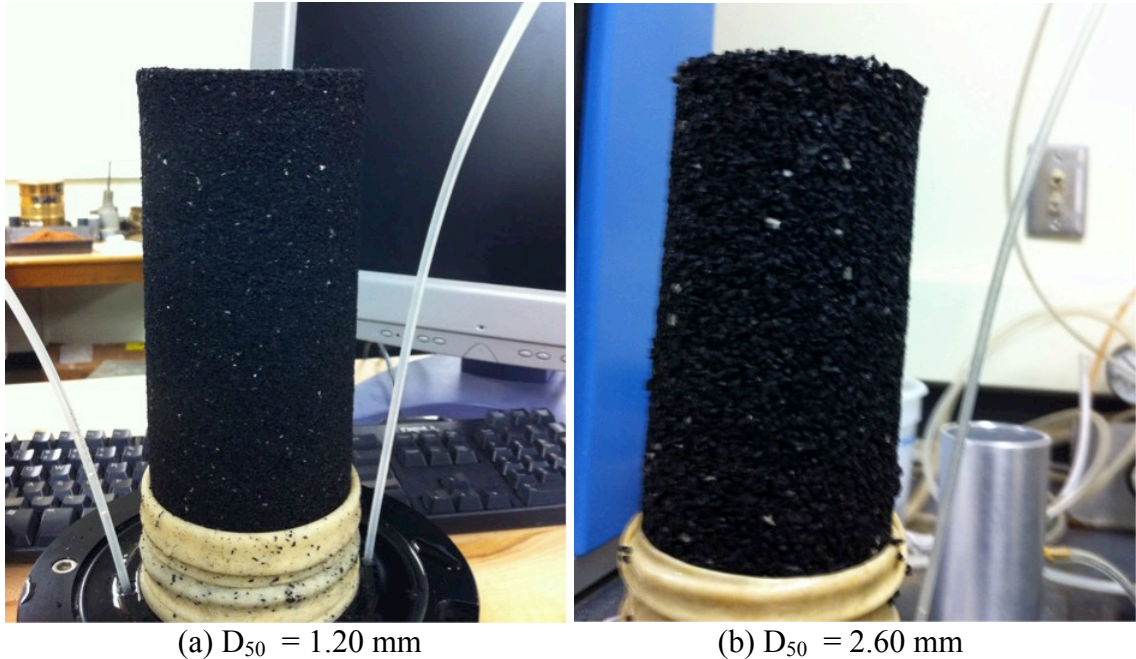
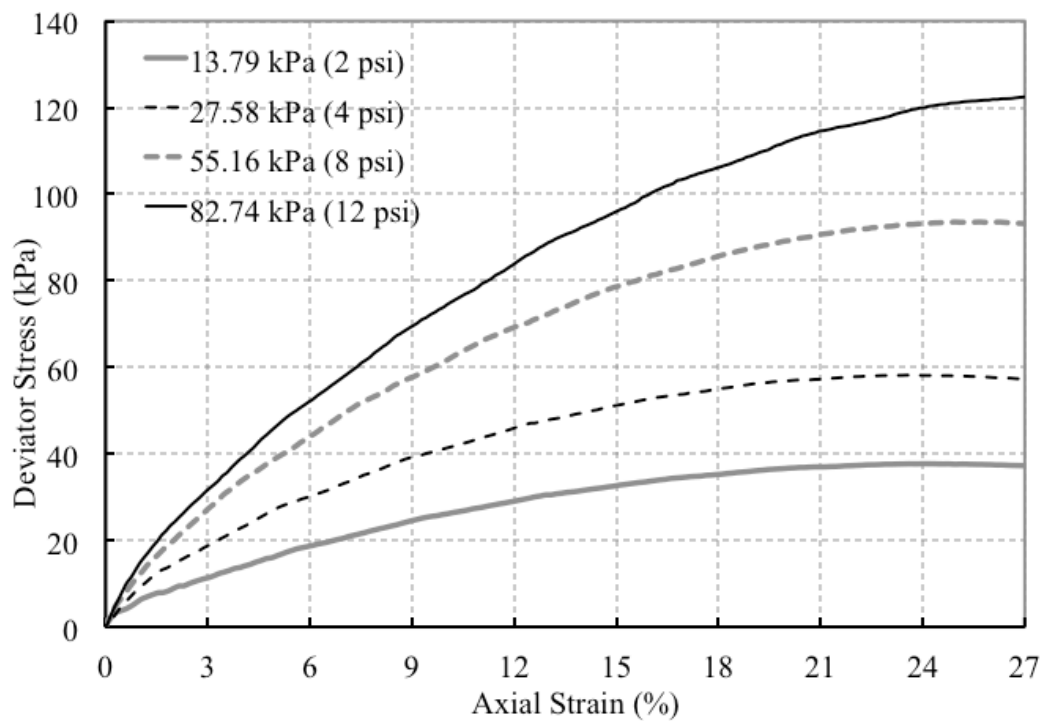


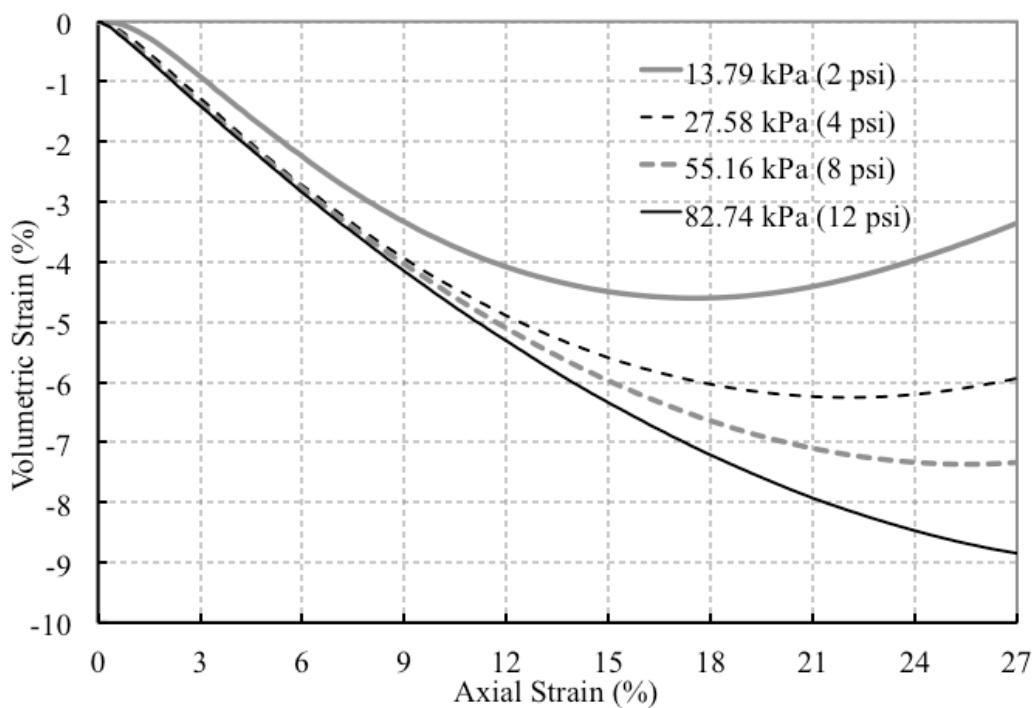
Figure 4.16: Blocks of TDA after applying an isotropic confining pressure

4.3.2 Effect of Particle Size in TDA Stress-Strain Characteristics

Although both TDA tested in this research are classified as granulated rubber per ASTM D6270 specifications shown in Table 2.1, both TDA samples presents different grain size characteristics as shown in Figure 4.1 and sieve analysis in Appendix A. Shape characteristics in terms of angularity are quite similar between them. However, TDA with $D_{50} = 2.60$ mm was found to be thicker and rougher than TDA with $D_{50} = 1.20$ mm (flatter) in addition to its higher particle size. Figure 4.17 show the stress-strain curves obtained from the CD triaxial tests for TDA with $D_{50} = 2.60$ mm. Similar to TDA with $D_{50} = 1.20$ mm, it was found high level of deformation before reaching at apparent peak and its behavior was mainly contractive according to Figure 4.17 (b).



a) Deviator stress versus axial strain



b) Volumetric strain versus axial strain

Figure 4.17: Consolidated drained triaxial tests results for TDA material ($D_{50}=2.60\text{mm}$)

The main objective of this section was to evaluate the impact of a difference in particle size might have on TDA strength and stiffness. For clarity, Figures 4.18 through 4.21 show the stress-strain curves comparing the behavior of both TDA particle sizes at the four different confining pressures. Coarser TDA exhibit higher strength than finer TDA samples, and such increment was between 8% and 11% when comparing the peak deviatoric stress observed at each confining pressure. Coarser TDA ($D_{50}=2.60\text{mm}$) was found to be stiffer as well as shown in Figure 4.22 where secant Young's modulus were calculated for each specimen and each confining pressure at 50% of the peak or maximum deviatoric stress observed. Increments between 21% and 29% percent in young modulus are obtained for the coarser TDA; and stiffness of the both TDA particle sizes seems to be stress-dependent since Young's moduli tend to increase with the confining pressure, which is a characteristic behavior of granular soils as well.

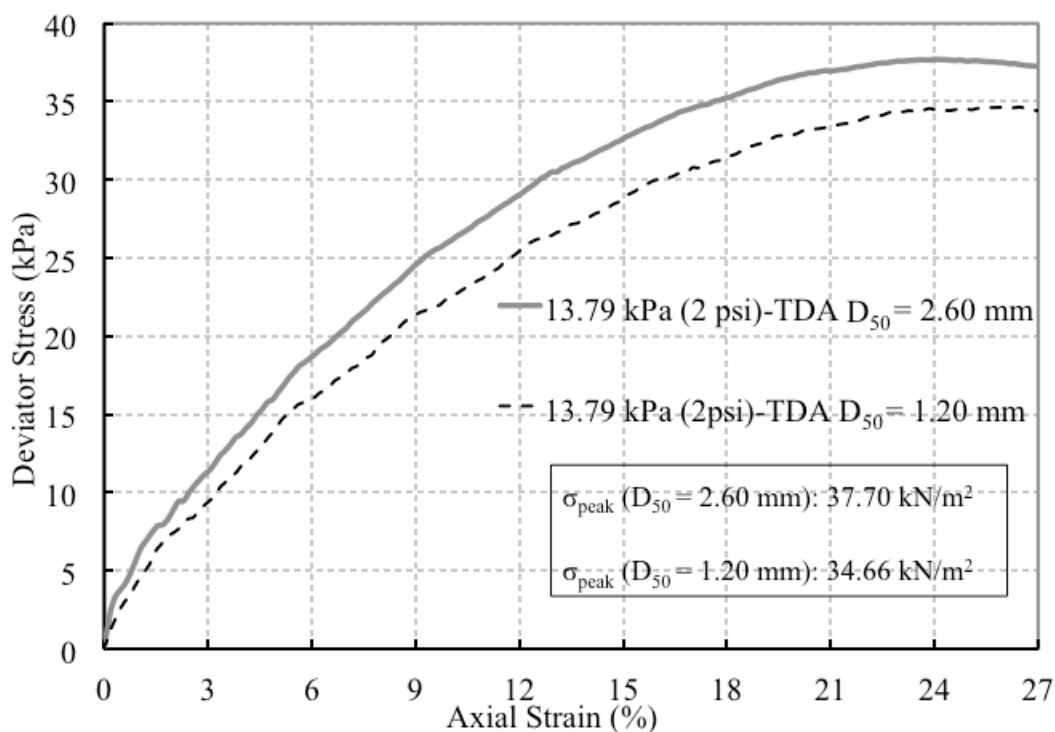


Figure 4.18: Consolidated drained triaxial tests results for TDA materials at 13.79 kPa

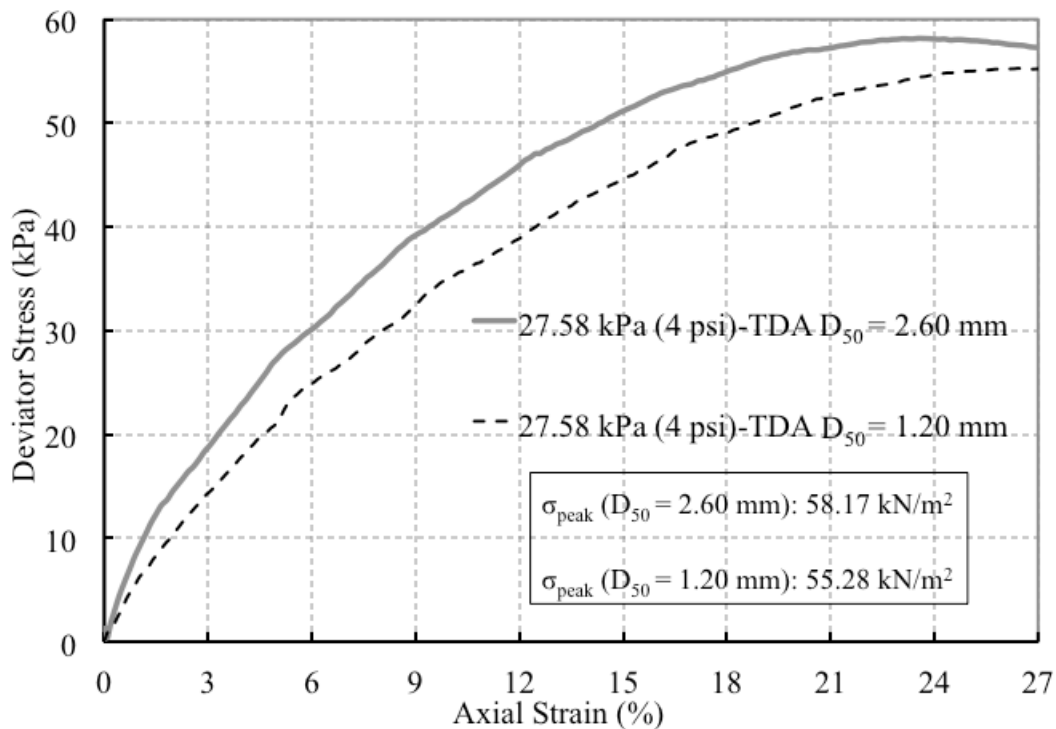


Figure 4.19: Consolidated drained triaxial tests results for TDA materials at 27.58 kPa

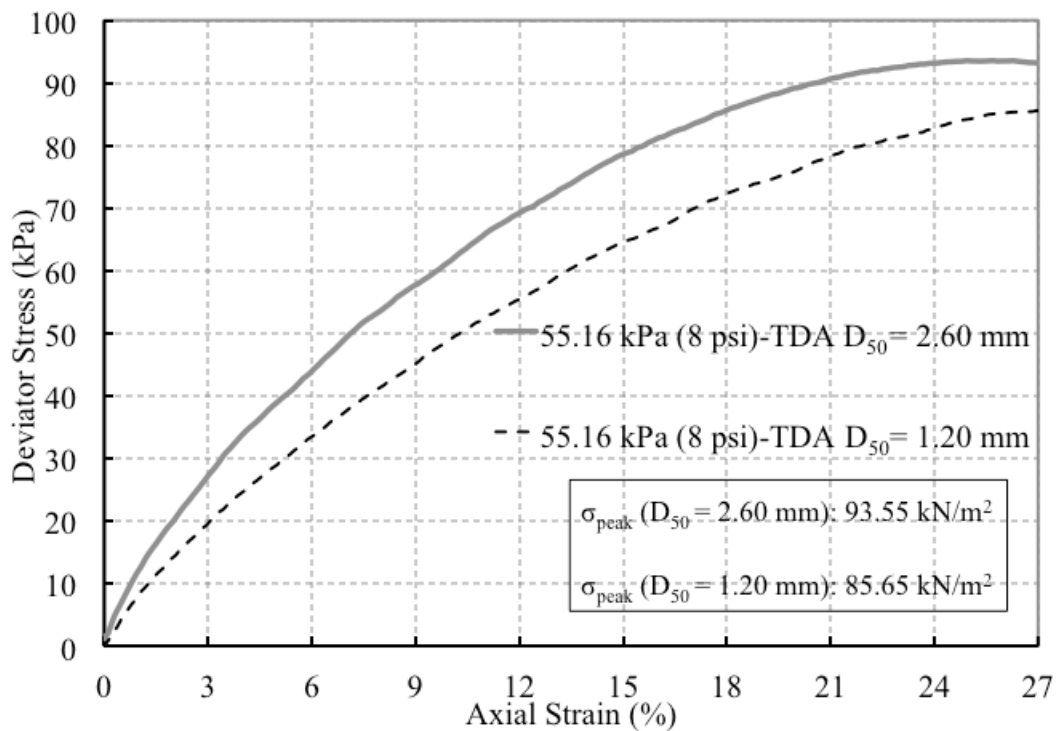


Figure 4.20: Consolidated drained triaxial tests results for TDA materials at 55.16 kPa

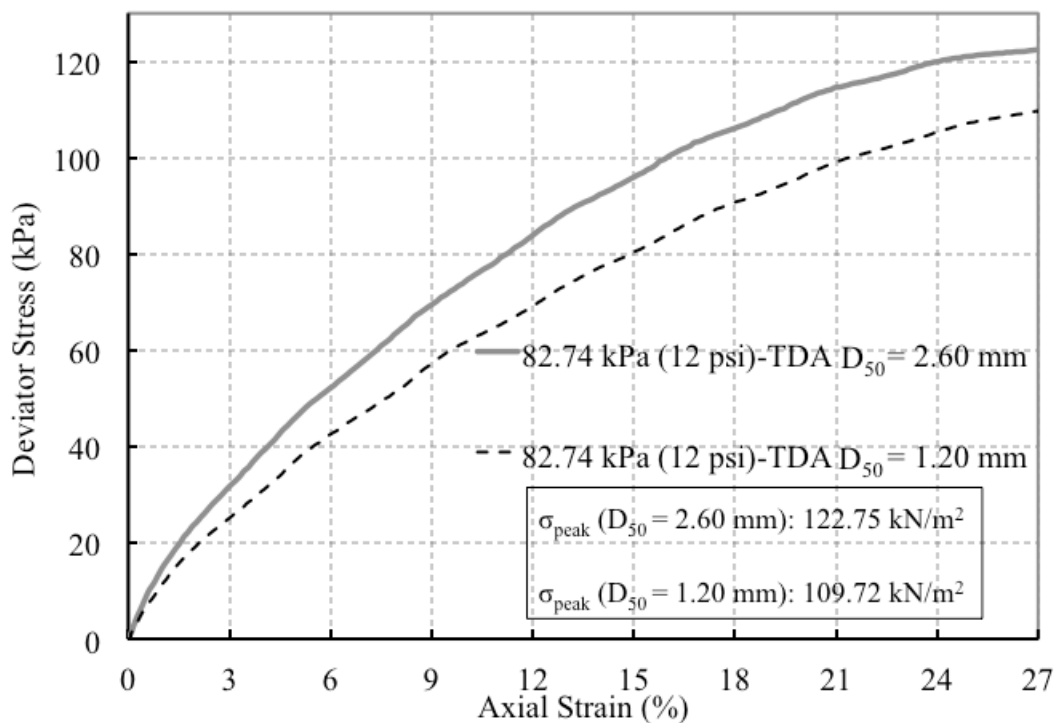


Figure 4.21: Consolidated drained triaxial tests results for TDA materials at 82.74 kpa

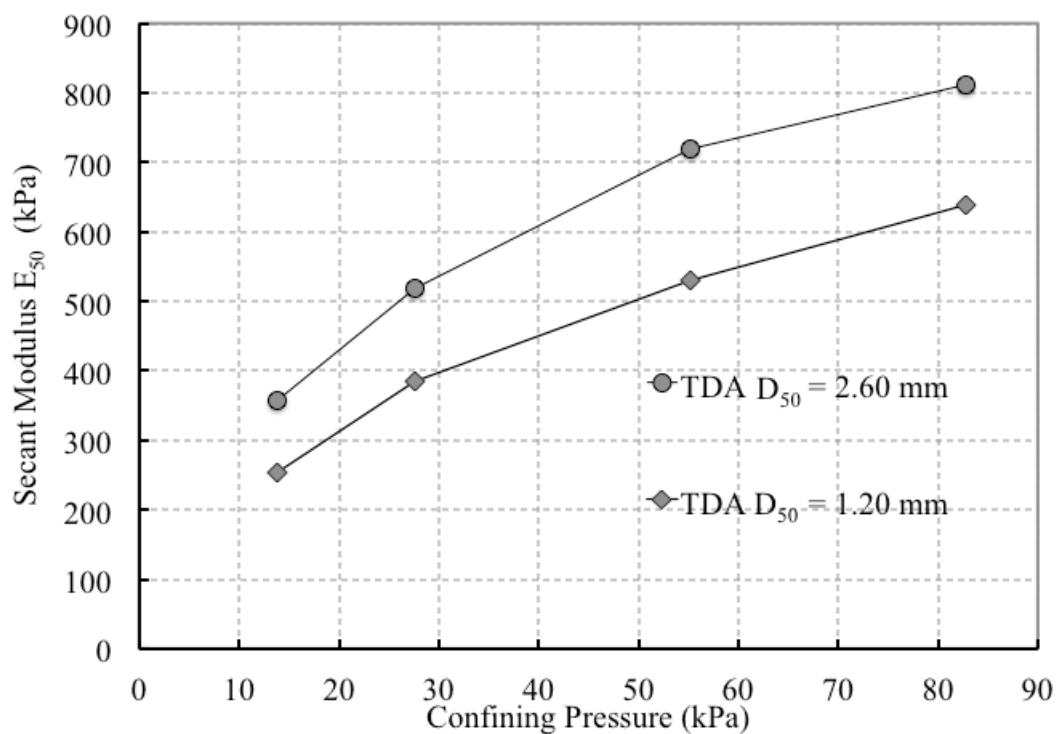


Figure 4.22: Secant modulus (E_{50}) for both TDA particle size

The same analysis of the shear strength parameters variation with axial strain previously explained in section 4.5 was done for the coarser TDA. Figure 4.23 shows the shear strength parameters determination in the p-q plane using both regressions again at 15% axial strain and Figure 4.24 shows the stress path at peak strain. For clarity, other axial strain level analysis can be found in Appendix C while Table 4.3 shows a summary of the results.

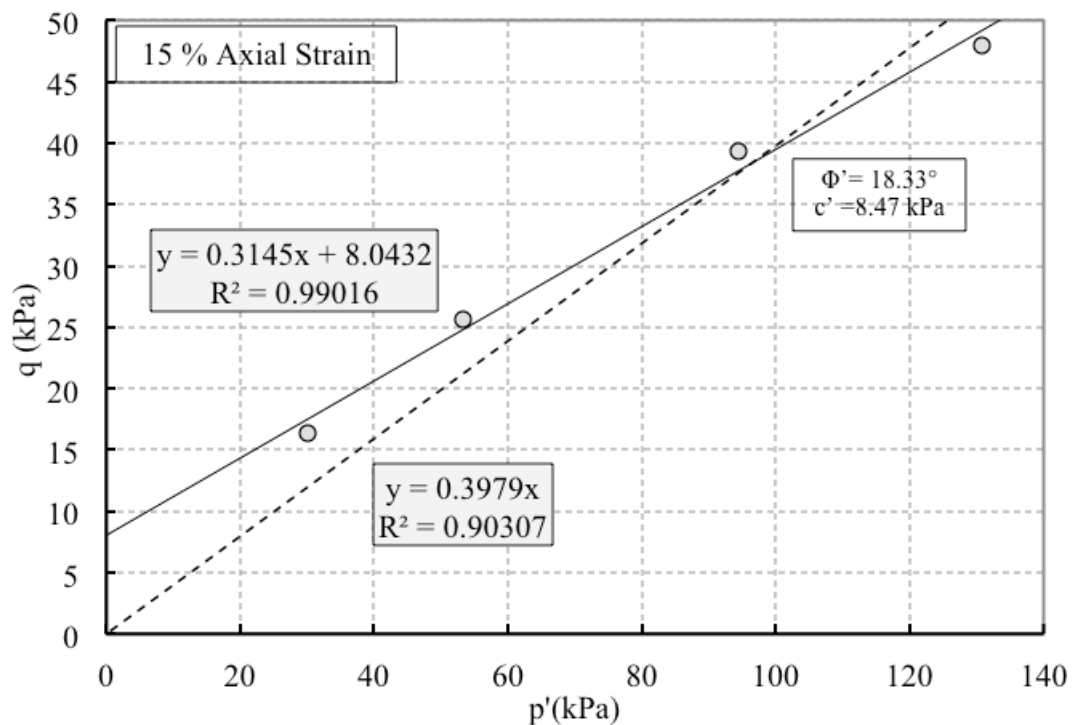
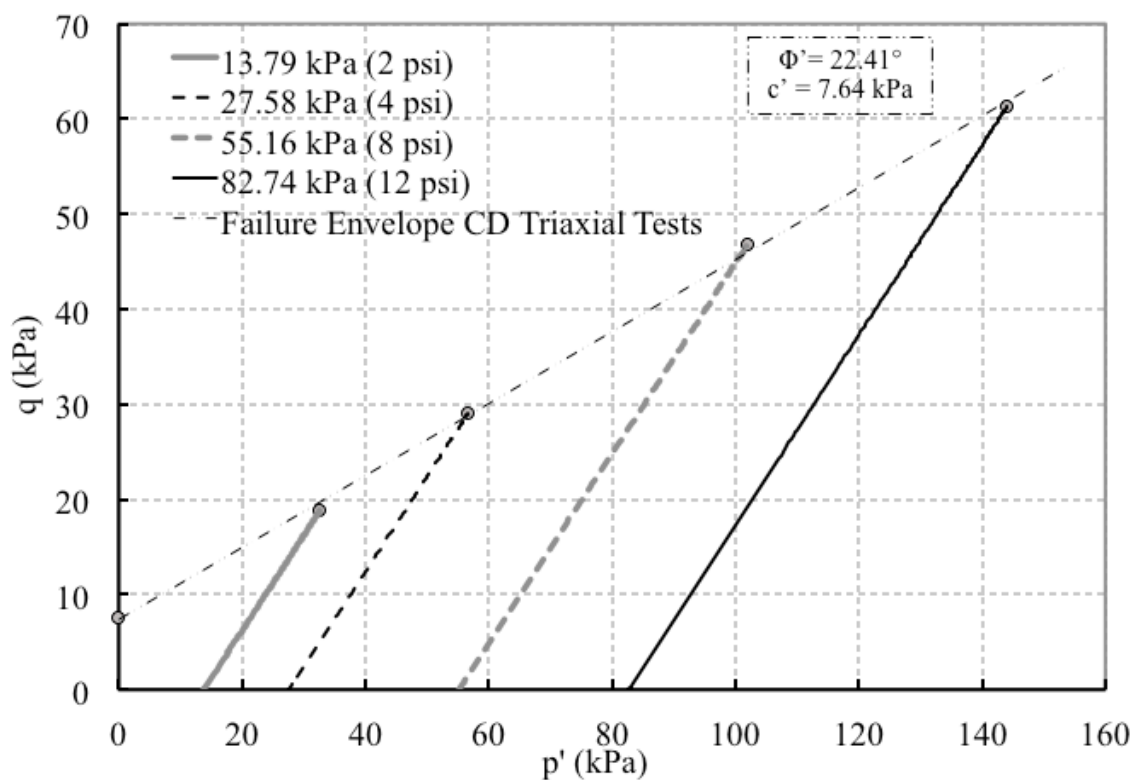


Figure 4.23: Shear strength parameters determination for TDA ($D_{50}=2.60\text{mm}$) at 15 % axial strain

Table 4.3: TDA $D_{50}=2.60\text{mm}$ shear strength parameters (CD triaxial tests)

Axial Strain (%)	Failure Envelope with y-axis intercept			Failure Envelope Through origin ($c' = 0$)	
	ϕ' ($^\circ$)	c' (kPa)	R^2	ϕ' ($^\circ$)	R^2
5	10.04	5.58	0.970	14.18	0.767
10	14.93	7.58	0.985	19.91	0.857
15	18.33	8.47	0.990	23.45	0.903
20	20.76	8.48	0.995	25.59	0.936
Peak ($\approx 25\%$)	22.41	7.64	0.998	26.62	0.960

Figure 4.24: Stress path for TDA ($D_{50}=2.60\text{mm}$) at peak axial strain

From Figures 4.23 and 4.24, it is observed again that both a cohesion intercept and a friction angle seem to better represent the shear characteristics of TDA rather than only a friction angle (zero intercept regression). Comparing the friction angles obtained for both TDA particle sizes, it is observed that friction angles obtained for the coarser

TDA ($D_{50}=2.60\text{mm}$) are in the order of 2 degrees higher than those of the finer TDA ($D_{50}=1.20\text{mm}$) as shown in Figure 4.25. This increase in shear strength is directly related to the higher strength observed in the stress-strain curves (Figures 4.18 through 4.21) for the coarser TDA when compared to the finer TDA. Differences in TDA shear strength parameters with different size particles have been documented (see Chapter 2). For example, Wu et al. (1997) reported friction angles which varies from 45 to 60 degrees for TDA sizes between 9.5 and 38 mm; Benda et al. (1995) reported friction angles between 17.4 and 25.8 degrees for TDA sizes between 2.0 and 38 mm and 10% axial strain; and Ahmed et al. (1993) reported friction angles between 20.5 and 24.7 degrees for particles sizes between 13 and 25 mm at 20% axial strain.

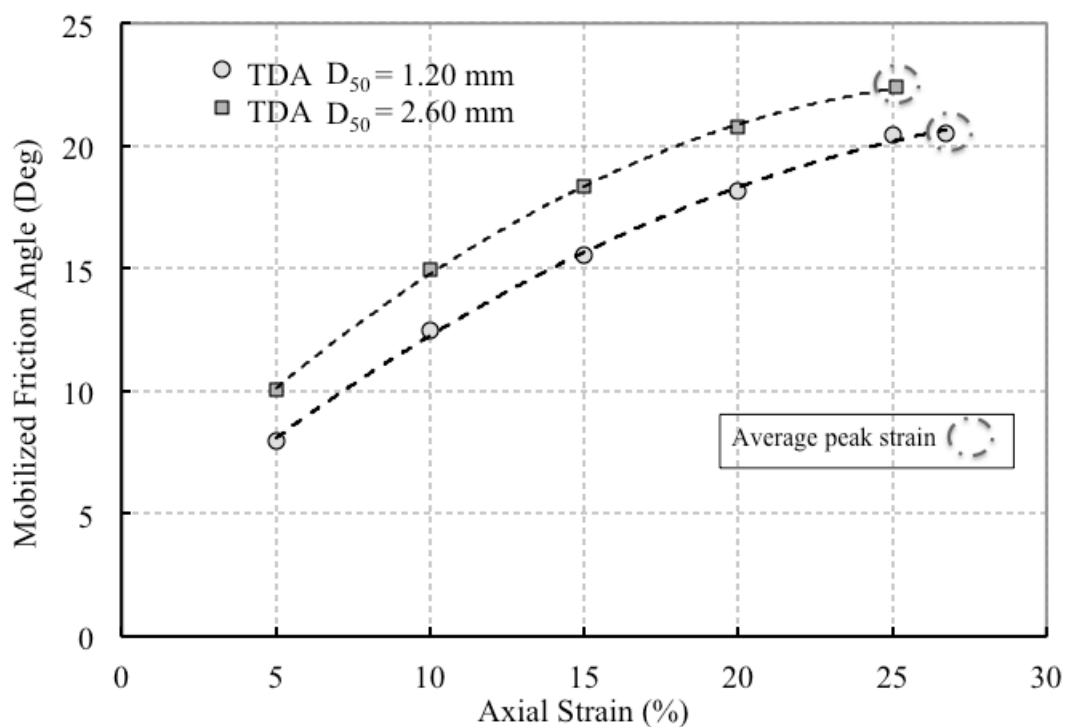


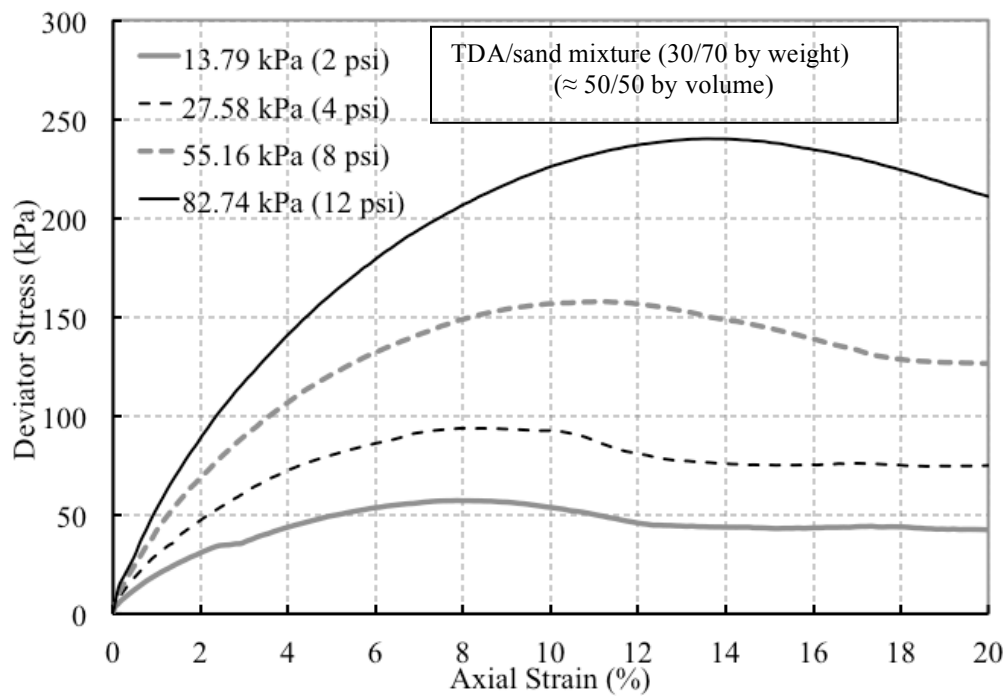
Figure 4.25: Comparison between TDA $D_{50}=1.20\text{ mm}$ and $D_{50}=2.60\text{mm}$ friction angles for different strain levels

The effect of grain size in the shear strength characteristics of granular soils is not often studied. However, researchers have found that the larger the maximum particle size, the higher the frictional angle (Kim and Ha 2014). The author attributed this to crushing of coarse soils. In general, the larger the particle diameter, the more the load applied to the particle diameter, which results in the occurrence of the particle crushing which would have a significant impact on the shear behavior of coarse-grain soils (Kim and Ha 2014). However, the increase in strength observed in the coarse TDA may not be the result of a crushing mechanism as in conventional granular soils. Due to the high deformable nature of TDA seems unlikely its particle would experience crushing. However, studies related to TDA crushing have not been performed to the best knowledge of this author. The increase in strength shown in Figures 4.18 through 4.21 that led to an increase in the friction angle for the coarse aggregate may be the result of two key factors. First, as the strain level increases there is more contact-to-contact area between the coarser TDA particles than the contact area between the finer TDA particles. Second, the shape slightly differs between both aggregates. Coarse TDA is thicker and rougher while finer TDA seems to be flatter and softer. Differences in shape could produce changes in the strength behavior of soils as well. A comparison between the two aggregates was shown in Figure 4.1, and additional microscope pictures can be found in Appendix A.

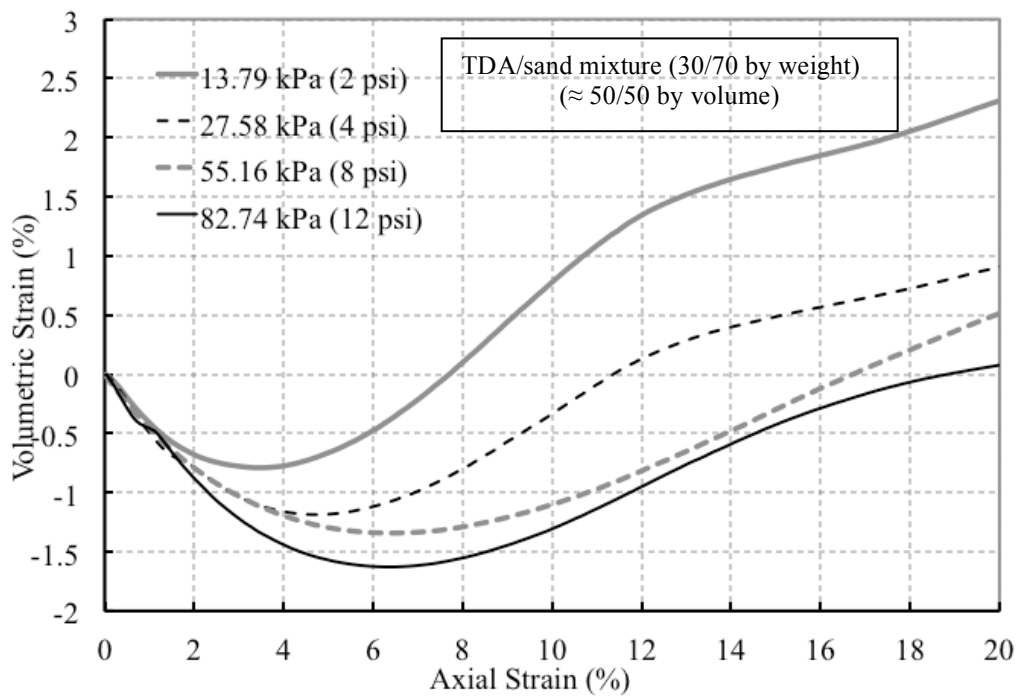
4.4 Triaxial Compression for TDA/sand Mixtures

The high level of compressibility exhibited by TDA raises the question of the conditions under which these materials could be placed in the field if deformations or settlements are a concern. Mixing TDA with conventional granular material may lead to a reduction in the level of deformation expected in the aggregate due the high stiffness of sand when compared to TDA as previously shown in Section 4.5. This section describes the stress-strain behavior of TDA/sand aggregates mixed in two different ratios: rubber/sand = 30/70 and 10/90 (by weight,%) which corresponds to a 50/50 and 20/80 ratio by volume approximately. TDA material used for mixture specimens was TDA- $D_{50}=1.20$ mm and Nevada sand. All samples were prepared in a dense state with a relative density close to 90%. Figures 4.26 and 4.27 shows the stress-strain curves and the change in volume obtained from CD triaxial tests for both mixtures.

Tests results show initially a contraction behavior up to 5% and 1% axial strain for the 30/70 and 10/90 mixtures respectively where a well-defined dilatant behavior starts governing up to these levels of strains for both mixtures. A well-defined peak failure deviatoric stress was observed for both mixtures as well before 15% axial strain which is the maximum level of strain to select shear strength parameters according to ASTM standard. After reaching a peak deviatoric stress, both mixtures exhibit strain-softening characteristics.

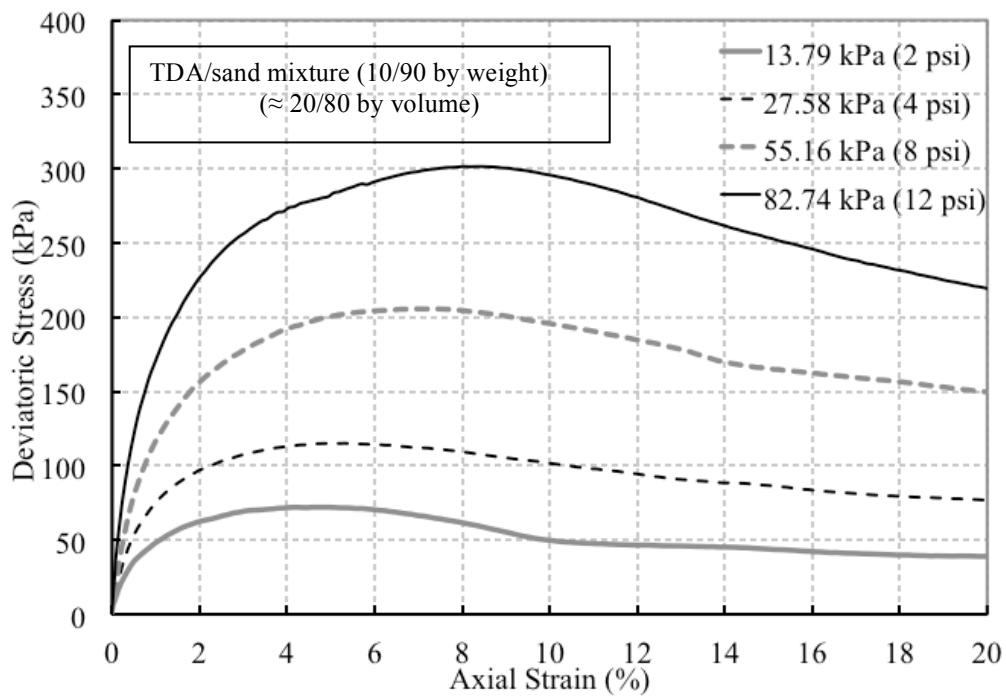


a) Deviator stress versus axial strain

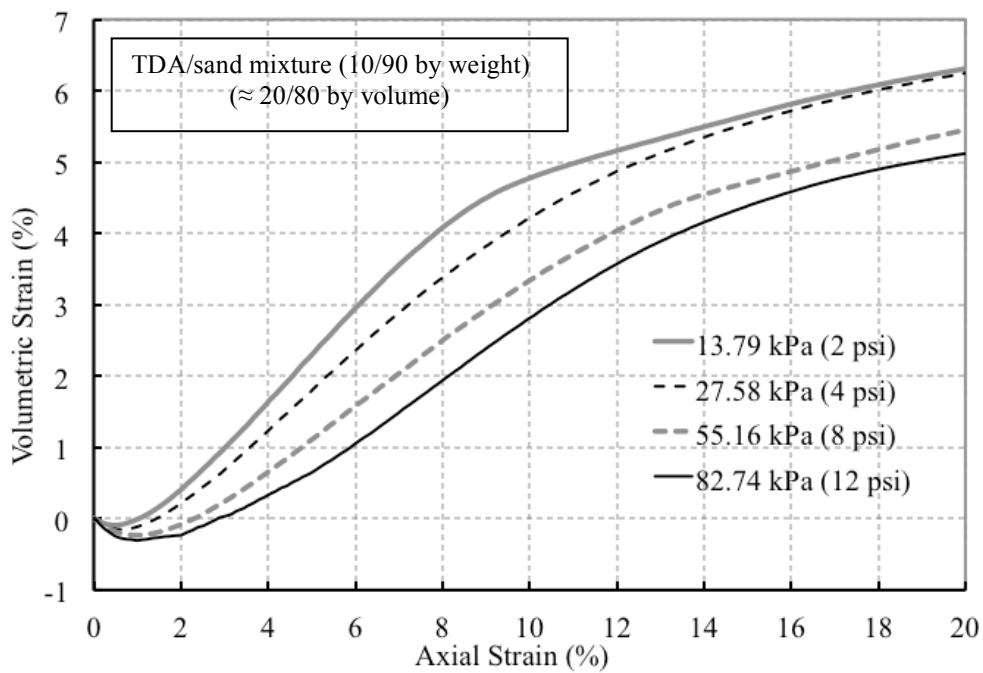


b) Volumetric strain versus axial strain

Figure 4.26: Consolidated drained triaxial tests results for TDA/sand mixture (30/70 by weight)



a) Deviator stress versus axial strain



b) Volumetric strain versus axial strain

Figure 4.27: Consolidated drained triaxial tests results for TDA/sand mixture (10/90 by weight)

Figures 4.28 and 4.29 show the shear strength parameters obtained from the p-q plane for both mixtures at peak strain. Although the cohesion component does not seem to be negligible, a very good fit of the failure envelope was attained when it was forced through the origin as well (as indicated in Tables 4.4 and 4.5). These are important facts that differentiate the mixture behavior when compared to TDA alone where contraction behavior was predominant even at high strain levels (up to 27%), a well-defined peak was not observed at conventional level of deformation, and a good fit of the failure envelope neglecting the cohesion seems unreasonable.

Table 4.4: Shear strength parameters for TDA/sand mixture (30/70 by weight or 50/50 by volume)

Axial Strain (%)	Failure Envelope with y-axis intercept			Failure Envelope Through origin ($c' = 0$)	
	ϕ' (°)	c' (kPa)	R^2	ϕ' (°)	R^2
5	26.34	9.82	0.998	31.14	0.964
Peak ($\approx 10\%$)	34.57	5.16	0.999	36.61	0.996

Table 4.5: Shear strength parameters for TDA/sand mixture (10/90 by weight or 20/80 by volume)

Axial Strain (%)	Failure Envelope with y-axis intercept			Failure Envelope Through origin ($c' = 0$)	
	ϕ' (°)	c' (kPa)	R^2	ϕ' (°)	R^2
Peak ($\approx 5\%$)	38.59	5.72	0.999	40.56	0.997

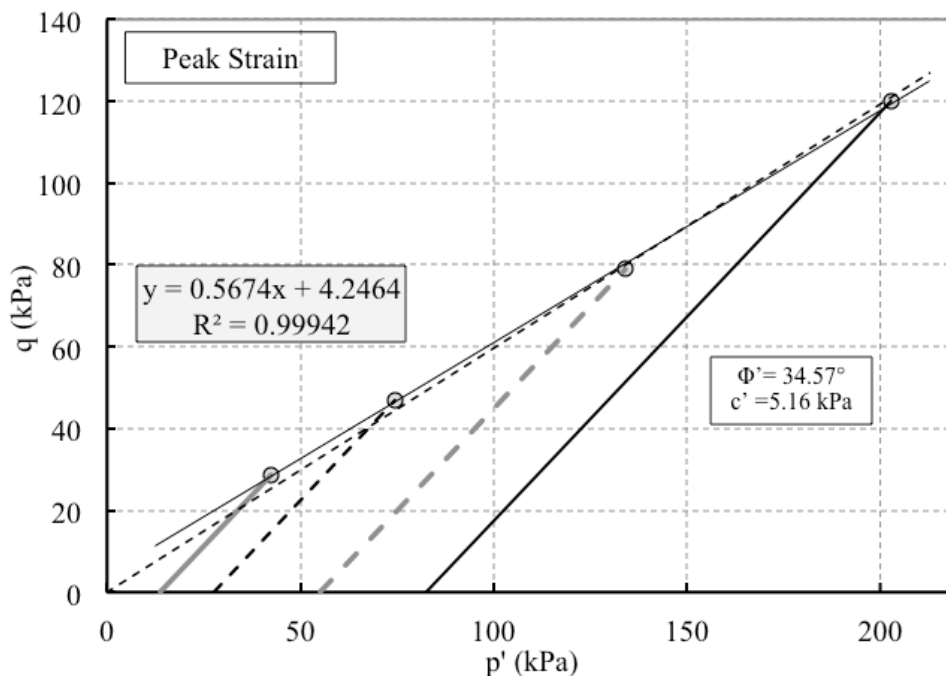


Figure 4.28: Shear strength parameters determination for TDA/sand mixture (30/70 by weight or 50/50 by volume) at peak strain ($\approx 10\%$)

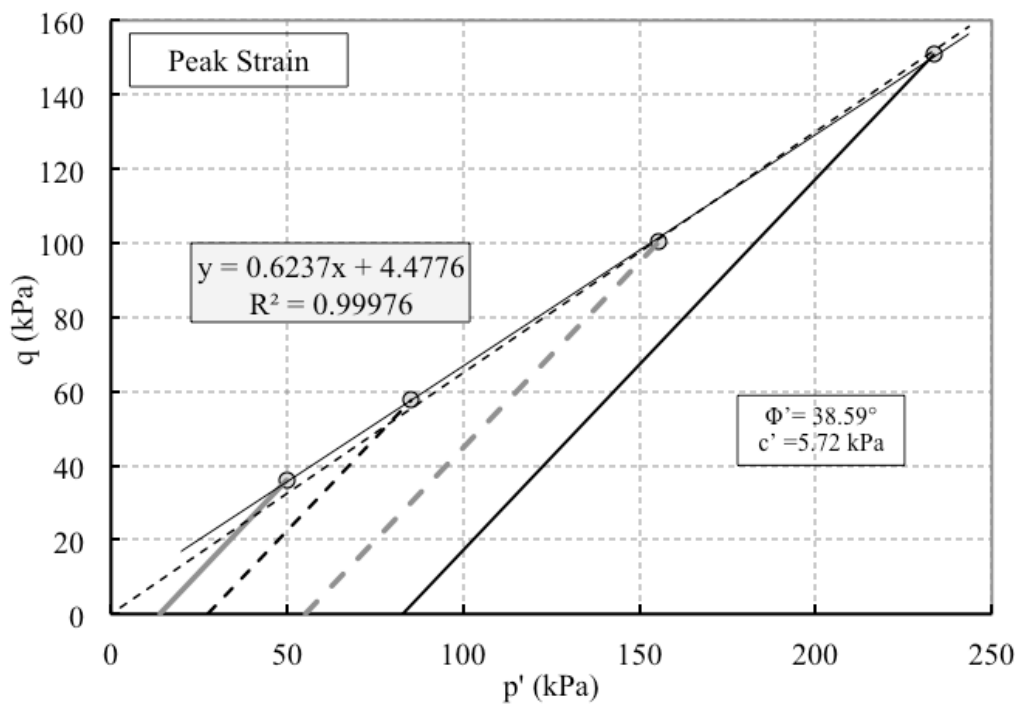


Figure 4.29: shear strength parameters determination for TDA/sand mixture (10/90 by weight or 20/80 by volume) at peak strain ($\approx 5\%$)

Figures 4.30 and 4.31 shows the stress-strain curves at a specific confining pressure for the different materials tested in this research excluding the coarser TDA, which were not used for the mixture specimens (other confining pressure curves can be found in Appendix C). The strength of the mixed material increased with increasing the amount of sand when compared to the TDA specimens primarily because the shear strength of sand is higher than the TDA strength as was discussed in Section 4.3. The stiffness of the mixed material increased dramatically when compared to TDA as well as shown in Figure 4.32 and 4.33 where 98, 96 and 83% increment in secant modulus are obtained for the Nevada sand, 10/90 mixture, 30/70 mixture respectively when compared to TDA; therefore the stiffness of the sand mainly predominated the behavior of the aggregate for the mixing proportions studied in this research.

The expected increment observed in mechanical properties in the mixtures when compared to TDA is not totally proportional or linear with the amount of sand provided to the mixture. For example, as seen in Figures 4.30 and 4.31, the inclusion of 10% by weight of TDA reproduced similar results to the 100% percent Nevada sand specimens in terms of strength.

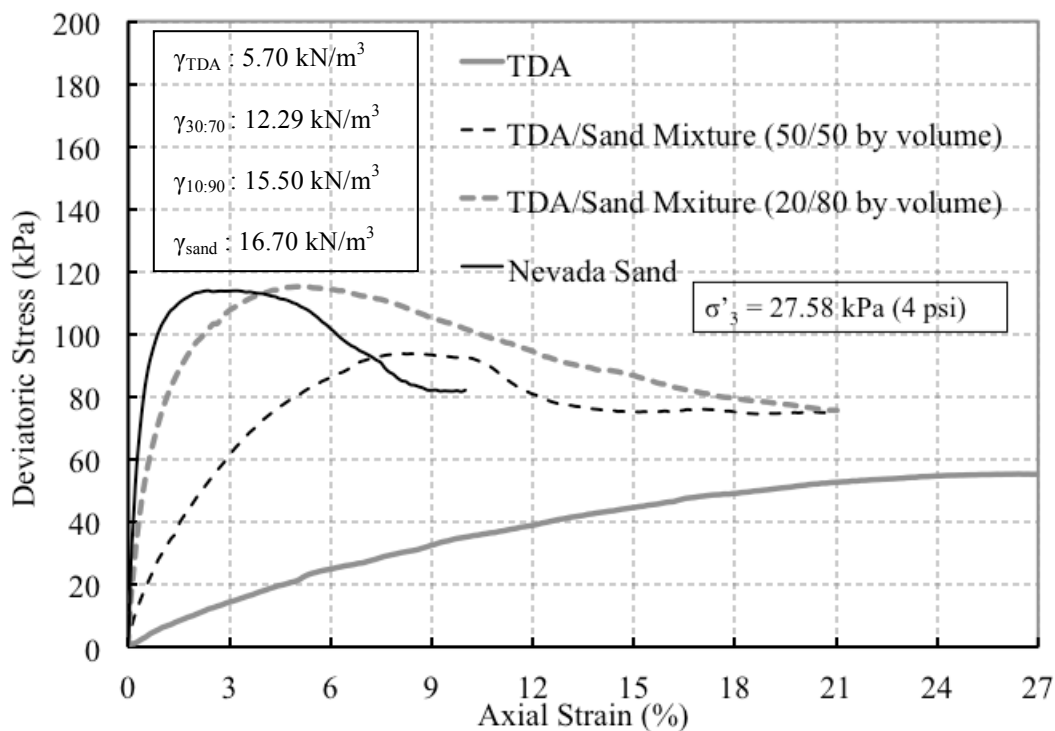


Figure 4.30: Stress-strain curves for all aggregates tested at $\sigma'_3 = 27.58 \text{ kPa}$

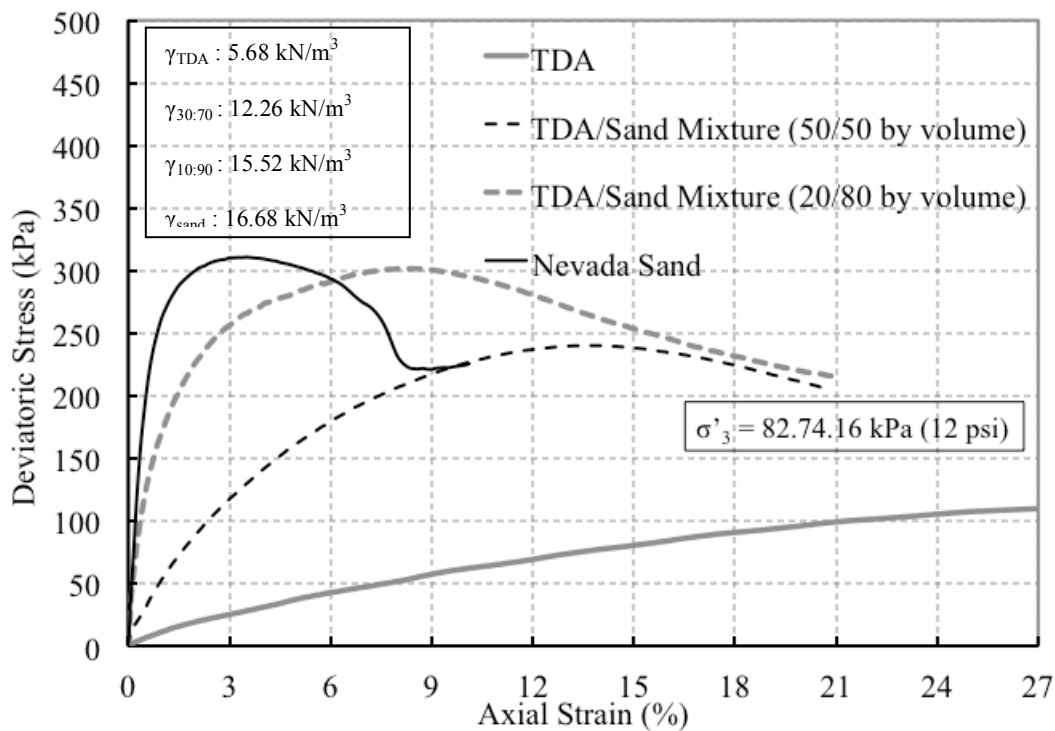


Figure 4.31: Stress-strain curves for all aggregates tested at $\sigma'_3 = 82.74 \text{ kPa}$

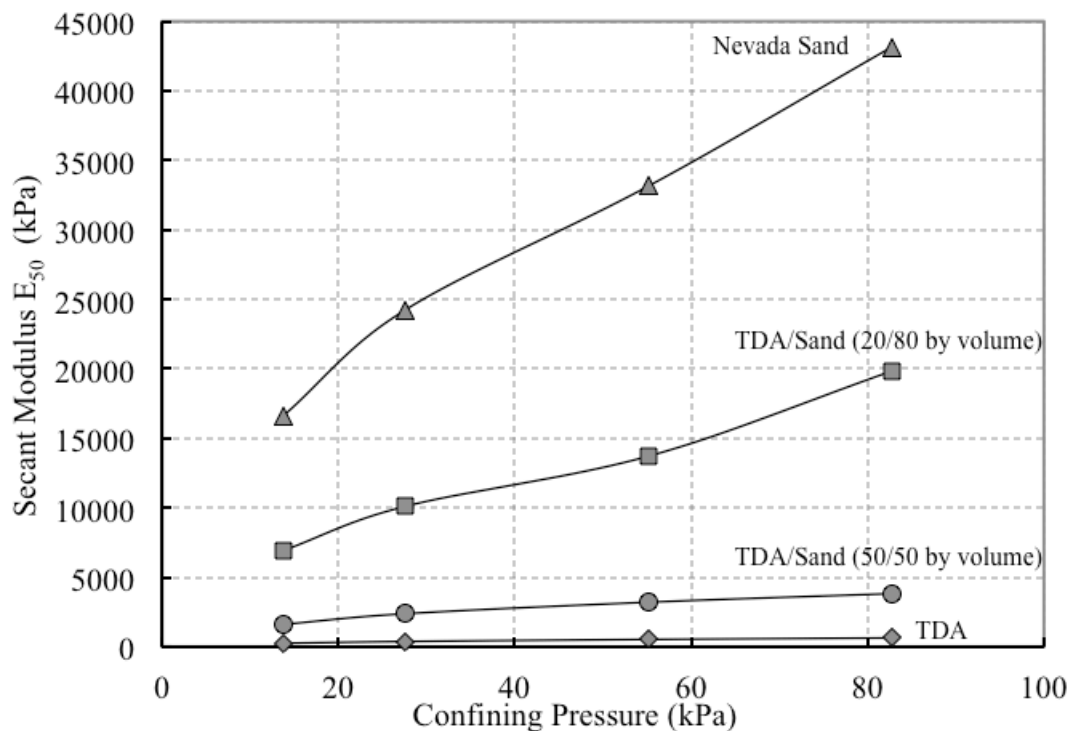


Figure 4.32: Variation of the secant modulus with the confining pressure

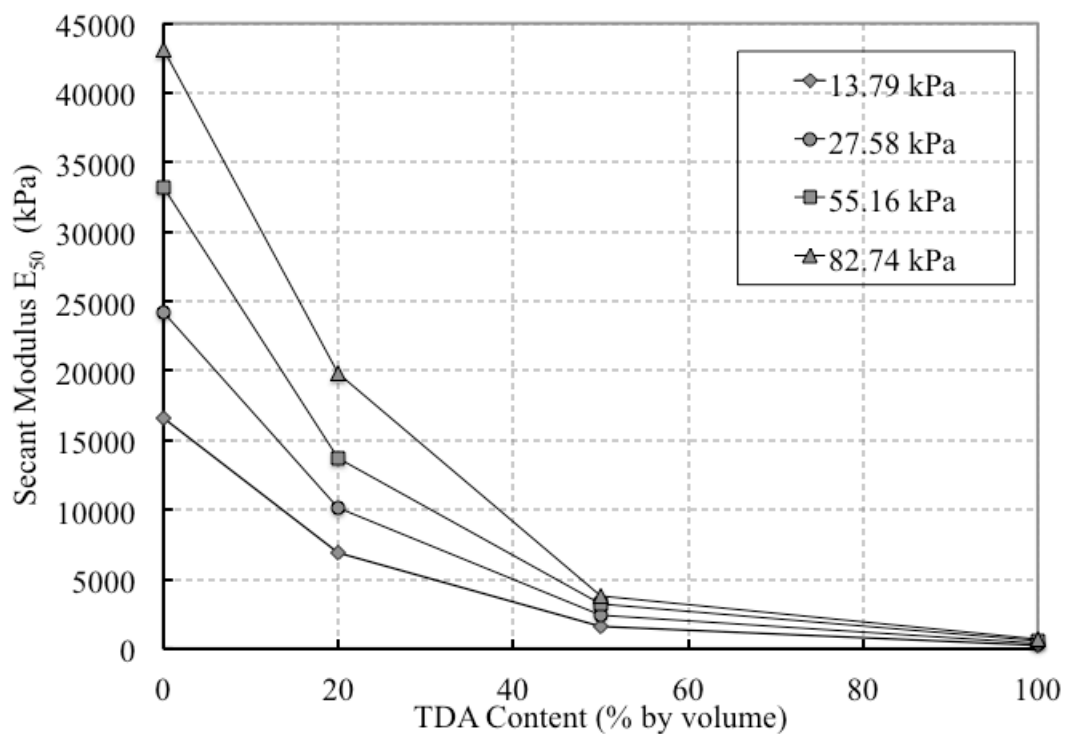


Figure 4.33: Variation of the secant modulus with TDA content

The shear strength parameters obtained in Tables 4.4 and 4.5 for both mixtures are compared to those of Nevada sand and TDA alone in Figure 4.34. For consistency, shear strength parameters are compared forcing the failure envelope through the origin. Acknowledging the fact that $c' = 0$ seems reasonable for Nevada sand and both mixtures as previously demonstrated but not for TDA, the friction angle for TDA plotted in Figure 4.34 corresponds to the maximum axial strain (Peak $\approx 27\%$) shown in Table 4.2 considering the failure envelope through the origin for which a R^2 Values of 0.94 was obtained. TDA contents presented in Figure 4.34 are presented as percentage by volume and not by weight as specimens were prepared in the lab following a gravimetric relation. The same procedure has been followed by other authors where mixture were proportioned by weight in lab settings and then volumetric relations were calculated (Youwai and Bergado 2003).

It was found that there is not significant difference in term of shear strength between mixtures with 20% TDA volumetric content and Nevada sand specimens. Therefore, a 20% inclusion of TDA by volume (10% by weight) would exhibit similar strength as 100% Nevada sand but the presence of TDA in the mixture would produce a loss in stiffness as shown in Figures 4.30 through 4.33. However, this loss may be within acceptable ranges considering that peak strength occurred at approximately 5% axial strain deformation, and the reuse of TDA in this proportion may not only reduce the environmental disposal concerns of tires but also be an alternative for geotechnical problems associated with low shear strength where filling materials may not composed only of competent granular material. Increases of 31% and 38% in the friction angle may be achieved for a TDA inclusion of 50% and 20% by volume, respectively.

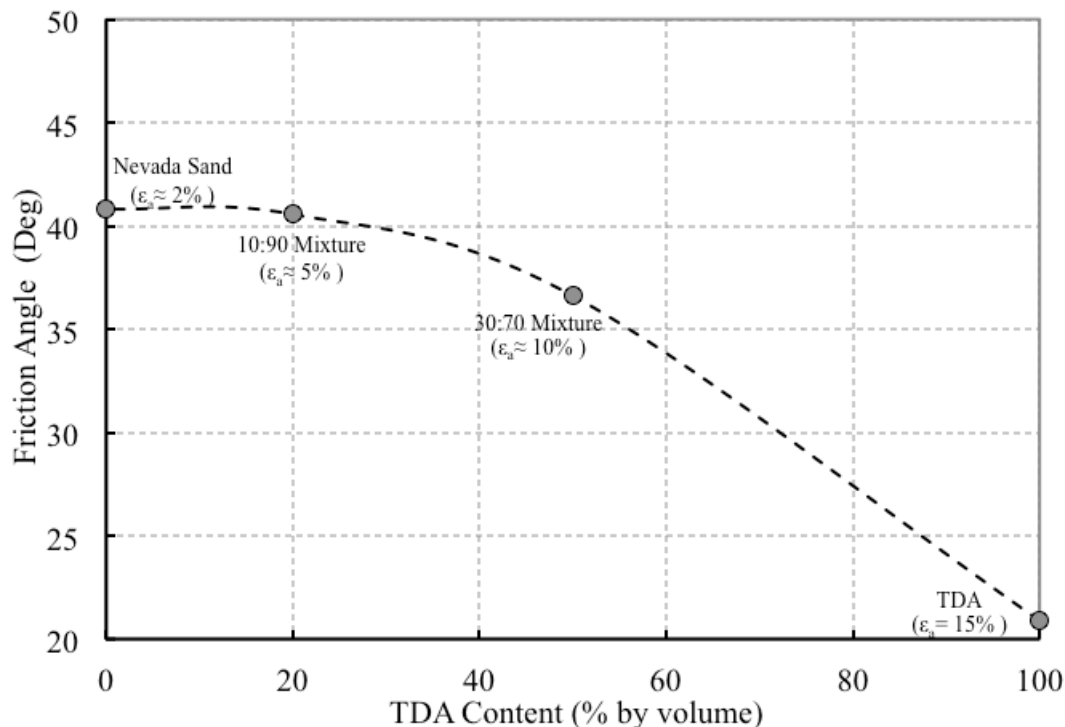


Figure 4.34: Variation of the friction angle with TDA content

The improvement observed in the mixture with 20% TDA may be the result of the friction between TDA-Sand particles. TDA particle may act as a reinforcement mechanism where tensile forces develop within TDA particles that are compressed by sand particles leading to strength similar to a specimen with 100% sand. Other studies have even found that TDA/sand mixtures can even exceed the shear strength characteristics of pure sand alone (Foose et al. 1996; Ghazavi and Sakhi 2005; Zornberg et al. 2004). However, friction angles obtained from these researches were based on large tire shreds sizes or tire chips with particles sizes much higher than TDA used in this research. Testing method has also varied among studies; For example Zornberg et al. (2004) performed drained triaxial tests using tire shreds with widths between 12.7 and 25.5 mm finding an optimum TDA content of approximately 35% by weight that produced the higher shear strength when compared to different sand relative densities and

different ratios of TDA length to width (aspect ratio). Foose et al. (1996) and Ghazavi et al. (2005) found higher strength in tire shreds/sand mixtures proportioned by volume using large scale direct shear equipment. The study performed by Youwai et.al (2003) did not report higher strength characteristics for any TDA/sand mixture; and the effect of aspect ratio and density was not studied by the authors either which is more agreement with the results found in this research; However, larger TDA particles sizes were used by Youwai et al. (2003) (16 mm maximum particle size).

Although this research did not involve as many variables as previous researchers, particularly in terms of the effect of density, particle size and aspect ratio, when it refers to mixtures; and acknowledging that TDA particle sizes differ in great amount. Higher friction angles may potentially occur in TDA/sand mixtures with the materials tested in this research. For example, although all specimens involved in this research have dense relative densities ($\approx 90\%$) but as TDA unit weight is lighter than Nevada sand, resulting densities in the mixtures were lower than Nevada sand specimens as shown in Figures 4.30 and 4.31 for the same dense state. However, in conventional soil mechanics it is well known that for sand in loose state, the shear strength characteristics will decrease (e.g. friction angle). Therefore, if a Nevada sand specimen were to be tested at a similar density of the mixture containing 20% TDA by volume; the resulting friction angle and strength of Nevada sand may in fact be lower than the mixture containing at least 20% TDA which would lead to the same conclusions as Zonberg et al. (2004) who compare the shear strength of TDA/sand mixtures and sand with two different relative densities. Other hypotheses regarding the effect of TDA particle size in the mechanical response of TDA/sand mixtures that could be made based on the results in this research is that

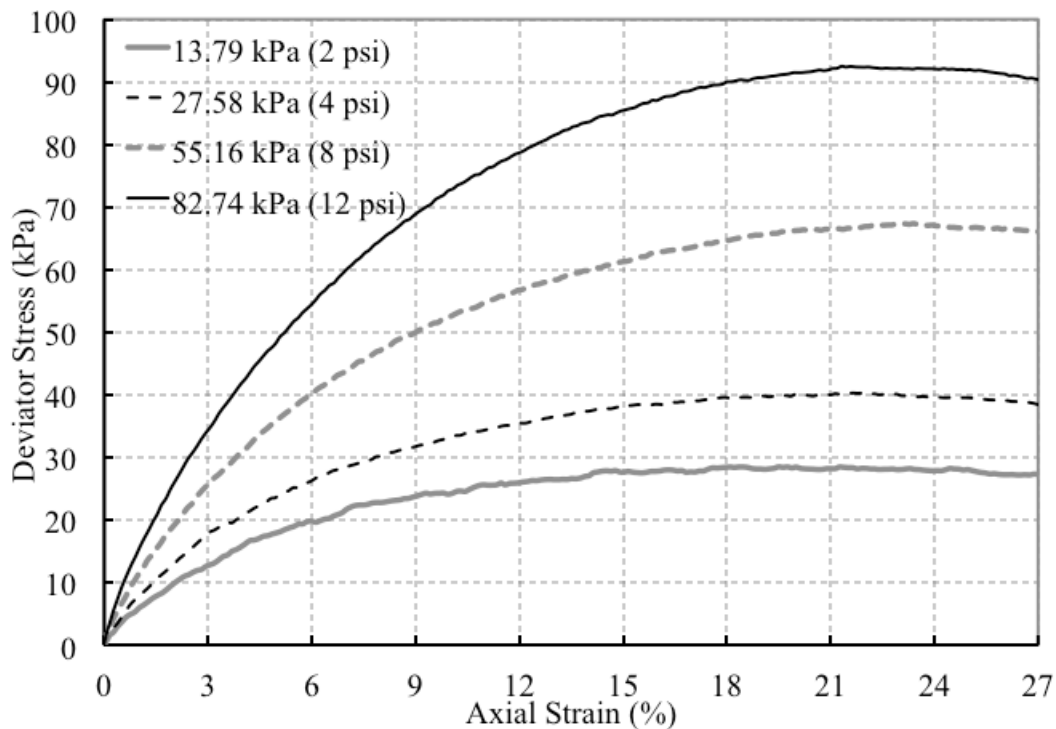
although, the finer ($D_{50} = 1.20$ mm) was used in the mixtures. Mixtures using the coarse TDA ($D_{50} = 2.60$ mm) may potentially lead to higher shear strength characteristics since as it was discussed in section 4.6 coarse TDA specimens exhibited higher strength. This led to higher friction angles when compared to the finer TDA which would be in agreement with other researchers where larger particles sizes produced higher shear strength characteristics in mixtures for a certain TDA content. However, these hypotheses are made based on conventional soil mechanics principles and previous results, verification recommended for future studies. In general, what can be concluded is that the improvement observed in shear strength for a certain proportion of TDA is the result of a reinforcement mechanism, but there is not a single variable to quantify the gain in strength since it would depend on the density, TDA particle sizes, and mixing proportions.

4.5 Stress-Strain Behavior of TDA Material Under CU Triaxial Compression

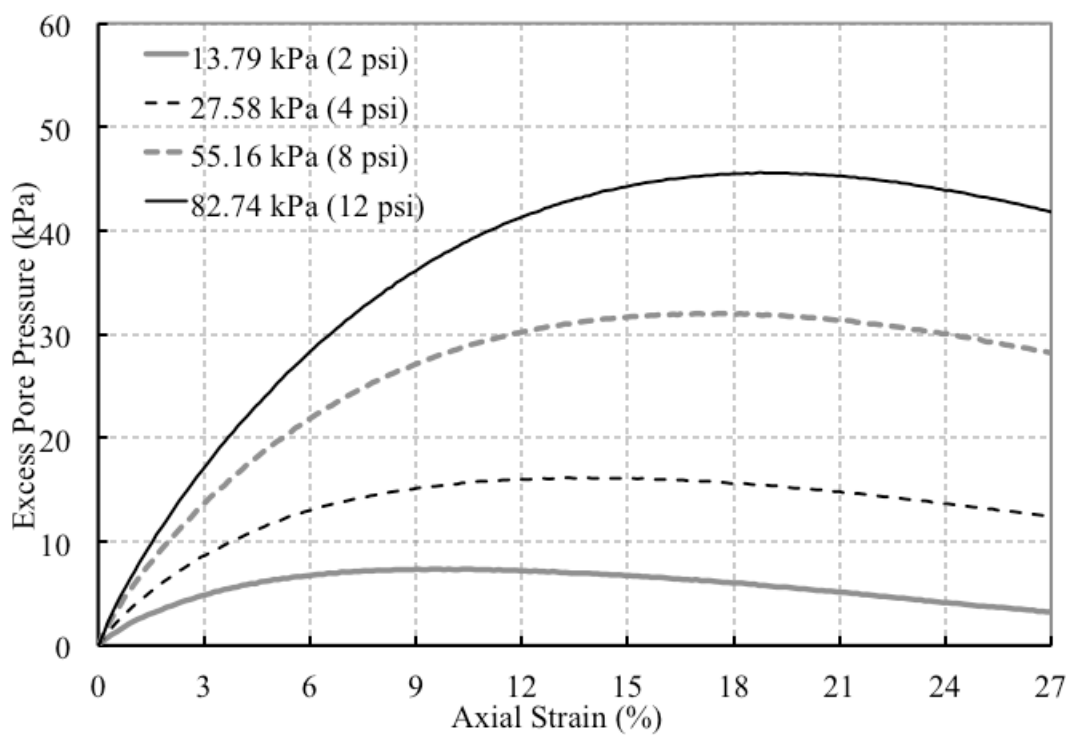
Most of the studies regarding stress-strain behavior of TDA materials have been performed under drained conditions as it was already discussed in Section 4.3 (CD triaxial tests). It is suspected that most researchers have focused on TDA behavior under drained conditions because in general TDA exhibits high permeability characteristics and drained conditions are expected to be the dominant situation in the field for most conventional applications. However, this research intended to study both drained (which was previously discussed) and undrained conditions as well in order to study stress-strain behavior and pore pressure generation in TDA. Figure 4.35 shows the stress-strain curves and excess pore pressure versus axial strain behavior obtained from the four CU triaxial tests performed on the TDA. It is observed that TDA generates positive pore pressures

which is in agreement with the results obtained for drained conditions and conventional soil mechanics for soil which predominant behavior while shearing is contractive under drained conditions. Physically, TDA would tend to contract and lose volume squeezing water out of the pores but it can not since drainage is blocked generating positive pore pressures.

Excess pore pressures appear to start dissipating for axial strain levels between 12 and 20%, depending on the confining pressure which may be an indication that the material would have a tendency to expand or swell drawing water into the pores generating a decrease in excess pore pressure. In terms of the variation of effective shear strength parameters with the axial strain obtained from the CU triaxial test, the same type of analysis as in the consolidated drained triaxial tests was performed for CU conditions. For clarity, effective shear strength parameters at different strain levels are summarized in Table 4.6, and all p-q plane figures can be found in Appendix C with the intention of not being repetitive since the procedure has been shown several times before.



a) Deviator stress versus axial strain



b) Volumetric strain versus axial strain

Figure 4.35: Consolidated undrained triaxial tests results for TDA material

Figure 4.36 shows the effective shear strength parameters at peak while Figure 4.37 shows a comparison between the effective stress paths (ESP) and total stress paths (TSP). It is observed that effective strength path shifts toward the left as a result of the positive pore pressures generated which produces a decrease in the effective stress. As expected the friction angle obtained for the total stress is considerable lower than the effective friction angle (36% lower). For comparison purposes shear strength parameters obtained from both regressions are shown in Figure 4.37. It is well known friction angles obtained from TSP are lower and in fact other authors have reported that it is common to find this value about one-half of the drained friction angle (Holtz and Kovacs 1981). This situation could be critical for short-term situations where undrained conditions could be the controlling failure mechanism specially in low permeability soils which is not the most commonly expected situation for TDA in the field.

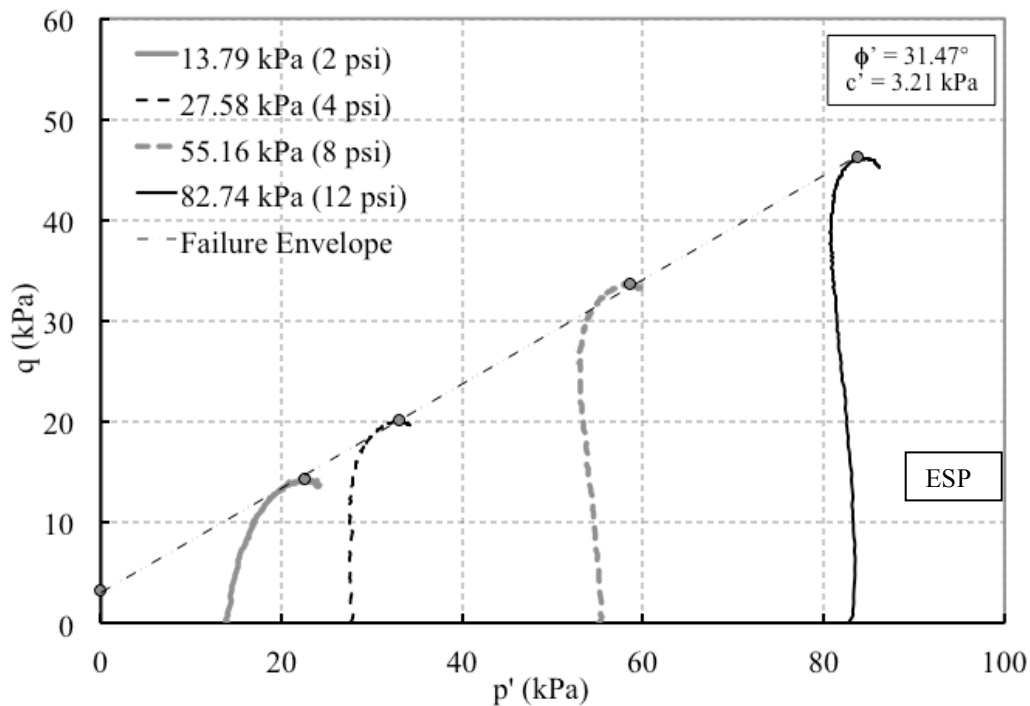


Figure 4.36: Effective shear Strength Parameters determination for TDA at peak from CU triaxial tests

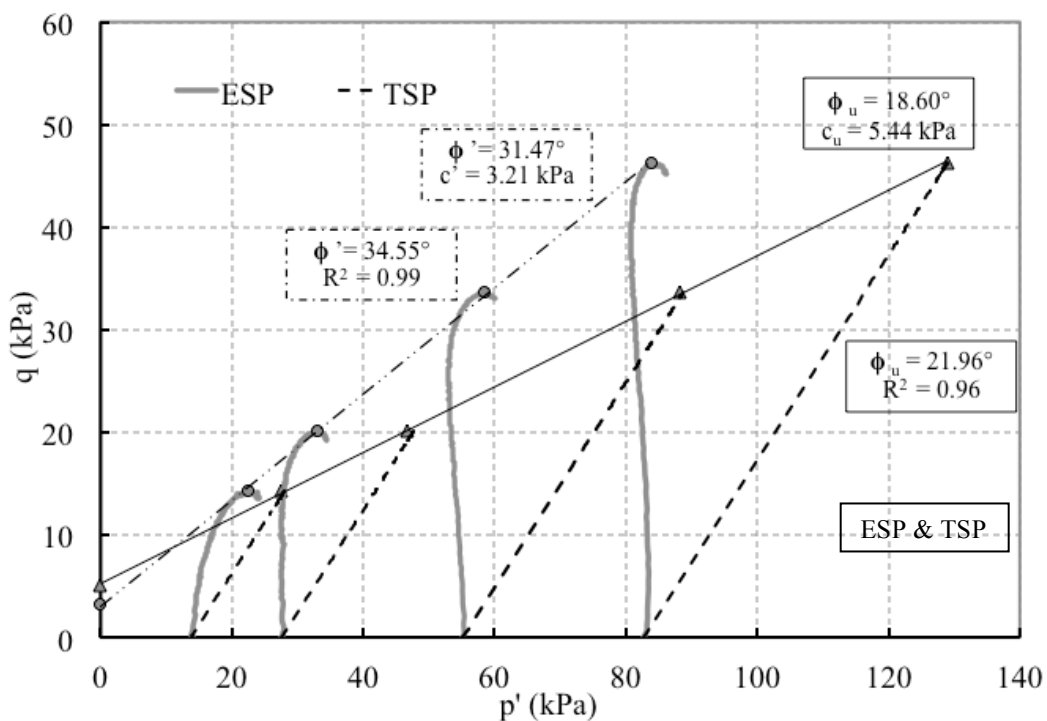


Figure 4.37: Comparison between effective and total stress paths for TDA CU tests

Table 4.6: Effective TDA shear strength parameters (CU triaxial tests)

Axial Strain (%)	Failure Envelope with y-axis intercept			Failure Envelope Through origin ($c' = 0$)	
	ϕ' (°)	c' (kPa)	R^2	ϕ' (°)	R^2
5	13.56	5.51	0.997	18.94	0.802
10	22.79	5.73	0.998	28.57	0.928
15	28.55	4.83	0.998	33.42	0.969
Peak ($\approx 22\%$)	31.47	3.21	0.999	34.55	0.990

TDA specimens seem to have a clear peak deviatoric stress at around 21% axial strain when tested under undrained conditions. However in certain situations, the failure criteria for soils under undrained conditions have been found to occur before the peak deviatoric stress by using the principal stress ratio (σ'_1 / σ'_3). Figure 4.38 show the resulting curves when using the previous criteria, and in fact peak principal stress ratios are found to occur at lower strain level than using the deviatoric stress failure criteria especially at lower confining pressures. However, there is negligible effect when the shear strength parameters are calculated using both criteria as shown in Figure 4.39. It is not possible to compare the results obtained in this section with other relevant studies since to the best of the knowledge of this author, published work related to undrained conditions in TDA was not available. Therefore, there may not be a clear consensus of all the variables involved in the problem yet.

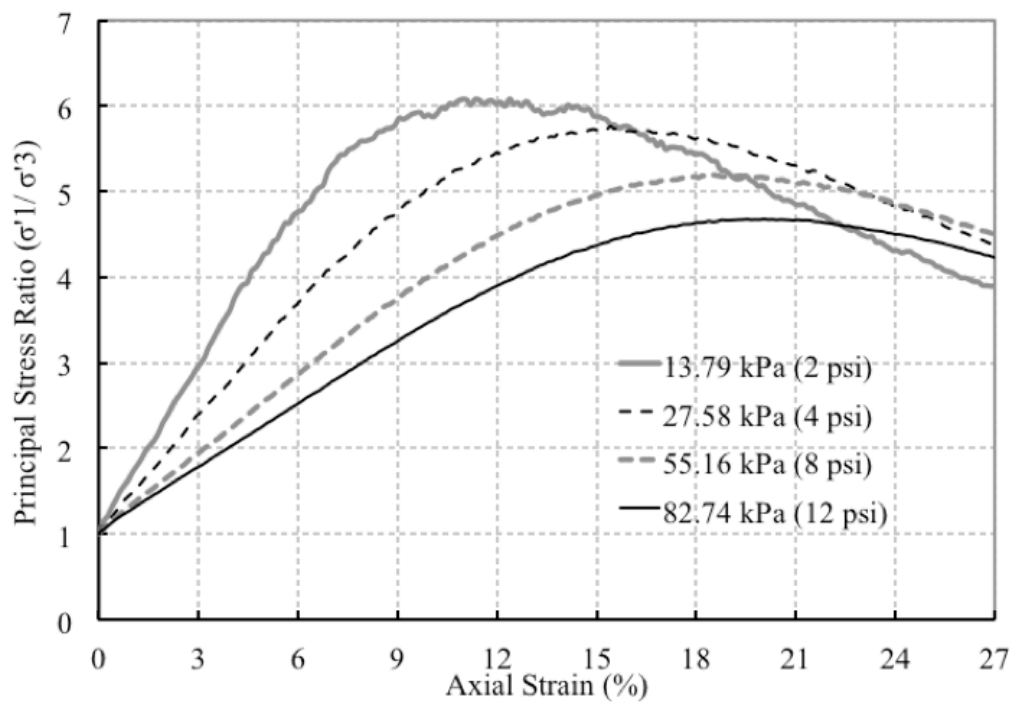


Figure 4.38: Comparison between effective and total stress paths for TDA CU tests

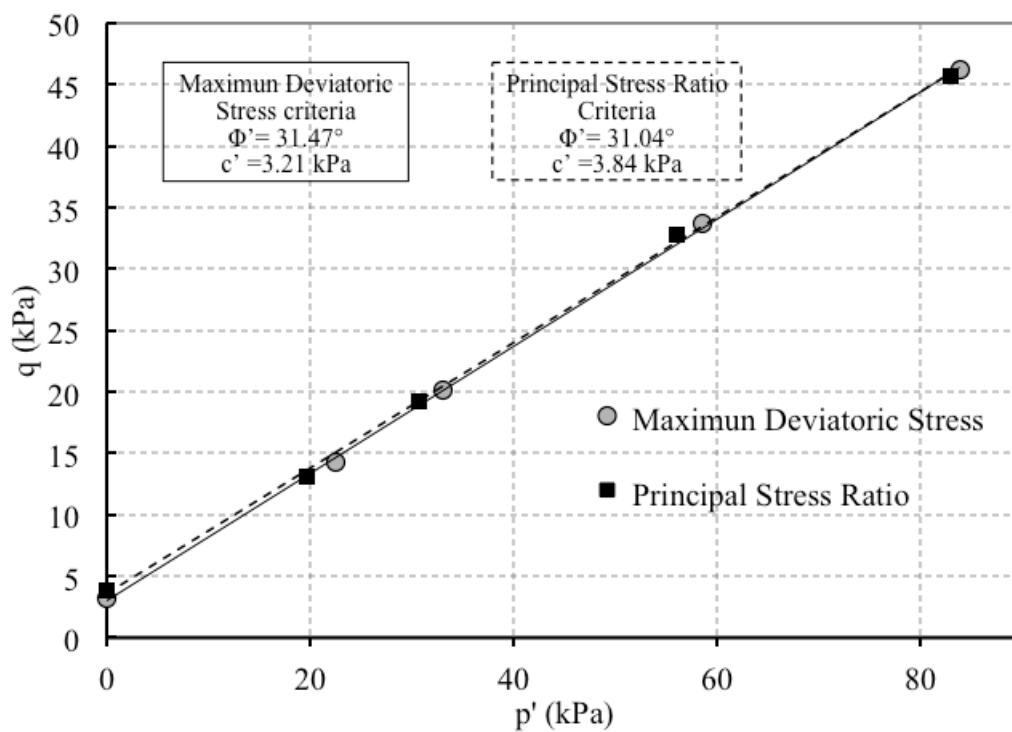
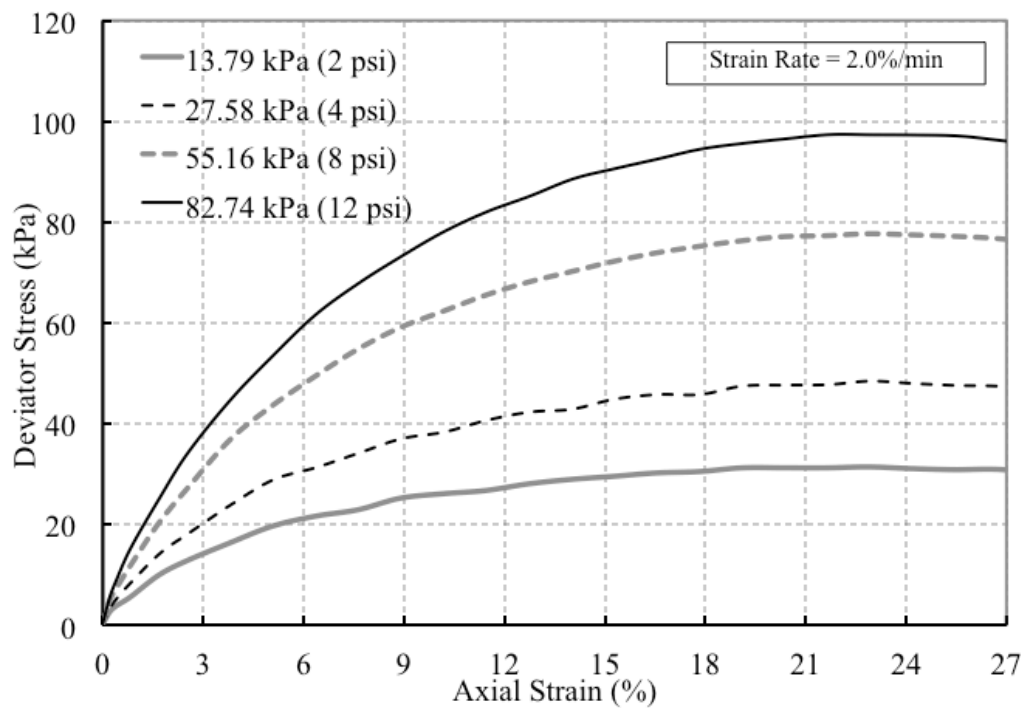


Figure 4.39: Shear strength parameters using peak deviatoric stress and principal stress ratio criteria

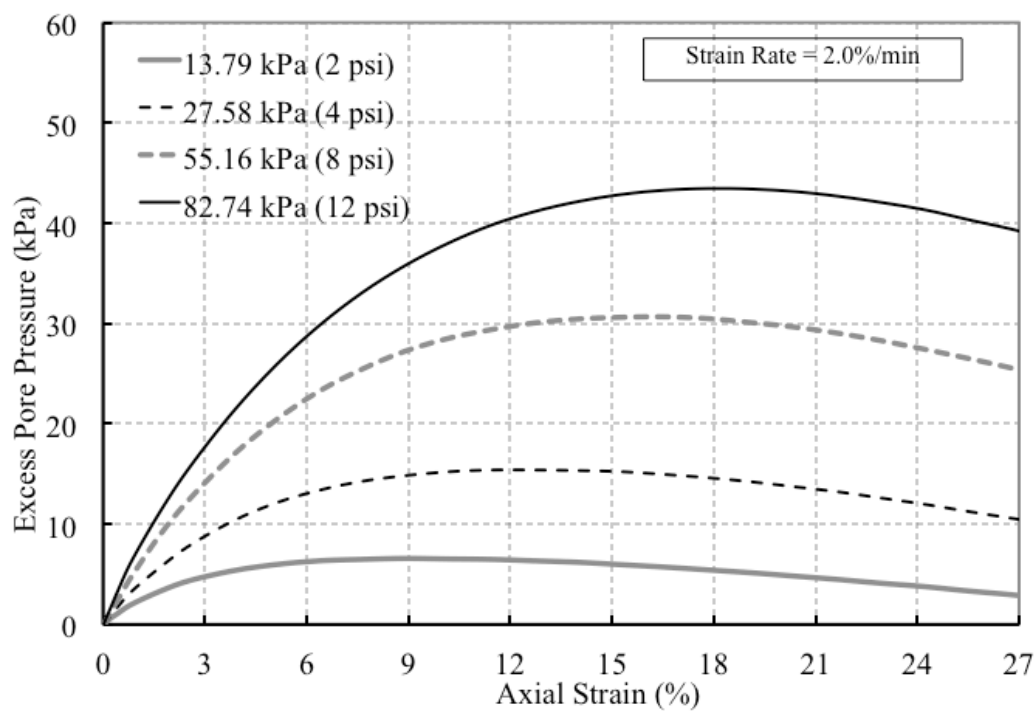
4.6 Effect of Strain Rate in TDA Stress-Strain Behavior

The stress-strain behavior of TDA was studied using two different strain rates while shearing. Strain-rate studies in rubber like materials has been broadly studied specially for mechanical applications (Amin et al. 2001) where the different strain rates produced an increase in stress due primarily to the viscosity effect of rubber.

Acknowledging the fact that TDA tested in this research is a granular media rather than a whole piece of rubber like is most mechanical applications and that temperature effects were not evaluated in this research, Figure 4.40 shows the stress-strain curves obtained from the CU triaxial tests at 2.0% axial strain. Curves from a lower strain rate (0.2%) were already presented in section 4.8. In order to compare the strain rate-effect in strength and excess pore pressure generation, Figures 4.41 and 4.42 show the deviatoric-stress and excess pore pressure vs axial strain curves at 82.74 and 55.16 kPa confining pressure respectively. Other confining pressures curves can be found in Appendix C. In general, higher strain-rate produces an increment in strength. Increments between 5% and 16% are attained for the ranges of confining pressures studied in this research. In terms of pore pressure generation, the high strain rate generates positive pore pressures as well which is consistent with the contractive behavior material. However, it is observed that pore pressures generated in the slow strain rate (0.2%/min) tests are slightly higher when compared to the higher strain rate tests (2.0 %/min). This may be to the results of slow strain rest having more time allowed to build-up excess pore pressure before dissipation process occurs while in the high strain rate tests the build-up generation process occurs faster.

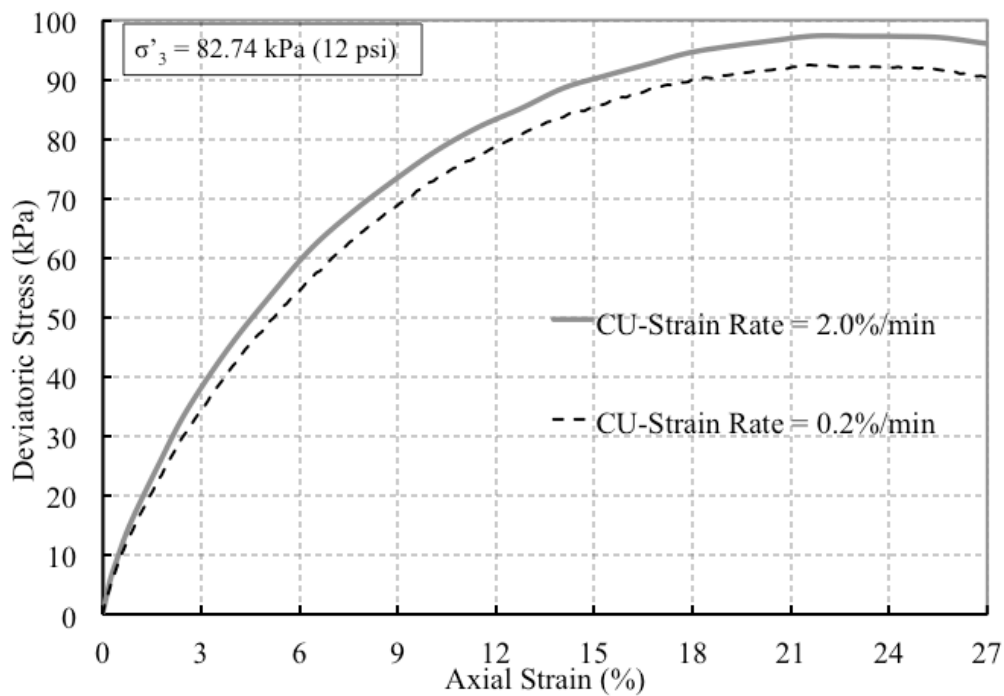


a) Deviator stress versus axial strain

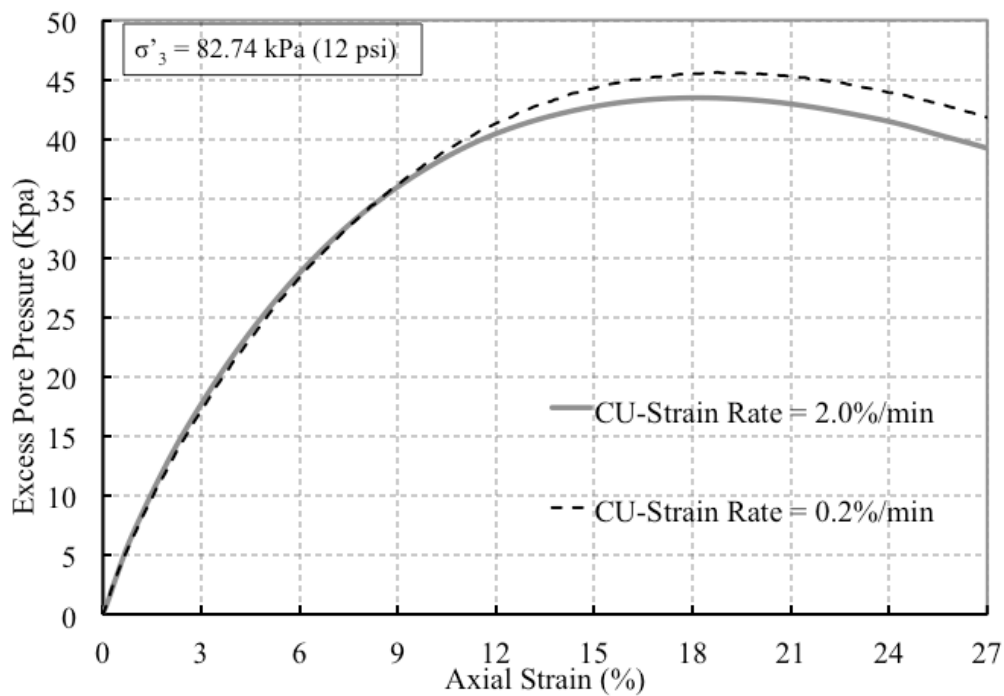


b) Volumetric strain versus axial strain

Figure 4.40: CU triaxial compression tests for TDA strain rate = 2.0%/min

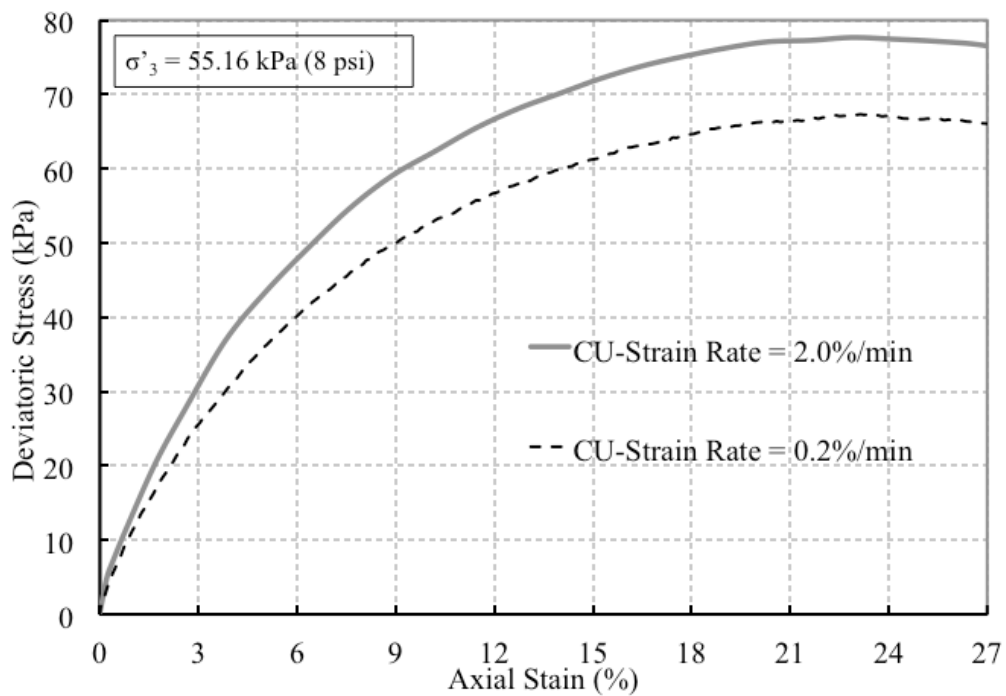


a) Deviator stress versus axial strain

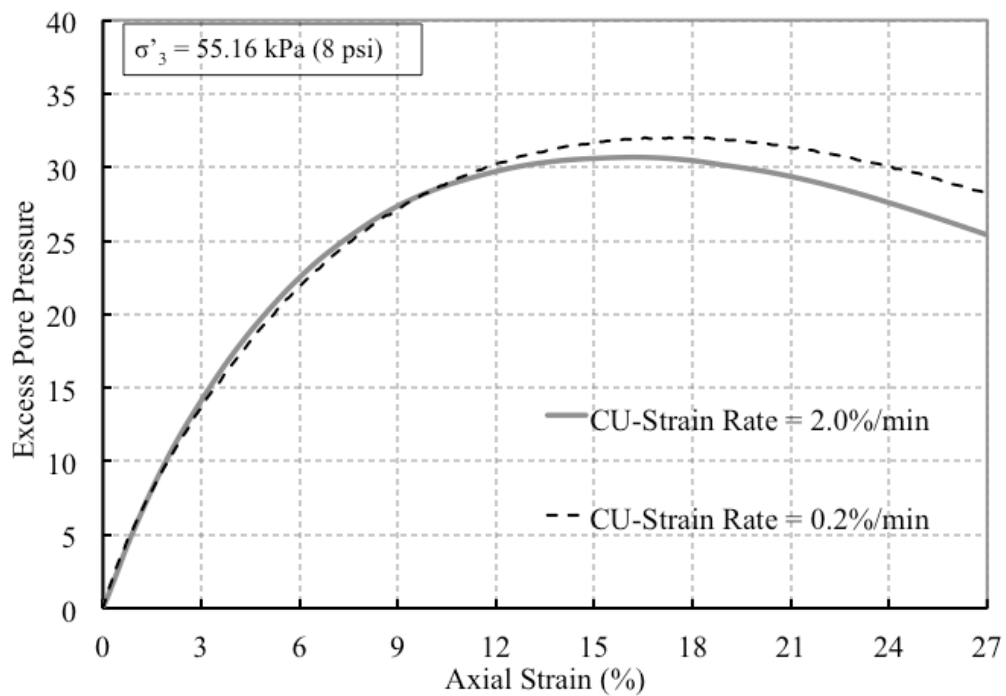


b) Volumetric strain versus axial strain

Figure 4.41: Comparison for consolidated undrained test at two different strain rates and 82.74 kPa confining pressure



a) Deviator stress vs axial strain



b) Volumetric strain versus axial strain

Figure 4.42: Comparison for consolidated undrained test at two different strain rates and 55.16 kPa confining pressure

The effect of the strain rate can also be observed in the stress-paths shown in Figure 4.43 where the increase in peak strength for the higher strain-rate can be observed again for all confining pressures (triangle symbols) when compared to the slow strain-rate (circle symbols). Effective stress paths are shifted more towards the right because even for similar values of excess pore pressures that occurred at low strain levels for both strain-rate, the effective vertical stresses are higher for the 2.0%/min axial strain which produces an increase in p' . However, the resulting shear strength parameters seem to have negligible effect for both strain-rates. Increases in peak deviatoric were also found for drained conditions (CD triaxial tests). Figure 4.44 shows the stress-strain curves obtained from CD triaxial tests at 2.0%/min. For comparison purposes, the results for one confining pressures are compared to the CD triaxial tests discussed in Section 4.4 are shown in Figure 4.45 (Other confining pressures can be found in Appendix C).

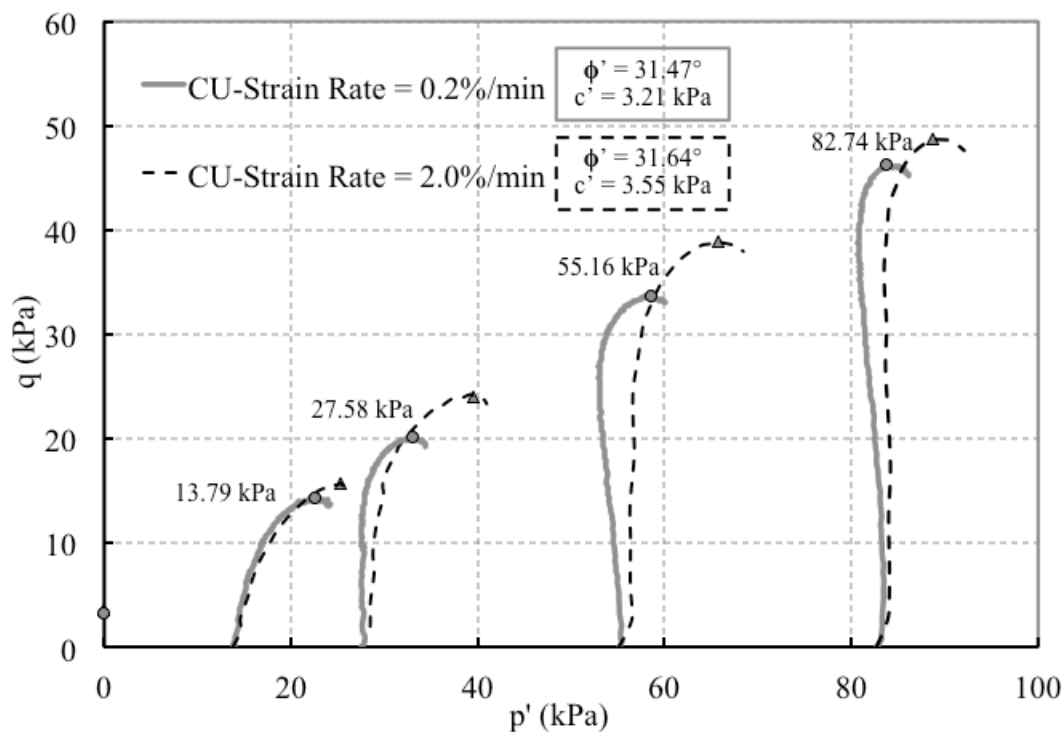


Figure 4.43: Effect of strain rate in the stress path for CU triaxial tests

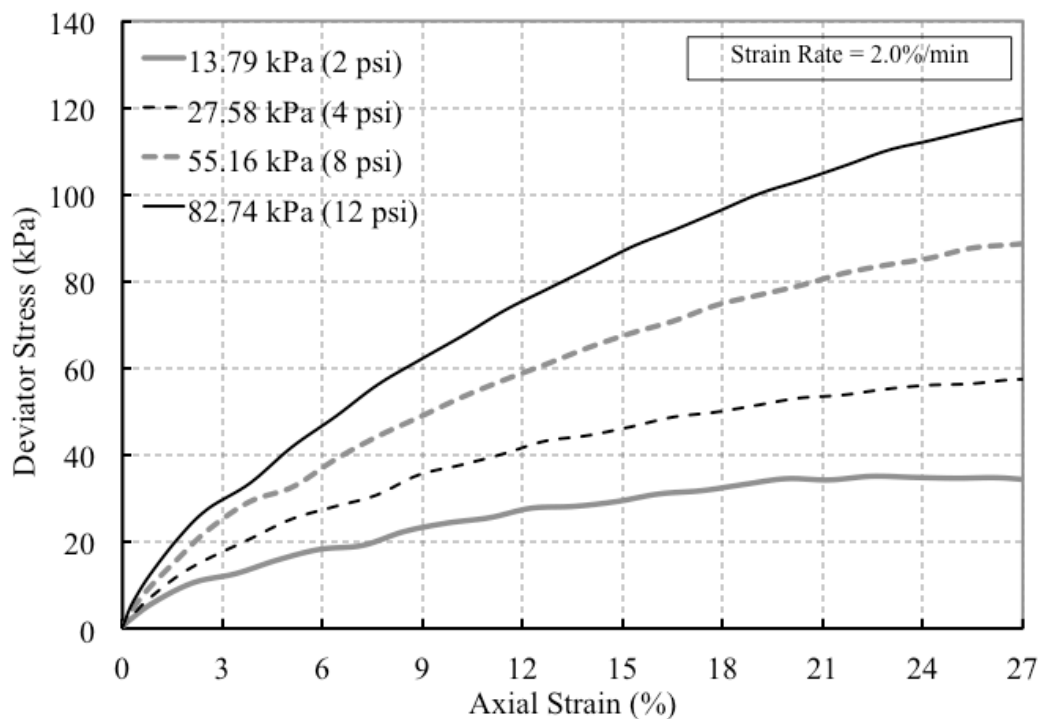


Figure 4.44: Consolidated drained triaxial tests results for TDA strain rate = 2.0%/min

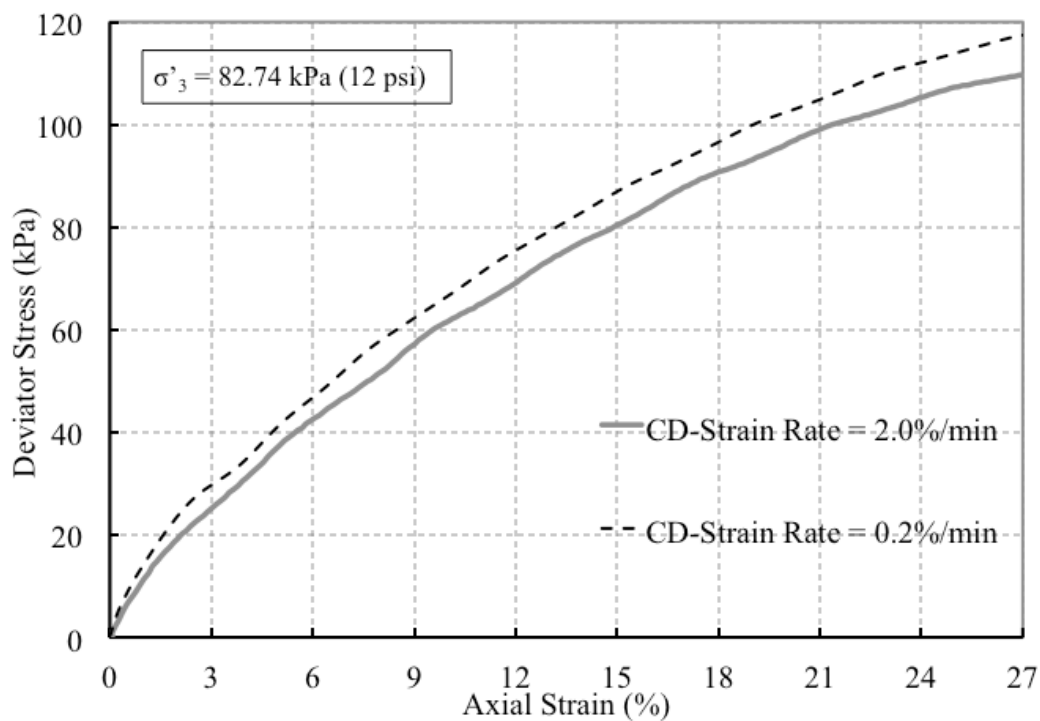


Figure 4.45: Comparison for consolidated drained test at two different strain rates and 82.74 kPa confining pressure

Increments between 2% and 6% in peak strength were observed for the level of confining pressures studied in this research under drained conditions for the higher strain rate, which is a slightly lower increment than the values obtained for undrained conditions. For both drainage conditions, an increment in stiffness was also observed as the strain rate increases as shown in Figures 4.42 and 4.45 where the slopes of the stress strain curves for 2.0%/min are steeper than those of the 0.2%/min strain rate producing an increment in modulus of elasticity. Table 4.7 presents a summary of the peak deviatoric stresses and secant modulus obtained for both drained condition while Figures 4.46 and 4.47 shows the differences in secant modulus for consolidated undrained and consolidated drained tests for both-strain rates, respectively.

Another aspect that is highlighted in Table 4.7 is the differences in peak strength and stiffness between both drained conditions. It was found that failure strength is higher for drained conditions than the undrained strength for both strain-rates which is expected and it is a true fact for conventional soils as well since its Mohr circles must be tangent to the effective Mohr failure envelope (Holtz and Kovacs 1981). For example, Figures 4.48 and 4.49 shows the comparison of two strain curves for CD and CU triaxial tests for confining effective stresses of 27.58 and 55.16, respectively.

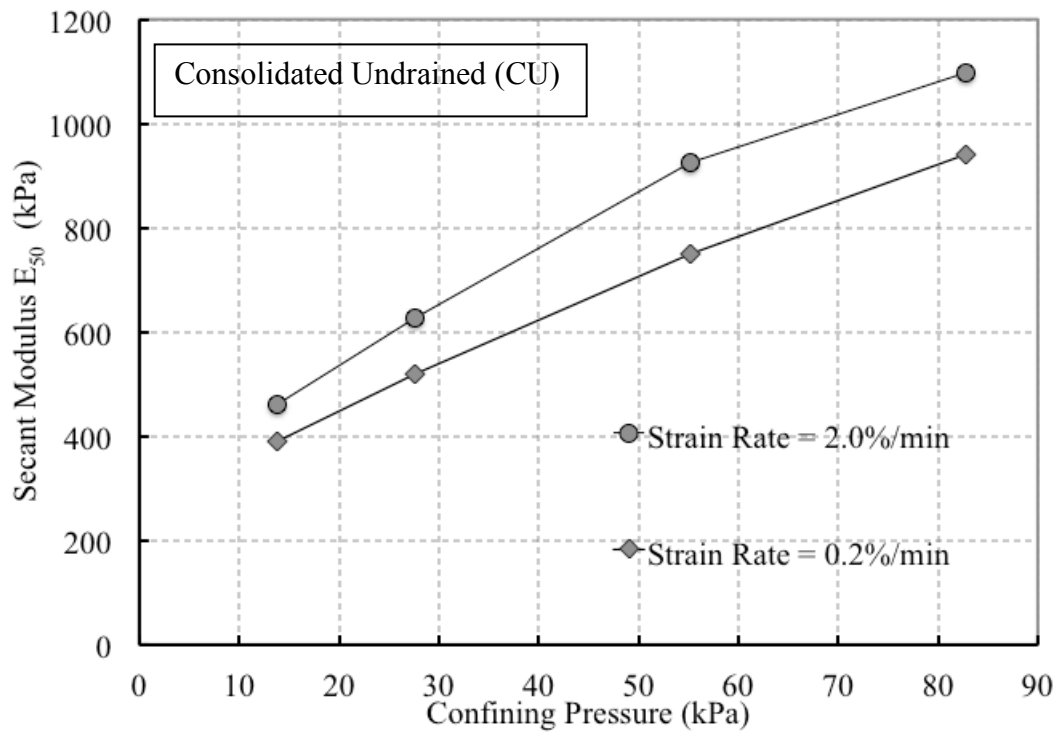


Figure 4.46: Secant modulus for consolidated undrained triaxial test

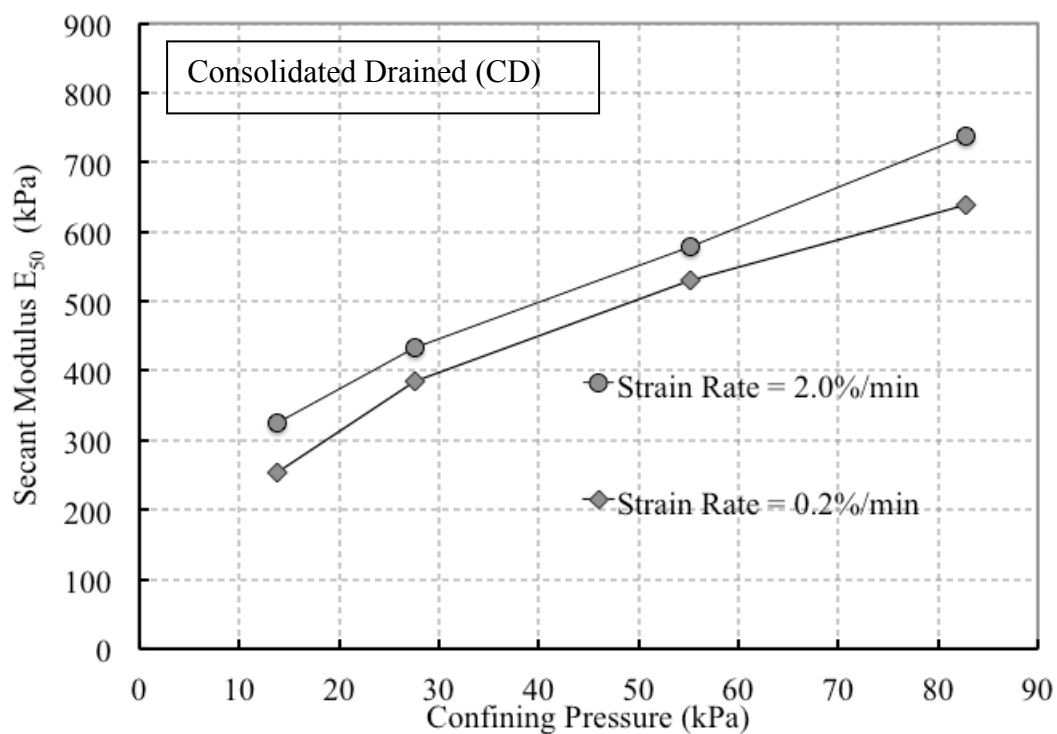


Figure 4.47: Secant modulus for consolidated drained triaxial test

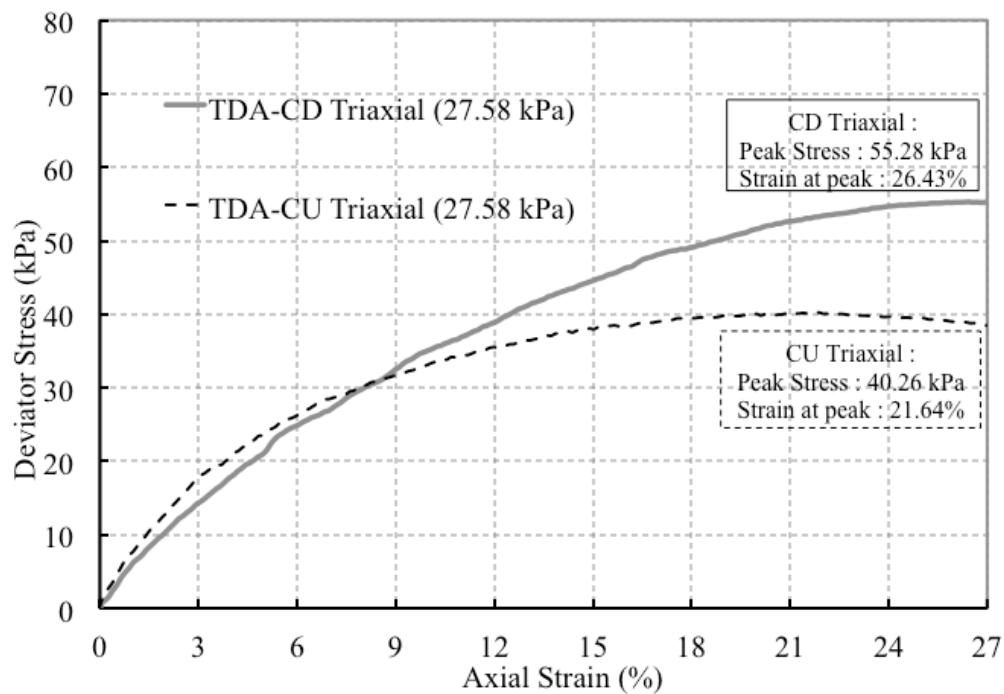


Figure 4.48: Comparison between CD and CU triaxial test at 0.2%/axial strain at 27.58 kPa confining pressure

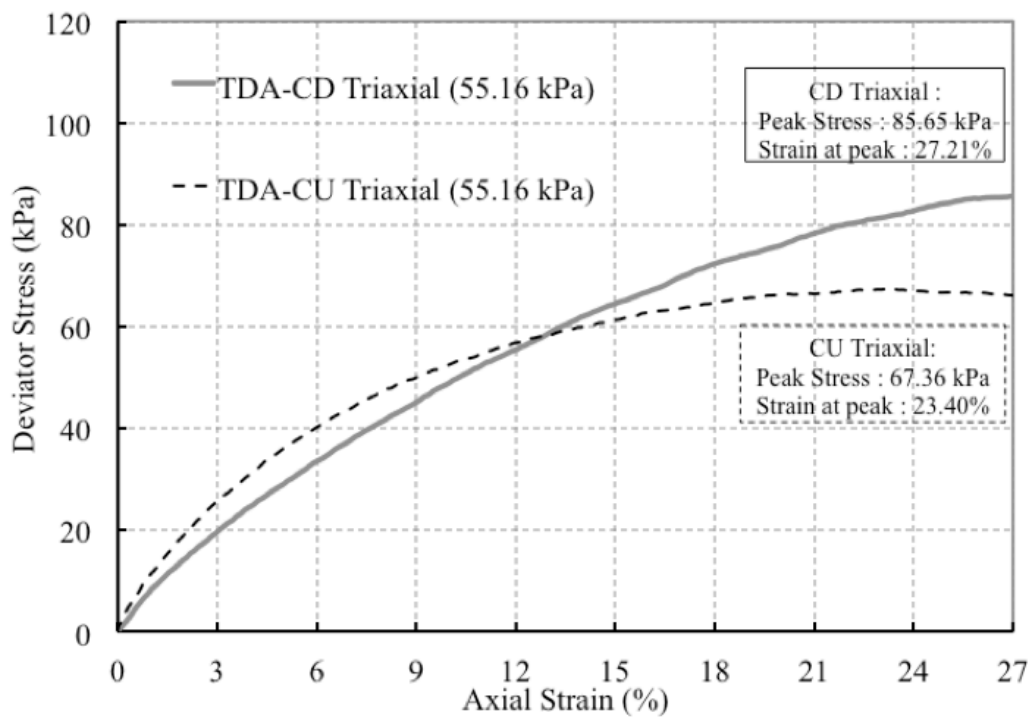


Figure 4.49: Comparison between CD and CU triaxial test at 0.2%/axial strain at 55.16 kPa confining pressure

Table 4.7: Effective TDA shear strength parameters based on CU triaxial tests

σ'_3 (kPa)	Consolidated Undrained				Consolidated Drained			
	0.2%/min		2.0%/min		0.2%/min		2.0%/min	
	σ_{peak} (kPa)	E_{50} (kPa)	σ_{peak} (kPa)	E_{50} (kPa)	σ_{peak} (kPa)	E_{50} (kPa)	σ_{peak} (kPa)	E_{50} (kPa)
13.79	28.45	389.73	31.37	461.32	34.66	253.73	35.07	324.72
27.58	40.26	520.16	47.94	625.85	55.28	383.89	57.33	434.32
55.16	67.36	748.44	77.67	924.64	85.65	529.36	88.48	579.06
82.74	92.49	941.85	97.35	1096.28	109.72	639.39	117.17	737.85

Besides the expected decrease in strength for the undrained tests shown in Figures 4.48 and 4.49 (the reader is referred to Appendix C for similar curves at different levels of confining pressures), Table 4.7 reveals that the contrary occur in terms of stiffness between the two drained conditions. Secant moduli of elasticity (E_{50}) were found to be approximately 30% higher for the undrained triaxial specimens for both strains rates as shown in Figures 4.50 and 4.51.

Acknowledging the fact that the study of two different strain rates may be limited to have a broader understanding of the strain rate effect in the mechanical behavior of TDA considering rubber viscolastic properties, and the scope of this research cover other important aspects regarding TDA characteristics. The results obtained are in general agreement with the behavior of conventional granular materials where strain rate effects have been historically studied. Increases in shear strength between 10% and 15% and modulus of elasticity at high strain-rates have been reported for granular soils by other researchers under drained and undrained conditions (Alzubaidi and Lafta 2013; Casagrande and Shannon 1948; Seed and Lundgren 1954; Whitman and Healy 1962). However, this topic should be further studied to explore if there is a strain-rate region

where there is no change in the mechanical properties (e.g strength and stiffness) or even if a decrease may eventually occur. Although, the confining pressures ranges studied in this research are reasonable considering the low density of TDA, a wider range of confining pressures may lead to different conclusions as well. However, testing TDA at high strain-rates may be a difficult task using triaxial techniques. TDA specimens were found to be quite deformable during the experiments, and their stability may not be as good as conventional soils for quick loadings during shearing, which could have induced unavoidable experimental errors.

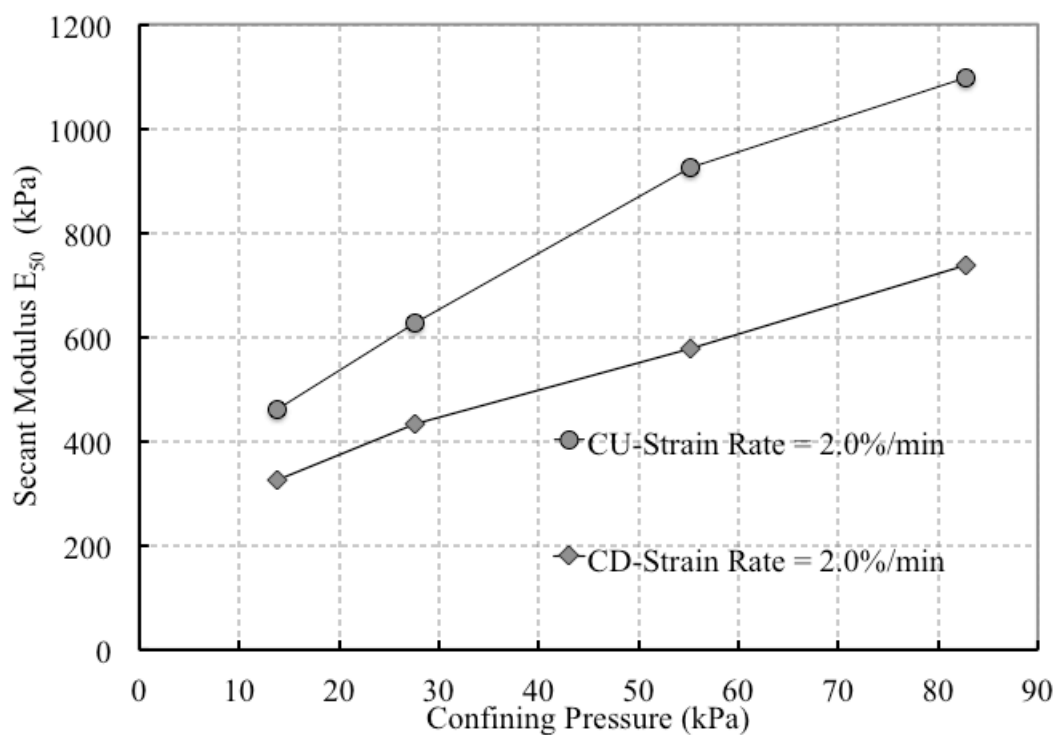


Figure 4.50: Secant modulus for both drained conditions at 2.0%/min

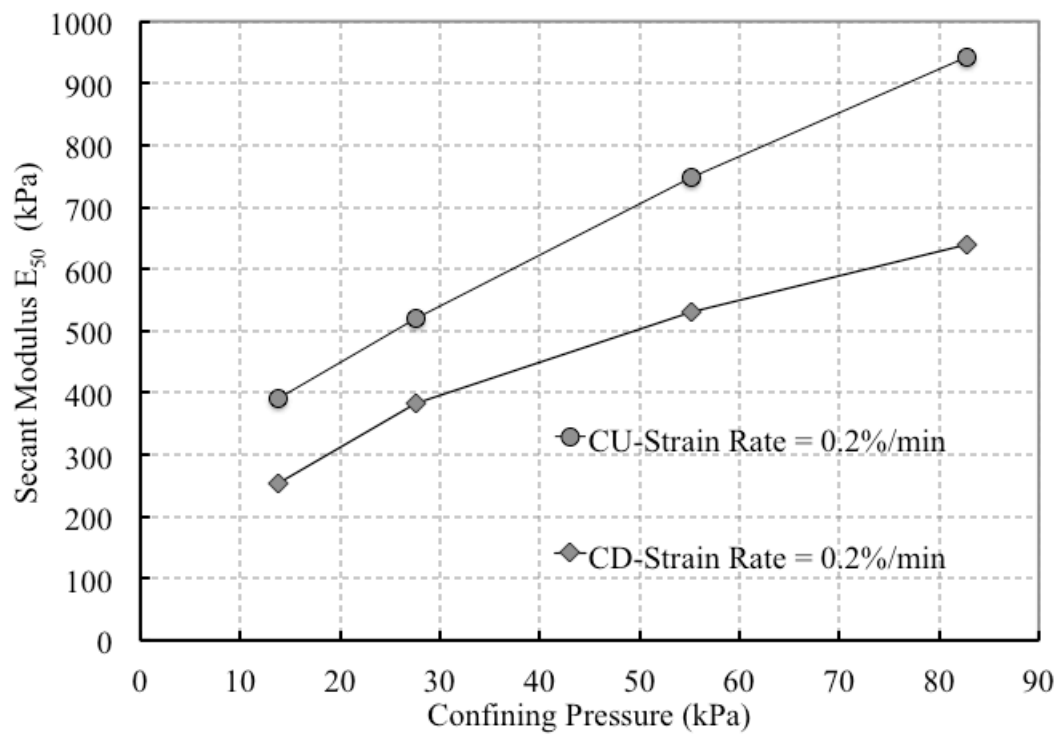


Figure 4.51: Secant modulus for both drained conditions at 0.2%/min

CHAPTER 5. SIMPLE SHEAR BEHAVIOR OF TDA AND TDA/SAND MIXTURES

5.1 Introduction

This chapter presents the results obtained from simple shear tests program carried out on samples composed of TDA, Nevada sand, and a TDA/sand mixture (50/50 by volume). The chapter describes the test set up and procedure used. Then the test results are presented and discussed. Results are divided into two parts: (i) 1-D compression during sample consolidation; and (ii) simple shear behavior and strength.

The inclusion of simple shear testing in the scope of the work of this research was considered important for the following reasons:

- The test includes a common stress path experienced in common geotechnical projects including retaining structures.
- The test yields valuable parameters such as G and shear stress versus shear strain behavior.
- Most of the research on TDA has included direct shear and compression triaxial techniques.

5.2 Simple Shear Test Set-up and Methodology

Simple shear tests were carried out on the same test materials described in the triaxial test program presented in chapter 4. The tests were carried out using ADVCSS device shown in Figure 5.1. The tests were carried out in general accordance with the recommendation of ASTM D6528 (ASTM 2007). The test matrix of the simple shear test program is shown in Table 5.1

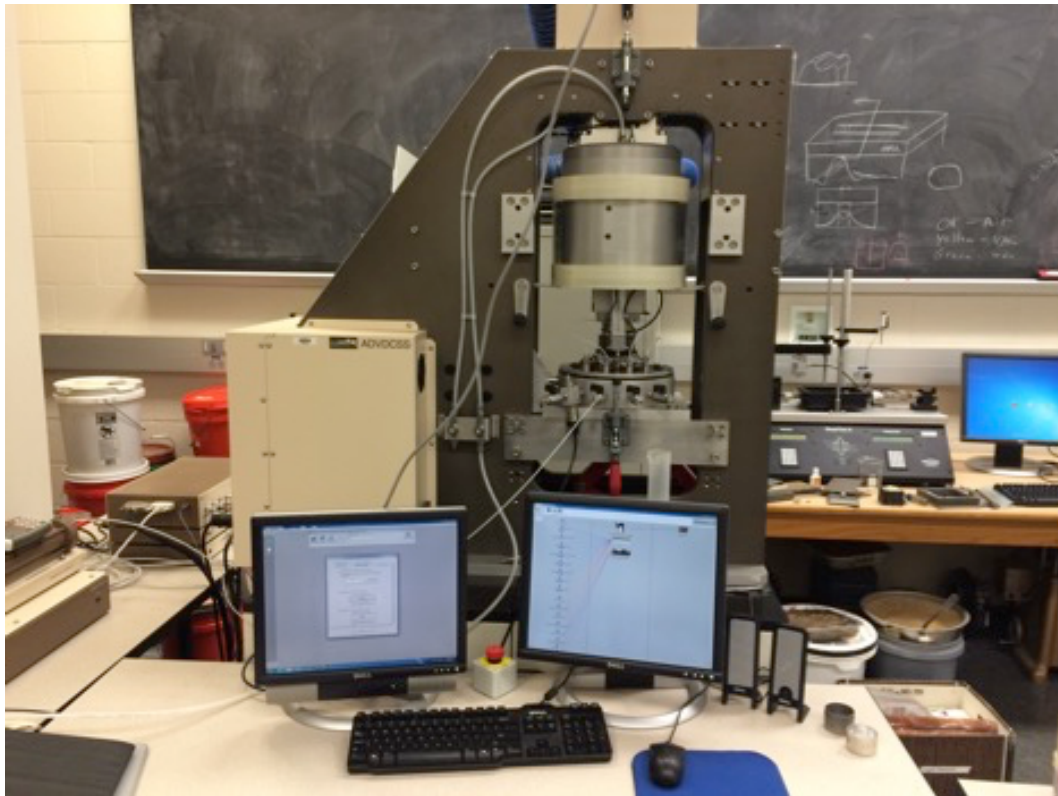


Figure 5.1: Advanced simple shear machine used in this research

All samples were prepared dry with target relative densities as close as possible as used in triaxial testing program ($D_r \approx 90\%$) Generally, the diameter and height of the specimens were approximately 70.22 mm and 20.0 mm respectively. Detailed

information regarding dimensions and initial densities of all simple shear tests can be found in Appendix C.

Simple shear test samples are prepared inside a stack of Teflon coated low friction retaining rings which in turn have an inner latex membrane as shown in Figure 5.2. The cylindrical soil specimen is prepared within the confining rings which enforces a condition of no lateral strain or K_0 -conditions. Detachable side prepared arms are clamped to the base pedestal to hold the specimen during preparation to decrease specimen disturbance as shown in Figure 5.3. Nevada sand and/or TDA are dry pluviated into the stack of rings and membrane using a funnel. The material is placed in thin layers and compacted lightly using a special tamping rod. Figure 5.3 shows the sample preparation set up and tools used. Once, specimen was prepared to the target density, the complete unit is placed onto the main testing frame as shown in Figure 5.4. Figure 5.5 shows a specimen during simple shear. During testing, the top of the specimen is connected to a piston or actuator, which applied the target vertical stress. The vertical actuator is totally fixed in the horizontal direction. The base of the specimen is connected to a horizontal actuator that will apply the shear loading at the specified rate. The vertical and horizontal displacements of the specimen are measured using the internal and external LVDT transducers of the device.

Table 5.1: Test matrix for simple shear test program

Test number	Material	Vertical Stress (kPa)	Shear strain rate (%/min)
SS-1	Fine TDA ($D_{50}=1.20\text{mm}$)	20	0.20
SS-2		40	
SS-3		80	
SS-4		120	
SS-5	Nevada-Sand ($D_{50}=0.15\text{mm}$)	20	0.20
SS-6		40	
SS-7		80	
SS-8		120	
SS-9	Coarse TDA ($D_{50}=2.60\text{mm}$)	20	0.20
SS-10		40	
SS-11		80	
SS-12		120	
SS-13	Fine TDA ($D_{50}=1.20\text{mm}$)	20	2.0
SS-14		40	
SS-15		80	
SS-16		120	
SS-17	TDA/sand Mixture (3/7 by weight) (50/50 by volume)	20	0.20
SS-18		40	
SS-19		80	
SS-20		120	



Figure 5.2: Simple shear sample membrane and stack of rings



Figure 5.3: Simple shear sample preparation

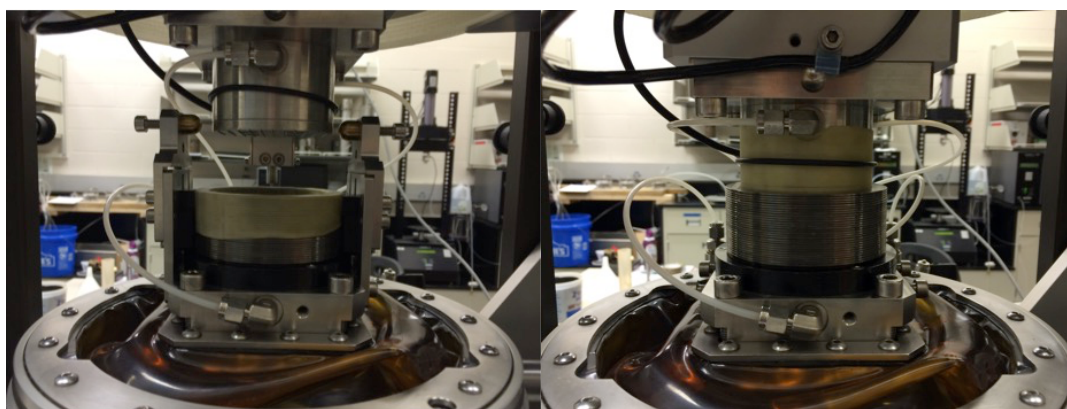


Figure 5.4: Simple shear sample installation in main machine

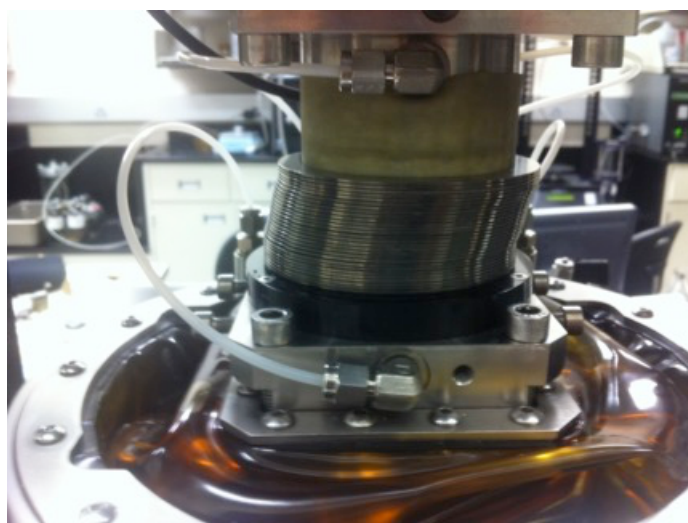


Figure 5.5: Simple shear specimen during shearing phase

The simple shear tests were carried out using two main phases: (i) Application of the specified vertical normal stress which results in 1-D compression of the sample; and (ii) application of horizontal shearing to the sample.

The first phase of vertical normal stress application was done with the vertical actuator of the device under a constant stress rate of 20 kPa/min. As indicated in Table 5.1, four normal stress levels were considered (20, 40, 80 and 120 kPa). During this test phase the vertical normal stress was held constant for a period of about 60 minutes. This was done to assess creep characteristics under 1-D compression conditions.

The second phase consisted in shearing the sample while keeping constant the vertical normal stress. The horizontal applied shear load was applied under shear strain controlled conditions. The two shear strain rates conditions used were $\dot{\gamma} = 0.2$ and 2.0%/min.

5.3 1-D Compression and Creep Results

Although a detailed study of TDA compressibility and creep characteristics is not the main purpose of this research, certain aspects of these topics could be evaluated during the consolidation phase prior to specimen shearing. Figure 5.6 shows the 1-D compression in terms of vertical axial strain vs time curves for the fine TDA and the target vertical normal stresses. Initially, specimens exhibit large deformation as consequence of the application of the target normal stress, which was applied using a load ramp at 20 kPa/min. As expected, the magnitude of axial deformation increases very rapidly as the normal stress increases. The curves show a marked slope decrease once the target vertical normal stress is reached. However, the curves do not become horizontal

since some creep deformation is exhibited by the different samples. This figure shows the slope at constant normal stress (creep) is higher with increasing stress level.

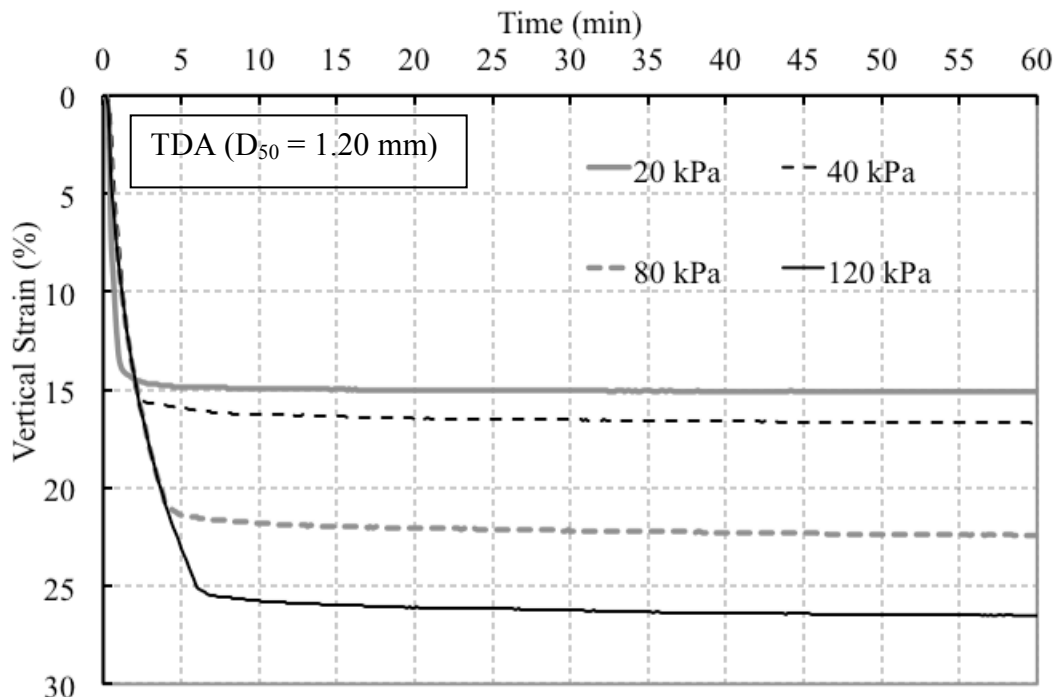


Figure 5.6: 1-D vertical strain versus time for dense fine TDA

The 1-D compressibility characteristics observed in the dense fine TDA are compared with the Nevada sand and TDA/sand mixture (50/50 by volume) in Figures 5.7 and 5.8 which corresponds to 1-D compression tests at 40 kPa and 120 kPa normal stress levels, respectively. In both figures “initial or instantaneous” 1-D deformation is the highest for the fine TDA. The level of initial vertical strains exhibited by the dense fine TDA samples were about 16% and 26% during the 1-D compression phase taken to vertical normal stress levels of 40 and 120 kPa, respectively. These strain levels are usually too large for most civil engineering applications. However, the 1-D compressibility decreases substantially for the 50/50 (by volume) TDA/Nevada sand mixture.

Initial vertical strain measured once the target vertical normal stress was reached is summarized for the different test materials in Figure 5.9. It can be seen in this figure that the level of initial vertical strain for the dense, fine TDA is approximately 24 times higher than those observed in the Nevada sand specimens. However, as mentioned above the 1-D compressibility decreases drastically for the 50/50 (by volume) TDA/sand mixture. Figure 5.9 shows the mixture material experienced levels of 1-D strain that were only approximately 5.5 times higher when compared to the values measured for the Nevada sand specimens. Therefore, the high 1-D stiffness of Nevada sand particle leads to considerable improvements when deformability issues are a concern (e.g. excessive settlements). High degree of 1-D compressibility of TDA compared to granular soils has been reported in the literature (Bosscher et al. 1997; Celis and Pando 2008; Drescher et al. 1999; Wartman et al. 2007).

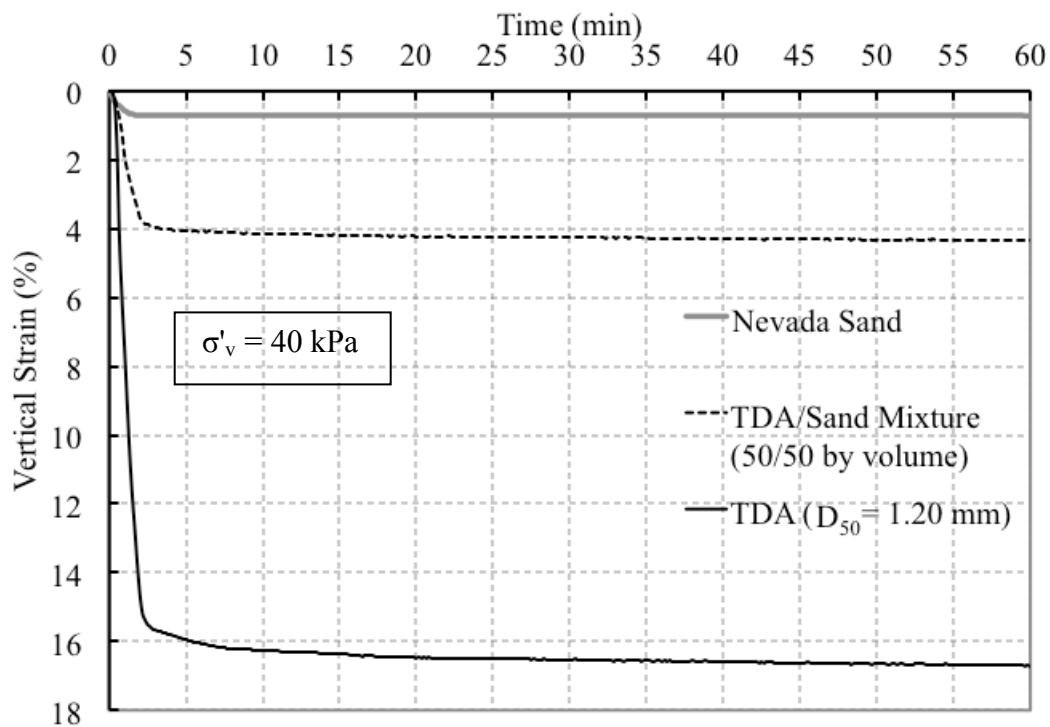


Figure 5.7: Comparison of strains from 1-D compression at 40 kPa normal stress

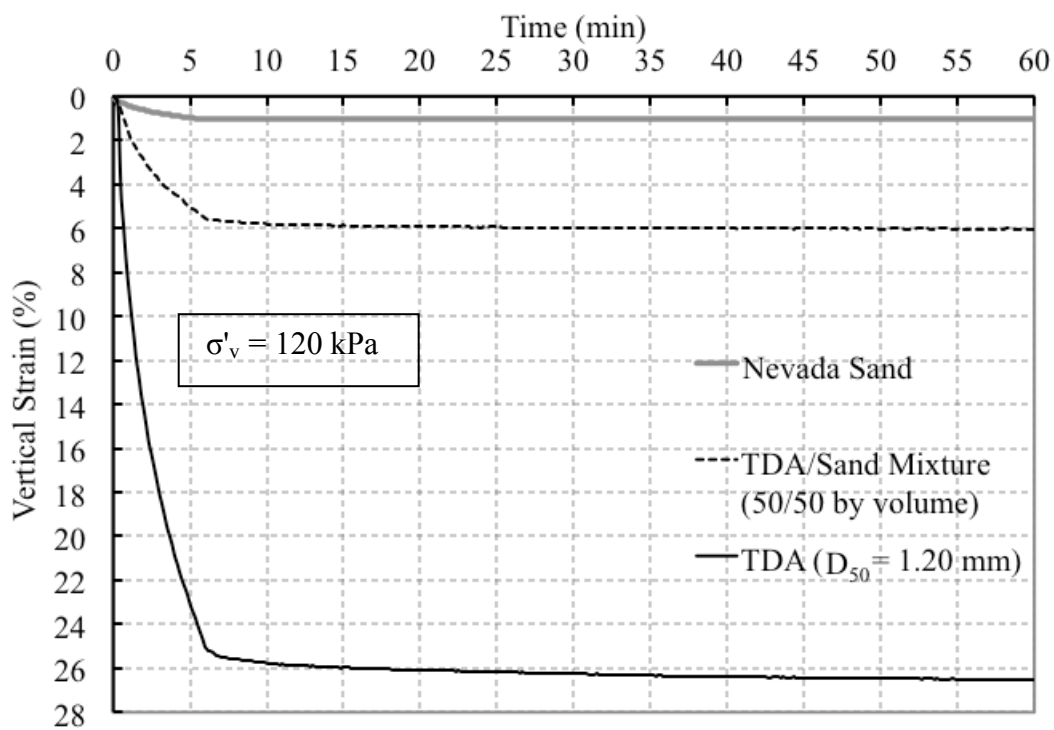


Figure 5.8: Comparison of strains from 1-D compression at 120 kPa normal stress

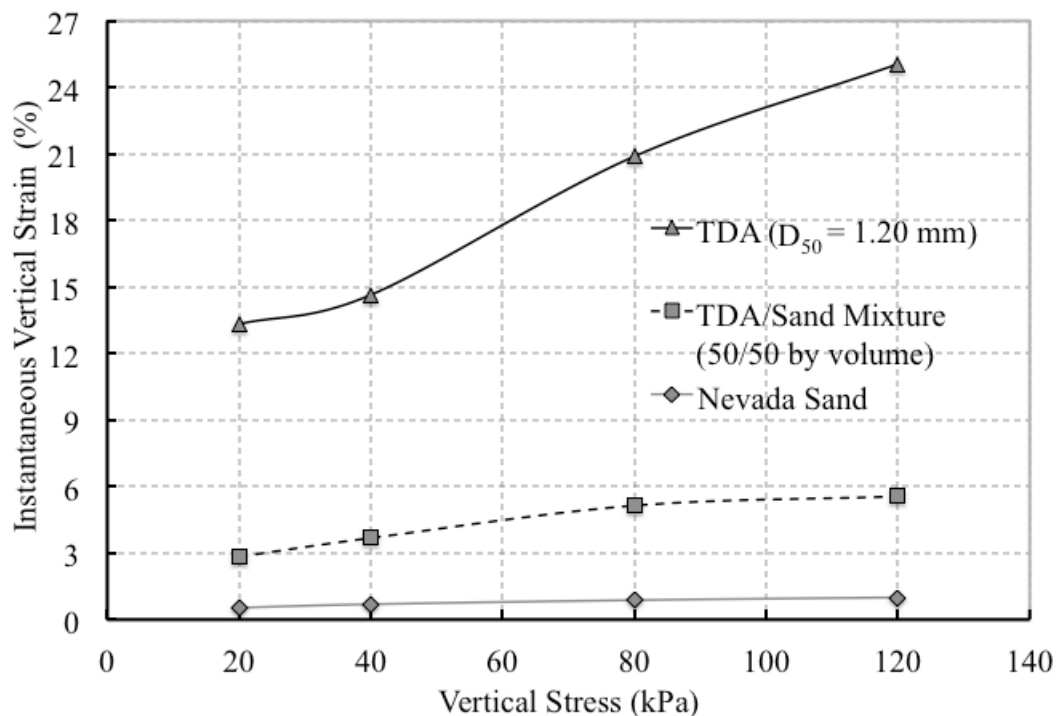
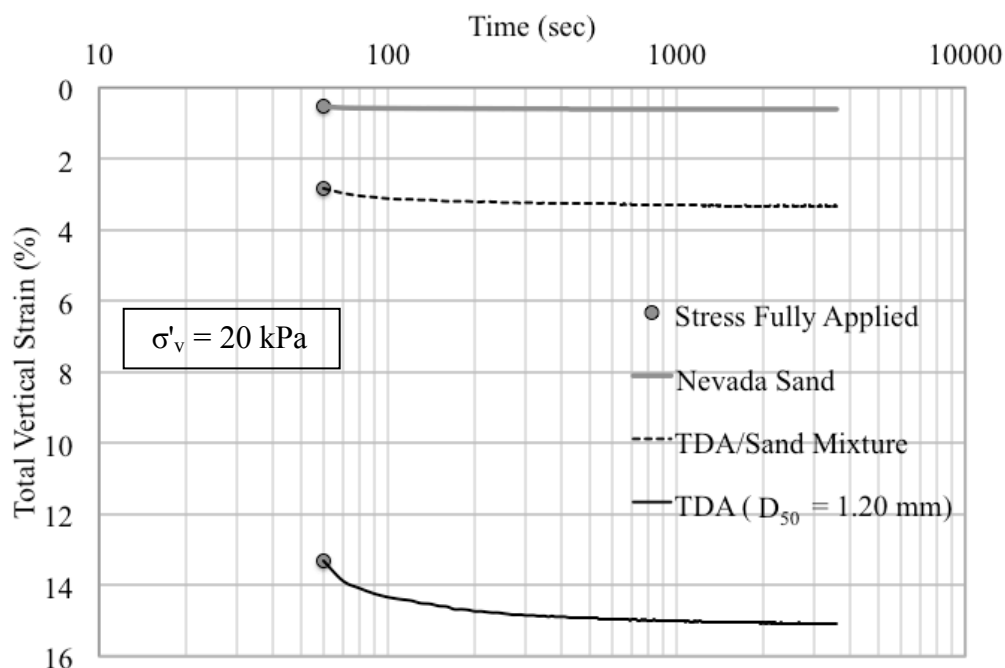


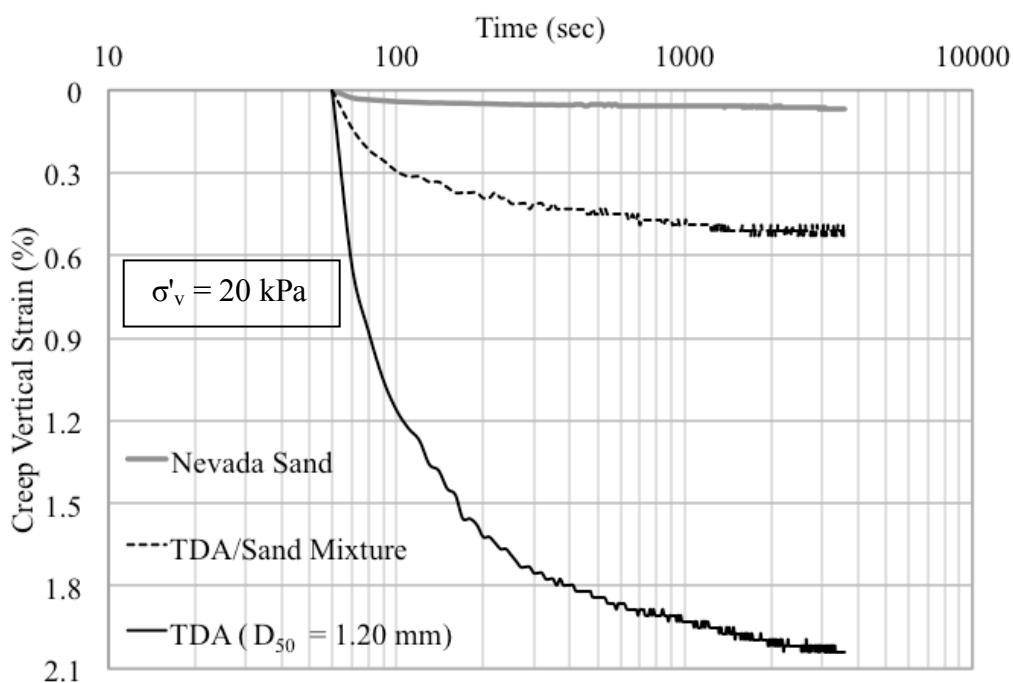
Figure 5.9: TDA vertical deformation for all materials at the end of the normal stress application

From Figures 5.7 and 5.8, it can be seen that the fine TDA seems to exhibit the most amount of 1-D creep since the vertical strains continued to increase slowly but at a faster rate when compared to the other test materials. 1-D creep is shown in after the normal stress is fully applied. For clarity, Figures 5.10 and 5.11 which show vertical strain versus log of time for 1-D compression at 20 and 80 kPa, respectively. The grey circles indicate the time where the target vertical stress was reached. Despite the short duration of only 60 minutes (3600 seconds) which is not enough time to fully assess 1-D creep effects, it is enough to observe the trends and initial levels of 1-D vertical deformations. These figures show that the Nevada sand samples stabilize or show negligible amounts of 1-D vertical strain after reaching the target normal stress (grey

circles). In contrast the TDA and TDA/sand mixture specimens continue to accumulate 1-D vertical strains past the grey circle or point of constant normal stress.

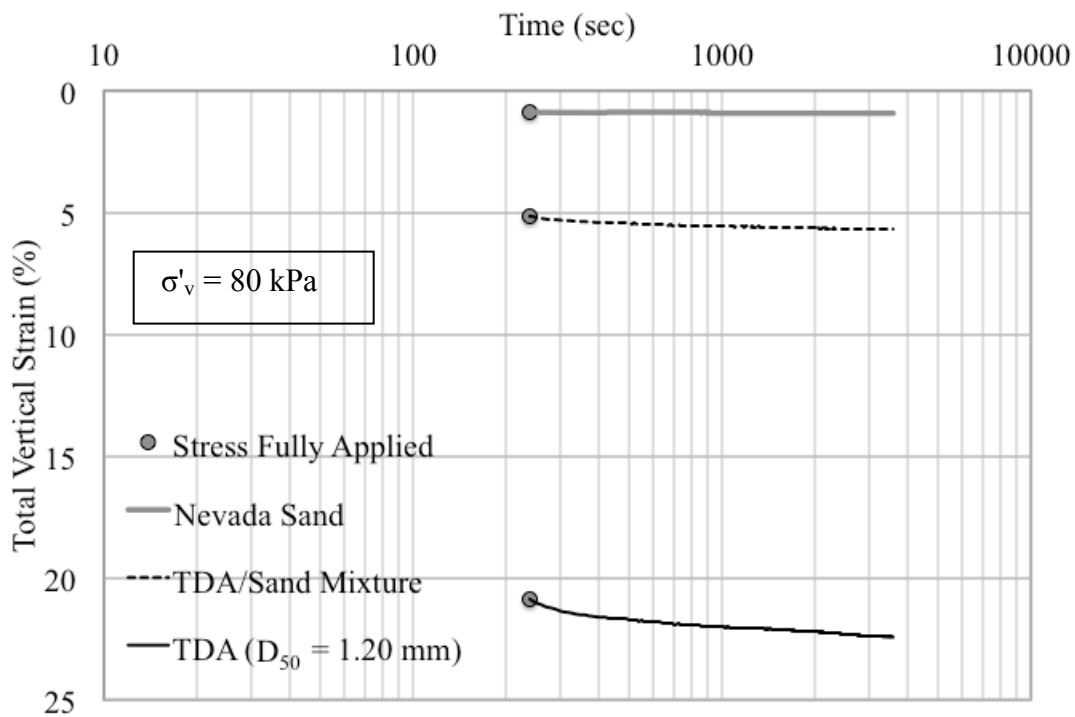


a) Analysis after vertical stress is fully applied

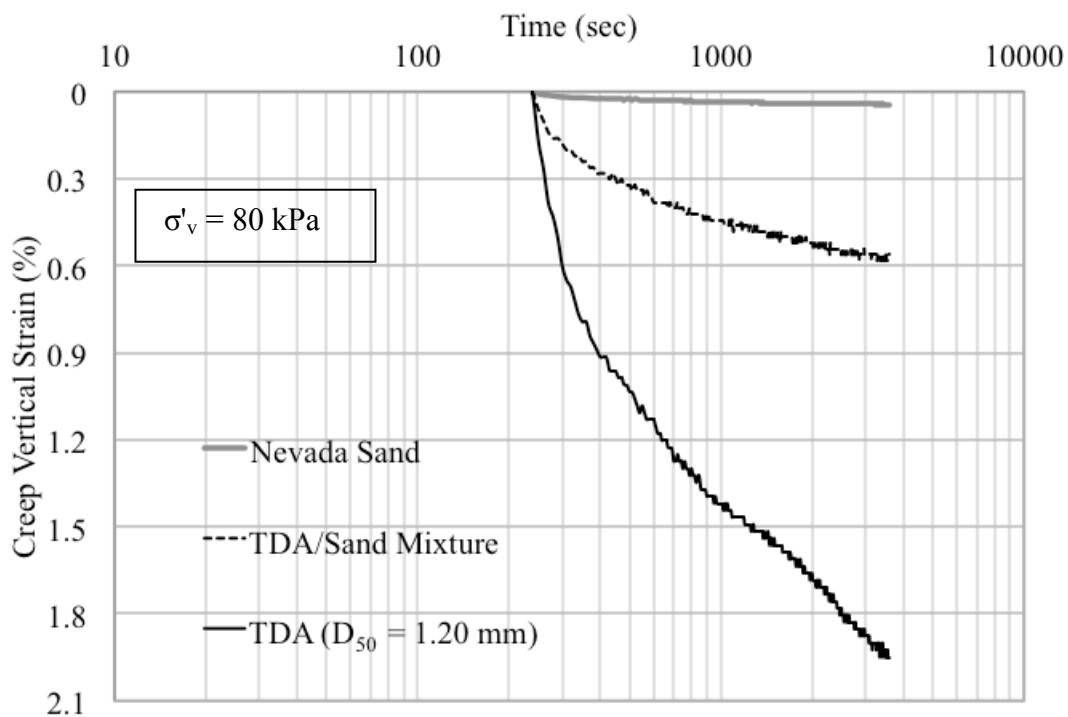


b) Vertical strains due to creep process

Figure 5.10: Analysis of deformations after vertical stress (20 kPa) is fully applied



a) Analysis after vertical stress is fully applied



b) Vertical strains due to creep process

Figure 5.11: Analysis of deformations after vertical stress (80 kPa) is fully applied

The continuous accumulation of vertical strains exhibited by the TDA specimens under constant normal stress levels is related to 1-D creep. This phenomenon has also been reported in TDA by Drescher et al. 1999; Wartman et al. 2007; and Celis and Pando 2008. The results show that creep rate is stress-dependent. Figures 5.10 and 5.11 show how TDA creep deformations increase in rate when increasing the normal vertical stress from 20 kPa to 80 kPa. The reader is referred to Appendix C for additional 1-D compression test results.

In conventional geotechnical engineering practice, it is common to quantify creep compressibility by means of a compression index (C_α) which is defined as follows:

$$C_\alpha = \frac{\Delta_{\epsilon_{vol}}}{\log\left(\frac{t_1}{t_2}\right)} \quad (5.1)$$

where:

$\Delta_{\epsilon_{vol}}$ = Change in volumetric strain.

t_2 and t_1 = Range of time when the creep compression is being calculated.

The previous expression corresponds to the slope of the vertical strain vs time curves shown in Figures 5.10(b) and 5.11(b). For this research t_2 was taken as 3600 seconds which is the end of the load application 1-D compression phase while t_1 was taken as a time that would be within the creep zone for all four vertical stresses. For consistency t_1 was taken as 500 seconds for all four vertical stresses. Figure 5.12 presents the creep compression index for the three different types of specimens.

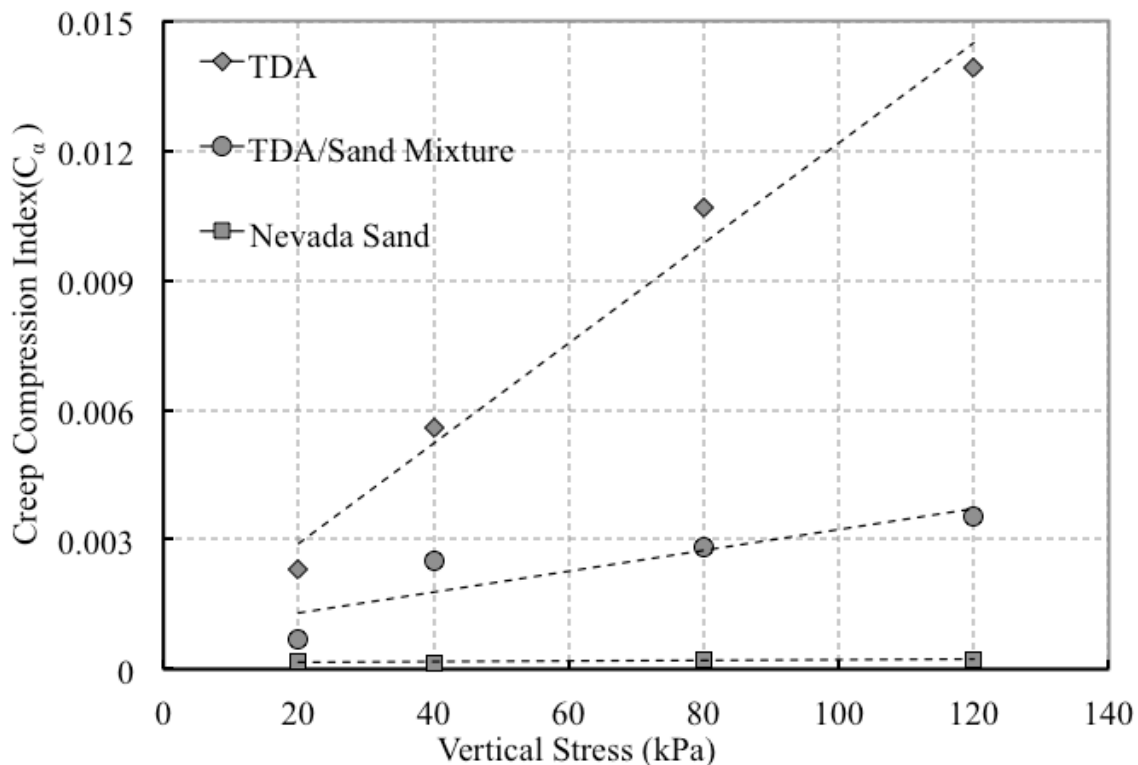


Figure 5.12: Creep compression index at different vertical stresses

The results obtained in Figure 5.12 indicates that TDA can exhibit a time dependent compression rate that could be between 14 to 63 times higher than the corresponding values measured for Nevada sand for the ranges of vertical stresses analyzed in this research. Substantial reductions in time-dependent compressibility can be achieved when both materials are mixed in an approximate 50/50 percent ratio (by volume) due to the high stiffness of the Nevada sand.

The TDA particle size was found to have some influence in the 1-D compression deformation characteristics. Coarser TDA ($D_{50} = 2.60$ mm), which was not compared with the rest of the materials, because TDA/sand mixtures do not contain this particle size, exhibits less levels of immediate compression when compared to the finer TDA ($D_{50} = 1.20$ mm) as shown in Figures 5.13 through 5.15. The magnitude of the decrease in

deformability seems to depend on the normal stress applied as shown in Figure 5.15. Coarser TDA vertical strains were found to be 49% and 37% lower than the finer TDA particles for 20 kPa and 40 kPa respectively. The decrease seems less pronounced at 80 kPa, and 120 kPa were 12% and 9% decreased in vertical strain were obtained respectively for the coarser TDA. Creep deformations seems to be higher for the coarser TDA aggregate when compared to the finer TDA at the same times as shown in Figure 5.16. This may be the result of finer TDA exhibiting higher degree of instantaneous deformation as shown in Figures 5.13 through 5.15 leading to a denser aggregate when secondary deformations occur. Therefore, time-dependent deformations would be reduced when compared to the coarser TDA, which particles are in a less packed state when creep deformations take place.

The results presented in this section indicate that in general the TDA exhibits a high degree of immediate 1-D compression. Although, the time allowed for 1-D compression of the TDA was limited; the results suggest that creep deformations may be a concern particularly for 100% TDA under high stress levels. High compressibility characteristics are attributed to the compression of its individual particles and the decrease of the TDA particle arrangement or skeleton which was found to have low axial stiffness (Chapter 4).

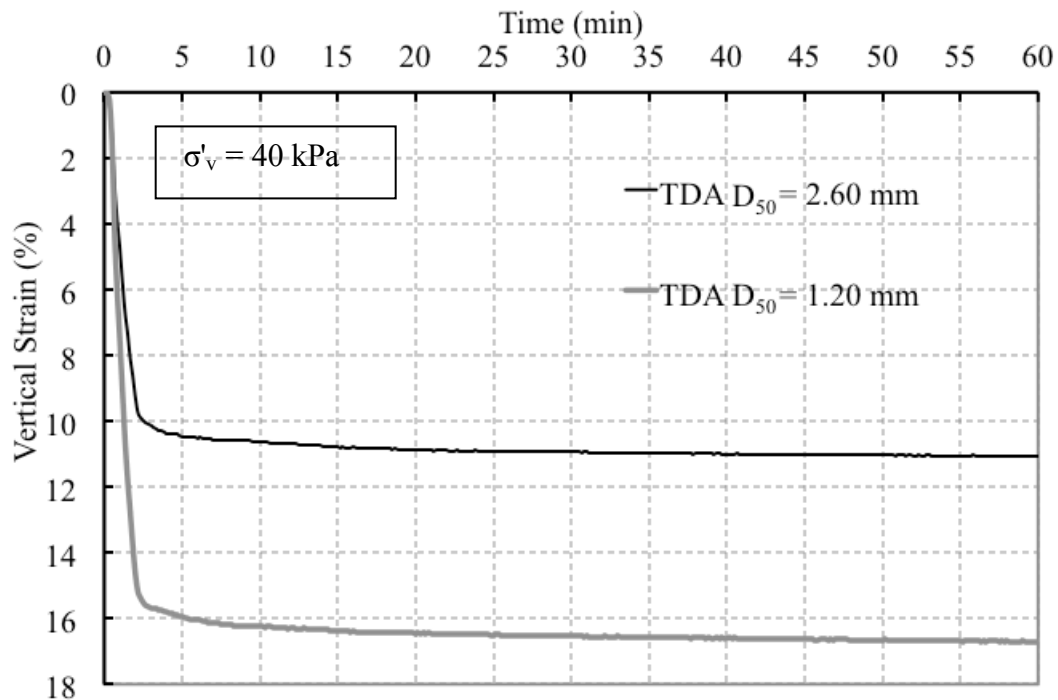


Figure 5.13: Comparison of 1-D compression for two TDA sizes at 40 kPa normal stress

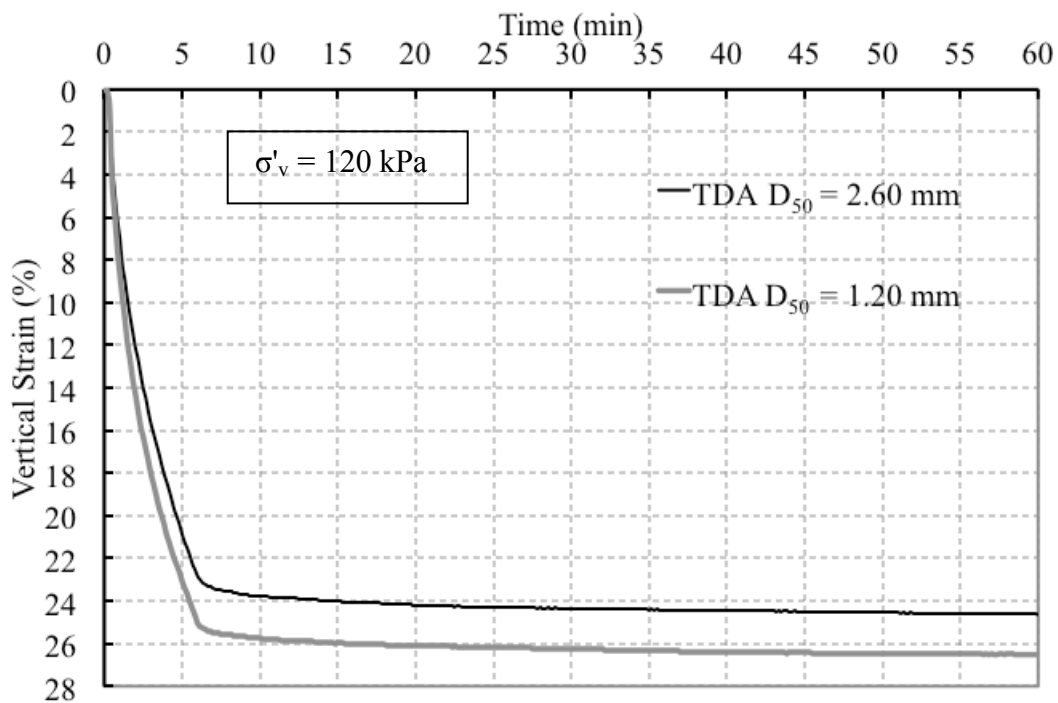


Figure 5.14: Comparison of 1-D compression for two TDA sizes at 120 kPa normal stress

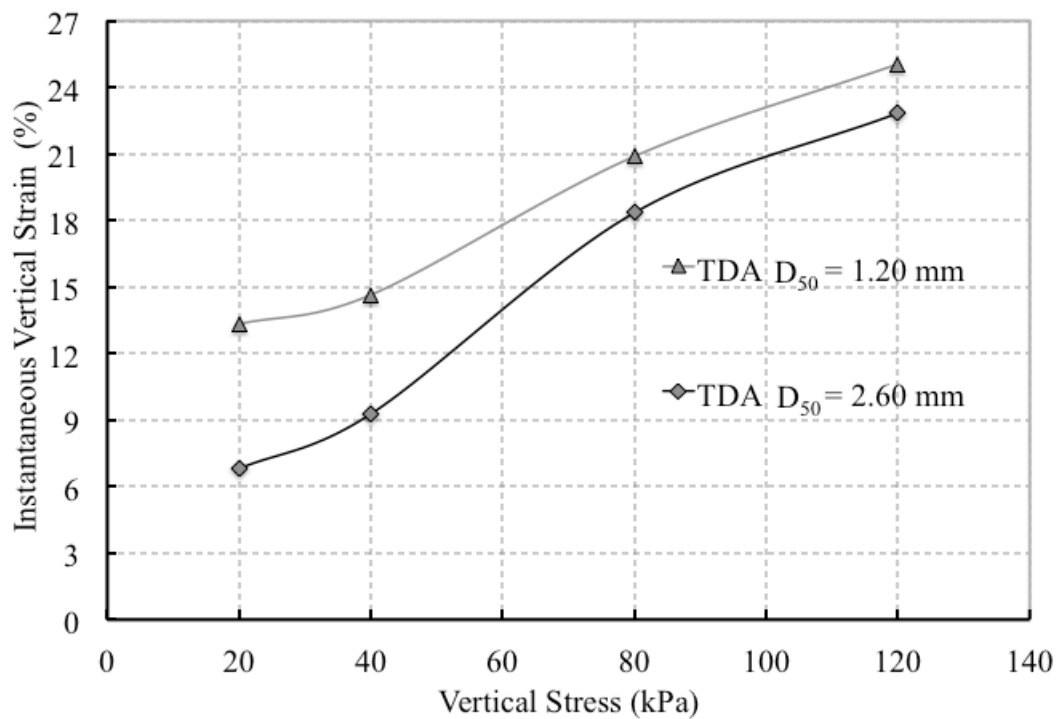


Figure 5.15: TDA vertical deformation for both TDA at the end of the normal stress application

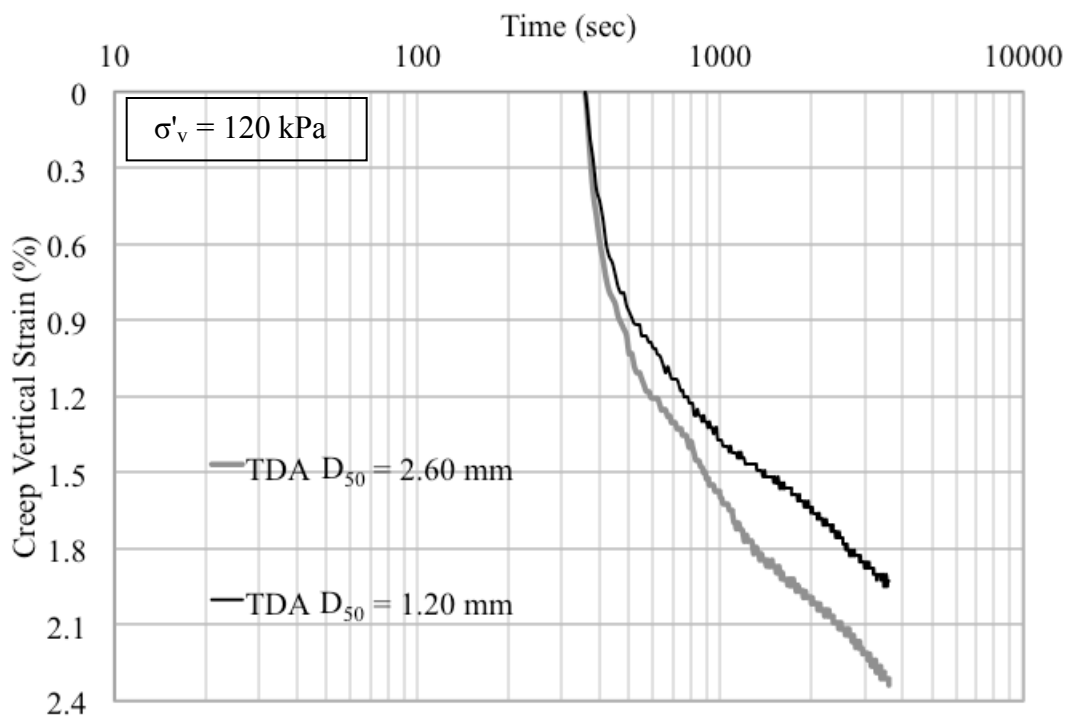


Figure 5.16: Creep vertical deformations for both TDA particle size

5.4 TDA Simple Shear Stress-Strain Characteristics

TDA simple shear behavior and strength was examined at the four different levels (Table 5.1). Figure 5.17 shows the resulting shear stress vs shear strain curves for the fine TDA ($D_{50} = 1.20$ mm). It is observed again that TDA exhibits a gradual increase of shear stress without reaching a clear failure peak shear stress even when sheared to strain values (γ) close to 50%. Figures 5.18 and 5.19 show similar curves for Nevada sand and TDA/mixture, respectively. A comparison of simple shear behavior of the three different test materials is presented Figures 5.20 through 5.22. As seen in these figures the TDA shear strength and stiffness are found to be considerably lower than those exhibited by the Nevada sand and TDA/sand mixture specimens.

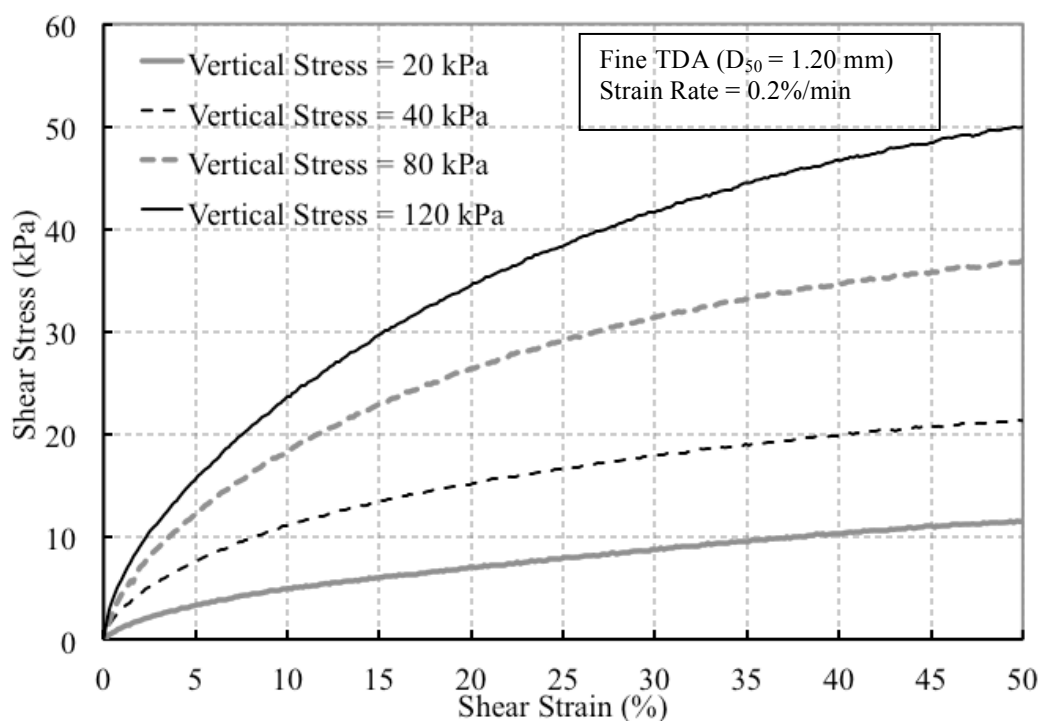


Figure 5.17: Simple shear stress-strain curves for fine TDA

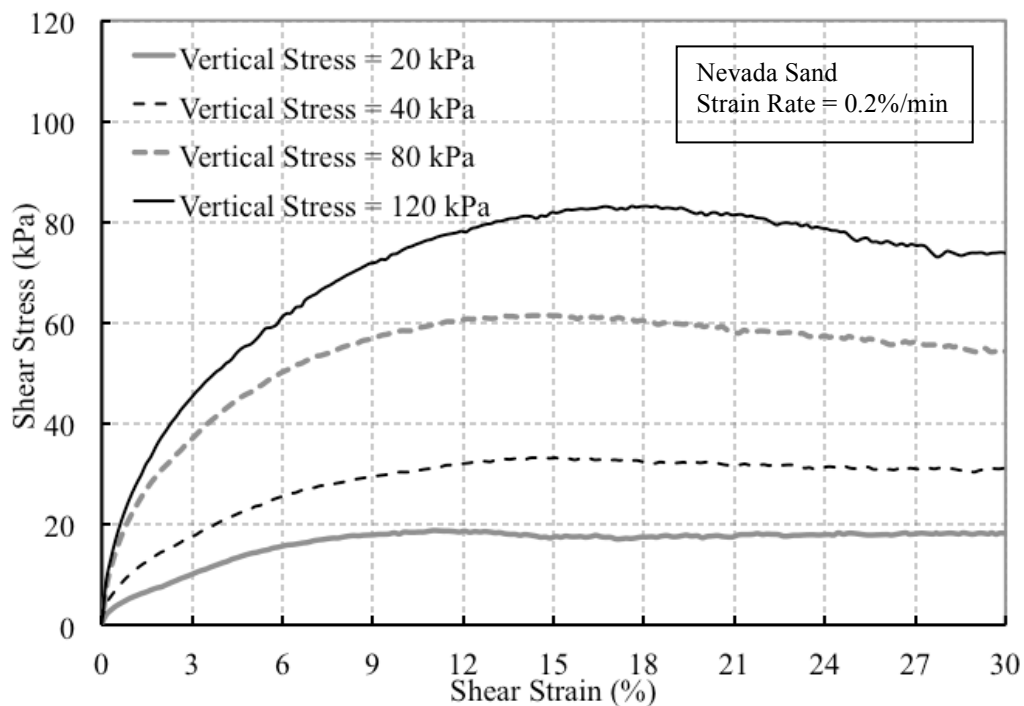


Figure 5.18: Simple shear stress-strain curves for Nevada sand

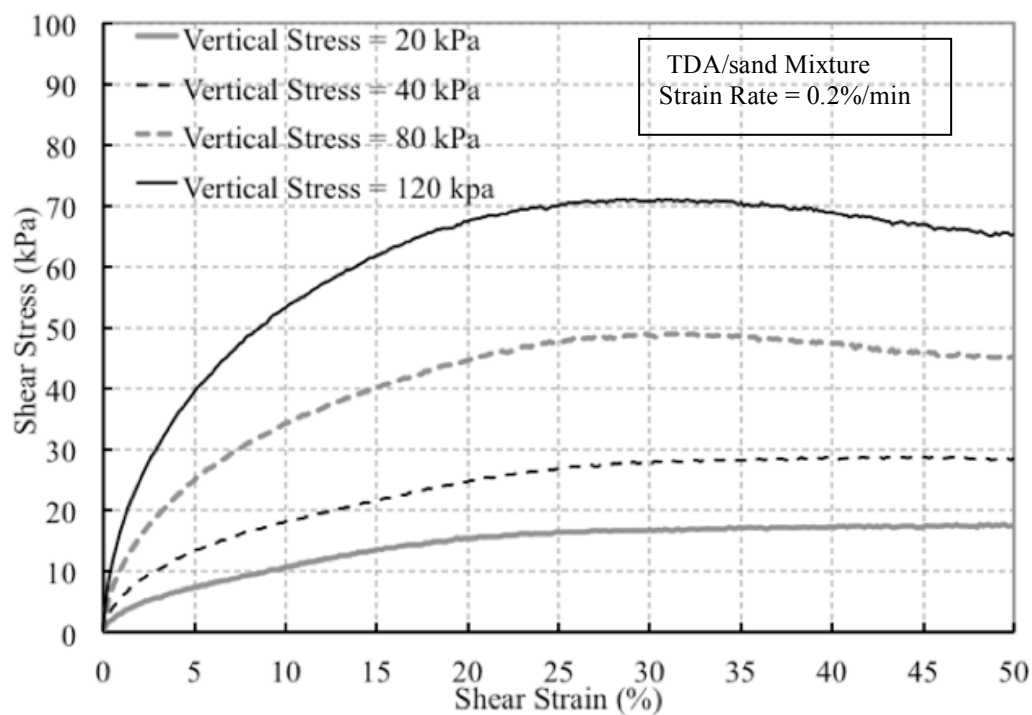


Figure 5.19: Simple shear stress-strain curves for TDA/sand mixture

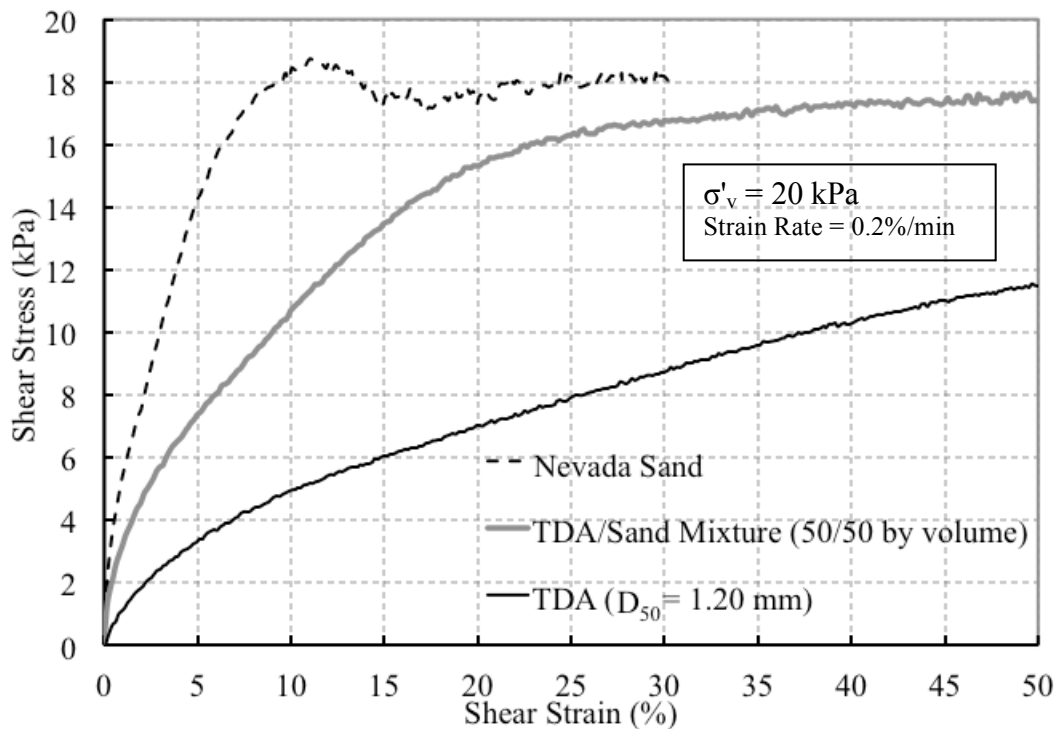


Figure 5.20: Stress-strain curves for TDA for the different specimens at 20 kPa

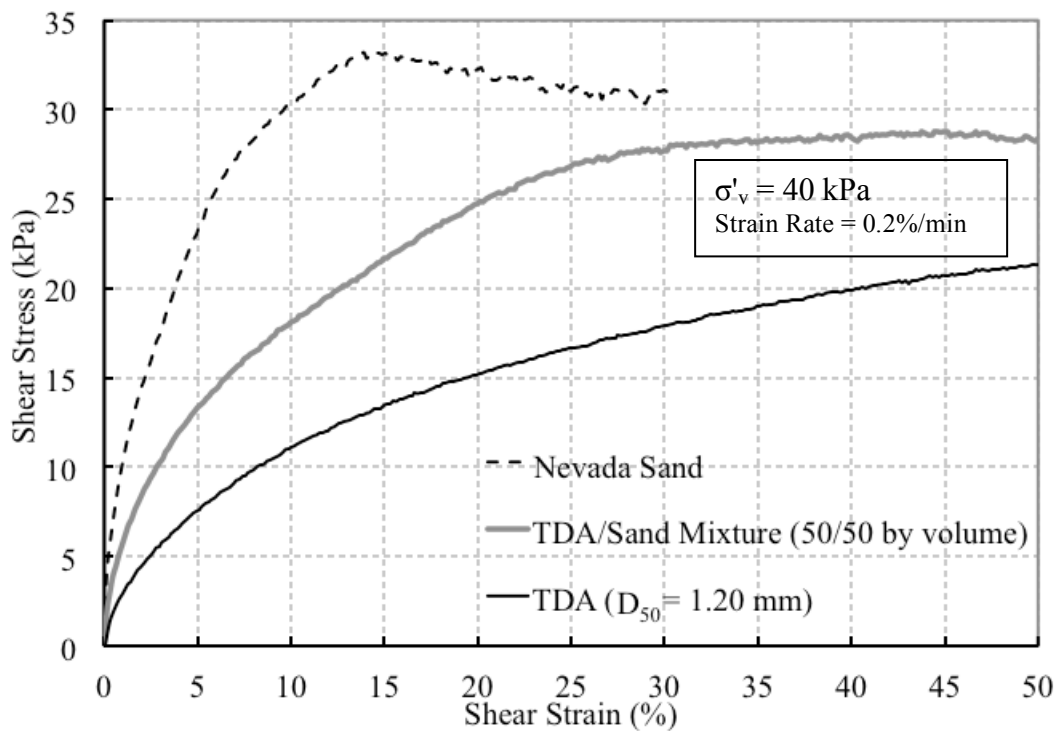


Figure 5.21: Stress-strain curves for TDA for the different specimens at 40 kPa

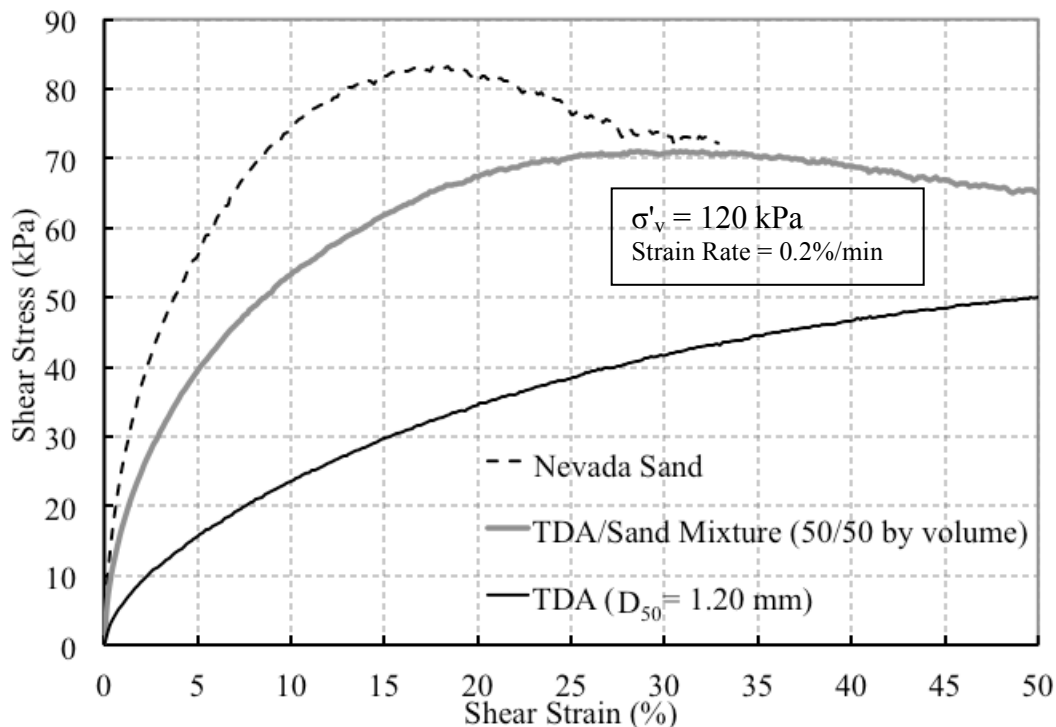


Figure 5.22: Stress-strain curves for the different specimens at 120 kPa

Nevada sand peak shear strengths were found approximately 39% higher than the maximum shear strength observed for TDA specimens for the range of vertical stresses analyzed. However, the level of deformation required for TDA to develop the maximum observed peak shear strength (50%) is much higher than the approximate failure peak shear stress observed for all four vertical stresses in the Nevada sand specimens ($\approx 15\%$). TDA shear strengths are found to be as much as 63% lower for the same Nevada sand failure shear strain. Nevada sand/ mixture specimens ($\approx 50/50$ by volume) exhibit an approximate 29% percent increment in shear strength when compared to the maximum observed TDA strength, and 37% when compared at the mixtures approximate peak strain ($\approx 35\%$).

For comparison purposes, the resistance to shear stress for all three types of specimens was determined by calculating a secant shear modulus (G) as suggested by ASTM D 6528. Figure 5.23 shows stress-strain curves at 80 kPa which was not shown before indicating the locations corresponding to the 50% peak shear stress. Figure 5.24 shows the calculated shear modulus values obtained at the four different vertical stresses. TDA shear stiffness was found to be between 81% and 89% percent lower than the Nevada sand specimen. Table 5.2 presents a summary of the principal mechanical properties obtained during this section.

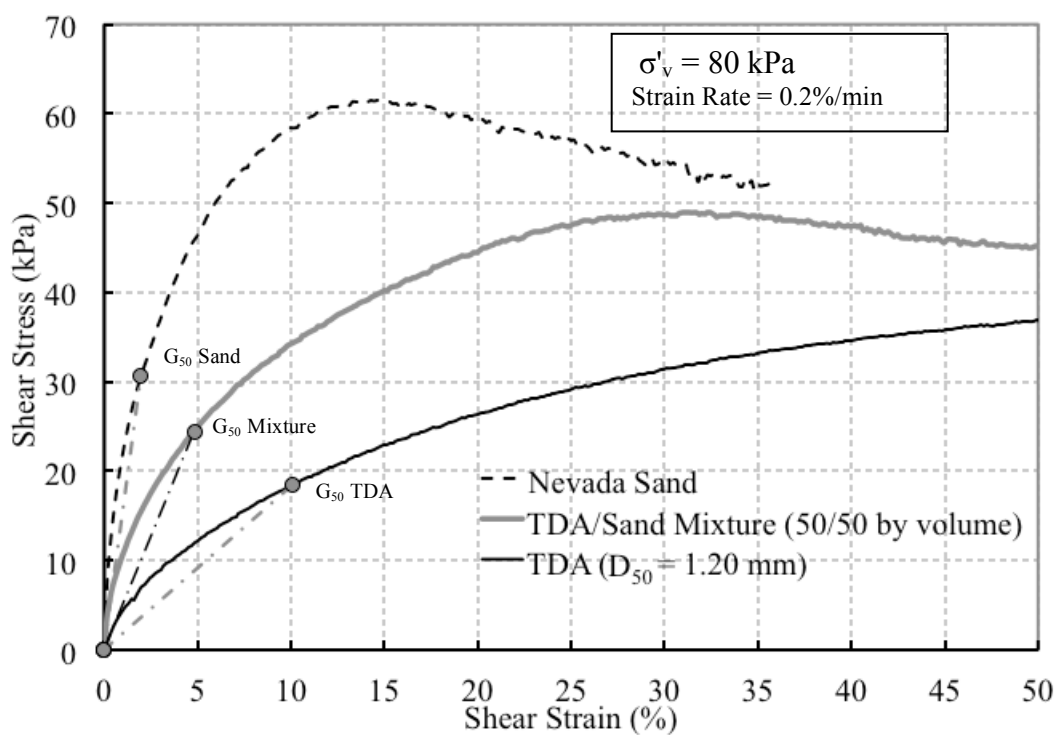


Figure 5.23: Determination of secant shear modulus for all specimens

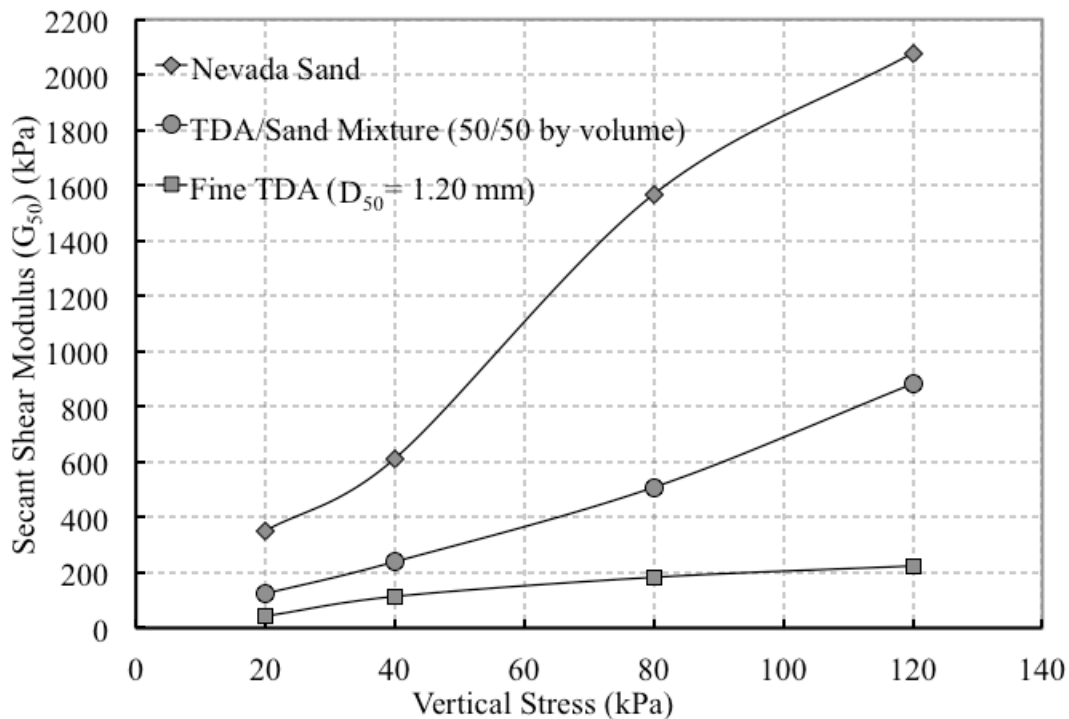


Figure 5.24: Variation of secant shear modulus with the vertical stress

Table 5.2: Summary of simple shear strength and G_{50} modulus

σ'_v (kPa)	TDA ($D_{50} = 1.20$ mm)			TDA/Nevada Sand (50/50 by volume)			Nevada Sand ($D_{50} = 0.15$ mm)	
	τ_{max} (kPa)	τ_{at} 15% (kPa)	G_{50} (kPa)	τ_{peak} (kPa)	τ_{at} 15% (kPa)	G_{50} (kPa)	τ_{peak} (15%) (kPa)	G_{50} (kPa)
20	11.49	6.04	41.86	17.39	13.46	123.61	18.69	351.36
40	21.33	13.48	113.98	28.80	21.70	239.58	33.20	612.59
80	36.89	22.90	183.30	48.93	40.20	508.58	61.47	1568.19
120	50.01	29.69	224.39	70.97	61.86	882.76	83.13	2078.36

5.4.1 TDA Particle Size and Shearing Strain Rate Effects on Simple Shear Behavior

The effect of TDA particle size in the shear strength was examined in the same manner as in the triaxial experimental program discussed in chapter 4. Figure 5.25 shows the stress-strain curves obtained for the coarser TDA ($D_{50} = 2.60$ mm). When the results are compared to the fine TDA ($D_{50} = 1.20$ mm) previously shown in Figure 5.17, it is found that an increase in particle size leads to an increase in shear strength as observed in Figures 5.26 and 5.27 for 20 kPa and 80 kPa, respectively. Coarser TDA exhibits an approximate 6% increase in shear peak strength when compared to the finer TDA. Improvement in the mechanical properties due to the increase in particle size is also achieved in terms of stiffness as shown in Figure 5.28, where an increased in secant shear modulus of approximately 10% is obtained for the coarser TDA specimens. Same tendencies were observed in the triaxial experimental program discussed in Chapter 4.

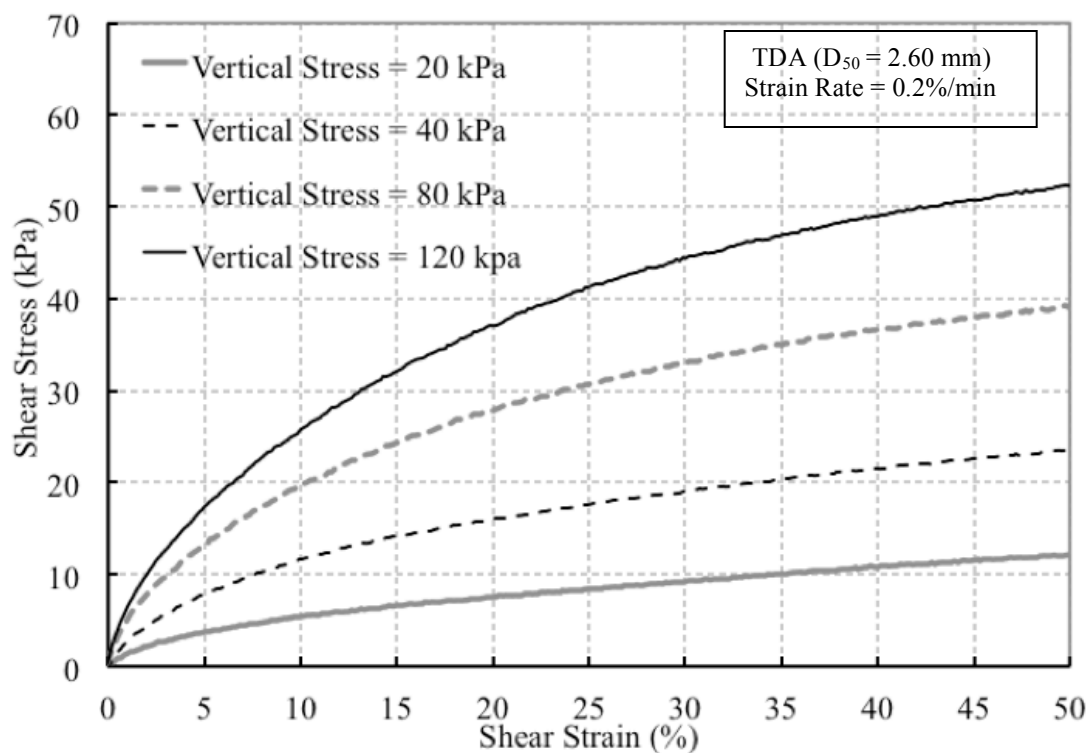


Figure 5.25: Stress-strain curves for coarser TDA ($D_{50} = 2.60$ mm) under simple shear

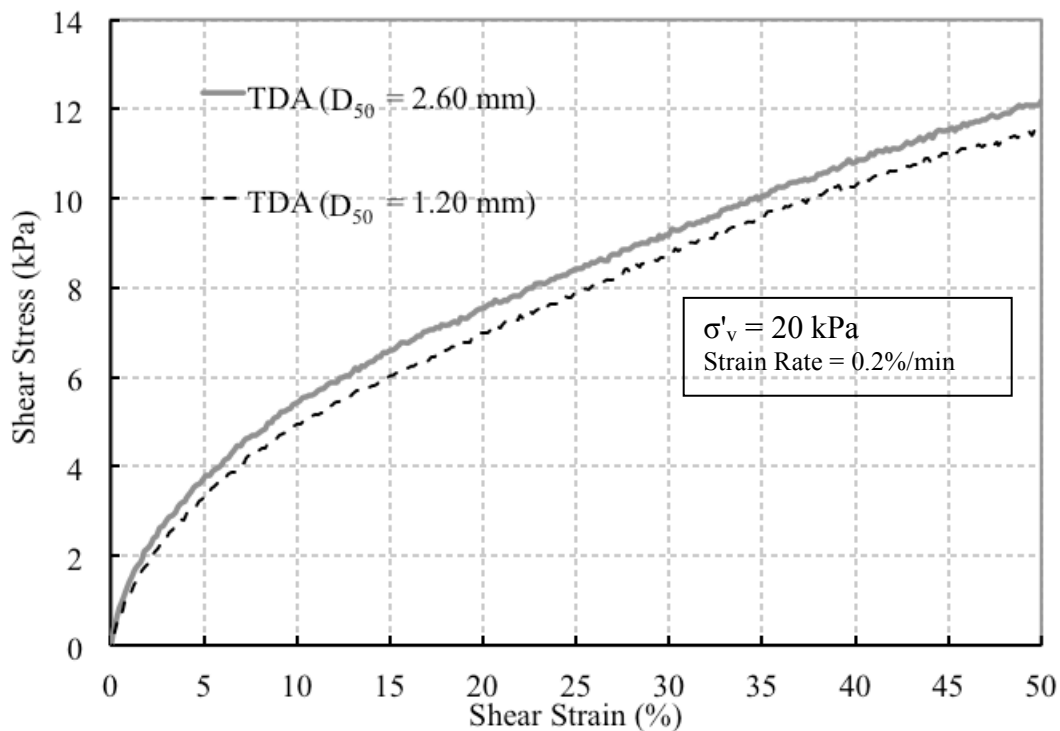


Figure 5.26: Stress-strain curves for different TDA particle size at $\sigma'_v = 20$ kPa

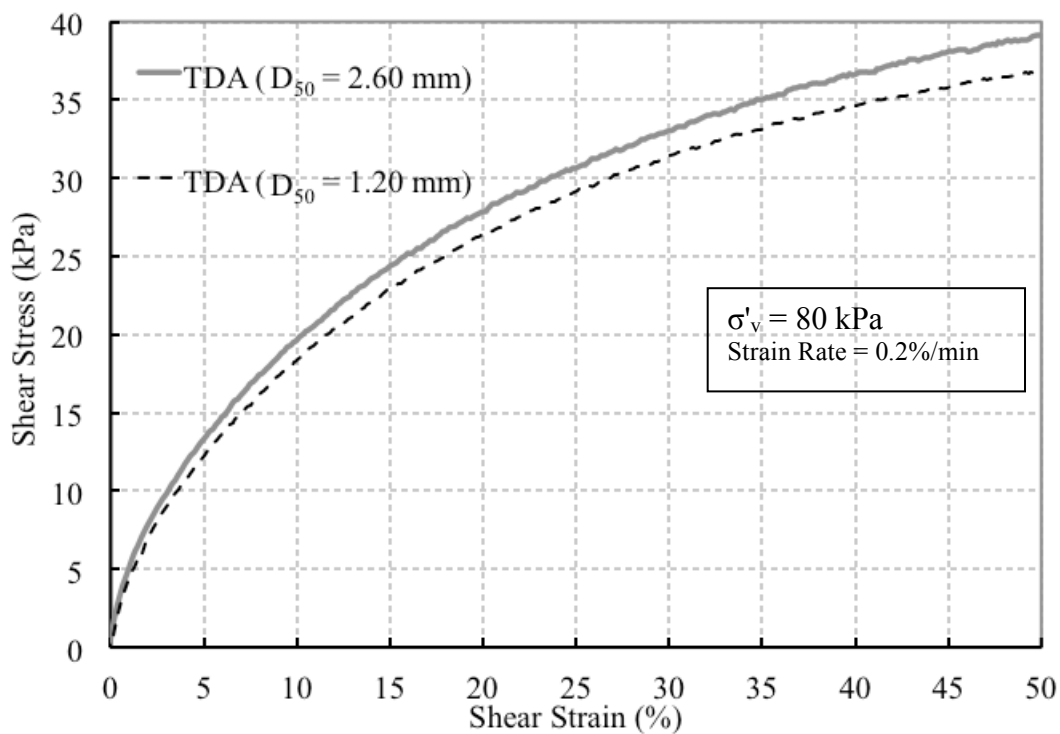


Figure 5.27: Stress-strain curves for different TDA particle size at $\sigma'_v = 80$ kPa

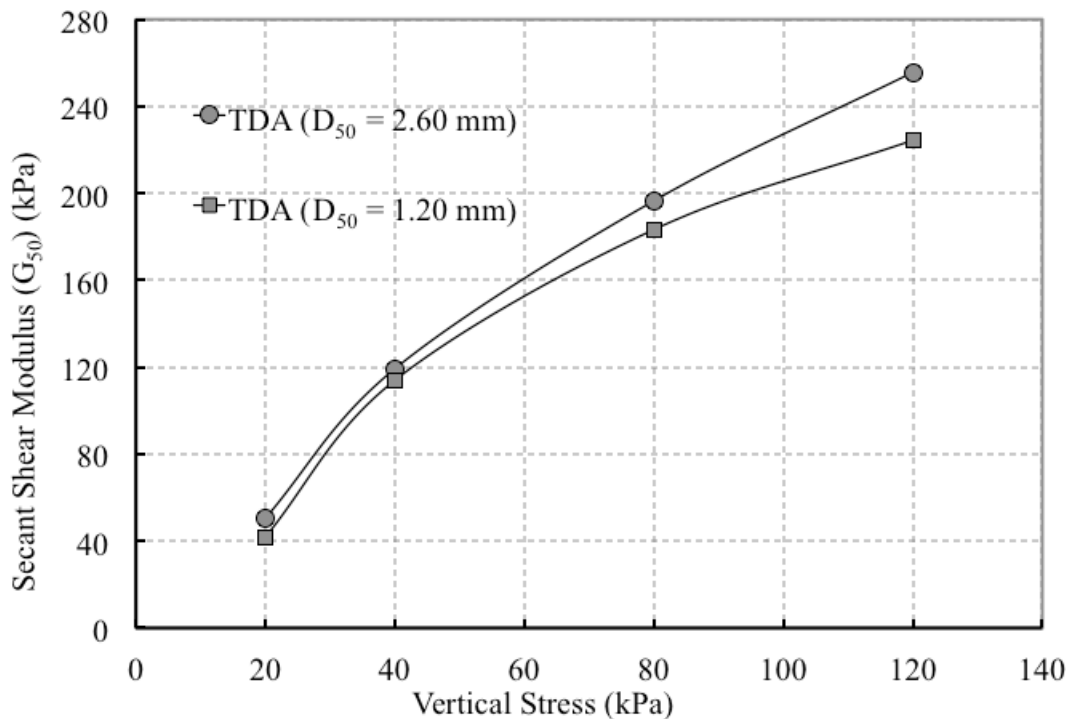


Figure 5.28: Secant shear modulus (G_{50}) for both TDA particle sizes

In terms of strain rate effects, Figure 5.29 shows the results of the simple shear test performed at a higher strain rate (2.0%/min). It is observed that peak shear stress increases with the applied vertical stress as expected. Comparing the results to those obtained in Figure 5.17 (0.2%/min), it is observed that peak shear stress increases as the shear rate increases as shown in Figures 5.30 and 5.31. An approximate increase between 4% and 8% in peak shear strength is obtained when the same normal stresses are compared for the two different strain rates.

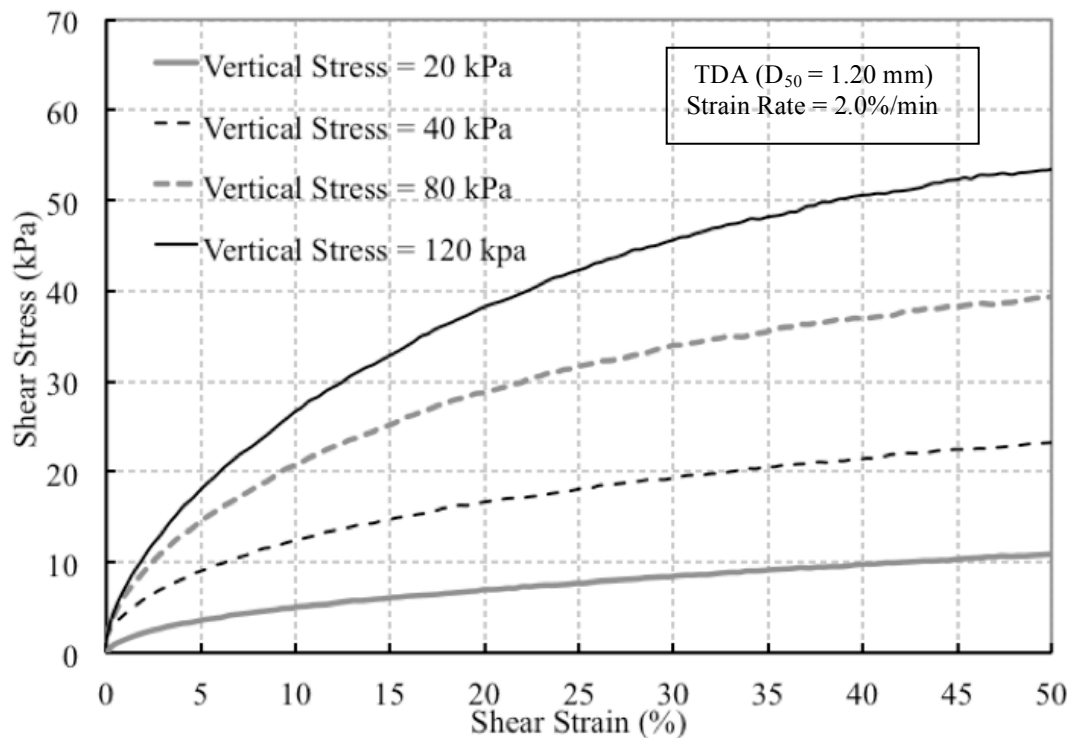


Figure 5.29: Simple shear stress-strain curves for fine TDA at $\dot{\gamma} = 2.0\%/min$

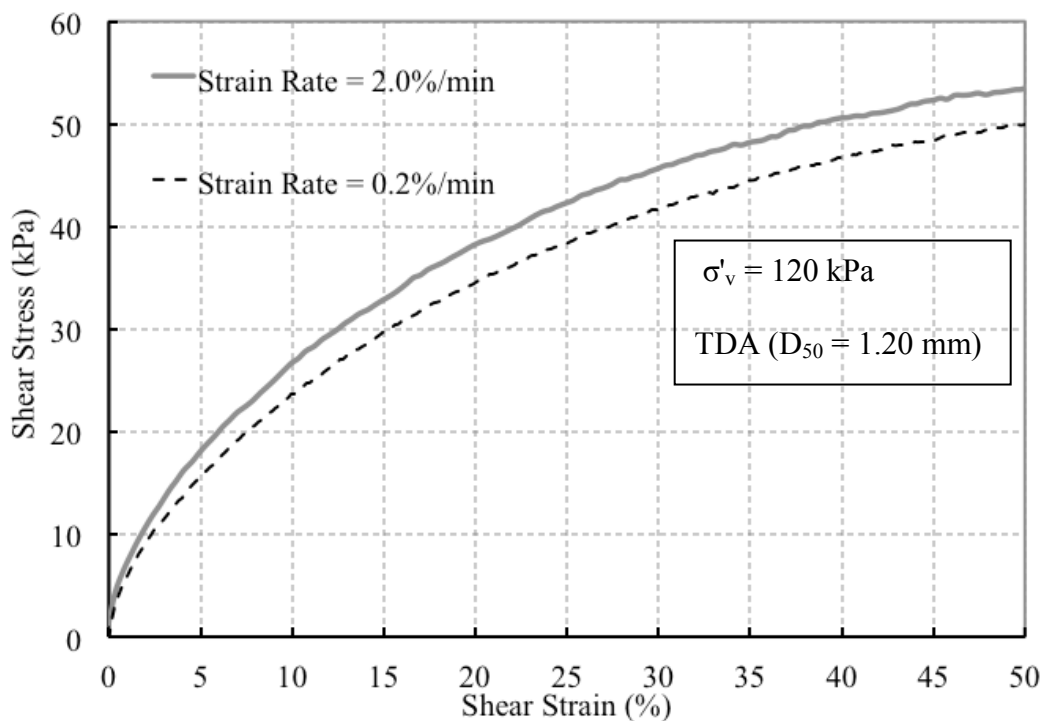


Figure 5.30: Simple shear stress-strain curves at different strain rates at $\sigma'_v = 120$ kPa

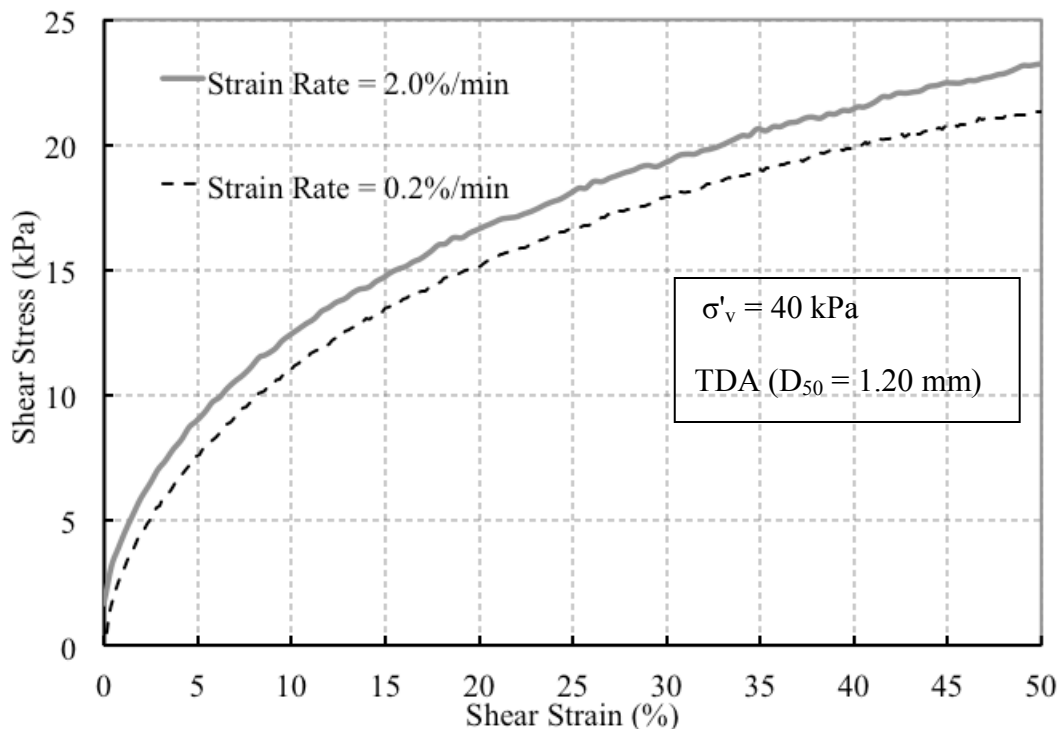


Figure 5.31: Simple shear stress-strain curves at different strain rates at $\sigma'_v = 40$ kPa

From the results, it is also observed that a rapid shearing rate (2.0%/min), TDA specimens tend to exhibit higher stiffness when compared to the slow shearing rate (0.2%/min) as shown in Figure 5.30. Secant shear moduli are found to be 16% higher for the rapid shear strain rate specimens. The results highlight the importance of strain rate effects for any material used in earth structures stability subjected to earthquakes or other forms of transient loads. In order not to make this document lengthy, additional stress-strain curves comparisons at different normal stresses are included in Appendix C. Acknowledging the fact that simple shear and triaxial test techniques are different in terms of the types of stresses and strains that are measured; their stress paths differ. The mechanical behavior tendencies in terms of strain-rate effects, particle sizes and

strength when compared to conventional granular materials are similar for both techniques.

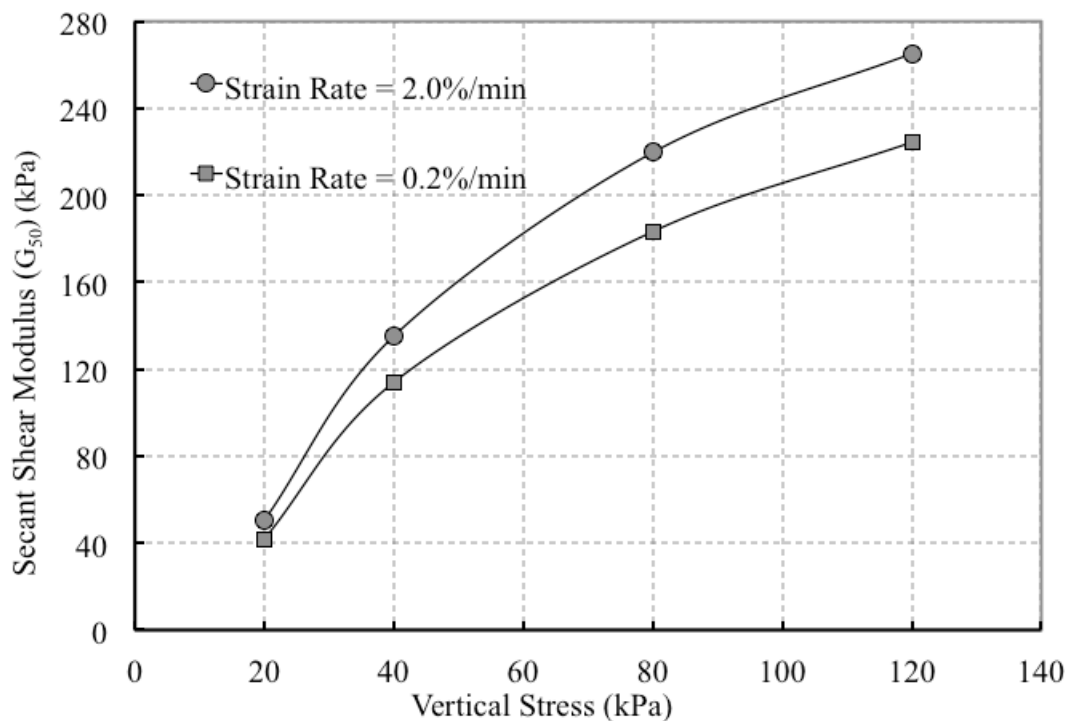


Figure 5.32: TDA secant shear modulus (G_{50}) at different strain rate

5.4.2 Estimation of the Friction Angle from the Simple Shear Test Results

Determination of shear strength parameters from simple shear tests results is a more complicated problem than determining shear strength parameters from triaxial and direct shear tests. Several authors have acknowledged the limitations when interpreting simple shear data (Atkinson et al. 1991; Budhu 1984; Kim 2009; McGuire 2011; Sivadas and Lee 2008; Wijewickreme et al. 2013).

During a simple shear the axes of stress rotate; and only the normal and shear stresses on the horizontal plane are measured making difficult to define the stress state within the specimen accurately. It has also been reported that specimen may be subjected

to a non-uniform distribution of stresses and strains which results in difficulties in interpreting the results obtained from simple shear tests (Budhu 1984). The approach illustrated in Figure 5.33 was followed in order to estimate the friction angles for the materials tested. The inner Mohr circle in Figure 5.33 represents the at rest condition state for which the horizontal stress is not accurately known during the test. The famous Jaky's expression $(1 - \sin(\phi'))$ was used to estimate K_0 values taking the friction angles obtained from the triaxial test indicated in chapter 4 at peak or 27% axial strain for the TDA.

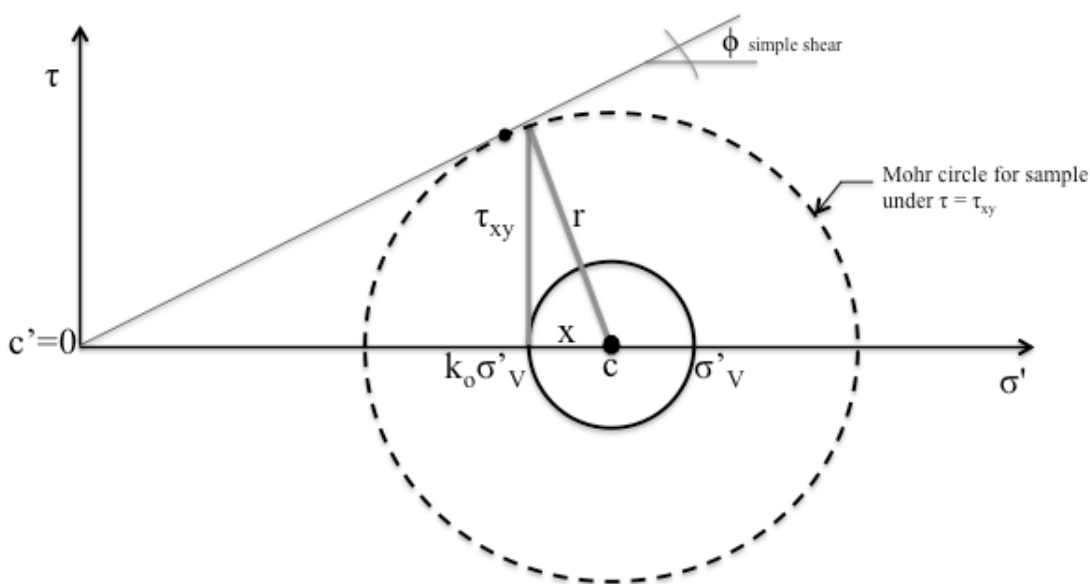


Figure 5.33: Stress state approach to estimate friction angles from simple shear test

The dashed Mohr circle represents the failure Mohr circle at a corresponding vertical stress (σ'_v). The shear stress measured in the horizontal plane in the test is represented by τ_{xy} . The stress corresponding to r measured from the center of the circles c which theoretically would be tangent to the Mohr-Coulomb failure envelope needs to be

calculated. The gray triangle represents the geometry of the variable involved where the distance x can be determined from the horizontal and vertical stresses as follows:

$$x = \frac{\sigma'_v - k_o \sigma'_v}{2} \quad (5.2)$$

By trigonometry the radius r from the Mohr circle for the sample under shear stress τ_{xy} can be computed as:

$$r = \sqrt{\left(\frac{\sigma'_v - k_o \sigma'_v}{2}\right)^2 + (\tau_{xy})^2} \quad (5.3)$$

Figure 5.32 shows the resulting friction angles obtained for TDA ($D_{50} = 1.20$ mm), TDA/sand mixture and Nevada sand. The TDA peak friction angle is 38% lower than that of Nevada sand. However, a clear failure peak was not observed for the TDA samples even for shear strains levels of up to 50%. Improvement in shear strength are observed when both materials are mixed in an approximate 50/50 proportion by volume since peak friction angle for this the mixture ratio were found to be only 11% lower than the corresponding values obtained for the Nevada sand.

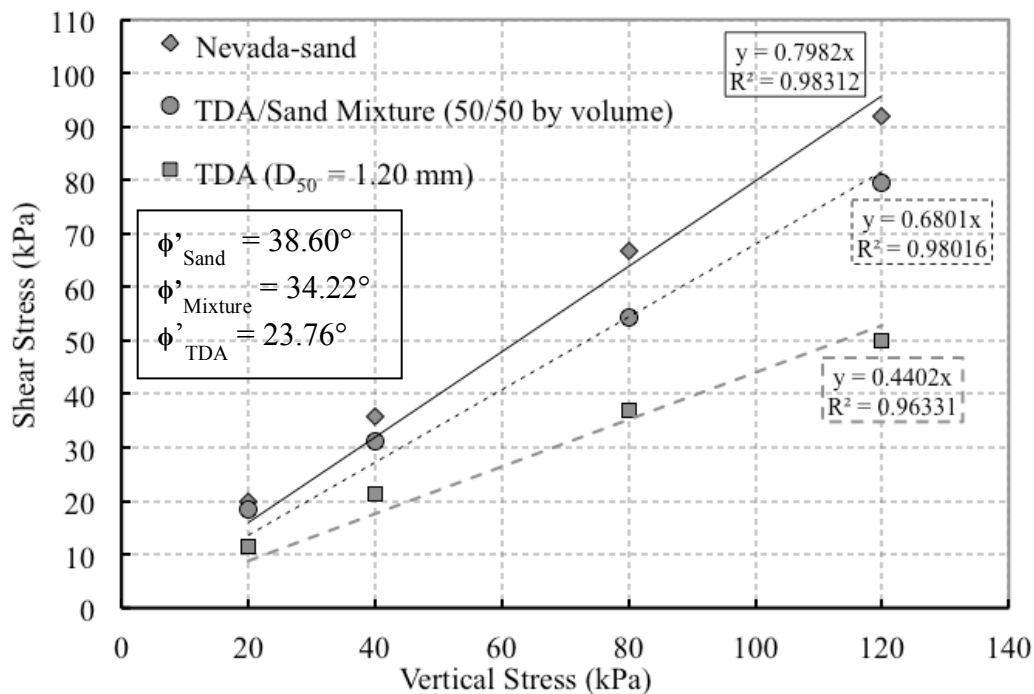


Figure 5.34: Estimation of friction angles from simple shear tests results

5.4.3 Comparison Simple Shear vs Triaxial Friction Angles

Peak friction angles obtained from both tests are shown in Figure 5.35. Simple shear friction angles are found to be lower than those obtained using triaxial testing technique. Simple shear Nevada sand and TDA/sand mixture friction angle are 2.22 and 2.39 degrees lower respectively than the triaxial test values. A reduction of 1.35 and 1.69 degrees was obtained for both different TDA particle sizes analyzed. Other authors have reported lower friction angles in simple shear tests when compared to triaxial values (Atkinson et al. 1991; Budhu 1984; Rossato and Simonini 1991).

Besides the simple shear tests limitations previously explained, it should be clear that the parameters are expected to differ since both tests are designed to induce different stress conditions within the specimens. However, there are other aspects that may cause differences in both tests specially when using TDA. In order to compare parameters

among different techniques, it would be necessary to ensure that both techniques experience the same failure mode. Although, a clear peak was observed in the Nevada sand, and the mixture for both tests, it is hard to define what failure means in the TDA since a clear peak was not observed in the simple shear test and how can axial strains and shear strains be correlated to define a same failure criteria. However, it is important to clarify that although parameters obtained may not be comparable among them, each particular test could be more appropriate for a certain application. For example, strengths estimated from back analysis of embankments and slope failures have been reported to be in good agreement with the strength measured in simple shear tests (Sivadass and Lee 2008).

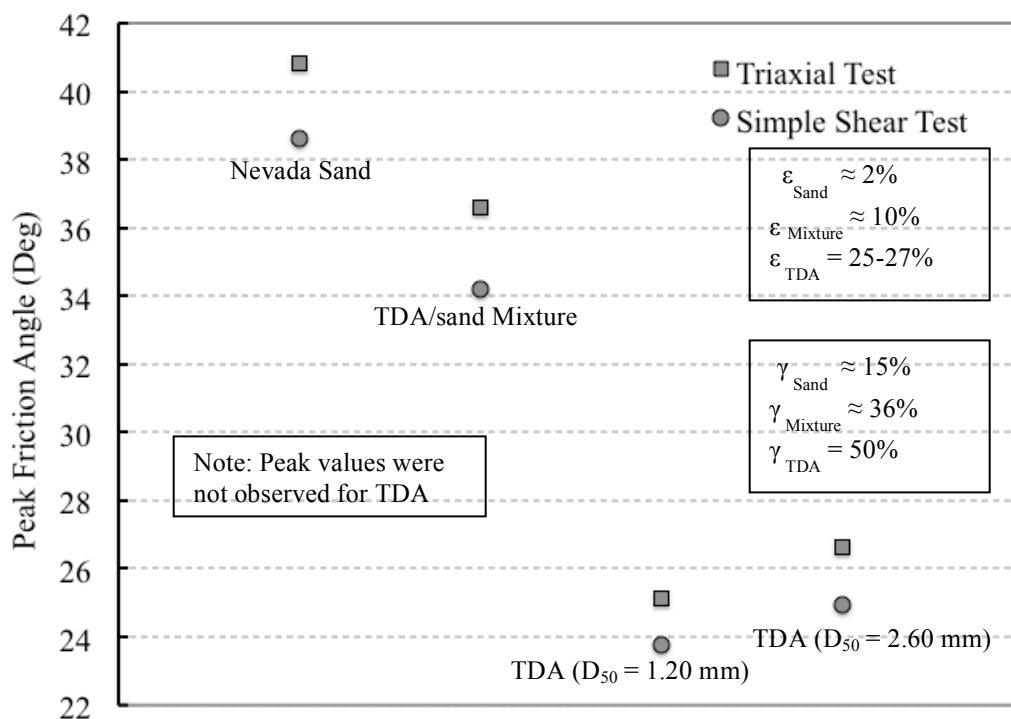


Figure 5.35: Comparison between simple shear and triaxial friction angle results

CHAPTER 6. FINITE ELEMENT MODELLING OF TDA TRIAXIAL COMPRESSION STRESS-STRAIN BEHAVIOR

6.1 Introduction

This chapter presents finite element modeling (FEM) analyses carried out for the consolidated drained triaxial test results discussed in Chapter 4. Three different constitutive models were chosen to explore their suitability and limitations to capture TDA stress-strain behavior.

The selection of the models was based on the interest to explore different scenarios. First, the use of a conventional hyperelastic model for rubber-like materials (typically not used for geotechnical applications). Second, the use of a conventional soil constitutive model and finally an elastic model applicable for granular polymer materials that incorporates a conventional geotechnical yield criterion.

The constitutive models selected and the software used for each of them are as follows:

- Hyperelastic Yeoh Model in ABAQUS
- Soil Hardening Model in PLAXIS
- Porous Elasticity Model in ABAQUS

6.2 Hyperelastic Constitutive Models

Several models have been developed in the past to help predict the large strain elasticity observed in isotropic elastomers such as rubber. Most have in common the use of a strain energy function or stored energy function. They rely on the base assumption

that rubber is a so-called Cauchy-elastic material, which means that the equilibrium state between the strain and stress tensors does not depend on the loading path (Ali and Sahari 2010). In other words the stress tensors is defined by the current state of deformation and not the path or history of deformation. A hyperelastic material is as an elastic material where the stress-strain relationship is derived from a strain energy density function (W) and not a constant factor, as shown schematically in Figure 6.1. In this figure, the left and right plots represent the stress-strain curves for hyperelastic and elastic materials, respectively. In both plots the area under the curve (W) represents the work or accumulated strain energy. The role of strain energy functions in hyperelastic materials is further described below.

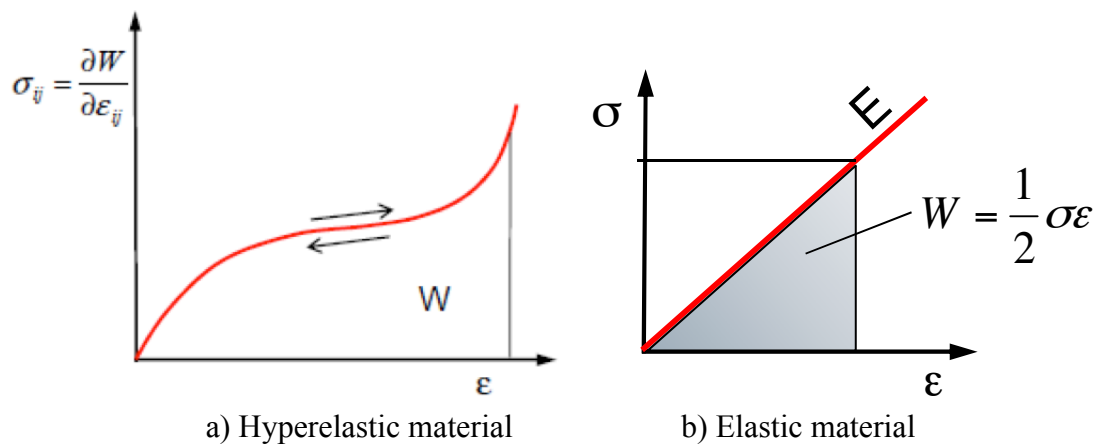


Figure 6.1: Stress-strain relationship as a function of energy function in hyperelastic material and elastic material (Jakel 2010)

To illustrate how energy functions govern the behavior of hyperelastic materials, let us start with the well known definition of the nominal or engineering strain (ϵ) of a simple rod of initial length (l_0) subjected to a tensile force that elongates the rod to a new length (l_1). For this situation strain is defined as follows: defined as the change in length divided by the original length:

$$\epsilon = \frac{l_1 - l_0}{l_0} = \frac{\Delta l}{l_0} \quad (6.1)$$

The stretch ratio (λ), another fundamental quantity often used to describe material deformation, is defined as the current length divided by the original length:

$$\lambda = \frac{l_1}{l_0} = \frac{l_1 - l_0 + l_0}{l_0} = \epsilon + 1 \quad (6.2)$$

For the simple case of a rod under uniaxial stress, there is an increase of energy associated with the elongation of the member. This energy is referred to strain energy which is equal to the work done by the tensile load (or stress) applied to the rod. The strain energy for this simple rod example can be computed as the area under a force versus deformation diagram. If we now define strain energy density (SED or W) of a material as the strain energy per unit volume, it can be shown that it is equal to the area under the stress-strain diagram as shown in Figure 6.1.

The description of the strain energy density (W) is much more complex for a 3-D stress state of a hyperelastic material. The strain energy density function in a hyperelastic material under a 3-D stress state is a function of the stretch invariants $W = f(I_1, I_2, I_3)$ or principal stretch ratios $W = f(\lambda_1, \lambda_2, \lambda_3)$.

Consider a deformation tensor: $\mathbf{F} = \left(\frac{\partial x}{\partial X} \right)$, where x and X are the material coordinates in the initial and deformed states. In the principal axis coordinates, the tensor \mathbf{F} is defined as:

$$\mathbf{F} = \begin{pmatrix} \lambda_1 & 0 & 0 \\ 0 & \lambda_2 & 0 \\ 0 & 0 & \lambda_3 \end{pmatrix} \quad (6.3)$$

Where $\lambda_1, \lambda_2, \lambda_3$ represent the material principal stretch ratios. Consequently, the determinant of \mathbf{F} is equal to volume variation: $\frac{dV}{V} = \det \mathbf{F} = \lambda_1 \lambda_2 \lambda_3$ and is denoted J . The modeling of hyperelastic materials relies on the definition of a strain density energy function W such that stress can be expressed as the derivative of W relative to strain tensor (\mathbf{E}):

$$\mathbf{S} = \frac{\partial W}{\partial \mathbf{E}} \quad (6.4)$$

Where the strain tensor \mathbf{E} is defined as follows:

$$\mathbf{E} = \frac{1}{2}(\mathbf{F}\mathbf{F}^T - \mathbf{I}) = \frac{1}{2}(\mathbf{B} - \mathbf{I}) \quad (6.5)$$

Tensor \mathbf{B} is also called the left Cauchy-Green deformation tensor which is defined in the same principal axis as:

$$\mathbf{B} = \begin{pmatrix} \lambda_1^2 & 0 & 0 \\ 0 & \lambda_2^2 & 0 \\ 0 & 0 & \lambda_3^2 \end{pmatrix} \quad (6.6)$$

The three stretch invariants are related to the principal stretch ratios in accordance to the following equations:

$$I_1 = \lambda_1^2 + \lambda_2^2 + \lambda_3^2 \quad (6.7)$$

$$I_2 = \lambda_1^2 \lambda_2^2 + \lambda_2^2 \lambda_3^2 + \lambda_3^2 \lambda_1^2 \quad (6.8)$$

$$I_3 = \det(\mathbf{B}) = \lambda_1^2 \lambda_2^2 \lambda_3^2 = J^2 \quad (6.9)$$

Deviatoric stretch ratios are the result of a division of stretch ratios by the cubic root of the strain tensor Jacobian determinant ($\lambda_1 \lambda_2 \lambda_3$), which expresses volume

variation. The expressions above are applicable to their deviatoric counterparts, just adding a bar above each variable. Models for rubber-like materials typically rely on the definition of new principal stretches and invariants, as follows:

$$\bar{\lambda}_i = \frac{\lambda_i}{J^{1/3}} \quad (6.10)$$

$$\bar{I}_1 = \frac{I_1}{J^{2/3}} \quad (6.11)$$

$$\bar{I}_2 = \frac{I_2}{J^{4/3}} \quad (6.12)$$

$$\bar{I}_3 = \frac{I_3}{J^{6/3}} = 1 \quad (6.13)$$

6.2.1 Selection of a Suitable Strain Energy Density Function for TDA Modeling

A variety of strain energy functions have been introduced to express stored energy as polynomials of \bar{I}_1 and \bar{I}_2 , or $\bar{\lambda}_1$, $\bar{\lambda}_2$, and $\bar{\lambda}_3$, and J (e.g., Polynomial model, Neo-Hookean, Mooney-Rivlin, Yeoh, Arruda-Boyce, among others). They all require material coefficients to be determined by means of uniaxial, biaxial and shear test data (Ali 2010). The main challenge is to select a proper strain energy function able to provide a good fit with the available experimental data. Complex polynomial models require several coefficients that will require a more extensive experimental program. In contrast more simplified strain energy density functions will likely involve fewer coefficients, but the physics governing the material behavior may not be well captured.

A general expression for the strain energy density of W is the so-called polynomial model, defined as:

$$W = \sum_{i,j=1}^n C_{ij} (\bar{I}_1 - 3)^i (\bar{I}_2 - 3)^j + \sum_{k=1}^m \frac{1}{D_k} (J - 1)^{2k} \quad (6.14)$$

The left summation term of Eq. (6.14) involves the first and second invariants of the deviatoric strain, while the right summation term involves the material volume variation. C and D are material constants that need to be determined from tests. The Cauchy stress tensor is then calculated according to the following equation:

$$\boldsymbol{\sigma} = \frac{2}{J} \left[\frac{1}{J^{2/3}} \left(\frac{\partial W}{\partial \bar{I}_1} + \bar{I}_1 \frac{\partial W}{\partial \bar{I}_2} \right) \mathbf{B} - \frac{1}{J^{4/3}} \frac{\partial W}{\partial \bar{I}_2} \mathbf{B} \mathbf{B} \right] + \left[\frac{\partial W}{\partial J} - \frac{2}{3J} \left(\bar{I}_1 \frac{\partial W}{\partial \bar{I}_1} + 2\bar{I}_2 \frac{\partial W}{\partial \bar{I}_2} \right) \right] \mathbf{I} \quad (6.15)$$

A reduced polynomial version may be used if dependence on \bar{I}_2 is not needed to fit the experimental data. The expression for W reduces to its most simple form in the Neo-Hookean model:

$$W = C_1(\bar{I}_1 - 3) + \frac{1}{D_1}(J - 1)^2 \quad (6.16)$$

However, by reducing the number of parameters and the order of the polynomial too much, the Neo-Hookean model may not be applicable for a wide range of strain levels. Abaqus documentation indicates that the Neo-Hookean model is typically accurate for strain level of less than 20% (ABAQUS 2011). Since the TDA materials tested in this research exhibited high degree of volume variation during triaxial testing, a higher order on the term involving J in Equation 6.16 was selected hoping it would yield a better representation of the observed TDA behavior. Therefore, the Neo-Hookean model was not considered a feasible alternative for this research. A higher order expression such as the so-called Yeoh model (ABAQUS 2011) was chosen to model the TDA drained triaxial tests discussed in Chapter 4. The strain energy density function prescribed by the Yeoh model is as follows:

$$W = \sum_{i=1}^3 C_{i0} (\bar{I}_1 - 3)^i + \sum_{k=1}^3 \frac{1}{D_k} (J - 1)^{2k} \quad (6.17)$$

Its derivation relative to deformation tensor gives the following stress tensor:

$$\boldsymbol{\sigma} = \frac{2}{J^{5/3}} [C_{10} + 2C_{20}(\bar{I}_1 - 3) + 3C_{30}(\bar{I}_1 - 3)^2] \left(\mathbf{B} - \frac{I_1}{3} \mathbf{I} \right) + \frac{2}{D_1} (J - 1) + \frac{4}{D_2} (J - 1)^3 + \frac{6}{D_3} (J - 1)^5 \quad (6.18)$$

Equation 6.18 was fit to the available test data using Excel solver to optimize parameters C and D before implementing the model in ABAQUS.

6.2.2 TDA Triaxial Simulations Using the Hyperelastic Yeoh Model

The hyperelastic model predictions were carried out using the finite element commercial software ABAQUS. Since triaxial compression tests are axisymmetric all simulations were performed using a two dimensional axisymmetric model as shown the one shown in Figure 6.2. This approach to model triaxial tests have been broadly documented and accepted (ABAQUS 2011; Surarak et al. 2012) . The triaxial tests samples dimensions were reported in chapter 4. Most samples tested had a diameter of about 2.8 inches and height of 6 inches. As shown in Figure 6.2, it was only necessary to create a mesh for the shaded area with dimensions 1.4 inches in diameter and 3 inches in height. All FE analyses for this case used a mesh consisting of 50 quadrilateral elements. The hyperelastic constitutive model of Yeoh was selected. Input parameters required according to Equation 6.18 are introduced in ABAQUS for each of the confining pressures.

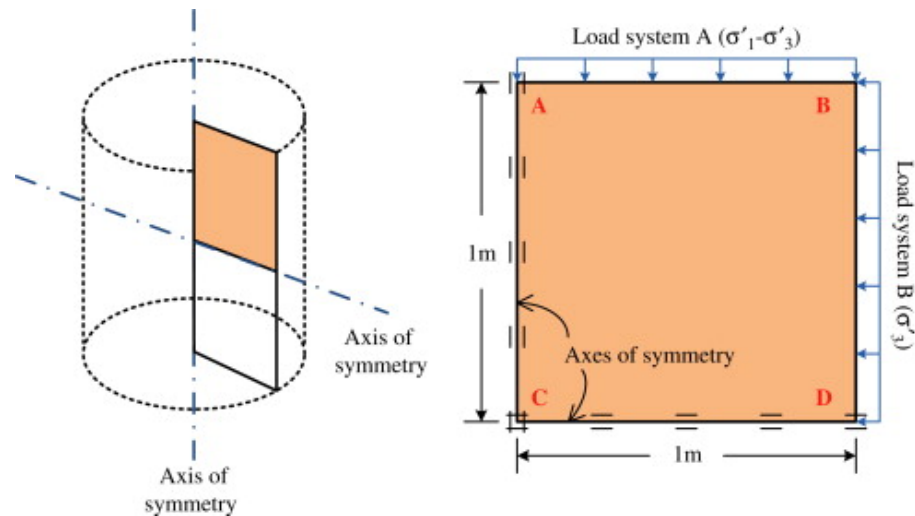


Figure 6.2: Axisymmetric representation of triaxial tests (Surarak et al. 2012)

The simulation of the triaxial compression was carried out in two steps. Step 1 represented the consolidation phase, where the corresponding confining pressure is specified applied. The second step represented the shearing phase. The boundary conditions of the model were selected as follows: on the bottom side, the vertical component of the displacement is fixed. The left hand side is a symmetry line with displacement in x equal to zero, and on the top surface a uniform downward displacement of 1 inch was applied slowly during the shearing phase. As an example, Figure 6.3 shows the third boundary condition created with the displacement applied in shearing phase, and the confining pressure applied during the consolidation phase (Step 1), corresponding to the 4 psi test (27.54 kPa).

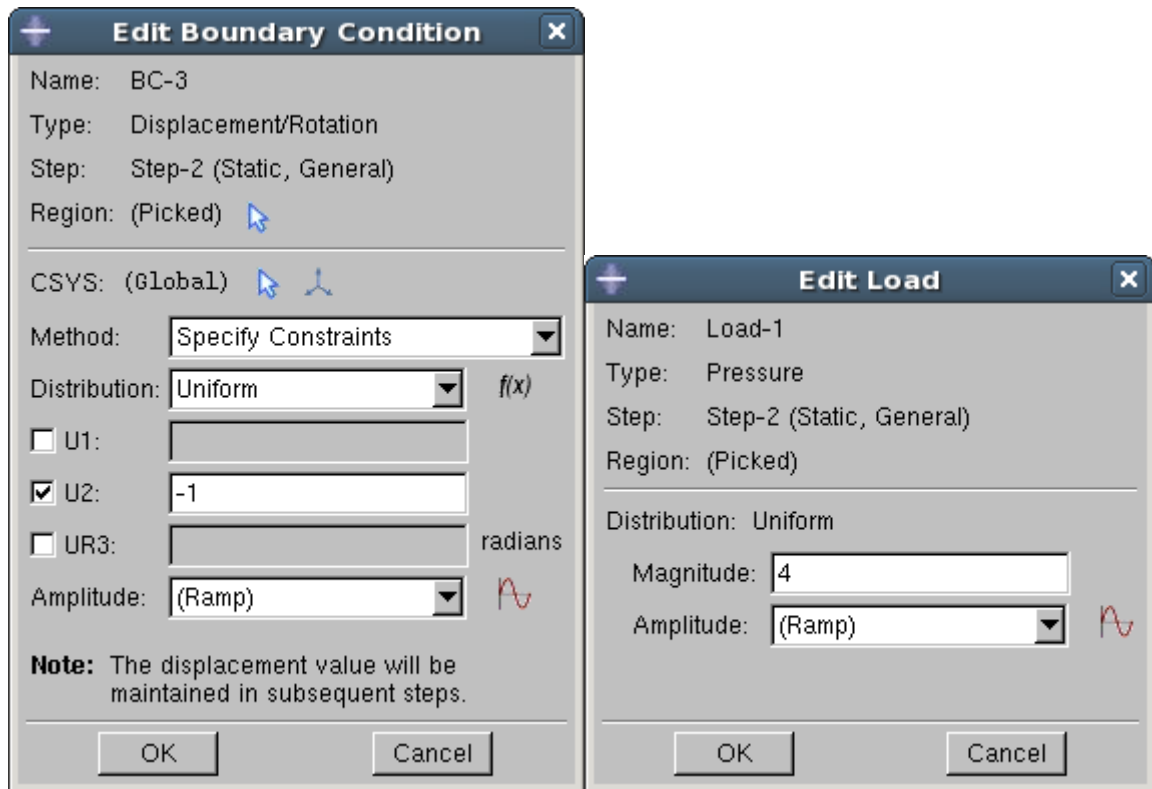


Figure 6.3: Screenshot from ABAQUS specifying displacement boundary condition BC-3 and confining pressure applied

Figure 6.4 shows the model with the boundary conditions created and the confining pressure applied. Figures 6.5 and 6.6 show the stresses and strains computed during the initial step of consolidation and shearing step, respectively. The high degree of deformability of the TDA materials can be observed in Figure 6.6 where the change of mesh height from the beginning of the test to the end of shearing phase is shown.

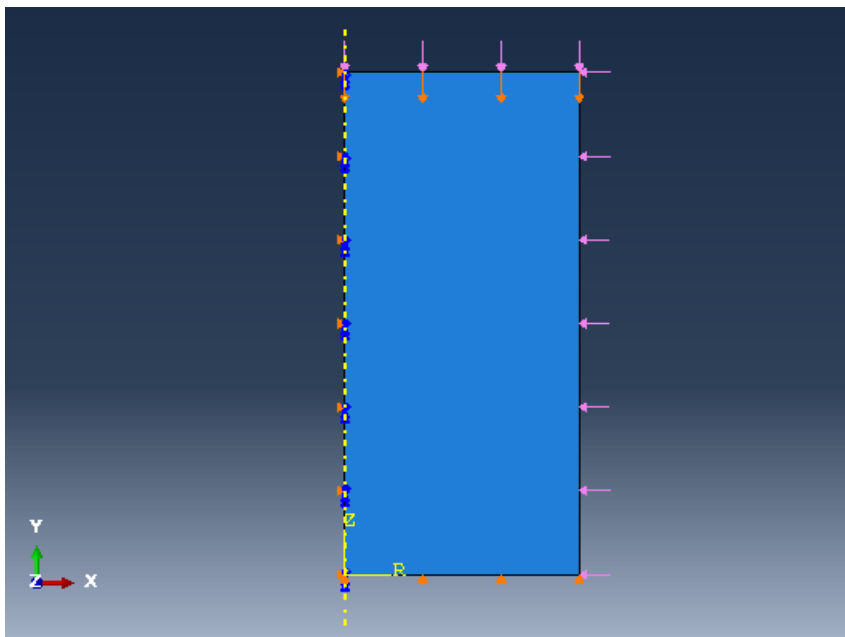


Figure 6.4: Screenshot of ABAQUS showing boundary conditions and applied confining pressure

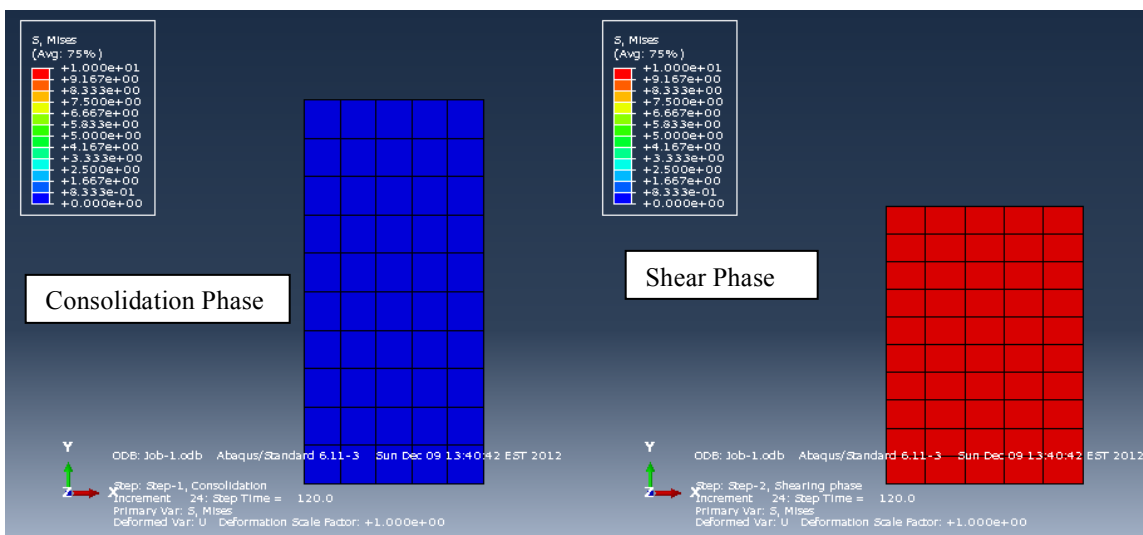


Figure 6.5: Screenshot of ABAQUS showing stresses for consolidation and shear phase

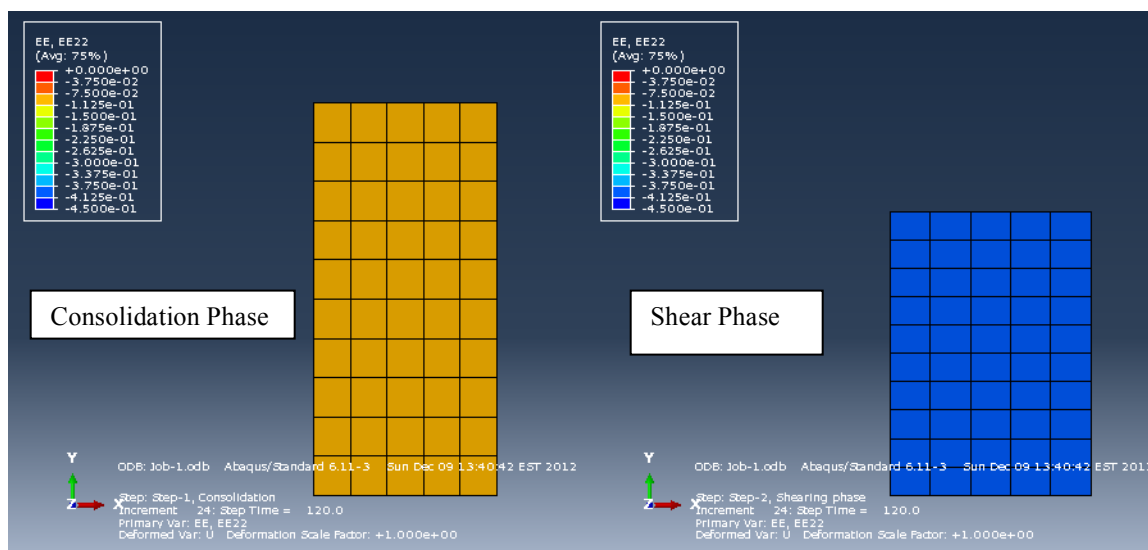
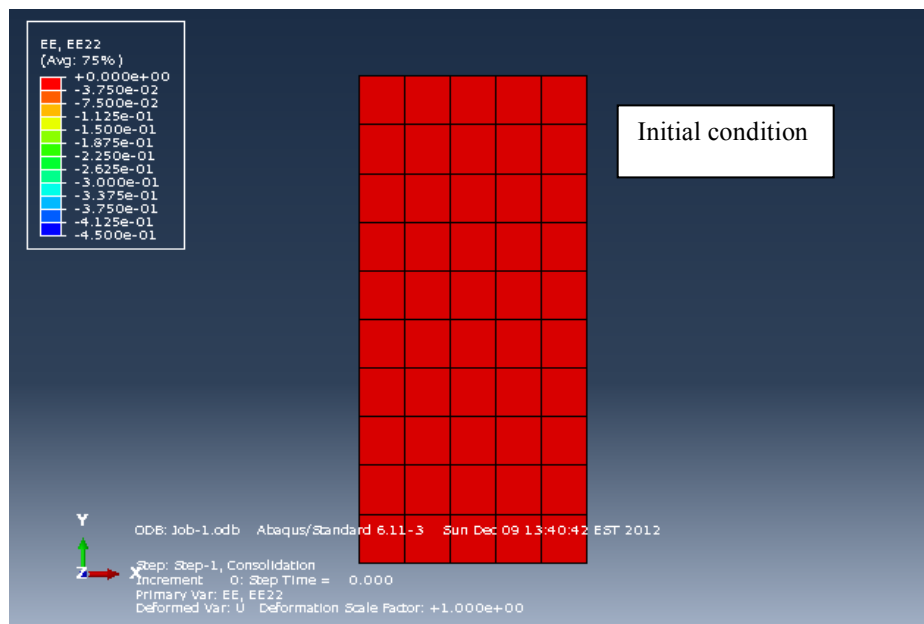


Figure 6.6: Screenshot of ABAQUS showing axial strains during initial stage, consolidation and shear phase

Figure 6.7 shows a comparison of the experimental and predicted stress-strain behavior of the fine TDA under drained triaxial compression. It is observed that the model appears to produce reasonable predictions compared to the experimental results. Table 6.1 presents the different model parameters used for the predictions for each

confining pressure level. Table 6.1 shows C parameters C_{10} , C_{20} and C_{30} had to be varied for the different confining stress levels. Parameters D were not varied for the different confining stress levels. This highlights a potential disadvantage of the Yeoh hyperelastic model, which requires manual updating of the C parameters as a function of confining stress level. For geotechnical engineering modeling this can be viewed as a model deficiency since most problems will involve variable stress levels and thus often use constitutive models that incorporate a stress dependency of stiffness and strength of the geomaterials involved. The Yeoh hyperelastic model captures adequately the influence of the volume change in the deviatoric stress as indicated by the D parameters and the right term on Equation 6.18. Although TDA may be considered a rubber like material, its behavior as an aggregate may differ from that of a solid rubber piece which may prevent Yeoh model from capturing the behavior properly.

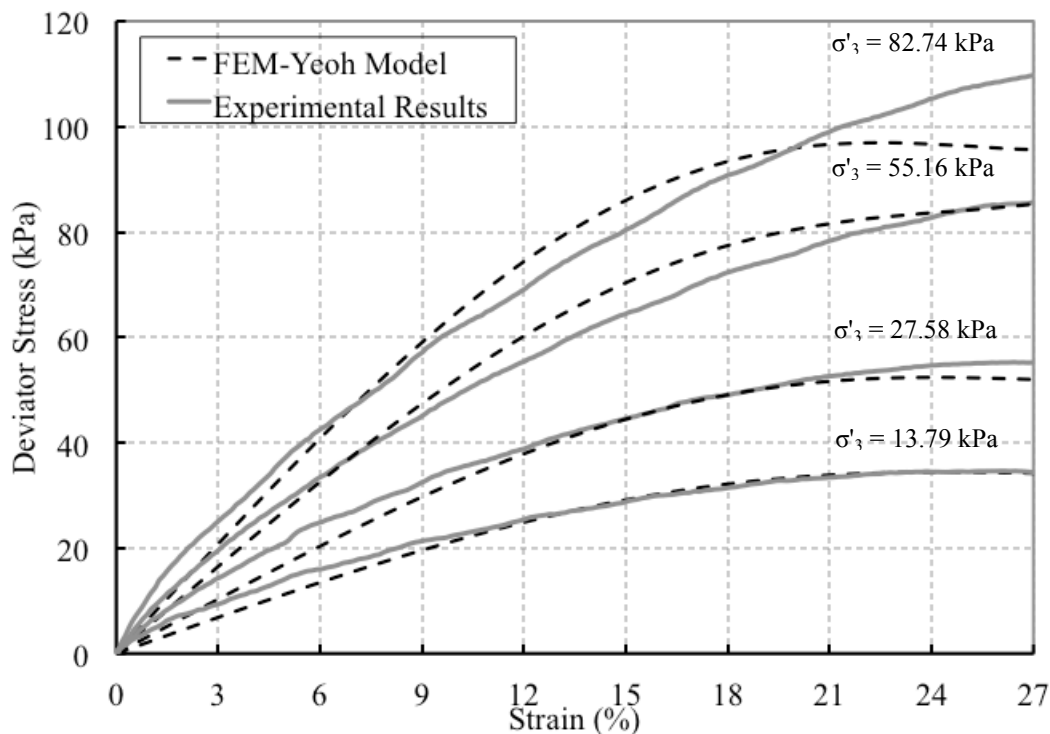


Figure 6.7: Comparison between FEM simulation and experimental results

Table 6.1: Summary of parameters determined for Hyperelastic Yeoh model

Parameters	$\sigma'_3 = 2$ psi (13.79 kPa)	$\sigma'_3 = 4$ psi (27.58 kPa)	$\sigma'_3 = 8$ psi (55.16 kPa)	$\sigma'_3 = 12$ psi (82.74 kPa)
C_{10}	5.818	8.155	11.353	12.809
C_{20}	-10.431	-14.620	-20.353	-22.963
C_{30}	10.969	15.375	21.404	24.148
D_1	0.0825			
D_2	0.0267			
D_3	0.00554			

6.3 Soil Hardening Constitutive Model

Another constitutive model evaluated for TDA triaxial compression behavior was the soil hardening model (SH). The SH model has been broadly used in FE analysis of different types of soils (soft and stiff soils). The SH model is based on the classical hyperbolic model formulated originally by Kondner (1963) and described further by Duncan and Chang (1970). However, the HS model is an extended model that supersedes the hyperbolic model for three main reasons: First, the model uses the theory of plasticity rather than elasticity. Second, it includes soil dilatancy; and it is able to include a yield cap (PLAXIS 2014). The SH model is considered a powerful tool that can model conventional geomaterials. However its applicability to predict the behavior of non-traditional aggregates such as TDA needs to be verified. Table 6.2 presents a summary of the parameters required for the model.

Table 6.2: Summary of parameters required for soil hardening model

Parameter	Definition
c'_{ref}	Cohesion
ϕ'	Friction angle
Ψ'	Dilatancy angle
E_{50}^{ref}	Reference stiffness modulus from triaxial test
E_{oed}^{ref}	Reference stiffness modulus from oedometer loading
E_{ur}^{ref}	Reference stiffness modulus from an unloading/reloading phase on triaxial
m	Power, modulus evolution depending on pressure level
ν_{ur}	Unloading/reloading Poisson's ratio
p^{ref}	Reference pressure
K_0^{nc}	At rest earth pressure coefficient for normal consolidated conditions
R_f	Failure ratio

The SH model uses the hyperbolic stress-strain relationship shown in Figure 6.8.

This figure shows the hyperbola that is defined by the following expression:

Failure criterion in the soil-hardening model is defined by the Mohr-Coulomb shear strength parameters (ϕ' and c') according to the following expression:

$$\varepsilon_1 = \frac{1}{E_i} \frac{q}{(1 - q/q_a)} \quad (6.19)$$

where :

ε_1 = Axial strain

q = Deviator stress ($\sigma_1 - \sigma_3$)

q_a = Asymptotic value for hyperbola

E_i = Initial tangential stiffness modulus

Figure 6.8 also shows the hyperbola is interrupted when the deviator stress reaches the failure load (q_f). The failure load is lower than the asymptotic value q_a that the hyperbolic stress-strain approaches gradually (towards infinity). The failure load is related to the asymptotic value as follows:

$$q_f = q_a \cdot R_f \quad (6.20)$$

Figure 6.8 also defines a secant soil stiffness E_{50} which corresponds to the slope of the secant line connecting the origin with the point in the stress-strain curve at a deviatoric stress level equal to 50% of the failure deviatoric stress. Finally this curve also shows a loading-unloading modulus (E_{ur}).

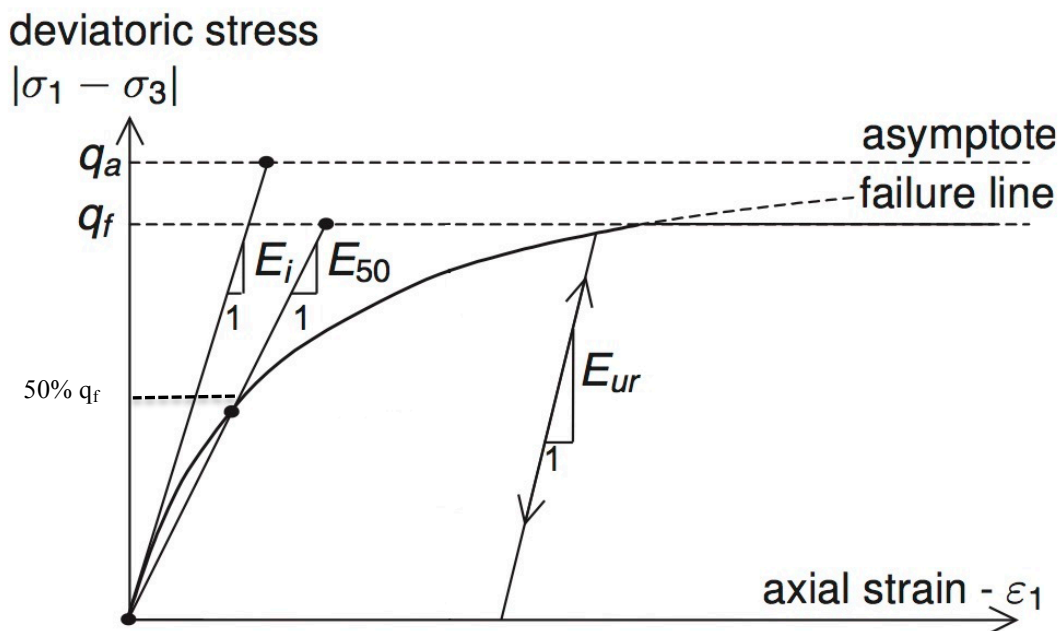


Figure 6.8: Hyperbolic stress-strain relation for soil-hardening model (PLAXIS 2014)

The parameters needed to specify the HS model are listed in Table 6.2. Their definition or purpose is provided bellow.

The SH model uses the Mohr-Coulomb failure criterion to define q_f as follows:

$$q_f = (c' \cot \phi' - \sigma'_3) \frac{2 \sin \phi'}{1 - \sin \phi'} \quad (6.21)$$

where :

c' = Effective cohesion intercept

ϕ' = Effective friction angle

σ'_3 = Effective minor principal stress (confining stress in a CD triaxial test)

As shown in Table 6.2 the HS model requires specifying the reference 50% secant stiffness modulus E_{50}^{ref} . This reference secant stiffness modulus corresponds to the E_{50} stiffness at a reference confining stress level (p^{ref}). The value of p^{ref} is also specified by the user and typically is selected as 1 atmosphere or 100 kPa. The HS model computes the 50% secant stiffness modulus as a function of confining stress level using the following expression

$$E_{50} = E_{50}^{ref} \left(\frac{c' \cos\phi' - \sigma'_3 \sin\phi'}{c' \cos\phi' + p^{ref} \sin\phi'} \right)^m \quad (6.22)$$

Where E_{50}^{ref} , c' , ϕ' and p^{ref} are as defined above. The exponent m in the above equation is the power law exponent that for most soils varies from 0.5 to 1.0 (PLAXIS 2014).

The initial tangential stiffness (E_i) can be obtained from the hyperbola equation (Equation 6.19) and the definition of E_{50} as follows:

$$E_i = \frac{2E_{50}}{2 - R_f} \quad (6.23)$$

The ratio between the failure asymptotic deviatoric stresses is given by the failure R_f in equation 6.22 which must be smaller than 1.

In case loading-unloading behavior is necessary, the E_{ur}^{ref} modulus may be obtained from tests during unloading cycles. In the same manner, oedometer modulus (E_{oed}^{ref}) can also be entered as input based on oedometer tests. However, PLAXIS recommends for many practical cases to take $E_{ur}^{ref} = 3E_{50}^{ref}$ while for E_{oed}^{ref} , it gives

certain suggestions in case experimental data for these modulus is not available (PLAXIS 2014).

6.3.1 FE Predictions of TDA, TDA-Mixtures and Nevada Sand CD Triaxial Tests Using the SH Model

FE predictions using the SH model model were carried out was used for the TDA, TDA/sand mixtures and Nevada sand under CD triaxial compression using the commercial software PLAXIS (PLAXIS 2014). The soil test module in PLAXIS was used for all the analysis since it allows simulating directly triaxial tests. For these analyses, axisymmetric model similar to the implemented in ABAQUS was used as shown in Figure 6.9.

The input parameters used for the SH model prediction of the different test materials are summarized in Table 6.3. It should be pointed out that the reference pressure was chosen as 55.16 kPa which corresponds to the confining pressure level used for one of the triaxial tests. The secant modulus (E_{50}) was determined from the experimental stress-strain curves in the triaxial tests. The Mohr-Coulomb shear strength parameters at failure were determined based on values reported in Chapter 4. The m power exponent and the failure ratio (R_f) were calibrated from the existing data. The final parameters for the model are summarized in Table 6.3. It is noted that the calibrated value of R_f for the TDA (0.59) is considerable lower than typical values reported in the literature for conventional granular materials ($R_f = 0.80$ to 0.90). However, Lee et al. (1999) reported using a similar failure ratio value equal to 0.61 for numerical predictions of the lateral pressures induced by the TDA backfill tested by Tweedie et al. (1998).

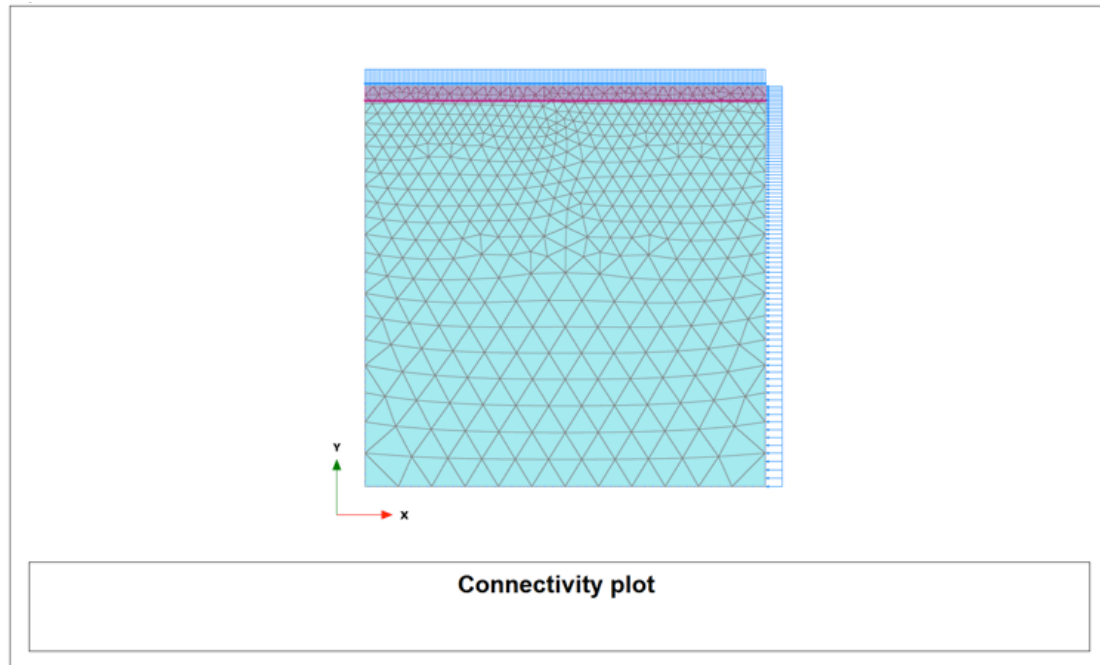


Figure 6.9: Triaxial axisymmetric model implemented in PLAXIS

Figures 6.10 through 6.12 show the stress-strain behavior for the Nevada sand, and the two TDA-Sand mixtures. As expected the SH model captures reasonably well the behavior of the Nevada sand. Similarly, the SH model is able to capture adequately the CD triaxial stress-strain behavior observed for the two mixtures. In contrast, the SH predicts the behavior of TDA within some limitations as shown in Figure 6.13. The model captures reasonably well the increase in stiffness with the confining pressure of the TDA material at lower axial strain levels (up to 7%). This prediction may be accepted or reasonable since most geotechnical designs would likely restrict axial strain levels to below 10% to avoid excessive settlements and deformations. However, the model underpredicts the TDA strength particularly for higher level of deformations. Figure 6.14 shows the prediction of the volumetric strain variation during shearing for TDA.

Table 6.3: Summary of parameters used for soil hardening model predictions

Material	ϕ' (deg)	c' (kPa)	E_{50} (kPa)	P_{ref} (kPa)	m	R_f
Nevada Sand	40.8	0	33151.61	55.16	0.52	0.85
TDA/sand Mixture (20/80 by volume)	38.67	5.85	13714.67	55.16	0.52	0.85
TDA/sand Mixture (50/50 by volume)	34.57	5.16	3207.11	55.16	0.60	0.69
100 % fine TDA	22.23	6.51	510.43	55.16	0.65	0.59

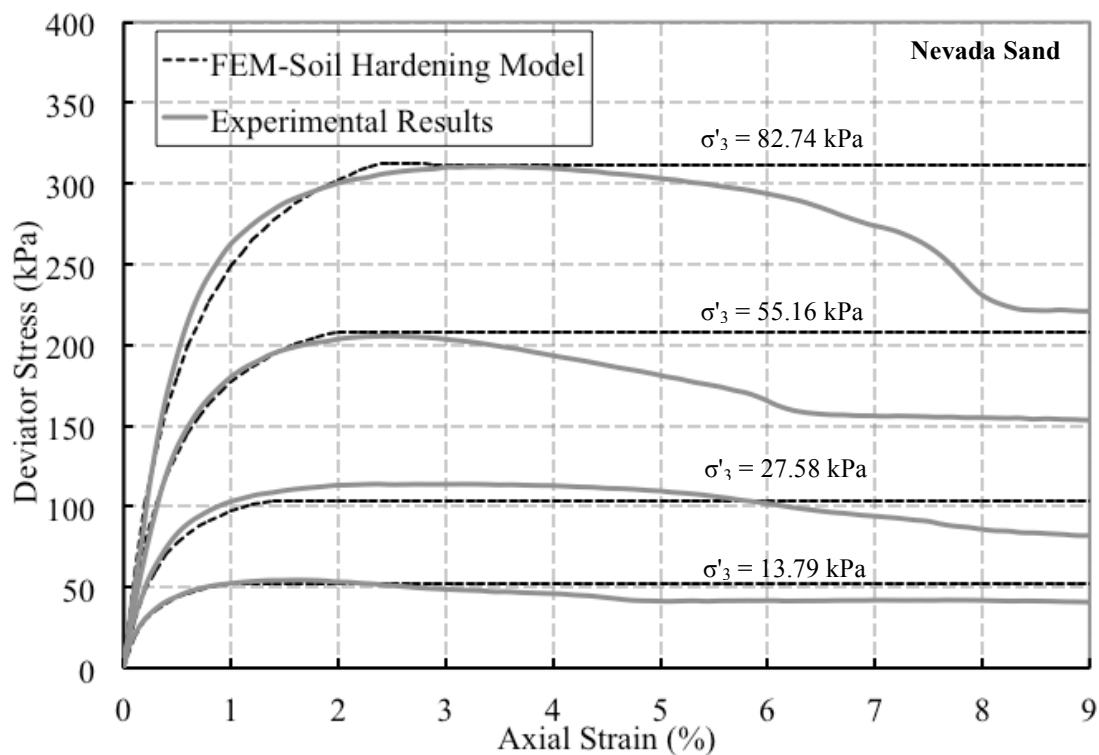


Figure 6.10: Soil hardening model results for Nevada Sand

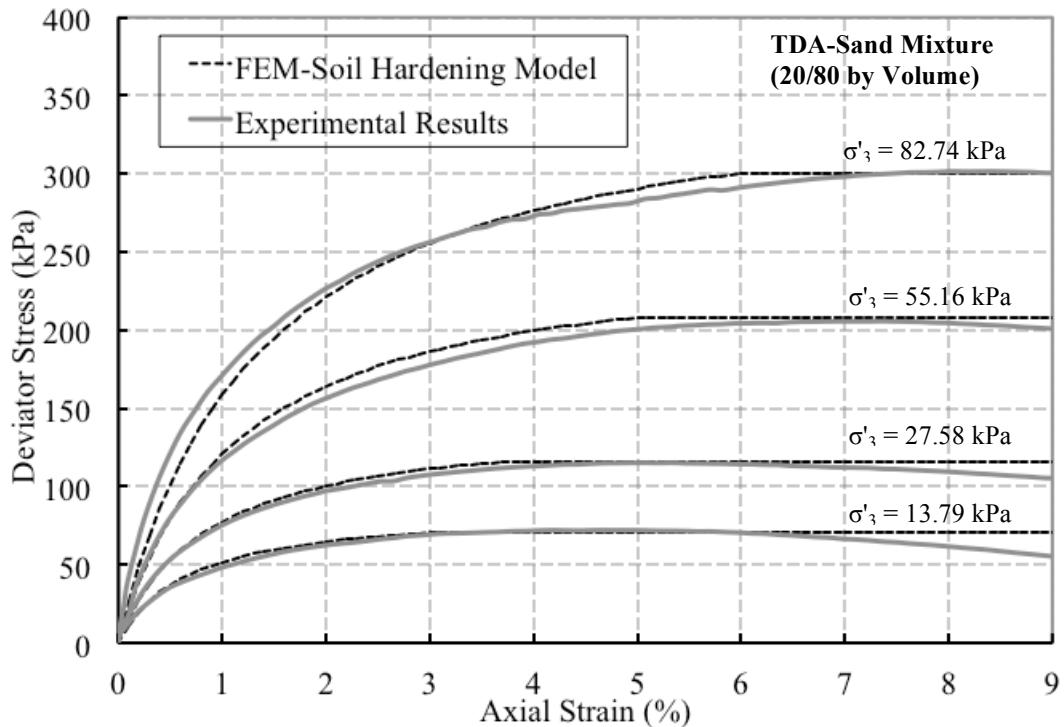


Figure 6.11: Soil hardening model results for TDA-Sand mixture (20/80 by volume)

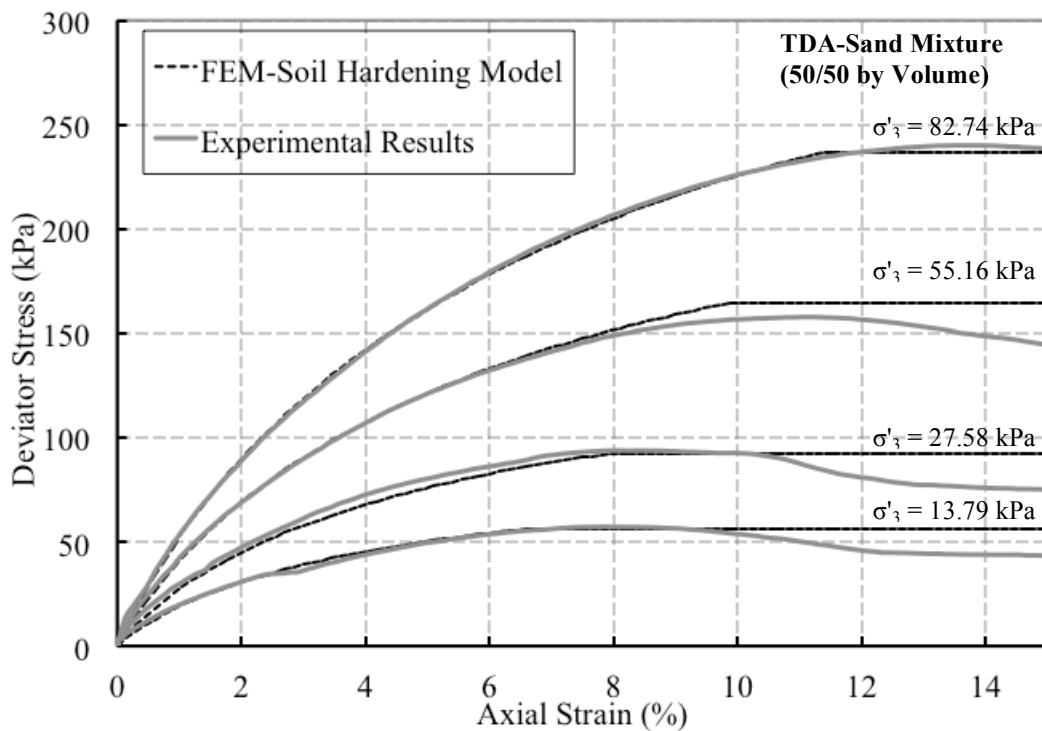


Figure 6.12: Soil hardening model results for TDA-Sand mixture (50/50 by volume)

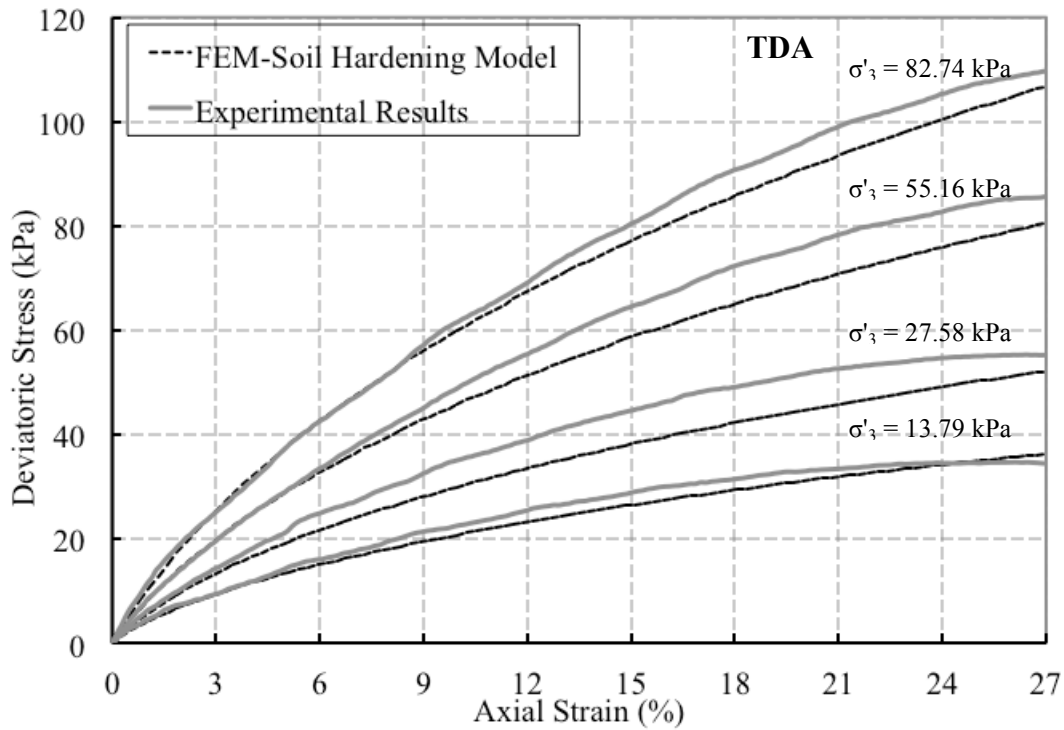


Figure 6.13: Soil hardening model results for TDA

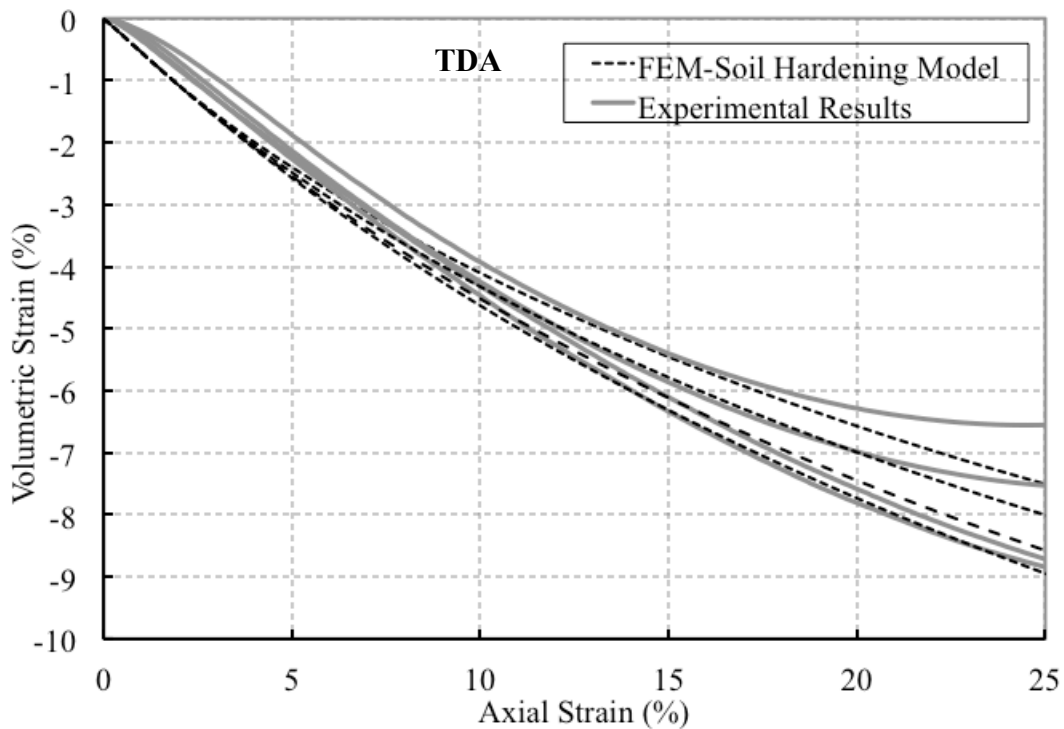


Figure 6.14: Volumetric change prediction during shearing for TDA

6.4 Porous Elasticity Constitutive Model

Triaxial compression behavior was also modeled using a porous elasticity model chosen as an alternative to the previous two modeling techniques. It was previously discussed that Yeoh model does not work properly for geotechnical applications because the model cannot capture the hardening of the TDA as a function of the confining pressure. Furthermore, the compressibility of TDA during consolidation phase is not negligible as conventional granular soils and it is a relevant factor that needs to be addressed when dealing with TDA. Therefore, an existing model that can moderately simulate both the compressibility (during consolidation) and the stiffness dependence on the confining pressure may result in a better representation of TDA behavior.

The porous elasticity model, included in ABAQUS, provides an attractive modeling approach since it provides a combination of features used for modeling porous or granular materials with features used to capture polymer behavior (ABAQUS 2011). TDA materials can be considered a combination of both granular material with some fraction of a polymer behavior related to the intrinsic nature of the rubber based particles. Additionally, this model is able to use an extension of the original Drucker-Prager model as a yield criteria, which is commonly used in conventional geomaterials. Finally, this model was considered given its flexibility when fitting triaxial compression test (ABAQUS 2011).

6.4.1 Porous Elasticity Model for the Consolidation Phase of CD Triaxial Tests

The porous elasticity model (ABAQUS 2011) is based on the experimental observations that in porous materials during elastic straining, the change in void ratio e and the change in the logarithm of the equivalent pressure stress p defined as:

$$p = -\frac{1}{3} \text{trace } \sigma \quad (6.24)$$

Are linearly related as:

$$de^{el} = -kd(\ln(p)) \quad (6.25)$$

Where k is a material parameter related to the compressibility behavior. If the tensile strength is nonzero, as shown in Figure 6.15, the equivalent relation shown in Equation 6.25 becomes:

$$de^{el} = -kd(\ln(p + p_t^{el})) \quad (6.26)$$

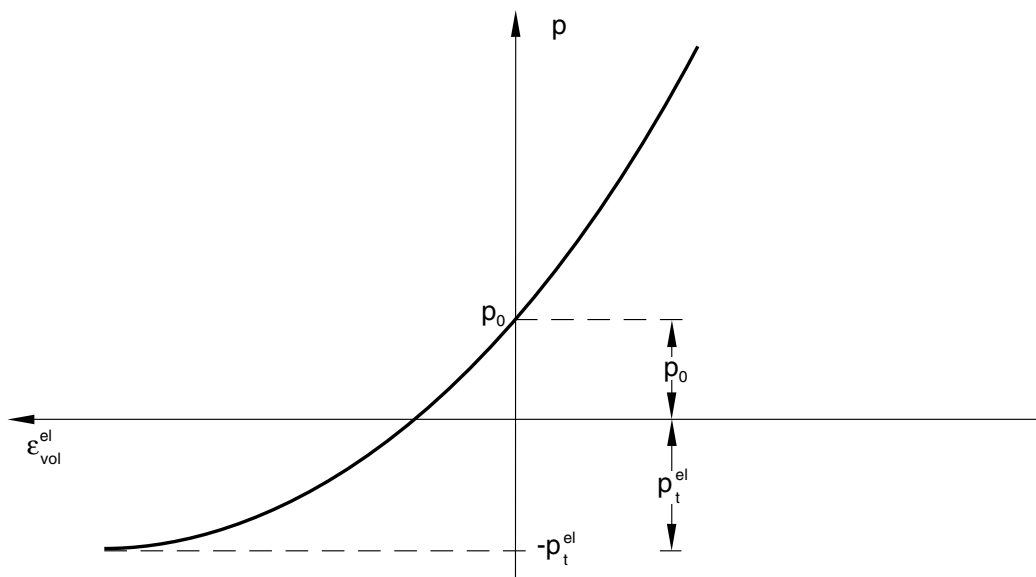


Figure 6.15 Porous elastic volumetric behavior (adapted from Abaqus 2011)

The volume change of the material sample is defined as:

$$J = \frac{1 + e}{1 + e_o} \quad (6.27)$$

Where e_o is the initial void ratio. Equation 6.27 is adapted to define the elastic volume change as a function of the elastic void ratio e^{el} as:

$$J^{el} = \frac{1 + e^{el}}{1 + e_o} \quad (6.28)$$

Integrating the linear relation, the volumetric elasticity relationship as reported by ABAQUS (2011) is as follows:

$$\frac{k}{1 + e_o} \ln \left(\frac{p + p_t^{el}}{p_o + p_t^{el}} \right) = 1 - J^{el} = 1 - \exp(\varepsilon_{vol}^{el}) \quad (6.29)$$

From equation 6.29, it is observed that the parameters to be determined in order to compute the volumetric change during consolidation are: κ , p_t^{el} and p_o . The initial void ratio for the TDA and the Nevada sand is a physical parameter that is known from the sample preparation and the specific gravity of the materials. Any mixture proportion void ratio was found to increase linearly from the average Nevada sand initial void ratio ($e_o \approx 0.56$) to the TDA average initial void ratio ($e_o \approx 0.98$). The goal of this section was not only to simulate the consolidation behavior of the materials tested during the triaxial program (Chapter 4) but also to develop equations based porous elasticity model that would allow estimating the compressibility behavior during consolidation. Additionally, an attempt was made to determine parameters for any mix ratio of TDA/Nevada sand mixture. Although, samples were prepared in the lab by mass proportions, the equivalencies in volume (which were already discussed in Chapter 4), will be used in the

development presented bellow. The main coefficient for the model is denoted f_r , which corresponds to the fraction of rubber (by volume). Therefore, the initial void ratio of any TDA/sand mixture can be computed as:

$$e_o = e_0^{sand} + (e_0^{rubber} - e_0^{sand}) f_r \quad (6.30)$$

The rest of the parameters were optimized by fitting Equation 6.29 in the Excel solver using the experimental data. Values of κ and p_t^{el} could be fitted with the same values at 0 and 20% rubber respectively ($\kappa_{sand} = 2.92 \times 10^{-3}$ $p_t^{el sand} = 0.1295$ kPa). However, the behavior for higher rubber contents was found to be very different. Transitioning from sand-influenced behavior to rubber-influenced behavior required introducing a threshold rubber content denoted herein as f_t . When the rubber fraction is greater than this threshold (f_t), κ was found to increase linearly while p_t^{el} was found to increase sharply as shown in Figures 6.16 and 6.17, respectively. From this optimization process, it was found that the behavior between the of TDA/sand mixture materials starts to change drastically at a rubber content of 37.4% ($f_t = 0.374$). Equations 6.31 through 6.34 are adapted for any TDA fraction (f_r) for the two identified zones as follows:

If $f_r \leq f_t$:

$$k = k^{sand} = 2.92 \cdot 10^{-3} \quad (6.31)$$

$$p_t^{el} = p_t^{el sand} = 0.1295 \text{ kPa} \quad (6.32)$$

If $f_r \geq f_t$:

$$k = k^{sand} + (k^{rubber} - k^{sand}) \frac{f_r - f_t}{1 - f_t} \quad (6.33)$$

$$p_t^{el} = p_t^{el \text{ sand}} + (p_t^{el \text{ rubber}} - p_t^{el \text{ sand}}) \exp\left(-\frac{f_r - f_t}{f_{rc}}\right) \quad (6.34)$$

It is important to note that for p_t^{el} value in Equation 6.34 instead of being equal to $\frac{f_r - f_t}{1 - f_t}$ was modified to an exponential term of the form of $\exp\left(-\frac{f_r - f_t}{f_{rc}}\right)$. This was done in order to produce a smooth, yet rapid transition to the observed rubber with apparent cohesion behavior. The term f_{rc} was also introduced to represent as the critical TDA fraction after the threshold fraction (f_t) required to capture the sharp increase observed in p_t^{el} . The values optimized for the parameters at any given TDA fraction f_t are as follows:

$$f_t = 0.374 \quad (6.35)$$

$$k^{rubber} = 0.220 \quad (6.36)$$

$$k = 2.92 \cdot 10^{-3} + 0.347(f_r - 0.374) \quad (6.37)$$

$$p_t^{el \text{ rubber}} = 9.676 \text{ kPa} \quad (6.38)$$

$$f_{rc} = 0.05 \quad (6.39)$$

$$p_t^{el} = 0.1295 + 9.547 \exp\left(-\frac{f_r - 0.374}{0.05}\right) \quad (6.40)$$

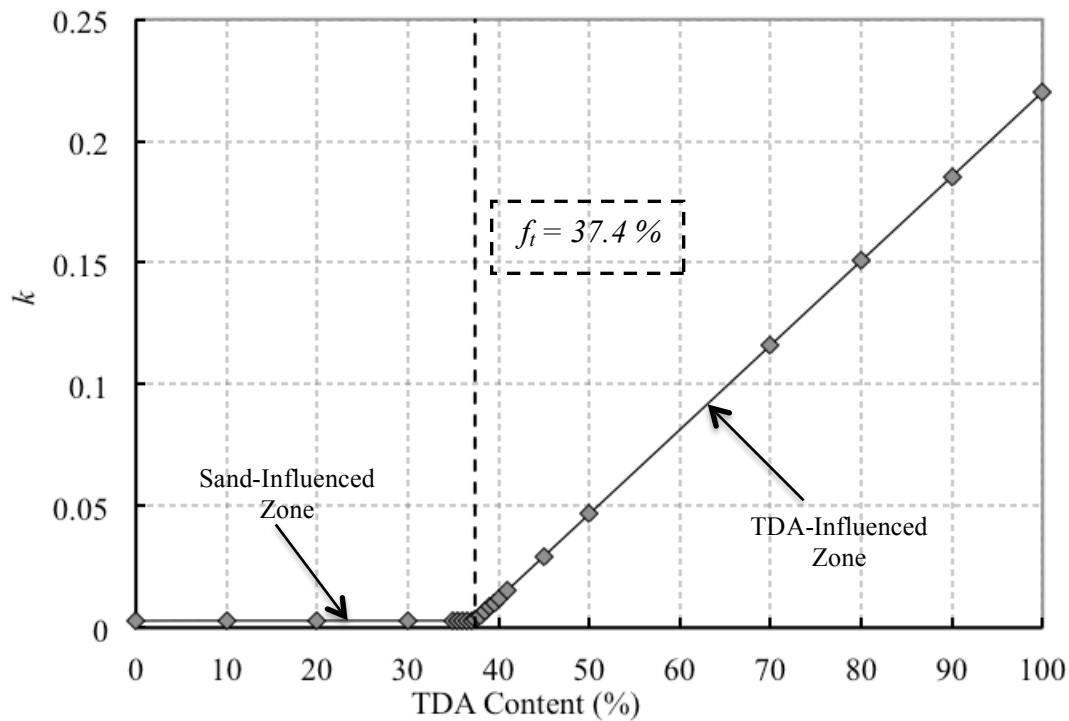


Figure 6.16: Analytical solution of k parameter obtained from the porous elasticity model

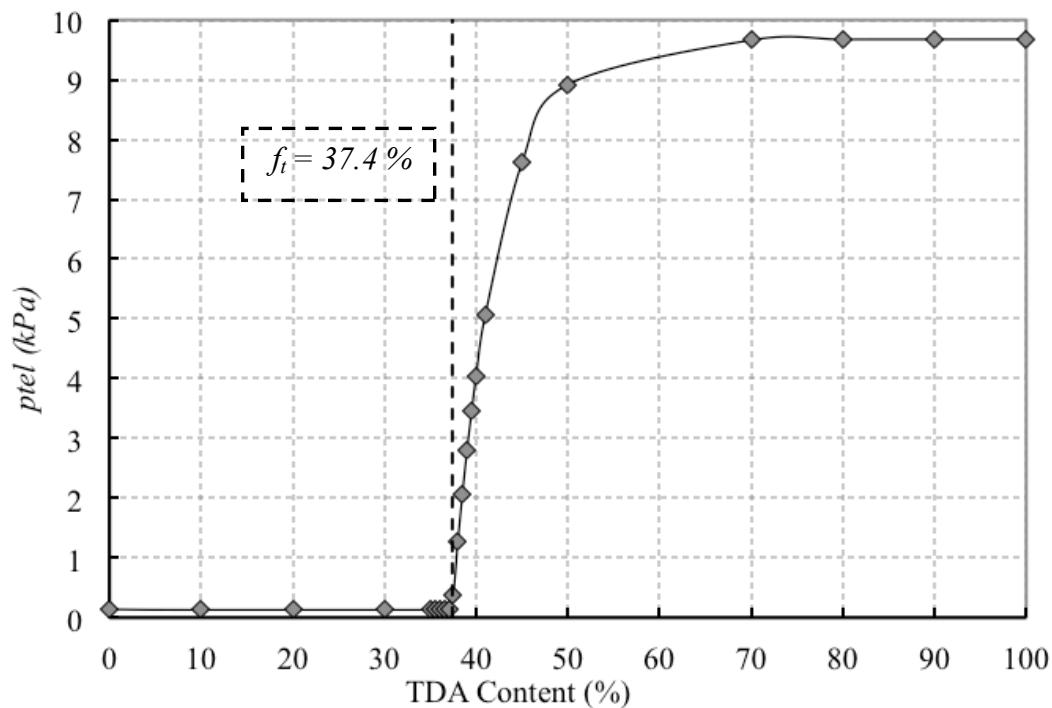


Figure 6.17: Analytical solution of p_t^{el} parameter from the porous elasticity model

The compressibility experimental response measured during the isotropic consolidation phase in the triaxial tests for the 50% and 100% TDA materials was to obtain the parameters in Equation 6.29. This was done using the Excel solver minimizing the difference between measurements and calculated results. The final parameters will be listed in the following subsection (Table 6.4). The values of k obtained seem reasonable since k is related to the compressibility of the material and the value for the Nevada sand is much lower compared to the k derived for the TDA. In terms of p_t^{el} , this parameter may be related to the apparent cohesion observed during the experimental triaxial testing of the TDA materials. Figure 6.18 shows the comparison between volumetric strains as a function of confining stress levels obtained at the end of the consolidation for the different materials tested.

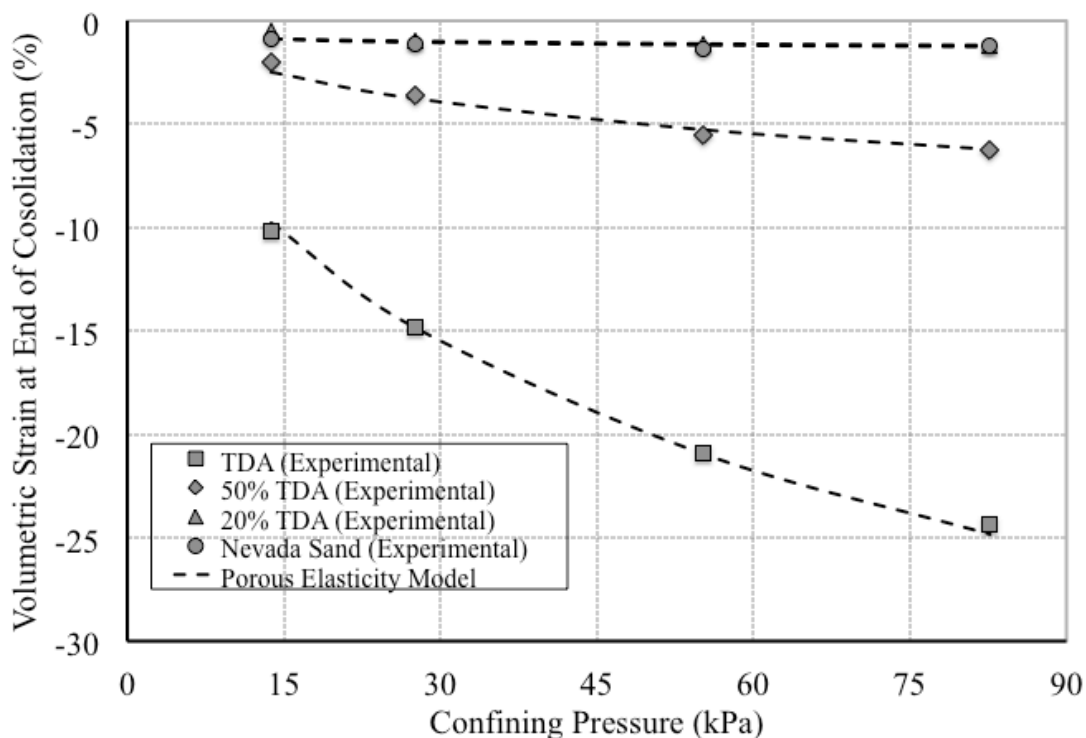


Figure 6.18: Predicted volumetric strains at the end of consolidation using Porous Elasticity Model

6.4.2 Predicted CD Triaxial Compression Behavior Using Porous Elasticity Model

The deviatoric elastic behavior in the porous elasticity model was defined by choosing a constant Poisson's ratio so that the deviatoric elastic stiffness increased with increasing pressure stress (ABAQUS 2011). During the drained shearing phase the material deformations are a result of elastic and plastic deformations. For the elastic component of the deformations, the shear modulus (G) is required and computed as follows:

$$G = \frac{3(1-2\nu)(1+e_0)}{2(1+\nu)k} (p + p_t^{el}) \exp(\varepsilon_{vol}^{el}) \quad (6.41)$$

Fixing a constant Poisson's ratio (ν) imposes a variable shear modulus G , which increases with increasing volume compression and pressure level, and decreases with increasing compressibility (k). It should be pointed out that e_0 , k , p_t^{el} and $J_{el} = \exp(\varepsilon_{vol}^{el})$ were calculated from previous models equations (consolidation phase). The value of Poisson's ratio was unknown. However, values of ν for different TDA materials have been reported in the literature ranging from 0.20 to 0.33 for different TDA sizes (Huggins 2012). The Poisson's ratio value was varied to produce an initial stiffness slope close to the experimental values measured in the triaxial tests. For the 100% fine TDA the best ν value was identified as 0.25. The variation in deviatoric stress during elastic loading can be determined as:

$$dS = 2 G d\varepsilon^{el} \quad (6.42)$$

The stress increase observed during initial elastic loading will eventually reach a predefined yield criterion. ABAQUS allows modeling the yield portion using extensions of the Drucker-Prager model. The exponent form shown in Figure 6.19 provided by

ABAQUS for granular / polymer models, was used since it offered better flexibility to model triaxial tests (ABAQUS 2011).

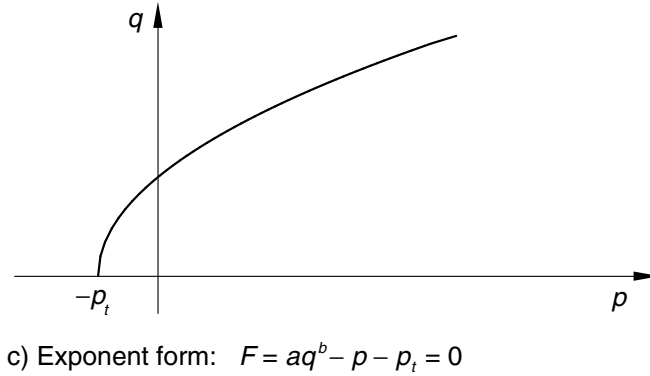


Figure 6.19: Drucker-Prager yield criteria for porous elasticity (ABAQUS 2011)

The Drucker-Prager yield criterion indicated in Figure 6.19 is defined as :

$$F = a\bar{\sigma}^b - (p + p_t^{el}) \quad (6.43)$$

or

$$\bar{\sigma} = \left(\frac{p + p_t^{el}}{a} \right)^{1/b} \quad (6.44)$$

Where a and b are material's parameters that needs to be calibrated. Progressive adjustments to the values of parameters a and b on maximum values of deviatoric stress ($\bar{\sigma}$) and the corresponding deviatoric pressure lead to consider a constant value for the parameter a equal to 0.6 for all materials tested. A constant value of 1 for parameter b was found to be adequate for low volume fractions of TDA. Essentially, this means that the sand strength increases linearly with increasing confining pressure. This is consistent with experimental observations during triaxial tests results where the failure envelopes did not show curvature at least for the confining pressures studied. At higher TDA

fractions, the b parameter value had to increased and eventually was fitted to a power law using the same f_t parameter defined in the previous subsection which results in the following set of equations:

If $f_r \geq f_t$, the b parameter used was based on:

$$b = b^{sand} + (b^{rubber} - b^{sand}) \left(\frac{f_r - f_t}{1 - f_t} \right)^n \quad (6.45)$$

Solving Equation 6.45 gives :

$$b^{rubber} = 1.143 \quad (6.46)$$

$$n = 0.78 \quad (6.47)$$

And for any TDA fraction by volume b parameter can be computed as follows:

$$b = 1 + 0.205(f_r - 0.374)^{0.78} \quad (6.48)$$

Once the corresponding parameters were optimized, the triaxial simulations for the different materials were performed using ABAQUS. The finite element models were the same as described in section 6.2 (Yeoh's hyperelastic model). Table 6.4 shows the final input parameters for the porous elasticity model. Figures 6.20 through 6.22 show the predicted CD triaxial stress-strain curves. It is observed that the porous elasticity model captures reasonable well the behavior of the materials within the elastic region of the stress-strain curves which may correspond to acceptable levels of deformation for the TDA in conventional applications. This model predicts the deviatoric stresses moderately well as shown in Figure 6.23. Although, the level of overprediction after the elastic portion seems considerable, conventional accepted models, such as Mohr-Coulomb, may lead to the same type of results.

Table 6.4: Summary of parameters used for soil porous elasticity model predictions

Material	k	pt_{el} (kPa)	e_o	ν	a	b
Nevada Sand	0.0029	0.129	0.56	0.25	0.60	1.00
TDA/sand Mixture (20/80 by volume)	0.0029	0.129	0.64	0.25	0.60	1.00
TDA/sand Mixture (50/50 by volume)	0.0467	8.91	0.77	0.25	0.60	1.045
100 % fine TDA	0.220	9.67	0.98	0.25	0.60	1.135

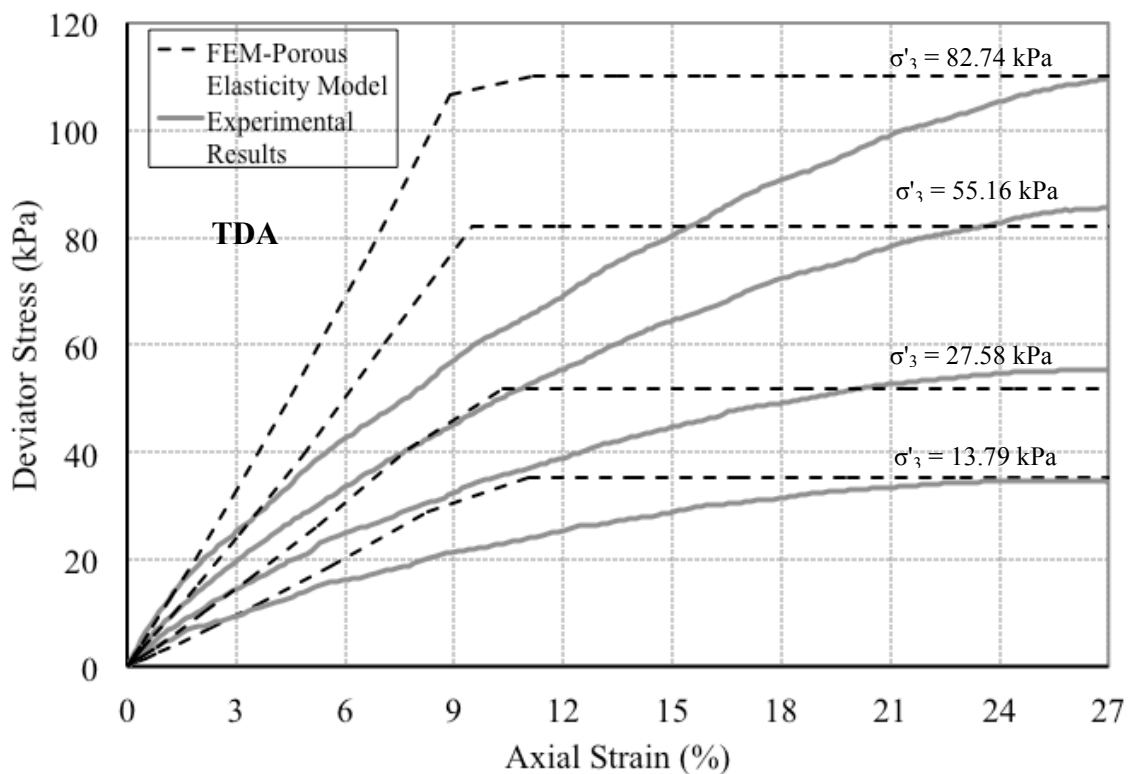


Figure 6.20: Porous elasticity model results for 100% fine TDA

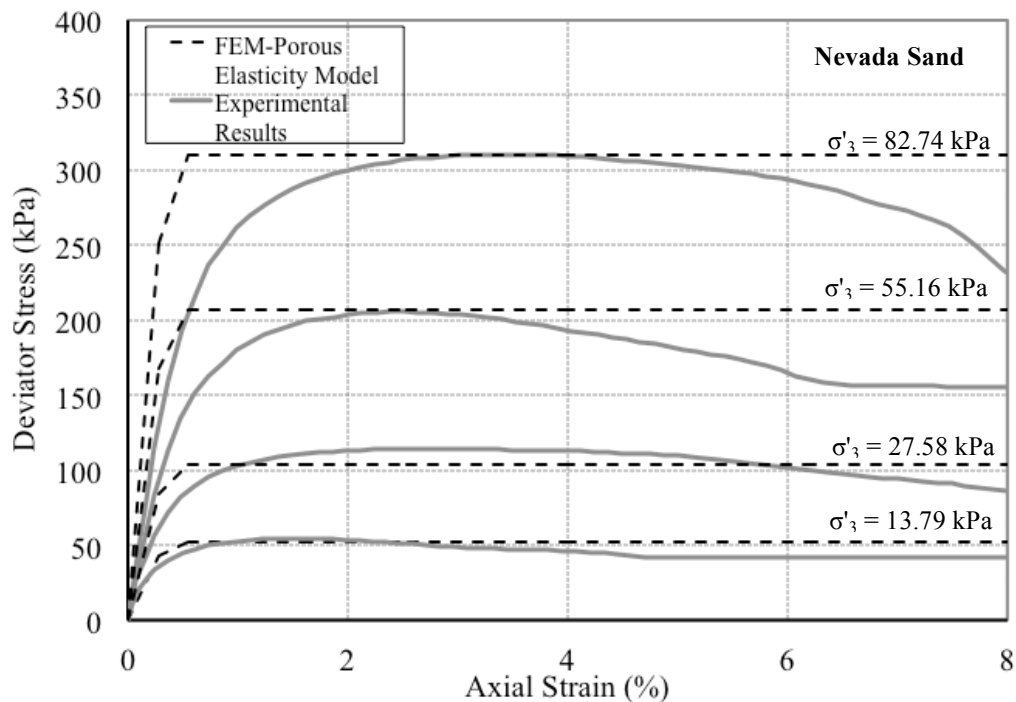


Figure 6.21: Porous elasticity model results for Nevada Sand

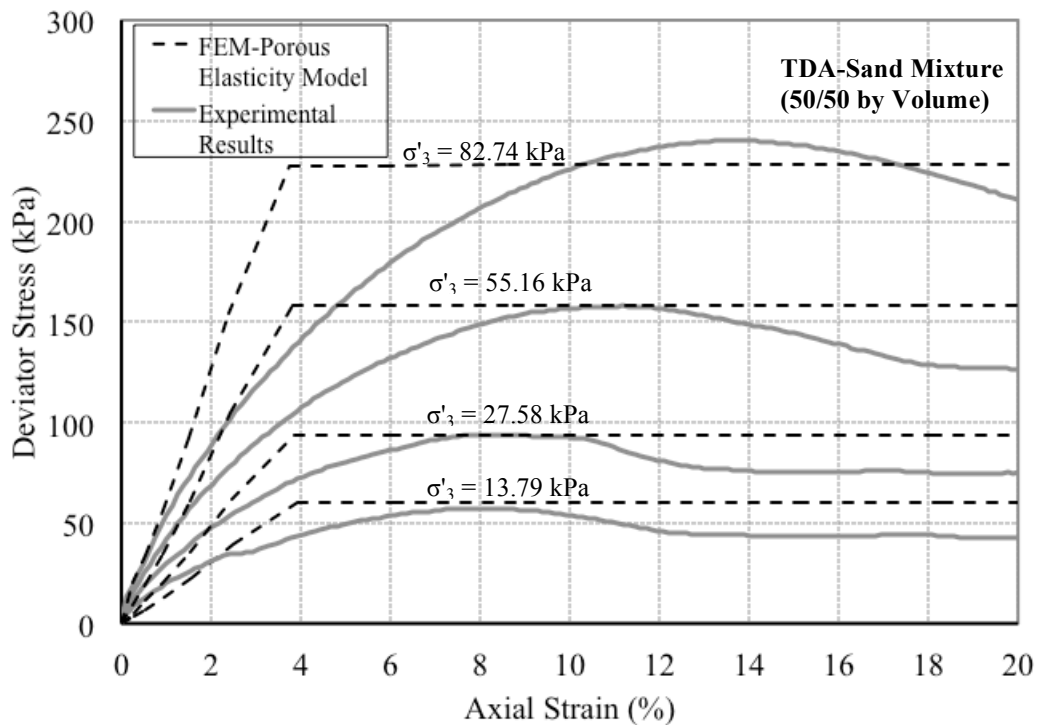


Figure 6.22: Porous elasticity model results for TDA-Sand mixture (50/50 by volume)

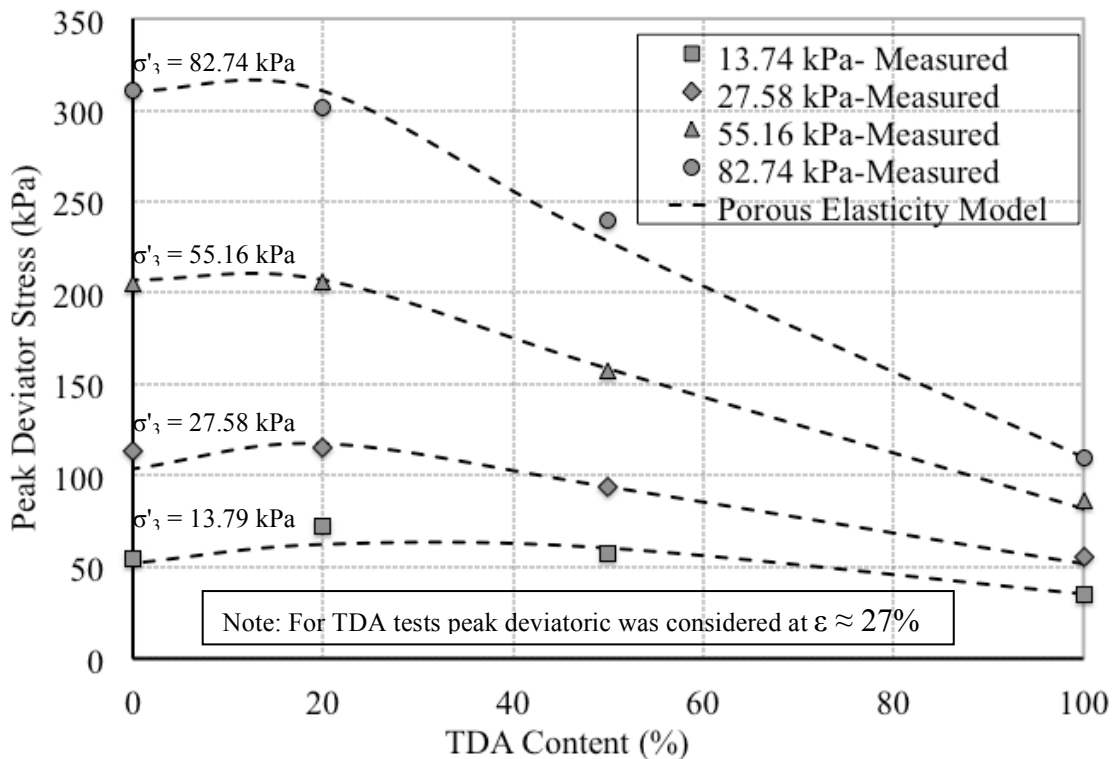


Figure 6.23: Deviatoric peak stress estimation for different TDA contents

6.4.3 Summary of Porous Elasticity Model Predictions

The main goal of the porous elasticity model was to evaluate the compressibility behavior of the TDA when compared to granular materials from the consolidation phase, which was possible by using Equation 6.29. The model allowed applying parameters obtained from the consolidation phase as an input for the triaxial simulations. This condition may be significant for materials with high degree of compressibility during consolidation such as TDA. Additionally an attempt to develop equations to compute model parameters for any TDA fraction in a mixture was explained. The model predicts reasonably well the behavior within the elastic region and the peak deviatoric stress for all materials tested.

CHAPTER 7. SUMMARY, CONCLUSIONS AND RECOMMENDATIONS FOR FUTURE WORK

7.1 Summary

The main goal of this dissertation was to study the engineering behavior of tire derived aggregates (TDA) and TDA/sand mixtures with emphasis on potential applications within the field of geotechnical engineering. The research activities were divided into three main components, as follows: 1) The study of lateral pressures generated by TDA backfill in retaining walls; 2) Mechanical properties with emphasis on the triaxial and simple shear stress-strain behavior and shear strength parameters for TDA and TDA/sand mixtures. All experimental work carried out in this research involved TDA particle sizes classified as granulated rubber which entails small shredded scrap tires pieces ranging from 0.425 to 12 mm; and 3) numerical predictions using finite element analyses of select triaxial compression tests from Component 2.

The lateral pressures on retaining walls was investigated by means of a series of geotechnical centrifuge tests carried out at the centrifuge facility at the Rensselaer Polytechnic Institute (RPI) in Troy, NY. The centrifuge tests involved tests for retaining walls at K_0 or at-rest earth pressure coefficient and under active conditions. The centrifuge tests involved using specialized tactile pressure sensors, which allowed accurate measurements of the lateral pressures (magnitude and distribution) generated by the different backfills considered. For the tests under at-rest conditions, three backfill materials were considered, namely TDA, TDA/Nevada Sand mixture (50/50 by volume),

and Nevada Sand. The active condition centrifuge tests were carried out using TDA/Nevada Sand mixture (50/50 by volume), and Nevada Sand as backfill. Both sets of centrifuge tests showed that classical lateral earth pressure theories commonly used to estimate lateral pressures on retaining walls with mineral soil backfills are not adequate for TDA backfills.

The second research component involved assessment of the mechanical properties of TDA and TDA/sand mixtures through geotechnical laboratory testing. Specifically stress-strain behavior was experimentally studied using two different testing techniques. First, drained and undrained triaxial compression tests were performed in order to evaluate the stress-strain characteristics of TDA and compare it to results from similar tests carried out on conventional sand and TDA/sand mixtures. Second, a series of simple shear tests were performed in order to evaluate the drained mechanical properties of the same test materials (TDA, TDA/Nevada Sand mixture, and Nevada Sand) tested under simple shear conditions. The simple shear testing program used similar sample conditions and stress levels as used for the triaxial program, in order to compare the behavior of these two testing procedures. The geotechnical tests showed the TDA material has a significantly lower stiffness and shear strength compared to a conventional silica sand tested under similar conditions.

The final component of this dissertation included an evaluation of three constitutive models, implemented by two different finite element (FE) software programs (ABAQUS and PLAXIS), to assess their suitability to predict the experimental results obtained from the CD triaxial tests presented in Chapter 4. The numerical predictions using FE analyses were reasonably close to the experimental results. However, this

numerical component highlighted the need to use more sophisticated constitutive models as opposed to those commonly used in geotechnical engineering practice in order to adequately capture the stress-strain behavior of TDA materials during triaxial compression experiments. Furthermore the numerical predictions of laboratory scale tests indicated that FE modeling may be adequate for predicting the behavior of larger scale problems such as field-scale retaining walls.

7.2 Conclusions

Based on the findings from geotechnical centrifuge tests, an experimental program based on triaxial compression and simple shear as well as finite element analyses, this author formed a number of conclusions. Those conclusions are summarized in the following subsections.

7.2.1 Centrifuge Tests Under At-rest Condition

Centrifuge tests under at-rest conditions were carried out for TDA, TDA/Nevada Sand mixture (50/50 by volume) and Nevada Sand. The main conclusions drawn from these tests are as follows:

- A reduction of 80% in the magnitude of the lateral pressure was obtained for the TDA backfill when compared to a Nevada Sand backfill.
- A slight increase in TDA lateral pressure with time was observed. This increase may be related to the compressibility of TDA particles which may result in creep.
- Pressure distributions measured using tactile pressure sensors showed that lateral pressures vary approximately linearly with depth for the TDA and Nevada Sand backfills.

- Lateral pressure distribution induced by a mixture of TDA/Nevada Sand backfill (50/50 by volume) seems to follow a polynomial distribution due to a rapid increase in lateral pressure toward the bottom of the retaining structure, which may be related to the segregation of Nevada Sand particles during the spinning process considering the difference in particle sizes within the mixture.
- An approximate 30% reduction in at-rest lateral pressure was observed for TDA/Nevada sand backfill (50/50 by volume) mixture when compared to the Nevada Sand backfill.
- The well-known Jaky's formula highly overpredicts the TDA lateral pressure coefficient (K_o) when compared to the experimental results. This may lead to conservative designs.
- The observed decrease in lateral pressures for TDA and TDA/sand mixture backfills is expected to bring economic benefits since less concrete and fewer reinforcement bars would be required for the structural elements.

7.2.2 Centrifuge Tests Under Active Conditions Using a Model Cantilever Wall

Based on the results obtained from the two cantilever retaining wall centrifuge models using TDA/sand mixture and Nevada Sand as backfill, the following major conclusions were drawn:

- TDA/sand mixture (50/50 by volume) backfill lateral pressures were found to be 35% lower than those obtained for the Nevada Sand backfill.
- Nevada Sand earth pressure coefficient was found to be within an acceptable range of prediction between experimental data and Rankine theory. However, the level of

overprediction for TDA/sand mixture (50/50 by volume) may not be within acceptable ranges, which can result in conservative designs.

- The level of wall movement required to reach active condition in a retaining wall using a TDA/sand mixture backfill seems to be lower than the typical values observed for retaining walls with conventional mineral backfills.
- The deflected shape of the retaining structure during the centrifuge test was found to be the result of combining two movements of the wall: rotation of the wall about the base and translation mode or sliding along the base.
- The combined translation-rotation movement mechanism could be explained by means of the classical theory of beams where the deflection curve of a cantilever beam was calculated to represent retaining wall displacement behavior.

7.2.3 Triaxial Compression Tests

Triaxial compression tests were carried out under drained and undrained conditions. Additionally, the effects of TDA particle size and shear strain rate were evaluated. Based on the results obtained from this experimental program, the following conclusions were drawn:

- The results obtained from the stress-strain behavior experimental program indicate that TDA exhibits a high degree of deformability as compared to conventional granular materials.
- Mechanical properties such as strength and stiffness are dramatically decreased for TDA when compared to granular soils.
- Apparent deviatoric failure peak stresses were not clearly observed at deformations higher than 20% axial strain for both drained and undrained conditions for the TDA.

Strength values based on such high values of strain may not be feasible to use in conventional design for most conventional civil applications. Therefore, the selection of strength parameters should be based on the expected or allowable deformation levels in the field.

- For triaxial drained conditions, TDA specimens exhibit contraction behavior or volume loss during shearing. However, TDA has a tendency to show a constant volumetric change at deformations close to 25% axial strain. Therefore, a steady state of deformation may be achieved at non-practical levels of deformation.
- For triaxial undrained conditions, TDA was found to generate positive excess pore pressures. This is consistent with volumetric change behavior observed in the drained conditions test and conventional soil mechanics where materials with predominant contractive behavior would tend to contract and squeeze water out of the pores which would produce positive pore pressures due to the blockage in drainage.
- A detailed analysis of the variation of shear strength parameters with the level of deformation in TDA revealed that the selection of shear strength parameters is highly dependent on the desired axial strain to be expected at any given application.
- Friction angles for the finer TDA tested in this research may vary from 8 to 21 degrees under drained conditions for axial strain ranges between 5% and 27%. The cohesion component seems to play an important role in the TDA shear strength behavior and may not be neglected.
- The increase in the mobilized shear strength parameters at different strain levels for TDA may be less influenced by particle rearrangement as in the Nevada sand. Deformability of TDA particles may play an important driving factor in the

- mechanics governing the increase in shear strength since the contact area between particles increases as the axial deformation achieves higher levels during shearing.
- TDA particle size has a direct impact on mechanical properties. It was observed that for the two TDA sizes tested ($D_{50} = 1.20$ mm and $D_{50} = 2.60$ mm), an increase in strength and stiffness was achieved for the coarser TDA samples. Increases in strength between 8% and 11%; and 21% and 29% for secant Young's modulus were obtained for the coarser TDA ($D_{50} = 2.60$ mm) in the confining stresses analyzed in this research.
 - Higher shear strain rates seem to produce higher TDA strength and stiffness. However, the range and number of strain rates analyzed in this research was limited. Therefore, a more rigorous study regarding the effect of strain rate is necessary considering the viscoelastic properties of rubber-like materials.
 - TDA exhibits high degree compressibility problems, which may result in lack of acceptance or limited use due to potential excessive settlement problems, may be improved by mixing TDA with conventional granular soils. Axial strains at a failure of approximately 5% and 10% were observed for TDA-Nevada Sand mixtures proportioned in ratios of 20/80 and 50/50 by volume, respectively. These levels of deformation may be within acceptable ranges for certain applications or standards.
 - Mechanical properties such as stiffness and strength also improved drastically for both mixtures due to the influence of the sand matrix in the aggregate. An inclusion of 20% of TDA in the mixture resulted in specimens with similar strengths and friction angles as the Nevada Sand specimens.

7.2.4 Simple Shear Tests

A laboratory program based on simple shear testing was performed in order to determine the shear strength characteristics and compressibility properties of TDA, TDA/Nevada Sand mixture (50/50 by volume) and Nevada Sand. The main conclusions follow:

- The tendencies observed during the triaxial experimental program under drained conditions in terms of strength and stiffness were similar as those obtained when the materials were tested by means of simple shear technique.
- Simple shear friction angles were found to be lower than those obtained using triaxial compression tests for all materials tested (TDA, TDA/sand mixture and Nevada Sand). The different stress condition created by each method applied to the specimens account for the differences in results.
- The experimental program carried out using simple shear technique also allowed access to 1-D compression behavior prior to shearing. The principal findings in terms of compressibility reveals that the level of instantaneous vertical strain in the TDA was approximately 24 times higher than that exhibited in the Nevada Sand tests.
- Instantaneous vertical strains for a TDA/sand mixtures (50/50 by volume) were found to be only 5.5 times higher than those of Nevada Sand specimens which verifies the important improvements achieved in terms of compressibility when both materials are mixed in equal proportions.
- The results also suggest that TDA creep secondary deformations may be a concern as well in TDA.

7.2.5 Finite Element Predictions of CD Triaxial Compression Tests Using Three Different Constitutive Models

Finite element (FE) analyses were carried out using the following constitutive models: i) Hyperelasticity model; ii) soil hardening model; and iii) porous elasticity. The FE analyses were used to predict the experimental results obtained from CD triaxial compression tests. The main conclusions follow:

- TDA behavior could not be modeled appropriately using a hyperelasticity modeling technique because such modeling cannot capture the confining stress dependence on the TDA stress-strain behavior.
- TDA/sand mixture behavior could be predicted reasonably well by the soil-hardening model. The applicability of the soil hardening model for TDA may be appropriate for up to 7% axial strain deformation, which is reasonable for the common deformation levels expected for most applications. For larger axial strain deformations, the model seems to underpredict TDA strength.
- The porous elasticity model seems an appropriate modeling technique for all materials within the elastic region of stress strain curves; moreover, the model could work reasonably well for materials where deviatoric peak stress is the design criteria since it is able to capture reasonably well the strength at failure.
- A high amount of volume loss during isotropic consolidation was observed during TDA triaxial compression tests, and the porous elasticity model did the best job of capturing this volume compression compared to the other two models used. Furthermore, the porous elasticity model is preferred when trying to numerically predict the compressibility behavior (volumetric change) during consolidation of TDA

materials because it allows simulation of compressibility behavior (volumetric change) during consolidation.

7.3 Recommendations for Future Work

Recommendations for future work and future studies on the feasibility of using TDA for civil engineering applications follow:

- More experimental results are needed from scaled models or field projects involving retaining structures that include TDA layers in the backfills.
- A study is needed showing measurement of TDA lateral pressures under passive conditions.
- For applications involving mixtures of TDA and sands, it is recommended to further assess in more detail the segregation problem observed in TDA/sand mixtures. As mentioned in Chapter 3, some segregation of Nevada sand was observed during the centrifuge models involving the 50/50 by volume mixtures. Segregation may be more prevalent for retaining structures backfill using a TDA based backfill involving coarser TDA sizes. Further investigations are recommended to investigate this issue.
- The experiments carried out in this research included two strain rate levels which were sufficient to highlight the strain rate dependency of some engineering properties. For civil engineering applications involving fast rates of loading it is recommended to carry out a more detailed study regarding of the effect of strain-rate in the TDA mechanical behavior.
- A study is needed to assess the influence of temperature on TDA mechanical properties in order to characterize the material for different field conditions and places.

- A feasibility study is needed to assess the value of using TDA mixed with other recycled aggregates possessing higher stiffness properties such as glass, bottom ash, and shingles. These properties would be considered for numerous infrastructure applications such as retaining structures and embankments.
- Study the applicability of using other numerical methods, such as the discrete element method, as a tool to predict TDA and TDA-soil behavior.

REFERENCES

- ABAQUS (2011). "Analysis User's Manual. Volume III : Materials." Simulia Corp., Providence, RI, USA, 1-677.
- Ahmed, I. (1993). "Laboratory Study on Properties of Rubber-Soils." Purdue University, Indiana. Joint Highway Research Project. Report No. FHWA/IN/JHRP-93/4.
- Ali, A., and Sahari, B. (2010). "A review of Constitutive Models for Rubber Like Materials." *American Journal of Engineering and Applied Science*, 3, 232-239.
- Alzubaidi, R., and Lafta, S. H. (2013). "Effect of Strain Rate on the Strength Characteristics of Soil-Lime Mixture." *Geotechnical and Geological Engineering*, 31(4), 1317-1327.
- Amin, A., Alam, M., and Okui, Y. (2001). "Nonlinear Viscoelastic Response of Elastomers : Experiments, Parameter Identification and Numerical Simulation." *Journal of Structural Engineering*, 47, 181-192.
- Arulmoli, K., Muraleetharan , K. K., Hossain, M. M., and Fruth, L. S. (1992). "VELACS Laboratory Testing Program-Soil Data Report." The Earth Technology Corporation, NSF, Washington, D.C.
- ASTM (2012). "Standard Practice for Use of Scrap Tires in Civil Engineering Applications." ASTM International (6270-08), 1-22.
- Atkinson, J. H., Lau, W. H. W., and Powel, J. J. M. (1991). "Measurement of Soil Strength in Simple Shear Tests." *Can. Geotech*, 28(2), 255-262.
- Aydilek, A., Madden, E. T., and Demirkan, M. (2006). "Field Evaluation of Leachate Collection Systems Constructed with Scrap Tires." *Journal of Geotechnical and Geoenvironmental Engineering*, 132(8), 990-1000.
- Baker, T. E., Allen, T. M., Jenkins, D. V., Money, D. T., Pierce, L. M., Christie, R. A., and Weston, J. T. (2003). "Evaluation of the Use of Scrap Tires in Transportation Related Applications in the State of Washington." Report to the Legislature as Required by SHB 2308, Department of Transportation, Washington., 1-275.
- Benda, C. (1995). "Engineering Properties of Scrap Tires Used in Geotechnical Applications." *Report 95-1*, Materials and Research Division Vermont Agency of Transportation, Montpelier, VT.
- Bosscher, P. J., Edil, T. B., and Kuraoka, S. (1997). "Design of Highway Embankments Using Tire Chips." *Journal of Geotechnical and Geoenvironmental Engineering*, 23(4), 295-304.

- Budhu, M. (1984). "On comparing Simple Shear and Triaxial Test Results." *Journal of Geotechnical Engineering*, 110(12), 1809-1814.
- Casagrande, A., and Shannon, W. L. (1948). "Strength of Soils Under Dynamic Loads." *ASCE*, 591-608.
- Cecich, V., Gonzales, L., Hoisaeter, A., Williams, J., and Reddy, K. (1996). "Use of Shredded Tires as Lightweight Backfill Material for Retaining Structures." *Waste Management & Research*(14), 433-451.
- Celis, H., and Pando, M. (2008). "Evaluacion de Mezclas de Arena y Goma Triturada como Rellenos de Muros de Contencion." Master Thesis, University of Puerto Rico at Mayaguez.
- Clough, W., and Duncan, J. M. (1971). "Finite Element Analyses of Retaining Wall Behavior." *Soil Mechanics and Foundations Division*, 97, 1657-1673.
- Collins, P. (1997). "Geotechnical Properties of Sand Lightweight Aggregate Mixtures." Master, Carleton University.
- Craig, W. H. "The Seven Ages of Centrifuge Modelling." *Proc., Constitutive and Centrifuge Modelling : Two Extremes*, Sarah Springman. Institute for Geotechnical Engineering, Swiss Federal Institute of Technology, 165-174.
- Dickson, T. H., Dwyer, D. F., and Humphrey, D. N. (2001). "Prototype tire-shred embankment construction." *Transportation Research Record 1775*, National Research Council, Transportation Research Board, Washington, D.C, 1-97.
- DOT (2012). "User Guidelines for Waste and Byproduct Materials in Pavement Construction." <<http://www.fhwa.dot.gov/publications/research/infrastructure/structures/97148/st4.cfm> %3E. (2015).
- Drescher, A., Newcomb, D., and Heimdahl, T. (1999). "Deformability of Shredded Tires." University of Minnesota. Sponsored by Minnesota Department of Transportation. Report No MN/RC-1999-13. St. Paul, Minnesota 55155, 1-150.
- Edinclair, A., Baykal, G., and Dengili, K. (2004). "Determination of Static and Dynamic Behavior of Recycled Materials for Highways." *Resources and Recycling* 42(3), 223-237.
- EPA (2015). "Common Wastes & Materials - Scrap Tires. Civil Engineering Applications." <http://www.epa.gov/osw/conserves/materials/tires/civil_eng.htm%3E. (April 7, 2015).
- Fang, Y. S., and Ishibashi, I. (1986). "Static Earth Pressures with Various Wall Movements." *Journal of Geotechnical Engineering*, 112(3), 317-333.

- Foose, G. J., Benson, C. H., and Bosscher, P. J. (1996). "Sand Reinforced With Shredded Waste Tires." *Journal of Geotechnical Engineering*, 122(9), 760-767.
- Garcia-Theran, M., Pando, M., Celis, H., and Abdoun, T. "Estimation Challenges of Lateral Pressures in Retaining Structures Using Granular Recycled Tire Aggregates as Backfill." *Proc., Geo-Congress 2014. Geo-Characterization and Modeling for Sustainability*, ASCE. Geotechnical Special Publication No.234 3666-3675.
- Geocomp-Corp. (2011). "Versatile Load Frame System for Running Fully Automated Unconfined Compression, Consolidation, Triaxial, Cyclic, CBR and Resilient Modulus Tests." 1-40.
- Ghazavi, M., and Sakhi, M. (2005). "Influence of Optimized Tire Shreds on Shear Strength Parameters of Sand." *International Journal of Geomechanics* 5, 58-65.
- Ha, D. (2007). "Evaluation of Ground Rupture Effect on Buried HDPE Pipelines." PhD, Rensselaer Polytechnic Institute.
- Harrop-Williams, K. O. (1989). "Geostatic Wall Pressures." *Journal of Geotechnical Engineering*, 115(9), 1321-1325.
- Helstrom, C. L., Weaver, J. W., and Humphrey, D. N. (2010). "Lateral Pressures Behind Retaining Walls Backfilled with Tire Derived Aggregate." http://www.haleyaldrich.com/downloads/publications/retaining_walls_tda.pdf%3E.
- Holtz, R., and Kovacs, W. (1981). *An Introduction to Geotechnical Engineering*, Prentice Hall, Englewood Cliffs, New Jersey.
- Hoppe, E. J., and Mullen, W. G. (2004). "Field Study of a shredded-embankment in Virginia." Virginia Transportation Research Council(A Cooperative Organization Sponsored Jointly by the Virginia Department of Transportation and the University of Virginia) In Cooperation with the U.S. Department of Transportation Federal Highway Administration Charlottesville, 1-55.
- Huggins, E. L. (2012). "Numerical and Realibility Analysis of Gravity Cantilever Retaining Walls Backfilled With Shredded Tires Subjected to Seismic Loads." Master, Clemson
- Humphrey, D. N. (1996). "Investigation of Exothermic Reaction in Tire Shred Fill Located in Ilwaco, Washington."Prepared for Federal Highway Administration, Washington, D.C.
- Humphrey, D. N. (1999). "Civil Engineering Applications of Tire Shreds." *The Tire Industry Conference*. Hilton Head, South Carolina, 1-16.

- Humphrey, D. N. (2004). "Effectiveness of Design Guidelines for Use in Tire Derived Aggregate as Lightweight Embankment Fill." *Recycled Materials in Geotechnics ASCE Civil Engineering Conference and Exposition* 61-74.
- Humphrey, D. N. "Tire Derived Aggregate as Lightweight Fill For Embankments and Retaining Walls." *Proc., Scrap Tire Derived Geomaterials-Opportunities and Challenges*, Taylor & Francis Group, 59-81.
- Humphrey, D. N., and Blumenthal, M. (2011). "The Use of Tire-Derived Aggregate in Road Construction." *Green Streets Highways 2010*, ASCE 2011, 1-15.
- Humphrey, D. N., and Katz, L. E. (2001). "Five-Year Study of the Water Quality Effects of Tire Shreds Placed Above the Water Table." Department of Civil and Environmental Engineering, University of Maine, 5711 Boardman Hall, Orono, ME, 1-7.
- Humphrey, D. N., Sandford, T. C., Cribbs, M. M., and Manion, W. P. (1993). "Shear Strength and Compressibility of Tire Chips for Use as Retaining Wall Backfill." *Transportation Research Record*, No.1422, National Research Council, Transportation Research Board, Washington, D.C., 29-35.
- Humphrey, D. N., and Swett, M. (2006). "Literature Review of Water Quality Effects of Tire Derived Aggregate and Rubber Modified Asphalt Pavement." University of Maine, Department of Civil and Environmental Engineering. Prepared for U.S. Environmental Protection Agency, 1-57.
- Humphrey, D. N., Whetten, N., Weaver, J., Recker, K., and Cosgrove, T. (1998). "Tire Shreds as Lightweight Fill for Embankments and Retaining Walls." *Geocongress 1998. Recycled Materials in Geotechnical Applications*, ASCE, Boston, MA, 51-65.
- ITASCA (2015). "FLAC. Explicit Continuum Modeling of Non-Linear Material Behavior in 2D." <<http://www.itascacg.com/software/flac%3E>.
- Jakel, R. (2010). "Analysis of Hyperelastic Materials with Mechanics-Theory and Application Examples." *Second SAXSIM I Technische Universitat Chemnitz*, 1-72.
- Kim, D., and Ha, S. (2014). "Effects of Particle Size on the Shear Behavior of Coarse Grained Soils Reinforce with Geogrid." *Materials*, 7, 963-979.
- Kim, Y. S. (2009). "Static Simple Shear Characteristics of Nak-dong River Clean Sand." *KSCE Journal of Civil Engineering*, 13(6), 389-401.
- Kutter, B. L., and Chen, Y. R. (1997). "Constant p' and Constant Volume Friction Angles Are Different." *Geotechnical Testing Journal*, 20(3), 304-316.
- Lambe, W., and Whitman, R. (1969). *Soil Mechanics*, John Wiley & Sons, New York.

- Lee, J. H., Salgado, R., Bernal, A., and Lovell, C. W. (1999). "Shredded Tires and Rubber-Sand as Lightweight Backfill." *Journal of Geotechnical and Geoenvironmental Engineering*, 125(2), 132-141.
- Li, X. S., and Dafalias, Y. F. (2000). "Dilatancy for Cohesionless Soils." *Geotechnique*, 50(4), 449-460.
- Liu, H., Mead, J., and Stacer, R. (1998). "Environmental Impacts of Recycled Rubber in Light Fill Applications : Summary & Evaluation of Existing Literature." University of Massachusetts, Chelsea Center for Recycling and Economic Development, 1-17.
- Madabhushi, G. (2015). *Centrifuge Modelling for Civil Engineers*, CRC Press. Taylor & Francis Group.
- Madabhushi, S. P. G. (2004). "Modelling of Earthquake Damage Using Geotechnical Centrifuges." *Current Science*, 87, 1405-1416.
- Masad, E., Taha, R., Ho, C., and Papagiannakis, T. (1996). "Engineering Properties of Tire/Soil Mixtures as a Lightweight Fill Material." *Geotechnical Testing Journal, ASTM*, 19(3), 297-304.
- McGuire, S. (2011). "Comparison of Direct Simple Shear Confinement Methods on Clay and Silt Specimens." Master, University of Rhode Island.
- Mei, G., Chen, Q., and Song, L. (2009). "Model for Predicting Displacement-Dependent Lateral Earth Pressure." *Can. Geotech*, 46, 969-975.
- Mills, B. (2008). "Recycled Tires as Lightweight Fill." *Annual Conference of the Transportation Association of Canada. Recycled Materials and Recycling Processes for Sustainable Infrastructure* Toronto, Canada, 1-14.
- Moo-Young, H., Sellasie, K., Zeroka, D., and Sabnis, G. (2003). "Physical and Chemical Properties of Recycled Tire Shreds for Use in Construction." *Journal of Environmental Engineering*, 129(10), 921-929.
- Nightingale, D. E., and Green, W. P. (1997). "An Unsolved Riddle: Tire Chips, Two Roadbeds, and Spontaneous Reactions." *Testing Soil Mixed with Waste or Recycled Materials*, ASTM STP 1275, West Conshohocken, PA, 265-285.
- O'Shaughnessy, V., and Garga, V. K. (2000). "Tire-Reinforced Earthfill. Part 3: Environmental Assessment." *Can. Geotech*, 37(1), 117-126.
- Palmer, M. C., O'Rourke, T. D., Olson, N., A., Abdoun, T., Ha, D., and O'Rourke, M. J. (2009). "Tactile Pressure Sensors for Soil-Structure Interaction Assessment." *Journal of Geotechnical and Geoenvironmental Engineering*, 135(11), 1638-1645.

Patenaude, S. M., and Wright, J. (2014). "Civil Engineering Applications Utilizing Tire Derived Aggregate (TDA)."

<<http://www.calrecycle.ca.gov/Tires/GreenRoads/Downloads/TDA.pdf>&3E.

PLAXIS (2014). "Material Models Manual." 1-2004.

Reddy, K., and Marella, A. (2001). "Properties of Different Size Scrap Tire Shreds: Implications on Using as Drainage Material in Landfill Cover Systems." *The Seventh International Conference on Solid Waste Technology and Management* October 2001, Philadelphia, PA, USA, 1-19.

RMA (2006). "Scrap Tire Markets in the United States." Rubber Manufacturers Association, 1-93.

RMA (2013). "2011 U.S. Scrap Tire Market Summary." Rubber Manufacturers Association, Washington, DC, 1-15.

Rossato, G., and Simonini, P. (1991). "Stress-Strain Behavior of Sands in Triaxial and Direct Simple Shear Tests." *Can. Geotech*, 28(2), 276-281.

Seed, H. B., and Lundgren, R. (1954). "Investigation of the Effect of Transient Loadings on the Strength and Deformation Characteristics of Saturated Sands." *ASTM* 54, 1288-1306.

Sherif, M. A., Fang, Y. S., and Sherif, R. I. (1984). "Ka and Ko Behind Rotating and Non-Yielding Walls." *Journal of Geotechnical Engineering*, 110(1), 41-56.

Sivadass, T., and Lee, C. Y. "Simple Shear Testing of Residual Soils with High Silt Content." *Proc., ICCBT 2008*, 1-16.

Soganci, A. S. (2014). "Strength Characteristics of Tire-Sand Mixtures." *Soil Mechanics and Foundation Engineering*, 51(6), 306-309.

Strenk, P. M., Wartman, J., Grubb, D. G., Humphrey, D. N., and Natale, M. F. (2007). "Variability and Scale-Dependency of Tire-Derived Aggregate." *Journal of Materials in Civil Engineering*, 19(3), 233-241.

Surarak, C., Likitlersuang, S., Wanatowski, D., Balasubramaniam, A., and Guan, H. (2012). "Stiffness and Strength Parameters for Hardening Soil Model of Soft and Still Bangkok Clays." *Soils and Foundations*, 52(4), 682-697.

Tandon, V., Velazco, D. A., Nazarian, S., and Picornell, M. (2007). "Performance Monitoring of Embankments Containing Tire Chips: Case Study." *Journal of Performance of Constructed Facilities*, 21(3), 207-214.

Tatlisoz, N., Benson, C., and Edil, T. (1997). "Effects of Fines on Mechanical Properties of Soil-Tire Chip Mixtures." *Testing Soil with Wst or Recycled Materilas*, K. B. L. Mark A. Wasemiller, ed., STP 1275, ASTM, Conshohocken, PA., 93-108.

Taylor, D. W. (1948). *Fundamentals of Soil Mechanics*, John Wiley & Sons, Inc., New York State College of Agriculture at Cornell University, Ithaca, NY.

Tweedie, J. J., Humphrey, D. N., and Sandford, T. C. (1998). "Full Scale Field Trials of Tire Shreds as Lightweight Retaining Walls Backfill : At Rest Conditions." *Transportation Research Board, 77th Annual Meeting* Washington, D.C., 1-21.

Tweedie, J. J., Humphrey, D. N., and Sandford, T. C. (1998). "Tire Shreds as a Lightweight Retaining Wall Backfill : Active Conditions." *Journal of Geotechnical and Geoenvironmental Engineering*, 124(11), 1061-1070.

Ubilla, J. O. (2007). "Physical Modeling of the Effects of Natural Hazards on Soil-Structure Interaction." Ph.D, Rensselaer Polytechnic Institute.

Valdez, J., and Evans, M. (2008). "Sand-Rubber Mixtures : Experiments and Numerical Simulations." *Can. Geotech*, 45, 588-595.

Wartman, J., Natale, M. F., and Strenk, P. M. (2007). "Immediate and Time-Dependent Compression of Tire Derived Aggregate." *Journal of Geotechnical and Geoenvironmental Engineering*, 133(3), 245-256.

Whitman, R., and Healy, K. A. (1962). "Shear strength of Sands During Rapid Loading." *Journal Soil Mech. Found. Div.*, 88, 99-132.

Wijewickreme, D., Dabeet, A., and Byrne, P. (2013). "Some observations on the State of Stresses in the Direct Simple Shear Test Using 3D Discrete Element Analysis." *ASTM*, 36(2).

Wu, W. Y., Benda, C. C., and Cauley, R. F. (1997). "Triaxial Determination of Shear Strength of Tire Chips." *Journal of Geotechnical and Geoenvironmental Engineering*, 123(5), 479-482.

Xiao, M., Ledezma, M., and Hartman, C. (2014). "Large-Scale Shear Testing of Tire Derived Aggregates (TDA)." *Proc., Geo-Congress 2014. Geo-Characterization and Modeling for Sustainability*, ASCE. Geotechnical Special Publication No.234, 3744-3753.

Yang, Z., Lohnes, R. A., and Kjartanson, B. (2002). "Mechanical Properties of Shredded Tires." *ASTM International*, 25(1), 44-52.

Yoon, S., Prezzi, M., Siddiki, N. Z., and Kim, B. (2006). "Construction of a test embankment using a sand-tire shred mixture as fill material." *Waste Management & Research*, 26, 1033-1044.

Youwai, S., and Bergado, D. (2003). "Strength and deformation characteristics of shredded rubber tire-sand mixtures." *Can. Geotech*, 40(2), 254-264.

Yowwai, S., and Bergado, D. (2004). "Numerical Analysis of Reinforced Wall Using Rubber Tire Chips-Sand Mixtures as Backfill Material." *Computers and Geotechnics*, 31, 103-114.

Zornberg, J. G., Cabral, A. R., and Viratjandr, C. (2004). "Behavior of Tire Shred-Sand Mixtures." *Can. Geotech*, 41, 227-241.

Zornberg, J. G., Costa, Y., and Vollenweider, B. (2004). "Mechanical Performance of a Prototype Embankment Backfill Built with Tire Shreds and Cohesive Soils." *TRB 2004 Annual Meeting* Washington, D.C, 1-20.

APPENDIX A: INDEX PROPERTIES

Table A.1: Sieve analysis for Nevada sand ($D_{50} = 0.15$ mm) ASTM D 422

Sieve No.	Sieve opening (mm)	Sieve weight (g)	Weight of sieve + soil retained (g)	Weight retained (gr)	Percent retained (%)	Cumulative percent retained (%)	Percent passing (%)
10	2.000	472.54	472.54	0	0	0	100
20	0.850	426.8	426.8	0.0	0.00	0.00	100.00
40	0.425	337.0	344.5	7.5	1.51	1.50	98.50
50	0.340	356.4	384.1	27.8	5.55	7.05	92.95
60	0.250	344.9	376.3	31.4	6.27	13.32	86.68
140	0.106	325.3	705.0	379.6	75.86	89.18	10.82
200	0.075	325.3	367.0	41.7	8.33	97.51	2.49
Pan	---	348.3	360.8	12.5	2.49	100.00	0.00
			$\Sigma =$	500.48	100.00		

Table A.2: Sieve analysis for TDA ($D_{50} = 1.2$ mm) ASTM D 422

Sieve No.	Sieve opening (mm)	Sieve weight (g)	Weight of sieve + soil retained (g)	Weight retained (gr)	Percent retained (%)	Cumulative percent retained (%)	Percent passing (%)
4	4.75	519.68	519.68	0	0	0	100
10	2.000	472.5	475.0	2.4	0.96	0.96	99.04
20	0.850	426.8	627.0	200.2	79.43	80.39	19.61
40	0.425	337.0	379.3	42.3	16.78	97.17	2.83
50	0.340	356.3	360.0	3.7	1.48	98.66	1.34
60	0.250	344.9	346.1	1.2	0.49	99.15	0.85
140	0.106	325.3	327.2	1.9	0.73	99.88	0.12
200	0.075	325.3	325.6	0.3	0.12	100.00	0.00
Pan	---	447.6	447.6	0.0	0.00	100.00	0.00
			$\Sigma =$	252.07	100.00		

Table A.3: Sieve analysis for TDA ($D_{50} = 2.6$ mm) ASTM D422

Sieve No.	Sieve opening (mm)	Sieve weight (g)	Weight of sieve + soil retained (g)	Weight retained (gr)	Percent retained (%)	Cumulative percent retained (%)	Percent passing (%)
4	4.75	519.68	519.68	0.00	0.00	0.00	100.00
10	2.000	472.54	666.90	194.36	73.80	73.80	26.20
20	0.850	426.81	495.54	68.73	26.10	99.90	0.10
40	0.425	336.98	337.09	0.11	0.04	99.94	0.06
50	0.340	356.25	356.35	0.10	0.04	99.98	0.02
60	0.250	344.88	344.93	0.05	0.02	100.00	0.00
140	0.106	325.32	325.32	0.00	0.00	100.00	0.00
200	0.075	326.31	326.31	0.00	0.00	100.00	0.00
Pan	---	447.55	447.55	0.00	0.00	100.00	0.00
			$\Sigma =$	263.35	100		

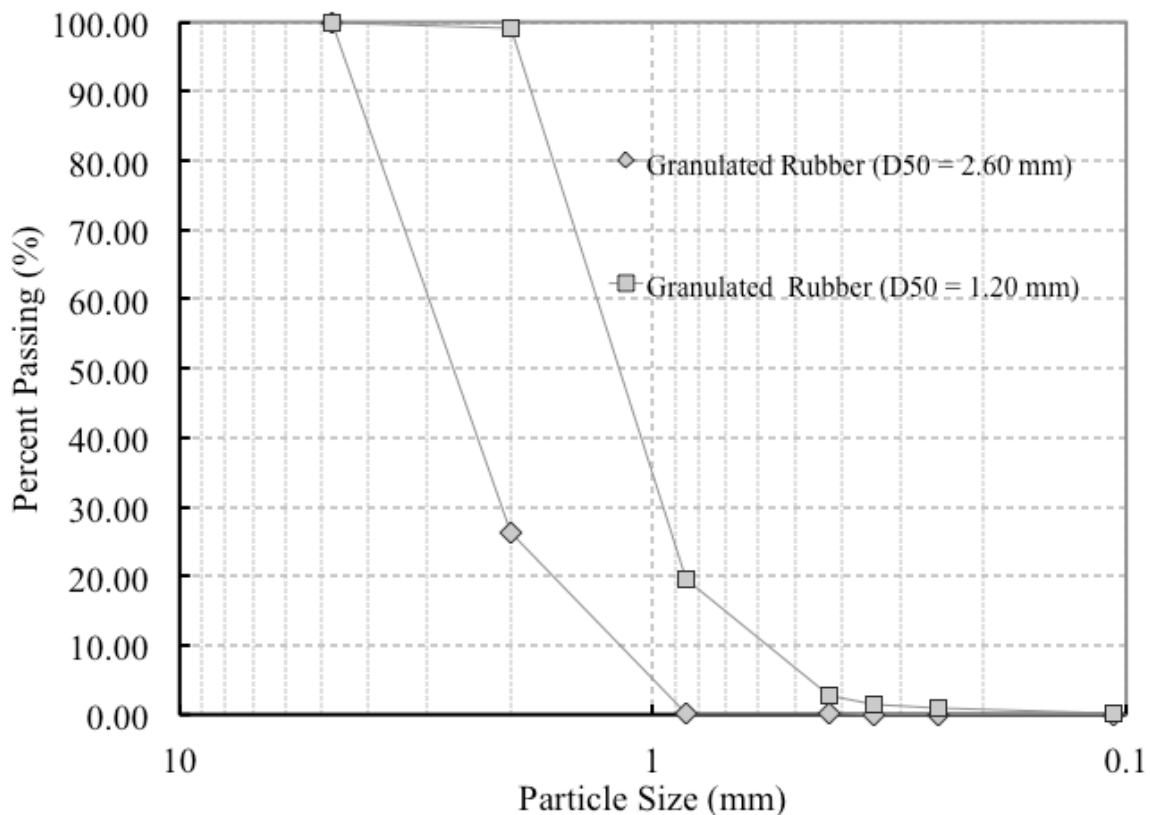


Figure A.1: Sieve analysis curves for TDA materials tested



Figure A.2: Sieve analysis for TDA material

Table A.4: Specific gravity results for materials tested (ASTM D854)

Material	MS (gr)	MP (gr)	MPW (gr)	MPWS (gr)	T (c°)	K	G _s	Average G _s
Nevada Sand	53.14	110.44	359.15	392.49	24	0.9991	2.68	2.67
	53.14	115.38	364.06	397.36	24	0.9991	2.68	
	53.14	112.51	361.21	394.32	24	0.9991	2.65	
TDA (D ₅₀ =1.2 mm)	27.8	110.44	359.11	362.96	24	0.9991	1.16	1.15
	27.8	115.38	364.1	367.37	24	0.9991	1.13	
	27.8	112.51	361.19	364.75	24	0.9991	1.15	
TDA (D ₅₀ =2.6 mm)	31.35	110.44	359.17	363.74	24	0.9991	1.17	1.17
	31.35	115.38	364.04	369.08	24	0.9991	1.19	
	31.35	112.51	361.16	365.57	24	0.9991	1.16	

Where:

MS = Mass of solids, MP = Mass of the picnometer, MPW = Mass of the picnometer + water, MPWS = Mass of the picnometer + water + solids, T = Temperature, K = Temperature correction factor, G_s = Specific gravity.

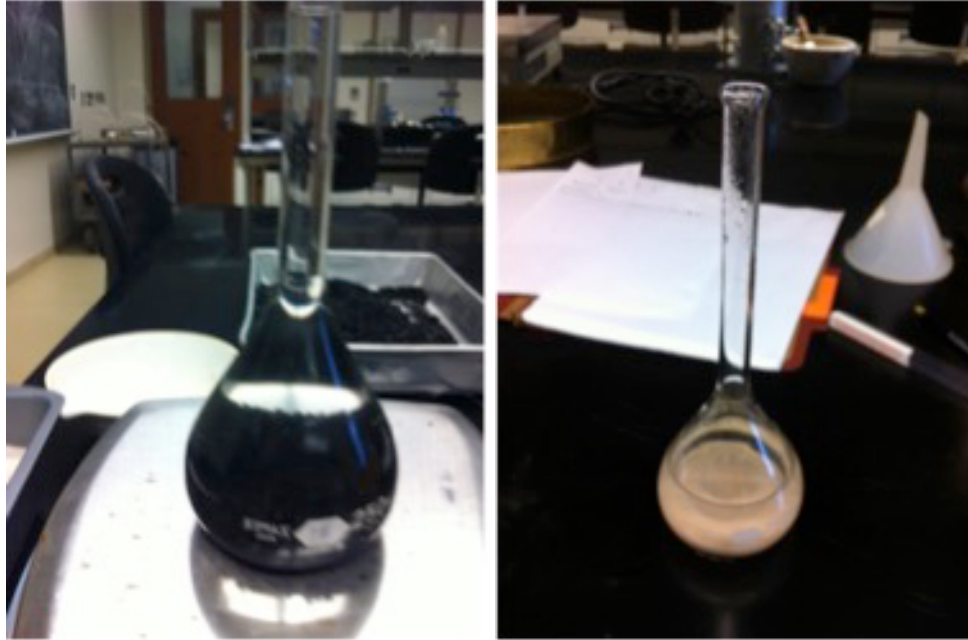


Figure A.3: Specific gravity test for TDA and Nevada sand

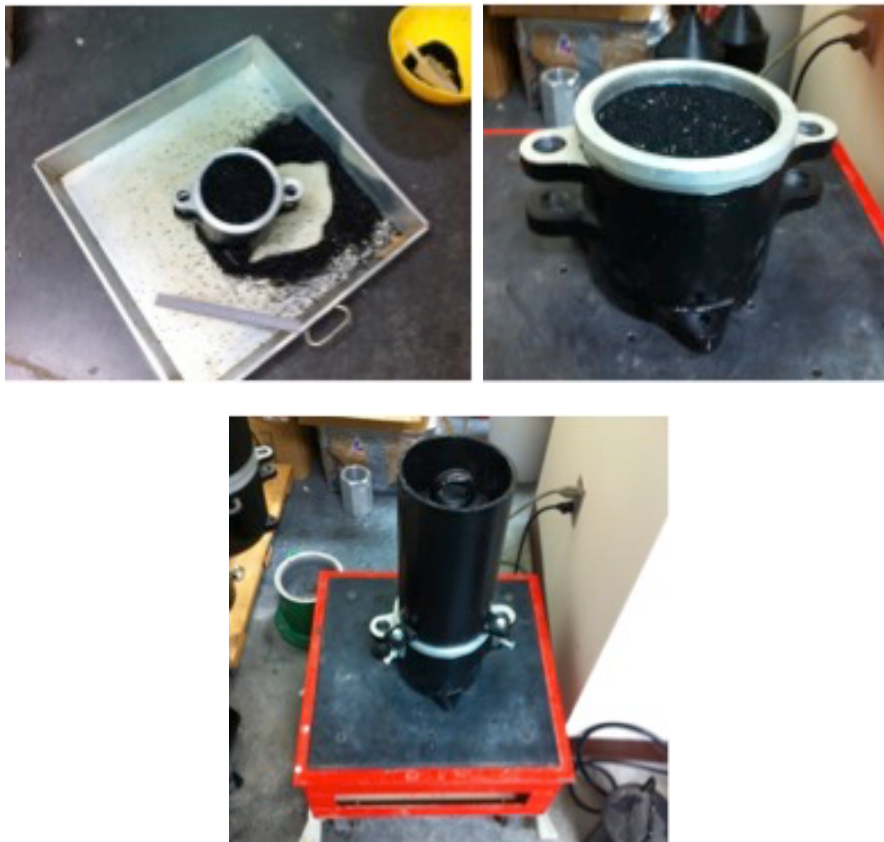


Figure A.4: Minimum and maximum density test

Table A.5: Minimum and maximum density tests (ASTM D 4253)

Minimum Density Test Data			
Parameter	TDA ($D_{50}=1.2$ mm)	TDA ($D_{50}=2.6$ mm)	Nevada Sand
Mold Height (cm)	15.558	15.558	15.558
Average Diameter (cm)	12.535	12.535	12.535
Mold Volume (m^3)	0.00192	0.00192	0.00192
Mold Weight (kg)	3.398	3.398	3.398
W mold + Solids (Kg)	4.328	4.322	6.123
W solids (Kg)	0.930	0.924	2.725
Minimum Density (kg/m^3)	484.37	481.25	1419.27
Minimum Unit Weight (kN/m^3)	4.75	4.72	13.92
Maximum Density Test Data			
$\Delta 1$ (mm)	26.46	27.17	28.67
$\Delta 2$ (mm)	30.21	27.35	28.58
$\Delta 3$ (mm)	29.58	27.76	28.02
$\Delta 4$ (mm)	28.33	26.38	28.92
$\Delta 5$ (mm)	27.97	26.69	28.31
$\Delta 6$ (mm)	26.22	27.56	28.09
Average Δ (cm)	2.81	2.72	2.84
Final Height (cm)	12.74	12.84	12.71
Final Volume (m^3)	0.001573	0.001585	0.001569
Maximum Density (Kg/m^3)	591.28	583.00	1736.64
Maximum Unit Weight (kN/m^3)	5.80	5.72	17.04

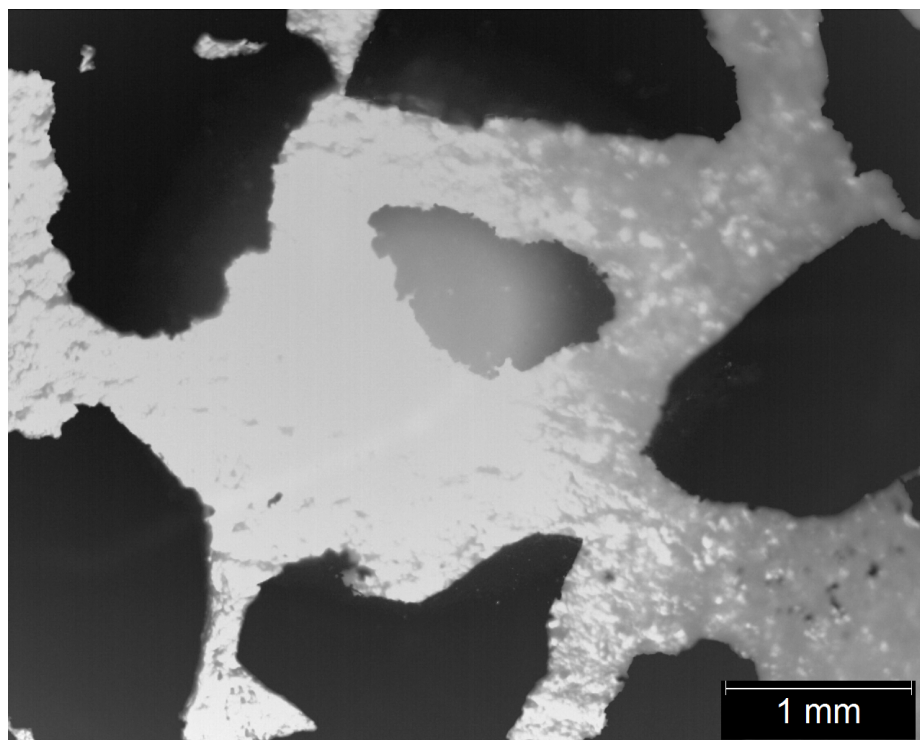


Figure A.5: Optical microscope x 25 Fine TDA

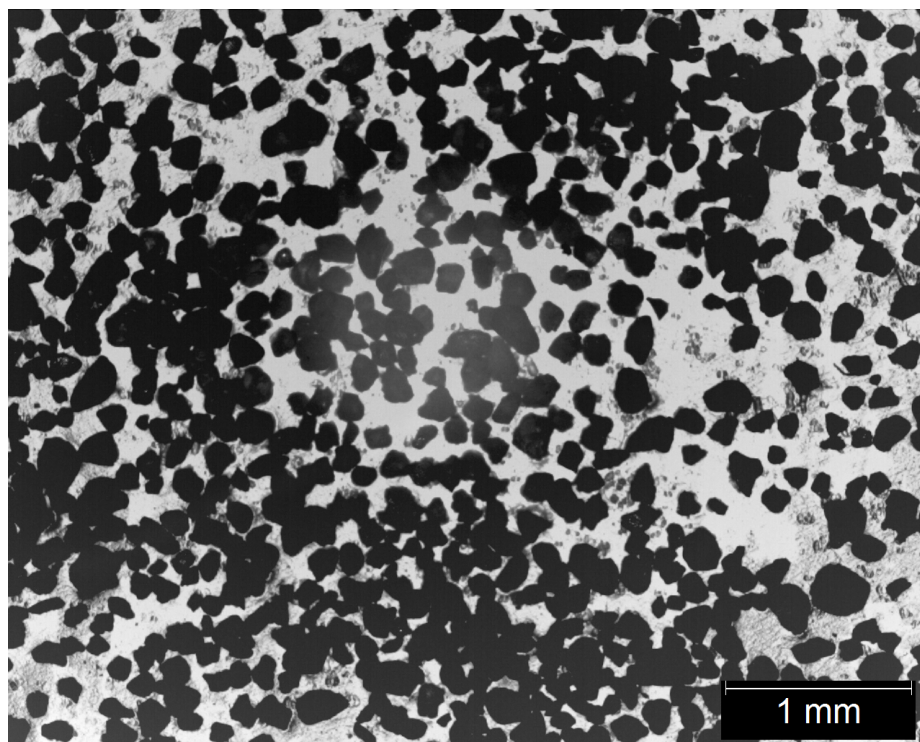


Figure A.6: Optical microscope x 25 Nevada sand

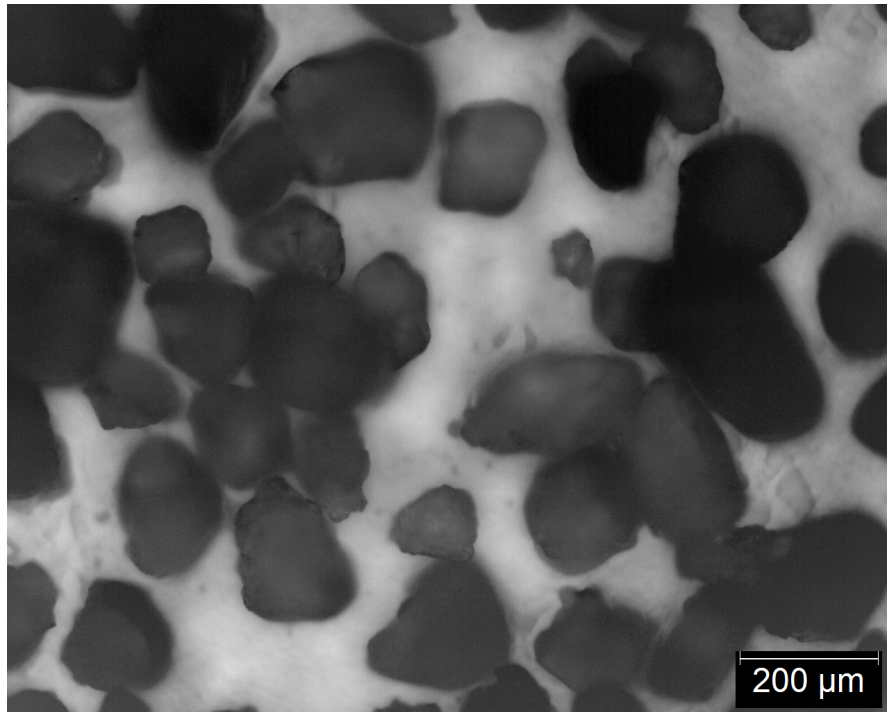


Figure A.7: Optical microscope x 100 Nevada sand



Figure A.8: Coarse TDA material tested in this research

APPENDIX B: ADDITIONAL INFORMATION ON CENTRIFUGE MODELS

B.1. Additional centrifuge model figures



Figure B.1: Aluminium retaining wall used in centrifuge tests

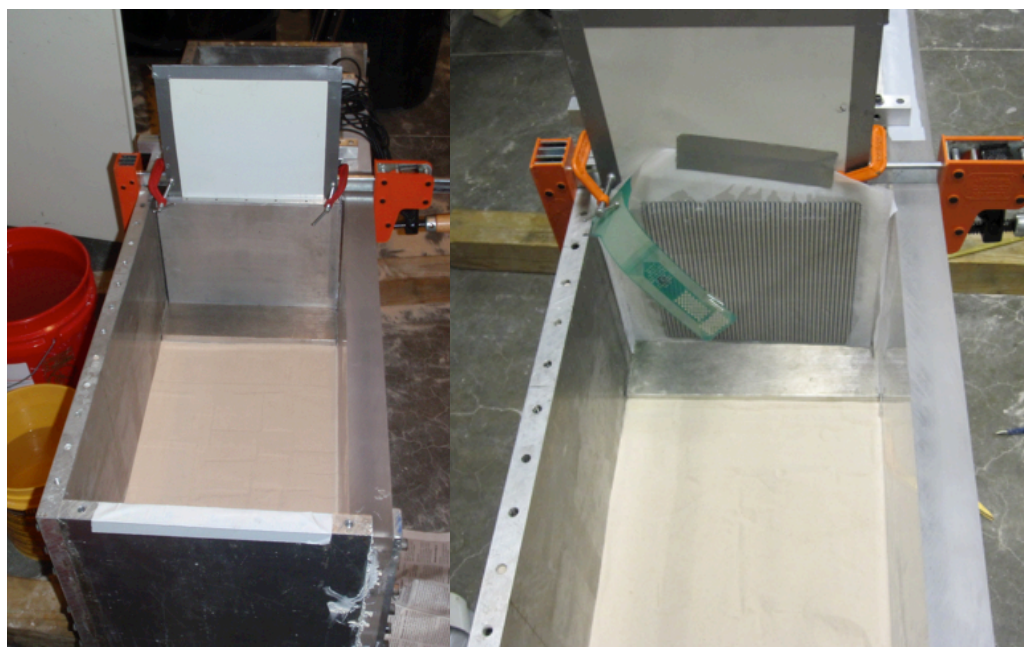


Figure B.2: Detail of aluminium retaining wall placement and sensor attachment to the wall for models 3 and 4

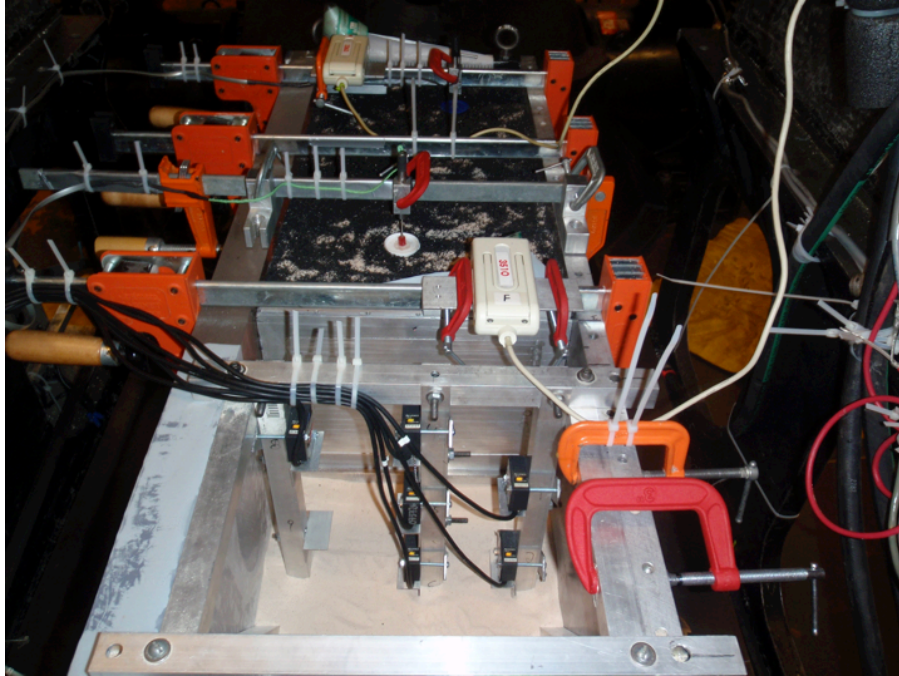


Figure B.3: Detail of laser sensors in front of the retaining wall face for model 4 in the centrifuge room

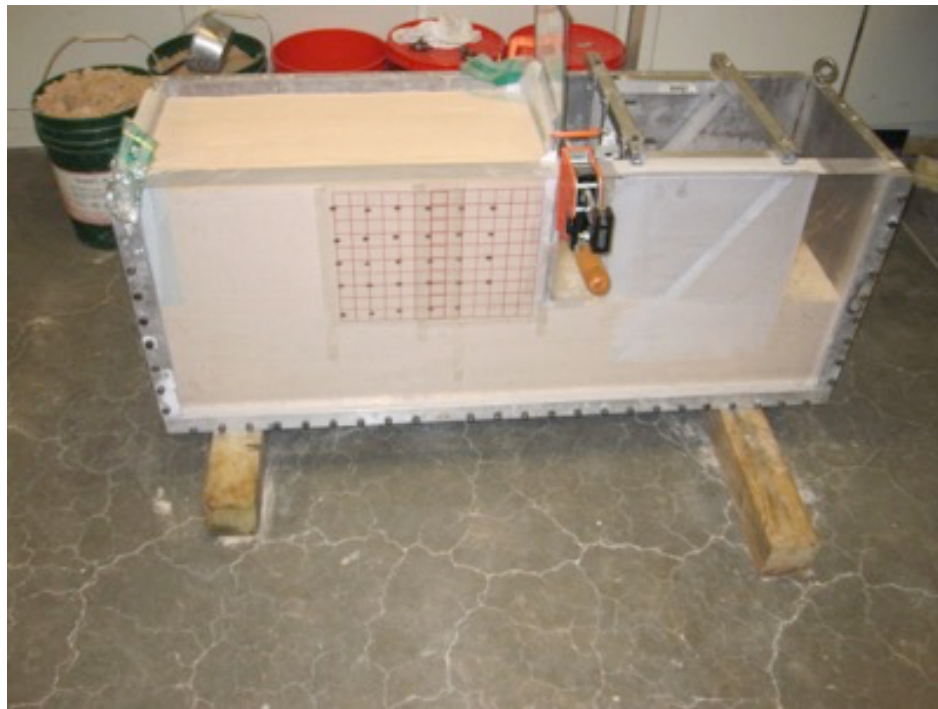


Figure B.4: Retaining wall model using Nevada sand

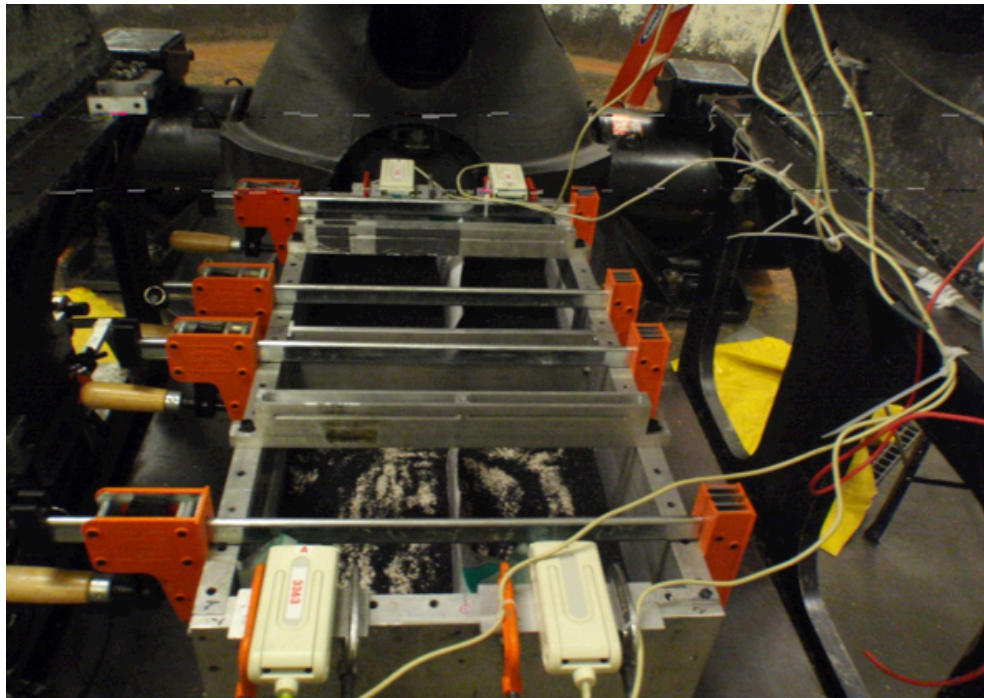


Figure B.5: Model 2 set up in the centrifuge room

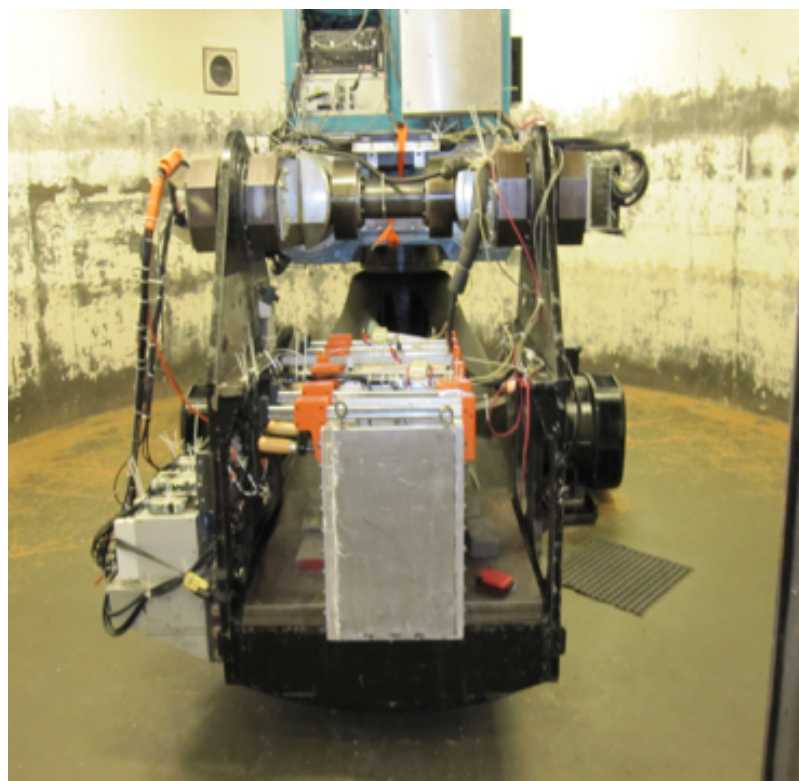


Figure B.6: Model 4 in centrifuge room to start spinning

B.2. Laser displacement sensors

Laser displacement sensors determine the distance from the sensor to an object (the face of the retaining wall for this research) by triangulation as shown in Figure 10.7. The specifications available and used at RPI were the Keyence LB-11 (sensor) and LB-70 (controller). Laser triangulation sensors determine the position of a target by measuring reflected light from the target surface. A 'transmitter' (laser diode) projects a spot of light to the target, and its reflection is focused via an optical lens on a light sensitive device or 'receiver'. If the target changes its position from the reference point the position of the reflected spot of light on the detector changes as well. The signal conditioning electronics of the laser detects the spot position on the receiving element and, following linearization and additional digital or analogue signal conditioning, provides an output.

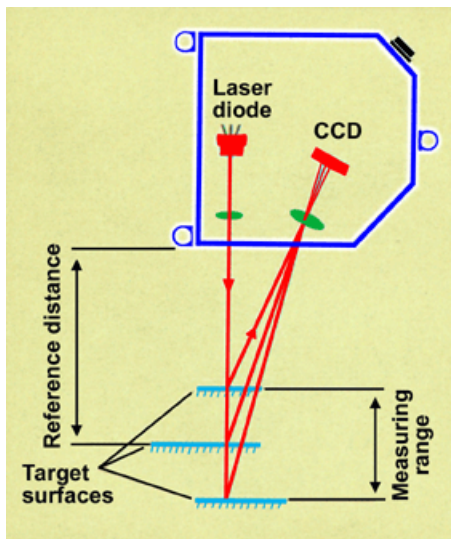


Figure B.7: Laser displacement sensor operation mechanism (adapted from www.sensorland.com)

This kind of sensor is capable of accurately measuring a dynamic movement without physical contact between the sensor and the moving object. More information about this kind of sensors can be found at <http://www.keyence.com/>.

The installation procedure consisted of connecting the sensor head to the sensor controller and turning on the sensor by activating the key power switch. The output of the sensor was monitored by putting a target (for example your hand) in front of the laser. If the target was too close or too far from the sensor head the light was expected to be red. If the target was within the sensor range the light was expected to be yellow and if the target was at the center of the sensor range the light was to be green. The output of the sensor is a change in voltage which was interpreted as a change in distance from the sensor to the target. Figure 10.8 shows the principal components of the sensor. The range of the sensor is +/- 4 cm from a reference distance of 10cm to the sensor head.

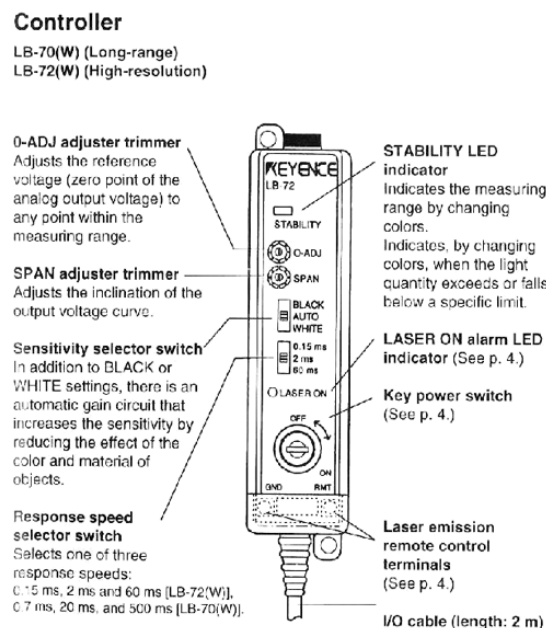


Figure B.8: Laser displacement sensor components (Adapted from Ubilla 2007)

B.3. Tactile pressure sensors

The tactile pressure sensor system is manufactured by Tekscan Inc. The Tekscan sensor sheet model 5250 with a pressure range up to 172 kPa (25 psi) was selected for this research. The 5250 sheet has a square shape of 246 mm by 246 mm (7.9 inches by 7.9 inches). The calibration was carried out by using the Tekscan equilibrator/calibrator. The equilibrator/calibrator is composed of mainly two parts: 1) the control panel, and 2) the loading cell. A pressure gage is attached to the loading cell to indicate the current pressure in the cell, which equals to the pressure applied on the sensor sheet (Ha 2007). Figure 10.9 shows a sketch of the calibration equipment while Figure 10.10 shows the tactile sensor inserted in the equipment to be equilibrated.

The procedure consisted of two stages: equilibration and calibration. Equilibration should be carried out before calibration. First, apply a uniform pressure to the entire area of the sensor. Then I-Scan software (the software for tactile sensor data acquisition) determines a gain (scale factor) for each sensel such that its Digital Output (DO) is equal to the average DO of all loaded sensels. This process compensates for the difference in sensitivity between sensels due to manufacturing, and/or repeated use of the sensor. Applying a uniform pressure is also useful as a quality assurance check on the sensor, to confirm that the sensor has an acceptable uniform output, is operating correctly, and no rows or columns have lost continuity.

Calibration is the process of correlating the digital output from the sensel to engineering units (force or pressure). Both single load calibration and two-load calibration can be used. The single load calibration is easy to perform and understand. However, it is not suitable for the case when there is a huge variation of output range over time. In those cases, two-load (non-linear) calibration should be used. The two-load

calibration utilizes a sophisticated algorithm, which processes the load distribution through a “histogram” method. The advantage of two-load (non-linear) calibration is that it may help reduce errors, and provide greater accuracy, especially if the total load in the experiment varies over large range. In this research, two-load calibration was performed at pressures of 0.5 psi and 15 psi.

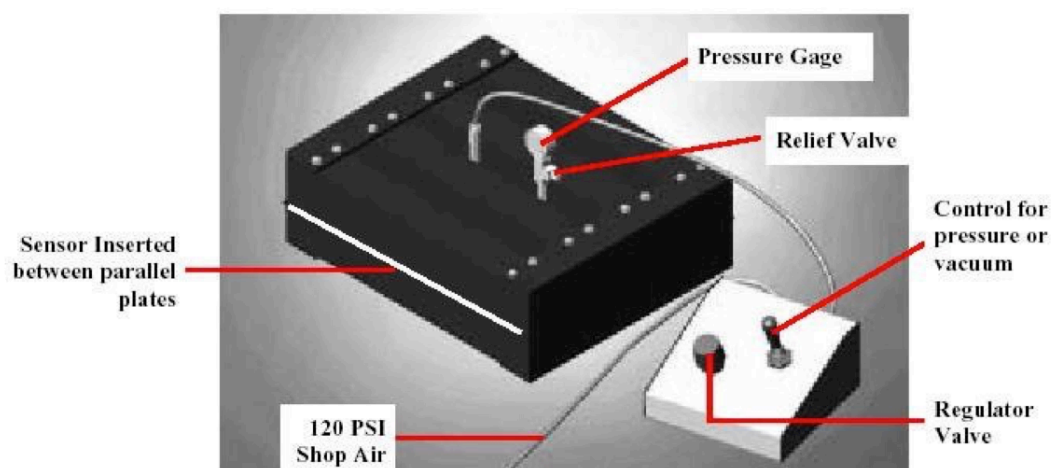


Figure B.9: Tactile sensor calibration equipment (Adapted from Ha 2007)



Figure B.10: Tactile sensor calibration equipment

As already known, tactile pressure sensors were used during this research to measure the lateral pressure along the height of the rigid containers. Figure 10.11 shows a snapshot of one of the tactile sensors during model 1. Each column in the figure represents the lateral pressure variation with depth along the container. The tactile sensor continuously records pressure during the tests

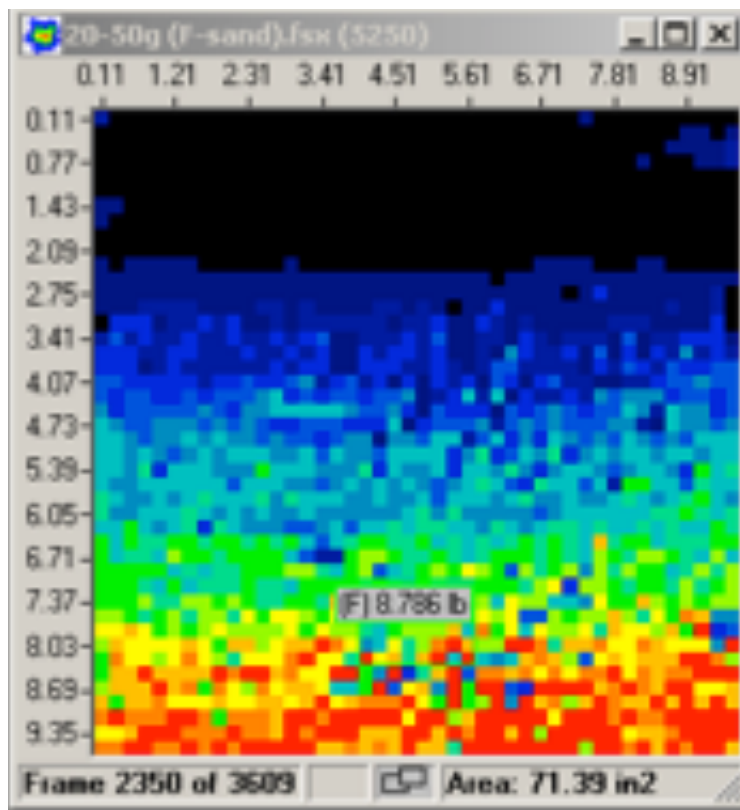


Figure B.11: Tactile pressure sensor print screen from I-Scan software

B.4. Samples of at-rest lateral pressure test results

Table B.1: At-rest lateral pressures at 40 g for backfills tested

Depth (m)	Normalized Depth	Lateral Pressure (kPa)			
		Nevada sand (Model 1)	TDA/sand Mixture (Model 1)	TDA/sand Mixture (Model 2)	TDA (Model 2)
0.00	0.00	0.00	0.00	0.00	0.00
0.23	0.03	1.19	0.61	0.69	0.00
0.45	0.06	2.53	0.55	0.76	0.21
0.68	0.09	4.32	1.10	0.90	0.34
0.91	0.12	6.11	1.84	1.17	0.55
1.13	0.15	7.45	2.02	2.21	0.55
1.36	0.18	9.24	2.58	3.59	0.76
1.59	0.21	10.88	3.19	2.34	0.76
1.81	0.24	13.12	3.44	3.65	1.24
2.04	0.27	14.61	4.91	5.31	1.72
2.27	0.30	16.84	7.12	6.55	2.96
2.49	0.33	18.93	10.25	5.72	2.48
2.72	0.36	22.06	11.90	5.72	2.96
2.95	0.39	23.10	15.28	7.65	2.76
3.17	0.42	22.21	11.84	12.13	3.31
3.40	0.45	25.19	10.98	13.79	3.03
3.63	0.48	26.53	11.11	12.82	3.86
3.85	0.52	27.57	12.76	10.89	4.14
4.08	0.55	29.21	12.95	12.82	5.10
4.31	0.58	30.85	14.91	10.96	4.83
4.53	0.61	31.60	15.89	14.48	5.58
4.76	0.64	32.64	13.87	13.38	6.07
4.99	0.67	33.39	17.06	17.72	6.27
5.21	0.70	34.43	18.29	14.75	6.76
5.44	0.73	35.47	17.98	17.10	6.62
5.67	0.76	36.52	30.44	33.09	6.83
5.89	0.79	37.56	28.17	28.41	7.79
6.12	0.82	38.60	21.78	28.82	8.00
6.35	0.85	39.65	24.61	16.55	9.38
6.57	0.88	40.69	29.58	20.27	9.10
6.80	0.91	41.73	36.94	29.65	9.17
7.03	0.94	42.78	40.81	29.30	8.76
7.25	0.97	43.82	43.45	43.85	9.86
7.48	1.00	44.86	37.12	44.54	10.89

Table B.2: TDA lateral pressure at different times for 40g-level

Depth (m)	LATERAL PRESSURE							
	TDA 5min (psi)	TDA 20min (psi)	TDA 60min (psi)	TDA 120min (psi)	TDA 5min (kPa)	TDA 20min (kPa)	TDA 60min (kPa)	TDA 120min (kPa)
0.00	0	0	0	0	0	0	0	0
0.23	0	0.01	0.01	0.01	0.00	0.07	0.07	0.07
0.45	0.03	0.04	0.04	0.04	0.21	0.28	0.28	0.28
0.68	0.05	0.06	0.06	0.06	0.34	0.41	0.41	0.41
0.91	0.08	0.08	0.08	0.08	0.55	0.55	0.55	0.55
1.13	0.08	0.08	0.1	0.08	0.55	0.55	0.69	0.55
1.36	0.11	0.1	0.09	0.09	0.76	0.69	0.62	0.62
1.59	0.11	0.11	0.1	0.1	0.76	0.76	0.69	0.69
1.81	0.18	0.19	0.18	0.18	1.24	1.31	1.24	1.24
2.04	0.25	0.24	0.24	0.23	1.72	1.65	1.65	1.59
2.27	0.43	0.43	0.43	0.42	2.96	2.96	2.96	2.90
2.49	0.36	0.41	0.39	0.39	2.48	2.83	2.69	2.69
2.72	0.43	0.45	0.45	0.43	2.96	3.10	3.10	2.96
2.95	0.4	0.45	0.42	0.41	2.76	3.10	2.90	2.83
3.17	0.48	0.57	0.51	0.53	3.31	3.93	3.52	3.65
3.40	0.44	0.51	0.51	0.51	3.03	3.52	3.52	3.52
3.63	0.56	0.61	0.59	0.6	3.86	4.21	4.07	4.14
3.85	0.6	0.66	0.64	0.65	4.14	4.55	4.41	4.48
4.08	0.74	0.8	0.78	0.79	5.10	5.52	5.38	5.45
4.31	0.7	0.76	0.75	0.75	4.83	5.24	5.17	5.17
4.53	0.81	0.9	0.89	0.89	5.58	6.21	6.14	6.14
4.76	0.88	0.94	0.9	0.91	6.07	6.48	6.21	6.27
4.99	0.91	0.98	0.95	0.98	6.27	6.76	6.55	6.76
5.21	0.98	1.07	1.03	1.05	6.76	7.38	7.10	7.24
5.44	0.96	1.07	1.05	1.05	6.62	7.38	7.24	7.24
5.67	0.99	1.09	1.06	1.08	6.83	7.52	7.31	7.45
5.89	1.13	1.24	1.2	1.21	7.79	8.55	8.27	8.34
6.12	1.16	1.25	1.23	1.23	8.00	8.62	8.48	8.48
6.35	1.36	1.5	1.45	1.48	9.38	10.34	10.00	10.20
6.57	1.32	1.44	1.46	1.46	9.10	9.93	10.07	10.07
6.80	1.33	1.41	1.39	1.41	9.17	9.72	9.58	9.72
7.03	1.27	1.43	1.42	1.42	8.76	9.86	9.79	9.79
7.25	1.43	1.5	1.5	1.47	9.86	10.34	10.34	10.14
7.48	1.58	1.69	1.65	1.68	10.89	11.65	11.38	11.58

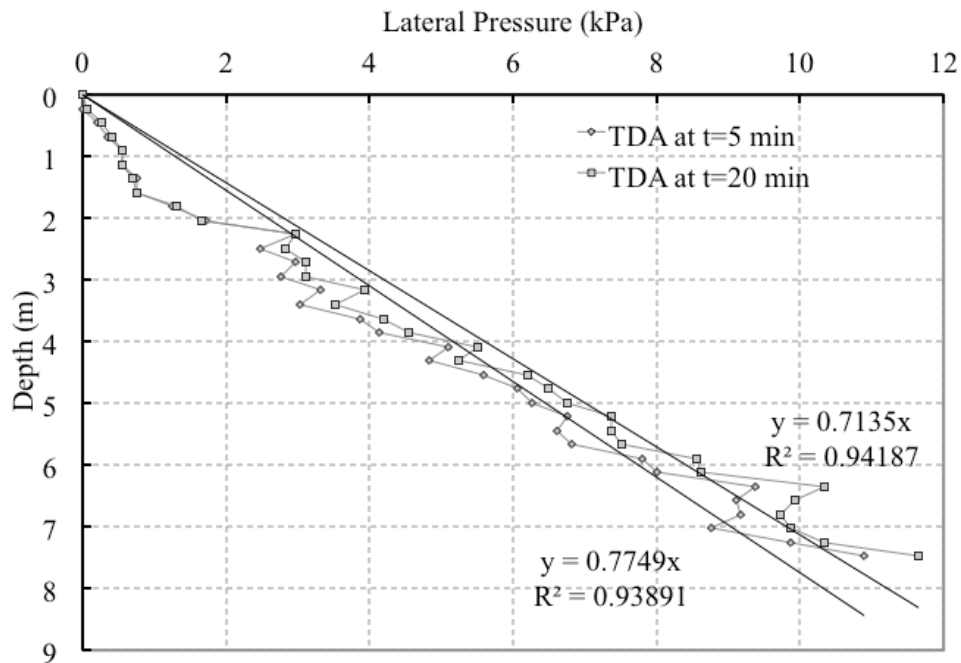


Figure B.12: Increase in lateral pressure with time for TDA backfill

B.5. Additional retaining wall model information

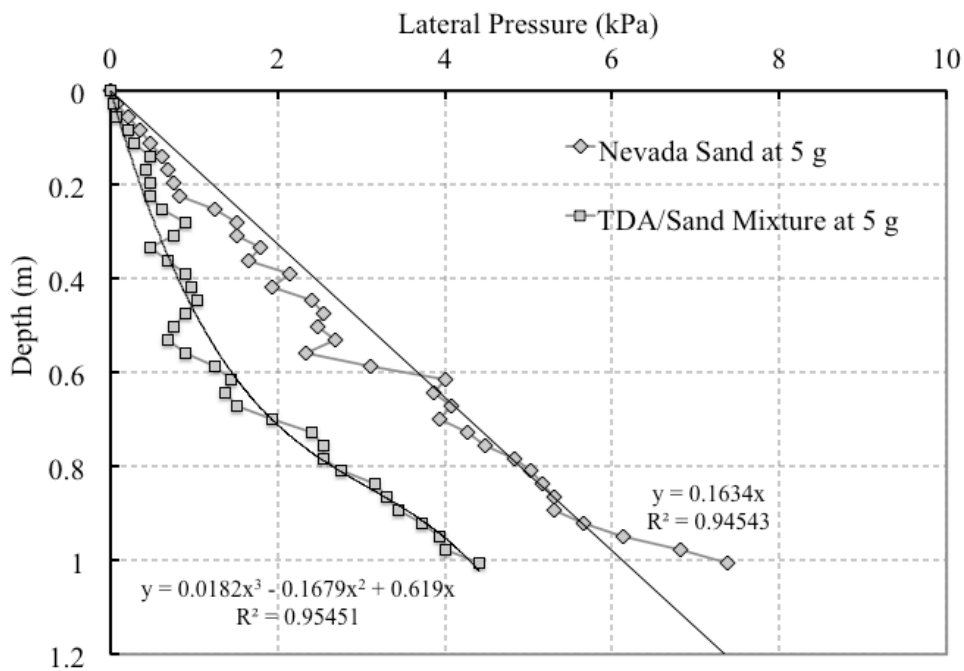


Figure B.13: Retaining wall centrifuge tests results at 5 g

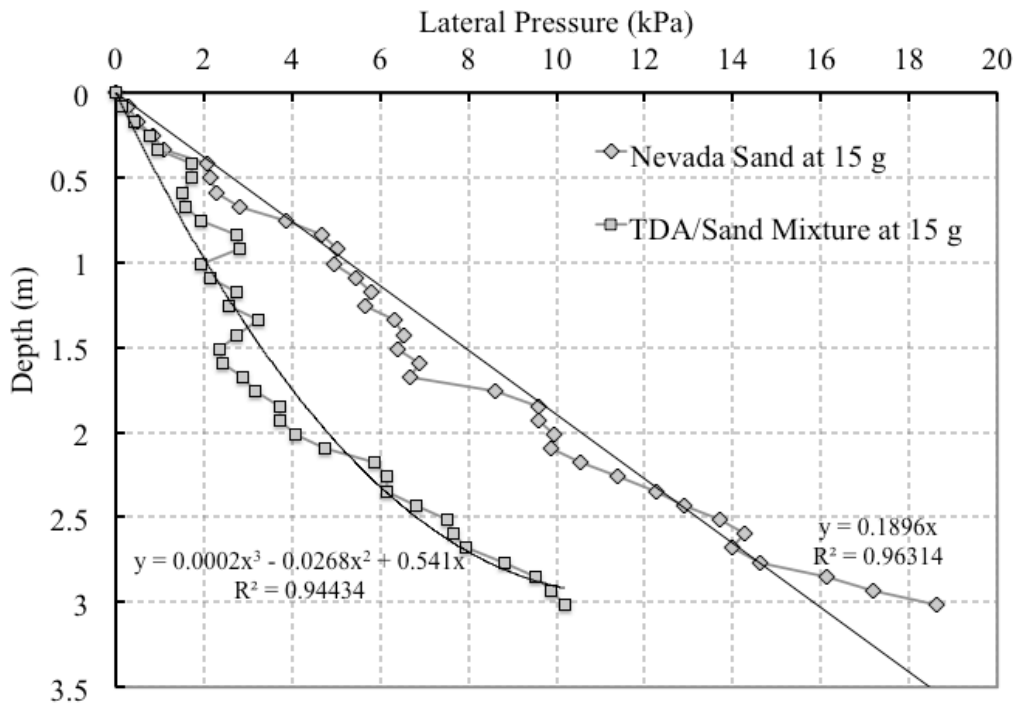


Figure B.14: Retaining wall centrifuge tests results at 15 g

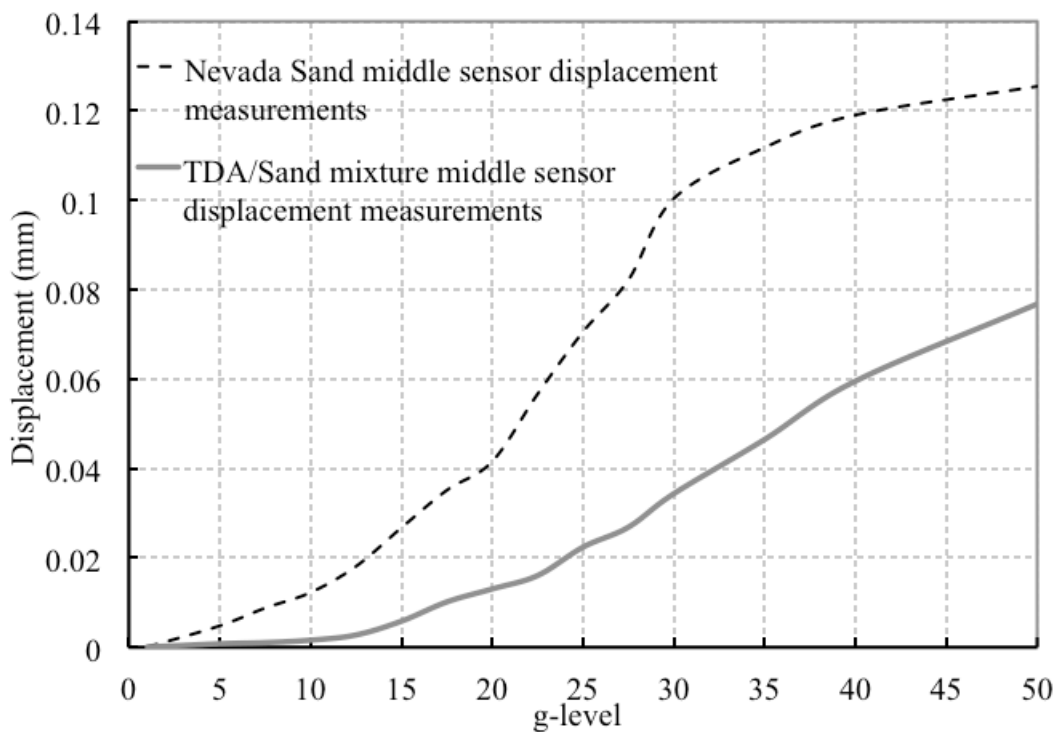


Figure B.15: Retaining wall displacements measurements for middle laser sensor

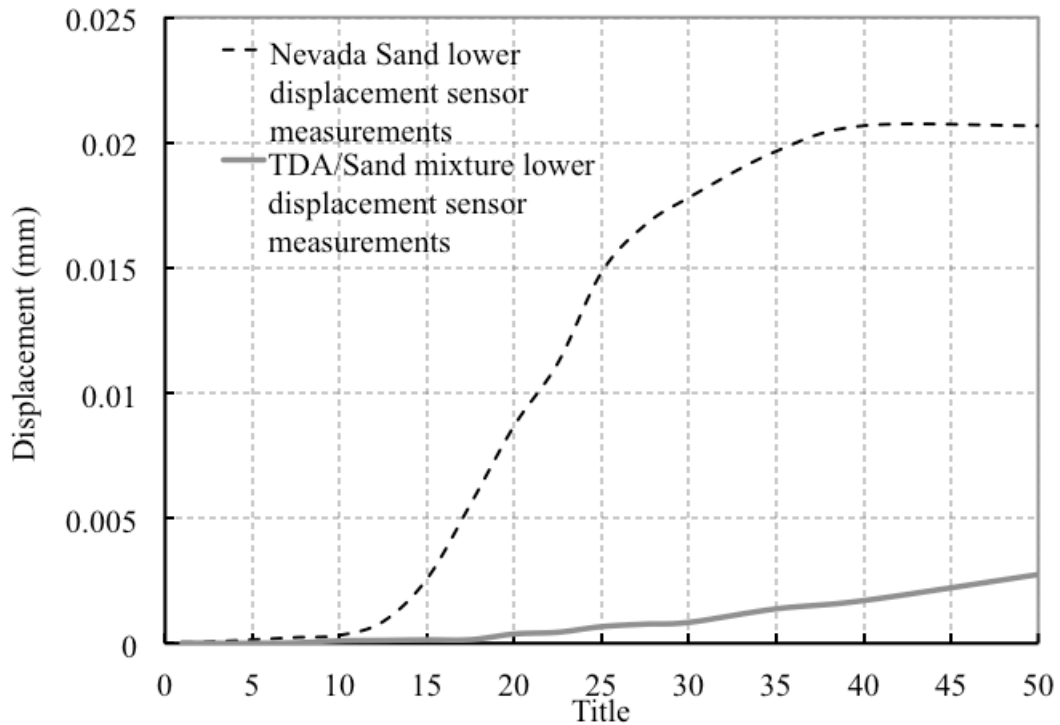


Figure B.16: Retaining wall displacements measurements for lower laser sensor

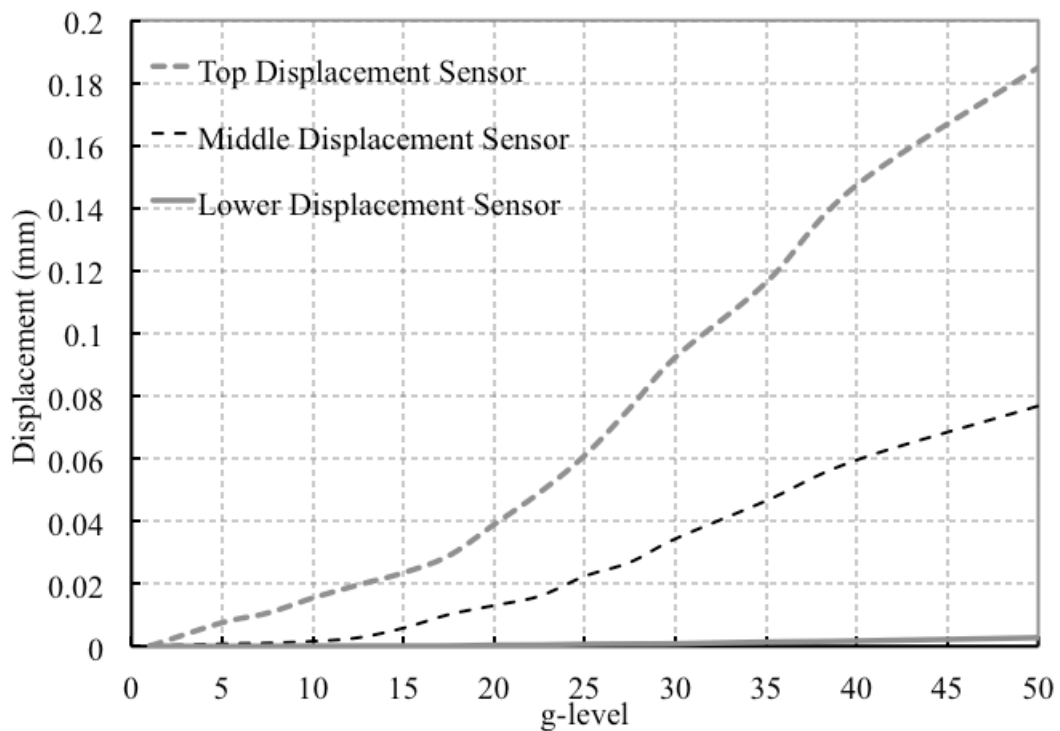


Figure B.17: Retaining wall displacements measurements for TDA/sand backfill mixture

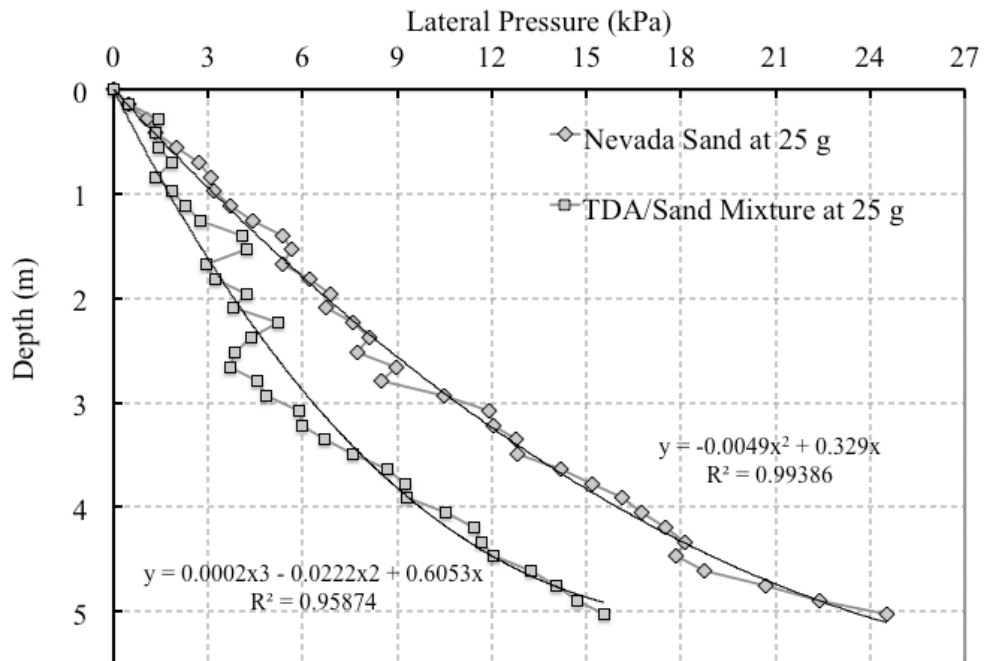


Figure B.18: Pressure distribution with depth using a second degree polynomial regression for Nevada sand backfill at 25 g (retaining wall)

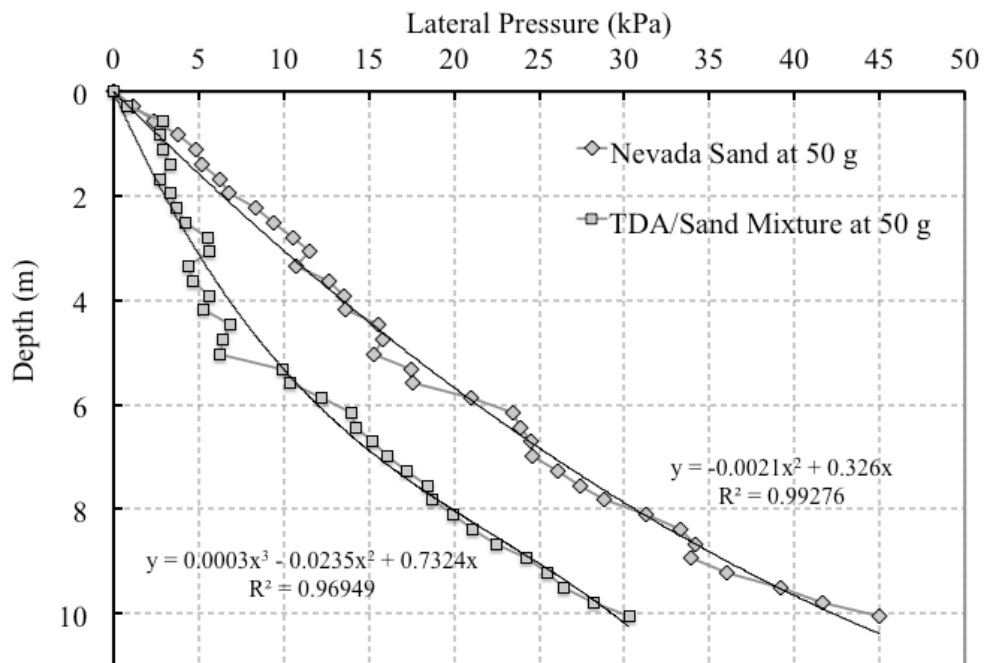


Figure B.19: Pressure distribution with depth using a second degree polynomial regression for Nevada sand backfill at 50 g (retaining wall)

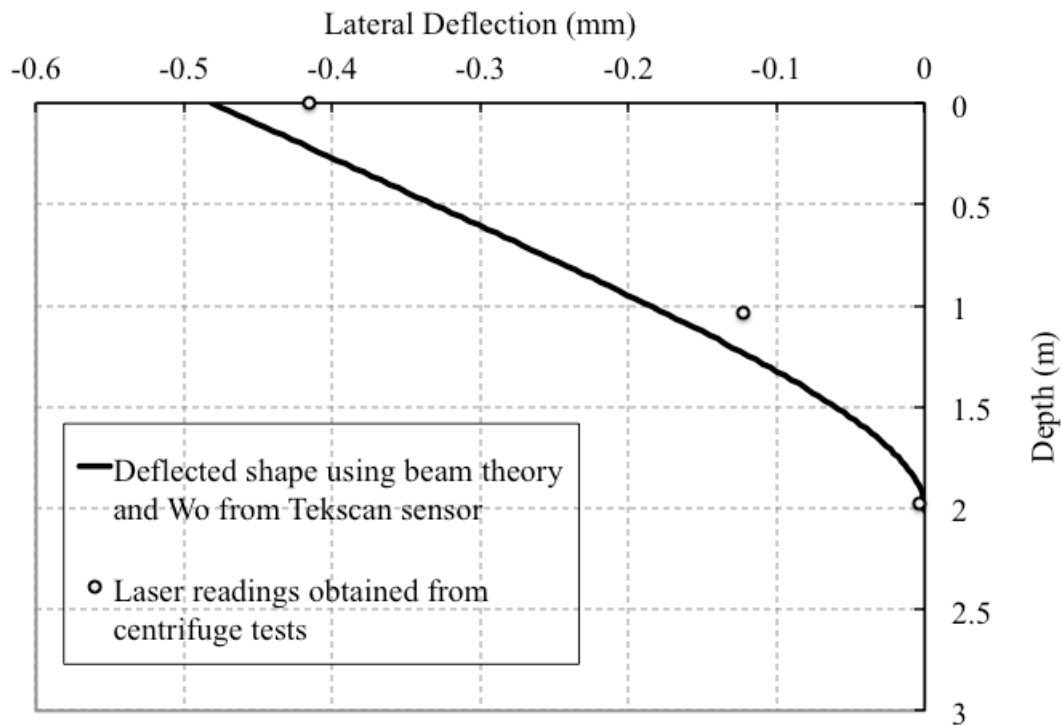


Figure B.20: Rotation + Translation retaining wall movement at 10 g

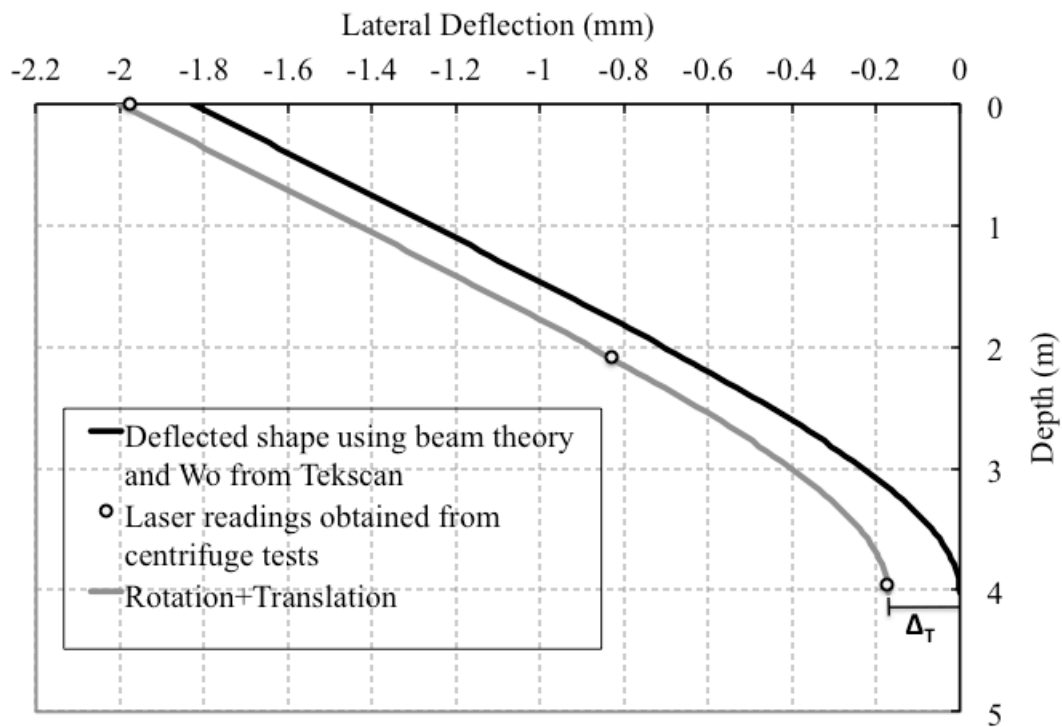


Figure B.21: Rotation + Translation retaining wall movement at 20 g

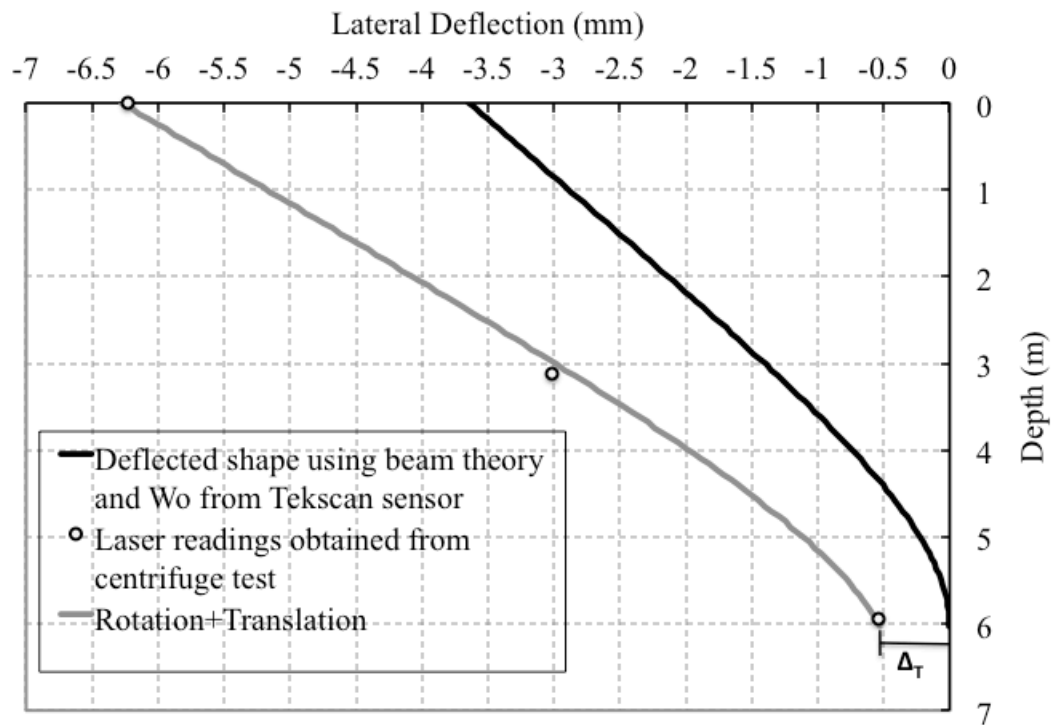


Figure B.22: Rotation + Translation retaining wall movement at 30 g

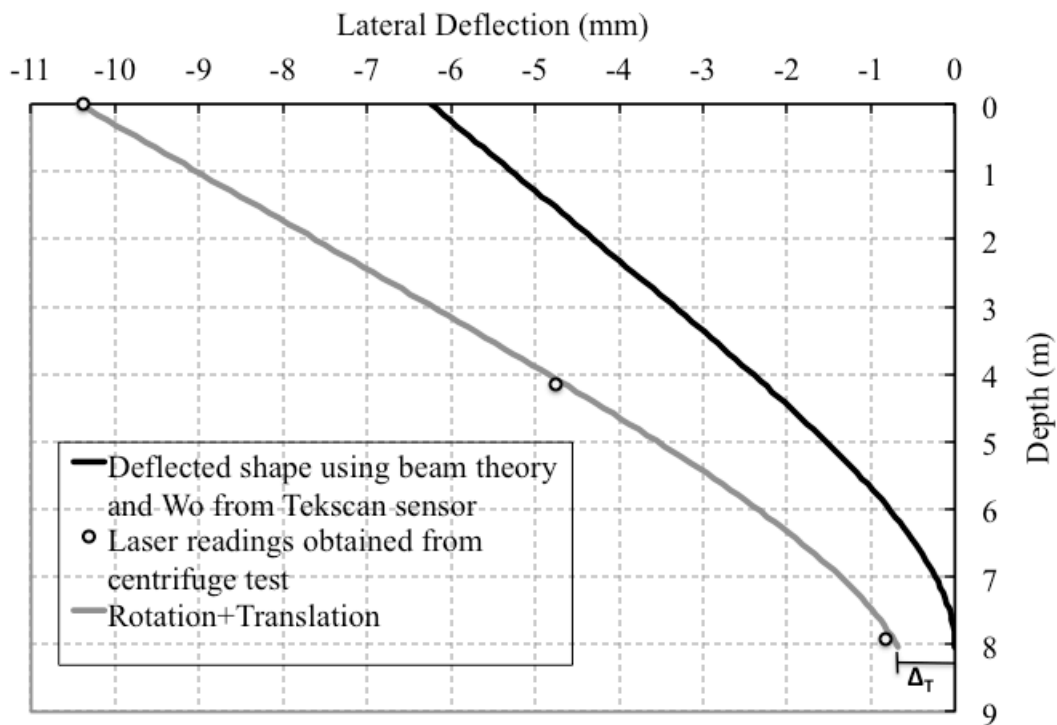


Figure B.23: Rotation + Translation retaining wall movement at 40 g

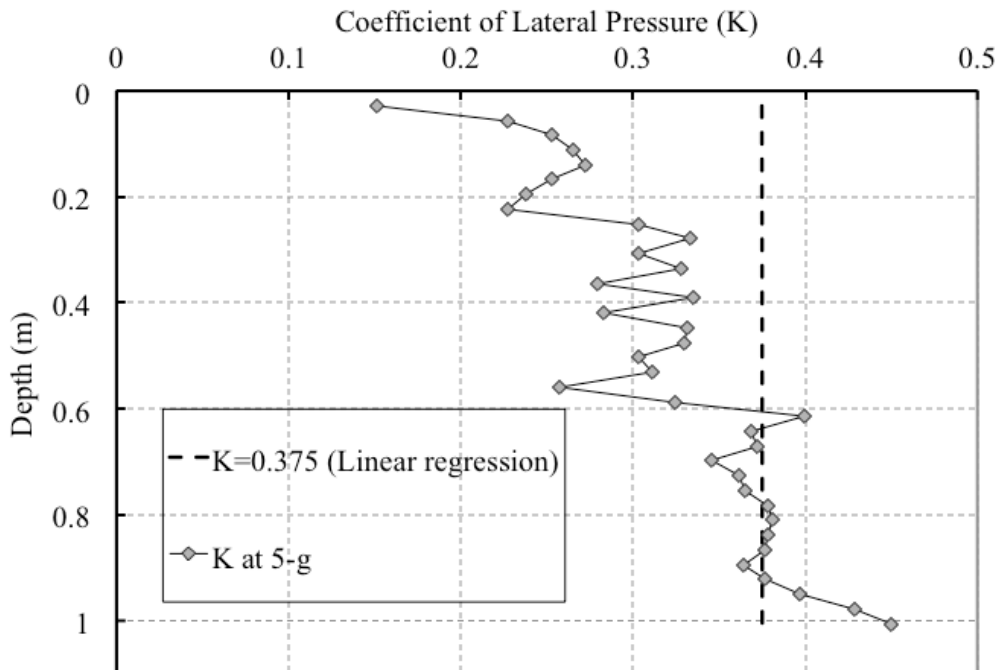


Figure B.24: Variation of the earth pressure coefficient K with depth for Nevada sand backfill in retaining wall model at 5 g (prototype dimensions)

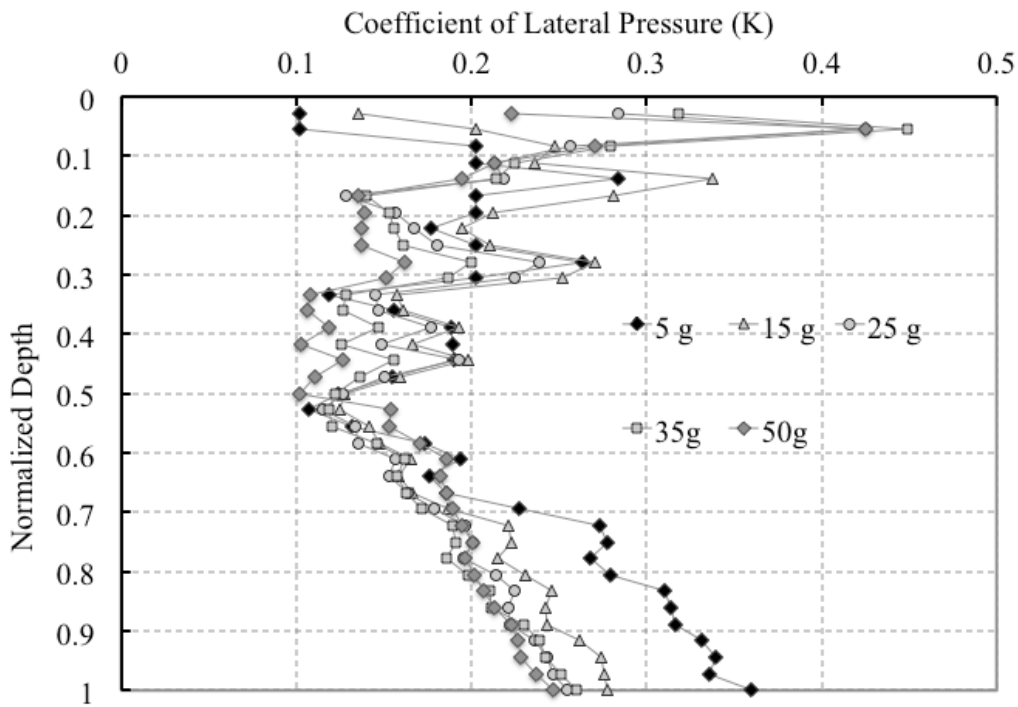


Figure B.25: Variation of the earth pressure coefficient K with depth for TDA/sand backfill in retaining wall model

Table B.3: Earth pressure lateral pressure retaining wall models at 5 g

Depth (m)	Pressure sand (kPa)	Pressure Mixture (kPa)	K Sand	K Mixture
0.000	0.000	0.000		
0.028	0.069	0.034	0.151	0.101
0.056	0.207	0.069	0.227	0.101
0.084	0.345	0.207	0.252	0.203
0.112	0.483	0.276	0.265	0.203
0.140	0.621	0.483	0.273	0.284
0.168	0.689	0.414	0.252	0.203
0.196	0.758	0.483	0.238	0.203
0.224	0.827	0.483	0.227	0.177
0.251	1.241	0.621	0.303	0.203
0.279	1.517	0.896	0.333	0.263
0.307	1.517	0.758	0.303	0.203
0.335	1.793	0.483	0.328	0.118
0.363	1.655	0.689	0.280	0.156
0.391	2.137	0.896	0.335	0.188
0.419	1.931	0.965	0.283	0.189
0.447	2.413	1.034	0.331	0.190
0.475	2.551	0.896	0.330	0.155
0.503	2.482	0.758	0.303	0.124
0.531	2.689	0.689	0.311	0.107
0.559	2.344	0.896	0.258	0.132
0.587	3.103	1.241	0.325	0.174
0.615	3.999	1.448	0.399	0.193
0.643	3.861	1.379	0.369	0.176
0.671	4.068	1.517	0.372	0.186
0.699	3.930	1.931	0.345	0.227
0.726	4.275	2.413	0.361	0.273
0.754	4.482	2.551	0.365	0.278
0.782	4.826	2.551	0.379	0.268
0.810	5.033	2.758	0.381	0.279
0.838	5.171	3.172	0.379	0.311
0.866	5.309	3.309	0.376	0.314
0.894	5.309	3.447	0.365	0.317
0.922	5.654	3.723	0.376	0.332
0.950	6.136	3.930	0.397	0.340
0.978	6.826	3.999	0.428	0.336
1.006	7.377	4.413	0.450	0.360

Table B.4: Earth pressure lateral pressure retaining wall models at 15 g

Depth (m)	Pressure sand (kPa)	Pressure Mixture (kPa)	K Sand	K Mixture
0.000	0.000	0.000		
0.084	0.276	0.138	0.202	0.135
0.168	0.483	0.414	0.177	0.203
0.251	0.827	0.758	0.202	0.248
0.335	1.103	0.965	0.202	0.236
0.419	2.068	1.724	0.303	0.338
0.503	2.137	1.724	0.261	0.281
0.587	2.275	1.517	0.238	0.212
0.671	2.827	1.586	0.259	0.194
0.754	3.861	1.931	0.314	0.210
0.838	4.688	2.758	0.343	0.270
0.922	5.033	2.827	0.335	0.252
1.006	4.964	1.931	0.303	0.158
1.090	5.447	2.137	0.307	0.161
1.173	5.792	2.758	0.303	0.193
1.257	5.654	2.551	0.276	0.167
1.341	6.343	3.241	0.290	0.198
1.425	6.550	2.758	0.282	0.159
1.509	6.412	2.344	0.261	0.128
1.593	6.895	2.413	0.266	0.124
1.676	6.688	2.896	0.245	0.142
1.760	8.618	3.172	0.301	0.148
1.844	9.584	3.723	0.319	0.166
1.928	9.584	3.723	0.305	0.159
2.012	9.928	4.068	0.303	0.166
2.096	9.860	4.757	0.289	0.186
2.179	10.549	5.861	0.297	0.221
2.263	11.376	6.136	0.309	0.223
2.347	12.273	6.136	0.321	0.215
2.431	12.893	6.826	0.326	0.231
2.515	13.721	7.515	0.335	0.245
2.598	14.272	7.653	0.337	0.242
2.682	13.996	7.929	0.320	0.243
2.766	14.617	8.825	0.324	0.262
2.850	16.134	9.515	0.348	0.274
2.934	17.168	9.860	0.359	0.276
3.018	18.616	10.204	0.379	0.278

Table B.5: Earth pressure lateral pressure retaining wall models at 25 g

Depth (m)	Pressure sand (kPa)	Pressure Mixture (kPa)	K Sand	K Mixture
0.000	0.000	0.000		
0.140	0.552	0.483	0.242	0.284
0.279	1.034	1.448	0.227	0.425
0.419	1.310	1.310	0.192	0.257
0.559	1.999	1.448	0.220	0.213
0.699	2.689	1.862	0.236	0.219
0.838	3.103	1.310	0.227	0.128
0.978	3.172	1.862	0.199	0.156
1.118	3.723	2.275	0.205	0.167
1.257	4.413	2.758	0.215	0.180
1.397	5.378	4.068	0.236	0.239
1.537	5.654	4.206	0.226	0.225
1.676	5.378	2.965	0.197	0.145
1.816	6.205	3.241	0.210	0.146
1.956	6.895	4.206	0.216	0.177
2.096	6.757	3.792	0.198	0.149
2.235	7.584	5.240	0.208	0.192
2.375	8.136	4.344	0.210	0.150
2.515	7.722	3.861	0.189	0.126
2.654	8.963	3.723	0.207	0.115
2.794	8.481	4.551	0.186	0.134
2.934	10.480	4.826	0.219	0.135
3.073	11.928	5.861	0.238	0.157
3.213	12.066	5.998	0.231	0.153
3.353	12.755	6.688	0.234	0.164
3.493	12.824	7.584	0.225	0.178
3.632	14.203	8.687	0.240	0.196
3.772	15.168	9.239	0.247	0.201
3.912	16.134	9.308	0.253	0.195
4.051	16.754	10.549	0.254	0.214
4.191	17.513	11.445	0.257	0.224
4.331	18.133	11.652	0.257	0.221
4.470	17.857	12.066	0.245	0.222
4.610	18.754	13.238	0.250	0.236
4.750	20.684	14.065	0.267	0.243
4.890	22.408	14.686	0.281	0.247
5.029	24.545	15.582	0.300	0.254

Table B.6: Earth pressure lateral pressure retaining wall models at 35 g

Depth (m)	Pressure sand (kPa)	Pressure Mixture (kPa)	K Sand	K Mixture
0.000	0.000	0.000		
0.196	0.827	0.758	0.260	0.318
0.391	1.793	2.137	0.281	0.449
0.587	2.896	1.999	0.303	0.280
0.782	3.378	2.137	0.265	0.224
0.978	3.723	2.551	0.234	0.214
1.173	4.826	1.999	0.252	0.140
1.369	4.688	2.551	0.210	0.153
1.565	5.861	2.965	0.230	0.156
1.760	6.895	3.447	0.240	0.161
1.956	7.377	4.757	0.232	0.200
2.151	8.343	4.895	0.238	0.187
2.347	7.584	3.654	0.198	0.128
2.543	8.963	3.930	0.216	0.127
2.738	9.791	4.895	0.219	0.147
2.934	9.860	4.482	0.206	0.125
3.129	11.101	5.929	0.218	0.156
3.325	11.445	5.516	0.211	0.136
3.520	11.032	5.240	0.192	0.122
3.716	12.480	5.378	0.206	0.119
3.912	12.342	5.723	0.194	0.120
4.107	15.306	7.308	0.229	0.146
4.303	16.823	8.481	0.240	0.162
4.498	16.823	8.618	0.230	0.157
4.694	17.306	9.308	0.226	0.163
4.890	17.168	10.204	0.216	0.171
5.085	18.478	11.721	0.223	0.189
5.281	19.512	12.273	0.227	0.191
5.476	20.615	12.411	0.231	0.186
5.672	22.063	13.652	0.239	0.198
5.867	23.718	15.031	0.248	0.210
6.063	24.614	15.582	0.249	0.211
6.259	24.338	17.513	0.239	0.230
6.454	25.786	18.754	0.245	0.239
6.650	28.062	19.650	0.259	0.243
6.845	29.785	20.960	0.267	0.251
7.041	32.612	22.270	0.284	0.260

Table B.7: Earth pressure lateral pressure retaining wall models at 50 g

Depth (m)	Pressure sand (kPa)	Pressure Mixture (kPa)	K Sand	K Mixture
0.000	0.000	0.000		
0.279	1.103	0.758	0.242	0.223
0.559	2.413	2.896	0.265	0.425
0.838	3.792	2.758	0.278	0.270
1.118	4.826	2.896	0.265	0.213
1.397	5.171	3.309	0.227	0.194
1.676	6.274	2.758	0.230	0.135
1.956	6.757	3.309	0.212	0.139
2.235	8.343	3.723	0.229	0.137
2.515	9.377	4.206	0.229	0.137
2.794	10.549	5.516	0.232	0.162
3.073	11.514	5.654	0.230	0.151
3.353	10.756	4.413	0.197	0.108
3.632	12.686	4.688	0.214	0.106
3.912	13.514	5.654	0.212	0.119
4.191	13.583	5.240	0.199	0.103
4.470	15.513	6.895	0.213	0.127
4.750	15.858	6.412	0.205	0.111
5.029	15.306	6.205	0.187	0.101
5.309	17.444	9.928	0.202	0.154
5.588	17.582	10.411	0.193	0.153
5.867	20.960	12.204	0.219	0.171
6.147	23.442	13.927	0.234	0.186
6.426	23.925	14.272	0.229	0.182
6.706	24.545	15.168	0.225	0.186
6.985	24.614	16.065	0.216	0.189
7.264	26.131	17.237	0.221	0.195
7.544	27.372	18.409	0.223	0.200
7.823	28.820	18.685	0.226	0.196
8.103	31.233	19.926	0.237	0.202
8.382	33.302	21.098	0.244	0.207
8.661	34.198	22.477	0.242	0.213
8.941	33.922	24.270	0.233	0.223
9.220	36.060	25.442	0.240	0.227
9.500	39.162	26.407	0.253	0.228
9.779	41.644	28.200	0.261	0.237
10.058	45.023	30.268	0.275	0.247

APPENDIX C: ADDITIONAL INFORMATION ON TRIAXIAL AND SIMPLE SHEAR TESTS

C.1. Additional triaxial tests details



Figure C.1: Filling of triaxial cell in the lab and pre-saturation process

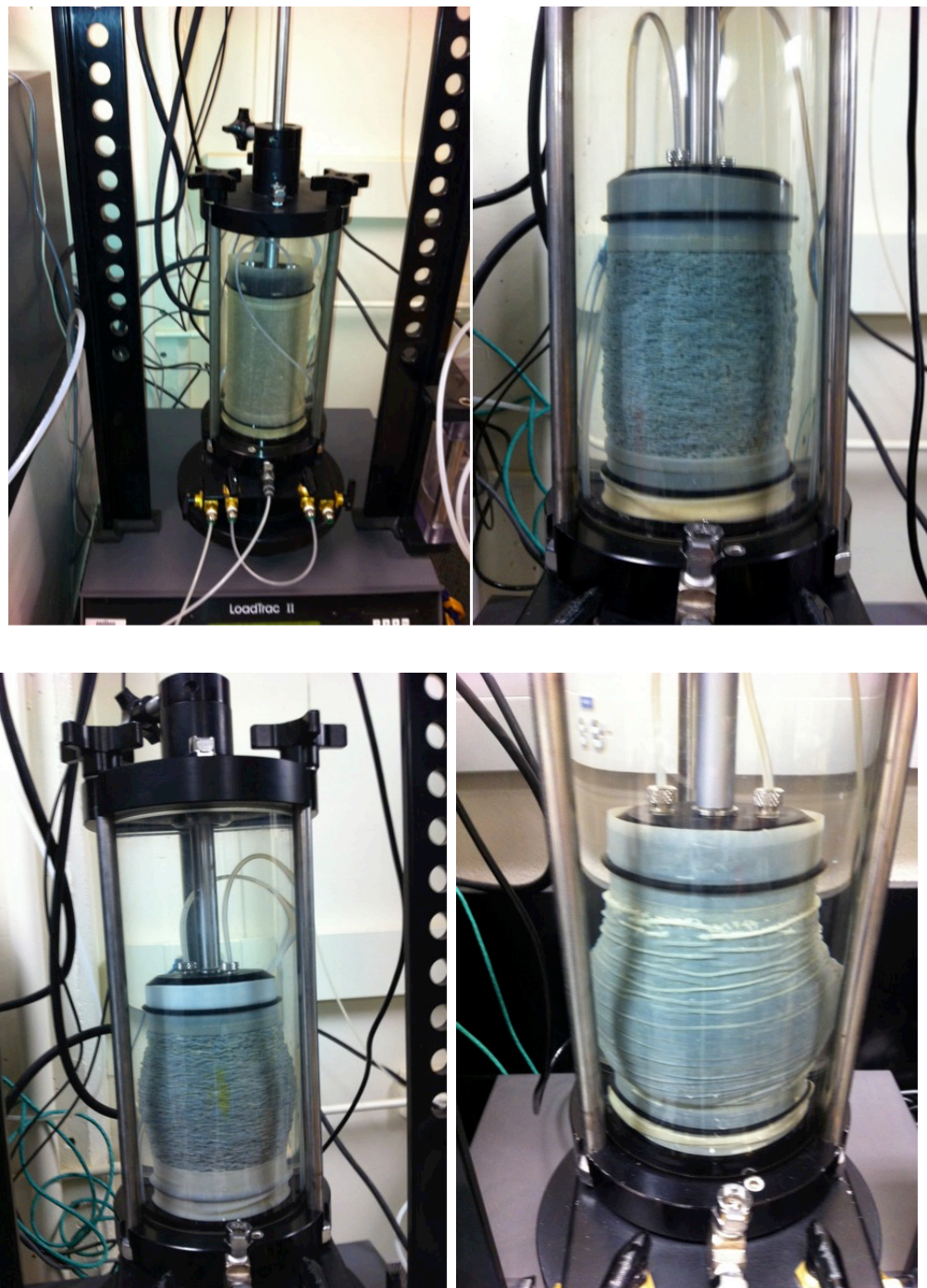


Figure C.2: CD Triaxial test from beginning of shearing phase to the end

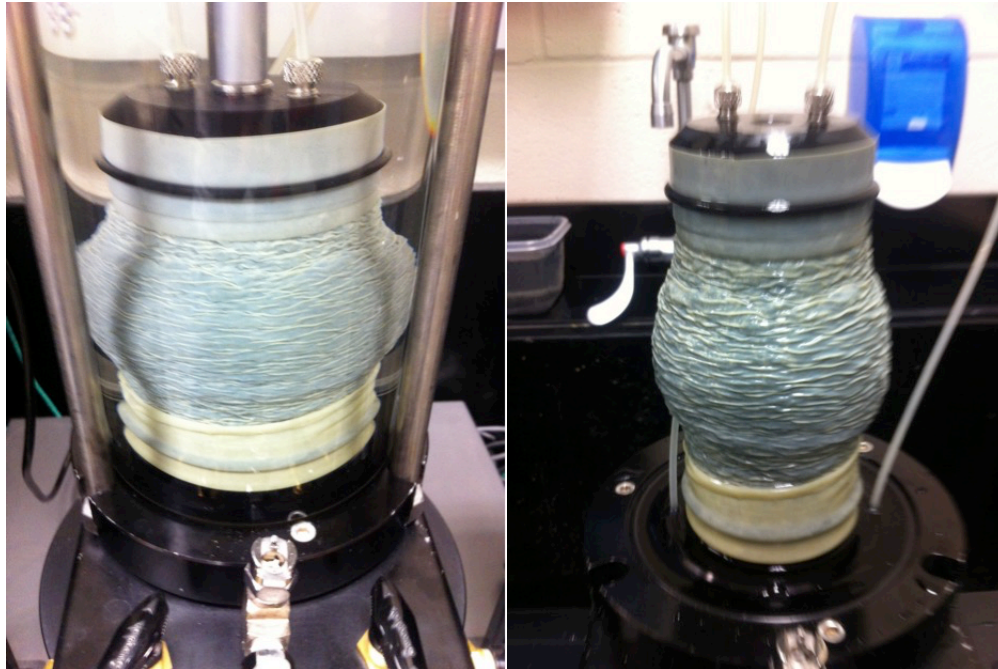


Figure C.3: TDA sample after shearing (right : sample inside chamber, left: sample outside chamber)



Figure C.4: Triaxial sample preparation mold and sample after mold removal



Figure C.5: 3/7 ratio TDA/sand mixture preparation and shearing failure



Figure C.6: 1/9 ratio TDA/sand mixture preparation and shearing failure

Table C.1: Triaxial tests initial conditions

Test number	Material	Mass (gr)	Height (mm)	Diameter (mm)	Density (gr/cm ³)
TR-1	TDA (D ₅₀ =1.20mm)	350	152.15	71.1	0.5794
TR-2		350	152.08	70.98	0.5816
TR-3		350	151.01	71.11	0.5836
TR-4		350	152.46	71.09	0.5784
TR-5	Nevada Sand	1020	152.42	71.12	1.6845
TR-6		1020	150.76	71.11	1.7036
TR-7		1020	151.02	71.08	1.7021
TR-8		1020	151.34	71.06	1.6994
TR-9	TDA (D ₅₀ =2.60mm)	350	152.23	71.1	0.5791
TR-10		350	152.08	71.05	0.5805
TR-11		350	151.99	71.11	0.5798
TR-12		350	151.55	71.02	0.5830
TR-13	TDA (D ₅₀ =1.20mm)	350	152.18	71.06	0.5799
TR-14		350	152.25	70.99	0.5808
TR-15		350	151.86	71.1	0.5805
TR-16		350	151.44	71.03	0.5832
TR-17	TDA (D ₅₀ =1.20mm)	350	152.13	71.07	0.5799
TR-18		350	151.88	71.1	0.5804
TR-19		350	151.94	71.02	0.5815
TR-20		350	151.55	71.1	0.5817
TR-21	TDA (D ₅₀ =1.20mm)	350	151.99	71.11	0.5798
TR-22		350	152.11	70.99	0.5813
TR-23		350	152.22	71.04	0.5801
TR-24		350	151.37	71.12	0.5820
TR-25	TDA/sand Mixture (3/7)	754	152.24	71.12	1.2467
TR-26		754	151.98	71.02	1.2524
TR-27		754	152.01	71.11	1.2490
TR-28		754	152.16	71.05	1.2498
TR-29	TDA/sand Mixture (1/9)	955	152.24	71.12	1.5791
TR-30		955	152.18	71.11	1.5801
TR-31		955	152.21	71.11	1.5798
TR-32		955	152.07	71.09	1.5822

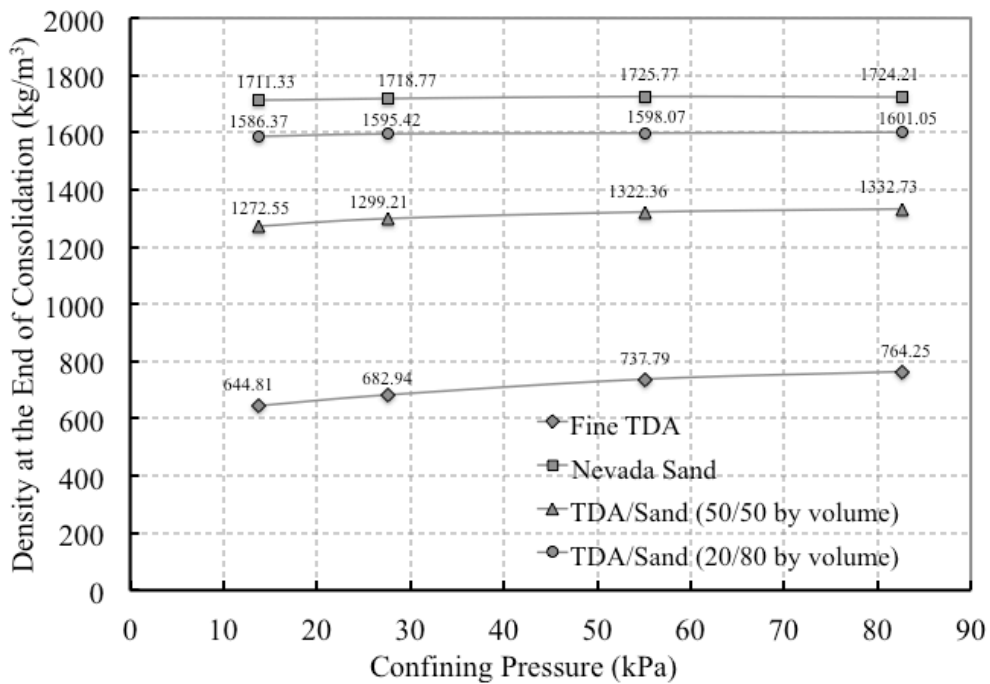


Figure C.7: Variation of density with confining pressure during consolidation phase

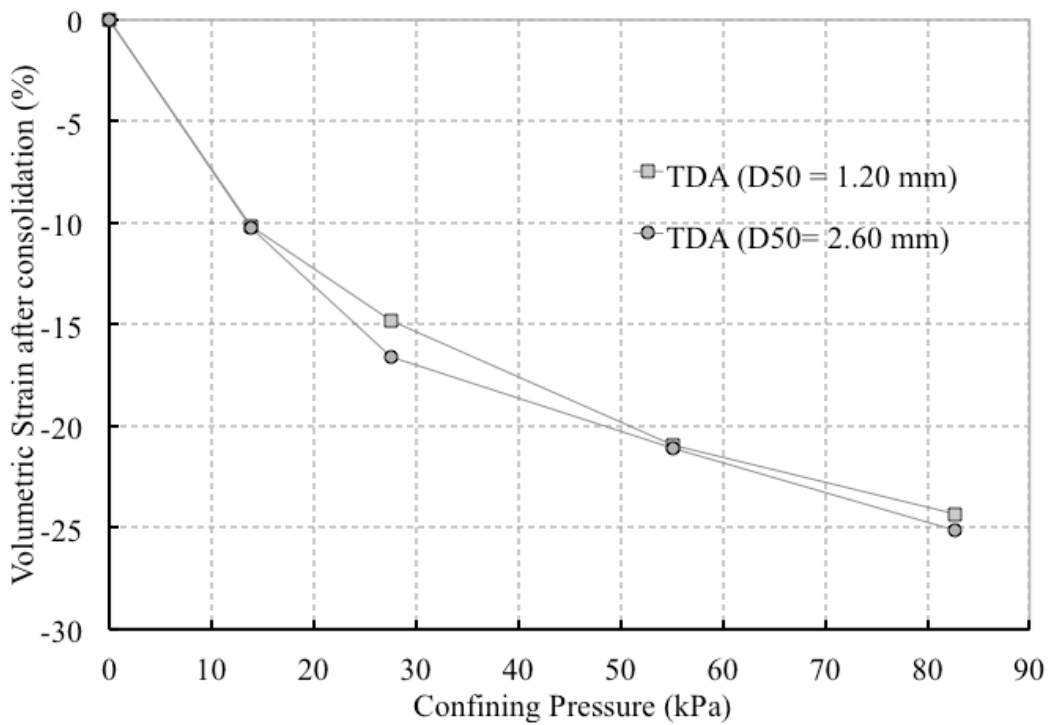


Figure C.8: Variation of volume during consolidation phase for both TDA materials tested in this research

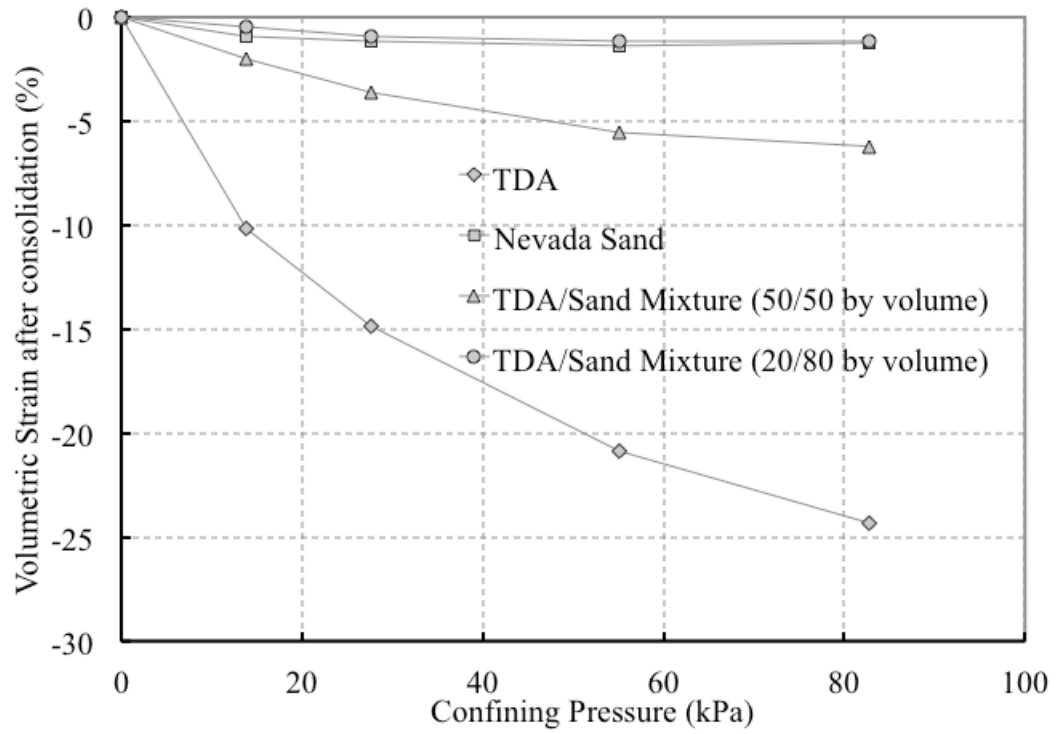
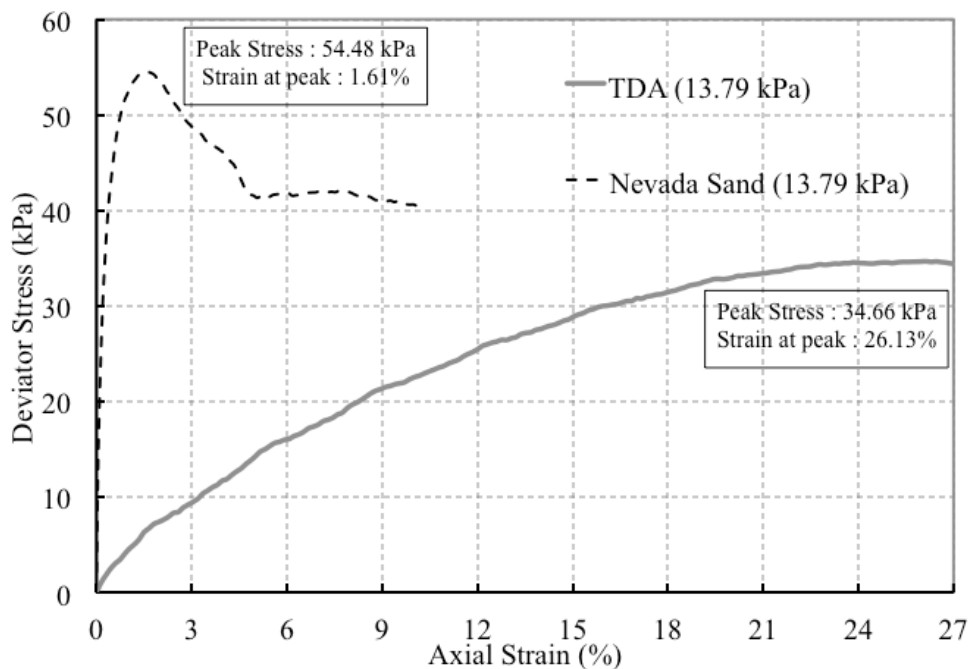
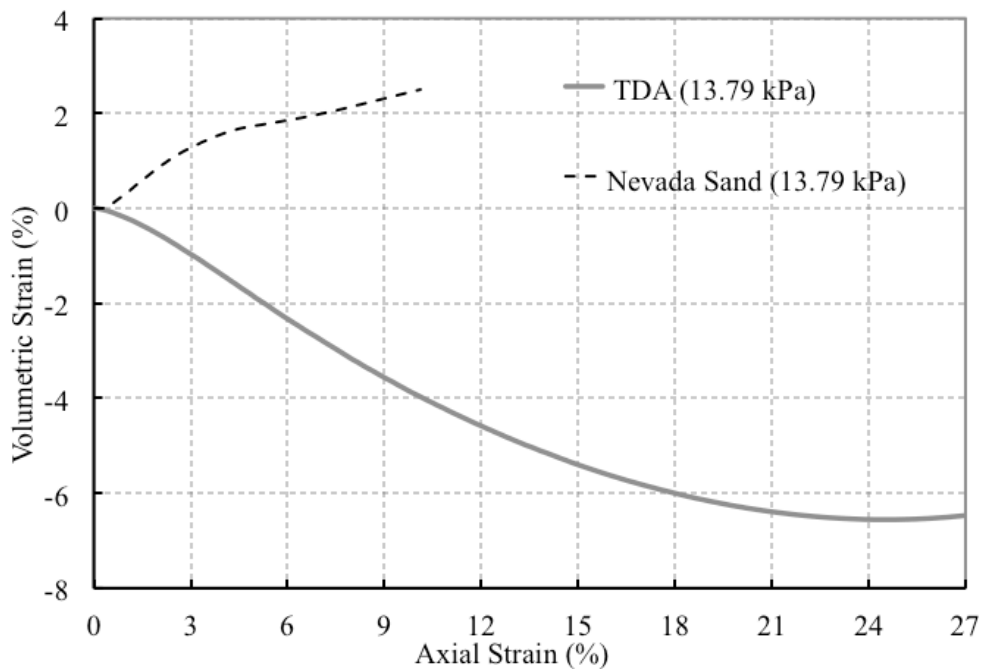


Figure C.9: Variation of volume during consolidation phase for all different aggregates

C.2. Additional CD stress-strain behavior information not included in chapter 4

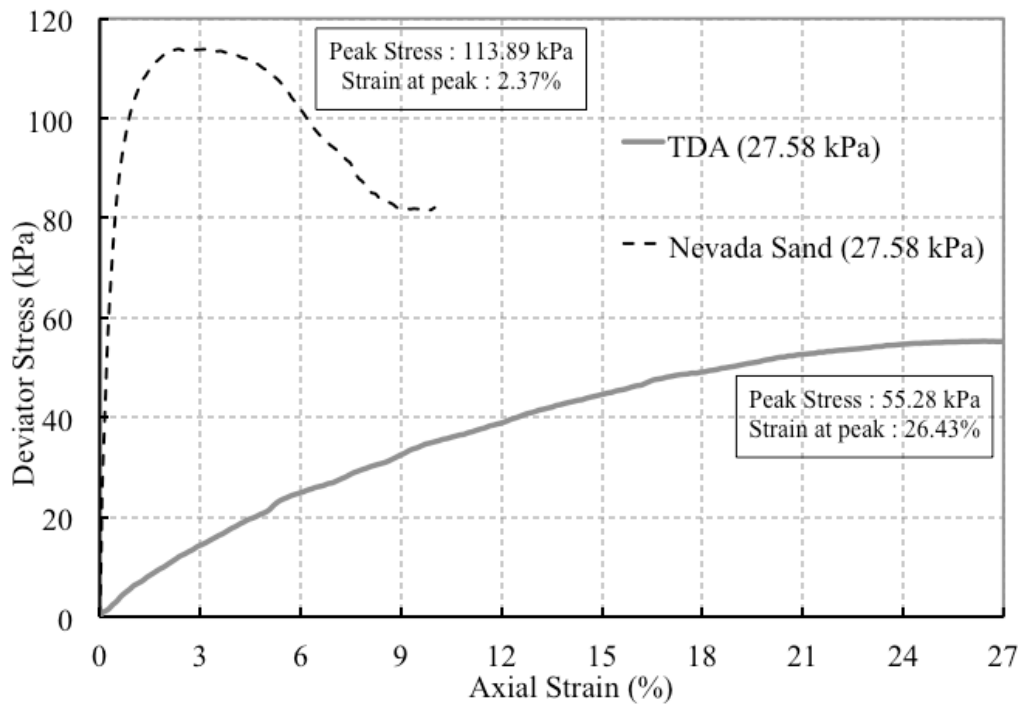


a) Deviator stress versus axial strain

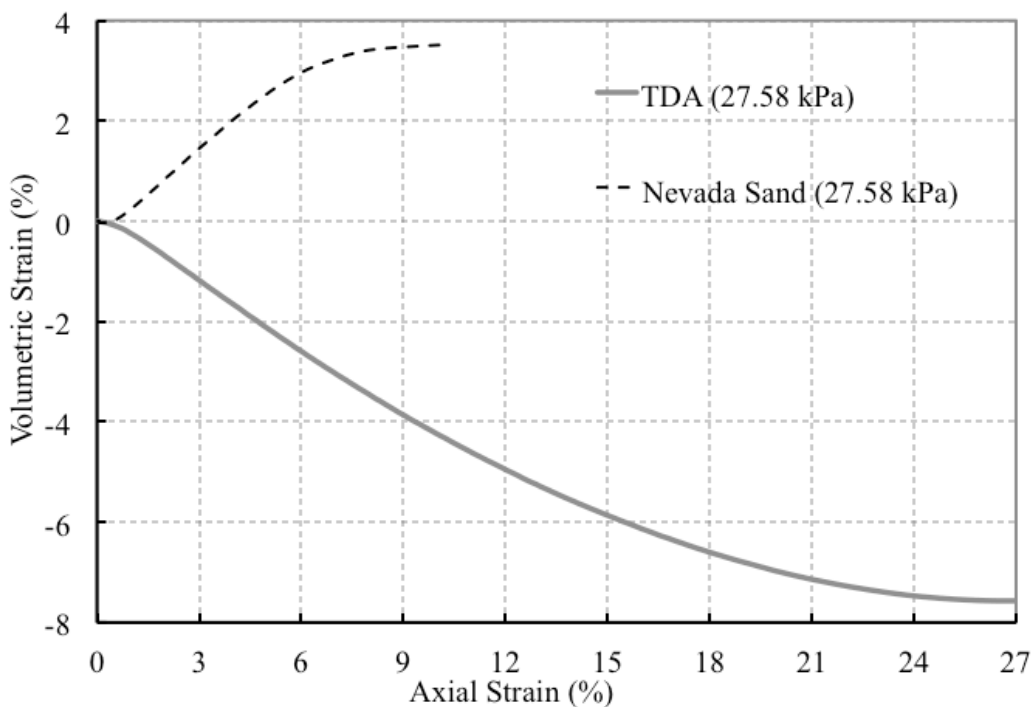


b) Volumetric strain versus axial strain

Figure C.10: Comparison between TDA material and Nevada sand for CD triaxial test at 13.79 kPa confining pressure

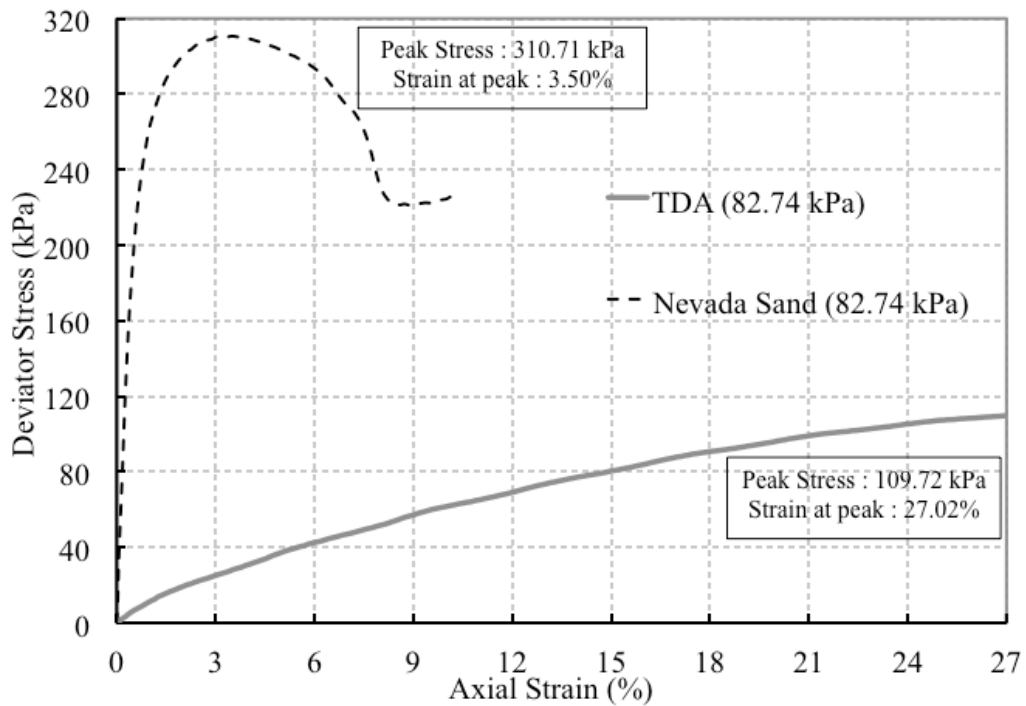


a) Deviator stress versus axial strain

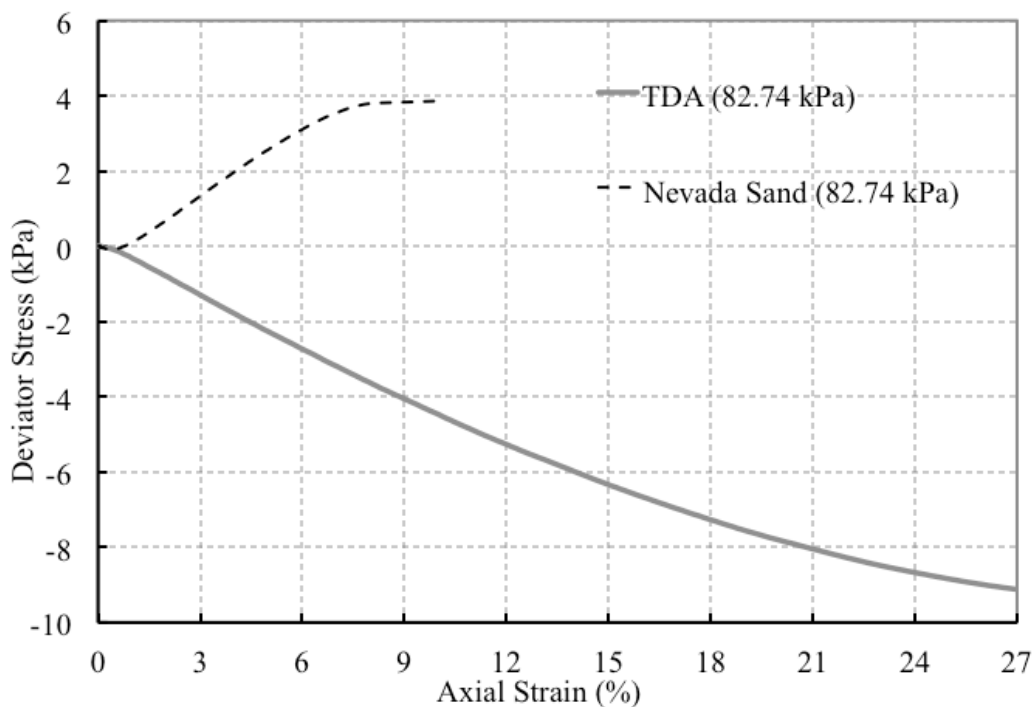


b) Volumetric strain versus axial strain

Figure C.11: Comparison between TDA material and Nevada sand for CD triaxial test at 27.58 kPa confining pressure



a) Deviator stress versus axial strain



b) Volumetric strain versus axial strain

Figure C.12: Comparison between TDA material and Nevada sand for CD triaxial test at 82.74 kPa confining pressure

C.3. Shear strength parameters determination not included in chapter 4

Table C.2: Shear strength parameters determination at 5% axial strain

sigma-3	Deviatoric	sigma-1f	p'	q	Strain
(kPa)	(kPa)	(kPa)	(kPa)	(kPa)	(%)
13.79	14.24	28.03	20.91	7.12	5
27.58	21.18	48.76	38.17	10.59	5
55.16	28.94	84.10	69.63	14.47	5
82.74	37.24	119.98	101.36	18.62	5

Regressions:

Intercept	Angle	c'	Φ'
(kPa)	(deg)	(kPa)	(deg)
4.70	7.92	4.75	8.00
0.00	11.45	0.00	11.69

Table C.3: Shear strength parameters determination at 10% axial strain

sigma-3	Deviatoric	sigma-1f	p'	q	Strain
(kPa)	(kPa)	(kPa)	(kPa)	(kPa)	(%)
13.79	22.54	36.33	25.06	11.27	10
27.58	35.06	62.64	45.11	17.53	10
55.16	48.95	104.11	79.64	24.48	10
82.74	61.60	144.34	113.54	30.80	10

Regressions:

Intercept	Angle	c'	Φ'
(kPa)	(deg)	(kPa)	(deg)
6.81	12.18	6.97	12.47
0.00	16.58	0.00	17.32

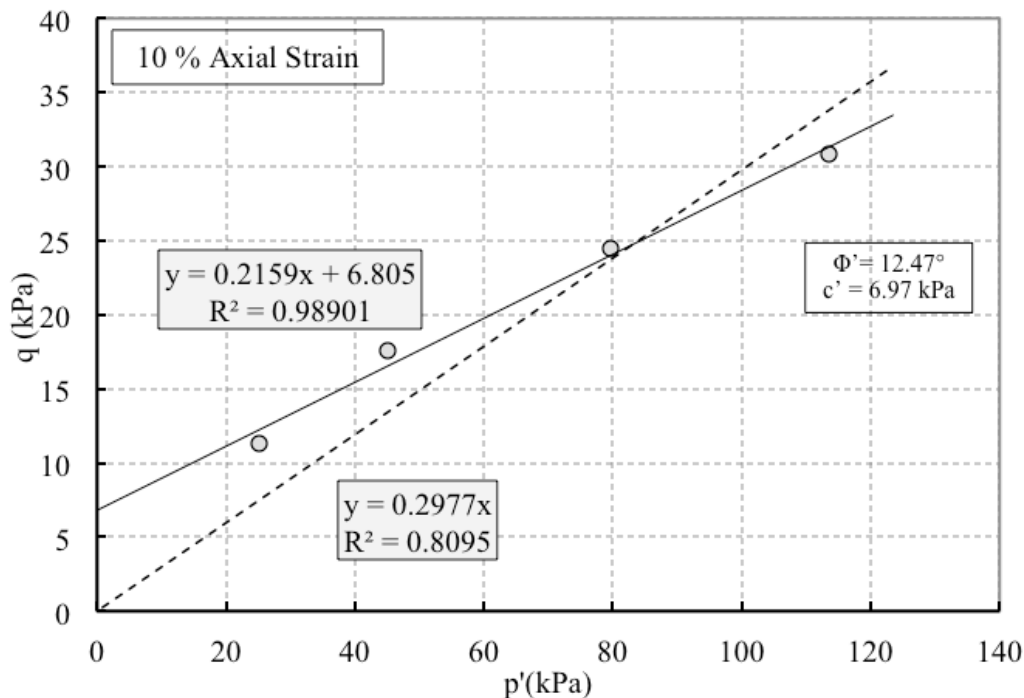


Figure C.13: Shear strength parameters determination for TDA at 10% axial strain (CD triaxial test)

Table C.4: Shear strength parameters determination for TDA at peak

sigma-3 (kPa)	Deviatoric (kPa)	sigma-1f (kPa)	p' (kPa)	q (kPa)	Strain to failure (%)
13.79	34.66	48.45	31.12	17.33	26.13
27.58	55.28	82.86	55.22	27.64	26.43
55.16	85.65	140.81	97.99	42.83	27.21
82.74	109.72	192.46	137.60	54.86*	27.25

*Actual peak was not observed for the 12 psi sample. Values was taken as the maximum deviatoric stress observed in the test at 27.50% axial strain

Regressions:

Intercept (kPa)	Angle (deg)	c' (kPa)	Φ' (deg)
7.44	19.32	7.94	20.52
0.00	22.99	0.00	25.11

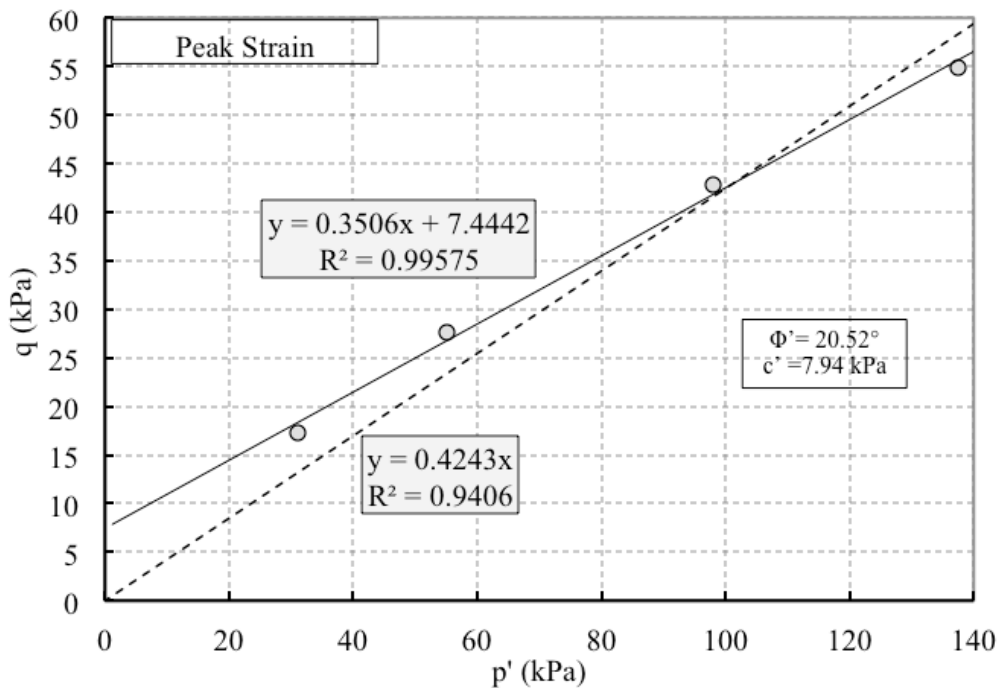


Figure C.14: Shear strength parameters determination for TDA ($D_{50}=2.60\text{mm}$) at peak for CD triaxial test .

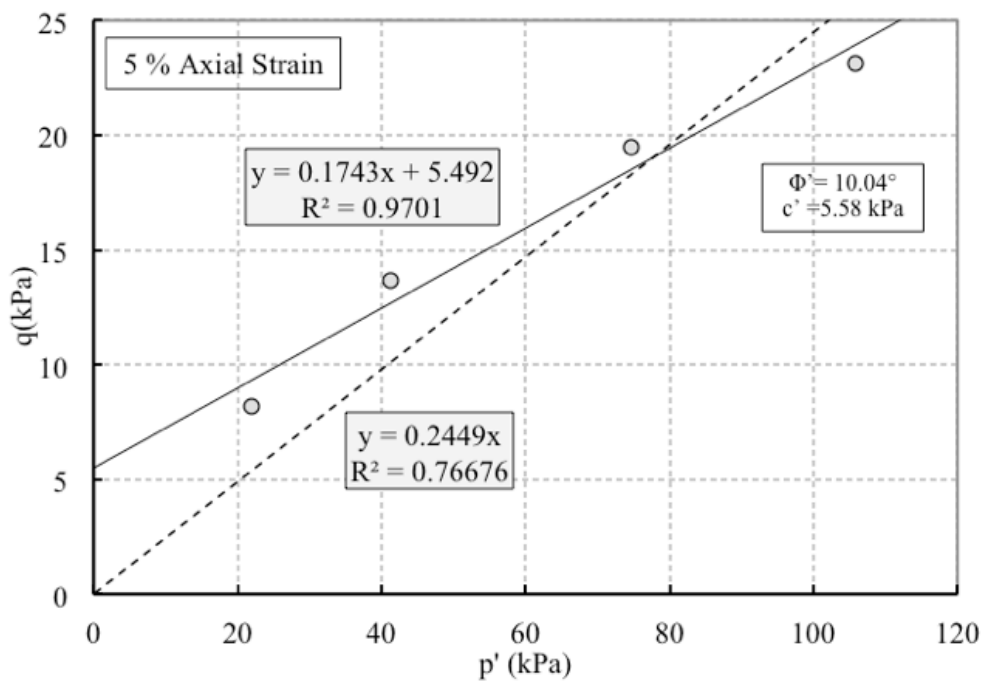


Figure C.15: Shear strength parameters determination for TDA ($D_{50}=2.60\text{mm}$) at 5 % axial strain (CD triaxial test)

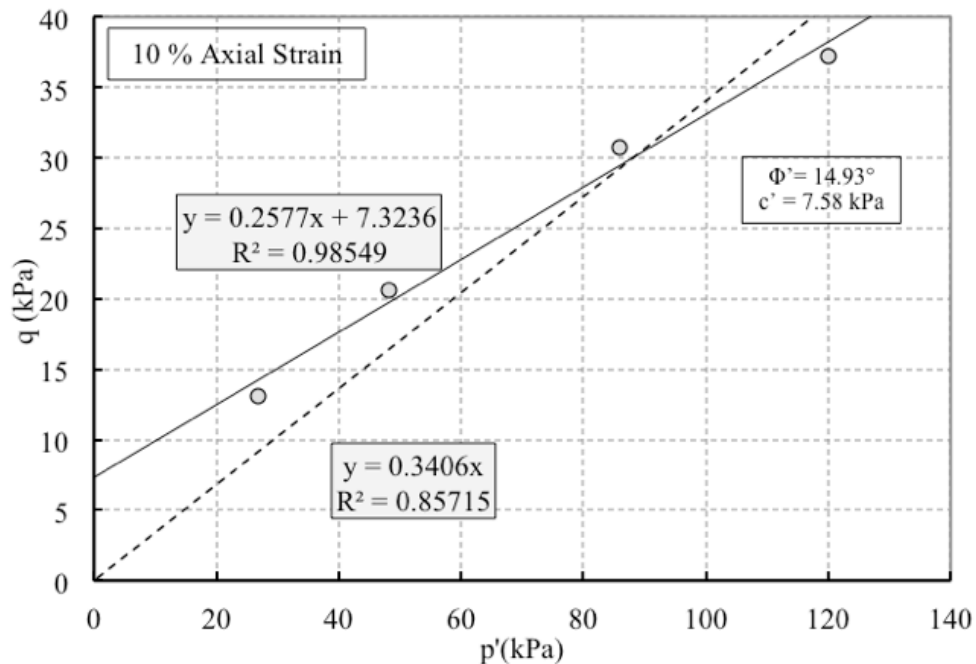


Figure C.16: Shear strength parameters determination for TDA ($D_{50}=2.60\text{mm}$) at 10 % axial strain (CD triaxial test)

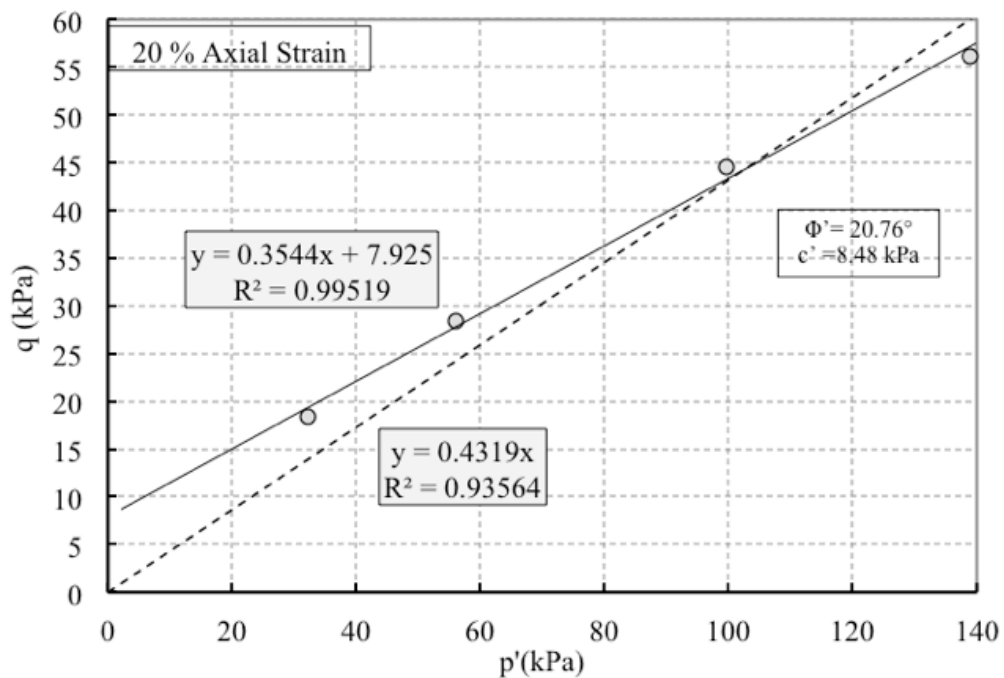


Figure C.17: Shear strength parameters determination for TDA ($D_{50}=2.60\text{mm}$) at 20 % axial strain (CD triaxial test)

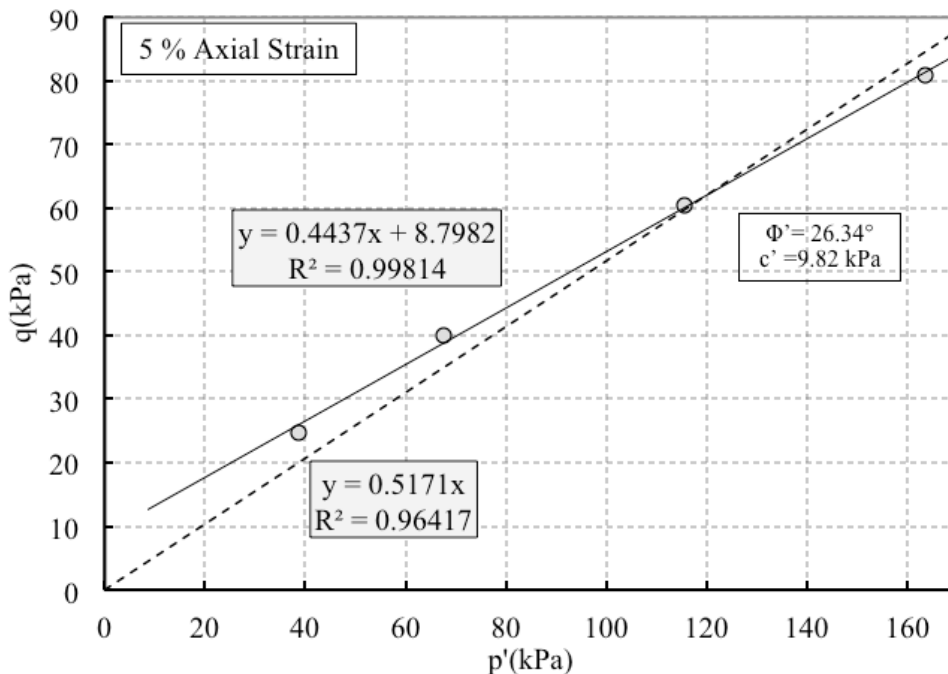


Figure C.18: Shear strength parameters determination for TDA/sand mixture (30:70 by weight) at 5% axial strain

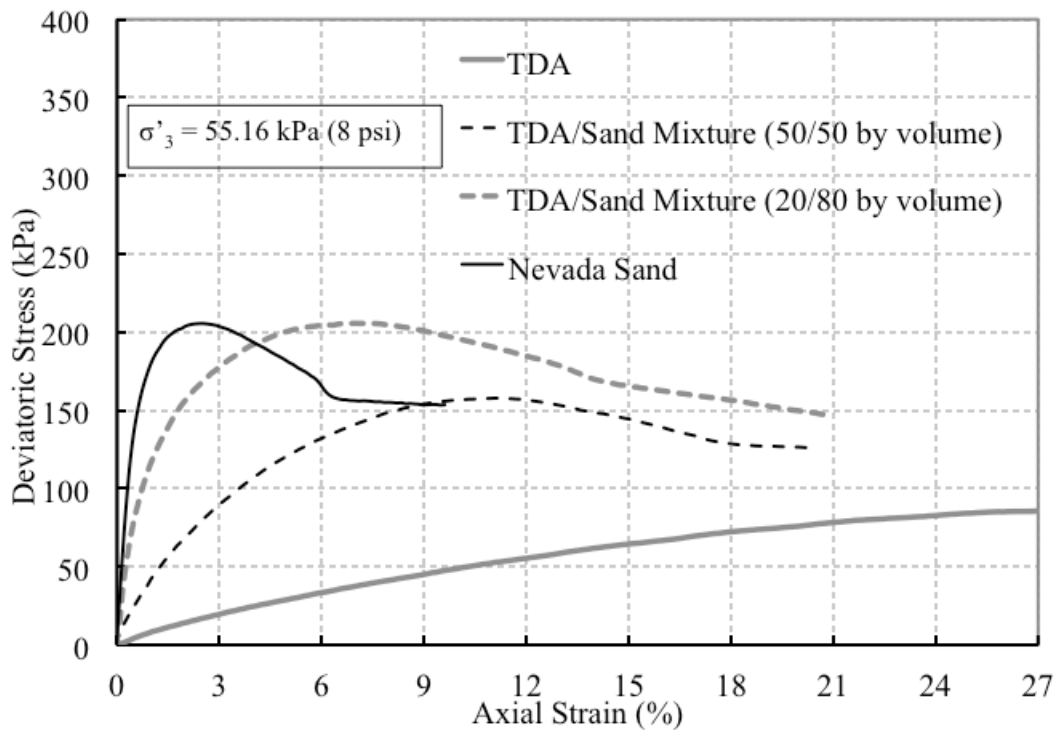


Figure C.19: Stress-strain curves for all aggregates tested at $\sigma'_3 = 55.16$ kPa

C.4. Additional CU stress-strain behavior information not included in chapter 4

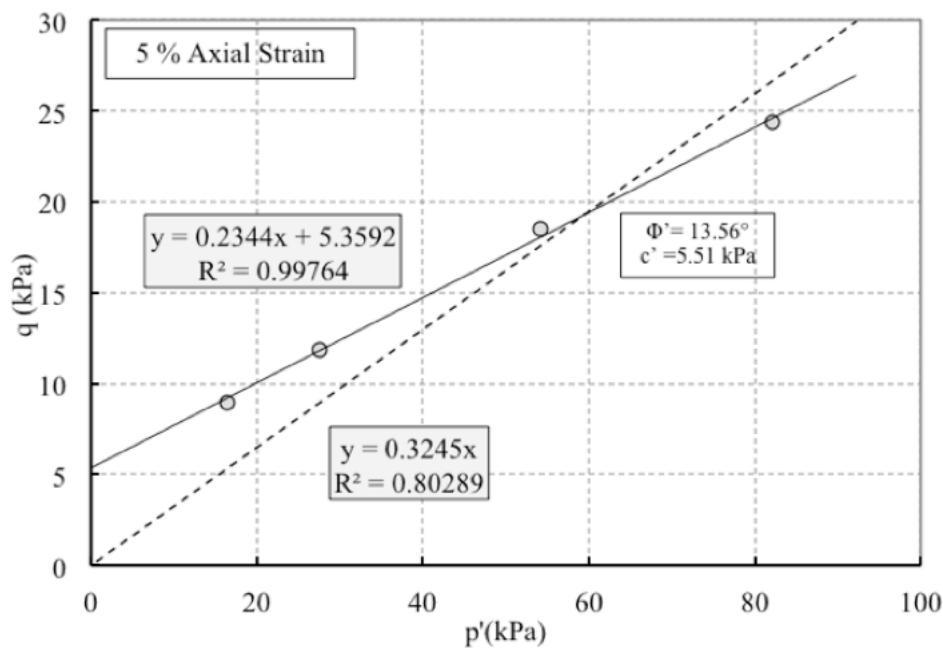


Figure C.20: Effective shear strength parameters determination for TDA at 5% axial strain (CU triaxial test)

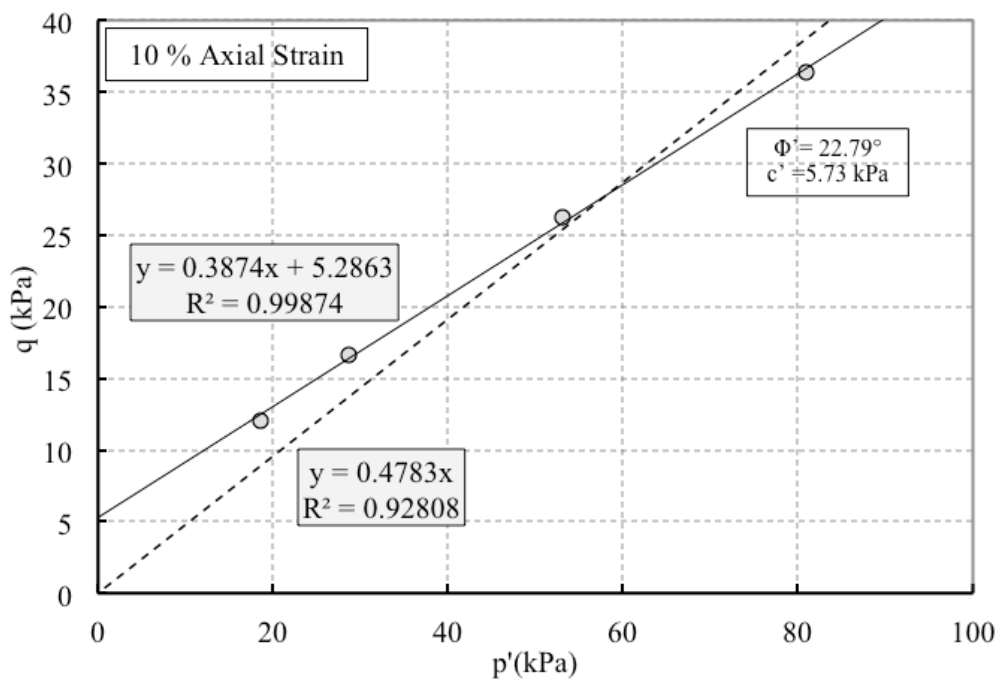


Figure C.21: Effective shear strength parameters determination for TDA at 10% axial strain (CU triaxial test)

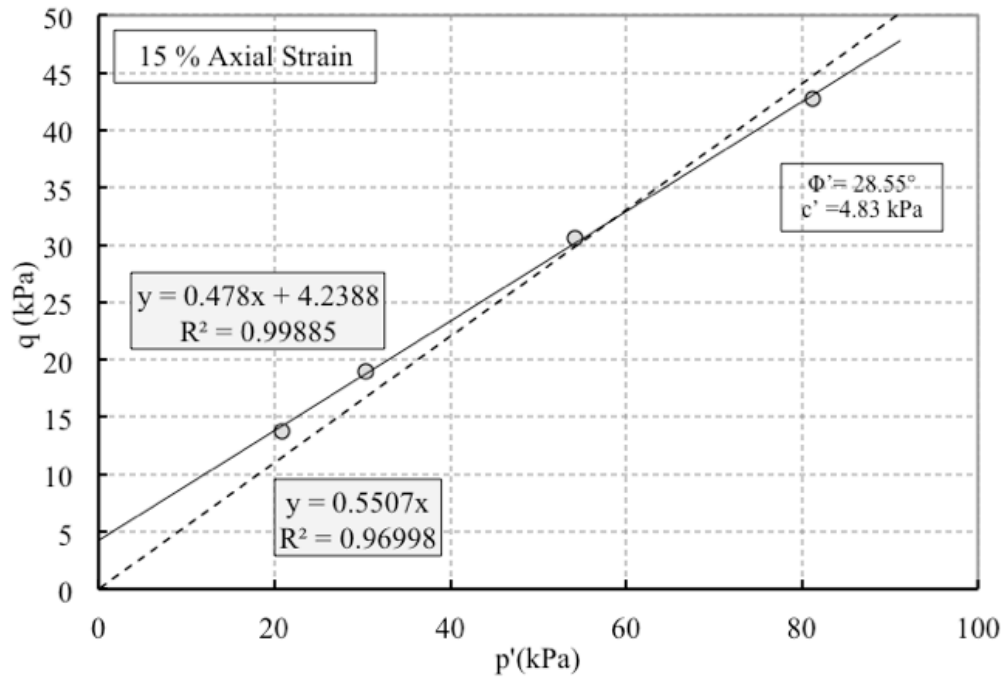


Figure C.22: Effective shear strength parameters determination for TDA at 15% axial strain (CU triaxial test)

C.5. Additional strain-rate effects not included in Chapter 4

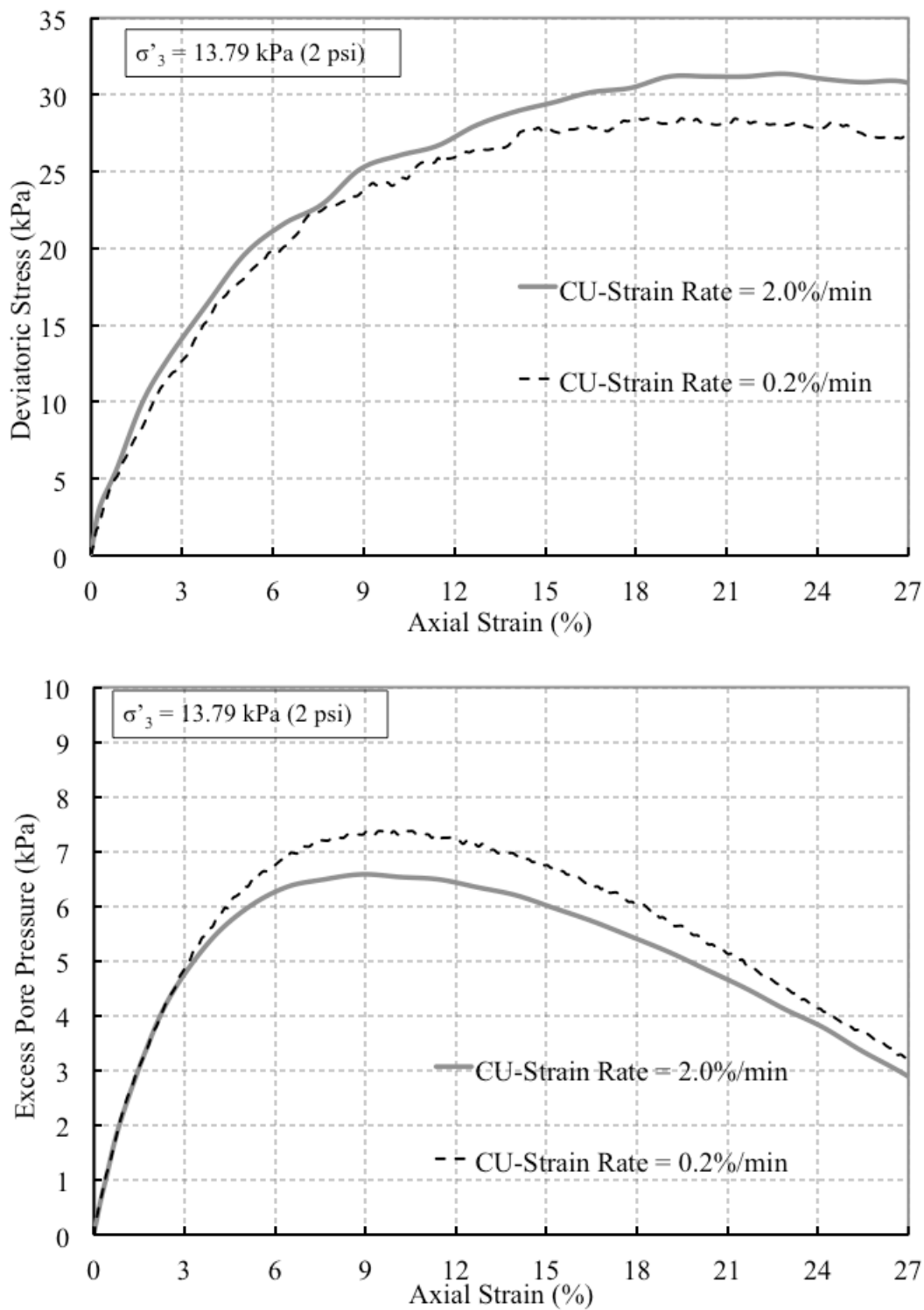


Figure C.23: Comparison for consolidated undrained test at two different strain rates at 13.79 kPa confining pressure

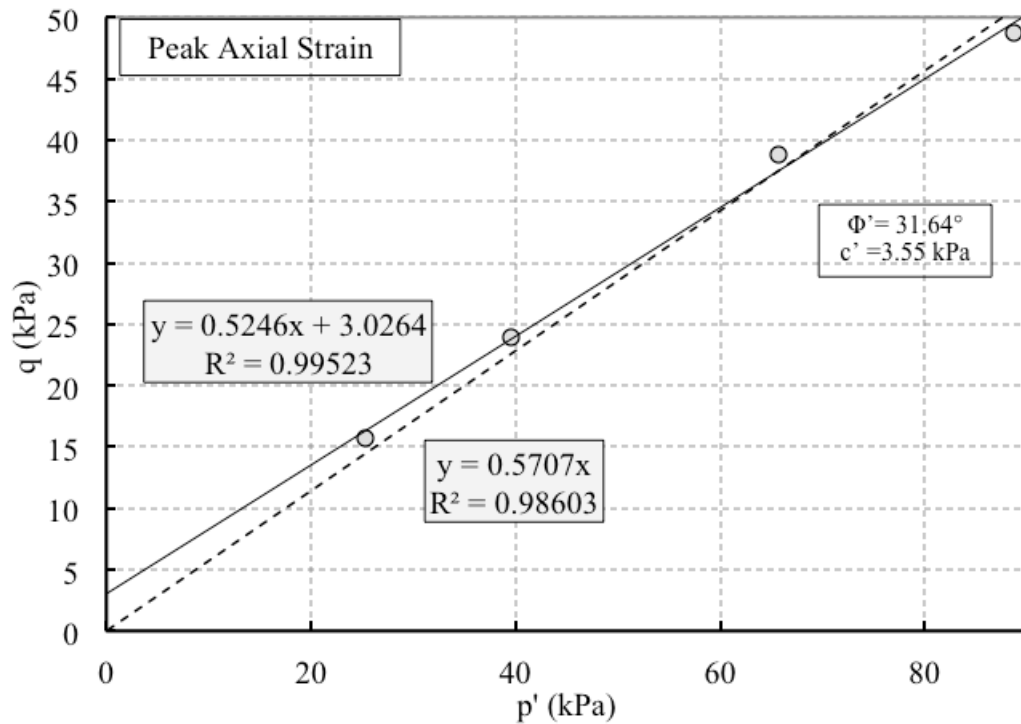


Figure C.24: shear strength parameters for CU-Triaxial test at 2.0%/min strain rate

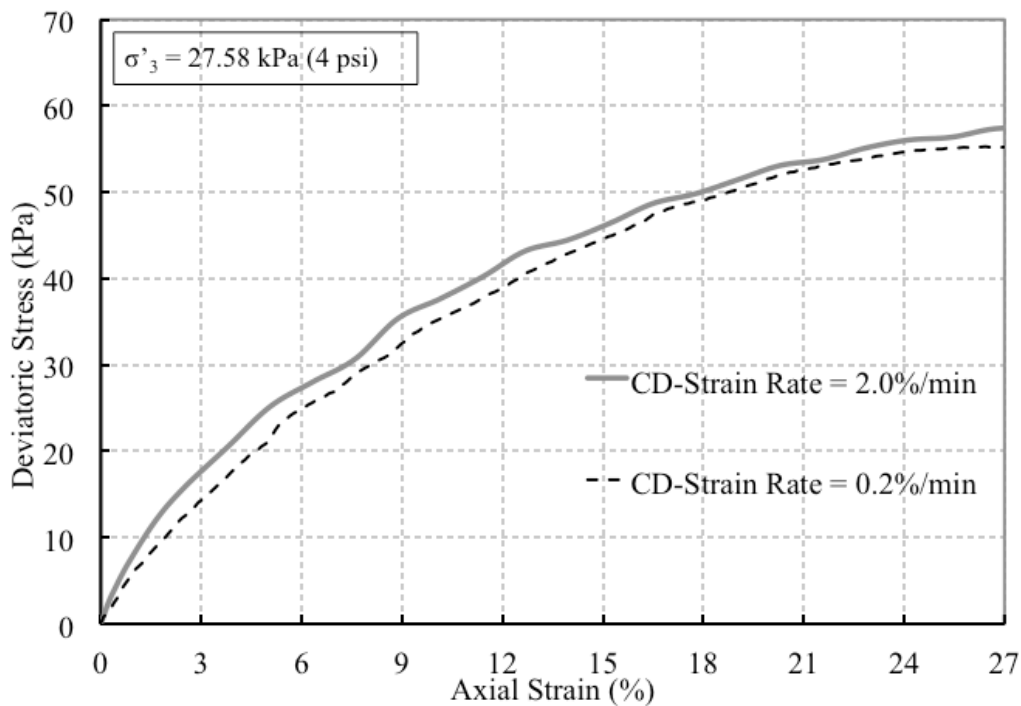


Figure C.25: Comparison for consolidated drained test at two different strain rates at 27.58 kPa confining pressure

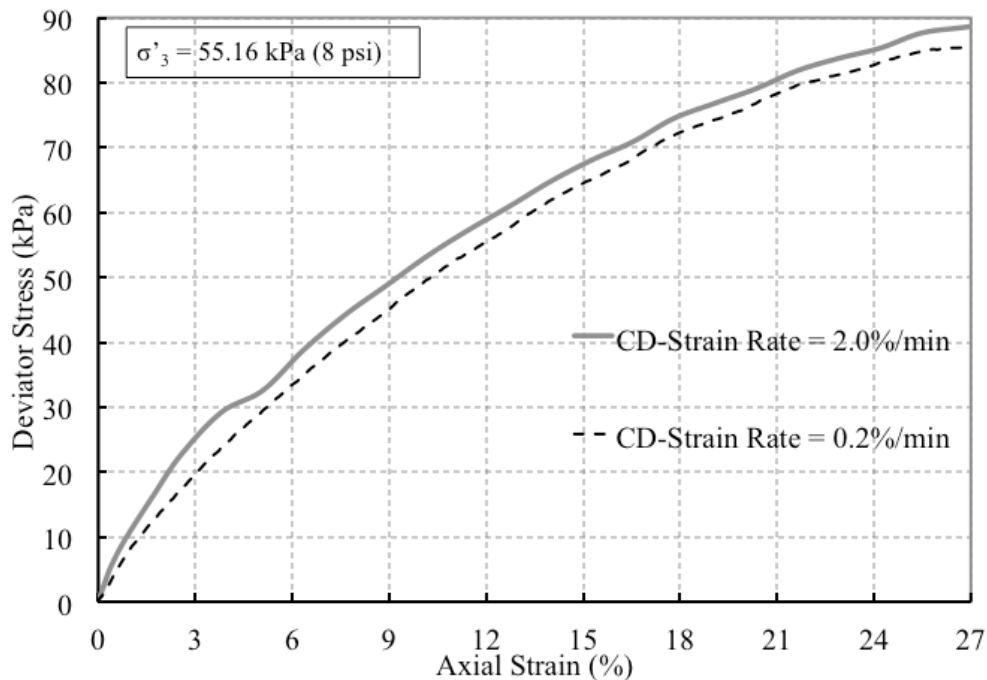


Figure C.26: Comparison for consolidated drained test at two different strain rates and 55.16 kPa confining pressure

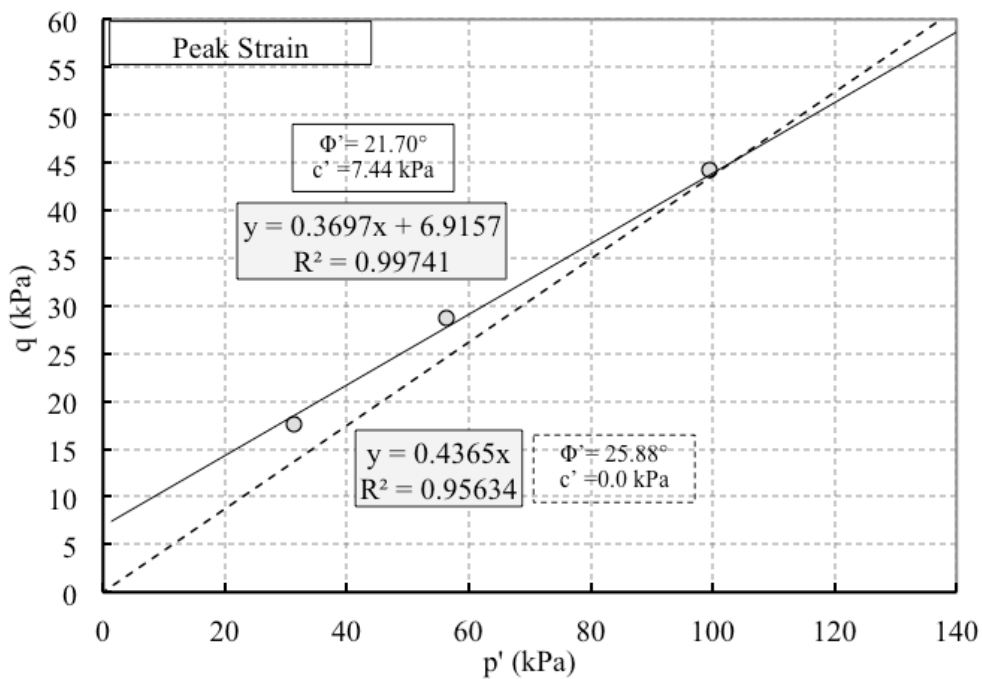


Figure C.27: Shear strength parameters determination for CD-Triaxial test at 2.0%/min strain rate

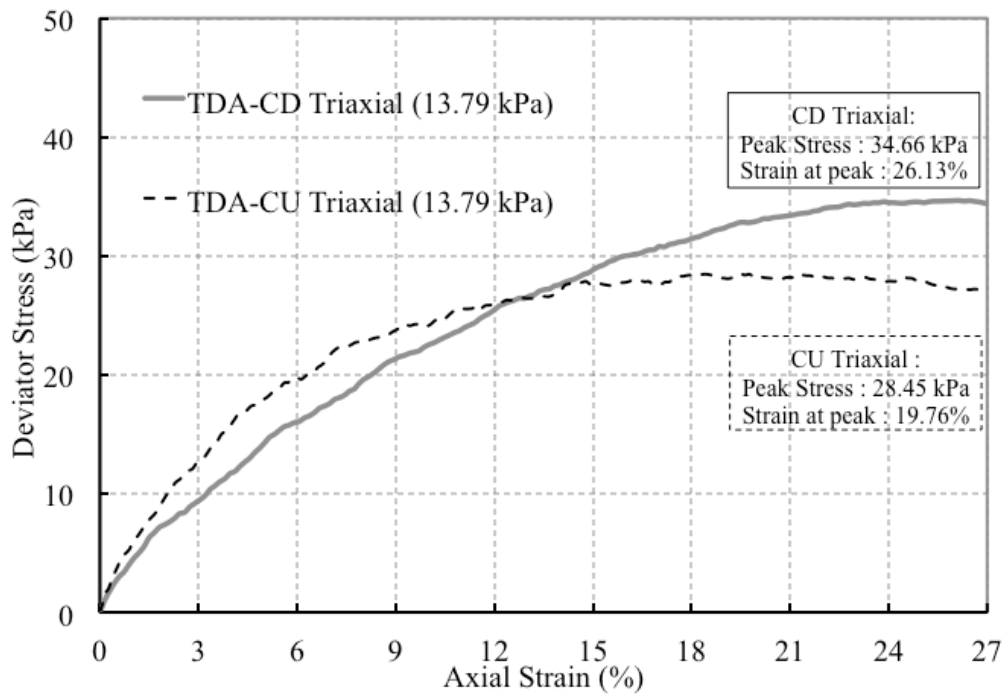


Figure C.28: Comparison between CD and CU triaxial tests at 0.2%/min strain rate (13.79 kPa confining pressure)

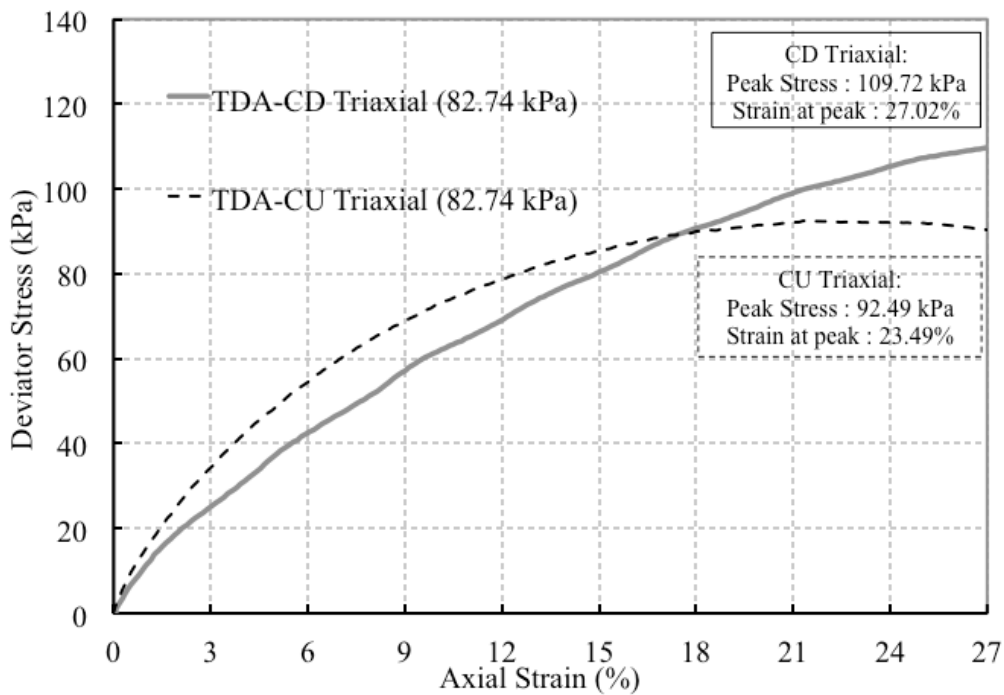


Figure C.29: Comparison between CD and CU triaxial tests at 0.2%/min strain rate (82.74 kPa confining pressure)

C.6. Simple shear test additional information not included in chapter 5

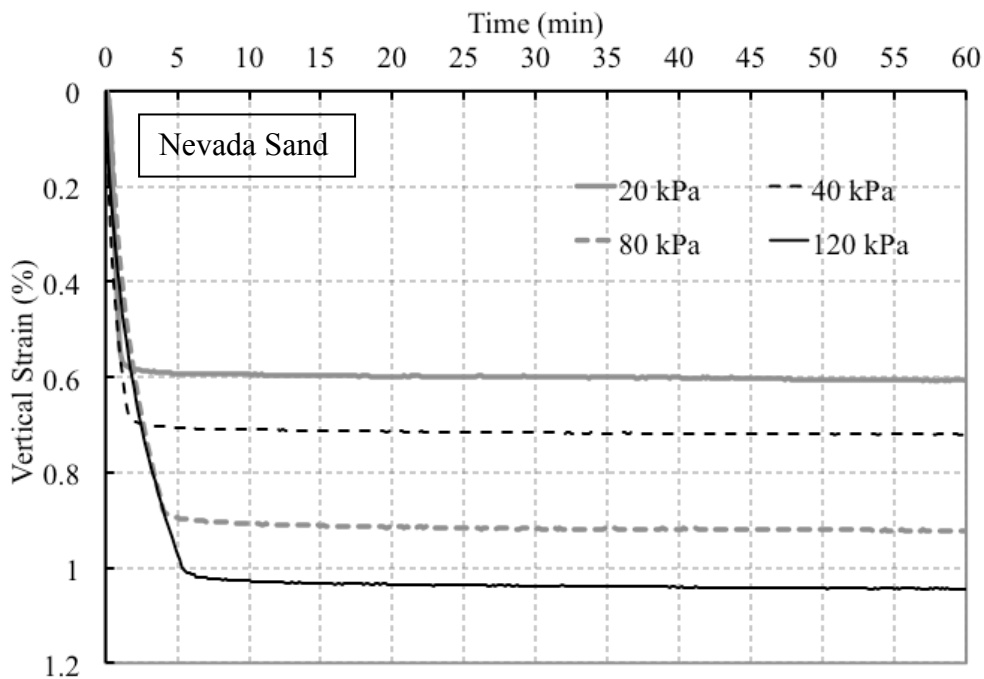


Figure C.30: Nevada sand deformation at different normal stresses during consolidation

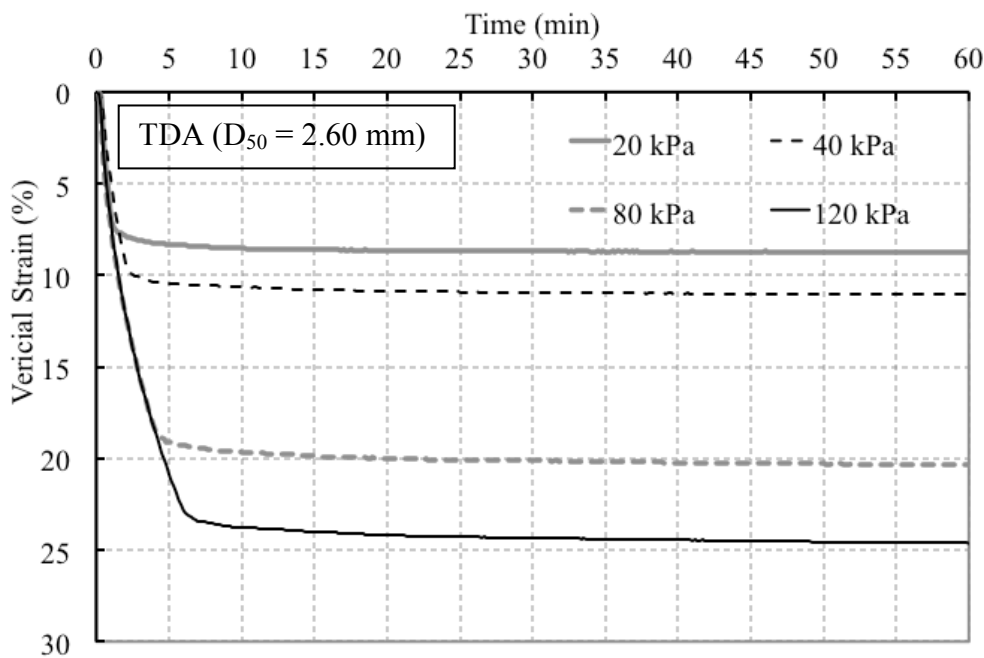


Figure C.31: TDA ($D_{50} = 2.60$ mm) deformation at different normal stresses during consolidation

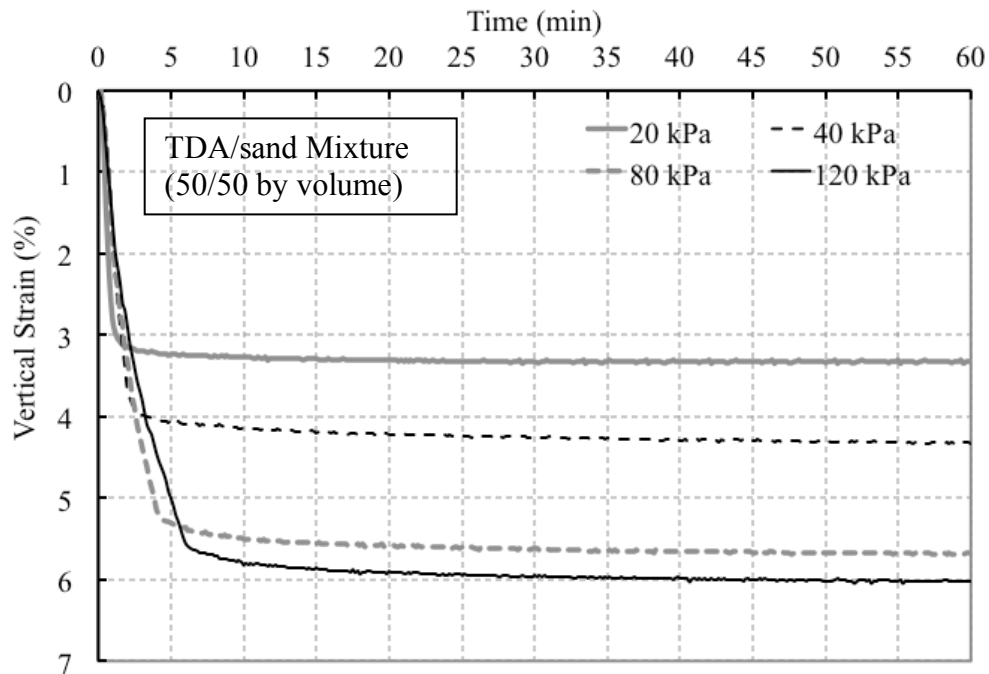


Figure C.32: TDA/sand mixture (50/50 by volume) deformation at different normal stresses during consolidation

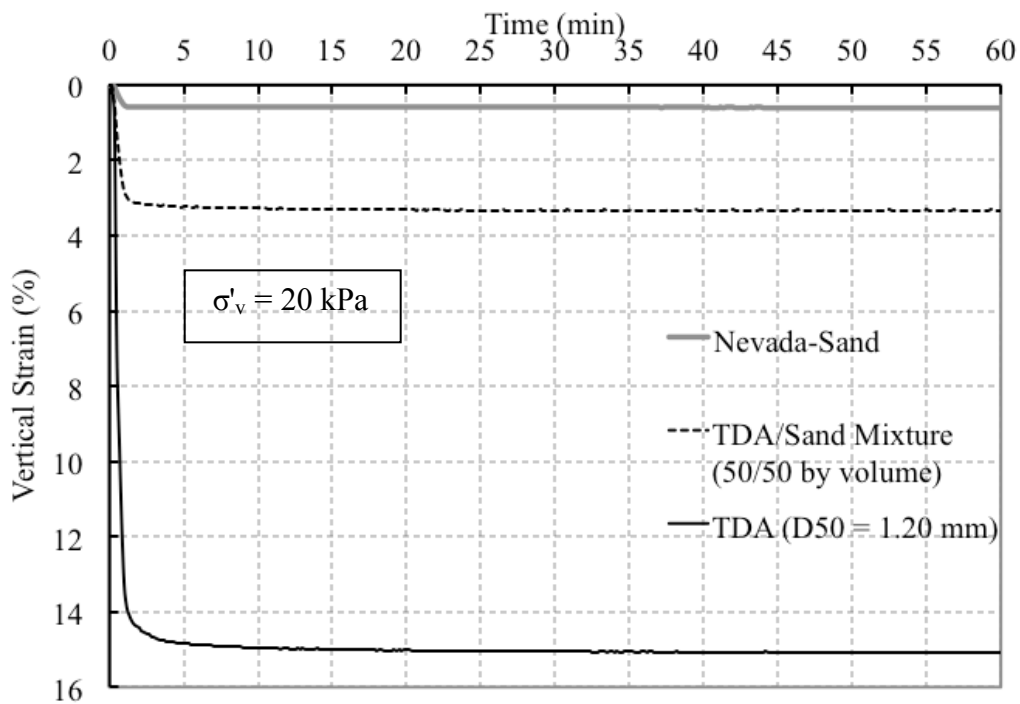


Figure C.33: Deformation of the different types of materials during consolidation at 20 kPa

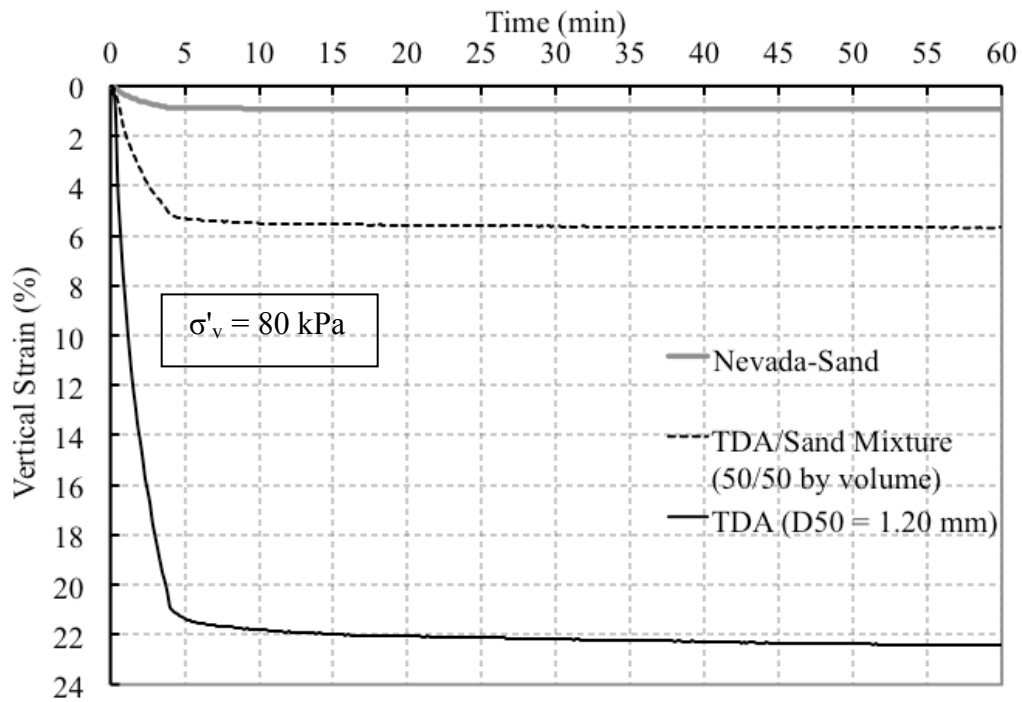


Figure C.34: Deformation of the different types of materials during consolidation at 80 kPa

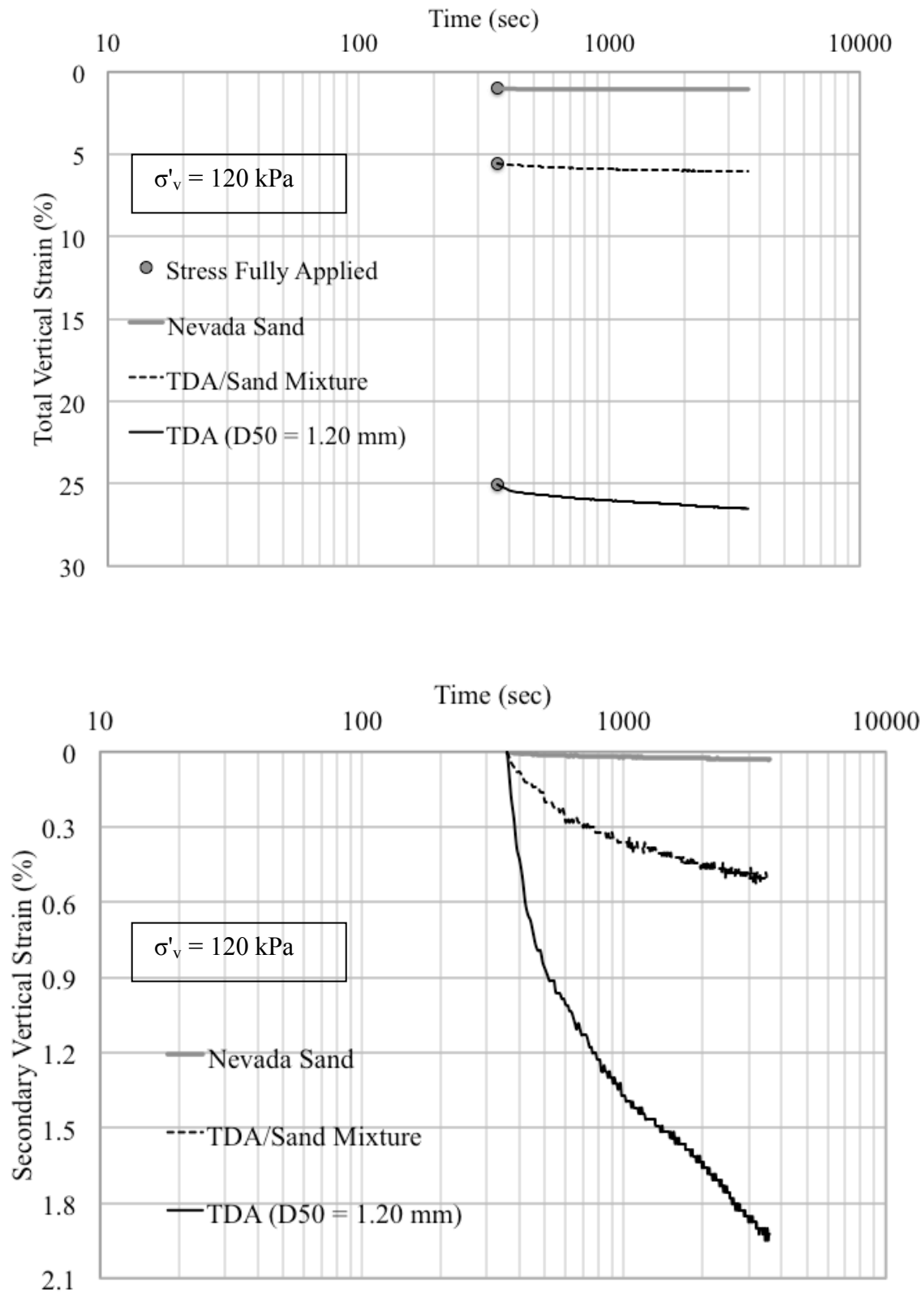


Figure C.35: Secondary deformation for the different types of materials during consolidation at 120 kPa

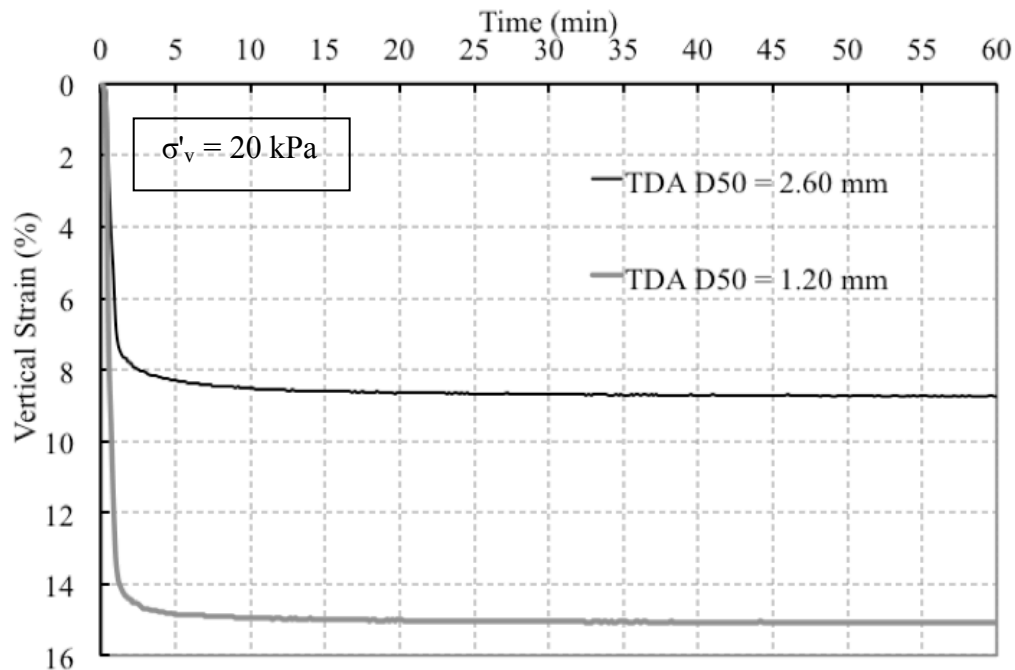


Figure C.36: Comparison of deformation during consolidation for both TDA particle size at 20 kPa

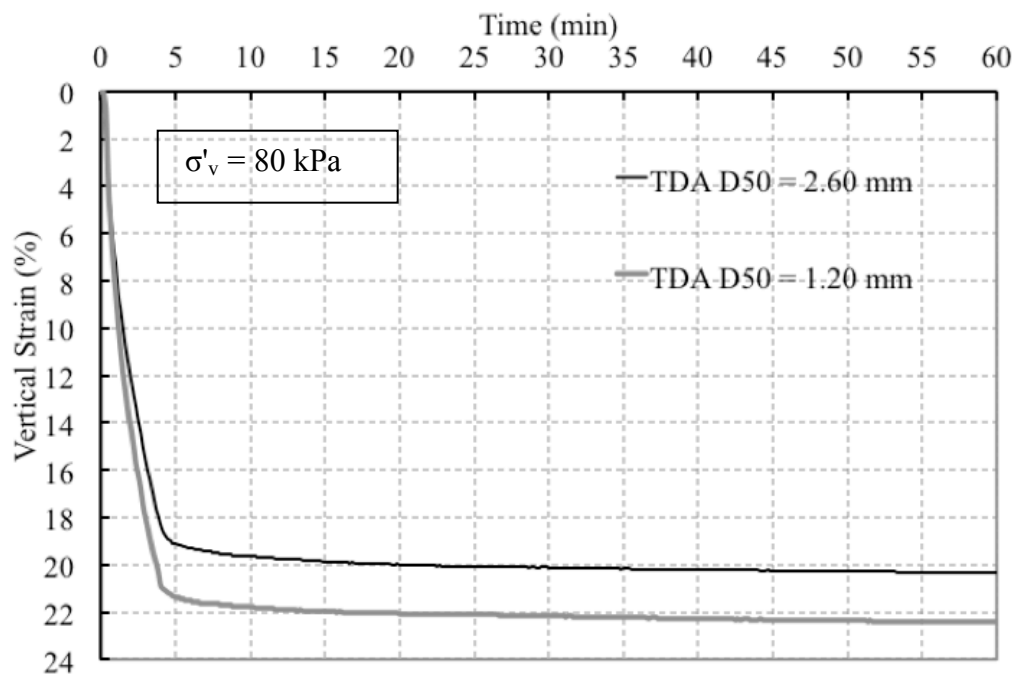


Figure C.37: Comparison of deformation during consolidation for both TDA particle size at 80 kPa

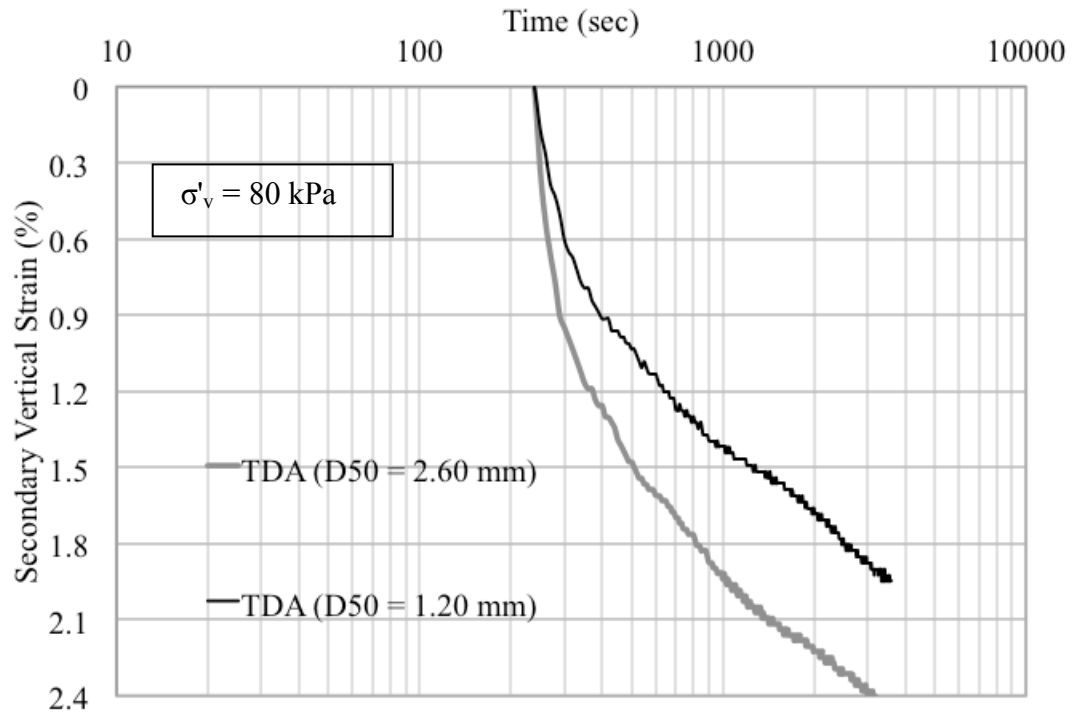


Figure C.38: Secondary deformation for both TDA particle size at 80 kPa

C.7. Simple shear test additional information (Shear phase)

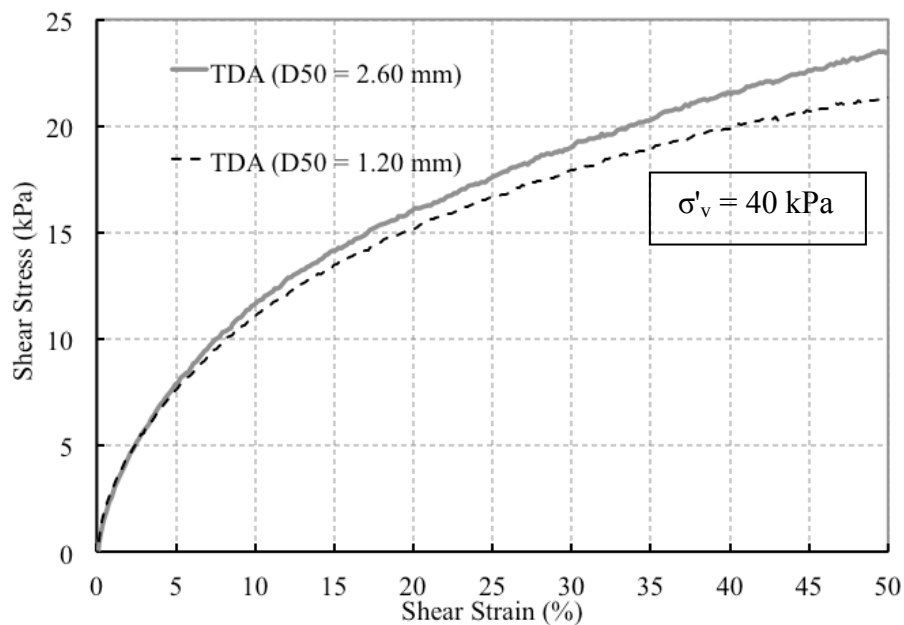


Figure C.39: Effect of TDA particle size in stress-strain behavior during simple shear at 40 kPa

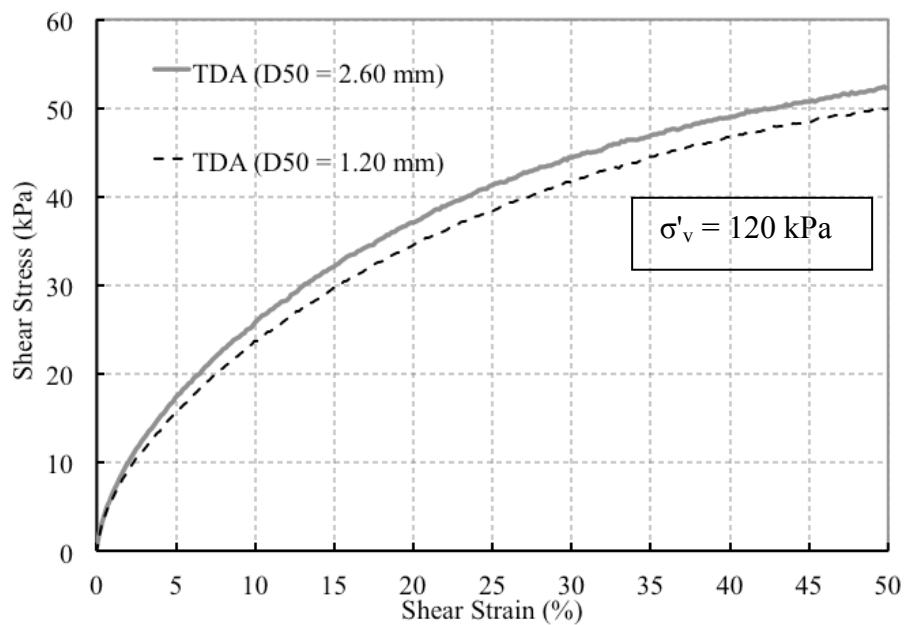


Figure C.40: Effect of TDA particle size in stress-strain behavior during simple shear at 120 kPa

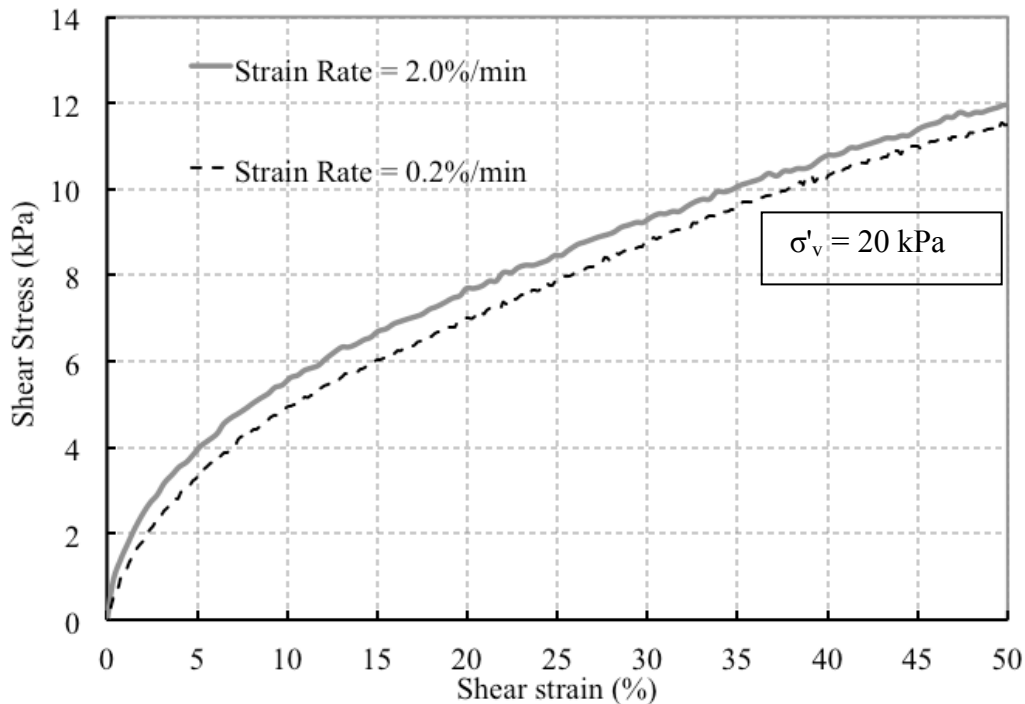


Figure C.41: Effect of strain-rate in TDA stress-strain behavior during simple shear at 20 kPa

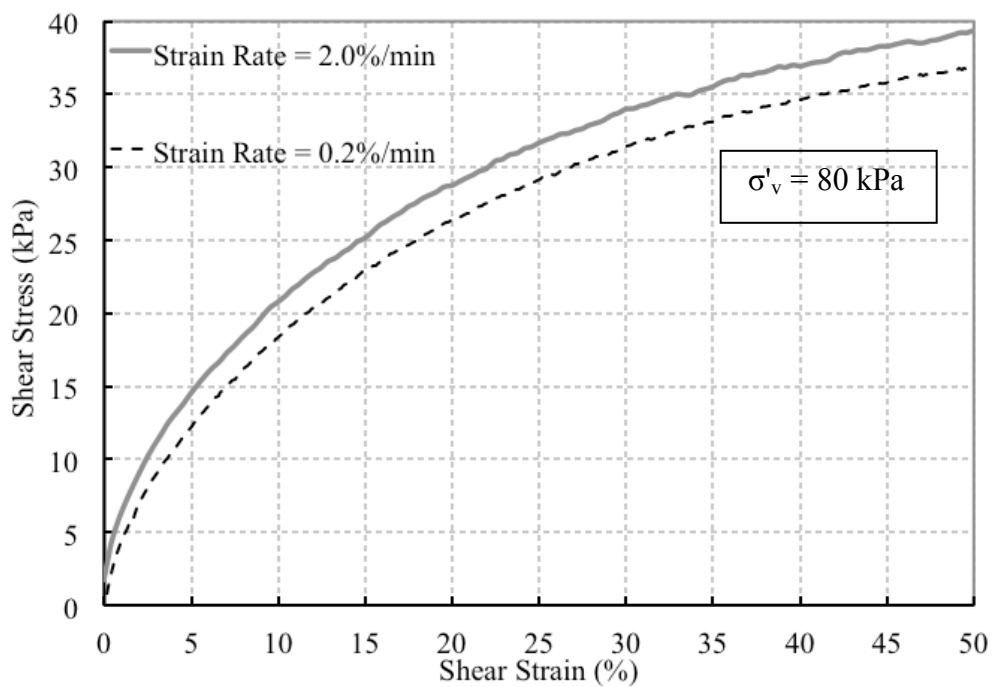


Figure C.42: Effect of strain-rate in TDA stress-strain behavior during simple shear at 80 kPa